Transactions of the ASME®

Technical Editor,
H. L. JULIEN (1998)
Associate Technical Editors
Advanced Energy Systems
M. J. MORAN (1996)
Fuels and Combustion Technologies
D. W. PACER (1994)
Gas Turbine
E. M. GREITZER (1994)
R. KIELB (1996)
S. SAMUELSEN (1996)
Internal Combustion Engine
W. CHENG (1996)
Nuclear Engineering
H. H. CHUNG (1996)
Power
P. H. GILSON (1996)

BOARD ON COMMUNICATIONS
Chairman and Vice-President
R. D. ROCKE

Members-at-Large
T. BARLOW, T. DEAR, L. KEER,
J. KITTO, W. MORGAN, E. M. PATTON,
S. PATULSKI, R. E. REDER, R. SHAH,
A. VAN DER SLUYS, F. M. WHITE,
J. WHITEHEAD

OFFICERS OF THE ASME
President, J. H. FERNANDES
Exec. Director
D. L. BELDEN
Treasurer
R. A. BENNETT

PUBLISHING STAFF
Mng. Dir., Publ.
CHARLES W. BEARDSLEY
Managing Editor,
CORNELIA MONAHAN
Sr. Production Editor,
VALERIE WINTERS
Production Assistant,
MARISOL ANDINO

Transactions of the ASME, Journal of Engineering for Gas Turbines and Power (ISSN 0742-4795) is published quarterly (Jan., Apr., July, Oct.) for $130.00 per year by The American Society of Mechanical Engineers, 345 East 47th Street, New York, NY 10017. Second class postage paid at New York, NY and additional mailing offices. POSTMASTER: Send address changes to Transactions of the ASME, Journal of Engineering for Gas Turbines and Power, c/o THE AMERICAN SOCIETY OF MECHANICAL ENGINEERS, 22 Law Drive, Box 2300, Fairfield, NJ 07007-2300.
CHANGES OF ADDRESS must be received at Society headquarters seven weeks before they are to be effective. Please send old label and new address.
PRICES: To members, $40.00, annually: to nonmembers, $136.00.
Add $24.00 for postage to countries outside the United States and Canada.
STATEMENT from By-Laws. The Society shall not be responsible for statements or opinions advanced in papers or . . . printed in its publications (B 7.1, para. 3).
COPYRIGHT © 1994 by The American Society of Mechanical Engineers. Authorization to photocopy material for internal or personal use under circumstances not falling within the fair use provisions of the Copyright Act is granted by ASME to libraries and other users registered with the Copyright Clearance Center (CCC) Transactional Reporting Service provided that the base fee of $3.00 per article is paid directly to CCC, 27 Congress St., Salem, MA 01970. Request for special permission or bulk copying should be addressed to Reprints/Permission Department.
INDEXED by Applied Mechanics Reviews and Engineering Information, Inc.
Canadian Goods & Services Tax Registration #126148048

Journal of Engineering for Gas Turbines and Power

Published Quarterly by The American Society of Mechanical Engineers
VOLUME 116 • NUMBER 1 • JANUARY 1994

TECHNICAL PAPERS

1 A Novel High-Temperature Ejector-Topping Power Cycle
B. Z. Freedman and N. Lior

8 Engineering-Economic Optimization of a Fuel Cell Cogeneration Plant
Y. Matsumoto, R. Yokoyama, and K. Ito

15 First- and Second-Law Analysis of Steam-Turbine Cogeneration Systems
M. A. Habib

20 CTCC Cogeneration Systems and Steam Supply Availability: An Investigation of Dynamic Availability
J. M. Franceschi

26 The Modular High-Temperature Gas-Cooled Reactor: A Cost/Risk Competitive Nuclear Option
H. L. Gotschall

32 Optimal Sizing of a Gas Turbine Cogeneration Plant in Consideration of Its Operational Strategy
R. Yokoyama, K. Ito, and Y. Matsumoto

39 Evaluation of Brayton and Rankine Alternatives for Diesel Waste Heat Exploitation
J. B. Woodward

46 Modeling and Analysis of Gas Turbine Performance Deterioration (92-GT-395)
A. N. Lakshminarasimha, M. P. Boyce, and C. B. Meher-Homji

53 Performance and Emission Levels in Gas Turbine Plants (92-GT-220)
F. Bozza, R. Tuccillo, and G. Fontana

63 The Effectiveness of Heat Transfer From Flue Gases to Ammonia-Water Mixtures
I. Kuštrin and M. Tuma

68 Development of Gas Turbine Steam Injection Water Recovery (SIWR) System (92-GT-87)
H. B. Nguyen and A. den Otter

75 Infrared Signature Suppression for Marine Gas Turbines: Comparison of Sea Trial and Model Test Results for the DRES Ball IRSS System (92-GT-310)
A. M. Birk and D. VanDam

82 TEMPER—A Gas-Path Analysis Tool for Commercial Jet Engines (92-GT-315)
D. L. Doel

90 Integration of Turbo-Expander and Turbo-Ramjet Engines in Hypersonic Vehicles (92-GT-204)
B. Zellner, W. Sterr, and O. Herrmann

98 Flow Separation in Shock Wave Boundary Layer Interactions (92-GT-205)
A. Hamed and A. Kumar

104 Air-Breathing Hypersonic Cruise: Prospects for Mach 4-7 Waverider Aircraft (92-GT-437)
I. M. Blankson

116 Numerical Simulation of the Flow Field Around Supersonic Air-Intakes (92-GT-206)
G. Freskos and O. Penenhoat

124 Thrust Vectoring/Reversing Tactics in Air-to-Air Combat (92-GT-362)
C. W. Boppe and R. P. Martorella

133 Transient Phenomena in Compressor Stations During Surge (92-GT-24)
K. K. Botros

143 Foothills Decompression/Recompression Facilities—Unique Power Recovery Application in Gas Pipelines (92-GT-26)
S. R. Kitt and B. D. Rose

152 Axial Inlet Conversion to a Centrifugal Compressor With Magnetic Bearings (92-GT-25)
T. Novecosky

156 Compressor Fault Identification From Overall Performance Data Based on Adaptive Stage Stacking (92-GT-28)
K. Mathioudakis and A. Stamatis

165 Optimizing Automated Gas Turbine Fault Detection Using Statistical Pattern Recognition (92-GT-29)
E. Loukis, K. Mathioudakis, and K. Papailiou

172 An Infrared Pyrometry System for Monitoring Gas Turbine Blades: Development of a Computer Model and Experimental Results (92-GT-80)
M. de Lucia and C. Lanfranchi

178 Fault Signatures Obtained From Fault Implant Tests on an F404 Engine (92-GT-82)
R. W. Eustace, B. A. Woodyatt, G. L. Merrington, and A. Runacres

(Contents Continued on page 19)

Downloaded 03 Jun 2010 to 171.66.16.159. Redistribution subject to ASME license or copyright; see http://www.asme.org/terms/Terms_Use.cfm

Contents (Continued)

184 The Effect of Compressor Rotor Tip Crops on Turboshaft Engine Performance (92-GT-83)
P. C. Frith

190 Tools for Diagnosing Case Deflections and Alignment on a Power Utility Combustion Turbine (92-GT-179)
H. R. Simmons, A. J. Smalley, R. W. Frischmuth, G. Lapini, and G. Robinson

198 Fatigue Life Estimation Procedure for a Turbine Blade Under Transient Loads (92-GT-78)
N. S. Vyas and J. S. Rao

207 Analysis of General Electric Model 7001 First-Stage Nozzle Cracking (92-GT-311)
H. L. Bernstein, R. C. McClung, T. R. Sharron, and J. M. Allen

217 Structural Evaluation and Testing of Swept Compressor Rotor
S. Aksoy, B. Mitlin, and H. Borowy

223 Detonation-Wave Technique for On-Load Deposit Removal From Surfaces Exposed to Fouling: Part I—Experimental Investigation and Development of the Method
K. Hanjalić and I. Smajević

231 Detonation-Wave Technique for On-Load Deposit Removal From Surfaces Exposed to Fouling: Part II—Full-Scale Application
K. Hanjalić and I. Smajević

237 Powder Metallurgy Repair of Turbine Components (92-GT-312)
K. A. Ellison, P. Lowden, and J. Liburdi

243 A High-Speed Capacitance-Based System for Gaging Turbomachinery Blading Radius During the Tip Grind Process (92-GT-365)
A. G. Sheard, G. C. Westerman, B. Killeen, and M. Fitzpatrick

250 The Evolutions of Thermal Barrier Coatings in Gas Turbine Engine Applications (92-GT-203)
S. M. Meier and D. K. Gupta

258 Microstructural Investigations of Plasma-Sprayed Yttria Partially Stabilized Zirconia TBC (In Relation to Thermomechanical Resistance and High-Temperature Oxidation Mechanisms) (92-GT-317)
S. Alpérine and L. Lelait

266 Thermal Fracture of Multilayer Ceramic Thermal Barrier Coatings (92-GT-318)
Y. R. Takeuchi and K. Kokini

272 Thermal Barrier Coatings on Turbine Blades by Plasma Spraying With Improved Cooling (92-GT-319)
T. Cosack, L. Pawlowski, S. Schneiderbanger, and S. Sturlese

ANNOUNCEMENTS

38 Change of address form for subscribers

Inside back cover Information for authors

Downloaded 03 Jun 2010 to 171.66.16.159. Redistribution subject to ASME license or copyright; see http://www.asme.org/terms/Terms_Use.cfm

A Novel High-Temperature Ejector-Topping Power Cycle

B. Z. Freedman[1]

N. Lior

Department of Mechanical Engineering and Applied Mechanics, University of Pennsylvania, Philadelphia, PA 19104-6315

A novel, patented topping power cycle is described that takes its energy from a very high-temperature heat source and in which the temperature of the heat sink is still high enough to operate another, conventional power cycle. The top temperature heat source is used to evaporate a low saturation pressure liquid, which serves as the driving fluid for compressing the secondary fluid in an ejector. Due to the inherently simple construction of ejectors, they are well suited for operation at temperatures higher than those that can be used with gas turbines. The gases exiting from the ejector transfer heat to the lower temperature cycle, and are separated by condensing the primary fluid. The secondary gas is then used to drive a turbine. For a system using sodium as the primary fluid and helium as the secondary fluid, and using a bottoming Rankine steam cycle, the overall thermal efficiency can be at least 11 percent better than that of conventional steam Rankine cycles.

1 Introduction

To increase thermal power generation efficiency, there is a continuing effort to increase the cycle's top temperature. While the temperature of combustion is in excess of 1700°C, most of the power generated in the world is by steam Rankine cycles where the maximal steam temperature is about 560°C (1050°F) (Babcock and Wilcox, 1978), and gas turbines operate up to about 1200°C (2200°F). These temperature limitations are incurred due to the combined effects of temperature, pressure, and dynamic forces on the cost and life of the plant. The critical components are the turbine blades and bearings, and the superheater piping in steam cycles.

Another problem that limits the use of higher temperature (when coal is the fuel) in present-day power plants is ash deposition. The temperature in the superheater must be low enough so that the ash entrained by the burned gas will stay solid and would not stick to the tubes. On the other hand, at temperatures higher than those that can be used in current steam plants, above 870°C (1600°F) (Babcock and Wilcox, 1978) the molten ash has a low enough viscosity to flow off the tubes without accumulating. This phenomenon is indeed used in slag-tap and cyclone type furnaces to remove a part of the ash from the flue gases. Parts of such furnace walls, which are water cooled, are kept hot enough so that the ash deposited on them flows down into a slag tank. These types of boilers discharge less ash to the plant environment and need smaller ash separation equipment. If the temperature of the superheater convection tube-bank could also be high enough, the flue gases will be even cleaner and perhaps no particle emission control equipment would be needed.

The high combustion temperatures in regular or cyclone furnaces [in some cases over 1700°C (3000°F)] require a large and costly radiant space for cooling the burned gases to thermomechanically acceptable levels.

In summary, it is highly desirable to operate at higher temperatures that not only will improve efficiency but will also reduce the size and cost of furnaces and will help solve the problem of controlling flue gas ashes. Construction materials are available today, and better ones are continuously becoming available, which are sufficiently durable for extended periods of time at the higher temperatures required, if operated under low stress. Unfortunately, the high steam pressures in modern Rankine plants, which can reach 24 MPa (3500 psia), limit the possibility of raising the boiler temperature considerably. Blade, bearing, and dynamic problems also limit gas turbine operating temperatures.

Topping Rankine cycles were developed (but not on a commercial scale), which allow the use of high-temperature boilers at relatively low pressures. The topping cycle fluid (such as mercury) has a vapor pressure much lower than that of water, and can thus be boiled at temperatures closer to that of combustion (about 1500 K) but at pressures much lower than that of water. The vapor expands in a turbine and then condenses while transferring its heat to the water in the lower temperature Rankine cycle. The efficiency of such topping cycles is potentially indeed higher than that of conventional nontopping cycles, but the topping cycles still require a very high-temperature turbine, which is not available.

The novel cycle described here (Fig. 1) and patented (Freedman, 1989) is also a topping one, but instead of expanding the very hot gases in a turbine, it uses them to compress another gas in an ejector. Most noteworthy, the combustion gases, which are too hot to be used in a turbine, are cooled thereby to a level acceptable for use in present day turbines by a process that produces compression work of another gas. From the Second-Law viewpoint, the straight cooling of combustion gases from the combustion temperature to that acceptable for turbine operation, as practiced in conventional boilers, destroys completely the exergy contained between these two tem-

[1]Current address: Hoshaia, D. N. Nazareth Illit 17915, Israel.

Contributed by the Advanced Energy Systems Division for publication in the JOURNAL OF ENGINEERING FOR GAS TURBINES AND POWER. Manuscript received by the Advanced Energy Systems Division October 21, 1991; revision received June 22, 1992. Associate Technical Editor: M. J. Moran.

Copyright © 1994 by ASME
Downloaded 02 Jun 2010 to 171.66.16.122. Redistribution subject to ASME license or copyright; see http://www.asme.org/terms/Terms_Use.cfm

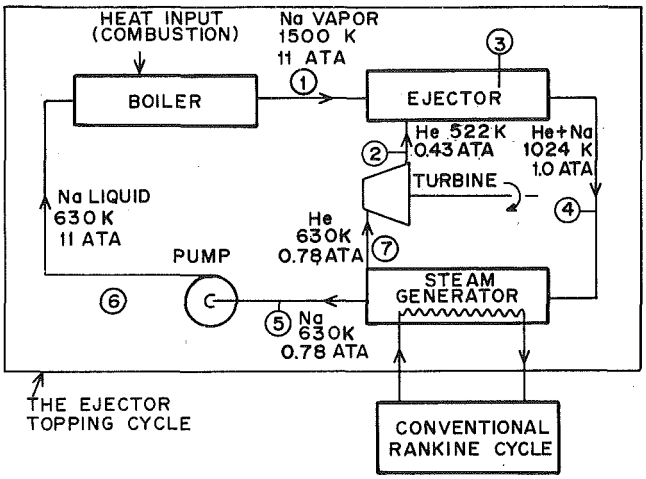


Fig. 1 Flow diagram of a high-temperature ejector-topping cycle

peratures. Here we accomplish the same cooling with concomitant production of useful work, clearly an important exergetic improvement. The ejector, as opposed to turbines, can operate at very high temperatures because of its inherently simple construction and absence of moving parts, which result in very low mechanical stresses and high reliability.

Although ejectors have relatively low efficiencies, the ejector-based topping cycles may have an overall higher efficiency than that of the above-described current turbine-based topping cycles, because of two major advantages: (1) The ejector can tolerate higher temperatures than a turbine can, and (2) it could use working fluids that have thermophysical properties superior to those that can be used in turbine topping cycles.

In the following, some aspects of the proposed system are discussed and an illustrative example is analyzed. The fluids chosen in this example were helium (the secondary fluid) and sodium (as the primary fluid). It is believed that helium is a good choice as a turbine fluid because of its low molecular weight and its high specific heat ratio, although it is harder to compress in the ejector. Sodium was chosen because there is experience in using it in high-temperature energy systems, and its thermophysical properties seem to be more promising than those of other candidate materials. It is possible that other working fluid pairs are better, and a thorough thermoeconomic selection study is desirable.

2 The Ejector

2.1 Introduction. The ejector uses energy from the sodium vapor to compress the helium from the pressure at the turbine outlet on back to the pressure of the turbine inlet (Fig. 1). In addition, it also supplies the pressure needed to overcome the pressure drop in the heating side of the steam generator. The compression is done by direct momentum exchange between the helium and the sodium through mixing and shear forces. Some important features of the ejector in the proposed system are described below. More information about ejectors in general can be found in Bonnington and King (1972), Bonnington and Hemmings (1976), and ASHRAE (1988).

2.2 Pressures. The mixing takes place in a convergent mixing section where the helium enters at subsonic velocity and the sodium at supersonic velocity. The mixing is done at a pressure that is lower than the pressure at the turbine outlet, and kept constant during the mixing.[2] There is an optimal mixing pressure for each situation that can be calculated using basic ejector theory. The pressure of the sodium vapor is reduced to the mixing pressure, which may be 30 times lower, by expanding the sodium vapor in a supersonic nozzle. After the mixing, the gas mixture is also supersonic and is compressed and slowed down, first by shock waves in a supersonic diffuser and then by expansion in a subsonic diffuser.

Increasing the pressure and temperature of the sodium increases the compression of the helium. The compression ratio of the ejector, i.e., the ratio of the helium pressures after and before the compression, is determined in an overall system analysis, and will be discussed below.

2.3 Condensation Processes. Sodium condensation may occur in the supersonic nozzle where its temperature may drop below the saturation pressure. This condensation will not be completed because of the tendency of the high-velocity gases to delay the condensation and to leave the vapor in a supercooled state (determining the fraction that does condense may need experimentation). If the amount of sodium condensing is too large, the heat released in the process may choke the flow and the ejector will not be able to compress the helium. If, on the other hand, only a small fraction of the sodium will condense, the ejector performance may even be slightly improved (ASHRAE, 1988). Condensation may also occur near the ejector outlet. In either case, this problem can be taken into consideration in the analysis, and averted to large extent in practice (say, by causing condensation to take place as near to the ejector outlet as possible).

2.4 Configuration. Many configurations of the ejector are possible, including the cylindrical and ring shapes shown in Fig. 2. Each of them contains the four basic elements: mixing section, supersonic nozzle(s), supersonic diffuser, and subsonic diffuser. The flow in the ejector can be axial or axial with rotation around the axis—"cyclone type." The cylindrical axial flow ejector is the only type that is well known and has a large theoretical and empirical data base. Cylindrical cyclone-type ejectors were described in the literature but their theoretical treatment is much more complicated and empirical data are scarce.

2.5 Ejector Computation. Exact computation of even the simplest kind of ejector needs sophisticated computer codes, which must be augmented by empirical correlations when condensation occurs during the process (cf. Mikkelson and Addy, 1974; VKI, 1975; Ortwerth, 1978; ESDU, 1986). In the analysis performed here, and based on the well-validated approaches and empirical data described in the above-mentioned references, the foundation was a one-dimensional inviscid approximation of adiabatic ideal gas flow. State-of-the-art empirical correction coefficients were used to obtain more realistic re-

[2]There are ejectors in which the pressure is not constant during the mixing.

Nomenclature

A = area
C_p = specific heat at constant pressure
C_v = specific heat at constant volume
H = enthalpy
k = specific heat ratio = C_p/C_v
m = mass flow rate
m_i = mass of species i
M = Mach number
P = pressure
T = temperature
V = volume
W = molecular weight
W_t = turbine work output
α = compressibility
ΔH = enthalpy difference
χ = molar mass ratio

Subscripts

a = air for combustion
g = gas
o = stagnation
tot = total

Downloaded 02 Jun 2010 to 171.66.16.122. Redistribution subject to ASME license or copyright; see http://www.asme.org/terms/Terms_Use.cfm

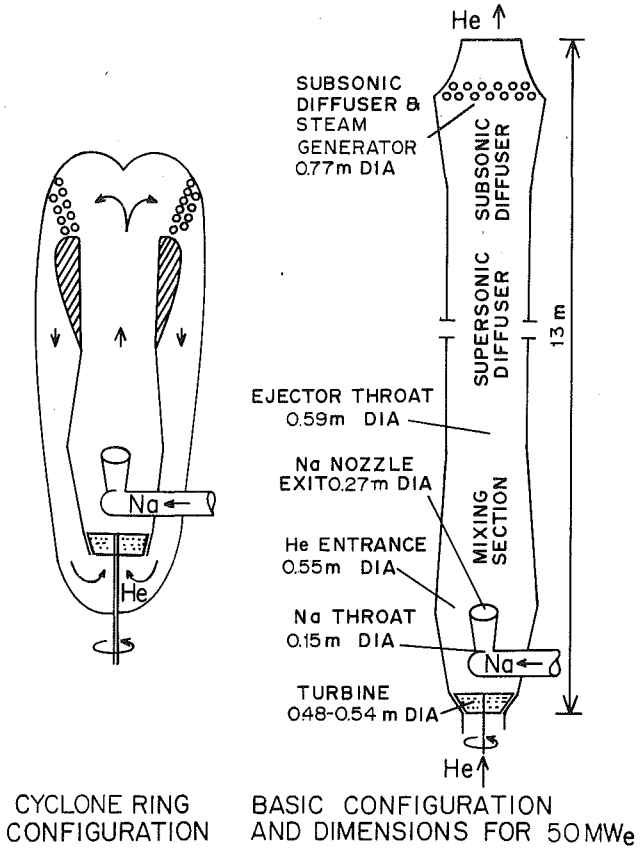


Fig. 2 Two ejector configurations

sults. The computer program developed solves a conventional model of supersonic constant pressure ejectors, which uses the laws of conservation of mass, momentum, and energy together with one-dimensional gas dynamic relationships between the flow parameters before and after a normal shock wave.

The following computational procedure was followed: (1) The parameters for the primary and secondary flows at the entrance are chosen, and the momentum of the flows is calculated, (2) it is assumed that there exists a downstream section in which the flow is totally mixed and has uniform properties, consistent with the assumption of a constant pressure duct, and the momentum there is computed by using the momentum conservation equation, (3) the temperature and mass flow rate of the mixed flow are computed using the conservation equations of mass and energy, (4) the pressure and velocity of the mixed flow are then computed, (5) if the mixed flow is supersonic, it is assumed that it decelerates through a normal shock wave and its exit pressure is thus found, (6) the pressure is then reduced by 25 percent to account for deviations from ideal ejector theory (see more below), checks are made to ensure that the entropy has not increased, and this whole procedure is repeated by systematic corrections in the inlet parameters until the exit pressure equals the desired one.

As stated above, a conservative empirical value of 25 percent stagnation pressure loss due to friction inside the ejector that is not accounted for by the theory was employed in the program. Condensation effects in the supersonic nozzle are assumed to reduce the mass of helium that can be compressed by 5 percent from the mass computed by the program.

The vapor pressure of the sodium needs to be known for calculating the equilibrium state of the mixture at the ejector outlet. This is given by Eq. (1) taken from Fink and Leibovitz (1981):

$$\ln P = 18.832 - 13113/T - (1.0948)\ln T + (1.977)10^{-4}T \quad (1)$$

where P = vapor pressure of the sodium, ATA, and T = temperature, K.

The total pressure P_{tot} is the sum of the partial pressures; according to Dalton's law it is related to the molar mass ratio by

$$\chi = \frac{m_{Na}}{m_{He}} = \left(\frac{P_{Na}}{P_{tot} - P_{Na}}\right)\frac{W_{Na}}{W_{He}}. \quad (2)$$

In cases where the mixture temperature is below the dew point, the latent heat of evaporation of sodium and the average specific heat capacity of the mixture need to be known for determining the equilibrium state. The calculation is done by guessing an equilibrium temperature, and calculating the sodium concentration at this temperature and the amount of sodium that needed to be condensed to reach this concentration. A check is made then to find whether the heat added by condensation increased the mixture temperature to the guessed one, and the initial guess is corrected if needed.

3 The Steam Generator

The steam generator produces the steam needed for the lower-temperature conventional Rankine cycle by heat transfer from the mixture of sodium and helium emerging from the ejector in a process that condenses the sodium and cools the helium and the condensed sodium. The pressures and temperatures of the steam are those used in boilers, superheaters, reheaters, and economizers of conventional power plants. The heat transfer rates in the steam generator are much higher than in fuel-fired boilers and are higher even than those found in liquid sodium steam generators, thus reducing significantly the required heat transfer area needed. These and other features of the steam generator are discussed below in more detail.

On the steam side the pressure is high and the heat transfer rates are similar to those found in conventional boilers. The main difference is in the coefficient of heat transfer on the gas side. This side is a partial condenser, where a large fraction of the heat transfer is by condensation of the sodium: In the example calculated in Section 6 below it is 75 percent of the total heat. The condensation heat transfer coefficient between pure sodium and steam generator tubes is two orders of magnitude larger than the heat transfer coefficient between combustion gas and the tubes. When the sodium vapor is mixed with the helium, the heat transfer coefficient of the mixture is between that of helium and that of condensing sodium. As a result, in parts of the steam generator where the sodium concentration is not too low, the gas side resistance to heat transfer can be neglected. In the steam generator section where water is evaporated, the heat transfer rate is determined, therefore, mainly by the thermal conductivity of the tubes. In the steam generator region where the sodium concentration is low, the heat transfer coefficient is that of the high-speed helium, which is still 10 to 20 times higher than that of combustion gases in furnaces. These high velocities are possible because the low density of the helium makes it possible to reach higher velocities than can be reached by air for a similar pressure drop. A part of the heat is transferred by the condensed (liquid) sodium, which also has a very high convective heat transfer coefficient. It should be noted that at the same time the tube design and materials must be such as to resist erosion by the sodium droplets.

The tubes in the steam generator are free from the ash deposition and the associated lowering of the heat transfer coefficients, which take place in fuel-fired systems.

The selection of the temperature of the gas leaving the steam generator and entering the turbine (station 7 in Fig. 1) is determined primarily by the need to condense and thus separate all the sodium. Higher temperatures not only allow undesirable condensation of sodium in the turbine, but also transfer more

Downloaded 02 Jun 2010 to 171.66.16.122. Redistribution subject to ASME license or copyright; see http://www.asme.org/terms/Terms_Use.cfm

of the heat to the lower temperature Rankine cycle, and thus the overall system improvement, achieved by the topping cycle, is reduced.

It should be noted that the coexistence of sodium and water in the same heat exchanger (albeit separated by tube walls) requires special safety measures to prevent their direct contact. There is, however, significant experience with heat exchangers that use liquid sodium and water, particularly from the liquid metal fast breeder reactor programs in a number of countries, and both knowledge and safety are continuously being improved (Bliem et al., 1985).

Measures are needed to prevent sodium droplet entrainment by the helium before it enters the turbine. The droplets may damage the turbine and also increase the sodium concentration in the mixture passing through the turbine and compressed by the ejector, thus reducing the system efficiency. A two-step separation process is possible: first, cooling of the gas mixture to below the sodium dew point alongside with maximization of the contact between the mixture and the condensing liquid sodium, followed by inertial or electrostatic separation of the condensed sodium droplets from the mixture. The separation process produces, however, a pressure drop that would otherwise have been used to produce more power by the turbine, and thus a proper tradeoff between these two effects is needed. It may be noted that we have accounted for the incomplete sodium separation by assuming that 5 percent was not condensed (Section 6).

4 The Sodium Boiler

4.1 Furnace Features. The sodium is evaporated in a fossil fuel-fired furnace, which is operated at higher temperature than used for conventional steam boilers. To achieve the high temperature, combustion is proposed to be done in a cyclone furnace (although other furnaces are also possible), a small chamber in which a high-speed rotating air stream is used to burn the fuel in an almost adiabatic process. The air needed for the combustion is heated in a high-temperature air heater by exchanging heat with the burned gases leaving the furnace. The combustion temperature is determined by the temperature of the entering air, the quality of the fuel, the amount of excess air, and the amount of heat lost through the walls. Conventional cyclone furnaces operate at temperatures of about 2300°C, and can reach 3500°C and more if special high-temperature air heaters are used (Bliem et al., 1985).

It should be noted that operation at such temperatures tends to increase NO_x production, which could be controlled by catalytic methods for NO_x separation from the stack gas or by the use of advanced combustor concepts, such as the radiatively-conductively stabilized burner described by Tang et al. (1980, 1981). It should, however, be noted that the higher efficiency of the proposed system also results in a proportionally smaller quantity of fuel and combustion products, including CO_2.

The furnace walls are covered, on the fire side, by an insulating layer of molten ash, and its temperature is kept at the desired level by the boiling sodium on the other side. The hot gas leaving the cyclone chamber heats the main convection bank in which the sodium is evaporated. The combustion temperature, amount of excess air, temperatures of the burned gases entering the air heater and of the air leaving it, and other relevant parameters, can be determined from an overall heat balance, as shown in Section 6 below.

When compared to conventional fuel-fired steam boilers, the higher conductivity and the heat of evaporation of sodium, and the fact that the fraction of heat transferred in the boiling process is about 75 percent of the total heat exchanged for sodium and only about 50 percent for H_2O, it was found that the overall heat exchange area needed in the sodium furnace is ten to twenty times smaller than that needed to generate steam for the same amount of heat transferred (see Section 6 below). In addition, the specific heat of Na vapor is large (twice that of high temperature steam), and thus the Na mass flow rate is relatively small.

The lower pressure and density of the sodium vapor make the volume needed for its containment quite large. In summary, the sodium boiler is characterized by a small heat exchange area, low sodium mass flow rate, low pressure, high temperature, and high vapor volume.

4.2 Construction Materials. Even the newest metal alloys suffer from a relatively short operating life at these high temperatures, where creep has a very significant effect on reducing the allowable temperature and stress (cf. AGARD, 1966). Higher temperature operation can be attained by a combination of proper design and materials. An example of improved design is a fire-tube boiler in which the tensile loads on the hot surfaces of the tubes are replaced by compressive loads. Compressive yield strength is generally higher than tensile yield strength and the effect of creep is less significant. This can be accomplished by passing the hot combustion products through tubes that are immersed in liquid sodium. Based on knowledge of the properties of the high-temperature alloys that could be used, it is estimated that such a fire-tube boiler can operate at 1500 K (2240°F, which results in pressure of 1.08 MPa) for a number of years without failure (cf. AGARD, 1966).

Higher temperatures may be attained with nonmetals: graphite, ceramics, or composite materials. Graphite has excellent stability at high temperature and it does not creep. Its yield strength increases with the temperature and its value is approximately 5000 psi (33.3 MPa), high enough to be used for pressure tubes up to 10 MPa with reasonable wall thickness. Unfortunately, it is chemically attacked by the hot sodium and by oxygen. The only way it can be used is by isolating it from contact with the surrounding gases. Coating is a successful way to prevent oxidation of graphite at high temperatures (Hausner, 1966) and continuous improvements are being made in graphite coatings for uses such as re-entry vehicles and rocket nozzles. It might also be possible to isolate graphite tubes by metal alloy sheathes, which might retain isolation qualities despite the fact that they are plastic at those high temperatures.

Ceramic materials are continuously being improved for use in high-temperature energy systems, and impressive advances have been made in recent years (ASM, 1985). It seems reasonable that ceramic materials for the high-temperature, low-pressure boilers will be developed earlier than the materials for use in high-temperature turbines. There is a good chance that operation at 2000 K and higher would be possible in the near future by using new construction materials.

5 Pump and Turbine

The work required by the pump is very small compared to the work done by the turbine and it can be calculated using the compressibility (α) of sodium liquid. Knowing the compressibility and density of liquid sodium (6×10^{-3} K^{-1}, and 850 kg/m^3 at 600 K, respectively, Fink and Leibovitz, 1981) we can calculate the enthalpy difference of the liquid sodium before and after the pump, i.e., the work done by the pump assuming ideal isothermal compression:

$$\left(\frac{\partial H}{\partial P}\right)_T = V - T\left(\frac{\partial V}{\partial T}\right)_P = V(1 - T\alpha), \tag{3}$$

$$\Delta H = \int_{P1}^{P2} V(1 - T\alpha)dP = V(1 - T\alpha)(P_2 - P_1) = 0.42 \text{ kJ/kg}.$$

This is only about 0.1 percent of the work done by the turbine, as will be shown in the next section. Liquid sodium pumps, of several types, are described by Sittig (1956).

Downloaded 02 Jun 2010 to 171.66.16.122. Redistribution subject to ASME license or copyright; see http://www.asme.org/terms/Terms_Use.cfm

Table 1 Fluid parameters at the various stations in Fig. 1

	Fluid	T K	P MPa	W	k	m kg/s	M	A cm²
1	Na, gas	1500	0.108	23	1.5	1.0	0.2	28
2	He	522	0.043	4	1.67	0.340	0.7	123
3	He + Na,g	871	0.10	10	1.605	1.34	0.4	121
4	Na;g + Na,l + He	1024	0.10	10	1.605	1.34	0.4	266
5	Na,l	630	0.08	23	----	1.0	----	
6	Na,l	630	1.08	23	----	1.0	----	
7	He	630	0.08	4	1.67	0.340	0.4	105

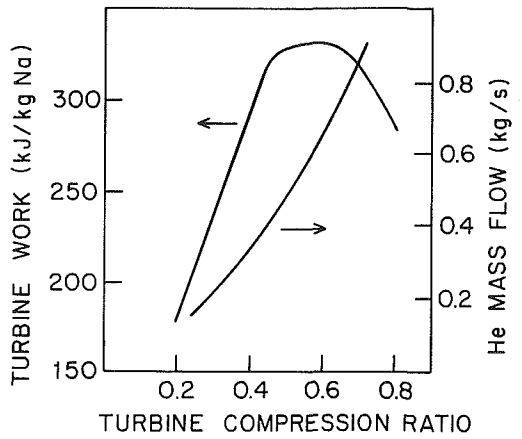


Fig. 3 Turbine work and helium mass flow rate as a function of ejector compression ratio for the example analyzed

Because the turbine is operated at a relatively low compression ratio, only a few stages will be needed along the flow direction and it thus should not be too large in that direction. The high specific volume requires, however, a relatively large cross-sectional area for the flow and hence a larger diameter.

6 Analysis of an Example

6.1 The Approach and Basic Assumptions. To provide quantitative performance predictions of this novel cycle, a full analysis of a conceptual system, using helium and sodium and producing 50 MWe, was performed employing for the ejector analysis the computer program described in section 2.5 above. The performance of the other components and of the entire system was calculated by employing mass and energy balances. The cycle and its main parameters are described in Fig. 1 and Table 1 (to simplify the description, the air preheater is not shown in Fig. 1). These describe a system that may be the closest to practical realization at this time, and the parameters have values that, although sometimes arbitrary, are used in the modeling of conventional systems. A conservative estimate of all losses was taken, and no optimization was performed yet. Consequently, it is quite likely that the real losses and the use of other combinations of parameters will yield better performance results. The results presented below were typically rounded to the nearest significant digit.

The first step in the analysis was to choose the compression ratio of the ejector. The compression ratio of the turbine is that of the ejector, minus the pressure drops in the steam generator and droplet separator. As can be seen from the results for this example shown in Fig. 3, a compression ratio of about 0.6 gives the maximal turbine work. Lower compression ratios require smaller mass flow rates of He (and thus result in smaller-size systems). We have chosen a compression ratio of 0.43, where the work output is reduced by only 3 percent from the maximal possible, but which allows a reduction of almost 50 percent in the helium mass flow rate from that needed for the maximal work output.

Table 2 Ejector parameters as computed by the computer program (entries marked with an asterisk are input parameters)

Parameters locations		m kg/s	Po MPa	P MPa	To K	T K	M	W	k	A cm²
Before mixing start	Na	1.0 *	1.08 *	0.029	1500 *	451	3.048	23. *	1.5 *	36.2
	He	0.380	0.043 *	0.029	522 *	448	0.7	4. *	1.67 *	135.
At ejector outlet		1.38	0.1 *		871			10	1.605	
At sodium nozzle throat		1.0	1.08		1500		1.0	23.	1.5	9.6
At ejector throat		1.38	0.153	0.029	871		1.688	10	1.605	135

Using this information and the ejector-design computer program described in Section 2.5, the results shown in Table 2 were obtained. The sodium mass flow rate was chosen as 1 kg/s for simplicity.

The work done by the turbine, W_t, was computed by assuming isentropic expansion of an ideal gas. Gas turbines operating at similar pressure ratios attain isentropic efficiencies of up to about 95 percent (cf. Hill and Peterson, 1965), but since the operating pressure in this cycle is lower than in conventional gas turbines, the isentropic turbine efficiency in this example was assumed to be 80 percent.

Pressure losses in the steam generator and sodium droplet separator were assumed to be 22 percent of the compression ratio generated by the ejector. The turbine expansion ratio will be, therefore, 0.55.

It was assumed that the fuel is high-quality coal with an HHV of 32,000 kJ/kg, burned with 15 percent excess air, that the combustion efficiency of the sodium boiler is conservatively 0.82 and that the heat losses through the furnace walls are about 3 percent (Babcock and Wilcox, 1978).

To effect complete evaporation of the sodium in the boiler, it was assumed that the temperature of the combustion products leaving the sodium boiler is 50 K higher than the boiling temperature in the boiler; in our example it will be, therefore, 1550 K.

The ejector for such topping cycles is rather large, and the heat loss through its exterior surface was thus evaluated. The average temperature on the ejector inner wall is 700 K and the temperature difference across the wall is, therefore, 400 K, about half of the temperature difference in conventional steam boilers. It was assumed conservatively that the heat loss per unit area was approximately 0.4 kW/m^2 (250 Btu/ft^2/hr), typical to conventional boilers (Babcock and Wilcox, 1978). Based on the dimensions shown in Fig. 2, the surface heat loss is of the order of 10 kW, negligible relative to the 50 MW produced.

Consistent with the conservative approach used in the evaluation of the proposed cycle, it was assumed that its bottoming Rankine cycle has state-of-the-art high efficiency, including a supercritical boiler with feedwater heating (all internal heat sources that can be used in the cycle are used regeneratively) and no reheat. While reheat, which is usually used in conventional Rankine systems, would decrease the amount of steam produced, the overall cycle efficiency would almost not change at all.

6.2 Properties. The specific heat of He is practically constant in the entire operating temperature range, so C_p = 5.2 kJ/kg°C and C_p/C_v = 1.67 were used (Reynolds and Perkins, 1977; Rohsenow and Hartnett, 1973). The average specific heat of the combustion products (with 5 percent moisture) at the high-temperature side of the boiler was taken as 1.46 kJ/kg K

Downloaded 02 Jun 2010 to 171.66.16.122. Redistribution subject to ASME license or copyright; see http://www.asme.org/terms/Terms_Use.cfm

Table 3 Main results of the sample system analyzed

Power, kW/(kgNa/s):	
heat supplied by the coal	5730
helium-turbine work output	238
bottoming Rankine cycle work output	2124
air preheat available from the stack gas	3380
Mass flow rates, (kg/s)/(kgNa/s):	
the combustion products	3.24
the combustion air	3.06
bottoming cycle steam	2.2
The temperature of the combustion products, K:	
entering the sodium boiler, T_{g1}	2300
leaving the sodium boiling section	1550
leaving the sodium sensible-heating section in the boiler, T_{g3}	1290
leaving the stack	420
The temperature of the combustion air, K:	
ambient	300
entering the Na boiler furnace	1110
The conditions of the bottoming Rankine cycle:	
feedwater inlet to steam generator	400 K
steam exit	810 K, 24 MPa

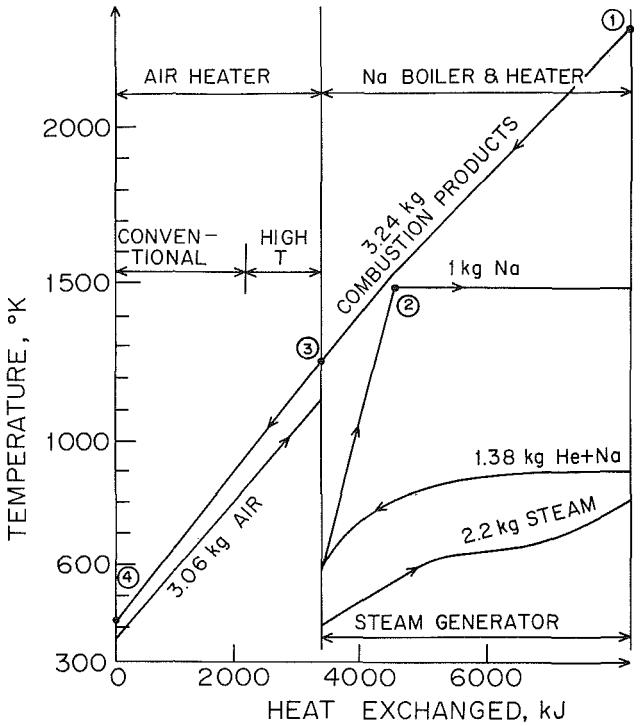


Fig. 4 Thermal balance of the system

and at the low-temperature end as 1.34 kJ/kg K (Babcock and Wilcox, 1978). The temperature dependence of the specific heat of air, both in the combustion air preheater and in the combustion chamber, were taken into account. The properties of sodium as a function of temperature were obtained from Fink and Leibovitz (1981).

6.3 Results and System Efficiency. The results of the analysis of this specific power cycle configuration are summarized in Table 3 and Fig. 4. Since the combustion air is preheated to 1110 K, a temperature higher than that in conventional Rankine power plants, it is noted that in the air-heater area and the air-heater blower, power would increase by about 30 percent. At the same time, as discussed in Section 4.1 above, the heat transfer rates in the proposed sodium boiler are much higher than those in steam boilers, resulting in a reduction of boiler air blower power consumption. This fact, and the relatively small energy consumption of the air blowers in the conventional case, lead to the conclusion that the air preheat in the proposed bottoming cycle would have an insignificant effect on the overall system efficiency improvement.

Table 4 Inefficiency sources and their values in the example analyzed; * indicates inclusion in the overall efficiency of the lower temperature

Inefficiency source	value	remarks
Pressure loss inside the ejector	25% of the work done in an ideal top cycle	literature-based estimate section 2.5
Pressure loss in the steam generator and droplet separator	22% "	estimate
Decrease in helium mass flow rate due to condensation in primary nozzle and incomplete separation	10% "	estimate
Loss in possible turbine work due to less than optimum compression ratio used to reduce system size	3% "	see Section 6.1
Turbine efficiency	80%	"
Heat loss from ejector external surface	0.002% of the total heat supplied by the fuel	"
Combustion efficiency	82% *	"
Excess air needed for the combustion	15% of the * stoichiometric amount	"
Sodium boiler heat exchange efficiency	94%	Table 3
Air heater efficiency	80% *	"

Table 5 Features of different 50 MW sodium-helium ejector-topping cycles (the middle column, in bold letters, is the case fully worked out in the paper)

Boiler Pressure, MPa	0.2	1.08	**1.08**	5.0	5.0
Boiler Temperature, K	1250	1500	**1500**	2000	2000
Ejector Outlet Pressure, MPa	0.02	0.02	**0.1**	0.1	0.5
Efficiency improvement over 40% steam plant	6 %	9 %	**6 %**	11 %	8 %
Diameter of Ejector Throat, cm	128	160	**57**	74	29

Based on the calculated results, about 20 kg/s of sodium are needed for the production of the designated 50 MWe by the ejector-topped power plant, requiring 111,000 kW of fuel heat. Assuming that the bottoming steam cycle has an overall efficiency of 40 percent (this includes the power consumption by the preheat and combustion air blowers, water pumps, and other auxiliaries) and if no topping cycle is used, the work done by the steam turbine, W_s, with the same amount of heat input is therefore 44,400 kW.

If the topping cycle is used, the work done by the helium (topping cycle) turbine, W_{He} = 4764 KW, and the work done by the steam cycle turbine, W_{st}, is

$$W_{st} = (111{,}000 - 4{,}764)0.4 = 42{,}494. \quad (4)$$

The net power gain due to the addition of the ejector topping cycle is thus 4764 − (44,400 − 42,494) = 2858 kW, and the improvement relative to the conventional steam cycle without topping is thus 100 (2858/44,400) = 6.4 percent. The assumed and calculated system inefficiencies are summarized in Table 4.

Performance estimations under a variety of operating conditions shown in Table 5 have indicated possible efficiency improvements of up to 11 percent.

Downloaded 02 Jun 2010 to 171.66.16.122. Redistribution subject to ASME license or copyright; see http://www.asme.org/terms/Terms_Use.cfm

7 Conclusions

The concept of a novel high-temperature ejector-topping cycle was described. It was shown that with this method the efficiency of heat cycles can be improved by allowing the use of temperatures higher than those that current gas turbines can tolerate. This is made possible by using at these highest temperatures an ejector, which inherently has no moving parts, and by operating the entire topping cycle under relatively low pressures. Even with currently available construction materials, operating temperatures of over 1500 K can be reached, at pressures of about 1.1 MPa. Using sodium as the primary ejector fluid and helium as the secondary, an analysis of the cycle at these conditions indicated a 6.4 percent efficiency improvement over a conventional steam Rankine cycle without topping. Additional calculations indicated efficiency improvements up to 11 percent. No attempt was made as yet to optimize the fluids or operating conditions, and it is expected that even better efficiency improvements can be attained.

Thermodynamically, it is noteworthy that in this cycle the combustion gases, which are too hot to be used in a turbine, are cooled to a level acceptable for use in present day turbines by a process that produces compression work of another gas. From the Second-Law viewpoint, the straight cooling of combustion gases from the combustion temperature to that acceptable for turbine operation, as practiced in conventional boilers, completely destroys the exergy contained between these two temperatures. Here we accomplish the same cooling with concomitant production of useful work, clearly an important exergetic improvement.

Other improvements were noted in that the high-temperature operation allows the use of a much smaller furnace (the sodium boiler) with practically no ash accumulation or emission problems. This holds good promise for coal utilization.

This work is a description of the first effort to reduce the proposed concept to practice. It was shown that this cycle is technologically feasible, but its economic attractiveness still needs to be investigated. The exploration of other ways to utilize the concept and other working fluids is recommended and is indeed under way. One preferable research direction is the use of air and/or steam as the working fluids of the topping cycle, and there is a good chance that this direction will yield practical and improved systems.

References

AGARD, 1966, *Materials Properties Handbook, Vol. 4: Heat Resisting Alloys*, North Atlantic Treaty Organization Advisory Group for Aerospace Research and Development, Neuilli-sur-Seine, France.

ASHRAE, 1988, *Equipment Handbook*, American Society of Heating, Refrigerating, and Airconditioning Engineers, Atlanta, GA 30329.

ASM, 1985, *Engineering Application of Ceramic Materials—Source Book*, American Society for Metals, Metals Park, OH 44073.

Babcock and Wilcox, 1978, *Steam, Its Generation and Use*, Babcock & Wilcox, 161 E. 42nd St., New York, NY 10017.

Bliem, C., et al., 1985, *Ceramic Heat Exchanger Concept and Materials Technology*, Noyes Publications, Park Ridge, NJ.

Bonnington, S. T., and King, A. L., 1972, *Jet Pumps and Ejectors—A State of the Art Review Bibliography*, BHRA Fluid Engineering, Cranfield, Bedford, United Kingdom.

Bonnington, S. T., and Hemmings, J. A. G., 1976, *Jet Pumps and Ejectors*, BHRA Fluid Engineering, Cranfield, Bedford MK430AJ, United Kingdom.

ESDU, 1986, *Ejectors and Jet Pumps—Design and Performance for Compressible Air Flow*, Engineering Science Data Unit, Item No. 84029, 251–259 Regent Str., London W1R 7AD, United Kingdom.

Fink, J. K., and Leibowitz, L., 1981, "Calculation of Thermophysical Properties of Sodium," *Proc. Eighth ASME Symp. on Thermophysical Properties*, J. V. Sengers, ed., ASME, New York, Vol. 2.

Freedman, B.-Z., 1989, "Use of Ejectors for High Temperature Power Generation," U.S. Patent No. 4,843,823 (assigned to the University of Pennsylvania).

Hausner, H. H., 1966, *Coatings of High Temperature Materials*, Plenum Press, New York.

Hill, P. G., and Peterson, C. R., 1965, *Mechanics and Thermodynamics of Propulsion*, Addison-Wesley, Reading, MA.

Mikkelson, C. D., and Addy, A. L., 1974, "An Investigation of Gas Dynamic Flow Problems in Chemical Laser Systems," Report UILU-ENG-74-4009, Department of Mechanical and Industrial Engineering, Univ. of Illinois at Urbana.

Ortwerth, P. J., 1978, "On the Rational Design of Compressible Flow Ejectors," AIAA Paper No. 78-1217.

Reynolds, W. C., and Perkins, H. C., 1977, *Engineering Thermodynamics*, McGraw-Hill, New York.

Rohsenow, W. M., and Hartnett, J. P., 1973, *Handbook of Heat Transfer*, Ch. 2, McGraw-Hill, New York.

Sittig, M., 1956, *Sodium, Its Manufacture, Properties and Uses*, Reinhold Publishing Corp., New York.

Tang, H., Churchill, S. W., and Lior, N., 1980, "The Formation of Thermal and Fuel NO_x for Radiantly Stabilized Combustion," *Proc. Combustion Institute's 18th Int. Symp. on Combustion*, pp. 73–80.

Tang, H., Churchill, S. W., and Lior, N., 1981, "The Effect of Fuel of Fuel-Sulfur on NO_x Formation in a Refractory Burner," in: *Research Trends in Air Pollution Control: Scrubbing, Hot-Gas Clean-up, Sampling and Analysis*, R. Mahalingham and A. J. Engel, eds., AIChE Symposium Series, No. 211, Vol. 77, pp. 77–86.

VKI, 1975, *Ejectors*, VKI Lecture Series 79, von Karman Institute.

Downloaded 02 Jun 2010 to 171.66.16.122. Redistribution subject to ASME license or copyright; see http://www.asme.org/terms/Terms_Use.cfm

Y. Matsumoto
Manager,
Technical Research Center,
The Kansai Electric Power Co., Inc.,
3-11-20, Nakoji, Amagasaki,
Hyogo, 661 Japan

R. Yokoyama
Associate Professor.
Mem. ASME

K. Ito
Professor.
Mem. ASME

Department of Energy Systems Engineering,
University of Osaka Prefecture,
1-1, Gakuen-cho, Sakai,
Osaka, 593 Japan

Engineering-Economic Optimization of a Fuel Cell Cogeneration Plant

The feasibility of fuel cells in cogeneration applications is studied from engineering and economic viewpoints by using an optimization approach. Capacities of fuel cell cogeneration units and auxiliary devices are determined together with maximum utility demands so as to minimize the annual total cost by considering the plant's annual operational strategy. This optimization problem is solved efficiently by considering the hierarchical relationship between unit sizing and operational planning problems. Through a numerical study on a plant for installation in a hotel and office building with a maximum electrical demand of 1000 kW, the effect of initial capital cost of fuel cell cogeneration units is examined from the perspective of the plant capacity, economics, and energy savings. The results show that a fuel cell cogeneration plant may have better economic and energy-saving characteristics than a conventional gas engine cogeneration plant with a reduction in the capital cost of fuel cell.

Introduction

Fuel cells, which have developed rapidly as an electrical power source in aerospace flights, are expected to be used as on-site power-generating devices in coming years. The reason for this expectation is that fuel cells have the advantage of lower air pollution, lower noise and vibration, and higher generating efficiency than most other power-generating devices such as diesel and gas engines, and gas turbines. Further, the thermal energy recovered from fuel cell power units can be used in cogeneration applications. In addition to the technological development of fuel cells and related peripheral devices, many field tests for their practical use as cogeneration devices have been performed (e.g., Appleby, 1987; Appleby and Foulkes, 1989; Yamamoto et al., 1992). However, the high initial capital cost of fuel cells has inhibited their commercial or public use, and future widespread application depends on a significant reduction in initial capital cost. It is therefore important to investigate the feasibility of fuel cells in cogeneration applications from both engineering and economic viewpoints.

The objective of this paper is to conduct such a feasibility study. An optimization approach is suitable for evaluating critical effects of fuel cells in cogeneration applications. An optimal sizing method for cogeneration plants has been proposed that considers the plants' annual operational strategies for variations of energy demands (Yokoyama et al., 1991). In this paper, the previously suggested method is used to determine capacities of fuel cell cogeneration units and auxiliary devices together with maximum utility demands to minimize annual total cost. The effect of the initial capital cost of fuel cell cogeneration units on the plant capacity, economics, and energy savings is investigated.

First, an optimization method is described to solve the problem in a short computational time by considering the hierarchical relationship between unit sizing and operational planning problems. Second, the optimization problem is formulated for a fuel cell cogeneration plant. Finally, a numerical study is carried out on a plant for installation in a hotel and office building with a maximum electrical demand of 1000 kW.

Plant Configuration

A simple schematic diagram of the plant investigated in this paper is shown in Fig. 1. Equipment symbols are explained in the nomenclature. Electricity is supplied to users by operating phosphoric acid fuel cells and purchasing electricity from an outside electric power company. Electricity is also used to drive pumps, cooling towers, and other auxiliary machinery in the plant. Exhaust heat generated from fuel cell cogeneration units is assumed to be recovered in the form of hot water, and it is used for a cascaded thermal energy supply. Cold water for space cooling is supplied by both single-stage and gas-fired absorption refrigerators. Hot water for space heating and other purposes is supplied by recovered exhaust heat, gas-fired absorption refrigerators, and gas-fired boilers. Surplus exhaust heat is disposed of by radiators.

There are many alternative options concerning the capacities of the above equipment and the requirements for purchased electricity and natural gas. It is important to determine equipment capacities and maximum utility demands on a rational basis from a long-term viewpoint. For example, an important relationship exists between the capacities of fuel cell cogeneration units and the maximum demand for purchased electricity. That is, if the capacities of units are underestimated, the effect

Contributed by the Advanced Energy Systems Division for publication in the JOURNAL OF ENGINEERING FOR GAS TURBINES AND POWER. Manuscript received by the Advanced Energy Systems Division February 10, 1992; revision received June 16, 1992. Associate Technical Editor: M. J. Moran.

Copyright © 1994 by ASME
Downloaded 02 Jun 2010 to 171.66.16.122. Redistribution subject to ASME license or copyright; see http://www.asme.org/terms/Terms_Use.cfm

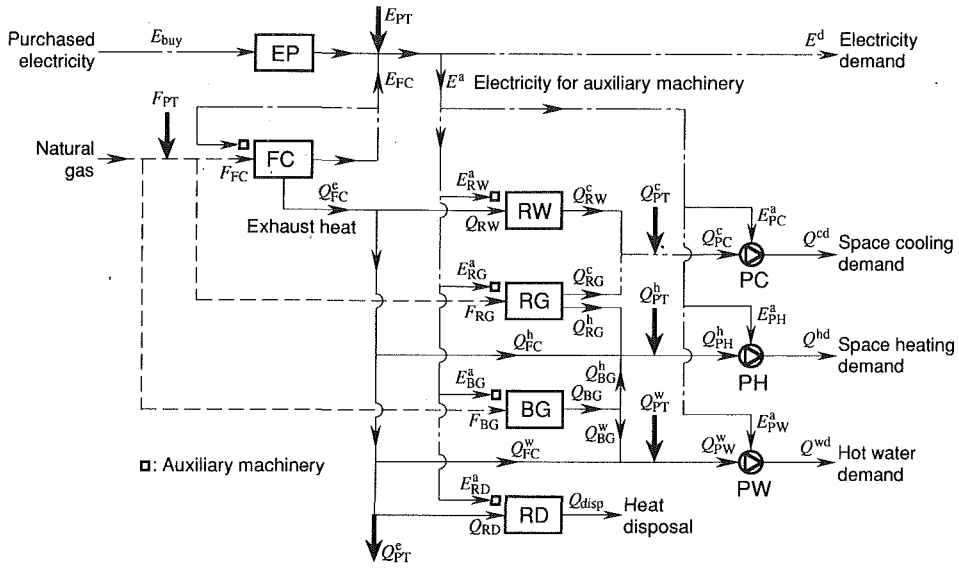


Fig. 1 Configuration of a fuel cell cogeneration plant

of introducing units becomes relatively small; conversely, if they are overestimated, the availability of units decreases. It is difficult to establish this balance because the plant's operational strategy for the seasonal and hourly variations of both electricity and thermal energy demands must be simultaneously considered. In this paper, an optimization method is adopted to solve this problem in a simple and rational manner.

Optimization Method

Basic Concept. The objective is to minimize the annual total cost from the economic viewpoint. The annual total cost may be evaluated as the sum of the annual capital cost and annual running cost by the annualized costs method (Witte et al., 1988). The annual capital cost of each piece of equipment is considered as a function of its capacity. The annual running cost for purchases of electricity and natural gas is the sum of the customer, demand, and energy charges. The demand charge is considered as a function of the maximum demand, and the energy charge is calculated from the plant's operational strategy.

The constraint equations consist of performance character-

Nomenclature

Equipment symbols (subscripts)

BG = gas-fired boiler
EP = equipment for purchasing electricity
FC = fuel cell cogeneration unit
PC, PH, PW = pumps
RD = radiator
RG = gas-fired absorption refrigerator
RW = single-stage absorption refrigerator

Energy quantities

E = electric power, kWh/h
F = natural gas consumption (measured at standard conditions), m^3/h
Q = heat flow rate, Mcal/h

Other symbols

C = initial capital cost of equipment, yen
C_c = annual capital cost, yen/y
C_d = annual customer and demand charges, yen/y
C_e = annual energy charge, yen/y
C_t = annual total cost, yen/y
i = interest rate
J_o = objective function in optimal operational planning problem, yen/h
J_s = objective function in optimal sizing problem, yen/y
N = number of equipment installed
p, q, r, s, t, u = performance characteristic values of equipment
R = capital recovery factor
v = ratio of salvage value to initial capital cost of equipment
α = initial capital cost per kW of fuel cell cogeneration unit, yen/kW
δ = binary variable expressing operational status
η = size parameter of equipment
κ = life of equipment, y
λ = penalty cost, yen/kWh, yen/m^3
φ = unit cost of utility energy charge, yen/kWh, yen/m^3
Ψ = unit cost of utility customer charge, yen/month
ψ = unit cost of utility demand charge, yen/(kW·month), yen/(m^3/h·month)
$\overline{(\ )}$, $\underline{(\ )}$ = upper and lower bounds, respectively

Superscripts

a = auxiliary machinery
c = space cooling
d = demand
e = exhaust heat
h = space heating
w = hot water supply

Subscripts

buy = purchased electricity
disp = heat disposal
gas1, gas2 = natural gas
n = index for each piece of equipment
PT = virtual energy flow

Downloaded 02 Jun 2010 to 171.66.16.122. Redistribution subject to ASME license or copyright; see http://www.asme.org/terms/Terms_Use.cfm

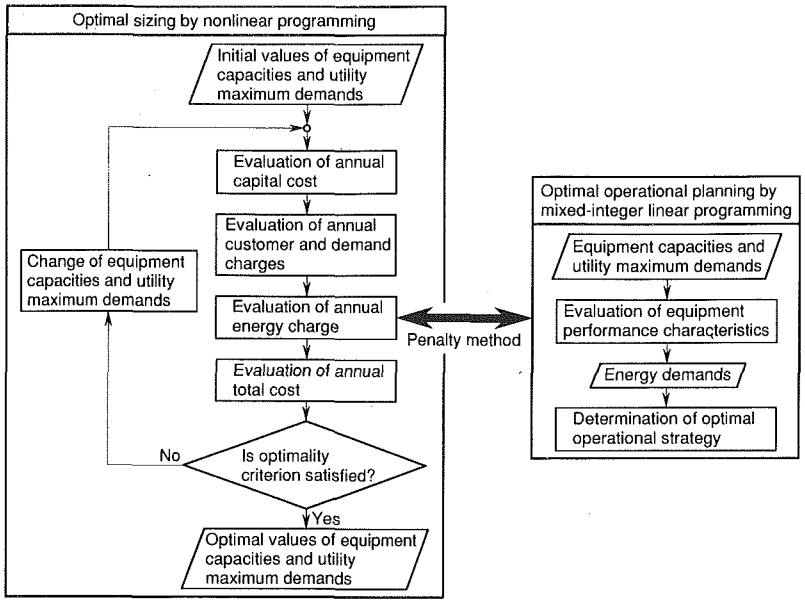


Fig. 2 Hierarchical optimization method of determining plants' sizes and operational strategies

istics for each piece of equipment, maximum demand contracts for utilities, and energy balance relationships for each energy flow. These constraints are considered for the average hourly energy demands estimated on several representative days in a year. In addition to these average energy demands, peak energy demands in summer and winter must be recognized in order to consider equipment and other energy source requirements to supply energy during peak periods. Since the performance characteristics of equipment change with capacity, they should be considered as functions of the latter.

Design variables are composed of equipment capacities and maximum demands on supplying utilities in the sizing problem, and the variables expressing operational strategy in the operational planning problem. Although the capacity of each piece of equipment is selected from a set of discrete values for a practical design, it is regarded as a continuous variable in this paper. The operational strategy is expressed by the binary and continuous variables, which correspond to the on/off status of operation and energy flow rates, respectively.

Hierarchical Optimization. In order to solve the problem in a short computational time, a hierarchical optimization method shown in Fig. 2 is adopted (Yokoyama et al., 1991). At the upper level, the optimal sizing problem is formulated as a nonlinear programming problem, in which optimal values of equipment capacities and maximum utility demands are determined so as to minimize the annual total cost. The constraints given above are not explicitly taken into account at this level, and the only ones considered are those that restrain virtual energy flows. At the lower level, for a plant whose equipment capacities and maximum utility demands are given at each searching step, the operational strategy is assessed and the annual energy charge is evaluated. In this paper, the operational strategy is obtained using an optimal operational planning method proposed earlier (Ito et al., 1990). In this procedure, virtual energy flows are added to the energy flows already existing so that any plant may satisfy energy demands at each searching step. The virtual energy flows play the role of supplying additional energy only if the plant is too small to satisfy energy demands. For that purpose, a penalty cost is imposed on virtual energy flows. At the upper level, as information on the occurrence of virtual energy flows is given in the iterative process, the design variables change automatically to avoid the virtual energy flows, i.e., to satisfy the energy demands.

This hierarchical optimization by the penalty method reduces drastically the number of design variables to be determined simultaneously, and consequently enables us to efficiently solve the sizing problem by considering the operational planning problem. The sequential linear programming method is adopted to solve the nonlinear programming problem (Cheney and Goldstein, 1959). The optimal operational planning problem is formulated as a mixed-integer linear programming problem, and it is solved by the branch and bound method (Garfinkel and Nemhauser, 1972). The specific algorithm adopted here is based on the Land-Doig method (Land and Doig, 1960).

Formulation of Optimization Problem

Prior to the formulation of the optimization problem, symbols denoting energy flow rates are defined as also shown in Fig. 1. Bold arrows in Fig. 1 indicate the virtual energy flows. Although only one unit is shown for each kind of equipment, there may be plural units. The subscript n for the nth of plural units is omitted in Fig. 1.

Optimal Sizing Problem. As stated above, annual energy demands are satisfied by imposing constraints on the annual maximum values of virtual energy flows. The constraints are expressed by

$$\left.\begin{aligned} \max_t E_{PT} &\le 0 \\ \max_t Q^c_{PT} &\le 0 \\ \max_t Q^h_{PT} &\le 0 \\ \max_t Q^w_{PT} &\le 0 \\ \max_t Q^e_{PT} &\le 0 \\ \max_t F_{PT} &\le 0 \end{aligned}\right\}, \tag{1}$$

where $\max_t$ denotes the annual maximum value.

The objective function is formulated in the following way. The annual capital cost of equipment C_c is expressed by

$$\begin{aligned} C_c = \{R(1-v)+iv\}\{&N_{FC}C_{FC}(\eta_{FC}) \\ &+N_{RW}C_{RW}(\eta_{RW})+N_{RG}C_{RG}(\eta_{RG}) \\ &+N_{BG}C_{BG}(\eta_{BG})+N_{RD}C_{RD}(\eta_{RD})+C_{EP}(\eta_{EP})\}, \end{aligned} \tag{2}$$

where N is the number of pieces of equipment installed, C and

Downloaded 02 Jun 2010 to 171.66.16.122. Redistribution subject to ASME license or copyright; see http://www.asme.org/terms/Terms_Use.cfm

Table 1 Tariffs of purchased electricity and natural gas

Utility	Equipment	Period	Unit cost		
			Customer charge	Demand charge	Energy charge
Purchased electricity	–	All months	–	ψ_{buy} = 1 660 yen/(kW•month)	φ_{buy} = {15.33 (Jul.~Sep.), 13.93 (Other months)} yen/kWh
Natural gas	FC, RG	Apr.~Oct.	Ψ_{gas1} = 2 000 yen/month	ψ_{gas1} = 1 000 yen/(m³/h•month)	φ_{gas1} = 48.87 yen/m³
	FC, RG BG	Nov.~Mar. All months	Ψ_{gas2} = 6 410 yen/month	–	φ_{gas2} = 108.93 yen/m³

η are respectively the initial capital cost and the size parameter of each piece of equipment, v is the ratio of salvage value to initial capital cost, and i is the interest rate. The capital recovery factor R is defined by

$$R = i(1+i)^{\kappa}/\{(1+i)^{\kappa}-1\}, \quad (3)$$

where κ is the life of equipment. In Eqs. (2) and (3), it is assumed for simplicity that the values of v and κ are common to all kinds of equipment, and that plural pieces of the same capacity are installed for each kind of equipment, although this method can use other assumptions. Maintenance costs for equipment, including the cost for fuel cell stack replacement, are considered as part of the initial capital costs. Other costs such as taxes, insurance, etc., are not considered in this paper.

The annual running cost is calculated as the sum of the customer, demand, and energy charges of purchased electricity and natural gas. Since there is a variety of tariffs regarding these utilities, it is difficult to formulate the annual running cost generally. For the tariffs shown in Table 1, the customer plus demand charges C_d and the energy charge C_e are respectively formulated as follows:

$$C_d = \sum_{m} \psi_{buy}\overline{E}_{buy} + \sum_{m_{gas1}} \Psi_{gas1} + \sum_{m_{gas1}} \psi_{gas1}\overline{F}_{gas1} + \sum_{m} \Psi_{gas2} \quad (4)$$

and

$$C_e = \sum_{t} \varphi_{buy}E_{buy} + \sum_{t_{gas1}} \varphi_{gas1}\left(\sum_{n=1}^{N_{FC}} F_{FCn} + \sum_{n=1}^{N_{RG}} F_{RGn}\right) + \sum_{t_{gas2}} \varphi_{gas2}\left(\sum_{n=1}^{N_{FC}} F_{FCn} + \sum_{n=1}^{N_{RG}} F_{RGn}\right) + \sum_{t} \varphi_{gas2}\sum_{n=1}^{N_{BG}} F_{BGn}, \quad (5)$$

where $\overline{E}_{buy}$ and $\overline{F}_{gas1}$ are respectively the maximum demands for purchased electricity and natural gas, and Ψ, ψ, and φ are respectively the unit costs of customer, demand, and energy charges. The symbols $\sum_{m}$ and $\sum_{t}$ denote the summations over annual total months and hours, respectively. As shown in Table 1, two kinds of tariff are adopted for natural gas, and quantities regarding each are denoted by subscripts gas1 and gas2, respectively. The symbols $\sum_{m_{gas1}}$ and $\sum_{t_{gas1}}$ denote the summations over the months and hours during which the first kind is adopted, and the symbol $\sum_{t_{gas2}}$ the ones over the hours during which the second kind is adopted.

As a result, the objective function to be minimized J_s, the annual total cost C_t, is defined by

$$J_s = C_t = C_c + C_d + C_e. \quad (6)$$

The size parameters, η_{FC}, η_{RW}, η_{RG}, η_{BG}, η_{RD}, and η_{EP}, and the maximum utility demands, $\overline{E}_{buy}$ and $\overline{F}_{gas1}$, are determined so as to minimize the objective function of Eq. (6), subject to the constraints of Eq. (1). In this procedure, the values of virtual energy flows in Eq. (1), E_{PT}, Q^e_{PT}, Q^h_{PT}, Q^w_{PT}, Q^e_{PT}, and F_{PT}, and the utility consumptions in Eq. (5), E_{buy}, F_{FCn}, F_{RGn}, and F_{BGn}, are calculated from the operational planning. Any quantities may be adopted as the size parameters, if they are representative of capacities. For example, maximum outputs are satisfactory as size parameters.

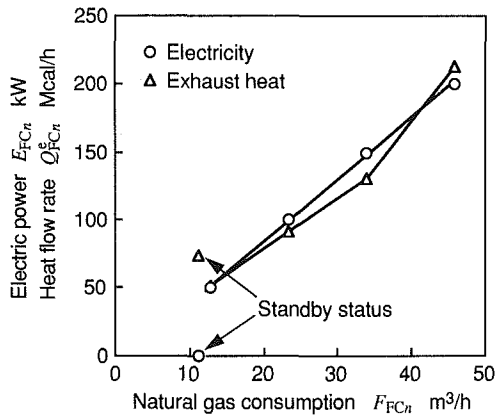


Fig. 3 Performance curves of a 200 kW fuel cell cogeneration unit

Optimal Operational Planning Problem. The operational strategy is assessed so as to minimize the hourly energy charge for given energy demands. This objective function is consistent with that stated above in the formulation of the optimal sizing problem. In order to avoid a tedious description of the formulation of the optimal operational planning problem, only a portion of the governing equations are discussed here.

First, the performance characteristics of each piece of equipment are formulated as constraints. For example, performance characteristics of a particular 200 kW fuel cell cogeneration unit are displayed in Fig. 3 as the relationship between electrical or thermal output and natural gas consumption. Discrete points corresponding to rated load, part-load, and standby status are based on real field test data. According to these data, the general performance characteristics of fuel cell cogeneration units are formulated by

$$\left.\begin{aligned}
&E_{FCn} = p_{FC}(\eta_{FC})F_{FCn} + q_{FC}(\eta_{FC})(\delta'_{FCn} + \delta''_{FCn})\\
&Q^e_{FCn} = p^e_{FC}(\eta_{FC})F'_{FCn} + q^e_{FC}(\eta_{FC})\delta'_{FCn}\\
&\qquad + r^e_{FC}(\eta_{FC})F''_{FCn} + s^e_{FC}(\eta_{FC})\delta''_{FCn}\\
&\qquad + t^e_{FC}(\eta_{FC})(1-\delta'_{FCn}-\delta''_{FCn})\\
&F_{FCn} = F'_{FCn} + F''_{FCn} + u_{FC}(\eta_{FC})(1-\delta'_{FCn}-\delta''_{FCn})\\
&\underline{F}'_{FC}(\eta_{FC})\delta'_{FCn} \le F'_{FCn} \le \overline{F}'_{FC}(\eta_{FC})\delta'_{FCn}\\
&\underline{F}''_{FC}(\eta_{FC})\delta''_{FCn} \le F''_{FCn} \le \overline{F}''_{FC}(\eta_{FC})\delta''_{FCn}\\
&\delta'_{FCn} + \delta''_{FCn} \le 1\\
&\delta'_{FCn},\ \delta''_{FCn} \in \{0,\ 1\}
\end{aligned}\right\} \quad (n = 1, 2, \ldots, N_{FC}), \quad (7)$$

where E_{FCn}, Q^e_{FCn}, and F_{FCn} are the electrical output, thermal output, and natural gas consumption, respectively. The first and second equations imply that the relationship between electrical or thermal output and natural gas consumption is expressed by piecewise linear equations, extracted directly from Fig. 3. The third equation indicates that the natural gas con-

Downloaded 02 Jun 2010 to 171.66.16.122. Redistribution subject to ASME license or copyright; see http://www.asme.org/terms/Terms_Use.cfm

sumption is divided into three parts: the consumption at lower part-load status F'_{FCn}, that at higher part-load status F''_{FCn}, and that at standby status $u_{FC}(\eta_{FC})$. These are identified by two binary variables, δ'_{FCn} and δ''_{FCn}; i.e., the lower part-load status is expressed by setting $\delta'_{FCn}=1$ and $\delta''_{FCn}=0$; the higher part-load status by $\delta'_{FCn}=0$ and $\delta''_{FCn}=1$; and the standby status by $\delta'_{FCn}=\delta''_{FCn}=0$. The fourth and fifth equations limit the natural gas consumption at the lower and higher part-load status, respectively. Since the performance characteristics change with the size, the performance characteristic values, $p_{FC}(\eta_{FC})$, $q_{FC}(\eta_{FC})$, $p^e_{FC}(\eta_{FC})$, $q^e_{FC}(\eta_{FC})$, $r^e_{FC}(\eta_{FC})$, $s^e_{FC}(\eta_{FC})$, $t^e_{FC}(\eta_{FC})$, and $u_{FC}(\eta_{FC})$, and the lower and upper bounds on the natural gas consumption, $\underline{F}'_{FC}(\eta_{FC})$, $\overline{F}'_{FC}(\eta_{FC})$, $\underline{F}''_{FC}(\eta_{FC})$, and $\overline{F}''_{FC}(\eta_{FC})$, are expressed as functions of the size parameter η_{FC}. Performance characteristics of other pieces of equipment are formulated in a similar way.

Next, energy requirements based on supply-demand relationships are formulated for each energy flow in Fig. 1. For example, the following equations are obtained for electricity flow:

$$\left.\begin{aligned}&\sum_{n=1}^{N_{FC}} E_{FCn}+E_{buy}+E_{PT}=E^a+E^d\\ &E^a=\sum_{n=1}^{N_{RW}} E^a_{RWn}+\sum_{n=1}^{N_{RG}} E^a_{RGn}+\sum_{n=1}^{N_{BG}} E^a_{BGn}+\sum_{n=1}^{N_{RD}} E^a_{RDn}\\ &\qquad+\sum_{n=1}^{N_{PC}} E^a_{PCn}+\sum_{n=1}^{N_{PH}} E^a_{PHn}+\sum_{n=1}^{N_{PW}} E^a_{PWn}\end{aligned}\right\}. \quad (8)$$

In addition, the following inequalities must be satisfied between maximum demands and consumptions of utilities:

$$E_{buy}\le\overline{E}_{buy} \quad (9)$$

and

$$\sum_{n=1}^{N_{FC}} F_{FCn}+\sum_{n=1}^{N_{RG}} F_{RGn}-F_{PT}\le\overline{F}_{gas1}, \quad (10)$$

where Eq. (10) is applied only to the hours during which the first kind of tariff is adopted for natural gas.

The objective function to be minimized J_o, the hourly energy charge, changes with the hours. For example, it is formulated by

$$J_o=\varphi_{buy}E_{buy}+\varphi_{gas1}\left(\sum_{n=1}^{N_{FC}} F_{FCn}+\sum_{n=1}^{N_{RG}} F_{RGn}\right)+\varphi_{gas2}\sum_{n=1}^{N_{BG}} F_{BGn}+\lambda(E_{PT}+Q^c_{PT}+Q^h_{PT}+Q^w_{PT}+Q^e_{PT}+F_{PT}) \quad (11)$$

for the hours during which the first kind of tariff is adopted for natural gas. In Eq. (11), λ is the penalty cost, and it should be given a value much larger than the values of utility costs φ_{buy}, φ_{gas1}, and φ_{gas2} in the numerical calculation, as required in the hierarchical optimization process stated above.

The operational strategy is determined so as to minimize the objective function of Eq. (11), subject to constraints such as Eqs. (7)-(10). If a given plant satisfies the annual energy demands, all values of the penalty terms in Eq. (11) become zeros, and the constraint in the optimal sizing problem, Eq. (1), is satisfied. Otherwise, some of the penalty terms have positive values, and consequently Eq. (1) is violated. However, in this optimization algorithm, the equipment capacities and maximum utility demands change automatically so as to satisfy Eq. (1).

Numerical Study

The method stated above is used to evaluate the feasibility of fuel cells in cogeneration applications in a hotel and office building subjected to a maximum electrical demand of 1000 kW. The effect of initial capital cost per kW of fuel cell cogeneration units on the plant capacity, economics, and energy savings is investigated. All values are stated in yen, which is equivalent to about 7.8×10^{-3} dollars based on the recent exchange rate.

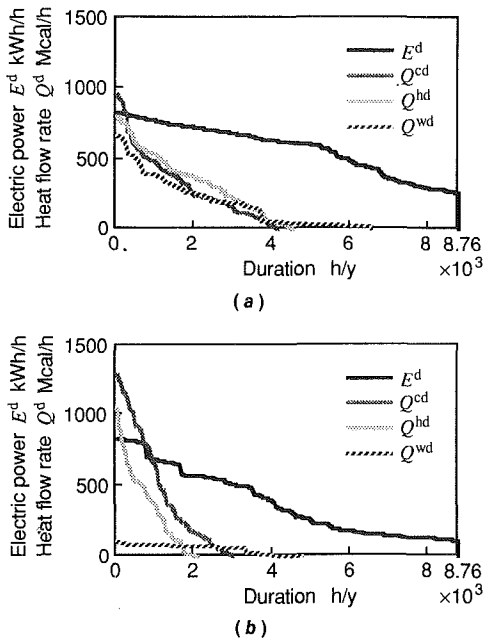


Fig. 4 Load duration curves of energy demands: (*a*) hotel; (*b*) office building

Input Data. Figures 4(*a*,*b*) show the annual load duration curves indicating variations of hourly energy demands for the hotel and office building, respectively. Here, one representative day is considered for each month, and hourly energy demands are estimated as input data for each representative day. In addition to these average energy demands, peak energy demands in summer and winter are also estimated by multiplying the average energy demands in August and January by 1.2, respectively.

Only one piece of each kind of equipment is assumed to be installed. The functions expressing the performance characteristic values of equipment are determined from actual data using curve-fitting by the least-squares method. The expressions for the initial capital costs of equipment are assumed to be linear with respect to their capacities. For the fuel cell cogeneration units, the initial capital cost is defined by

$$C_{FC}(\overline{E}_{FC})=\alpha\overline{E}_{FC}, \quad (12)$$

and a parametric study is carried out with respect to the initial capital cost per kW, α. The representative values of the performance characteristics and initial capital costs are summarized in Table 2. For purchased electricity and natural gas, the tariffs shown in Table 1 are used. In evaluating the annual capital cost, it is assumed that the ratio of salvage value to initial capital cost $v=0$, the interest rate $i=0.1$, and the life $\kappa=15$ y.

Results and Discussion. Figures 5(*a*,*b*) show the relationship between the initial capital cost per kW of fuel cell cogeneration unit, α, and the optimal equipment capacities for the hotel and office building cases, respectively. In the hotel case, the optimal capacity of the fuel cell cogeneration unit becomes zero in the range of α more than 0.8×10^6 yen/kW. Under those circumstances, a conventional plant without any fuel cell cogeneration unit is superior in the long-term economics because of the high cost of the fuel cell cogeneration

Downloaded 02 Jun 2010 to 171.66.16.122. Redistribution subject to ASME license or copyright; see http://www.asme.org/terms/Terms_Use.cfm

Table 2 Performance characteristic values and initial capital costs of equipment

Equipment	Performance characteristic value		Initial capital cost
Fuel cell cogeneration unit	Electrical generating efficiency Exhaust heat recovery efficiency	0.38 (Rated load) 0.46 (Rated load)	α yen/kW
Single-stage absorption refrigerator	COP	0.70	64.7×10^3 yen/(Mcal/h)
Gas-fired absorption refrigerator	COP Thermal efficiency	1.17 (Space cooling) 0.94 (Space heating)	50.6×10^3 yen/(Mcal/h)*
Gas-fired boiler	Thermal efficiency	0.90	12.2×10^3 yen/(Mcal/h)
Radiator	Electricity consumption rate	0.011 kW/(Mcal/h)	14.9×10^3 yen/(Mcal/h)
Equipment for purchasing electricity	—		50.2×10^3 yen/kW

* The capacity is defined as that for space cooling.

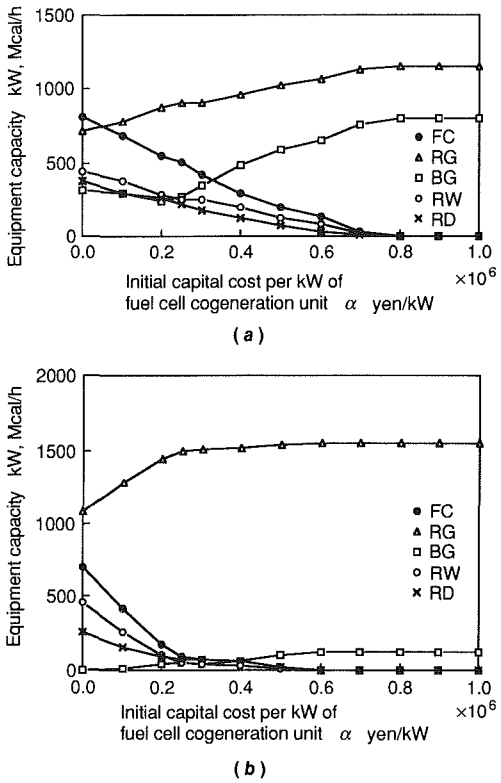


Fig. 5 Relationship between initial capital cost per kW of fuel cell cogeneration unit and optimal values of equipment capacities: (*a*) hotel; (*b*) office building

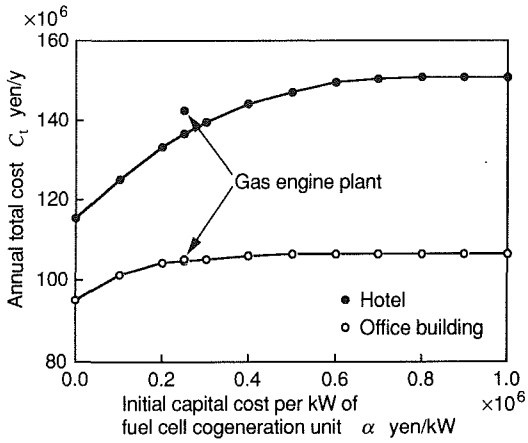


Fig. 6 Relationship between initial capital cost per kW of fuel cell cogeneration unit and annual total cost

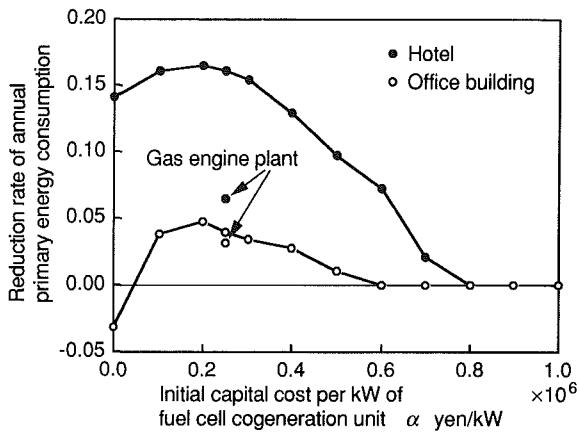


Fig. 7 Relationship between initial capital cost per kW of fuel cell cogeneration unit and reduction rate of annual primary energy consumption

unit. In the range of α less than 0.8×10^6 yen/kW, as may be expected, the optimal capacity increases gradually with a decrease in α. In the office building case, however, the optimal capacity is very low even for $\alpha=0.25\times10^6$ yen/kW, and it increases drastically in the range of α less than 0.25×10^6 yen/kW. This is due to the difference between the hotel and office building energy demand patterns, as shown in Fig. 4; i.e., although the peak values of thermal energy demands in the office building case are larger than those in the hotel case, their duration is shorter, and consequently the operational effect of introducing the fuel cell cogeneration unit becomes lower.

Figure 6 shows the relationship between the initial capital cost per kW of fuel cell cogeneration unit, α, and the annual total cost C_t as the objective function. This figure includes the data on a gas engine cogeneration plant obtained by setting the initial capital cost per kW of cogeneration unit at 0.25×10^6 yen/kW. The annual total cost for the fuel cell plant is less than that for the gas engine plant. This is because the electrical generating efficiency of a fuel cell cogeneration unit is higher than that of a gas engine cogeneration unit, while the exhaust heat recovery efficiency is lower. This combination of features matches the energy demand patterns of both the hotel and office building cases. In the office building case, the difference between annual total cost for the fuel cell plant and the gas engine plant is much less than that in the hotel case. This also reflects the difference in energy demand patterns stated above.

Figure 7 shows the relationship between the initial capital cost per kW of fuel cell cogeneration unit, α, and the reduction in annual primary energy consumption by virtue of increasing fuel cell capacity. The latter is an important criterion for energy savings, and it shows how much annual primary energy consumption can be reduced by introducing a cogeneration plant instead of a conventional plant. The primary energy consumption represents both purchased electricity and natural gas converted into primary energy, with the total thermal efficiency of purchased electricity corresponding to 0.35 of the higher heating value. In the range of α more than 0.2×10^6 yen/kW, the reduction increases with a decrease in α, since the fuel cell capacity increases accordingly. In the range of α less than 0.2×10^6 yen/kW, however, the reduction decreases as the fuel cell capacity becomes oversized with the consequence that much

Downloaded 02 Jun 2010 to 171.66.16.122. Redistribution subject to ASME license or copyright; see http://www.asme.org/terms/Terms_Use.cfm

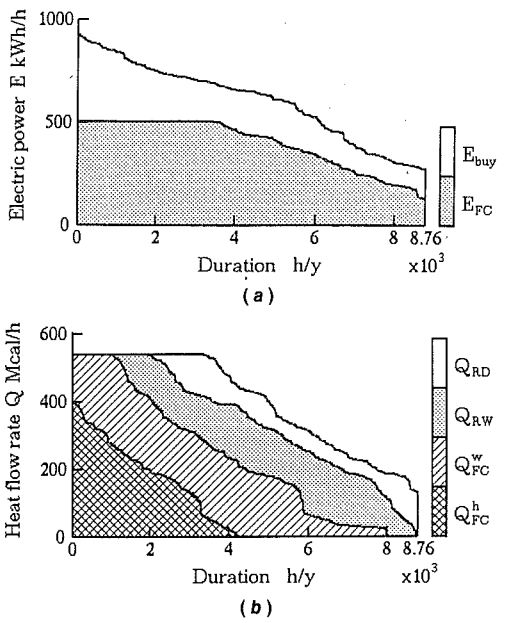


Fig. 8 Load duration curves of energy supply (hotel, $\alpha = 0.25 \times 10^6$ yen/kW): (*a*) electricity supply; (*b*) exhaust heat utilization

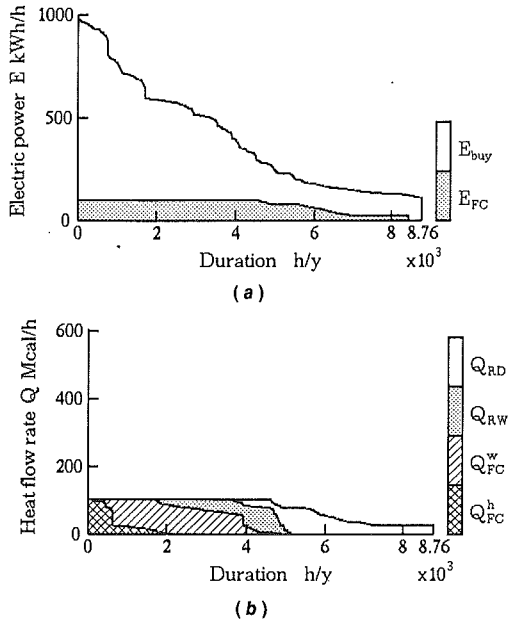


Fig. 9 Load duration curves of energy supply (office building, $\alpha = 0.25 \times 10^6$ yen/kW): (*a*) electricity supply; (*b*) exhaust heat utilization

exhaust heat must be disposed of. Application in the hotel case is more advantageous not only from the economic viewpoint but also from the energy-saving viewpoint.

Figures 8 and 9 show the load duration curves of energy supply for the initial capital cost per kW of fuel cell cogeneration unit $\alpha = 0.25 \times 10^6$ yen/kW in the hotel and office building cases, respectively. The difference between the hotel and office building cases is also apparent from these figures. For the hotel case, although the capacity of the fuel cell cogeneration unit is large, exhaust heat is used efficiently for thermal energy supply. In the office building case, even though the capacity of fuel cell cogeneration unit is very small, the unit operates at part-load status during about half a year, and consequently about one third of exhaust heat is disposed of.

Conclusions

The feasibility of fuel cells in cogeneration applications has been studied from engineering and economic viewpoints by using an optimization approach. A numerical study has been carried out on a plant for installation in a hotel and office building with a maximum electrical demand of 1000 kW. The following principal results have been obtained:

1 The optimization method employed determines the values of equipment capacity and maximum utility demand rationally and simply, by considering operational strategies for variations of both electricity and thermal energy demand.

2 The effect of initial capital cost of fuel cell cogeneration unit on plant capacity, economics, and energy savings has been clarified.

3 The difference in energy demand pattern has a significant influence on plant capacity, economics, and energy savings.

4 Due to its higher electrical generating efficiency, a fuel cell cogeneration plant may have better economic and energy saving characteristics than a conventional gas engine cogeneration plant.

Acknowledgments

The authors would like to express their gratitude to Mr. M. Matsuo, an engineer of Matsushita Electric Industrial Co., Ltd., for his helpful contribution to the numerical calculation in this research.

References

Appleby, A. J., 1987, *Fuel Cells: Trends in Research and Applications*, Hemisphere Publishing, Washington, DC.

Appleby, A. J., and Foulkes, F. R., 1989, *Fuel Cell Handbook*, Van Nostrand Reinhold, New York.

Cheney, E. W., and Goldstein, A. A., 1959, "Newton's Method for Convex Programming on Tchebycheff Approximation," *Numerical Mathematics*, Vol. 1, pp. 253–268.

Garfinkel, R. S., and Nemhauser, G. L., 1972, *Integer Programming*, Wiley, New York.

Ito, K., Yokoyama, R., Akagi, S., and Matsumoto, Y., 1990, "Influence of Fuel Cost on the Operation of a Gas Turbine-Waste Heat Boiler Cogeneration Plant," ASME Journal of Engineering for Gas Turbines and Power, Vol. 112, pp. 122–128.

Land, A. H., and Doig, A. G., 1960, "An Automatic Method of Solving Discrete Programming Problems," *Econometrica*, Vol. 28, pp. 497–520.

Witte, L. C., Schmidt, P. S., and Brown, D. R., 1988, *Industrial Energy Management and Utilization*, Hemisphere Publishing, Washington, DC.

Yamamoto, H., Matsumoto, Y., and Mizumoto, Y., 1992, "Field Test of a 200 kW On-Site Fuel Cell at a Hotel," *Proceedings of the International Fuel Cell Conference*, pp. 91–94.

Yokoyama, R., Ito, K., and Matsumoto, Y., 1991, "Optimal Sizing of a Gas Turbine Cogeneration Plant in Consideration of Its Operational Strategy," *Proceedings of the 5th International Symposium and Exposition on Gas Turbines in Cogeneration, Repowering and Peak-Load Power Generation*, pp. 363–370.

Downloaded 02 Jun 2010 to 171.66.16.122. Redistribution subject to ASME license or copyright; see http://www.asme.org/terms/Terms_Use.cfm

First- and Second-Law Analysis of Steam-Turbine Cogeneration Systems

M. A. Habib
Mechanical Engineering Department,
King Fahd University
of Petroleum and Minerals,
Dhahran, Saudi Arabia

The paper presents an analysis of a cogeneration plant. The performance of the plant is compared to a conventional plant with separate production of process heat and power. The analysis is first- and second-law based and, therefore, quantifies the irreversibilities of the different components of each plant. In the cogeneration plant, the heat required in the boiler can be obtained either from fuel firing (condensing or back-pressure turbine plant) or from exhaust gases of a simple gas turbine (gas turbine cogeneration plant). The present study compares the two methods. The influence of the heat-to-power ratio and the process pressure on the thermal efficiency, utilization factor, and irreversibilities of the different components of each plant is presented. The results show that the total irreversibility of the cogeneration plant is lower by 38 percent compared to the conventional plant. This reduction in the irreversibility is accompanied by an increase in the thermal efficiency and utilization factor by 25 and 24 percent, respectively. The results show that most irreversible losses are due to boiler.

Introduction

Cogeneration is the simultaneous production of power and process heat. Cogeneration is needed because many industries (e.g., sugar, dyeing, and fertilizers) require process heat at low pressure. Boilers at these low pressures are very large. In most of these applications, steam is produced at high pressure and is then throttled to the process pressure. During the throttling process, although the enthalpy is constant as given by the first law, available energy is wasted due to irreversibility according to the second law of thermodynamics. A turbine (back-pressure or condensing) is usually installed in place of the throttling valve to decrease the boiler pressure to that of the process. Thus, process steam as well as power are simultaneously produced by a single plant, which is called a cogeneration plant.

The studies by Rice (1987), and Huang and Wang (1987) provided first- and second-law analyses of gas turbine cogeneration units. Baughn and Kerwin (1987) and Baughn and Bagheri (1987) provided a prediction technique for a gas turbine cogeneration unit. In addition to the fact that these studies concentrated only on the gas turbine units, they did not quantify the irreversibility losses of the different components of each plant. Such quantification is essential for the plant designer and engineer to spot the cause of the major losses. Recent studies by Horlock (1987) and Huang (1990) for condensing turbine and gas turbine cogeneration plants, respectively, indicate the great influence of the heat-power ratio and the process pressure on the performance of the cogeneration plant.

In the present study, a computational procedure is provided for the first- and second-law analysis of a general cogeneration plant. The study is aimed at the quantification of the influence of the heat–power ratio and the process pressure on the thermal efficiency, utilization factor, and irreversibility rates of the different components of the cogeneration plant. Both cases of back-pressure or condensing turbine and gas turbine cogeneration units are considered. The work is also aimed at comparing the cogeneration plant to the conventional plant. A conventional plant has separate production of power and process heat.

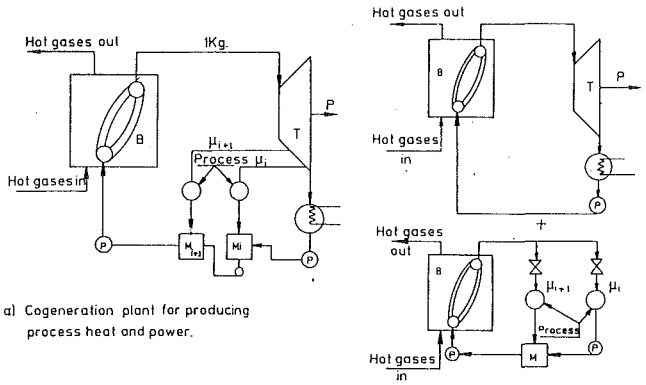
Cycle Description

Figure 1 presents a schematic diagram of the cogeneration cycle and the conventional cycle. The cogeneration cycle is generally a condensing turbine. In the limit where all the boiler steam is consumed in the process such that there is no steam flow rate in the condenser, then it is called a back-pressure turbine. The water-steam in the boiler can be heated by hot gases from fuel burned in the steam generator or from exhaust of a simple gas turbine unit. In the conventional plant power is obtained from Rankine-cycle plant and process steam is obtained from a separate boiler unit in which steam is throttled to the required process pressure. The power was fixed through all the present calculations and the two plants are compared at same process-steam mass-flow rate and power. The results are presented in terms of the heat–power ratio and the process pressure.

The present calculations were obtained at a fixed power output of 20 MW. The pressure and temperature at exit of the boiler are 100 bar and 500°C, respectively, and the condenser pressure is 10 kPa. In each comparison with a conventional

Contributed by the Power Division for publication in the JOURNAL OF ENGINEERING FOR GAS TURBINES AND POWER. Manuscript received by the Power Division November 18, 1991. Associate Technical Editor: R. W. Porter.

Copyright © 1994 by ASME
Downloaded 02 Jun 2010 to 171.66.16.122. Redistribution subject to ASME license or copyright; see http://www.asme.org/terms/Terms_Use.cfm



a) Cogeneration plant for producing process heat and power.

b) Separate-units plant for producing process heat and power (conventional plant).

Fig. 1 Flow diagram of the cogeneration and conventional steam plants

plant, the same process mass-flow rate was considered. The inlet temperature of the hot gases, Fig. 1, is 2000 K in the case of the back-pressure/condensing turbine plant and 800 K in the case of the gas turbine plant. Extraction of process steam was limited to one extraction at a fraction of the boiler pressure as given by P_r. The isentropic efficiencies of the turbines and compressors are 90 percent and the pumping work is neglected. The properties of the hot gases were assumed to be similar to those of air. The boiler combustion losses were not considered throughout the present calculations and therefore, the calculations were based on the heat input rather than the energy in the fuel input.

Cycle Analysis

(a) **The Cogeneration Plant.** Considering the mass-flow rate used for the process i per kg of the mass flow exiting from the boiler is μ_i then the mass fraction entering the condenser is $1-\Sigma_1^n \mu_i$. The total process mass is $\Sigma_1^n \mu_i$ and the total mass flow rate at the exit of the boiler is given as

$$\dot{m}_s = P/\left[h_b - \sum_1^n \mu_i h_i - \left(1 - \sum_1^n \mu_i\right) h_c \right] \tag{1}$$

The process heat is given by

$$\dot{Q}_p = \dot{m}_s * \left[\sum_1^n \mu_i (h_i - H_i) \right] \tag{2}$$

The thermal efficiency is given by

$$\eta = P/\dot{m}_s (h_b - H_b) \tag{3}$$

The utilization factor is

$$UF = \left[P + \sum_1^n \mu_i (h_i - H_i) \right] \Big/ \dot{m}_s (h_b - H_b) \tag{4}$$

The irreversibility rates of the different components are expressed as

$$\dot{I}_T = \left[\dot{m}_s \left(\mu_i s_i + \left(1 - \sum_1^n \mu_i\right) s_c - s_b \right] T_0 \right. \tag{5}$$

$$\dot{I}_b = \left\{ \dot{m}_s (s_b - S_b) + \dot{m}_g \left[\int_{\text{in}}^{\text{out}} c_p \, dT/T - R \ln p_{\text{out}}/p_{\text{in}} \right] \right\} T_0 \tag{6}$$

$$\dot{I}_c = \left[\dot{m}_s \left(1 - \sum_1^n \mu_i\right) * (S_c - s_c) + \dot{Q}_c/T_0 \right] T_0 \tag{7}$$

$$\dot{I}_p = \dot{m}_s \left\{ \left[\sum_1^n \mu_i (S_i - s_i) \right] + \sum_1^n \Delta S_j \right\} T_0 \tag{8}$$

where the increase in the process entropy, ΔS_j, for liquid or solid of constant specific heat is given by

$$\Delta S_j = \mu_j (h_j - H_j) * \ln (T_{2j}/T_{1j})/(T_{2j} - T_{1j}) \tag{9}$$

where T_{2j} and T_{1j} are the final and initial temperatures of the process j.

$$\dot{I}_H = \dot{m}_s \left\{ \left(1 - \sum_{i+1}^n \mu_i\right) * S_{i+1} - \left[\left(1 - \sum_i^n \mu_i\right) * S_i + \mu_i s_i \right] \right\} T_0 \tag{10}$$

where $\dot{m}_g$ is given by the following expression:

$$\dot{m}_g \int_{\text{in}}^{\text{out}} c_p \, dT = \dot{m}_s (h_b - H_b) \tag{11}$$

In the case of the gas turbine cogeneration plant, the pinch point was checked. Thus, $\dot{m}_g$ was obtained by applying the energy balance on the superheater and boiler sections only.

(b) **The Conventional Plant.** In the case of the conventional plant the steam mass flow rate, the heat added, the thermal efficiency, and the utilization factor are calculated as follows:

$$\dot{m}_s = P/(h_{b1} - h_c) \tag{12}$$

$$\dot{Q}_b = \dot{m}_s (h_{b1} - H_{b1}) + \dot{m}_p * (h_{b2} - H_{b2}) \tag{13}$$

Nomenclature

c_p = specific heat at constant pressure
H = enthalpy of water or condensate
h = enthalpy of steam
I = irreversibility rate
$\dot{m}$ = mass flow rate
p = power
P_r = process pressure/boiler pressure
$\dot{Q}$ = rate of heat transfer
R = gas constant
S = entropy of water
s = entropy of steam
T = temperature
UF = utilization factor
η = thermal efficiency
λ = process heat power ratio
μ = extracted mass fraction

Subscripts

b = boiler
$b1$ = boiler for power production
$b2$ = boiler for process heat
c = condenser
g = gases
$g1$ = gases of boiler for power production
$g2$ = gases of boiler for process heat
H = heater
in = input
o = ambient
out = output
p = process steam
s = steam
T = turbine
th = throttling

Downloaded 02 Jun 2010 to 171.66.16.122. Redistribution subject to ASME license or copyright; see http://www.asme.org/terms/Terms_Use.cfm

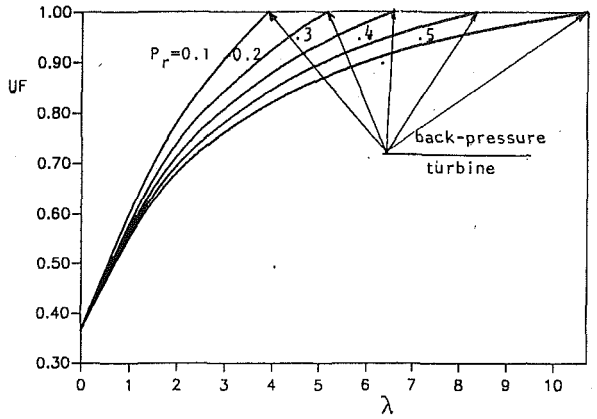


Fig. 2 Influence of the heat-power ratio of the Utilization Factor

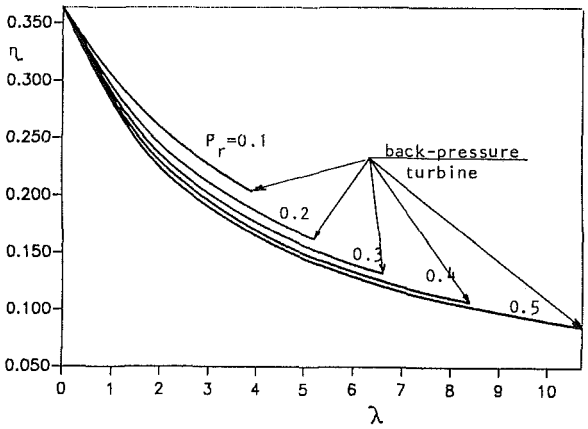


Fig. 3 Influence of the heat-power ratio of the thermal efficiency

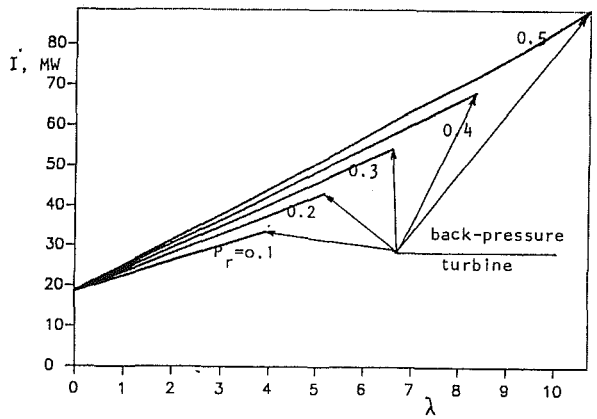


Fig. 4 Influence of the heat-power ratio on the total irreversibility rate

$$\eta = P/\dot{Q}_b \tag{14}$$

$$UF = (P+\dot{Q}_p)/\dot{Q}_b \tag{15}$$

$$\dot{I}_b = \left\{ \dot{m}_s(s_{b1}-S_{b1}) + \dot{m}_p(s_{b2}-S_{b2}) + \dot{m}_{g1}\left[\int_{in}^{out} c_p\,dT/T - R\ln p_{out}/p_{in}\right] + \dot{m}_{g2}\left[\int_{in}^{out} c_p\,dT/T - R\ln p_{out}/p_{in}\right]\right\} T_0 \tag{16}$$

$$\dot{I}_T = \dot{m}_s(s_c - s_b)T_0 \tag{17}$$

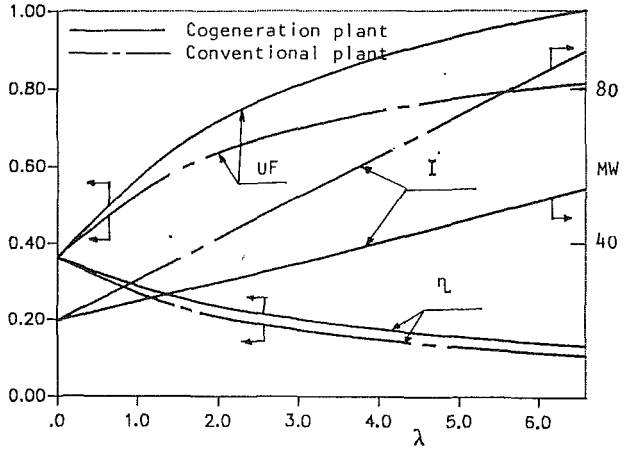


Fig. 5 Comparison of the performance of the cogeneration and conventional plants at $P_r = 0.3$

$$\dot{I}_p = \dot{m}_s\left\{\left[\sum_1^n \mu_i^*(S_i - s_i)\right] + \sum_1^n \Delta S_j\right\} T_0 \tag{18}$$

$$\dot{I}_{th} = \dot{m}_s \sum_1^n \mu_i (s_b - s_p) T_0 \tag{19}$$

Results

The influences of the heat-power ratio on the utilization factor, thermal efficiency, and total irreversibility rate are shown in Figs. 2-4, respectively. As shown by Fig. 2, the utilization factor increases sharply to a maximum value. The value of this maximum increases as the pressure ratio decreases. At low values of process pressure this maximum value approaches 1.0 and corresponds to the back-pressure turbine case. Figure 3 indicates that η decreases with the heat-power ratio. However, the decrease in η is limited to a minimum value corresponding to the back-pressure turbine case. At a certain value for λ, the efficiency decreases as the process pressure increases. Figure 4 indicates the corresponding total irreversibility rate and confirms the results of Fig. 3 for the efficiency.

A comparison of the thermal efficiency, utilization factor, and total irreversibility rate between the cogeneration plant and the conventional plant is shown in Fig. 5. The figure indicates that the efficiency and the utilization factor are generally smaller in the conventional plant as compared to the cogeneration plant. In contrast to this, the irreversibility rates are higher in the case of the conventional plant at all values of λ. It is also shown by this figure that the superiority of the cogeneration plant over the conventional plant is improved as λ increases. At $\lambda = 6.6$, the efficiency and utilization factor are larger in the case of the cogeneration plant by 25 and 24 percent, respectively, as compared to the conventional plant. Corresponding irreversibility rates are lower by 38 percent at $\lambda = 6.6$. The irreversibility rates of the different components of the two plants are shown in Fig. 6. The process heat is same. Most of the irreversibility losses are largely due to the boiler. Also throttling is an addition to the major losses in the conventional plant.

The influence of the process pressure on the thermal efficiency, utilization factor, and irreversibility rate of the cogeneration plant as compared to a conventional plant is shown in Fig. 7. The figure shows that these parameters are nearly uninfluenced by the pressure ratio in the case of the conventional plant. In the cogeneration plant, both the efficiency and utilization factor decrease while the irreversibility rate increases as the pressure ratio increases. The figure shows that the efficiency and utilization factor are better in the case of the

Downloaded 02 Jun 2010 to 171.66.16.122. Redistribution subject to ASME license or copyright; see http://www.asme.org/terms/Terms_Use.cfm

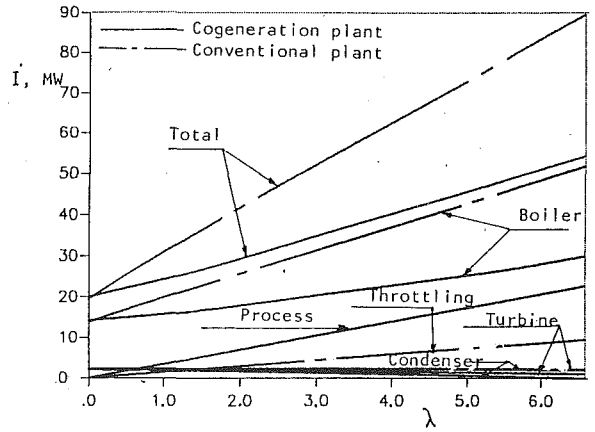


Fig. 6 Comparison of the irreversibility rates of the different components of the cogeneration and conventional plants at $P_r = 0.3$

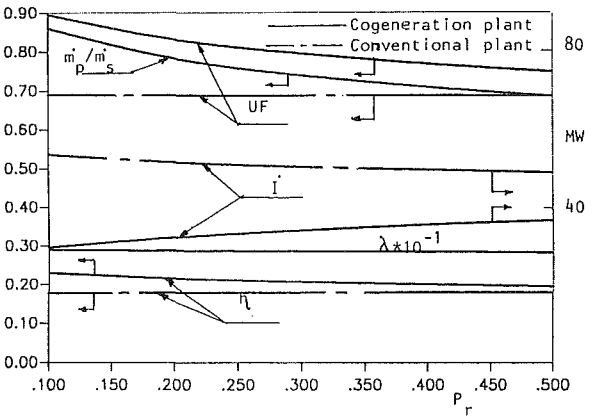


Fig. 7 Influence of the process pressure on the performance of the cogeneration plant ($\dot{m}_p = 100$ t/h)

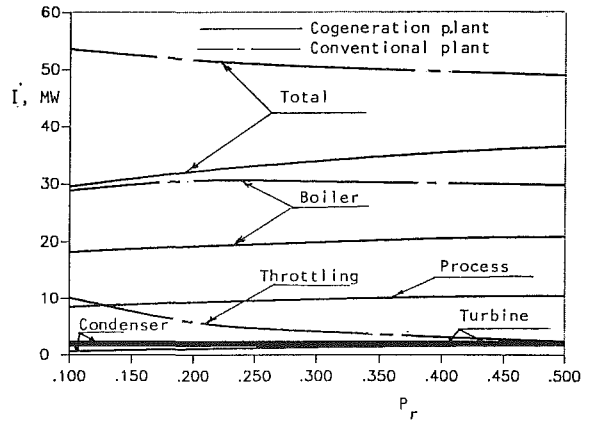


Fig. 8 Influence of the process pressure on the irreversibility rates of the different components of the cogeneration and conventional plants ($\dot{m}_p = 100$ t/h)

cogeneration plant. On the other hand, the irreversibility rate is less as compared to the conventional plant. However, the difference in these values for the two plants are reduced as the process pressure increases. This may be attributed to the fact that increasing the pressure ratio reduces the throttling pressure difference (between the boiler pressure and the process pressure). Thus, the irreversibility rate of the throttling process is decreased and, therefore, the two plants approach the same performance figures. This is confirmed by Fig. 8, which provides a comparison of the irreversibility rates of the different components of the cogeneration and conventional plants. Figure 8 shows also that the major difference between the two plants is due to the irreversibility rate of the boiler, which is higher for the conventional plant.

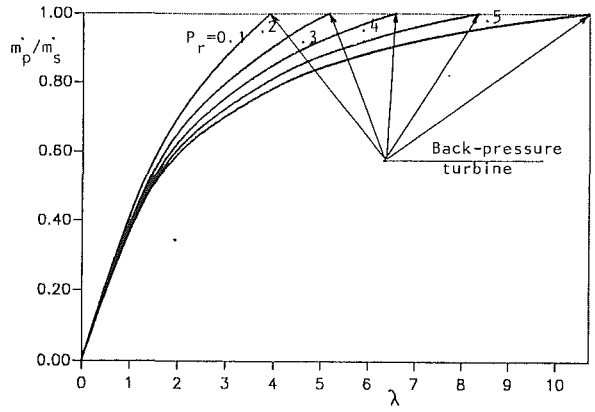


Fig. 9 The process-mass fraction versus the process-heat ratio

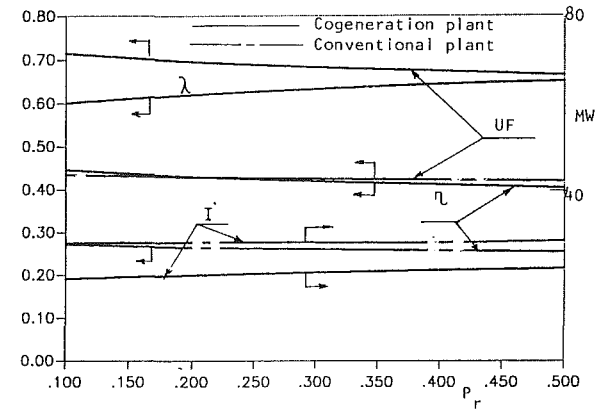


Fig. 10 The performance of the gas turbine unit and conventional plant

Figure 9 provides the required process-mass fraction ratio required for process heat-power ratio. As shown by the figure, the process-mass fraction increases rapidly with λ and the rate of this increase is reduced at high values of λ. As the pressure ratio increases, the mass fraction increases and reaches unity for the back-pressure turbine at low values of the process pressure. Figure 10 presents the influence of the process pressure on the distributions of the thermal efficiency, utilization factor, and irreversibility rate for the combined-cycle back-pressure gas turbine cogeneration and conventional plants. These results were found at the same power output and heat-power ratio and confirm the results of Huang (1990) for the influence of the process pressure and Horlock (1987) for the influence of the heat-power ratio. The figure shows that the total irreversibility rate for the combined-cycle gas turbine is less than for the conventional plant. Figure 11 presents the distribution of the irreversibility rates of the different components of the gas turbine cogeneration plant. The low irreversiblity rate of the gas turbine cogeneration unit is attributed to the low value of the boiler irreversibility rate as shown by Fig. 11. In this case, the difference between gas temperature and steam temperature is small and thus the irreversibility rate of the boiler is small.

Conclusions

First and second-law analysis of cogeneration plants was performed. The results indicate that, at all heat-power ratios, the thermal efficiency, utilization factor, and irreversibility rates are far better in the cogeneration plant as compared to the conventional plant. The differences in these values are 25,

Downloaded 02 Jun 2010 to 171.66.16.122. Redistribution subject to ASME license or copyright; see http://www.asme.org/terms/Terms_Use.cfm

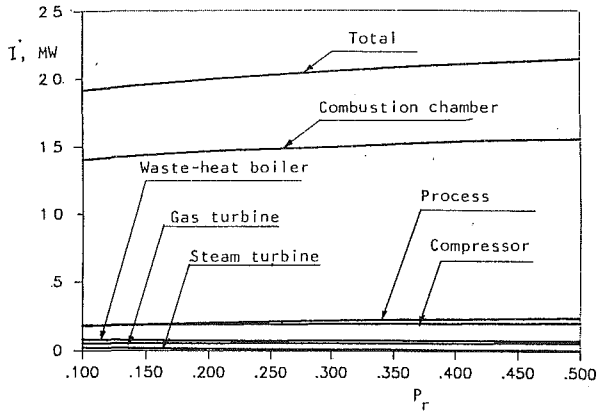


Fig. 11 Distribution of the irreversibility rates of the different components of the gas turbine cogeneration plant

24, and 38 percent, respectively, at $\lambda = 6.6$. The results indicate that the boiler is the major contributer to the total irreversibility. The results also indicate that the performance figures are much better in the case of gas turbine as compared to the conventional plant. This is also attributed to the low boiler losses in the gas turbine plant.

Acknowledgments

Support by the King Fahd University of Petroleum and Minerals for this research project is acknowledged.

References

Baughn, J. W., and Bagheri, N., 1987, "The Effect of Thermal Matching on the Thermodynamic Performance of Gas Turbine and IC Engine Cogeneration Systems," ASME JOURNAL OF ENGINEERING FOR GAS TURBINES AND POWER, Vol. 109, pp. 39–45.

Baughn, J. W., and Kerwin, R. A., 1987, "A Comparison of the Predicted and Measured Thermodynamic Performance of Gas Turbine Cogeneration System," ASME JOURNAL OF ENGINEERING FOR GAS TURBINES AND POWER, Vol. 109, pp. 32–38.

Horlock, J. H., 1987, "Approximate Analysis of Feed and District Heating Cycles for Steam Combined Heat and Power Plant," *Proceedings of the Institution of Mechanical Engineers*, Vol. 201, No. A3, pp. 193–200.

Huang, F. F., and Wang, L., 1987, "Thermodynamic Study of an Indirect Fired Air Turbine Cogeneration System With Reheat," ASME JOURNAL OF ENGINEERING FOR GAS TURBINES AND POWER, Vol. 109, pp. 16–21.

Huang, F. F., 1990, "Performance Evaluation of Selected Combustion Gas Turbine Cogeneration Systems Based on First and Second-Law Analysis," ASME JOURNAL OF ENGINEERING FOR GAS TURBINES AND POWER, Vol. 112, pp. 117–121.

Rice, I. G., 1987, "Thermodynamic Evaluation of Gas Turbine Cogeneration Cycles: Part 1—Heat Balance Method Analysis," ASME JOURNAL OF ENGINEERING FOR GAS TURBINES AND POWER, Vol. 109, pp. 1–7.

Downloaded 02 Jun 2010 to 171.66.16.122. Redistribution subject to ASME license or copyright; see http://www.asme.org/terms/Terms_Use.cfm

CTCC Cogeneration Systems and Steam Supply Availability: An Investigation of Dynamic Availability

J. M. Franceschi
Principal Engineer,
Inst. & Control Engineering,
Ebasco Services Inc.;
Doctoral Candidate,
Dept. of Applied Science,
New York University,
New York, NY

The ability of an industrial cogeneration project to satisfy its steam supply contract was investigated using dynamic simulation. This study of unit behavior performance focused on steam capacity control during expected operational transients, from the trigger event to system recovery. Transients specified in the project steam sale contract include the conditions of unit upset and the dynamic interruption criteria. Performance is measured by the quantitative steam supply variables of pressure, flow, temperature, enthalpy (at the battery limit) and response time following the disturbance of a combustion turbine (CT) trip. A unit especially configured for steam supply uses an availability strategy for response to a CT loss, which requires back-up equipment in the boiler island to activate in time to compensate for disturbance effects without loss of steam-sale continuity as defined in the contract. Dynamic simulation was used to validate seamless transitions of plant alignments from one mode to another during the specified scenarios. A discussion of steady-state availability and facility power block structure sets the context for the investigation.

Introduction

In the diversity of today's energy business, Combustion Turbine Combined Cycle (CTCC) facilities are often proposed for steam supply applications. High efficiencies, minimal footprints, favorable environmental permitting, reduced construction schedules, and innovative financing have contributed to CTCC application success. Meeting availability goals with the proper number and individual unit capacities is crucial and independent of unit type. Unit mix defines the power block structure and sets the availability characteristics of the design. The intent of this paper is to establish the response of the presented CTCC power block structure to the reliability concern, established from industry failure data, of a gas turbine trip. The response of the facility and the equipment supplied to mitigate the effects of the failure will enhance the industry's knowledge base concerned with the application of CTCCs for steam supply systems. Designs evolve based on steady-state mass, energy, and capital exchanges at the facility boundary (battery limits) and from the yearly scheduled capacity profile of the steam user's system. The ability of any CTCC cogeneration facility to meet steam supply availability requirements is evidenced by power block structure performance registered on its yearly duty cycle. Cycle availability issues become apparent when information on the steam host system, the steam supply boundary guarantee points, and the facility duty cycle is compared. A working definition of steam supply interruption and electrical service interruption penalties is necessary to set operational requirements and quantify unavailability effects. To eliminate the uncertainty of risk, detailed measurement of availability achievement, static and dynamic, is conducted. Steady-state and dynamic simulations used in these evaluations are information intensive. Modeling entails data concentration of unit configuration, duty cycle or transient conditions, Balance of Plant (BOP) components, and unit interconnections.

Steady-state availability calculations, based on industrial reliability data, produce a quantitative availability rating for the power block structure. Recent studies by Shor and Griffin (1990) and Shor (1988) investigate industry-wide CTCC reliability data for the major component systems (HRSG, CTG, BOP) of installed CTCC units. Although the overall unit failure rate for CTCC facilities exceeds conventional boiler units because of the additional CTG equipment system, the many other positive attributes of CTCC systems along with their availability ratings merit their consideration as design alternatives for industrial steam supply systems. CTCC component systems availability data allow numerics to be applied to design configurations of the major component systems. Loss experience also leads to particular transients being common knowledge to the industry, one such common disturbance being a CT trip. North American Electric Reliability Council (NERC) Generating Availability Data System (GADS) equipment avail-

Contributed by the Power Division for publication in the JOURNAL OF ENGINEERING FOR GAS TURBINES AND POWER. Manuscript received by the Power Division March 6, 1992. Associate Technical Editor: R. W. Porter.

Copyright © 1994 by ASME
Downloaded 02 Jun 2010 to 171.66.16.122. Redistribution subject to ASME license or copyright; see http://www.asme.org/terms/Terms_Use.cfm

ability data are used to review the CTG, HRSG, and BOP systems.

Availability data show that CTCC BOP component structure and reliability track equipment experience in conventional fossil boiler plants. This CTCC/Conventional Boiler BOP relationship is established by the NERC GADS data over the period 1976 to 1985. The Fossil Units-All Fuel Types BOP equivalent availability factor (EAF) was 98.75 percent. The BOP EAF for Combined Cycle Units over the same period was 97.92 percent, a small differential effect on CTCC unit availability. As for the HRSG, GADS data also show that boiler EAFs, conventional and HRSGs, share similar (95 percent) availability ratings. This indicates no availability differential between conventional fossil boiler plants and HRSGs, with boiler tube leaks the number one cause of forced outage. The record for CTCC combustion turbines, however, has shown a significant contribution to unit unavailability, even though their EAF has improved since 1976 (NERC GADS, 1985a).

In the period 1976 to 1985, NERC GADS cogeneration system data for equivalent availability factor (EAF) on combustion turbines show an increase from the upper 70 percent range to the upper 80 percent range. Shor and Griffin (1990) attribute even higher availability achievements and trends to newly installed combustion turbines (CTs), which utilize triplex control systems. For CTCC systems, their calculations utilize a MTBF value of 2400 h for CTs, which produces a frequency of failure of .000417 failures/h,[1] supporting the view that newly installed CTs have developed considerably better availability ratings than the industrial data shows. The reworking of the CT MTBF value shown in Table 1 of Shor and Griffin (1990) changes the CT frequency of failure from 0.00166 failures/h (600 h MTBF) to 0.000417 failures/h. Here, failure frequency is taken as the number of component failures per unit of operating time. This may change the current failure philosophy regarding CTCC major component systems, making the HRSG failure rate (0.000429) comparable to CTs and the overall CTCC unit failure rate about twice conventional boiler units.

Knowledge about the working characteristics of CTCC components, no matter how profound, reveals nothing of system behavior. Dynamics of the configuration of elements connected in a CTCC system, as for all systems, cannot be understood from causal, linear relationships. Experience with the boiler-furnace primarily designed to produce steam from the radiant heat transfer of combustion, for example, does not directly translate to the HRSG designed to produce steam from the convective heat transfer of hot gas. Response to the same disturbances can be markedly different between these steam generator designs. Dynamic availability models and simulation are tools for developing critical knowledge of system behavior at a financially significant time—before commitment to construction.

Dynamic availability analysis includes measuring system response to a disturbance and affirming the ability of the unit to ride through upsets while remaining within steam supply tolerances. The integration of components is an inherent aspect of building a simulation, ensuring that produce-as-intended operational modes can be met.

One dynamic analysis conducted for a prescribed upset investigated the scenario of a CT trip of a two-unit CTCC power block structure. Included was the ability of back-up equipment systems to initiate properly (the event control means) and supply steam continuously through the upset. Typical of validation work, once the design proved successful for the particular simulation, focus shifted into an offshoot study of how to sequence the back-up components properly, which must operate to remain above a minimum steam sale. The thermodynamic configuration of the HRSG governs the ability to survive the transient. Selection and evaluation of the operational actions after CT trip were aimed at meeting the upset

Table 1 Steam sale provision and interruption criteria

STEAM SALE PROVISION	INTERRUPTION CRITERIA
Net Process Steam Flow 88kg/sec (700,000 lb/hr) Each CTG/HRSG Train Producing 44 kg/sec (350,000 lb/hr)	Continuous Uninterrupted Service
Net Process Steam Pressure 2240 kPa (325 psia)	1896 kPa (275 psia) Minimum 2344 kPa (340 psia) Maximum
Net Process Steam Temperature 285°C (545°F)	10°C (50°F) Superheat Minimum During Transient
	Minimum Values Reached Within 10 minutes of One CTG/HRSG Train Loss
	System Recovery to Steam Sale Provision Values Attained Within 20 minutes of One CTG/HRSG Train Loss

[1]Frequency of failure is the reciprocal of mean time between failure (MTBF). Some reports utilize 600 h as a MTBF value, which is more in line with the GADS data.

Nomenclature

Acronyms

BOP = Balance of Plant
BFP = Boiler Feed Pump
CT = Combustion Turbine
CTCC = Combustion Turbine Combined Cycle
CTG = Combustion Turbine Generator
EAF = Equivalent Availability Factor
GADS = Generating Availability Data System
HRSG = Heat Recovery Steam Generator
NERC = North American Electric Reliability Council
MTBF = Mean Time Between Failure
MTTR = Mean Time To Restore
PBS = Power Block Structure

Variables

f_r = failure rate, failure/h
$MTTR_{CT}$ = mean time to repair for CT, h
N_{CT} = number of combustion turbines running
N_{op} = number of units operating
$N_{T2\text{-}1}$ = number of transitions from 2 CT running to 1 CT running per year, events/yr
t_{op} = yearly operating deviations of operational alignment, h/yr
t_{oppt} = yearly operating duration of operational alignments based on loss of 1 unit's CT, h/yr
WHEDR = steam user header flow, kg/s
WUNIT1 = steam flow of Unit 1, kg/s
WUNIT2 = steam flow of Unit 2, kg/s
PHEDR = steam user header pressure, kPa
THEDR = steam user header temperature, °C
HHEDR = steam user header enthalpy, kJ/kg
HRISER = evaporator riser enthalpy, kJ/kg
DHRISR = evaporator riser enthalpy derivative, kJ/kg/s
YBURNR = duct burner fuel control valve position, fraction open

Downloaded 02 Jun 2010 to 171.66.16.122. Redistribution subject to ASME license or copyright; see http://www.asme.org/terms/Terms_Use.cfm

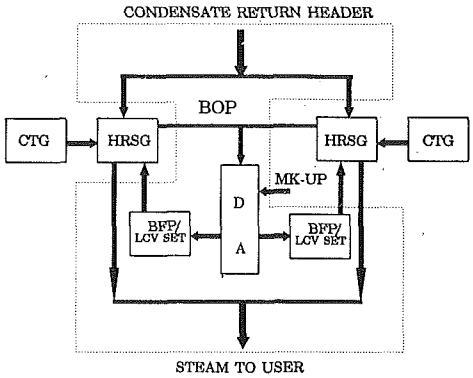


Fig. 1 Power block structure

requirements of the service interruption criteria. The structure of the model, the investigation results, and the conclusions are presented below.

Unit Power Cycle and Statement of Operational Risk

In overview, the power block structure is comprised of two industrial frame CTGs connected to individual natural circulation HRSGs. The CTG produced 178,773 kJ/s (610 MBtu/h) of thermal energy at an exhaust temperature of 532°C (990°F) and 71 MW of electric power at the 21°C (70°F) ambient condition. The HRSGs supplied steam to the steam user at 2240 kPa (325 psia) and 285°C (545°F). It consisted of a single pressure evaporator designed to produce, at any ambient condition, a maximum of 88 kg/s (700,000 #/h) steam from each unit with duct firing. The net process steam guarantee point of 44 kg/s (350,000 #/h) of steam per unit w/o duct burning was selected as the operational case CT trip for investigation. This guarantee point or operational mode is at the highest duty time (>60 percent) expected over the year, considering 3 weeks of scheduled maintenance for each unit.

The power block structure of the facility is represented in Fig. 1. Condensate return {70 percent at 99°C (210°F)} from the steam user was sent through backend feedwater coils in each boiler before entering the deaerator along with demineralized make-up. A common deaerator at 262 kPa (38 psia) with multiple deaeration vessels was provided for both units with individual pegging steam supply from each HRSG to its separate deaereation vessel. Three 50 percent boiler feed pumps per unit were supplied along with redundant level control valves. Boiler feed was sent through the economizer to the evaporator where the steam leaving then runs through two superheaters with a duct burner positioned between them. The duct burner pilot is in continuous service. The steam connection of each unit to the header feeding the process user was water-attemperated from a boiler feed supply. Electrical energy was sent to the grid.

The steam sale provision and interruption criteria are summarized in Table 1. The model simulated all fluid and gas thermodynamic exchanges according to classic power industry methods, the first-principles bases of which are similar to those described by Shor et al. (1983).

Investigation of operational alignment states, which Shor and Griffin (1990) describe as availability state probabilities, can formally determine the multitude of unit alignments in relation to their steam supply capacities. In this way, the various high-risk operational unit alignments where unit loss would trigger a minimum steam capacity violation penalty can direct the reliability design.

The operating mode or alignment of risk for the facility featured in the investigation is two units running with the forced loss of one combustion turbine.

In this scenario, unless a reliability-enhancing strategy is provided to preempt the consequences, CT loss violates the minimum steam service guaranteed to the user. The strategy explored features a duct burner, firing in the boiler of the nontripped unit, at the time of the CT trip. The firing rate chosen doubles steam capacity, thereby compensating for the lost CT/HRSG train. Even though the investigation chose to use a CT trip, the reliability enhancement strategy (fired duct burner) assumes the CT and the HRSG have the same failure probability.

The reference approach of the investigation, for making up the steam capacity lost with the loss of the CTG, is replacing the CTG/HRSG train capacity by step-increasing production from the other, still-running train.

Alternate strategies proposed included continuous-running induced draft fans on the tripped HRSG train. This feature provides the capability to replace the CT flow and support duct burner combustion on the tripped CT train, to handle the disturbance. Since this strategy does not replace a failed CTG/HRSG train, it ranked low in the priority list for investigation.

Without the luxury of additional CTG/HRSG trains, the two unit PBS alignment exhibits numerical risk as part of the yearly duty cycle. Shor and Griffin (1990) summarize their lessons learned stating "that if the plant is well designed to avoid common mode failures and its individual parts have low forced outage rates and low scheduled outage factors, the most important remaining variable is the ratio of installed steam capacity to minimum acceptable steam flow to prevent refinery upset" (Shor and Griffin, 1990). As the installed capacity to minimum acceptable steam flow increases, the number of loss occurrences per year decreases. While not the condition of the featured PBS, this trend signals the significance of extra installed capacity.

Continuous unit duty cycles regulate the number of high risk transitions in the facility at-risk exposure. For the featured PBS, both units are in service 60 percent of the year and the number of transitions from 2 CTCC units to 1 CTCC unit (violating steam capacity) can be calculated (Shor and Griffin, 1990). If t_{op} is the yearly operation time of the alignment in hours, f_r is the CT failure rate in failures/h/CT and N_{CT} is the number of turbines operating, the number of transitions per year $N_{T2\text{-}1}$ is

$$N_{T2\text{-}1} = t_{op} * f_r * N_{CT}$$

When t_{op} is 4953 h, which includes the above scheduled outage statements, f_r equivalent to 0.000417 failures/h/CT (Shor and Griffin, 1990) and the number of units operating 2, $N_{T2\text{-}1}$ becomes 4.13 transitions per year. Assuming 4 CT trips per year do not have an effect on the steam capacity, because the reliability enhancement strategy works successfully, then the operating alignment for the post-trip state is established as 1 unit running producing 88 kJ/kg (700,000 lb/h) of steam. Therefore, the yearly exposure rate (number of transitions) together with the mean time to restore (MTTR) value for a combustion turbine, determines the operating duration of this post-trip one-unit alignment. This one-unit alignment duty time is equal to the number of transitions per year $N_{T2\text{-}1}$ multiplied by the MTTR of a CT, or

$$t_{oppt} = N_{T2\text{-}1} * \mathrm{MTTR}_{CT}$$

For a MTTR of 24 hours for CTs as reported by Lofe et al. (1987), t_{oppt} becomes 99 hours. This post-trip operating condition does not include other yearly duty cycle operating alignments for the unit at this steam capacity; it is post-trip only. Applying the same analysis as above for the two unit operating alignment to this case, the number of transitions from one unit at 88 kg/s (700,000 lb/h) to no units or violation of steam sale can be determined. As above,

Downloaded 02 Jun 2010 to 171.66.16.122. Redistribution subject to ASME license or copyright; see http://www.asme.org/terms/Terms_Use.cfm

$$N_{T1\text{-}0} = t_{oppt} * f_r * N_{op}$$

with t_{oppt} being 99, here f_r is, for the overall *unit*, 0.000976 failures/h/unit and N_{op} units operating equal to 1, giving a transition rate of 0.096 transitions/yr or 1 every 10 years. Therefore, if the two-unit operating scenario could survive a CT trip, the steam sale risk probability would be once every 10 years. If this reliability-enhancing strategy (duct firing to replace the lost steam capacity) is an effective control for the postulated event, it can replace the need for having an additional CTCC unit running or having standby boilers constantly in service in anticipation of the disturbance.

With failure rate information, penalties attributed to the interruption can be calculated with confidence, economic impacts assessed, and other alternatives developed and investigated. If a third unit were to be included in the PBS featured in Fig. 1, the MTTR value in the evaluation of t_{oppt} above would be set as the start-up time of the third unit and not the MTTR of the CT used above (assuming the third unit was not down for scheduled outage). This would substantially change the transition rate $N_{T1\text{-}0}$ above. If we estimate the start-up time of the third unit to be two hours and define this as the MTTR, the new value for t_{oppt} would be 8.6 h/yr giving a $N_{T1\text{-}0}$ of 0.008 transitions a year from one unit operating at 88 kJ/kg to no units operating or steam sale violation. A $N_{T1\text{-}0}$ of 0.008 corresponds to one steam sale violation every 125 years, a substantial reduction of risk.

Model Modular Configuration of Components and Controls

The model modular configuration is comprised of a connected network of modular software routines, which reflect the CTCC equipment types and emulate the process flow diagram. These modules are individually parameterized with physical and operating data to "make them live." The physical data transform the generic software module, i.e., an economizer, into the specific component installed in the design. The operating data initialize the process parameters of the module to the operating mode at which the transient will occur. Module decomposition mimics the exact equipment types employed in CTCC systems (i.e., evaporators, attemperators, integral deaerators, duct burner, pipe, valve, etc.), which is a common attribute of modern day industrial dynamic simulations.

Both CTG/HRSG trains are included to insure the proper system dynamics would be represented by the simulation. This couples the inherent physics of residual steaming in the boiler and feedwater makeup of the tripped unit to the dynamics of firing the untripped unit. Combustion turbine exhaust conditions were handled, for simplicity, as a boundary condition using data from trip curves supplied by the CTG vendor.

The internal modular configuration of the HRSG model, beginning at the CTG exhaust, included two superheat modules with a duct burner between them, a natural circulation evaporator, an economizer, and a feedwater heater coil. Vendor heating surface data were utilized for the physical parameterization of these modules. The duct burner was configured as a fuel valve boundary condition merging with the HRSG gas flow downstream of the high-temperature superheater.

Steam sendout to the thermal host from the high-temperature superheat sections also supplies augmentation steam (excess process steam) to the CTG, which then passes through individual desuperheating stations. The steam from the first unit is merged with second unit steam and sent to the steam user. Piping from the final superheater outlet of each unit to the steam junction process header was included as pipe resistance modules, but without thermal losses (because lengths were short). Pipe resistance modules with thermal loss were included for the long steam sendout pipe from the process header to the thermal host facility connection. Both the augmentation steam to the CTG and the thermal host steam sendout were configured as outlet flow boundary conditions.

Feedwater to each HRSG economizer is provided from separate BFP module sets (3–50 percent pumps) with redundant level control valves. Feed pump module data was acquired from the pump specification. BFP suction is taken from the deaerator, which has a controlled and an uncontrolled makeup. Deaerator module physical data were obtained through vendor information. The controlled make-up water to the deaerator from the condensate make-up system is configured as a fluid pressure boundary condition in series with a make-up level control valve module. The uncontrolled make-up comes from normal condensate return, which flows through the FWHs and is then sent to the deaerator. Pegging steam to the deaerator is provided from evaporator drum steam flowing through a pressure control valve at each unit. Blowdown from both HRSG evaporators is headered and sent to a pressurized blowdown tank with flash steam returned to the deaerator. Blowdown tank module sizing was performed in accordance with Ebasco Standard MNE-83, "Continuous Blowdown Flash Tanks."

Evaporator drum level is controlled using a three element Proportional-Integral (P-I) controller module with final superheater steam and economizer feed flows and drum level as the control variables. The deaerator condensate make-up valve is controlled using a single element P-I controller module for deaerator level. Control for the pegging steam valve is provided using a single element controller, which controls deaerator pressure. Augmentation steam was controlled using a single element P-I controller with final superheater steam outlet pressure as its control variable. Desuperheating was controlled using a single element P-I controller using final superheater discharge temperature. The control configuration for the duct burner fuel control valve used a single element P-I controller based on the thermal host's header pressure.

Operational data for module parameterization of simulated initial conditions was obtained from the steady-state heat balance at 21°C (70°F) ambient conditions. The model was first run to validate the steady-state conditions of the heat balance. After controller tuning the model was run to the steady-state ambient condition. For this steady-state point, all the variables of the model were saved as an initial condition file to be used to begin the transient exercise.

Back-up Equipment Sequence of Operation

An operational instruction program file was prepared to guide the simulation through the operational sequence threat to the steam supply. The sequence of instructions placed in this file begins with the loading, into the simulation, of the stored 21°C (70°F) conditions to initialize to operating point. The transient exercise then begins by tripping the CT of Unit 1. Upon CT trip, automatic actions taken through control logic involve the setting of the feedwater control valve on Unit 1 to a minimum position and closing both units CTG steam augmentation valves. On the untripped Unit 2, after a time delay (3–5 s) corresponding to the duct burner flame detection safety system, the duct burner fuel control valve is set to 40 percent open, simulating the opening of the duct burner fuel block valve. The "block valves open" condition is maintained for 30 seconds, for boiler tube protection, before the fuel control valve is ramped full open with the valve having a stroke time of 10 seconds.

Supplying some energy into the boiler within the time window is crucial. A preset time demand (10 s) holds the burner fuel control valve wide open, regardless of control signal (steam user header pressure). After this time demand signal has elapsed the duct burner fuel control system is transferred to automatic. The controlling header pressure with Unit 2 is then at the pretip pressure setpoint 2240 kPa (325 psia). This control strategy is

Downloaded 02 Jun 2010 to 171.66.16.122. Redistribution subject to ASME license or copyright; see http://www.asme.org/terms/Terms_Use.cfm

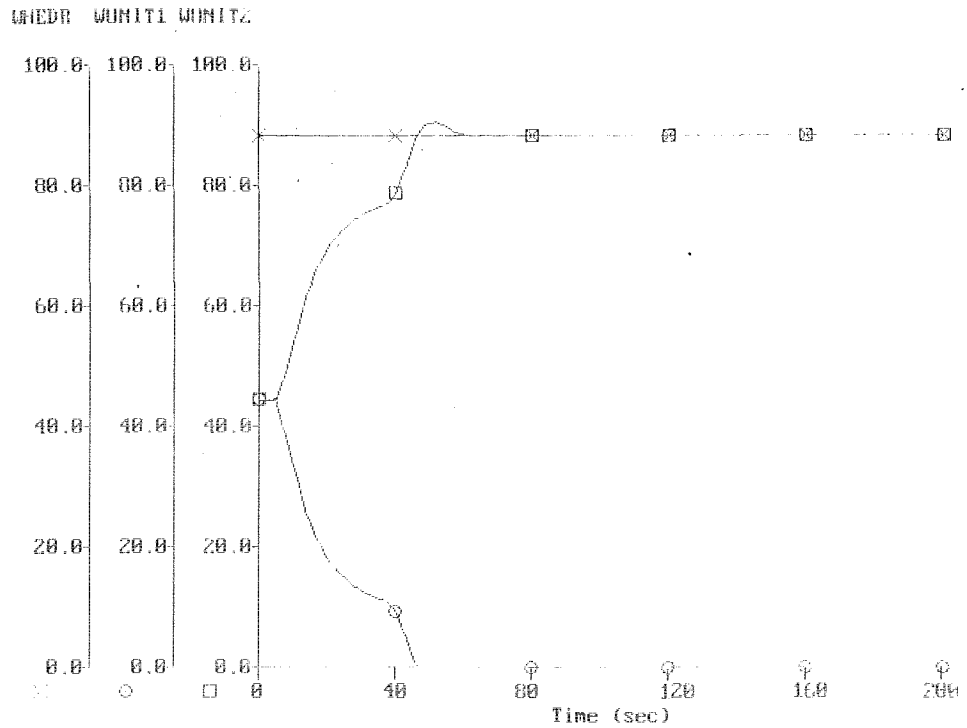


Fig. 2 Steam user and unit steam flows

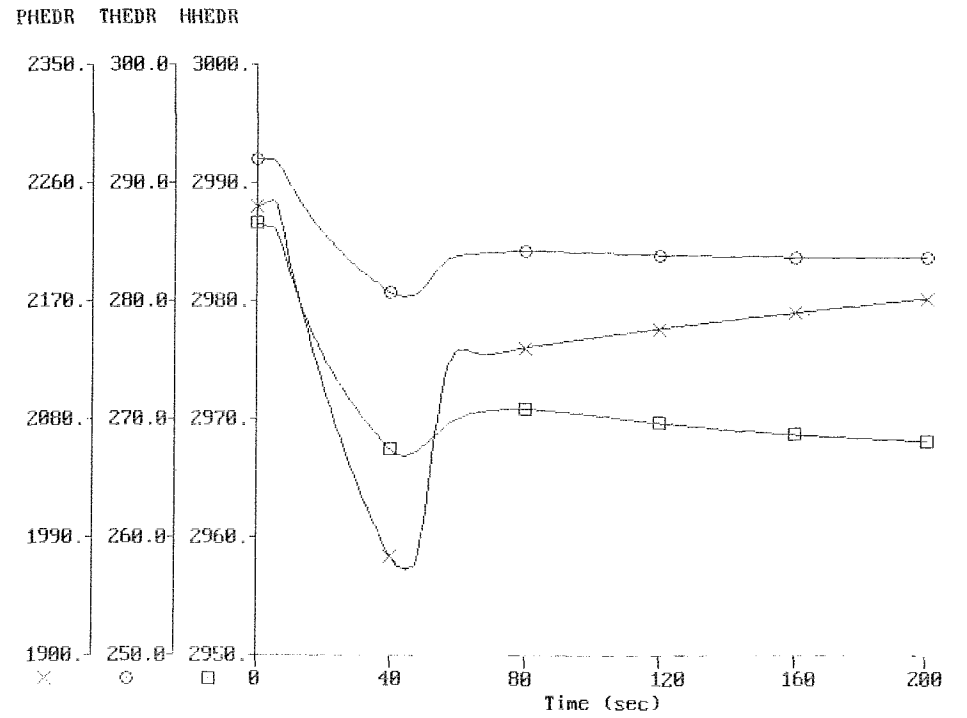


Fig. 3 Steam user header pressure, temperature, and enthalpy

based on the initial condition that both units were running at 44 kg/s each at trip initiation. For other unit steaming rates the timing sequence of this control system may be inappropriate to achieve control over the disturbance. Control strategies are being developed to handle a wide range of steaming capacities.

Results

The parametric responses to the transient are shown in Figs. 2 and 3. Comparing these data to the criteria of Table 1 confirms success of the design in meeting the upset requirements during the remarkably short scenario. Figure 2 plots unit 1 (WUNIT1) and 2 (WUNIT2) steam flow and the combined steam flow to the steam user (WHEDR) in kg/s. Figure 3 graphs the steam header pressure (PHEDR) in kPa, the temperature (THEDR) in °C, and enthalpy at the header to the steam user (HHEDR) in kJ/kg.

Downloaded 02 Jun 2010 to 171.66.16.122. Redistribution subject to ASME license or copyright; see http://www.asme.org/terms/Terms_Use.cfm

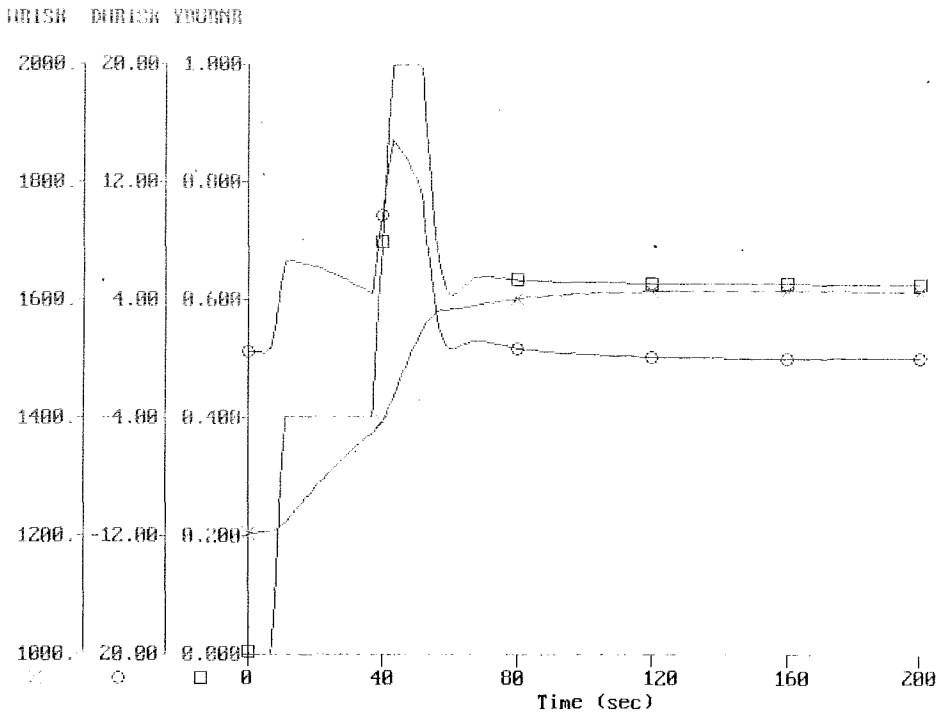


Fig. 4 Boiler steam enthalpy, enthalpy derivative, and duct burner fuel valve position

Conclusions

The simulation-derived response curves show that (for CTCC cycles), the internal HRSG evaporator sections steam rapidly. The enormous surface area of the imbedded stream finned tube arrangement sets the stage for swift steam production changes. The single pressure evaporator at a low thermodynamic pressure in conjunction with a low exit gas temperature exhibits an inherent quick-response characteristic. With Fig. 4 showing the enthalpy (HRISR) in kJ/kg and the enthalpy derivative (DHRISR) in kJ/kg s during the transient in relation to the duct burner valve position (YBURNR), the high sensitivity of the steaming rate to duct burner movement can be noted.

For a fast response steaming requirement, such as maintaining steam supply service to the user during an upset, this sensitivity can be an asset. Validation that unit performance meets customer requirements, in terms of a production schedule and stated availability, can be achieved through dynamic simulation early in the project. Initially, the PBS common nonintegral deaerator was selected due to pressure excursions related to HRSG integral deaerator designs when subjected to temperature transients (duct burner firing) in the gas flow (Franceschi, et al., 1991). As a second alternative design, HRSGs using an integral deaerator will be investigated. This scheme decouples the commonality of the PBS shown in Fig. 1, increasing the reliability of the PBS regarding common mode failure. The use of dynamic simulation to evaluate the performance of design alternatives before commitment to build can deliver large benefits to the project.

Acknowledgments

Important support for the modeling effort was provided by several colleagues and associates at Ebasco. S. Statz, F. Elfers, A. DeMagistris, and J. VanName provided critical idea exchange related to the modeling structure and results. Data development for CTG curves was provided by M. Leon. Steady-state operating data were provided by D. Carbone and F. Lazbin. Corporate direction of simulation efforts was provided by D. G. Price, V. P. Chief Engineer Instrumentation and Control and A. C. Cagnetta, General Manager Region 1 Fossil Division. Continued professional guidance was provided by W. L. Livingston of Ebasco and Dr. G. Miller of NYU. Critical simulation support was provided by G. Kosowski of Trax Corporation.

References

Franceschi, J., Statz, S., and Van Name, J., 1991, "Operability Concerns Related to Three-Pressure Combined Cycle Power Plants," presented at the EPRI Conference on Power Plant & Power System Training Simulators and Modeling, Miami Beach, FL, Apr. 18.

Lofe, J. J., Pourciau, J. L., and Richwine, R. R., 1987, "Availability Predictions for Combustion Turbines, Combined Cycle, and Gasification-Combined Cycle Power Plants," presented at the Joint ASME/IEEE Power Generation Conference, Miami Beach, FL, Oct., Paper No. 87-JPGC-Pwr-64.

North American Electric Reliability Council, 1985a, Generating Availability Data System, "Equipment Availability Report 1976-1985," Princeton, NJ, p. 131.

North American Electric Reliability Council, 1985b, Generating Availability Data System, "Equipment Availability Report 1985," Princeton, NJ, p. 133.

Shor, S. W. W., Smith, L. P., and Dixon, R. R., 1983, "Modular Modeling System (MMS): A Code for the Dynamic Simulation of Fossil and Nuclear Power Plants," Electric Power Research Institute, Report CS/NP-2989, Palo Alto, CA.

Shor, S. W. W., 1988, "Availability of Combined Cycle Plants With Recent Model Gas Turbines," presented at the Joint ASME/IEEE Power Generation Conference, Philadelphia, PA, Sept. 25-29, Paper No. 88-JPGC/Pwr-30.

Shor, S. W. W., and Griffin, R. F., 1990, "Design of Cogeneration Plants to Provide Reliable Continuous Steam Supply," *Cogeneration and Combined Cycle Plants, Design, Interconnection, and Turbine Applications*, presented at the ASME 1990 International Joint Power Conference, Boston, Oct. 21-25.

Downloaded 02 Jun 2010 to 171.66.16.122. Redistribution subject to ASME license or copyright; see http://www.asme.org/terms/Terms_Use.cfm

The Modular High-Temperature Gas-Cooled Reactor: A Cost/Risk Competitive Nuclear Option

H. L. Gotschall
Gas-Cooled Reactor Associates,
10240 Sorrento Valley Rd., Suite 300,
San Diego, CA 92121

The business risks of nuclear plant ownership are identified as a constraint on the expanded use of nuclear power. Such risks stem from the exacting demands placed on owner/operator organizations of current plants to demonstrate ongoing compliance with safety regulations and the resulting high costs for operation and maintenance. This paper describes the Modular High-Temperature Gas-Cooled Reactor (MHTGR) design, competitive economics, and approach to reducing the business risks of nuclear plant ownership.

Introduction

The National Academy of Engineering estimates a 60 percent growth in world-wide electricity consumption over the next thirty years, with the contribution from nuclear power expected to double [1]. Even though failure to meet energy needs will mean diminished standards of living for people in developed nations and the worsening of a marginal existence for those in third-world countries, it is by no means certain that the nuclear option will be in a position to fulfill the role identified for it. While the current generation of nuclear plants has established an impressive record of safe operation, the exacting demands placed on owner/operators to demonstrate ongoing compliance with safety regulations and the resulting high costs for operation and maintenance threaten to price the nuclear option out of the U.S. market. The cost and organizational strains associated with establishing and demonstrating ongoing regulatory compliance continue to be the dominant risks of U.S. nuclear plant ownership.

If nuclear power is to sustain and expand its role as an economic source of energy in the world market, advanced reactors must address these risks. A key innovative aspect of the Modular High-Temperature Gas-Cooled Reactor (MHTGR) is the extent to which reliance on passive features potentially shifts a substantial portion of the economic risks associated with demonstrating regulatory compliance from the plant owner/operator to the vendor/supplier where they can be more efficiently contained. Doing so will make the MHTGR an attractive option to a broad range of prospective owner/operators who may otherwise view the nuclear option as too demanding and risky.

A primary justification for proceeding with commercial MHTGR development in parallel with advanced light water reactor (ALWR) certification is its potential to establish an approach to safety regulation that significantly reduces the risks of nuclear plant ownership.

Contributed by the Nuclear Engineering Division and presented at the Joint Power Generation Conference, San Diego, California, October 6-10, 1991. Manuscript received by the Nuclear Engineering Division June 12, 1991. Associate Technical Editor: S. M. Cho.

Description of the MHTGR Plant

A philosophy underlying the MHTGR design concept is to facilitate the extensive use of conventional power plant equipment and practices based on the safety characteristics of the reactor. This requires that the unit size be limited and the reactor be configured so that fission products are retained within ceramic-coated fuel particles for the full range of licensing basis events. These functions are accomplished without reliance on operator actions and auxiliary power sources (other than batteries) such that safety-related equipment is limited to selected systems within and proximate to the reactor module.

The design under consideration within the U.S. Commercial MHTGR Program is rated at 450 MWt per module. A current description of the design with illustrations is available in [2]. The reactor components are contained within three steel vessels: a reactor vessel, a steam generator vessel, and a connecting cross vessel. The reactor vessel is approximately the same size as that of a large boiling water reactor and contains the core, reflector, and associated supports. Core reactivity is controlled through top-mounted penetrations that house the control rod drive mechanisms and the hoppers containing boron carbide pellets for reserve shutdown. These penetrations are also used as access for refueling and inspection.

The reactor core and the surrounding graphite neutron reflectors are supported on a steel core support plate at the lower end of the reactor vessel. The reactor core is an assembly of prismatic graphite fuel blocks with hexagonal cross sections. The fuel is in the form of coated particles of low-enriched fissile uranium oxycarbide. The fuel particles are bonded together to form fuel compacts that are contained in sealed vertical holes in the graphite fuel blocks. The fuel blocks are stacked in columns that form an annular core configuration. Unfueled graphite blocks fill the center and surround the active core to form the reflector.

Heat transfer during power operation or normal decay heat removal operation is accomplished by circulating helium coolant down through the core to the hot plenum. The helium then flows through a coaxial hot duct inside the cross vessel to a once-through helical bundle steam generator. After passing downward over the steam generator tubes, the cool helium is

Copyright © 1994 by ASME
Downloaded 02 Jun 2010 to 171.66.16.122. Redistribution subject to ASME license or copyright; see http://www.asme.org/terms/Terms_Use.cfm

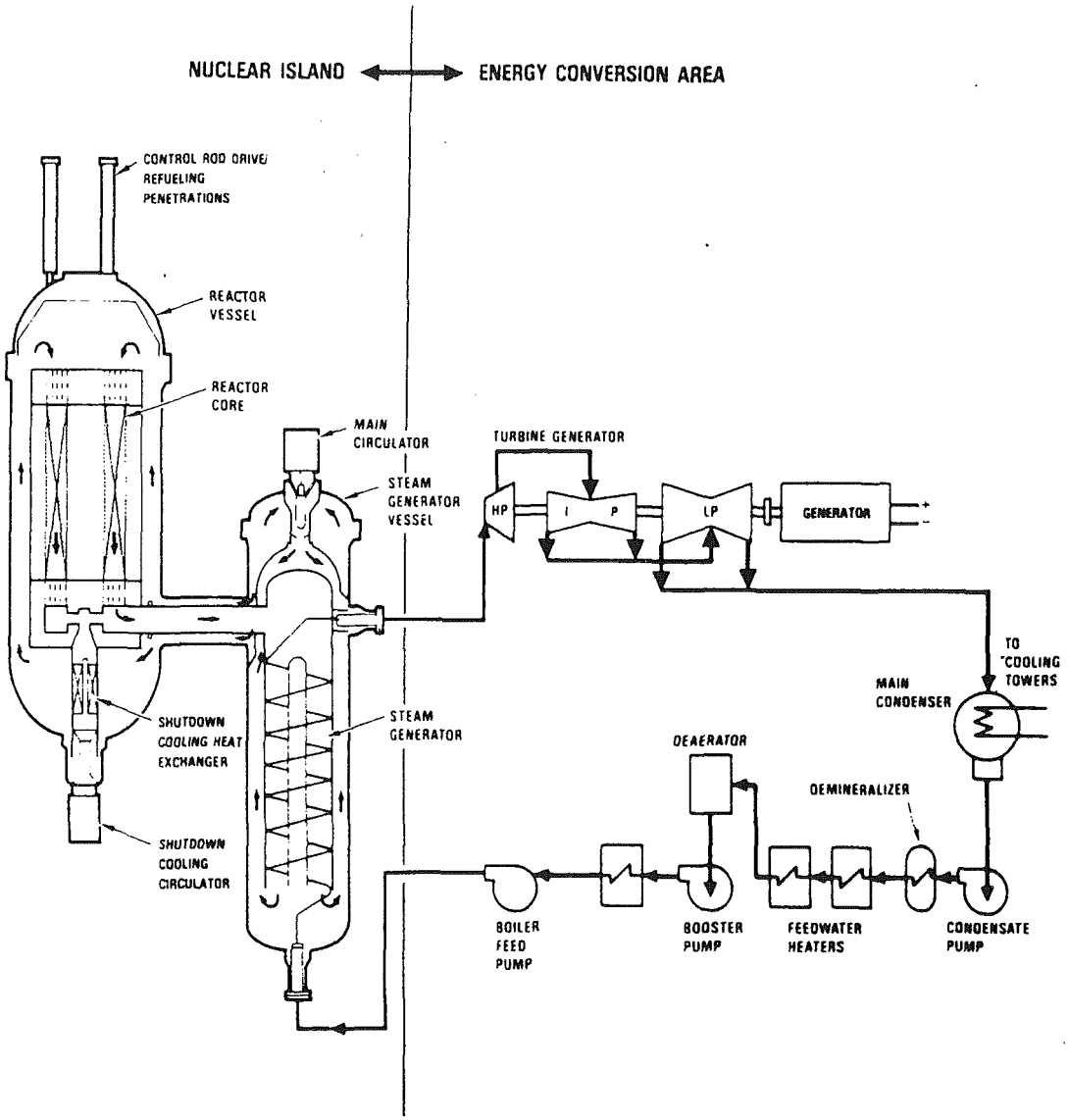


Fig. 1 MHTGR schematic flow diagram

channeled upward within the annulus between the steam generator vessel and shroud to the main circulator inlet.

The main circulator is a submerged electric motor-driven, two-stage axial compressor with active magnetic bearings. The helium is discharged from the circulator and flows through the annulus of the cross vessel and hot duct and then upward to the cold plenum above the core.

To enhance plant availability, a separate shutdown cooling system (SCS) is provided for rapid heat removal when the primary heat transport system requires maintenance. The heat exchanger and circulator for this system are mounted at the bottom of the vessel. Use of the system allows hands-on maintenance to begin within 24 hours after plant shutdown.

The reactor modules are individually housed in adjacent, but separate, reinforced concrete silo structures located below grade and covered by a common maintenance hall, as shown in Fig. 1. The below-grade location provides significant benefits by reducing the seismic amplifications typical of above-grade structures and lowering the plant profile. All components and systems for each module required to meet regulatory requirements are independent of other modules and are localized within the individual concrete structures.

An important aspect of the MHTGR safety concept is the capability to dissipate core decay heat passively to the atmosphere. Decay heat is transferred by conduction, convection, and radiation from the core to the reactor cavity cooling system (RCCS) located in the concrete silo structure. Using above-grade air intake structures, the RCCS channels naturally convect outside air down through the enclosed ducts and panels that line the below-grade reactor cavity. The warmed air is exhausted through return ducts to above-grade outflow structures. The RCCS operates continuously and requires no operator actions or active equipment.

The MHTGR plant design incorporates four functionally independent, reactor-module/turbine-generator power units. The plant consists of two separate well-defined areas, the Nuclear Island (NI) and the Energy Conversion Area (ECA). The reactor modules and all other safety-related and radionuclide control systems are located on the NI within a doubly fenced security boundary. The ECA envelopes plant facilities that are not on the NI. Since the plant has been designed to require no safety-related operator actions, the four reactor module-turbine generator power units are controlled from a single nonsafety-related control room located in the ECA. The prin-

Downloaded 02 Jun 2010 to 171.66.16.122. Redistribution subject to ASME license or copyright; see http://www.asme.org/terms/Terms_Use.cfm

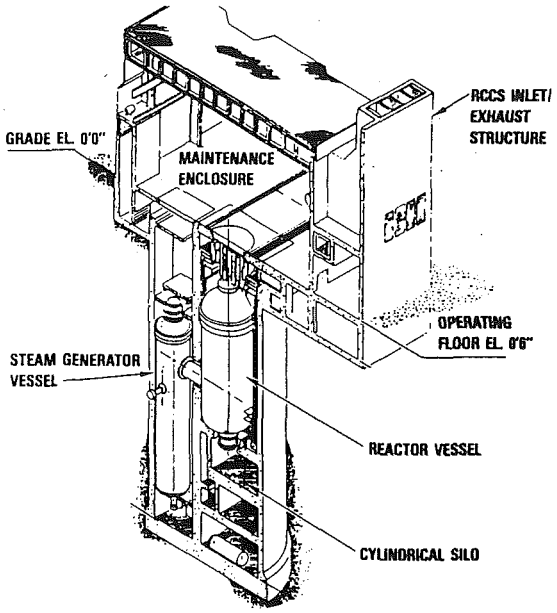


Fig. 2 MHTGR reactor building

cipal structures in the ECA are the operations center, which contains the nonsafety-related control room, the turbine generator building, and the station cooling towers.

Steam from each reactor module is supplied to an adjacent turbine generator in the ECA. The net energy conversion efficiency of each reactor-module/turbine-generator power unit is approximately 38.4 percent. Thus, each power unit is capable of independently producing a net output of 173 MWe. A simplified schematic flow diagram for a power unit is shown in Fig. 2. The MHTGR plant has a net electrical output of approximately 692 MWe. Key performance parameters for the recommended plant are summarized in Table 1.

The MHTGR safety concept provides defense-in-depth against the release of fission products. Fission products are retained by successive static structural barriers: the fuel particle coatings, the graphite matrix, the steel reactor module vessels, and the below-grade concrete silo. The reactor is configured such that the integrity of these barriers is ultimately protected by self-limiting reactor characteristics and passive systems; i.e.:

- If reactivity control systems (i.e., control rod and reserve boron carbide pellet systems) are unavailable, nuclear heat generation is limited by the reactor negative temperature coefficient.
- If all active cooling systems (i.e., the primary and shutdown cooling systems) are unavailable, decay heat is dissipated by conduction, convection, and radiation to the passive reactor cavity cooling system.
- The effects of chemical attack are controlled by the use of an inert coolant, helium, and the material properties of the fission product barriers.

This approach to nuclear safety is developmental, particularly with regard to assigning the principal fission product retention function to the fuel coatings.

Economic Assessment

MHTGR economic assessments are based on the assumption that the safety attributes will permit the extensive use of conventional equipment and practices. This section provides a summary comparison of projected economics for a mature commercial MHTGR plant with an alternative coal plant. Estimated costs are shown in greater detail in [2].

In accordance with Department of Energy (DOE) guidelines

Table 1 4 × 450 MWt MHTGR plant key performance parameters

Plant	
Number of power units	4
Thermal power	1800 MWt
Electrical output	692 MWe, Net
Net thermal efficiency	38.4 percent
Power unit	
Thermal power per unit	450 MWt
Electrical output per unit	173 MWe, net
Reactor module	
Core power density	6 W/CC
Helium inlet temperature	288°C (550°F)
Helium outlet temperature	704°C (1300°F)
Helium pressure	7.07 MPa (1025 psia)
Steam pressure	17.2 MPa (2500 psia)
Steam temperature	538°C (1000°F)
Feedwater pressure	23.8 MPa (3450 psia)
Feedwater temperature	193°C (380°F)

Table 2 4 × 450 MWt MHTGR target plant capital costs (1990$)

Total direct costs (M$)	721
Total indirect costs (M$)	278
Base construction costs	
Total (M$)	999
Total ($/KWe)	1444
Contingency (M$)	200
Total overnight costs	
Total (M$)	1199
Total ($/KWe)	1733
Interest during construction (M$)	171
Total capital cost	
Total (M$)	1370
Total ($/KWe)	1980

[3], a mature commercial plant is defined as corresponding to a cumulative deployed capacity of 4500 MWe. The competitive goal for this plant, termed the Target Plant, is that the evaluated mean busbar costs (30-year, constant dollar, levelized) will be 20 percent less than a comparably sized, reference coal plant. All cost estimates and analyses in this report are in accordance with DOE guidelines.

The financial structure and related parameters assumed for this assessment are representative of those for an investor-owned utility [3].

The MHTGR busbar cost includes the capital, nonfuel operation and maintenance (O&M), fuel and plant decommissioning expenses, and is expressed as cost per unit energy generation (mills/kWh). Details of these costs are discussed below.

Plant Capital Costs. Input to the capital cost estimate for the MHTGR Target Plant was provided by MHTGR Program contractors and integrated by Gas-Cooled Reactor Associates (GCRA). Capital costs for the reactor plant equipment (excluding vessels and heat exchangers) were developed by General Atomics. Vessel and heat exchanger costs were developed by ABB/Combustion Engineering Nuclear Power (ABB/CENP). Costs for the other capital expenditures (equipment, field labor, and field material) necessary to construct the NI were developed by Bechtel National, Inc. Costs for all the capital expenditures (equipment, field labor, and field material) necessary to construct the ECA were developed by Stone & Webster Engineering Corporation with support from ABB/CENP for the plant control system. GCRA developed the estimate of the owner's costs (project management, permit fees, taxes, insurance, staff training, etc.) that are incurred before plant startup and included in the plant capital cost.

The plant capital cost estimates are summarized in Table 2. In this table, the total of the cost accounts is identified as the base construction cost. A contingency is added to the base construction cost to develop the estimated total overnight cost.

Downloaded 02 Jun 2010 to 171.66.16.122. Redistribution subject to ASME license or copyright; see http://www.asme.org/terms/Terms_Use.cfm

Table 3 4 × 450 MWt MHTGR target plant O&M costs (1990M$/yr)

Staff salary and payroll taxes	15.3
Central support group participation	5.0
Maintenance materials (at 84 percent capacity factor)	6.1
Control rods and replaceable reflector)	4.2
Administrative and general costs	12.4
Total (M$/yr)	43.0

Table 4 4 × 450 MWt MHTGR target plant busbar costs (1990$)

Plant data	
Thermal power (MWt)	1800
Net electric rating (MWe)	692
Capacity factor (percent)	84
Cost data	
Total capital cost (M$)	1370
Levelized capital cost (M$/yr) (at 9.58 percent fixed charge rate)	131.0
O&M costs (M$/yr)	43.0
Fuel cycle cost (M$/yr)	51.2
Decommissioning costs (M$/yr)	3.6
Total revenue requirement (M$/yr)	228.8
Busbar cost (mills/KWh)	
Capital	25.8
O&M	8.4
Fuel	10.1
Decommissioning	0.7
Total (mills/KWh)	45.0

The contingency is developed at approximately the three-digit level of the cost estimate structure and summed for a single entry. The contingency adder establishes a 50 percent confidence level (most likely) cost estimate. An allowance for interest costs during construction (also known as Allowance for Funds Used During Construction, or AFUDC) is added to the overnight cost for the total capital cost estimate.

Nonfuel Operation and Maintenance Costs. The assessment of MHTGR O&M requirements is based on an evaluation performed by the GCRA Utility Working Group [4]. Key assumptions for the MHTGR Target Plant were that the expectations of the Nuclear Regulatory Commission (NRC), the Institute of Nuclear Power Operations (INPO), and nuclear insurers will have evolved as a result of earlier successful projects and that operational licensing requirements consistent with the following attributes will have been accepted:

- The off-site consequences of licensing basis events, including those attributable to operator error by omission or commission, are benign to the extent that planning for sheltering and evacuation of the public is not required.
- Licensing requirements are met without reliance on the control room, its contents, auxiliary power supply (other than batteries), or operator actions to mitigate accidents.
- The safety-related equipment to be maintained to current nuclear industry standards is limited to selected systems within and proximate to the reactor module and all other equipment may be maintained to commercial non-nuclear power plant standards.

As a result, it is estimated that an on-site operating staff of 335 personnel is required. Staff and other O&M costs are given in Table 3. A key assumption is that a central operational support group will have been formed to provide training and technical support services to member owner/operator organizations.

Fuel Cycle Costs. The fuel cycle costs are based on a three-year fuel cycle with half the core reloaded on an 18 month cycle. Fuel fabrication costs and fuel burnup costs were developed by General Atomics. The 30-year levelized fuel cycle costs for the target MHTGR plant applying the utility ownership parameters and nuclear fuel cost parameters in [3] are, in terms of 1990 mills/kWh, as follows: fabrication—3.71, fuel—5.34 and waste—1.00, for a total of 10.05.

Table 5 Reference 640 MWe coal plant capital cost estimate (1990$/KWe)

Direct costs	1033
Indirect costs (w/o owner's)	267
Owner's costs	130
Total overnight costs	1430
AFUDC	211
Total capital cost ($/KWe)	1641

Decommissioning Costs. A decommissioning scoping cost estimate of $135M (1990$) was projected for the MHTGR plant design based on a review of current decommissioning cost estimates and the unique characteristics of the MHTGR. Funding for decommissioning was assumed to be accumulated during a plant's economic life by means of an external sinking fund.

Busbar Costs. The levelized busbar cost results are given in Table 4. It is noted that these costs assume a capacity factor of 84 percent. This figure is based on GCRA's evaluation of historical turbine plant availability data that showed an incremental advantage of approximately four percentage points for four small (~150 MWe) versus one large (~600 MWe) turbine-generator(s) for the MHTGR. Reactor designers identified no barriers to achieving a corresponding level of performance. This incremental difference in capacity factor is used in comparisons with fossil options using a single turbine-generator configuration.

MHTGR Economic Competitiveness

The economic competitiveness assessment is based on comparison of the MHTGR busbar generation costs with a comparably sized conventional pulverized coal plant. By the turn of the century, escalation of fuel cost is expected to render oil- or gas-fired plants less economic than coal. Coal-fired plants that employ alternative combustion technologies, such as the fluidized bed, are expected to be competitive, but current cost projections do not indicate these plants will be more economic than the conventional pulverized coal plant.

A reference coal plant size was selected to have the same thermal power rating as the MHTGR plant. The MHTGR plant has a thermal power rating of 1800 MWt (4 × 450) and produces about 692 MWe. An 1800 MWt pulverized coal plant would produce about 640 MWe based on a representative thermal efficiency of about 35.5 percent (9600 Btu/kWh heat rate).

The reference coal plant capital cost estimate was determined from detailed estimates developed by DOE [5], and the Electric Power Research Institute (EPRI) [6], plus actual plant cost results. Since plant capital costs are somewhat dependent on plant location, a single site was selected for comparison of the plant costs. This site is the hypothetical "Middletown" site located in the Northeastern United States. The resultant reference coal plant costs are given in Table 5.

The reference coal plant O&M cost estimate was determined using DOE guidelines [3], as was the reference delivered cost of coal ($1.70/MBtu in 1990$), which is intended to be representative of high-sulfur coal for the Middletown site. The real escalation rate (i.e., escalation in excess of inflation) of coal was set at 1 percent/year.

Using the same guidelines, the cost estimate for decommissioning a 640 MWe coal plant is approximately $14 million (1990$).

A comparison of the busbar costs for the 4 × 450 MWt MHTGR plant with the coal plant is given in Table 6. The

Downloaded 02 Jun 2010 to 171.66.16.122. Redistribution subject to ASME license or copyright; see http://www.asme.org/terms/Terms_Use.cfm

Table 6 4 × 450 MWt MHTGR target plant comparison with coal (1990$)

	1800 MWt MHTGR	1800 MWt Coal
Electric rating (MWe)	692	640
Capacity factor (percent)	84	80
Total capital costs		
Total (M$)	1370	1050
Total ($/kWe)	1980	1641
Busbar costs (mills/KWh)		
Capital	25.8	23.0
O&M	8.4	7.9
Fuel	10.1	22.1
Decommissioning	0.7	0.1
Total (mills/KWh)	45.0	53.0

goal for the Target Plant is a 30-year levelized busbar cost advantage of 20 percent less than coal. The evaluated economic margin for the 4 × 450 MWt MHTGR plant relative to the reference coal plant is reasonably close to the goal. For the reference coal cost and real escalation rate, the MHTGR has about a 15 percent cost advantage. This advantage increases with increasing coal costs and real escalation, and decreases when these factors decrease. A parametric analysis of the effect of these factors on the MHTGR's busbar cost advantage is given in Fig. 3.

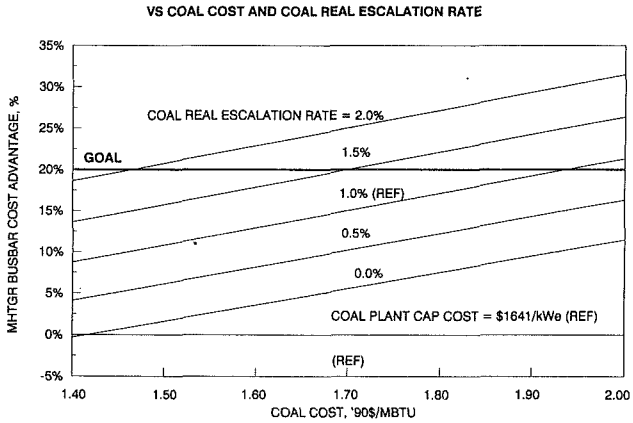


Fig. 3 4 × 450 MWt MHTGR target plant economic advantage versus coal cost and coal real escalation rate

Reducing the Risks of Nuclear Plant Ownership

While there is a wide variation in the degree of success experienced with current nuclear plants, average data show that nuclear lost its historical production cost advantage over coal about three years ago and the gap is widening. When production costs are added to fixed costs, the capital cost intensive nuclear plants are far more expensive than coal [6]. In 1988, the EPRI Nuclear Power Division Advisory Committee held round table discussions to identify the reasons for O&M cost increases. The primary factor was related to nuclear safety regulations and utility response to those regulations, which have led to large corporate and plant staffs [8]. A valid concern is that further O&M cost increases can preclude the nuclear option.

Further, the discipline and vigilance required to establish and continuously verify the ongoing safety of current nuclear plants have placed utility personnel in extremely high-stress working environments. Current plants have been found to be very exacting, requiring progressive levels of checks, audits and signoffs, all corroborated by voluminous records documenting strict adherence to quality control standards during essentially all aspects of plant operation and maintenance. In some cases, more than 30 percent of the plant staff is dedicated to training, and it has been necessary to make radical changes to satisfy NRC and INPO expectations with regard to steps taken to instill discipline and rigor. These factors all combine to create a rigidity that stifles individual initiative, reduces plant availability, and increases overhead on plant operating costs. Unfortunately, nuclear plant ownership has often meant imposing changes on previously successful corporate cultures. The prospect that it may be necessary to reorganize the owner/operator corporate structure and culture to accommodate a nuclear plant represents a business risk that is difficult to quantify in monetary terms, but one that has a profound bearing on the future of the industry.

While the industry at large and all advanced nuclear programs are addressing these issues, a conclusion within GCRA is that a major incentive for MHTGR deployment is its potential for reducing the costs and risks associated with nuclear plant operational licensing requirements. Because current plants rely on multiple active systems and field constructed fission product barriers, heavy emphasis is placed on the regulation of construction, operation, and maintenance activities. While off-site functions such as design, materials procurement, and component fabrication of safety systems are also subject to regulatory purview, plant safety is ultimately dependent on the integrated performance of various, often complex, systems and structures at the plant. Consequently, the regulation of field activities pertaining to the plant as a whole has been particularly intense. Experience has shown that this approach is prone to financial risks since each location entails a unique combination of owner, site, project organization, labor supply and public interest groups. This requires each nuclear project to face anew the challenges of developing disciplined field and plant organizations and establishing rigorously documented proof of compliance with regulations.

Whereas the primary focus for nuclear safety regulation of current plants is on activities at the plant site, the MHTGR concept permits a shift in regulatory focus to the off-site manufacture of passive components and systems. Two key aspects of the MHTGR safety concept contribute to the technical basis for this shift. First, the MHTGR relies on successive static structural barriers to provide defense-in-depth against the release of fission products. Challenges to those barriers are limited by plant operating systems; and their integrity is ultimately protected by passive, self-limiting reactor characteristics that control heat generation and dissipation. As a result, the MHTGR approach to defense-in-depth permits relatively greater emphasis to be placed on design verification, which can be accomplished as an element of design certification testing and not repeated at each installation. Moreover, because of the reduced scope of plant equipment subject to regulatory purview and the relative simplicity of safety system and component interfaces, risks associated with nuclear safety regulations in replicating the design at dispersed sites are minimized.

The second aspect of the MHTGR safety concept that reduces risks of noncompliance with nuclear regulations at the site is the fact that both the first and second principal fission product barriers can be factory fabricated to nuclear standards. The nuclear safety function of the first principal barrier, the ceramic coatings on the fuel kernel, is to prevent the release of fission products. While the technology to manufacture ceramic-coated fuel to the necessary quality level is developmental, the intent is to produce fuel encapsulated in ceramic coatings with structural integrity verifiable in the fashion of a nuclear-grade vessel bearing an ASME N-stamp. The second principal fission product barrier, the reactor vessel, serves nuclear safety functions for both the prevention and mitigation of fission product releases. Its preventive functions include control of reactor core geometry (heat generation) by static structural forces and control of peak core temperatures (heat dissipation) by radiative heat transfer. The reactor vessel also provides an impermeable boundary for the mitigation of any fission product releases from the coated fuel particles.

Downloaded 02 Jun 2010 to 171.66.16.122. Redistribution subject to ASME license or copyright; see http://www.asme.org/terms/Terms_Use.cfm

In summary, key aspects of the MHTGR safety concept permit regulations to focus on offsite design verification and the factory fabrication of the fuel and components. This approach reduces the scope of on-site operating functions subject to nuclear safety regulation and emphasizes the monitoring and inspection of the fuel and passive systems and components, most of which will be automated. Accordingly, the need for staff and equipment trained and poised for rapid intervention of nuclear incidents is dramatically reduced. Similarly, reducing the scope of safety-related plant equipment reduces exposure to sabotage and the extent of areas within the plant subject to security restrictions. As a result, freedom of movement about the plant is enhanced, as is the productivity of maintenance labor. The MHTGR safety concept simplifies the means by which safety functions are accomplished and reduces the burden of demonstrating compliance with regulations.

For the MHTGR, the implications of this are twofold: (*a*) The focus of sophisticated, high-technology labor and stringent regulations can reside in the corporate cultures of the fuel and reactor suppliers, which are more readily adapted to the discipline and rigor required for reliable nuclear safety than that of the diverse owner/operator industry, and (*b*) the organizational capability and culture of the owner/operator organization can be more nearly on a par with that required for non-nuclear options.

An additional business risk mitigation aspect of the MHTGR is the capability it provides the owner/operator to add relatively small increments of power (i.e., 173 MWe). This attribute results as a by-product of limitations placed on unit size to provide for fission product retention within the fuel particle coatings as noted previously. This feature allows the owner/operator a greater degree of flexibility in adapting planned capacity additions to external factors such as changes in load growth or financial circumstances. It also enhances overall system reliability since relatively small increments of generation capacity require less reserve margin.

Conclusions

At its early state of design development, the MHTGR Target Plant is assessed to be reasonably close to its economic goal of a 20 percent busbar cost advantage relative to coal. A key distinguishing feature is its potential to reduce the risk of nuclear plant ownership. For this outcome to be realized, it will be necessary to:

- Develop the capability to manufacture ceramic-coated fuel in commercial quantities of the quality required for its fission product containment function and to define the role of the regulator in that process.
- Conduct reactor development and demonstration testing as an element of NRC design certification.
- Establish the fuel and reactor module vendor/supplier infrastructure.
- Mount a systematic effort, sustained throughout design development and initial projects, to evolve regulatory provisions appropriate to the MHTGR.

Once the extensive use of conventional power plant equipment and practices is established, the MHTGR will offer a cost/risk competitive nuclear option to a broad range of owner/operators. Additional factors contributing to this conclusion are (*a*) the flexibility offered by the MHTGR to add generation capacity in small increments and (*b*) the increasing complexity and risk confronting fossil options as a result of more stringent regulation of emissions.

References

1 "Energy, Production, Consumption and Consequences," National Academy of Engineering, 1990.

2 "Utility/User Requirements for and Assessment of the Modular High Temperature Gas-Cooled Reactor," Gas-Cooled Reactor Associates Report 91-002, June 1991.

3 "Cost Estimate Guidelines for Advanced Nuclear Power Technologies," Oak Ridge National Laboratory Report TM-1007/R2, Mar. 1990.

4 "Utility Projections of Operation and Maintenance Costs for Modular HTGR Plants," Gas-Cooled Reactor Associates Report 90-005, Mar. 1990.

5 "Nuclear Energy Cost Data Base," Department of Energy Report NI-0095, Sept. 1988.

6 "TAG™, Technical Assessment Guide," Electric Power Research Institute Report P-6587-L, Vol. 1, Revision 6, Sept. 1989.

7 "Rising O&M Costs May Impede Nuclear Power Revival," *Power Engineering Magazine*, Mar. 1991.

8 Marston, T. U., "Nuclear Power Plant Cost Control," Electric Power Research Institute, Apr. 5, 1989.

Downloaded 02 Jun 2010 to 171.66.16.122. Redistribution subject to ASME license or copyright; see http://www.asme.org/terms/Terms_Use.cfm

R. Yokoyama
Associate Professor.
Mem. ASME

K. Ito
Professor.
Mem. ASME

Department of Energy Systems Engineering,
University of Osaka Prefecture,
1-1, Gakuen-cho, Sakai,
Osaka, 593 Japan

Y. Matsumoto
Manager,
Technical Research Center,
The Kansai Electric Power Company, Inc.,
3-11-20, Nakoji, Amagasaki,
Hyogo, 661 Japan

Optimal Sizing of a Gas Turbine Cogeneration Plant in Consideration of Its Operational Strategy

An optimal planning method is proposed for the fundamental design of cogeneration plants. Equipment capacities and utility maximum demands are determined so as to minimize the annual total cost in consideration of the plants' annual operational strategies for the variations of both electricity and thermal energy demands. These sizing and operational planning problems are formulated as a nonlinear programming problem and a mixed-integer linear programming problem, respectively. They are solved efficiently in consideration of their hierarchical relationship by a penalty method. A numerical example about a gas turbine plant is given to ascertain the validity and effectiveness of the proposed method.

Introduction

As dispersed and small-scale energy systems, cogeneration plants have been introduced increasingly for commercial and public purposes in Japan. In order to utilize their high economical and energy-saving potentials, planners are urged to propose good plans for the fundamental design of cogeneration plants. For example, it is considered an important subject to determine rationally equipment capacities and utility maximum demands, especially capacities of prime movers and a maximum demand of purchased electricity. This is because if the capacities of prime movers are underestimated, the effect of introducing cogeneration plants becomes relatively small, and contrarily if they are overestimated, the availability of prime movers decreases. However, this subject is very difficult to solve since it is necessary to take account of the plants' annual operational strategies for the variations of both electricity and thermal energy demands.

At present, a trial and error method is used conventionally to determine plants' sizes; i.e., economical and energy-saving properties are evaluated only for several alternatives regarding equipment capacities and utility maximum demands, among which the best alternative is selected. Additionally, the thermal- or electric-following strategies are adopted conventionally as operational strategies for prime movers. These conventional approaches have the disadvantage that the high economical and energy saving potentials cannot necessarily be utilized. Therefore, it is necessary to develop a rational method of determining plants' sizes and operational strategies.

From the above-stated viewpoint, the authors first proposed an optimal planning method of determining the operational strategies of cogeneration plants, and ascertained its effectiveness by carrying out case studies on several types of gas turbine plants (Ito et al., 1987, 1988, 1990a, 1990b; Ito and Yokoyama, 1989). However, it appears that there is no rational and practical method of determining the plants' sizes. For example, several authors proposed optimization approaches to the plant sizing by taking account of only a few energy demand patterns (Papoulias and Grossmann, 1983; Johnson et al., 1985; Horii et al., 1987). However, these approaches cannot apply directly to the sizing of cogeneration plants for commercial and public purposes, because the energy demands fluctuate seasonally and hourly, and it is necessary to consider hundreds of energy demand patterns.

The purpose of the present paper is to develop an optimal planning method of determining the sizes of cogeneration plants in consideration of their annual operational strategies. First, the main factors to be taken into account at the fundamental design stage are categorized, and the concept of the optimal planning method is described. Secondly, the optimization problem is formulated concretely for a simple cycle gas turbine cogeneration plant. Lastly, a numerical example is given about a plant used for district heating and cooling.

Optimal Planning Method

Main Factors in Fundamental Design. Economic or energy-saving properties are often used as evaluation criteria in the fundamental design of cogeneration plants, and they are influenced by many factors. Figure 1 shows these main factors categorized into (*a*) plant, (*b*) input energy, (*c*) output energy, (*d*) energy management, and (*e*) environment. These factors should be taken into account comprehensively. In this paper, the factors with the symbol ● or ◆ are regarded as design

Contributed by the International Gas Turbine Institute and presented at the International Cogen-Turbo Symposium and Exposition, Budapest, Hungary, September 3-5, 1991. Manuscript received at ASME Headquarters August 1992. Associate Technical Editor: L. A. Riekert.

Copyright © 1994 by ASME
Downloaded 02 Jun 2010 to 171.66.16.122. Redistribution subject to ASME license or copyright; see http://www.asme.org/terms/Terms_Use.cfm

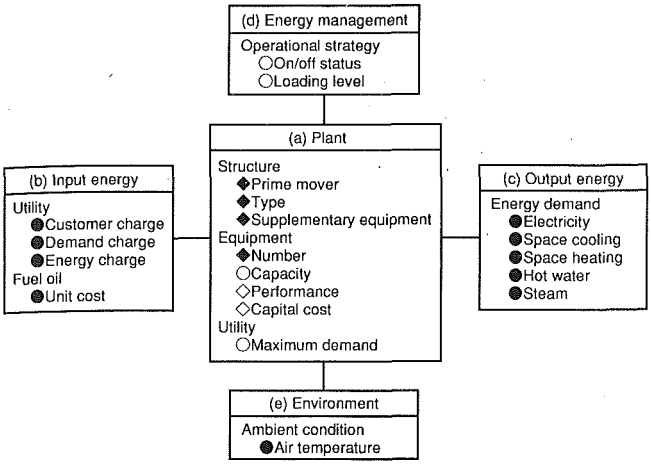


Fig. 1 Main factors to be taken into account in the fundamental design of cogeneration plants

specifications, those with ○ as design items to be determined in the design process, and those with ◇ as design characteristics to be determined together with the design items. Namely, equipment capacities and utility maximum demands are determined together with the plant's operational strategy for a given plant structure, utility tariff, energy demand, and ambient condition. Though the factors with ◆ are treated as design specifications here, they may also be regarded as design items. In this case, there exist many configurations regarding the plant structure. The method to be proposed is used to determine the size for each configuration and to select the best one.

Basic Concept of Optimal Planning Method. In this paper, the annual total cost is minimized from the viewpoint of long-term economics. It is evaluated as the sum of the annual capital cost and annual running cost on the basis of the annualized costs method (Witte et al., 1988). The annual capital cost of each piece of equipment is considered a function of its capacity. The annual running cost of each utility is the sum of the customer/demand charges and energy charge. The demand charge is considered a function of the utility maximum demand, and the energy charge is calculated from the plant's operational strategy.

As constraints, it is necessary to consider performance characteristics of each piece of equipment and energy balance relationships of each energy flow for average hourly energy demands estimated on several representative days in one year. In addition to the average energy demands, peak energy demands in summer and winter must be considered for equipment to supply energy during the peak periods. Here, since performance characteristics of equipment change with the capacities, they should be considered as functions of the capacities.

Design variables are composed of equipment capacities and utility maximum demands in the sizing problem, and the variables expressing the operational strategy in the operational planning problem. Though the capacity of each piece of equipment is selected from a set of discrete values in the practical design, it is regarded as a continuous variable in this paper. The operational strategy is expressed by the binary and continuous variables, which correspond to the on/off status of operation and energy flow rates, respectively (e.g., Ito et al., 1990a).

Hierarchical Optimization by Penalty Method. As stated in the introduction, the above planning problem is a large-scale and complex one since it includes the annual operational problem. It takes much computation time to optimize all the design variables simultaneously. In order to solve the problem efficiently, we propose a hierarchical optimization method: Equipment capacities and utility maximum demands are determined at the upper level; the operational strategy is assessed at the lower level; both levels are interconnected with each other by a penalty method.

This hierarchical optimization procedure is shown in Fig. 2. At the upper level, the optimal sizing problem is formulated as a nonlinear programming problem, in which optimal values of equipment capacities and utility maximum demands are searched so as to minimize the annual total cost. The constraints stated above are not taken into account explicitly, and only the constraints are considered that force virtual energy flows not to arise. At the lower level, for a plant with the

Nomenclature

Equipment symbols (subscripts)

- BA = gas-fired auxiliary boiler
- BW = waste heat recovery boiler
- EP = equipment for purchasing electricity
- GT = gas turbine generator
- PC = pump for supplying cold water
- RE = electric compression refrigerator
- RS = steam absorption refrigerator

Energy quantities

- E = electric power, MWh/h
- F = natural gas consumption (measured at standard conditions), m^3/h
- Q = heat flow rate, MWh/h

Other symbols

- C = initial capital cost of equipment, yen
- C_c = annual capital cost, yen/y
- C_d = annual customer and demand charges, yen/y
- C_e = annual energy charge, yen/y
- C_f = annual total cost, yen/y
- h = limit ratio of heat disposal to exhaust heat
- i = interest rate
- N = number of equipment installed
- p, q, r, s = performance characteristic values of equipment
- R = capital recovery factor
- v = ratio of salvage value to initial capital cost of equipment
- δ = binary variable expressing on/off status of operation
- η = size parameter of equipment
- κ = life of equipment, y
- λ = penalty cost, yen/MWh, yen/m^3
- φ = unit cost of utility energy charge, yen/MWh, yen/m^3
- Ψ = unit cost of utility customer charge, yen/month
- ψ = unit cost of utility demand charge, yen/(MW·month), yen/(m^3/h·month)
- $\overline{(\ )}$, $\underline{(\ )}$ = upper and lower bounds, respectively

Superscripts

- a = auxiliary machinery
- c = space cooling
- d = demand
- s = steam

Subscripts

- buy = purchased electricity
- disp = heat disposal
- gas = natural gas
- n = index for each piece of equipment
- PT = virtual energy flow

Downloaded 02 Jun 2010 to 171.66.16.122. Redistribution subject to ASME license or copyright; see http://www.asme.org/terms/Terms_Use.cfm

equipment capacities and utility maximum demands given at each searching step, the operational strategy is assessed and the annual energy charge is evaluated. In this paper, the operational strategy is assessed using an optimal operational planning method proposed by the authors (e.g., Ito et al., 1990a). Here, it may be done using such a conventional strategy as thermal- or electric-following strategies. In this procedure, virtual energy flows are added to the energy flows actually existing for any plant given at each searching step to satisfy the energy demands. The virtual energy flows play the role that they supply energy additionally only if the plant is too small to satisfy the energy demands. For that purpose, a penalty cost is imposed on the occurrence of virtual energy flows. At the upper level, given information about the occurrence of virtual energy flows, the design variables change their values automatically so as not to cause the virtual energy flows, or so as to satisfy the energy demands.

The introduction of this penalty method reduces drastically the number of design variables to be determined simultaneously, and consequently enables us to solve efficiently the sizing problem in consideration of the operational planning problem. The sequential linear programming method is adopted as a solving method of the nonlinear programming problem (Cheney and Goldstein, 1959). The optimal operational planning problem is formulated as a mixed-integer linear programming problem, and it is solved by the branch and bound method (Garfinkel and Nemhauser, 1972). The concrete algorithm adopted here is based on the Land–Doig method (Land and Doig, 1960).

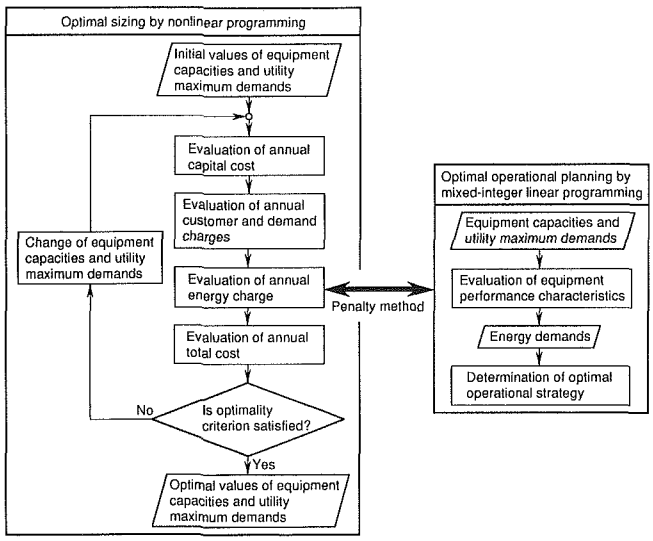


Fig. 2 A hierarchical algorithm of determining plants' sizes and operational strategies

Formulation for a Gas Turbine Plant

For a simple cycle gas turbine cogeneration plant, the optimal sizing problem is formulated together with the optimal operational planning problem.

Plant Structure. Figure 3 illustrates the structure of the plant investigated as an example. Equipment symbols are explained in the nomenclature. Although only one unit is illustrated for each kind of equipment, there may be several units. Solid lines, dot-dash lines, two dots-dash lines, dotted lines, and broken lines denote the flows of steam, electricity, cold water, exhaust gas, and natural gas, respectively. Bold arrows denote the virtual energy flows. An energy quantity is defined for each energy flow.

Electricity is supplied to users by the parallel running of gas turbine generators and purchasing electricity from an outside electric power company. Electricity is also used to drive electric compression refrigerators, pumps, and other auxiliary machinery in the plant. Exhaust heat generated by the gas turbines is recovered by waste heat recovery boilers, and it is reused for several kinds of thermal energy in a cascade way. The surplus exhaust heat is disposed of through the exhaust gas damper. The shortage of steam is supplemented by gas-fired auxiliary boilers. Cold water for space cooling is supplied by electric compression and steam absorption refrigerators. Steam is used for space heating and other miscellaneous purposes.

The capacities of each kind of equipment except the pumps are determined optimally together with the maximum demands of purchased electricity and natural gas. Here, it is assumed that the capacity of equipment for purchasing electricity is equal to the electricity maximum demand.

Optimal Sizing Problem. As stated above, the annual energy demands are satisfied by imposing constraints on the annual maximum values of virtual energy flows. That is, the constraints are expressed by

$$\left.\begin{aligned} \max_t E_{PT} \le 0 \\ \max_t Q^c_{PT} \le 0 \\ \max_t Q^s_{PT} \le 0 \\ \max_t F_{PT} \le 0 \end{aligned}\right\}, \tag{1}$$

where $\max_t$ means the annual maximum value.

The objective function is formulated in the following way. The annual capital cost of equipment C_c is expressed by

$$\begin{aligned} C_c = \{R(1-v)+iv\}\{&N_{GT}C_{GT}(\eta_{GT}) + N_{BW}C_{BW}(\eta_{BW}) \\ &+ N_{BA}C_{BA}(\eta_{BA}) + N_{RE}C_{RE}(\eta_{RE}) + N_{RS}C_{RS}(\eta_{RS}) \\ &+ C_{EP}(\eta_{EP})\}, \end{aligned} \tag{2}$$

where N is the number of pieces of equipment installed, C and η are respectively the initial capital cost and the size parameter

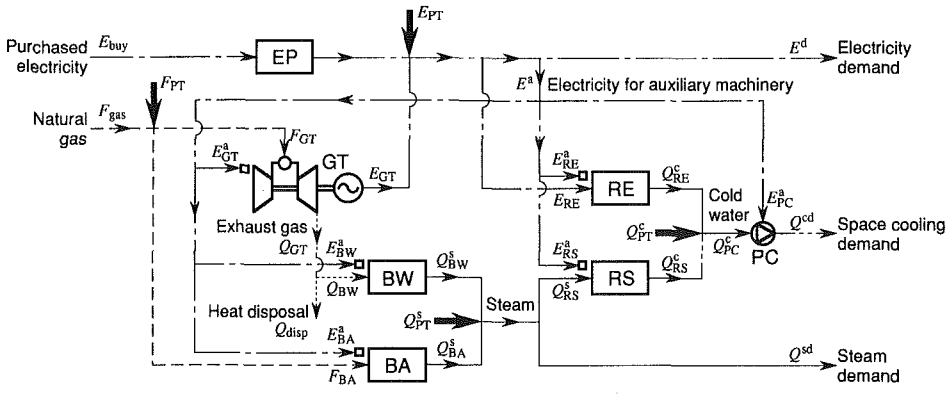


Fig. 3 Structure of a simple cycle gas turbine cogeneration plant

Downloaded 02 Jun 2010 to 171.66.16.122. Redistribution subject to ASME license or copyright; see http://www.asme.org/terms/Terms_Use.cfm

Table 1 Tariff of purchased electricity and natural gas

Utility	Unit cost		
	Customer charge	Demand charge	Energy charge
Purchased electricity	–	$\psi_{buy} = 1.74$ $\times 10^6$ yen/(MW•month)	$\varphi_{buy} = \begin{cases} 10.77 & \text{(July–Sept.)} \\ 9.79 & \text{(Other months)} \end{cases}$ $\times 10^3$ yen/(MWh)
Natural gas	$\Psi_{gas} = 36.0$ $\times 10^3$ yen/month	$\psi_{gas} = \begin{cases} 1.20 & \text{(Apr.–Oct.)} \\ 3.20 & \text{(Other months)} \end{cases}$ $\times 10^3$ yen/(m^3/h•month)	$\varphi_{gas} = 30.88$ yen/m^3

of each piece of equipment, v is the ratio of salvage value to initial capital cost, and i is the interest rate. The capital recovery factor R is defined by

$$R = i(1+i)^\kappa / \{(1+i)^\kappa - 1\}, \tag{3}$$

where κ is the life of the equipment. In Eq. (2), it is assumed that the values of v and κ are common to all kinds of equipment, and that several pieces of the same capacity are installed for each kind of equipment. The annual running cost is calculated as the sum of the customer/demand charges and the energy charge of purchased electricity and natural gas. Since there is the variety of tariff regarding these utilities, it is difficult to formulate the annual running cost generally. For the tariff shown in Table 1, for example, the customer/demand charges C_d and the energy charge C_e are respectively formulated as follows:

$$C_d = \sum_m \psi_{buy} \bar{E}_{buy} + \sum_m \Psi_{gas} + \sum_m \psi_{gas} \bar{F}_{gas} \tag{4}$$

and

$$C_e = \sum_t \varphi_{buy} E_{buy} + \sum_t \varphi_{gas} F_{gas}, \tag{5}$$

where $\bar{E}_{buy}$ and $\bar{F}_{gas}$ are, respectively, the maximum demands of purchased electricity and natural gas, and Ψ, ψ, and φ are, respectively, the unit costs of customer, demand, and energy charges. Symbols $\sum_m$ and $\sum_t$ denote the summations over annual total months and hours, respectively. As a result, the annual total cost C_t, the objective function to be minimized, is defined by

$$C_t = C_c + C_d + C_e. \tag{6}$$

The size parameters η_{GT}, η_{BW}, η_{BA}, η_{RE}, η_{RS}, η_{EP}, and the utility maximum demands $\bar{E}_{buy}$, $\bar{F}_{gas}$ are determined so as to minimize the objective function in Eq. (6), subject to the constraints in Eq. (1). In this procedure, the values of virtual energy flows in Eq. (1) and utility consumptions in Eq. (5) are calculated from the operational strategy. Any quantities may be adopted as size parameters, if they are representative of capacities. For example, maximum outputs are satisfactory as size parameters.

Optimal Operational Planning Problem. On the basis of the optimal operational planning method, the operational strategy is assessed so as to minimize the hourly energy charge for the given energy demands. The objective function in this problem is consistent with that in the optimal sizing problem. The following equations are fundamentally the same as those used in the optimal operational planning method (e.g., Ito et al., 1990a), and only a short comment is given here.

Performance characteristics are first formulated for each kind of equipment as follows:

Gas turbine generator

$$\left.\begin{aligned} &E_{GTn} = p_{GT}(\eta_{GT}) F_{GTn} + q_{GT}(\eta_{GT}) \delta_{GTn} \\ &Q_{GTn} = r_{GT}(\eta_{GT}) F_{GTn} + s_{GT}(\eta_{GT}) \delta_{GTn} \\ &E^a_{GTn} = p^a_{GT}(\eta_{GT}) F_{GTn} + q^a_{GT}(\eta_{GT}) \delta_{GTn} \\ &\underline{F}_{GT}(\eta_{GT}) \delta_{GTn} \le F_{GTn} \le \bar{F}_{GT}(\eta_{GT}) \delta_{GTn} \\ &\delta_{GTn} \in \{0, 1\} \end{aligned}\right\} \quad (n = 1, \ldots, N_{GT}) \tag{7}$$

Waste heat recovery boiler

$$\left.\begin{aligned} &Q^s_{BWn} = p_{BW}(\eta_{BW}) Q_{BWn} + q_{BW}(\eta_{BW}) \delta_{BWn} \\ &E^a_{BWn} = p^a_{BW}(\eta_{BW}) Q_{BWn} + q^a_{BW}(\eta_{BW}) \delta_{BWn} \\ &\underline{Q}_{BW}(\eta_{BW}) \delta_{BWn} \le Q_{BWn} \le \bar{Q}_{BW}(\eta_{BW}) \delta_{BWn} \\ &\delta_{BWn} \in \{0, 1\} \end{aligned}\right\} \quad (n = 1, \ldots, N_{BW}) \tag{8}$$

Gas-fired auxiliary boiler

$$\left.\begin{aligned} &Q^s_{BAn} = p_{BA}(\eta_{BA}) F_{BAn} + q_{BA}(\eta_{BA}) \delta_{BAn} \\ &E^a_{BAn} = p^a_{BA}(\eta_{BA}) F_{BAn} + q^a_{BA}(\eta_{BA}) \delta_{BAn} \\ &\underline{F}_{BA}(\eta_{BA}) \delta_{BAn} \le F_{BAn} \le \bar{F}_{BA}(\eta_{BA}) \delta_{BAn} \\ &\delta_{BAn} \in \{0, 1\} \end{aligned}\right\} \quad (n = 1, \ldots, N_{BA}) \tag{9}$$

Electric compression refrigerator

$$\left.\begin{aligned} &Q^c_{REn} = p_{RE}(\eta_{RE}) E_{REn} + q_{RE}(\eta_{RE}) \delta_{REn} \\ &E^a_{REn} = p^a_{RE}(\eta_{RE}) E_{REn} + q^a_{RE}(\eta_{RE}) \delta_{REn} \\ &\underline{E}_{RE}(\eta_{RE}) \delta_{REn} \le E_{REn} \le \bar{E}_{RE}(\eta_{RE}) \delta_{REn} \\ &\delta_{REn} \in \{0, 1\} \end{aligned}\right\} \quad (n = 1, \ldots, N_{RE}) \tag{10}$$

Steam absorption refrigerator

$$\left.\begin{aligned} &Q^c_{RSn} = p_{RS}(\eta_{RS}) Q^s_{RSn} + q_{RS}(\eta_{RS}) \delta_{RSn} \\ &E^a_{RSn} = p^a_{RS}(\eta_{RS}) Q^s_{RSn} + q^a_{RS}(\eta_{RS}) \delta_{RSn} \\ &\underline{Q}^s_{RS}(\eta_{RS}) \delta_{RSn} \le Q^s_{RSn} \le \bar{Q}^s_{RS}(\eta_{RS}) \delta_{RSn} \\ &\delta_{RSn} \in \{0, 1\} \end{aligned}\right\} \quad (n = 1, \ldots, N_{RS}) \tag{11}$$

Pump for supplying cold water

$$\left.\begin{aligned} &E^a_{PCn} = p^a_{PC} Q^c_{PCn} + q^a_{PC} \delta_{PCn} \\ &\underline{Q}^c_{PC} \delta_{PCn} \le Q^c_{PCn} \le \bar{Q}^c_{PC} \delta_{PCn} \\ &\delta_{PCn} \in \{0, 1\} \end{aligned}\right\} \quad (n = 1, \ldots, N_{PC}) \tag{12}$$

In these equations, for each kind of equipment the capacity of which is to be determined, performance characteristic values and lower/upper bounds of input energy are expressed as functions of the size parameter η.

From Fig. 3, energy balance and supply-demand relationships are formulated for each energy flow as follows:

Electricity

$$\left.\begin{aligned} &\sum_{n=1}^{N_{GT}} E_{GTn} + E_{buy} + E_{PT} = \sum_{n=1}^{N_{RE}} E_{REn} + E^a + E^d \\ &E^a = \sum_{n=1}^{N_{GT}} E^a_{GTn} + \sum_{n=1}^{N_{BW}} E^a_{BWn} + \sum_{n=1}^{N_{BA}} E^a_{BAn} \\ &\qquad + \sum_{n=1}^{N_{RE}} E^a_{REn} + \sum_{n=1}^{N_{RS}} E^a_{RSn} + \sum_{n=1}^{N_{PC}} E^a_{PCn} \end{aligned}\right\} \tag{13}$$

Exhaust gas

$$Q_{GTn} = Q_{BWn} + Q_{dispn} \quad (n = 1, \ldots, N_{GT}(=N_{BW})) \tag{14}$$

Downloaded 02 Jun 2010 to 171.66.16.122. Redistribution subject to ASME license or copyright; see http://www.asme.org/terms/Terms_Use.cfm

Table 2 Annual total and hourly maximum values of energy demands

	Annual total value GWh/y	Hourly maximum value MWh/h
Electricity	73.29	20.56
Space cooling	27.28	31.54
Steam	31.24	28.84

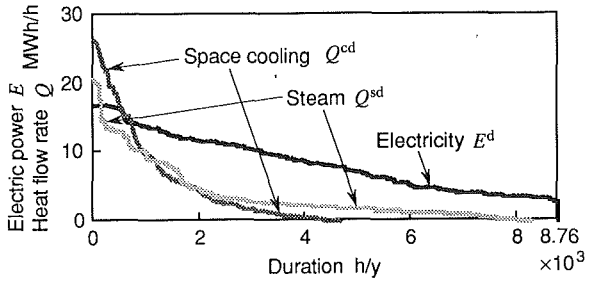


Fig. 4 Load duration curves for energy demands

Steam

$$\sum_{n=1}^{N_{BW}} Q^{s}_{BWn} + \sum_{n=1}^{N_{BA}} Q^{s}_{BAn} + Q^{s}_{PT} = \sum_{n=1}^{N_{RS}} Q^{s}_{RSn} + Q^{sd} \quad (15)$$

Cold water

$$\sum_{n=1}^{N_{RE}} Q^{c}_{REn} + \sum_{n=1}^{N_{RS}} Q^{c}_{RSn} + Q^{c}_{PT} = \sum_{n=1}^{N_{PC}} Q^{c}_{PCn} = Q^{cd} \quad (16)$$

Natural gas

$$F_{gas} + F_{PT} = \sum_{n=1}^{N_{GT}} F_{GTn} + \sum_{n=1}^{N_{BA}} F_{BAn} \quad (17)$$

In addition, the following relationships must be satisfied between maximum demands and consumptions of utilities:

Electricity

$$E_{buy} \le \overline{E}_{buy} \quad (18)$$

Natural gas

$$F_{gas} \le \overline{F}_{gas} \quad (19)$$

The hourly energy charge, the objective function to be minimized, is expressed by

$$\varphi_{buy} E_{buy} + \varphi_{gas} F_{gas} + \lambda (E_{PT} + Q^{c}_{PT} + Q^{s}_{PT} + F_{PT}), \quad (20)$$

where λ is the penalty cost, and it should be given a value much larger than the values of utility costs φ_{buy} and φ_{gas} in the numerical calculation.

The operational strategy is determined so as to minimize the objective function in Eq. (20), subject to the constraints in Eqs. (7)–(19). If a given plant satisfies the annual energy demands, all values of the penalty terms in Eq. (20) become zeros, and the constraint in the optimal sizing problem, Eq. (1), is satisfied. Otherwise, the penalty terms have a positive value, and consequently Eq. (1) is violated. However, in this optimization algorithm, the equipment capacities and utility maximum demands change their values automatically so as to satisfy Eq. (1).

Numerical Example

Input Data. The effectiveness of the proposed method is investigated through a numerical example about a simple cycle gas turbine cogeneration plant for district heating and cooling. In the district considered here, four office buildings and two hotels are to be constructed. The total floor area is about 384,000 m^2. For simplicity, it is assumed that the plant begins to supply energy to all buildings at the same time. Table 2

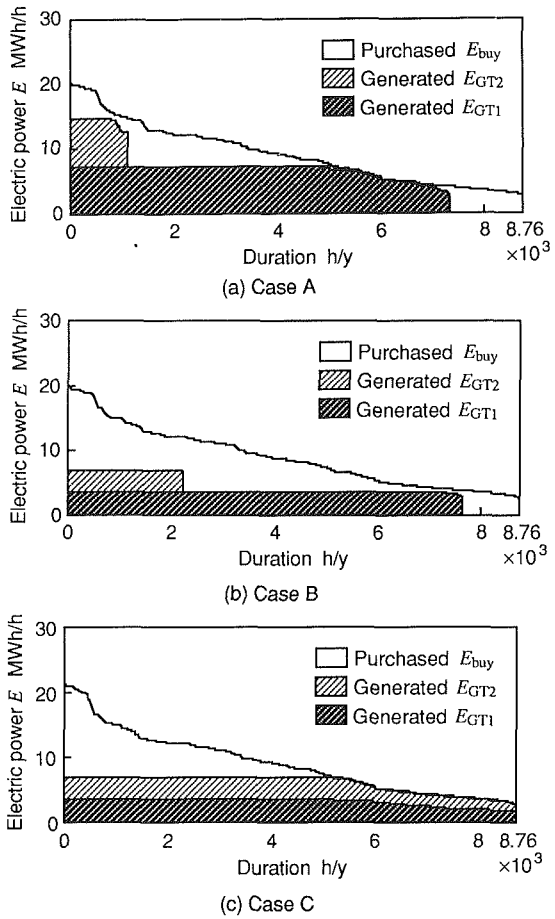


Fig. 5 Load duration curves for electricity supply

gives the annual total and hourly maximum values of electricity, space cooling, and steam demands. Figure 4 shows the load duration curves indicating the annual variations of hourly energy demands. Here, a weekday, a Saturday, and a holiday are considered representative days for each month; i.e., the operational strategy is investigated on 36 representative days throughout one year. Hourly energy demands are given as input data for each representative day. In addition to these average energy demands, peak energy demands in summer and winter are also given by multiplying the average energy demands on a weekday in August and January by 1.2, respectively. The functions expressing performance characteristic values and initial capital costs of equipment are determined from the actual data using the curve-fitting by the least squares method. The values shown in Table 1 are used for the tariff of purchased electricity and natural gas. In evaluating the annual capital cost, it is assumed that the ratio of salvage value to initial capital cost $v = 0$, the interest rate $i = 0.1$, and the life $\kappa = 15$ y.

The economical merits of cogeneration plants can be divided into three parts; i.e., they are due to (*a*) introduction of cogeneration plants, (*b*) optimal operational planning, and (*c*) optimal sizing. Here, these merits are evaluated separately by carrying out the following four case studies:

Case A: cogeneration plant with its size determined optimally by considering its optimal operational strategy

Case B: cogeneration plant with its size given a priori by considering its optimal operational strategy

Case C: cogeneration plant with its size given a priori by using the conventional electric-following strategy

Case D: conventional plant composed of a gas-fired auxiliary boiler and a steam absorption refrigerator

Downloaded 02 Jun 2010 to 171.66.16.122. Redistribution subject to ASME license or copyright; see http://www.asme.org/terms/Terms_Use.cfm

Table 3 Values of equipment capacities and utility maximum demands

Case			A	B	C	D
Plant			Cogeneration			Conventional
Size			Optimal	Nonoptimal		
Operational strategy			Optimal	Optimal	Electric-following	–
Equipment capacity	Gas turbine generator	$\overline{E}_{GT}$ MW	7.34	3.50	3.50	–
	Waste heat recovery boiler	$\overline{Q}^{s}_{BW}$ MW	13.22	7.26	7.26	–
	Gas-fired auxiliary boiler	$\overline{Q}^{s}_{BA}$ MW	2.41	14.34	14.34	28.84
	Electric compression refrigerator	$\overline{Q}^{c}_{RE}$ MW	0.17	5.82	5.82	–
	Steam absorption refrigerator	$\overline{Q}^{c}_{RS}$ MW	31.37	25.73	25.73	31.54
Utility maximum demand	Purchased electricity	$\overline{E}_{buy}$ MW	9.54	18.27	18.27	26.10
	Natural gas	$\overline{F}_{gas}$ $\times 10^3$ m^3/h	4.70	3.76	3.76	2.77

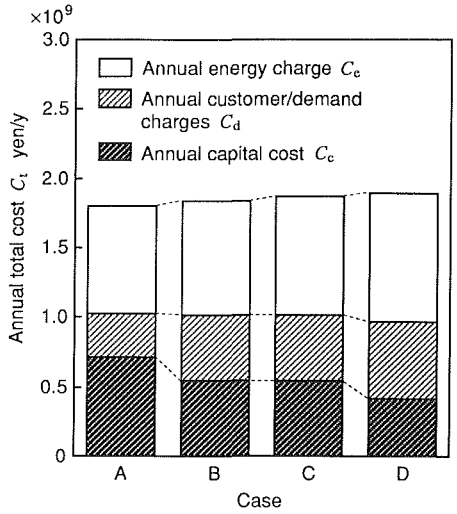


Fig. 6 Annual total cost and its items

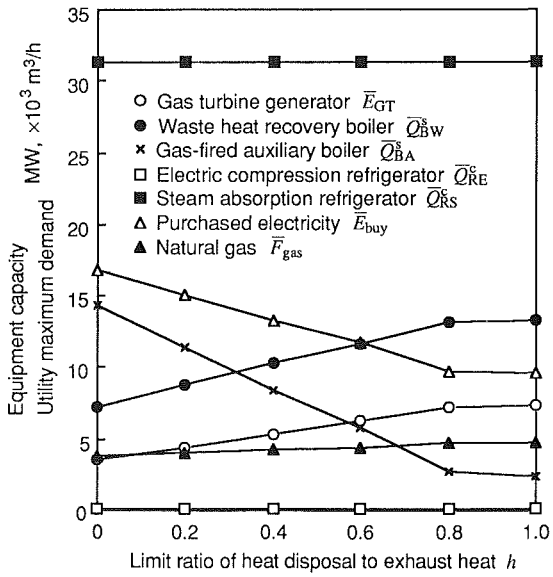


Fig. 7 Relationship between limit on heat disposal and optimal values of equipment capacities and utility maximum demands

It is assumed that two pairs of gas turbine generator/waste heat recovery boiler are installed in cases A to C, and that one unit is installed for other kind of equipment in all cases.

Results and Discussion. Table 3 shows the values of equipment capacities and utility maximum demands determined optimally for case A, and those values given a priori for cases B to D. For example, the capacity of gas turbine generators is discussed here. This value in case A is about twice as large as that in cases B and C. This result is understood from the annual operational strategy in the following way. Figure 5 shows the load duration curves for electricity supply, and (*a*) to (*c*) correspond to cases A to C, respectively. In case C, both gas turbine generators operate at base load status. In cases A and B, though the first gas turbine generator operates at base load status, the second one operates only at peak demand times. This is because by adopting the optimal operational strategy the second one stops so as not to dispose of a large amount of exhaust heat at times with low thermal energy demands. Additionally, the generating efficiency of gas turbine generators tends to increase with their capacity, and contrarily the thermal efficiency of exhaust heat recovery tends to decrease. As seen from Fig. 4, both space cooling and steam demands are relatively small as compared with the electricity demand in this district. Thus, in adopting the optimal operational strategy, gas turbine generators of larger capacity match this demand pattern.

Figure 6 shows the annual capital cost and its items for each case. In case D, though the annual capital cost is lower than those in other cases, the demand charge is higher because of a high maximum demand of purchased electricity, and the energy charge is also higher because of the conventional energy supply. In case C, in spite of a high capital cost, the introduction of the cogeneration plant leads to the reduction of both the demand and energy charges. In case B, the annual capital cost and the customer/demand charges are equal to those in case C, the energy charge decreases owing to the adoption of the optimal operational strategy. In case A, the annual total cost decreases further by optimizing both the plant's size and operational strategy. As a result, the reduction rate of annual total cost in cases A, B, and C to that in case D are 5.07, 3.43, and 1.50 percent, respectively. The differences in the annual total cost between cases C and D, B and C, A and B are due to the above-stated economical merits (*a*) to (*c*), respectively. This result shows that the economical merits can be obtained not only by introducing cogeneration plants but also by planning them optimally using the proposed method.

Although the result shown in Table 3 is determined optimally from the viewpoint of long-term economics, it is not satisfactory from the energy saving viewpoint. Namely, the capacity of gas turbine generators are so large that a large amount of exhaust heat must be disposed of. Hence, the optimization calculation is carried out again by adding the constraint that limits the heat disposal

$$Q_{dispn} \leq h\overline{Q}_{GTn} \quad (n = 1, \ldots, N_{GT}) \tag{21}$$

to the optimal operational planning problem. In Eq. (21), h is the limit ratio of heat disposal to exhaust heat generated from the gas turbine. Figure 7 shows the effect of the limit ratio h on the optimal values of equipment capacities and utility maximum demands. The constraint in Eq. (21) has little effect on the optimal values in the range of $0.8 \leq h \leq 1.0$. This is because a part of exhaust heat from the gas turbines is usually used for thermal energy supply. In the range of $h < 0.8$, however, the capacity of gas turbine generators decreases with

Downloaded 02 Jun 2010 to 171.66.16.122. Redistribution subject to ASME license or copyright; see http://www.asme.org/terms/Terms_Use.cfm

the limit ratio h. At the point of $h = 0$, the capacity becomes about a half of that without limit on heat disposal. This result shows that the plant's size should be determined rationally by considering its operational strategy carefully.

Conclusions

An optimal planning method for the fundamental design of cogeneration plants has been proposed on the basis of the mathematical programming. The optimal sizing problem of determining equipment capacities and utility maximum demands has been described together with the optimal operational planning problem of determining the plants' annual operational strategies. An algorithm by a penalty method has been given to solve these problems efficiently in consideration of their hierarchical relationship. Through a numerical example about a simple cycle gas turbine cogeneration plant, it has turned out that equipment capacities and utility maximum demands can be determined rationally and easily by the proposed method. It has also proved that economical merits are not only due to introduction of cogeneration plants but also due to optimal sizing and operational planning by the method.

Although this paper has dealt with a numerical example only about a simple cycle gas turbine cogeneration plant, the proposed method applies not only to other types of gas turbine plants but also to plants with different prime movers. In addition to optimal planning by the method, it is important to accumulate, analyze, and arrange the data on performance characteristics of equipment and energy demands for various categories of buildings. It appears that these activities lead to significant findings on the fundamental design of cogeneration plants.

References

Cheney, E. W., and Goldstein, A. A., 1959, "Newton's Method for Convex Programming on Tchebycheff Approximation," *Numerical Mathematics*, Vol. 1, pp. 253–268.

Garfinkel, R. S., and Nemhauser, G. L., 1972, *Integer Programming*, Wiley, New York, pp. 5–7.

Horii, S., Ito, K., Pak, P. S., and Suzuki, Y., 1987, "Optimal Planning of Gas Turbine Cogeneration Plants Based on Mixed-Integer Linear Programming," *International Journal of Energy Research*, Vol. 11, pp. 507–518.

Ito, K., Yokoyama, R., Horii, S., Matsumoto, Y., and Akagi, S., 1987, "An Optimal Operational Planning Model for Gas Turbine Cogeneration Plants," *Proc. of the 1987 Tokyo International Gas Turbine Congress*, Vol. I, pp. 97–104.

Ito, K., Yokoyama, R., Yamaguchi, T., Matsumoto, Y., and Akagi, S., 1988, "Optimal Operational Planning of a Gas Turbine Combined Heat and Power Plant Based on the Mixed-Integer Programming," *Proc. of the IFAC International Symposium on Power Systems Modelling and Control Applications*, pp. 13.4.1–13.4.7.

Ito, K., and Yokoyama, R., 1989, "Economic Feasibility Study of Some Cogeneration Plants for a Local Energy Center," *Proc. of the IFAC/IFORS/IAEE International Symposium on Energy Systems, Management and Economics*, pp. 181–186.

Ito, K., Yokoyama, R., Akagi, S., and Matsumoto, Y., 1990a, "Influence of Fuel Cost on the Operation of a Gas Turbine-Waste Heat Boiler Cogeneration Plant," ASME JOURNAL OF ENGINEERING FOR GAS TURBINES AND POWER, Vol. 112, pp. 122–128.

Ito, K., Yokoyama, R., and Matsumoto, Y., 1990b, "Optimal Operation of Cogeneration Plants With Steam Injected Gas Turbines," *Proc. of the 4th International Symposium and Exposition on Gas Turbines in Cogeneration, Repowering, and Peak-Load Power Generation*, pp. 93–100.

Johnson, S. M., Stubington, J. F., and Wood, R. M., 1985, "Cogeneration Plant Optimisation," *Chemeca 85*, pp. 371–376.

Land, A. H., and Doig, A. G., 1960, "An Automatic Method of Solving Discrete Programming Problems," *Econometrica*, Vol. 28, pp. 497–520.

Papoulias, S. A., and Grossmann, I. E., 1983, "A Structural Optimization Approach in Process Synthesis—I, Utility Systems," *Computers and Chemical Engineering*, Vol. 7, pp. 695–706.

Witte, L. C., Schmidt, P. S., and Brown, D. R., 1988, *Industrial Energy Management and Utilization*, Hemisphere Publ., Washington, DC, pp. 68–69.

Downloaded 02 Jun 2010 to 171.66.16.122. Redistribution subject to ASME license or copyright; see http://www.asme.org/terms/Terms_Use.cfm

Evaluation of Brayton and Rankine Alternatives for Diesel Waste Heat Exploitation

J. B. Woodward
Professor,
Naval Architecture & Marine Engineering,
University of Michigan,
Ann Arbor, MI 48109-2145

A diesel engine may produce exhaust-gas thermal energy in excess of that needed for turbocharging. Alternatives for exploitation of the energy by producing work may be direct expansion through a gas turbine (completing a Brayton cycle that begins with the engine's compression and combustion), or transfer of heat into a Rankine cycle. It is demonstrated that either alternative may have a domain in which it is superior in work done, or in exhaust volume per unit mass of diesel exhaust. Computation models are developed and demonstrated for finding the boundaries along which the Rankine and Brayton alternatives have equal merit in either work or exhaust volume.

Introduction

In a paper published in the JOURNAL OF ENGINEERING FOR GAS TURBINES AND POWER, Professor E. W. Beans (1990) establishes a basis for comparing the merits of Rankine and Brayton power cycles in circumstances where both may be candidates for the same application. Professor Beans makes the point that in spite of obvious differences, these two cycles share many features, and then develops a common mathematical model by which their relative merits can be judged.

The Beans analysis has a high degree of generality, and hence is valuable over a wide range of analyses, but it does have its limitations. For example, his Rankine analyses are limited to cycles that exhaust on the steam saturation line. This paper is not an attempt at a general improvement of his work; rather, the paper outlines a kindred method that is intended for use only within one limited area where Rankine versus Brayton competition exists. Because the method is less bound by the need to be general, it may offer greater insight and better accuracy within its limited area.

Area of Concern

The concern of this paper is the exploitation of the energy in diesel engine exhaust that exceeds the requirements of the turbocharger (Tanaka et al., 1985). This concern frequently appears with medium- and low-speed marine propulsion engines (Woodward, 1981), a particular diesel application that serves as the model for the exposition here.

Absent an excessively long stroke, a diesel cylinder cannot expand its working fluid to atmospheric pressure. In many familiar instances, the cylinder exhausts at a somewhat higher pressure into a gas turbine (an element of the turbocharger, of course). The gas turbine in turn exhausts at atmospheric pressure, but at a temperature on the order of several hundred degrees C above atmospheric. In some instances, the hot turbine exhaust gas is then used as the heat source for a Rankine bottoming cycle.

Advances in turbocharger efficiency have brought about circumstances in which the turbine does not require all of the energy available to it, particularly in the case of large (20,000 kW and up, roughly) low-speed marine engines. Some of the cylinder exhaust gas may therefore be diverted to other uses. If this excess gas is to be exploited, then two alternatives are offered:

1 Transfer the thermal energy of the excess gas to a Rankine bottoming cycle. The additional shaft work drives a generator, or may be added to the propulsion shaft work.
2 Expand the excess gas through a gas turbine that is in parallel with the turbocharger. The output of this turbine may also drive a generator, or may be added to the propulsion shaft work.

The use of a Rankine bottoming cycle downstream of the turbocharger is a long-established practice in marine propulsion. When that cycle is present, then the first alternative has the obvious merit of requiring no additional hardware, although components of higher rating may be required. The second requires additional hardware—the turbine itself, as well as piping and an extensive drive train. Nonetheless, the second alternative is the overwhelming favorite when marine engineering practice calls for exploitation of this bonus energy.

Weight and cost of hardware are factors in the choice between alternatives, but several thermodynamic factors are prominent, namely efficiency (i.e., fraction of exploitable energy converted to work) and volume flow rate of working fluid. Examination of these latter factors and their relative merits is the topic of this paper.

Thermodynamic Merits of the Brayton and Rankine Alternatives

Let's first note that the comparison to be made here is not

Contributed by the Advanced Energy Systems Division for publication in the JOURNAL OF ENGINEERING FOR GAS TURBINES AND POWER. Manuscript received by the Advanced Energy Systems Division June 28, 1991; revision received February 21, 1992. Associate Technical Editor: M. J. Moran.

Copyright © 1994 by ASME
Downloaded 02 Jun 2010 to 171.66.16.122. Redistribution subject to ASME license or copyright; see http://www.asme.org/terms/Terms_Use.cfm

truly between the two *cycles*. In the gas turbine alternative, the compression and heat addition processes of the power cycle are carried out in a diesel cylinder, and hence their parameters are not available for manipulation in the way the Rankine cycle pressures and temperatures are. Omitting the word "cycle" to speak of "Brayton alternative" and Rankine alternative" is therefore appropriate.

Because constant-pressure turbocharging is the universal practice for the low-speed diesels where waste-heat exploitation is most often used, the kinetic energy of cylinder exhaust gas is taken to be negligible. As a consequence, the availability of the gas is found to consist only of pressure and temperature components. Because the temperature component is by far the larger, the gas is referred to hereafter as the"heat source." In all calculations it is treated as a perfect gas with the properties of air. The objective to be pursued is conversion of the largest possible fraction of the pressure/temperature availability of this gas into work, while observing other possibly significant consequences such as volume flow rates.

Two measures of merit by which the alternatives are to be judged are therefore offered:

1 The fraction of the source availability converted to work.
2 The value at turbine exhaust of a volume parameter. The parameter used is volume of exhaust per unit mass of the heat source. For the Brayton alternative, this parameter is simply the working fluid specific volume; for the Rankine alternative it is the working fluid specific volume multiplied by the mass ratio of working fluid rate to heat source fluid rate.

Source Availability Converted to Work. In evaluating the first of these measures, the most direct approach is to calculate the work per unit mass of heat source done by each of the competing turbines. However, at this stage of the discussion it is more appropriate to take an indirect approach, namely to find the work by subtracting irreversibilities from the source availability. This approach more fully illuminates the reason why one alternative is superior to the other, and suggests the differing circumstances under which the other might be superior.

Four irreversibilities are to be found. They are caused by:

1 Temperature difference between the heat source and the turbine working fluid.
2 Unexploited availability remaining in the heat source after transfer of heat to the turbine working fluid.
3 Inefficiency of the turbine.
4 Availability remaining in discarded turbine working fluid.

With the Brayton alternative, the first two of these are zero since the turbine working fluid and the heat source are identical. With the Rankine alternative, the first two are always nonzero, since a finite temperature difference must appear between heat source and Rankine working fluid, since it is impractical to cool the heat source to the surrounding temperature, and since it is impractical to exploit the pressure component of heat-source availability. The third is always nonzero for both because turbine efficiencies are always less than 1.00; however, it is taken as zero here because the competing efficiencies are not likely to be greatly different, and affect the alternatives in about the same way. With the Rankine alternative, the fourth is always nonzero because a temperature difference must occur between condensing working fluid and the surroundings. With the Brayton alternative, the fourth is usually nonzero because the working fluid exhausting from the turbine is usually hotter than the surroundings. However, the Brayton exhaust temperature may equal the surrounding temperature, making this irreversibility zero.

An example illustrates the differing impact of the irreversibilities on the two alternatives. The irreversibilities are labeled I_1, I_2, etc., with the numbering matching the list used above.

General data for diesel exhaust heat source		
Pressure		0.20 MPa (2 atm)
Temperature		400°C
Surrounding temperature, pressure		25°C, atmospheric
Availability at above state		191.2 kJ/kg
Alternative data	Brayton	Rankine
Turbine inlet pressure	0.20 MPa	2.0 MPa
Turbine inlet temperature	400°C	212.4°C (saturated)
Pinch temperature difference	NA	30°C
Turbine exhaust pressure	atmospheric	0.007 MPa
Turbine efficiency	100 percent	100 percent
Results		
Working fluid mass ratio	1.0	0.0834 kg/kg source
I_1	0	25.7
I_2	0	89.3
I_3	0	0
I_4	70.3	6.8
Sum of irreversibilities	70.3	121.8
Work	120.9	69.4
Fraction, work/source availability	0.632	0.364

The methods of calculation employ standard textbook formulas (Van Wylen and Sonntag, 1965); they are outlined in Appendix 1.

The Brayton alternative is clearly superior in this example. Indeed, other examples would show this same superiority over a fairly wide range of heat source states. The listing of irreversibilities shows the cause: The Rankine alternatives suffers from two large irreversibilities that are always zero for its competitor. This circumstance may lead an observer to believe that the Brayton alternative is inherently superior in its efficiency. On the other hand, the fact that the high irreversibilities occur at different places for the two alternatives leads one to investigate heat source states different from that of the example, yet within the bounds of possibility. Are there such states that will show lower Rankine irreversibilities simultaneously with higher Brayton irreversibility? A repeat of the

Nomenclature

°C = degrees Celsius
c_p = constant-pressure specific heat, kJ/kg K
$f(\ )$ = function of
h = enthalpy, kJ/kg
I = irreversibility
k = ratio of specific heats
K = degrees Kelvin
m = mass ratio, kg working fluid to kg heat source
P = pressure, MPa
R = gas constant, N-m/kg K
T = temperature, °C or K
v = specific volume, m^3/kg
$\mathbf{u}$ = exhaust volume parameter, m^3/kg of heat source
w = work, kJ/kg of heat source
α = any constant
Δ = difference
η = efficiency
λ = $(k - 1)/k$
ξ = any system parameter value
ϕ = isentropic temperature ratio
ψ = availability
ω = any independent variable

Subscripts

B = Brayton
ex = exhaust state
fp = saturated liquid state at beginning of evaporation
p = pinch, as in pinch temperature difference
R = Rankin
sat = saturated state
so = source
stm = steam
0 = surrounding state

Downloaded 02 Jun 2010 to 171.66.16.122. Redistribution subject to ASME license or copyright; see http://www.asme.org/terms/Terms_Use.cfm

example with a heat source at higher temperature and lower pressure demonstrates the possibility.

General data for diesel exhaust heat source		
Pressure		0.15 MPa (1.5 atm)
Temperature		600°C
Surrounding temperature, pressure		25°C, atmospheric
Availability at above state		289.2 kJ/kg
Alternative data	Brayton	Rankine
Turbine inlet pressure	0.15 MPa	4.0 MPa
Turbine inlet temperature	600°C	250.4°C (saturated)
Pinch temperature difference	NA	30°C
Turbine exhaust pressure	atmospheric	0.007 MPa
Turbine efficiency	100 percent	100 percent
Results		
Working fluid mass ratio	1.0	0.1865 kg/kg source
I_1	0	34.7
I_2	0	68.9
I_3	0	0
I_4	193.7	14.6
Sum of irreversibilities	193.7	118.2
Work	95.5	171
Fraction, work/source availability	0.330	0.591

In the second example the temperature difference between heat source and Rankine working fluid is a much smaller fraction of the temperature difference between heat source and heat sink, causing the irreversibilities I_1 and I_2 to be a smaller burden on Rankine performance. The worsening of the Brayton alternative is obvious in the large increase in irreversibility I_4, a circumstance caused by a poor match between throttle pressure and temperature. This mismatch causes the turbine exhaust temperature to be higher than before, thus increasing the availability of the fluid that is thrown away by exhausting to the atmosphere.

Turbine Exhaust Volume. Specific volume of turbine exhaust is a major determinator of sizes of heat exchangers, pipes, and of the turbine itself. Since the mass flow rate of working fluid per unit of heat source is usually quite different in the two alternatives, a comparison of specific volumes only is insufficient. The parameter of comparison used here (symbolized **u**) is therefore the volume of turbine exhaust per unit mass of heat source. Using data from the examples just completed produces the following results:

	First example		Second example	
	Brayton	Rankine	Brayton	Rankine
Turbine exhaust volume per unit mass of heat source, m^3/kg	1.48	1.28	2.22	2.26

The volume parameter is not greatly different in either example, but the reversal of order in the outcome is also illustrated.

The Alternatives Compared

The example in which the Brayton work fraction is so evidently superior uses heat-source values that might be found with a low-speed marine diesel, and hence is the more typical of propulsion plants where bottoming cycles are used. This circumstance, plus the unique burdens that the irreversibilities I_1 and I_2 present to the Rankine alternative, underlie the widely held (but undocumented) belief that the Brayton alternative is inherently superior. However, higher exhaust temperatures are typical of high-speed engines. The second example therefore suggests that there indeed may be an exhaust state domain in which the Rankine alternative is the favored competitor. An investigation more general than random examples is therefore justified; the results for work/availability fraction over a wide range of heat source pressures and temperatures are presented

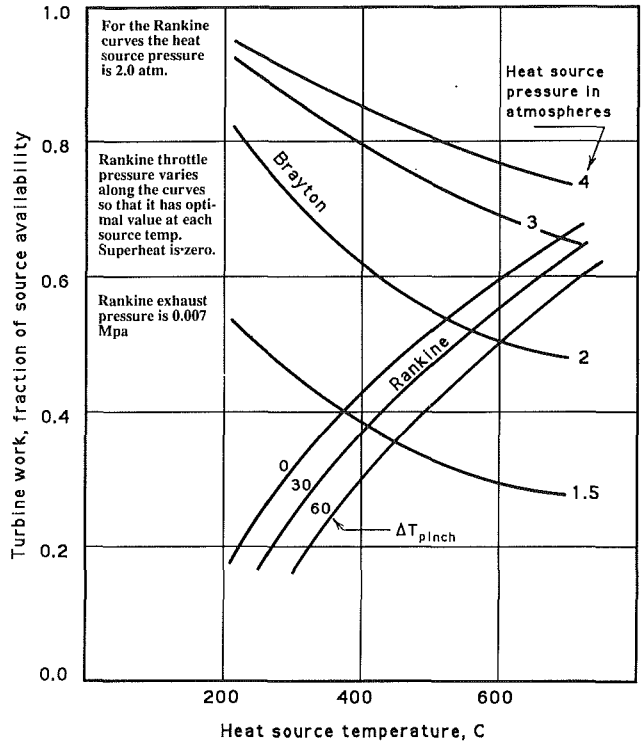


Fig. 1 Fraction of heat source availability converted to shaft work by Brayton and Rankine alternatives

by Fig. 1. The domains in which each alternative is superior are quite evident in this figure.

The effect of some variables found in Rankine cycle analysis are not evident in Fig. 1. They are noted, and their absence justified, following:

1 Throttle pressure. For a given heat source temperature, and with other variables held constant, a throttle pressure at which the work fraction is a maximum can be found. For the heat source temperature range shown in the figure, that pressure (with no superheat) ranges from approximately 1.5 mPa at the low end to 4.0 MPa at the other. The throttle pressure varies along the curves of Fig. 1, with the best value being used at each point. The Rankine curves may thus be described as "turbine work fraction at throttle pressures that are optimal for the stated heat source temperature."

2 Exhaust pressure. The turbine work fraction is a strong function of exhaust pressure. The curves of Fig. 2 are plotted for a pressure of 0.007 MPa, assumed to be about the lowest practicable for a Rankine bottoming cycle. The effect of variation is to be treated when a matching of Brayton and Rankine work fractions is explored in a later section.

3 Superheat. Given that the heat source temperature is close to that of the highest steam temperature, superheat would be accomplished more by reducing throttle pressure without reducing steam temperature than by simply raising steam temperature. The consequence here is largely that of shifting the unstated optimal throttle pressure along the curves, producing no visible effect in Fig. 1. Investigation shows that raising steam temperature without decreasing pressure likewise has little effect because a consequent reduction in the amount of steam generated offsets the increase in work done per unit mass of steam.

The temperature difference between heat source and steam does have a significant consequence. This difference is conveniently represented by a pinch temperature difference in the heat exchanger. The shift of the curves toward lower values of the work fraction caused by increasing pinch temperature difference is evident in the figure.

The similar comparison of Brayton and Rankine exhaust

Downloaded 02 Jun 2010 to 171.66.16.122. Redistribution subject to ASME license or copyright; see http://www.asme.org/terms/Terms_Use.cfm

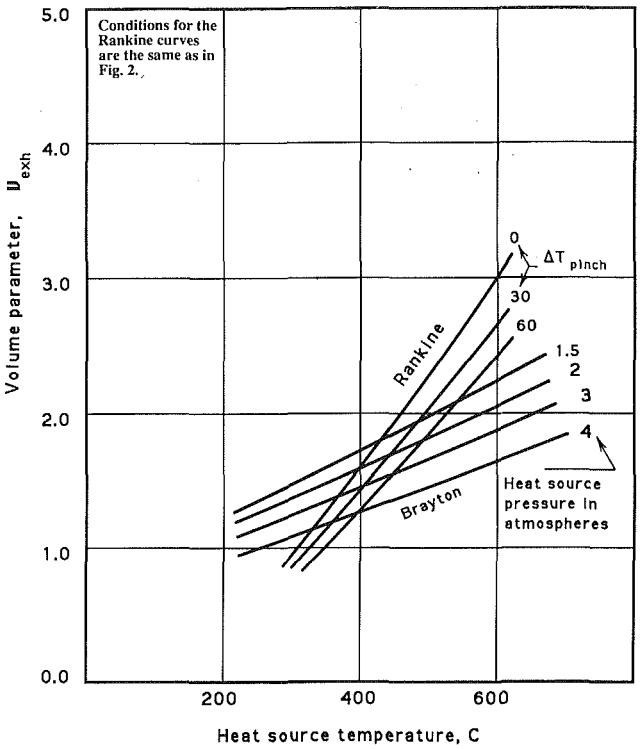


Fig. 2 Value of exhaust volume parameter u (volume of turbine exhaust per unit of mass of diesel exhaust heat source) for Brayton and Rankine alternatives

volume parameters is shown by Fig. 2. A division of the plane into domains favorable to one or the other alternative also appears here. For the Rankine curves, the plots represent optimal throttle pressure, steam saturated at the throttle, and exhaust pressure of 0.007 MPa, just as in Fig. 1. However, in this case a modest amount of superheat at the throttle does shift the Rankine curves a significant amount. This influence is omitted from Fig. 2 because it is treated when the boundary between Brayton and Rankine alternatives is explored in a later section.

A Computational Model for Boundaries Between Alternatives

Discussion and figures have indicated that for the values of diesel exhaust heat source pressure and temperature used here, either a Brayton turbine or a Rankine cycle may be superior in work production or in minimizing turbine exhaust volume flow rates. A computational model by which the contour of equal work performance between Brayton and Rankine can be mapped is expressed by

$$w_B(\alpha_B, \xi_B, \omega_B) = w_R(\alpha_R, \xi_T, \omega_R) \quad (1)$$

and a model by which the contour of equal volume-parameter performance can be mapped is expressed in quite similar fashion by

$$\mathbf{u}_B(\alpha_B, \xi_B, \omega_B) = \mathbf{u}_R(\alpha_R, \xi_R, \omega_R) \quad (2)$$

In these equations,

$\alpha \equiv$ constants such as specific heat
$\xi \equiv$ system parameter, i.e., variables that are likely to remain fixed along an equal-performance contour
$\omega \equiv$ an independent variable that varies along a contour

Expanding the Work-Equality Model. The computational models can be expanded into working form by introducing the equations implied in the examples (and described in Appendix 1). For example, the equal-work model (Eq. (1)) becomes

$$\eta_B c_p T_{so}(1-\phi) = \{\eta_R c_p[T_{so} - (T_{\text{sat}} + \Delta T_p)] \times / (h_{\text{stm}} - h_{fp})\}(h_{\text{stm}} - h_{ex}) \quad (3)$$

Equation (3) can also be expressed in terms of three-dimensional ratios as

$$1 = R_{\eta w} R_m R_h \quad (4)$$

where

$R_{\eta w} \equiv$ efficiency ratio $= \eta_R/\eta_B$
$R_m \equiv$ mass flow ratio $= c_p[T_{so} - T_{\text{sat}} + \Delta T_p)]/(h_{\text{stm}} - h_{fp})$
$R_h \equiv$ isentropic work ratio $= (h_{\text{stm}} - h_{ex})/c_P T_{so}(1-\phi)$

The dimensionless form would be useful in the pursuit of generality such as that advocated in the Beans paper (Beans, 1990). However, because the thrust of this paper is toward illuminating a limited area of comparison between Brayton and Rankine alternatives, only Eq. (3) is to be used.

The only α appearing in Eq. (3) is c_p, the constant-pressure specific heat of the heat source fluid. Any of the other symbols could represent either ξ or ω, depending on the analyst's task. Given the strong influence of exhaust pressure on the output of a Rankine cycle, a highly likely task is "given the heat source conditions, and given optimal values of pinch temperature difference and steam state, find if the Rankine alternative can match or exceed the Brayton alternative at an acceptable Rankine exhaust pressure." In such a case, the only ω is the exhaust enthalpy, h_{ex} (which is a function of P_{ex}); this instruction is followed here for purposes of illustration. The computational problem is to solve Eq. (3) (or Eq. (4)) for the unknown h_{ex}, which is a function of the independent variable P_{ex}.

Expanding the Volume-Equality Equation. For equality of the exhaust volume parameter **u**, Eq. (2) expands to

$$(R/P_0)T_{so}[1 - \eta_B(1-\phi)] = R_m v_{ex} f(\eta_R) \quad (5)$$

As is the case with Eq. (3), Eq. (5) can also be expressed in terms of three dimensionless ratios, but that route is not followed in this paper.

Presumably the same independent variable would be used both in finding the equal-work contour and the equal-volume-parameter contour. Exhaust pressure is a likely example, and in such case both v_{ex} and $f(\eta_R)$ are functions of that parameter.

Solving the Boundary-Contour Equations

The Work-Equality Equation. A quick trial-and-error solution can be made by hand calculation with the aid of a Mollier chart for steam properties. On the other hand, computer software for doing power cycle analysis, especially that which does its own table look-up for stream properties, has been a common resource for many years. The disadvantage in following this route to computation may be the complexity of adapting the programming to this particular problem, or of adapting its answers; such tasks may require as much work by the analyst as the hand calculation.

A compromise technique, which the author's experience suggests is likely to be the easiest alternative, is to construct a computational scheme that blends the use of a microcomputer with human look-up of stream properties. The remainder of this paper describes the method, using as an example the search for a Rankine exhaust pressure that marks the equal-merit boundary between Brayton and Rankine alternatives.

A solution to Eq. (3) is expedited by using

$$h_{ex} = h_{\text{stm}}(P_{ex}/P_{\text{stm}})^{\lambda} \quad (6)$$

When this is substituted into Eq. (3) with the appropriate value of λ, that equation is immediately solvable for the unknown P_{ex}. One may protest that in the region near its saturation line no fluid exhibits a constant value of λ. However,

Downloaded 02 Jun 2010 to 171.66.16.122. Redistribution subject to ASME license or copyright; see http://www.asme.org/terms/Terms_Use.cfm

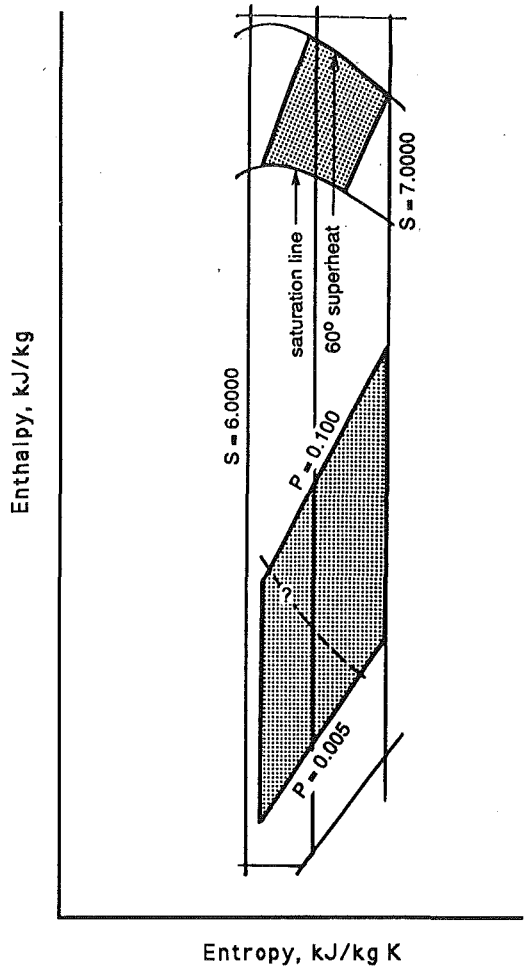


Fig. 3 A portion of the Mollier chart for steam. The highlighted areas show the likely limits for throttle and exhaust conditions for Rankine cycles using a diesel exhaust heat source. The line with question mark is the 20 percent liquid contour.

in this case several factors justify the use of this equation. They are

1 The range of h/P combinations is small, so that a single value of λ can be found to render satisfactory service, especially if only a rough survey of a Brayton–Rankine boundary is to be done.
2 If the error in the estimate is greater than can be tolerated, then a simple two-step procedure (to be outlined subsequently) can be applied.

A likely domain of h/P combinations for a Rankine expansion is pictured on the enthalpy–entropy plane in Fig. 3. The upper highlighted area is the region of throttle conditions, and the lower highlighted area is the region of exhaust conditions, at least for isentropic state lines. The lower area might be further reduced by strictures on moisture fraction of the steam as its exhaust. The dashed line labeled with a question mark is the 20 percent moisture contour, showing how even so generous a moisture limit produces a major shrinkage of the exhaust area.

What value of λ shall be used? A value of 0.066, found by a few trial-and-error solutions of Eq. (6) for λ, provides good answers in the lower part of the exhaust region of interest shown in Fig. 3 (i.e., near the 20 percent moisture boundary), but may give errors of 20 percent in P_{ex} near the upper edge. When such an error is unacceptable, a two-step procedure can produce an error of no more than 1 percent over the entire exhaust region.

In using the two-step procedure, one first finds a value of P_{ex} by solving Eq. (3) with the λ value of 0.066, and then might effect the second step as follows:

1 At the P_{ex} just found, read (e.g., on a Mollier chart) the value of h_{ex} that lies on the turbine expansion path.
2 Solve $\lambda = \ln(h_{ex}/h_{stm})/\ln(P_{ex}/P_{stm})$, using this h_{ex} while using the first-step P_{ex}.
3 Repeat the solution of Eq. (3) with the value of λ just found.

A very simple computational aid is illustrated in Appendix 2. It is a BASIC program having only four lines of calculation. Its simplicity is obtained by requiring the user to supply steam table values, to supply values of P_{ex} for trial, and to decide when the error in satisfying Eq. (3) is sufficiently small. A similar program for the volume-equality calculation is presented in Appendix 3.

The Volume-Equality Model. If P_{ex} is again used as a sample independent variable, then v_{ex} as a function of P_{ex} can be found in a manner analogous to Eq. (6), i.e.,

$$v_{ex} = v_{stm}(P_{ex}/P_{stm})^{\lambda} \tag{7}$$

An appropriate mean value for λ is -0.89. Just as with Eq. (6), this value may produce errors in P_{ex}, the Rankine exhaust pressure at which Rankine and Brayton alternatives have the same **u**, of up to 20 percent in some parts of the exhaust domain pictured in Fig. 3. Likewise, a second step of solution to reduce this error to around 1 percent can be used. The instructions for use with Eq. (6) can be used with Eq. (7), though applying them to specific volumes rather than enthalpies.

The efficiency term, $f(\eta_R)$, must account for the change in exhaust specific volume caused by an inefficient expansion through the turbine. Many empirical relationships might be devised; one that is suitable for the range $0.80 \le \eta_R \le 1.00$ is

$$f(\eta_R) = 1 + 5(1-\eta_R)[0.10 - 0.071(P_{ex} - 0.007)^{0.43}] \tag{8}$$

Surveys of the Brayton/Rankine Boundaries

Figure 4 demonstrates the mapping of contours of equal work from the same heat source, using Eqs. (3) and (6). Along any line representing a heat source state, the fraction of heat source availability converted to work is the same for both alternatives. Since higher P_{ex} reduces Rankine work, any point to the left of a contour represents Brayton > Rankine. For example, the figures shows that with heat source pressure 1.5 atm, temperature 600°C, the competing work fractions are equal when Rankine exhaust pressure is 0.23 MPa. If this pressure rises, Rankine work is reduced without any change to Brayton work. The domains in which each is superior is thereby determined.

Since reasonable amounts of superheat leave the curves of Fig. 4 virtually unchanged, the effect of superheat is not indicated. (With superheat, the increase in the Rankine Δh caused by higher temperature is offset by the consequent lower value of m.) On the other hand, pinch temperature difference in the heat exchanger is a strong influence. Each curve of the figure, made for a zero value of pinch temperature difference, is therefore shown modified by 60°C pinch ΔT.

Figure 5 demonstrates the mapping of contours of equal volume parameter **u**, using Eqs. (5) and (6). In this instance, both superheat and pinch temperature difference cause noticeable differences in the locations of the contours of equal **u**. To illustrate the magnitude of the difference, one of the contours from Fig. 5 (for $P_{so} = 1.5$) is repeated in Fig. 6, accompanied by plots of this curve as modified by one value of superheat and one of pinch temperature difference.

Conclusions

Comparison of Brayton and Rankine alternatives for ex-

Downloaded 02 Jun 2010 to 171.66.16.122. Redistribution subject to ASME license or copyright; see http://www.asme.org/terms/Terms_Use.cfm

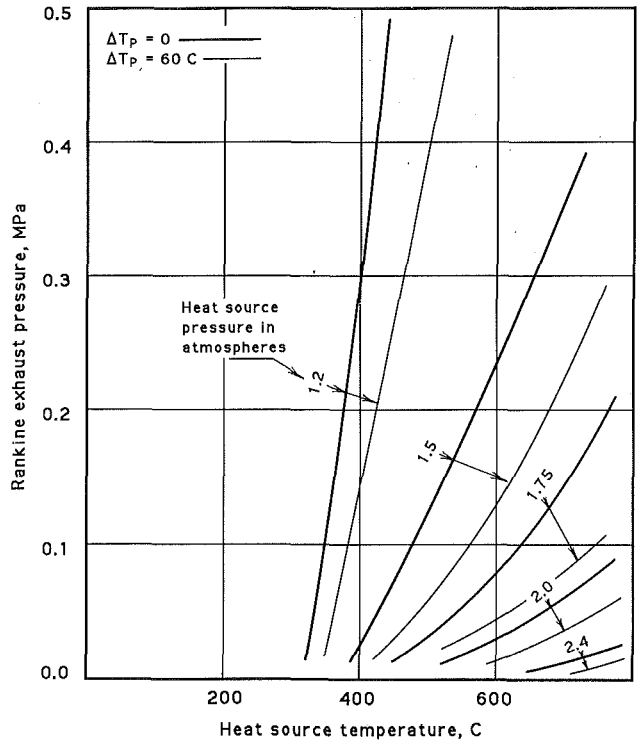


Fig. 4 Contours of equal work fraction (fraction of source availability converted to work) for Brayton and Rankine alternatives on the source-temperature/exhaust-pressure plane. The effect of pinch temperature difference is indicated.

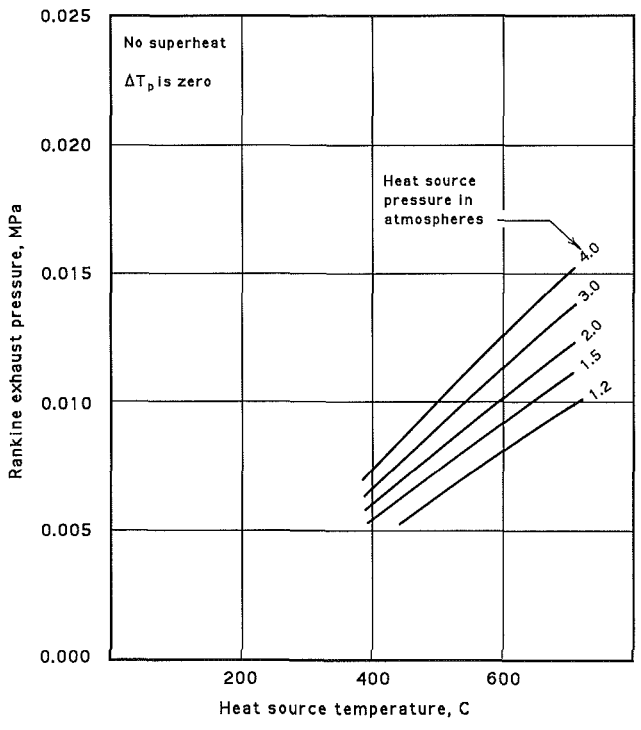


Fig. 5 Contours of equal exhaust volume parameters *v* for Brayton and Rankine alternatives on the source-temperature/exhaust-pressure plane

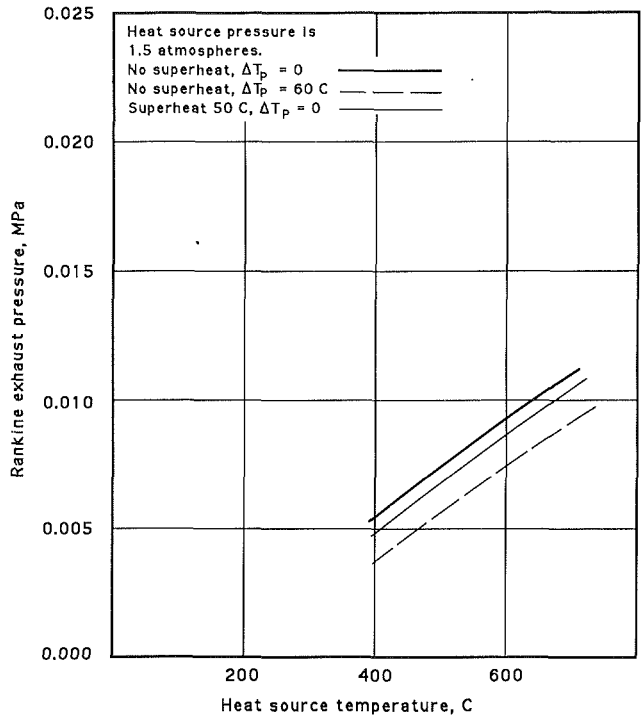


Fig. 6 A contour of equal exhaust volume parameter *v* for Brayton and Rankine alternatives to show effects of superheat at the Rankine throttle and pinch temperature difference. The curve for source pressure 1.5 atm is repeated from Fig. 5, but with the two variations added.

ploiting a diesel cylinder exhaust gas energy source shows that either may be superior in the fraction of source availability converted to work. High cylinder exhaust pressure and low temperature favor the Brayton alternative because this combination produces a low irreversibility for its exhaust while producing a high irreversibility for transfer of energy into a Rankine cycle. On the other hand, high cylinder gas temperature and low pressure reduce the Rankine irreversibilities while increasing that of Brayton alternative. Location of the contour of equal work fraction between the alternatives depends on Rankine exhaust pressure and on pinch temperature difference between its working fluid and the heat source. Superheat used in the Rankine alternative has a trivial effect. If Brayton and Rankine turbine efficiencies are approximately the same, then their influence is also trivial.

Volume flow rates at turbine exhausts also show a realm of superiority (taken to mean low volume flow rate) for each of the alternatives, but the difference between them is small. Generally, the Rankine value is favorable (low) when its work fraction is unfavorable (low), and vice versa.

The boundaries of equal performance between the alternatives can be mapped by formulas expressing the respective work quantities or exhaust volume quantities. Solution is expedited on the Rankine side by use of several empirical formulas that express steam states along the turbine expansion line.

References

Beans, E. W., 1990, "Comparative Thermodynamics for Brayton and Rankine Cycles," ASME JOURNAL OF ENGINEERING FOR GAS TURBINES AND POWER, Vol. 112, pp. 84–99.

Tanaka, S., Yabuki, S., Takahashi, S., Hamada, H., and Hatada, H., *1985*, "Design Considerations for Energy Efficient Propulsion Plants," presented at the spring meeting of the Society of Naval Architects and Marine Engineers, Norfolk, VA, May 21–24.

Van Wylen, G. J., and Sonntag, R. E., 1965, *Fundamentals of Classical Thermodynamics*, Wiley, New York.

Woodward, J. B., 1981, *Low Speed Marine Diesel*, Wiley, New York.

APPENDIX 1

Computational Formulas

Availability is found by the steady-flow formula

Downloaded 02 Jun 2010 to 171.66.16.122. Redistribution subject to ASME license or copyright; see http://www.asme.org/terms/Terms_Use.cfm

$$\psi = (h - h_0) - T_0(s - s_0) \quad \text{(A1)}$$

Enthalpy for the heat source and Brayton working fluid is found by

$$h = c_p T \quad \text{(A2)}$$

Enthalpy for the Rankine working fluid is found from tables, except for Eq. (6). Entropy for the heat source and Brayton working fluid is found by

$$s = c_p[\ln\ (T/T_0)] - R[\ln\ (P/P_0)] \quad \text{(A3)}$$

Entropy of the Rankine working fluid is found from tables. Temperature changes along an isentropic Brayton expansion line are found be

$$T_2 = T_1\phi \quad \text{(A4)}$$

where

$$\phi = (P_2/P_1)^{(k-1)k} \quad \text{(A5)}$$

with the symbol λ often used to represent $(k - 1)/k$. Enthalpy changes along an isentropic Rankine expansion line are found from following the entropy line in tables or on a chart. Specific volume for the heat source and Brayton working fluid is found by

$$v = (RT)/P \quad \text{(A6)}$$

Specific volume for the Rankine working fluid is found from tables, except for Eq. (7). Irreversibility is found by the difference between the net reversible work for a process and the actual work (in all cases where the calculation is made here, the actual work is zero). Reversible work is taken to be the change in availability.

APPENDIX 2

BASIC Program to Equate Work of Brayton and Rankine Alternatives

This program is used as an aid to a trial-and-error investigation of the Rankine exhaust pressure at which the two alternatives produce the same work from a common heat source.

```
10 REM*PROGRAM TO EQUATE RANKINE AND BRAYTON WORKS
20 PRINT "TYPE SOURCE PRESSURE (ATMOS) AND TEMPERATURE (C)"
30 INPUT PSO,TSO
40 PRINT "TYPE STEAM PRESSURE (MPA) AND ENTHALPY"
50 INPUT PSTM,HSTM
60 PRINT "TYPE SATURATION TEMP (C) AND LIQUID SAT ENTHALPY"
70 INPUT TSAT,HF
80 PRINT "TYPE PINCH TEMP DIFF"
90 INPUT DELTP
100 PRINT "TYPE YOUR EXPONENT"
110 INPUT POWER
120 PRINT "TYPE BRAYTON AND RANKINE TURBINE EFFICIENCIES"
130 INPUT ETAB,ETAR
140 PRINT "TYPE TRIAL VALUE OF PEXH"
150 INPUT PEXH
160 HEXH=HSTM*(PEXH/PSTM)^POWER
170 BRAY=ETAB*(TSO+273)*(1-(PSO^(-.2857)))
180 M=(TSO-(TSAT+DELTP))/(HSTM-HF)
190 RANK=M*ETAR*(HSTM-HEXH)
200 PRINT "BRAYWORK, RANKWORK: ";BRAY,RANK
210 GOTO 140
220 END
```

APPENDIX 3

BASIC Program to Equate Exhaust Volume Parameters of Brayton and Rankine Alternatives

This program is used as an aid to a trial-and-error investigation of the Rankine exhaust pressure at which the two alternatives produce the same exhaust volume parameter **u** from a common heat source.

```
10 REM*PROGRAM TO EQUATE RANKINE, BRAYTON VOLUME PARAMETERS
20 PRINT "TYPE SOURCE PRESSURE (ATMOSPHERES) AND TEMPERATURE (C)"
30 INPUT PSO,TSO
40 PRINT "TYPE STEAM PRESSURE (MPA), ENTHALPY, AND SPECIFIC VOLUME
50 INPUT PSTM,HSTM,VSTM
60 PRINT "TYPE SATURATION TEMP (C) AND LIQUID SAT ENTHALPY"
70 INPUT TSAT,HF
80 PRINT "TYPE PINCH TEMP DIFF"
90 INPUT DELTP
100 PRINT "TYPE YOUR EXPONENT"
110 INPUT POWER
120 PRINT "TYPE BRAYTON AND RANKINE TURBINE EFFICIENCIES"
130 INPUT ETAB,ETAR
140 PRINT "TYPE TRIAL VALUE OF EXHAUST PRESSURE (MPA)"
150 INPUT PEXH
160 PHI=PSO^(-.2857)
170 VOLBRAY=.00286*(TSO+273)*(1-ETAB*(1-PHI))
180 M=(TSO-(TSAT+DELTP))/(HSTM-HF)
190 VEXH=VSTM*(PEXH/PSTM)^POWER
200 VOLRANK=M*VEXH
210 VOLRANK=VOLRANK*(1+((1-ETAR)/.2)*(.1-.0708*(PEXH-.007)^.43))
220 PRINT "BRAY VOL, RANK VOL: ";VOLBRAY,VOLRANK
230 GOTO 140
240 END
```


Downloaded 02 Jun 2010 to 171.66.16.122. Redistribution subject to ASME license or copyright; see http://www.asme.org/terms/Terms_Use.cfm

A. N. Lakshminarasimha

M. P. Boyce

C. B. Meher-Homji

Boyce Engineering International Inc., Houston, TX 77099

Modeling and Analysis of Gas Turbine Performance Deterioration

The effects of performance deterioration in both land and aircraft gas turbines are presented in this paper. Models for two of the most common causes of deterioration, viz., fouling and erosion, are presented. A stage-stacking procedure, which uses new installed engine field data for compressor map development, is described. The results of the effect of fouling in a powerplant gas turbine and that of erosion in a aircraft gas turbine are presented. Also described are methods of fault threshold quantification and fault matrix simulation. Results of the analyses were found to be consistent with field observations.

Introduction

The ingestion of particles suspended in the air such as sand, dust, water droplets, ice, fly-ash, salt, etc., is the single most important factor causing performance deterioration in all types of gas turbines. Since gas turbines use roughly half a ton of air for each horsepower output for every 24 hours of operation, even if one part per million (ppm) enters the compressor, a 10,000 HP unit will ingest ten pounds of foreign material in a single day! With such a high rate of foreign particle ingestion, even a highly efficient filtering system can only mitigate but not eliminate the problem of gas turbine performance deterioration. Industrial and marine gas turbines foul due to continued operation in an environment that almost always contain dust particles, pollen, salt, and other impurities. The fouling problem is amplified if there are internal oil leaks near the blade surfaces. Among the different gas turbine applications, aircraft gas turbines are affected the most as they ingest dust not only during flight but also during landing and take off. Because of the high power setting during takeoff, a strong suction zone is induced at the engine inlet due to a vortex formed between the inlet and the ground. This suction pressure ingests runway gravel, puddles of water and ice, and salt spread on runways during winter. Similarly, during landing, the thrust reverser efflux blows runway dirt into air, which gets sucked into the engines.

Component (compressor or turbine) and engine performance will most certainly deteriorate with engine use. To cite a few incidents, several cases have been reported of engine loss of performance and flame-out on Boeing 747s at cruising altitudes as a result of volcanic ash (*Flight International*, 1982; *Aviation Week and Space Technology*, 1982). Incidents have occurred as recently as Dec. 1989 and June 1991 (Berton, 1989; Philips, 1991). The occurrence of severe fouling has been reported on Fairchild A-10 aircraft due to gun firing and ingestion of gun and severe loss of performance. From an economic point of exhaust into engine intakes (Scott, 1982) leading to engine stall view, a 1 percent increase in specific fuel consumption (SFC) from a single-engined aircraft of 45 aircraft fleet, could increase the expenditure due to additional fuel by a million dollars a year (Jay and Todd, 1978). In a typical power plant gas turbine, the increase in operating cost due to performance deterioration between major overhauls, which is approximately three years, is one and a half million dollars (Diakunchak, 1992). In the case of cogeneration plants, the loss of revenue due to reduced output can also be severe.

From operational, economic, and safety considerations, gas turbine performance deterioration has emerged as a very important topic of research. Fault classification, quantification, and identification are three essential steps in any turbine engine deterioration model development.

Since gas turbines have been in use for over four decades, fault classification is based on a significant base of reported operational problems. Generally, performance deterioration in gas turbines is due to:

1 Fouling: due to minute dust particles, pollen, salt spray and insects that are deposited on blade surfaces.
2 Erosion: of blade surfaces caused by particulate ingestion.
3 Tip clearance increase: of blade tips caused by particulate ingestion.
4 Water ingestion—during rain.
5 Foreign Object Damage (FOD): caused by hailstones, runway gravel, and bird ingestion.

Quantitative and qualitative descriptions of the effects of fouling and erosion deterioration mechanisms on both component and overall engine performance are provided ahead in detail.

Compressor Performance Simulation

The performance of compressors is normally depicted by means of the compressor characteristics, which describe the variation of compressor pressure ratio and efficiency with engine mass flow rate. In performance deterioration studies, the variation in the compressor map with engine usage is sought. Since performance maps are not supplied to the user, any

Contributed by the International Gas Turbine Institute and presented at the 37th International Gas Turbine and Aeroengine Congress and Exposition, Cologne, Germany, June 1-4, 1992. Manuscript received by the International Gas Turbine Institute February 11, 1992. Paper No. 92-GT-395. Associate Technical Editor: L. S. Langston.

Copyright © 1994 by ASME
Downloaded 02 Jun 2010 to 171.66.16.122. Redistribution subject to ASME license or copyright; see http://www.asme.org/terms/Terms_Use.cfm

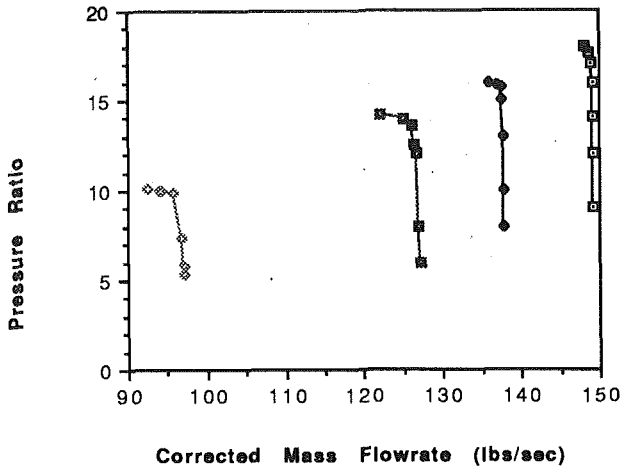


Fig. 1 LM2500-PE compressor performance simulation

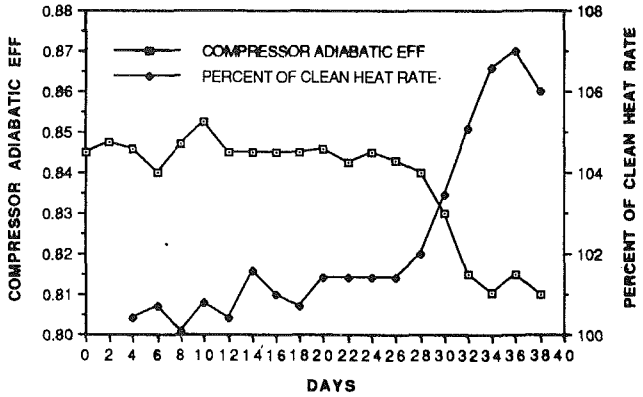


Fig. 2 Effects of fouling on an industrial gas turbine

simplified map generation technique would be extremely useful to the user, to aid in meaningful maintenance scheduling and trending of the performance variation of the component. Compressor performance simulation using a stage stacking technique has received a lot of attention in recent years due to its simplicity. The stage stacking procedure takes into account interrelationships among stages through compatibility of speed, mass flow, and energy. Thus, it provides a logical basis for examining the behavior of a multistage compressor subjected to deterioration in one or more stages. Additionally, it is possible to study the effects of different types of deterioration, using a stage stacking technique. Usually a gas turbine user has neither the compressor performance map or the stage characteristics for performance simulation. In such a situation, one can use the on-site performance measurement values of baseline compressor flow, efficiency, and the annulus area of the compressor gas path and use the generalized stage compressor characteristics (Saravanamuttoo and Lakshminarasimha, 1985, Muir et al., 1989; Siddigh and Saravanamuttoo, 1990) for compressor performance simulation. This procedure is iterative, as additional details of design stage pressure ratio, and stage inlet angles are unknown.

To accomplish such a procedure, generalized stage characteristics can be written in an equation form as:

$$Y = 1.0 - k\,\frac{(x - x_{\text{ref}})^2}{(x_{s,c} - x_{\text{ref}})^2}$$

where

- For a generalized stage pressure coefficient (ψ) curve, $X = \phi/\phi_{\text{ref}}$, $Y = \psi/\psi_{\text{ref}}$, $X_s = 0.6$, and $X_c = 1.3$; subscript "ref" refers to stage design condition.
- For a generalized stage efficiency (η) curve,

$$X = \frac{\tau/\tau_{\text{ref}}}{\phi/\phi_{\text{ref}}} \text{ and } Y = \frac{\eta}{\eta_{\text{ref}}}$$

where τ is the stage temperature rise coefficient.

Using the equation form of the generalized stage characteristics makes the implementation of an iterative method of compressor map development easier. To begin the calculation, an average design stage pressure coefficient using equal stage design pressure ratio, and inlet flow angle calculation (for the case under consideration) as described by Muir et al. (1988) was utilized. Figure 1 represents the compressor map simulated using on-site field measurement of a LM2500-PE gas turbine unit. The second lowest mass flow rate compressor operating point for each constant speed line represents a measured value. Iteration using the generalized stage characteristic for the highest constant rpm line of the compressor characteristic shown in Fig. 1 was required to match the field measurement point. For other off-design speeds very good agreement was obtained between field measurements and the simulated results.

Axial Compressor Fouling. Fouling of compressors in gas turbine power plant is perhaps the most significant operational problem faced by gas turbine operators. Aerodynamically, an axial flow compressor is a very sensitive component, requiring close manufacturing tolerances on the blading for the baseline performance to be achieved. Fouling of the blade surfaces reduces flow through the compressor, compressor pressure ratio, and its efficiency. This causes a reduction in gas turbine performance, decreasing power available and increasing the heat rate. Figure 2 shows the effect of fouling in a large gas turbine unit (Meher-Homji, 1990). Reduction in performance in the beginning is gradual but an exponential reduction in performance of gas turbine follows if the compressor is not washed in time. Performance deterioration due to fouling is, for the most part, recoverable. The type of wash depends on the fouling characteristics. Opinions have varied in the past as to whether compressor fouling affects the early stages, which are directly exposed to incoming air, or the later stages, where deposits may bake on because of the higher temperatures, making them difficult to remove by washing. Quantification of the effects of fouling is important from both detection and washing schedule considerations.

Very few publications quantify the effects of the basic factors affecting performance deterioration. Lakshminarasimha (1984), Saravanamuttoo and Lakshminarasimha (1985) and Muir et al. (1989) are among the few publications to quantify the effects of fouling. Compressor performance is simulated by the method of stage stacking. Fouling in individual stages is simulated by modifying the stage characteristics. Since the performance of the whole stage is represented by meanline conditions at rotor inlet and outlet, only the overall effect of fouling on a stage can be simulated. Prime factors causing the blade profile change, the amount and distribution of deposition along the blade span, which describe the process of fouling, are not considered. Two factors that describe the effects of fouling, reduction in the flow coefficient ($\delta\phi/\phi$, or the flow) and the efficiency coefficient (K_η, which describe the loss of efficiency due to blade profile change) are used to simulate fouling. For a given set of values of these two factors, stage characteristics could be modified to simulate a desired level of fouling. Various degrees and types of fouling in a stage can be obtained by giving different combinations of values to these factors.

Results of Fouling Simulation. A series of different fouling cases, which included fouling severity and fouling severity, were carried out on LM2500 compressor section. Figure 3 represents the effect of fouling stage location on compressor mass flow rate with $\delta\phi/\phi = 3$ percent and $K_\eta = 1$ percent. Reduction of compressor mass flow rate when either of the

Downloaded 02 Jun 2010 to 171.66.16.122. Redistribution subject to ASME license or copyright; see http://www.asme.org/terms/Terms_Use.cfm

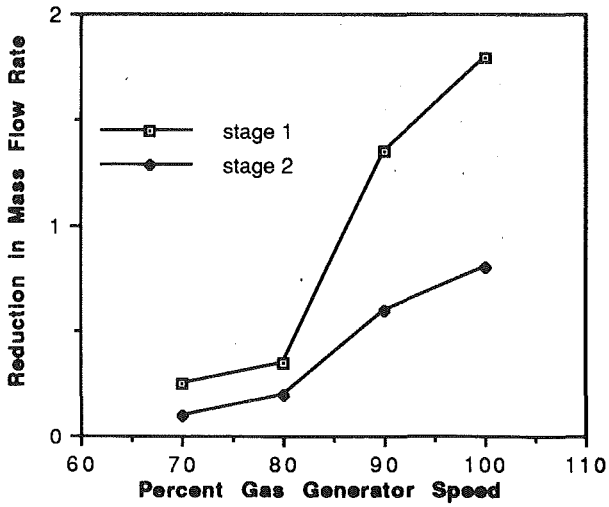


Fig. 3 Effect of fouling location on gas generator mass flow rate

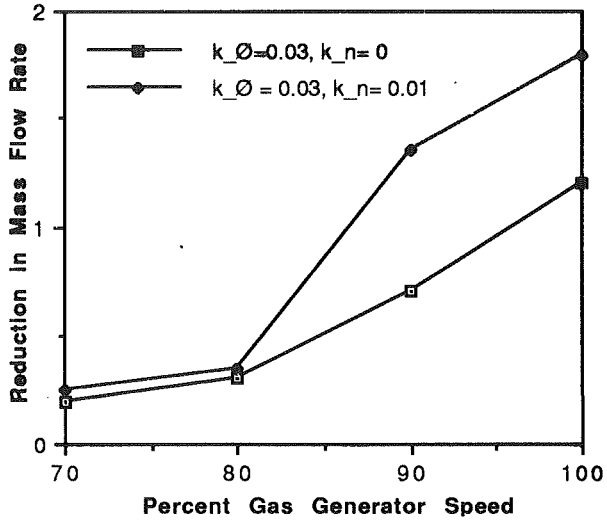


Fig. 4 Effect of first-stage fouling severity on compressor mass flow rate

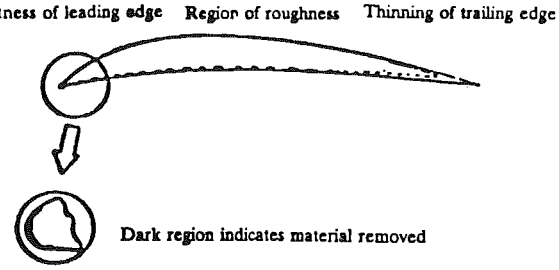


Fig. 5 Typical erosion pattern of a compressor blade

two stages gets fouled increases with compressor speed, with the first stage having the strongest influence. The reason for this is that the front stages affect the operating point of all succeeding downstream stages. The last stage had no effect at all and is therefore not shown in the figure. The reduction of mass flow rate due to two levels of fouling severity $\delta\phi/\phi = 3$ and 2 percent with $K_\eta = 1$ percent is shown in Fig. 4. A reduction of the compressor mass flow rate is greater at higher speed, thus indicating fouling severity can be more easily noticed at higher gas generator speeds than at low off-design speeds. Reduction of the compressor delivery pressure was also noticed in all the cases studied.

Erosion. Erosion of blade profile and tip clearance increase occur more frequently in aircraft engines than in industrial gas turbines. A detailed study of performance variation with engine usage is documented in the work related to NASA Aircraft Energy Efficient (ACEE) program. The results of this research are based on the two commonly used high-bypass turbofan engines used for civil aviation: the Pratt and Whitney JT9D (Jay and Todd, 1978) and the General Electric CF6 (Wulf, 1980). In all the cases studied, Specific Fuel Consumption (SFC) was found to increase with engine usage. The SFC increase was attributed to increases in tip clearance and airfoil contour changes in both compressor and turbine sections. As an example, Wulf (1980) points out that after 6000–8000 hours of engine operation, CF6 compressor blades had blunt leading edges and surface roughness had significantly increased. These unavoidable blade shape changes resulted in an increase in SFC. Due to the blunting of the leading edge alone, SFC had increased by almost 0.38 percent. The average surface roughness on the concave side of the blades had increased from 55 μin. to 120 μin., and caused SFC to increase by another 0.13 percent. Similar observations are also reported by Jay and Todd (1978). While low-pressure compressor erosion losses are due to surface roughness and tip clearance, erosion losses in a high-pressure compressor are created by blade length reduction and loss of air seal materials in addition to increase in roughness (Schwind and McMillan, 1982).

The engines used in the ACEE program are high bypass ratio turbofan engines. A large fraction of the power generated is absorbed by the fan section and would be comparable to the work absorbed by the compressor. A much larger effect would be observed in compressor performance in a low bypass ratio gas turbine such as the JT8D, but the fan loss would be smaller. Detailed physical deterioration measurements of airfoil contour changes, tip clearance variation, etc. have been compiled for the JT8D by Schwind and McMillan (1982). Since the high-pressure compressor had maximum deterioration, airfoil contour measurements were concentrated only on this component.

Erosion Simulation. In general, blade erosion is a complex function of the physical properties of the particles, blade material, and aerodynamic parameters such as particle mass flow, particle size, shape, velocity and direction of impingement, the geometry, and the material of the blade row. In view of this complexity, the prediction of erosion as well as the subsequent change in compressor performance is a complicated task. Typical erosion simulation involves two parts (Balan, 1984). First, leading edge blunting, chord length reduction, roughness and its distribution are calculated by using particle trajectory and erosion calculations. Second, pressure loss due to these changes is then calculated using an inviscid–viscous interaction technique. This procedure can be applied to a two-dimensional cascade. Application of this procedure to even a single-stage compressor is difficult and tedious and has not been carried out. For health monitoring or performance deterioration modeling applications, fault models should be simple and therefore simplifying assumptions are essential.

From a detailed research survey (Balan, 1984; Batcho et al., 1987; Tabakoff et al., 1990) typical regions of erosion can be depicted as shown in Fig. 5. In general, blade erosion can be described as blunting of the leading edge, thinning of the trailing edge, and as a general increase in blade surface roughness. Batcho et al. (1987) suggested a simple model, which took into account the change in lift coefficient due to chord reduction, based on simple airfoil theory. Tabakoff et al. (1990) improved this model by including the surface roughness effects and confirmed the model with the cascade and one-stage compressor experimental results of Balan (1984). The erosion simulation model can be summarized as follows:

The change in lift coefficient (C_l), due to chord reduction (δC) by erosion using thin airfoil theory is:

$$\delta C_l = 1.5\pi f(Z_0, C)$$

Downloaded 02 Jun 2010 to 171.66.16.122. Redistribution subject to ASME license or copyright; see http://www.asme.org/terms/Terms_Use.cfm

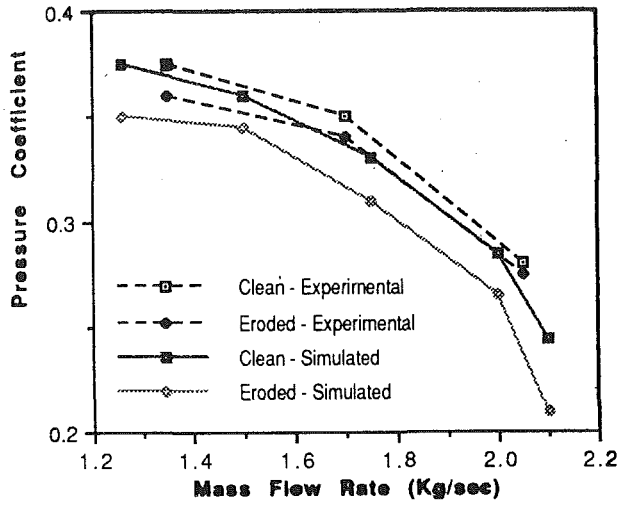


Fig. 6 Simulation of the effect of erosion on compressor performance

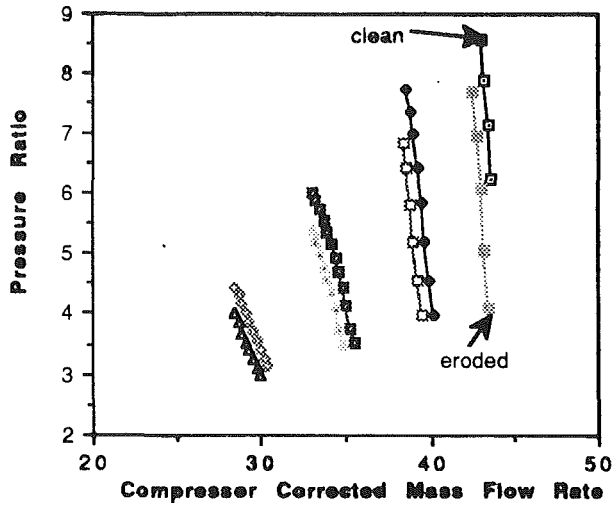


Fig. 7 85 Compressor performance simulation

where, if Z_0 is the maximum airfoil camber,

$$f(Z_0, C) = \frac{Z_0/C}{1 - \frac{\delta C}{C}}$$

This reduction in the lift coefficient can be used to calculate the reduction in the pressure coefficient (ψ) and the increase in the loss coefficient.

In addition to blade chord reduction, losses due to blade surface roughness (Tabakoff et al., 1990) could be translated in terms of pressure coefficient. Finally, for each stage, an altered stage performance can be obtained by subtracting the reduction in the pressure coefficient due to erosion from the uneroded pressure coefficient:

$$\psi_{\text{eroded}} = \psi_{\text{clean}} - \delta\psi_{\text{due to erosion}}$$

The result from the above erosion simulation is shown in Fig. 6 for a single-stage compressor. Considering the simplicity of the method, a good comparison can be seen between measured (Balan, 1984) and simulated results. This procedure was extended to a multistage compressor described by Milner et al. (1975). Using the stage stacking method described in the previous section, comparison between the measured and simulated clean or baseline compressor map was obtained. Since field erosion data for this compressor were not available, the erosion data for a compressor described by Schwind et al. (1982) for which inline service data were available was used in the simulation.

Results of this simulation summarized in Fig. 7 indicate that compressor erosion results in a reduction of both compressor mass flow rate and pressure ratio. Also, it can be concluded that reduction of mass flow and pressure ratio is dependent upon compressor speed, being higher at higher speeds. Additional numerical experiments were carried out by simulating cases when only front or rear stages were eroded. These results indicated that front stages have a greater impact on overall compressor performance compared to rear stages, as front stages affect all the stages following it. This is an important conclusion from both safety and economic viewpoints. If a gas turbine is to operate in dusty environments it is more advisable to use expensive highly erosion-resistant compressor blade material and/or coatings in front rather than rear stages, thus reducing both time between overhaul periods and increasing the safe operation time.

Effects of Component Performance Deterioration on Engine Performance Parameters

The power developed by a turbine is given by:

$$\text{Power} = \dot{m} C_p T_3 \left[1 - \frac{1}{\left(\frac{P_3}{P_4}\right)^{\frac{\gamma-1}{\gamma}}} \right]$$

The pressure P_3 entering the turbine is essentially the compressor discharge pressure minus the pressure drop in the combustion chamber. As the mass flow rate and the compressor delivery pressure drop due to deterioration, the work output of the turbine drops. In order to maintain the power output, the fuel control system would increase the fuel flow rate and hence the turbine inlet temperature. Since deterioration also causes the compressor efficiency to drop, the turbine work to maintain the same flow rate and compressor delivery pressure increases. These factors reduce the life of hot section components.

To illustrate the variation of the overall engine parameters due to fouling, the simulated compressor characteristics were matched with a gas generator turbine and a power turbine. The variations of power and specific fuel consumption as functions of compressor speed are shown in Figs. 8 and 9. The significant drop in power observed is primarily due to a reduction in air flow capacity of the compressor. It should be noted that a nominal 1 percent drop in compressor efficiency (if first stage) resulted in about 3 percent increase in SFC, due to changes in both pressure ratio and efficiency. Using the fouling simulation, a fault matrix was created for fouling. The results or parameter variations that indicate that fouling reduces the compressor mass flow and compressor delivery pressure, and increases the heat rate and SFC, are in good agreement with the fault matrix obtained from a database of field data for the fouling cases indicated in Table 1 (Boyce, 1984).

A newly installed engine initially has an unrecoverable degradation in performance caused by thermal distortions and blade tip rubs. This is followed by a gradual increase in viscous losses, which is partly recoverable. The level and time variation of this recoverable loss is component dependent. Figure 10, summarized from Jay and Todd (1978), indicates an almost linear variation in the reduction of both flow and efficiency of the low-pressure compressor (LPC) with the number of engine cycles, but shows almost an exponential reduction in these parameters for the high-pressure compressor (HPC) due to in-service deterioration. The nonzero intercept in Fig. 10 is indicative of the initial unrecoverable loss mentioned earlier. A similar trend is observed in Thrust Specific Fuel Consumption (TSFC) variation with the number of engine cycles shown in Fig. 11. Figure 11 also summarizes the relative effects of various types of deterioration, airfoil and seal erosion being

Downloaded 02 Jun 2010 to 171.66.16.122. Redistribution subject to ASME license or copyright; see http://www.asme.org/terms/Terms_Use.cfm

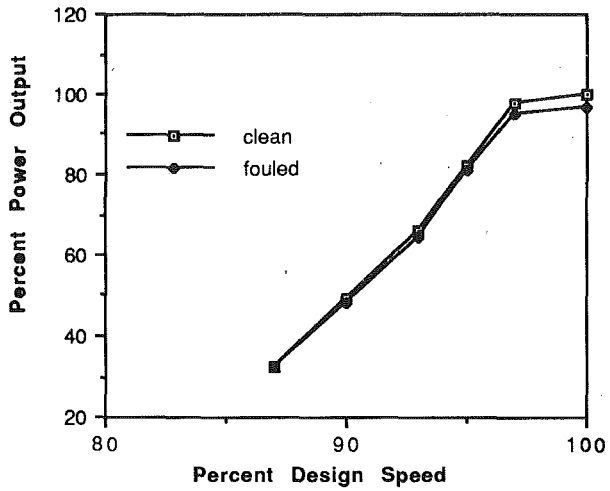


Fig. 8 Effect of fouling on power

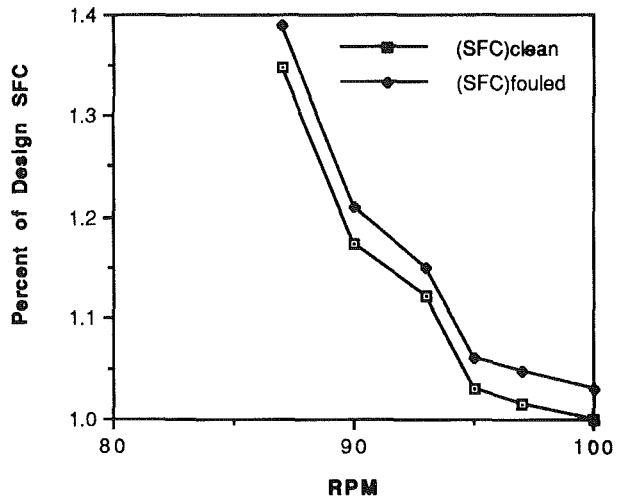


Fig. 9 Effect of fouling on SFC

the most prominent deterioration mechanisms. These results indicate clearly that as flight cycles increase, tip clearance, blade length loss, roughness and airfoil contour changes are the most observable characteristics that affect the engine performance. It should be noted here that the losses in flow and efficiency shown in the figures were obtained by experimentally measuring the component performance and then introducing this performance variation in a cycle analysis program to calculate the overall loss in flow and efficiency.

In any multistage machine, the performance of any stage depends upon upstream stages. The effect that each stage has on overall compressor performance depends upon the stage pressure ratio (which is proportional to stage loading) as well as the stage loading sequence of upstream and downstream stages. Many different performance deterioration case studies carried out by the lead author have indicated that the higher the stage loading, the greater the effect on the overall compressor performance. Hence, when highly loaded stages deteriorate, they have a greater impact on overall compressor performance deterioration. It was also found that, if the stage following a deteriorated stage has a higher loading, then it has a lower impact on the overall compressor performance. Thus stage loading while acting to amplify the deterioration filters the deterioration effect of upstream stages. This is an important observation to be noted while designing deterioration-tolerant machines.

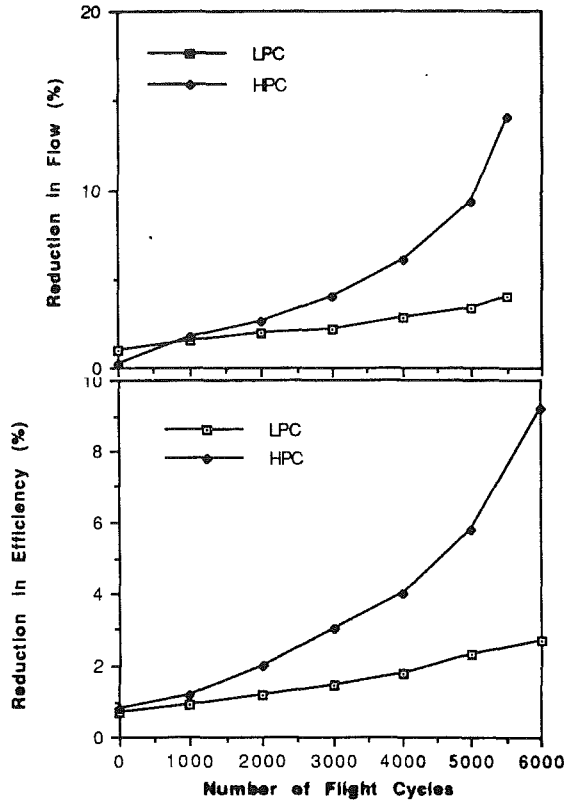


Fig. 10 Preliminary model of JT9D performance deterioration—reduction in flow and efficiency of the HP and LP compressor

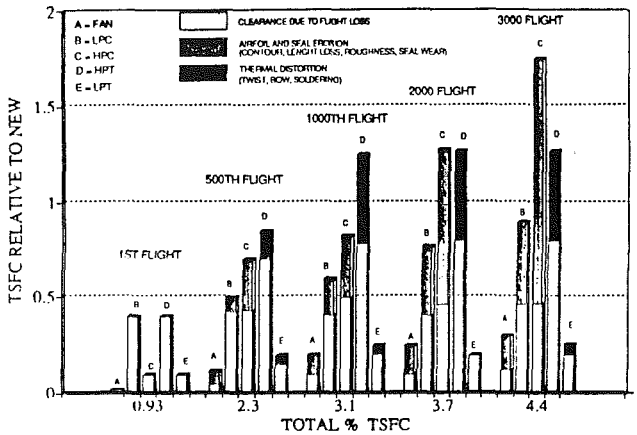


Fig. 11 Classification of JT9D performance deterioration, from Jay and Todd (1978)

Correlation of Stage Characteristics on the Overall Compressor Map: Fault Threshold Quantification

Two of the prime requirements of a prediction method suitable for Engine Health Monitoring (EHM) are that the method should be simple and the results be explicitly presented. The method of simulating fouling by modification of stage characteristics and obtaining overall performance by stage stacking becomes more difficult as the number of stages increases, because it becomes necessary to relate the performance of a greater number of stages to one another. When different stages have to be simulated for fouling using different combinations of fouling factors, the results obtained using the stage-stacking analysis becomes voluminous. Thus a correlation technique is essential in order to represent the behavior of each of the individual stages on the overall compressor map. Brown and Groh (1962) describe a suitable technique, adopted in the pres-

Downloaded 02 Jun 2010 to 171.66.16.122. Redistribution subject to ASME license or copyright; see http://www.asme.org/terms/Terms_Use.cfm

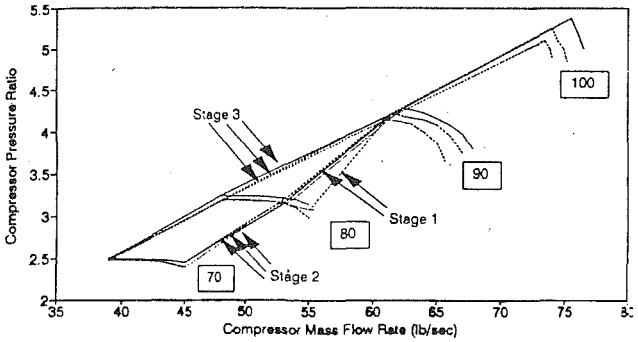


Fig. 12 Peak line compressor map

ent investigation. It is usually possible to locate a point on the stage characteristic where the pressure coefficient is maximum. The peak point separates stalled or overloaded stage operation from unstalled or underloaded operation. Ideal operation of a compressor stage occurs at a flow somewhere between the peak point and maximum efficiency point.

The procedure to obtain the peak line is as follows:

1 For each stage, the flow coefficient corresponding to the maximum pressure coefficient point on the stage characteristic is determined.
2 For each speed on the overall compressor map, and for each stage, the flow coefficient determined above is converted to equivalent mass flow and is plotted as a peak point on the speed line.
3 For each stage, corresponding peak points are joined together to obtain the peak line for that stage.

When peak lines of all stages are plotted on an ideal compressor map, where compressor operational boundaries are not cut off by stall and surge margins, they meet at a point close to the design speed. Such a point of coincidence is termed the match point of the compressor. At speeds above the match point, the peak lines of rear stages fall at higher mass flow than front stages, while below the match speed the situation is reversed. The order of the peak lines for a properly matched compressor should be in forward sequence (1, 2, 3, . . .) above the match point, and in reverse sequence below the match point speed. In real compressor situations, even though the sequence of peak lines should be maintained for safe compressor operation, peak lines of all the stages may not appear as they may be cut off by the operating boundaries of the compressor.

When a compressor stage deteriorates, its peak line shifts generally independently of the other stages, and the normal sequence of peak lines may be altered and can be detected. Such a change also results in a shift in the matching of the stages, and this variation can be observed. Whenever there is a change in the sequence of peak lines, one can also determine the threshold value of deterioration for the machine.

Peak lines for a variety of compressor fouling situations were analyzed. Unfortunately, measured peak line data were not available. However, peak lines from simulated stage characteristics and those obtained from measured stage characteristics of a five-stage compressor (Sandercock et al., 1956) agreed well, and the match point in both cases was found to be around 90 percent of the design speed. The peak line maps for the baseline (clean), a lightly fouled first compressor stage, and a heavily fouled first stage are plotted together in Fig. 12. As can be seen from the figure, fouling tends to unload the fouled stage, moving the peak line to lower mass flows and increasing the range of unstalled operation. This unloading effect extends to other stages downstream of the fouled stage, as is apparent in the movement of the second-stage peak line. Conversely, when fouling of the second stage was simulated, loading of the first upstream stage was observed. Increasing the degree of fouling of the first stage accentuated the unloading of the first stage and the shifts of overall engine performance increased. At this high degree of fouling ($\delta\phi/\phi$ = 8 percent and K_η = 1 percent) a mismatch in sequence of peak line was observed. Operating in such a condition could result in compressor surge indicating a threshold level for fouling. The determination of this threshold is valuable from an engine health monitoring standpoint.

Table 1 Compressor diagnostic matrix (Boyce, 1984)

Compressor Diagnostics								
	η_c	P_2/P_1	T_2/T_1	Mass Flow	Vibration	ΔT Bearing	Bearing Pressure	Bleed Chamber Pressure
Clogged filter		↓		↓				
Surge	↑	Variable		↓	Highly fluctuating	↑	↑	Highly fluctuating
Fouling	↓	↓	↑	↓	↑			
Damaged blade	↓	↓	↑	↓	↑			Highly fluctuating
Bearing failure					↑	↑	↓	

Conclusions

A procedure to simulate the effects of different types of faults on engine performance parameters has been described. Fouling and erosion of axial flow compressors are used as examples for the fault simulation. Fault simulation techniques based on subcomponent parameters is found to be effective as it takes into account the interdependency among subcomponents and allows for controlled fault simulation. Results from the axial compressor fault simulation indicate that control of performance of front stages is more important than rear stages. Fouling, which causes a reduction in compressor flow rate, results in a reduced compressor delivery pressure, power output, and increased SFC and heat rate. Erosion, on the other hand, causes a reduction in mass flow rate as a result of a reduced pressure ratio rise due to a reduced chord length. A peak line compressor map was shown to be useful to determine fault threshold levels. A simulation of fault matrix using compressor-turbine matching calculation was found to be in agreement with available field data.

Acknowledgments

The lead author is indebted to the valued guidance and support received during his graduate studies from Dr. Saravanamuttoo at Carleton University and Dr. Tabakoff and Dr. Hamed at the University of Cincinnati.

References

Aker, G. F., and Saravanamuttoo, H. I. H., 1989, "Predicting Gas Turbine Performance Degradation Due to Compressor Falling Using Computer Simulation Techniques," ASME JOURNAL OF ENGINEERING FOR GAS TURBINES AND POWER, Vol. 111, pp. 343-350.

Aviation Week and Space Technology, 1982, "Singapore Airlines," July 19, p. 29.

Balan, C., 1984, "Performance Deterioration of Cascades Exposed to Solid Particles," Ph.D. Dissertation, University of Cincinnati, Cincinnati, OH.

Batcho, P. F., Moller, J. C., Padova, C., and Dunn, M.G., 1987, "Interpretation of Gas Turbine Response Due to Dust Ingestion," ASME JOURNAL OF ENGINEERING FOR GAS TURBINES AND POWER, Vol. 109, pp. 344-352.

Bernton, H., 1989, "Redoubt Volcano Eruptions," *Washington Post*, 17th Dec.

Boyce, M. P., 1984, *Gas Turbine Engineering Handbook*, Gulf Publishing.

Brown, L. E., and Groh, F. G., 1962, "Use of Experimental Interstage Performance Data to Obtain Optimum Performance of Multistage Axial Compressor," ASME JOURNAL OF ENGINEERING FOR POWER, Vol. 84, pp. 187-194.

Diakunchak, I. S., 1992, "Performance Deterioration in Industrial Gas Turbines," ASME JOURNAL OF ENGINEERING FOR GAS TURBINES AND POWER, Vol. 114, pp. 161-168.

Downloaded 02 Jun 2010 to 171.66.16.122. Redistribution subject to ASME license or copyright; see http://www.asme.org/terms/Terms_Use.cfm

Flight International, 1982, "747 Glides," July 3, p. 2.

Jay, A., and Todd, E. S., 1978, "Effect of Steady Flight Loads on JT9D-7 Performance Deterioration," NASA CR-135407, 1978.

Lakshminarasimha, A. N., 1984, "Computer Simulation of Fouling in Axial Flow Compressors," M.Eng. Thesis, Carleton University, Ottawa, Canada.

Meher-Homji, C. B., 1990, "Gas Turbine Axial Compressor Fouling—A Unified Treatment of Its Effects, Detection and Control," ASME IGTI—Vol. 5.

Milner, E. J., et al., 1975, "Performance of a J85-13 Compressor With Clean and Distorted Inlet Flow," NASA TM-X-3304, Dec.

Muir, D. E., Saravanamuttoo, H. I. H., and Marshall, D. J., 1989, "Health Monitoring of Variable Geometry Gas Turbines for the Canadian Navy," ASME JOURNAL OF ENGINEERING FOR GAS TURBINES AND POWER, Vol. 111, pp. 244–250.

Philips, D., 1991, "Widely Used Jet Engines Checked for Corrosion Following Major Fire," *The Washington Post*, June 12.

Sandercock, D. M., et al., 1956, "Experimental Investigation of a Five-Stage Axial-Flow Research Compressor With Transonic Rotors in All Stages," Part I-II NACA RM E54G01, G24, F24, July.

Saravanamuttoo, H. I. H., and Lakshminarasimha, A. N., 1985, "A Preliminary Assessment of Compressor Fouling," ASME Paper No. 85-GT-153; *Turbomachinery International*, Sept. 1985, Vol. 26, No. 7.

Scott, W. B., 1982, "Fix Found for A-10 Residue Problem," *Aviation Week and Space Technology*, 8 Feb., pp. 47, 50.

Schwind, R. G., and McMillan, O. J., 1982, "Blade Erosion Effects on Aircraft-Engine Compressor Performance," NEAR TR 274, Sept.

Siddigh, F., and Saravanamuttoo, H. I. H., 1989, "Determination of the Impact of Compressor Fouling on Gas Turbine Performance Degradation," presented at the Eighth NRCC Symposium on Industrial Application of Gas Turbines, Ottawa, Canada, Sept.

Tabakoff, W., Lakshminarasimha, A. N., and Pasin, M., 1990, "Simulation of Compressor Performance Deterioration Due to Erosion," ASME *Journal of Turbomachinery*, Vol. 112, pp. 78–83.

Wulf, R. H., 1980, "CF6-6D Engine Performance Deterioration," NASA CR—19786, Jan.

Downloaded 02 Jun 2010 to 171.66.16.122. Redistribution subject to ASME license or copyright; see http://www.asme.org/terms/Terms_Use.cfm

Performance and Emission Levels in Gas Turbine Plants

F. Bozza

R. Tuccillo

Dipartimento di Ingegneria Meccanica per l'Energetica (D.I.M.E), Università di Napoli Federico II, Naples, Italy

G. Fontana

Dipartimento di Ingegneria Industriale, Università di Cassino, Cassino, Italy

The rise in gas turbine combustion chamber temperatures requires optimal choices to be made with regard not only to performance parameters but also with a view to resolving pollutant emission problems. For this reason, the authors have set up a gas turbine cycle model, which performs an accurate analysis of several processes, in terms of operating fluid chemical and thermodynamic properties. The model also enables prediction of NO_x formation based upon chemical kinetics and is able to relate the amount of pollutants to a number of operating parameters (e.g., cycle pressure ratio, fuel-to-air equivalence ratio, residence time in combustion chamber, etc.). It can also predict the effect of most usual NO_x reduction systems, such as water or steam injection. A comparison of several possible choices for the gas and combined cycles is then presented, in terms of thermodynamic performance (e.g., first and second law analysis) and nitric and carbon dioxide emissions. In order to find the best compromise between performance improvement and limitation of pollutant emission, enhanced gas cycles are also considered, such as STIG or intercooled-reheat cycles. Examples also refer to medium or low Btu gases, obtained from coal gasification, in order to show not only the possible advantages in terms of thermal NO_x reduction, but also the significant amounts of "fuel NO_x" that can arise from ammonia contained in the fuel.

Introduction

The technological development of gas turbine components in recent years has allowed a significant increase in operating parameter values (e.g., maximum pressure and temperature). The future of the gas turbine would thus seem to see it becoming more and more competitive compared with other types of thermal engines, as regards both power and efficiency levels that can be reached.

On the other hand, this evolution leads to a need for delving into the environmental impact of gas turbine power plants, and, in particular, into pollutant emissions and their contribution to the greenhouse effect. In fact, the higher levels of flame temperature that have characterized the process in recent combustors, produce an increase in thermal NO_x formation. Furthermore, the increased fuel-to-air ratios give rise to greater amounts of carbon oxide and dioxides, which contribute to both air pollution and greenhouse problems.

The above can be detected mainly when firing a conventional fuel, such as oil or natural gas. Particular problems, however, arise when a medium or low LHV fuel is adopted, such as a coal-derived gas. Depending on fuel composition, a strong reduction in thermal NO_x production can often be obtained, but usually an increase in carbon dioxide arises from a higher carbon-to-hydrogen ratio, which characterizes these kinds of fuel. In addition to that, the formation of "fuel NO_x" can be due to the greater quantity of nitrogenous species, such as ammonia, that can be contained in the fuel (Hung, 1975a; Folsom et al., 1980).

In recent papers (Fontana and Tuccillo, 1990; Bozza et al., 1991) the authors have demonstrated that the evolution of the classical thermodynamic parameters of gas turbine cycles should be controlled by including in the objectives not only maximum performance, but also constraints on pollutant production. In fact, some tendencies that could improve performance would also cause a very high increase in emissions. Hence, the systems for NO_x abatement are proving to be increasingly more expensive as regards both the more accurate fluid-dynamic design of combustion chamber (mainly in the case of dry combustors) and the consumption of demineralized injected water or steam (Aoyama and Mandai, 1984; Cerri and Arsuffi, 1988; Fitts et al., 1990; Nakata et al., 1990; Sato et al., 1990; Kreitmeier et al., 1991).

Basing on the considerations above, the authors propose, in this paper, a method for a detailed analysis of gas turbine thermodynamics and some insight also into emissions. To this end a model has been set up for cycle calculation, by including an accurate evaluation of gas composition and properties (Svhela and McBride, 1974). This allows reliable estimation of both the thermal and exergetic balances of the power plant: These also depend on the fuel adopted. The examples presented will, in fact, refer to gas turbine plants fired with either natural or coal-derived gas.

As regards power plant layout, the authors examine two up-to-date gas turbines of the heavy duty and the aero-derivative type, respectively. The latter is, in particular, analyzed in its actual configuration, for both dry and water or steam-injected operation. Performance and emission levels of the base engine

Contributed by the International Gas Turbine Institute and presented at the 37th International Gas Turbine and Aeroengine Congress and Exposition, Cologne, Germany, June 1-4, 1992. Manuscript received by the International Gas Turbine Institute February 21, 1992. Paper No. 92-GT-220. Associate Technical Editor: L. S. Langston.

Copyright © 1994 by ASME
Downloaded 02 Jun 2010 to 171.66.16.122. Redistribution subject to ASME license or copyright; see http://www.asme.org/terms/Terms_Use.cfm

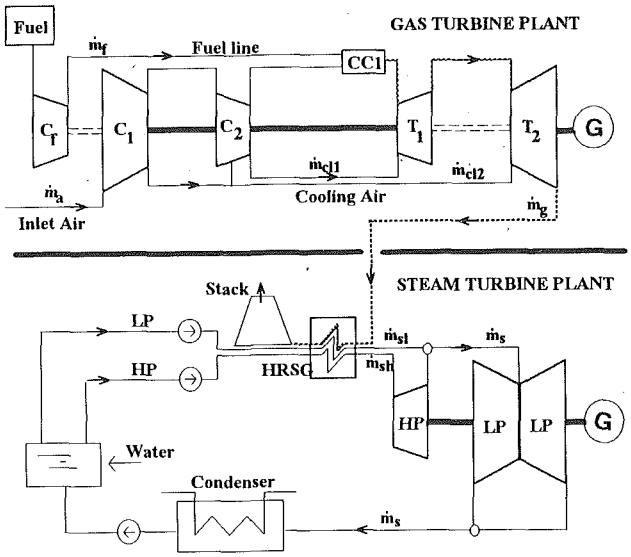


Fig. 1 Combined power plant layout

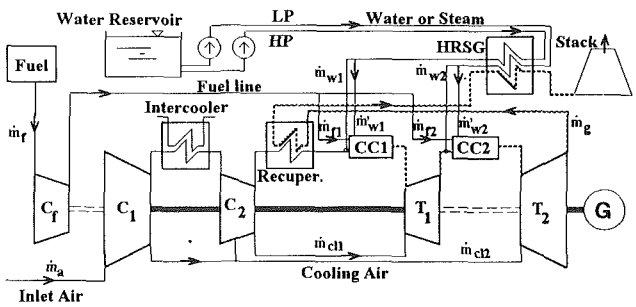


Fig. 2 General layout of enhanced cycle gas turbine plant with water or steam injection

are then compared with those of some alternative configurations, which could be obtained by adopting intercooled compression, regenerative exchangers or reheat cycles (El Masri, 1986, 1987, 1988).

The prediction of thermal NO_x formation is obtained through a model based on chemical kinetics, which relates this type of emission to several typical parameters such as the whole residence time within the combustor, the time fractions dedicated to primary and secondary combustion, the fuel-to-air ratio, and the dilution law. The model also accounts for the effects of water or steam injection into the combustor. A more realistic comparison among several fuels is made possible by some empirical correlations (Nakata et al., 1990), which were employed to predict fuel NO_x formation.

The results are presented in terms of several emission indices, which put into evidence either the concentration of noxious species in the exhaust or the amount of pollutant per unit of mechanical output. The latter will emphasize, therefore, the benefits of combined cycle plants and of any other system aiming to improve the performance level without altering the main combustion process.

Thermodynamic Analysis

Figures 1 and 2 show two general gas turbine plant layouts, which refer to general complex configurations that can easily be simplified by eliminating one or more components. Dashed lines between fuel and air compressors indicate that the mechanical linking of these two components does not really exist, but the fuel compression work should be taken into account in the plant energy balance. Similarly, the dashed connection of the two gas turbines signifies the possibility of either single or two-shaft arrangement.

In particular, Fig. 1 illustrates a classical simple cycle gas turbine plant layout with a dual pressure heat recovery steam generator (HRSG) for the bottoming steam power plant. Figure 2 refers to a more complex schema, which includes a number of modifications to the base layout of Fig. 1. In fact, both intercooled compression and reheated expansion are considered and the possibility of regenerative cycle is also included. In addition, the HRSG device allows steam injection upstream of the first combustion chamber, CC_1, and downstream of the high-pressure turbine, T_1 ($\dot{m}_{w1}$ and $\dot{m}_{w2}$ rates, respectively). Further rates of water or steam, $\dot{m}'_{w1}$ and $\dot{m}'_{w2}$, are supposed to be directly injected into the combustion chambers for thermal NO control.

In both schemes, internal air blade cooling was considered. The air rates, $\dot{m}_{cl1}$ and $\dot{m}_{cl2}$, and the number of blade elements that require cooling were determining by assigning the maximum metal temperature and by evaluating the related heat transfer effectiveness (El Masri, 1986, 1988).

To the end of performing energy and exergy balances, the following nondimensional quantities are introduced, as to summarize the mass flow conditions through the plant components in Figs. 1 and 2.

Nomenclature

b = availability, kJ/kg
EI = emission index
f, F = fuel-to-air ratio
h = enthalpy, kJ/kg
I = irreversibility loss, kJ/kg
k = kinetic constant, cm^3/mole s
$m, \dot{m}$ = mass, mass flow rate, kg, kg/s
M = mass per unit of inlet air, kg/kg_{air}
$dNO/d\tau$ = rate of NO formation, mole/cm^3s
[NO] = NO concentration, ppm
p = pressure, MPa
r = speed of reaction, mole/cm^3s
R = gas constant, kJ/kg K
s = entropy, kJ/kg K
T = temperature, K
W = work, kJ/kg
x_i = molar fraction
x_w, X_w = water or steam mass fraction
y, Y = air fraction
z, Z = gas fraction
β = pressure ratio
ϵ = exergy, kJ/kg
η = efficiency
ξ = exergetic value of fuel, kJ/kg
τ = time, ms
τ_r = residence time, ms
ϕ, Φ = equivalence ratio

Subscripts

a = air
$b, b1, b2$ = combustor
$c, c1, c2$ = compressor
cc = combined cycle
ch = chemical contribution
cl = cooling air
eq = chemical equilibrium
f = fuel
g = exhaust gas
gt = gas turbine
II = second law
m = mixture
P = plant
st = stoichiometric
$t, t1, t2$ = turbine
th = thermal
w = water or steam
0 = standard conditions

Superscripts

ch = chemical contribution
tm = thermomechanical contribution
$*$ = current combustion
$'$ = primary combustion
$''$ = secondary combustion

Downloaded 02 Jun 2010 to 171.66.16.122. Redistribution subject to ASME license or copyright; see http://www.asme.org/terms/Terms_Use.cfm

- The following ratios account for changes in mass flow due to cooling air bleeding and re-injection:

$$Y_1 = \frac{\dot{m}_a - \dot{m}_{cl1} - \dot{m}_{cl2}}{\dot{m}_a}; \quad Y_2 = \frac{\dot{m}_a - \dot{m}_{cl2}}{\dot{m}_a} \tag{1}$$

- Fuel-to-air and equivalence ratios in first and second combustion and in plant mass balance:

$$F_1 = \frac{\dot{m}_{f1}}{Y_1 \dot{m}_a}; \quad F_2 = \frac{\dot{m}_{f2}}{(Y_2 - Y_1 \Phi_1)\dot{m}_a}; \quad F = \frac{\dot{m}_{f1} + \dot{m}_{f2}}{\dot{m}_a} \tag{2}$$

$$\Phi_1 = \frac{F_1}{F_{st}}; \quad \Phi_2 = \frac{F_2}{F_{st}}; \quad \Phi = \frac{F}{F_{st}} \tag{3}$$

- Local and overall steam (or water) to air ratios:

$$X_{w1} = \frac{\dot{m}_{w1}}{Y_1 \dot{m}_a}; \quad X'_{w1} = \frac{\dot{m}_{w1} + \dot{m}'_{w1}}{Y_1 \dot{m}_a} \tag{4}$$

$$X_{w2} = \frac{\dot{m}_{w1} + \dot{m}'_{w1} + \dot{m}_{w2}}{Y_2 \dot{m}_a}; \quad X'_{w2} = \frac{\dot{m}_{w1} + \dot{m}'_{w1} + \dot{m}_{w2} + \dot{m}'_{w2}}{Y_2 \dot{m}_a} \tag{5}$$

$$X_w = \frac{\dot{m}_{w1} + \dot{m}'_{w1} + \dot{m}_{w2} + \dot{m}'_{w2}}{\dot{m}_a} \tag{6}$$

- Exhaust mass after first and second combustion:

$$M_{g1} = Y_1 (1 + X'_{w1} + F_1)$$

$$M_{g2} = Y_2 (1 + X'_{w2} + F_2) + Y_1 F_1 (1 - \Phi_2) \tag{7}$$

- Total exhaust mass downstream of the power turbine:

$$M_g = 1 + X_w + F \tag{8}$$

The above definitions lead to an easier estimation of the plant energy balance. The net gas turbine mechanical output per unit of air flow is thus expressed as follows:

$$W_{gt} = M_{g1} W_{t1} + M_{g2} W_{t2} - (W_{c1} + W_{c2}) \tag{9}$$

In particular, the specific works, W_{t1} and W_{t2}, are referred to the unit of gas flow entering the high-pressure and the low-pressure turbine, respectively. They are evaluated through an expansion model, which is in accordance with the original proposal of El Masri (1986, 1988) and has been modified by the authors in order to fit the particular features of the configurations examined (Bozza and Tuccillo, 1992). The values of W_{t1} and W_{t2} include effects of the cooled expansion and of cooling air addition to the main stream as well. Similarly, the compression works, W_{c1} and W_{c2}, account for any air bleeding that occurred upstream of the high-pressure compressor discharge.

In the authors' opinion, a more correct mechanical energy balance should include the gaseous fuel compression work, which can be of particular importance when low or medium Btu coal gases are considered. This leads to an alternative formulation of the net mechanical output of the gas turbine plant:

$$W_P = W_{gt} - F\, W_{cf} \tag{10}$$

The related first-law efficiencies are then evaluated as:

$$\eta_{gt} = \frac{W_{gt}}{F\ \mathrm{LHV}}; \quad \eta_P = \frac{W_p}{F\ \mathrm{LHV}} \tag{11}$$

The classical definitions of flow availability and exergy were adopted for the second law analysis of the energy conversion process (Bejan, 1988; Kotas, 1985; Moran, 1982):

$$b = h - T_0 s \tag{12}$$

$$\epsilon = \epsilon^{tm} + \epsilon^{ch} = (h - h_0) - T_0 (s - s_0) + R T_0 \sum x_{i0} \ln \frac{x_{i0}}{x_{ia}} \tag{13}$$

Hence the exergy definition comprehends both the thermomechanical and the chemical terms. The latter accounts for the maximum reversible work that could be obtained through the diffusion of the molecular species at the reference state, due to their different concentration in the exhaust (x_{i0}) and in the external environment (x_{ia}). As will be shown in the following, this will reveal significant differences that arise from the use of either natural or coal derived fuels.

The irreversibility losses, I, through the components of the plant layouts in Figs. 1 and 2 are given by:

- Losses in compression processes, I_c.
- Losses in the cooling heat exchanger. The difference in the exergetic value between the upstream and downstream conditions of the exchanger is considered as completely lost in the atmosphere.
- Steam–air mixing losses in injection downstream of the compressor or upstream of the T_2 turbine.
- Irreversibility losses in the combustion processes, I_b. These losses also include those related to fuel–air mixing and to water injection.
- Losses, I_t, in cooled expansion processes, also related to the gas–air mixing.
- Exergy destruction in heat recovery in the HRSG device or in the regenerative exchanger.

The above-listed exergy destructions also include the effects of the total pressure losses in the flow through the several components such as heat exchangers and combustors. A further source of destruction is the chemical exergy associated with the exhaust composition at the discharge of the whole gas turbine process:

$$I_{ch} = M_g \epsilon_g^{ch} \tag{14}$$

This amount could be, in fact, converted into work only by very special devices (i.e., for instance, a Van't Hoff box); a more realistic analysis would consider only the exhaust thermomechanical exergy as potentially convertible into work. Hence the maximum mechanical output, per unit of mass of air, which is obtainable from the gas turbine process, is given by:

$$W_{\max} = W_P + M_g\, \epsilon_g^{tm} \tag{15}$$

The total theoretical work $W_{\max}$ is introduced in the second law efficiency definition:

$$\eta_{II} = 1 - \frac{\Sigma\, I}{F\, \xi_{of}} = \frac{W_{\max}}{F\, \xi_{of}} \tag{16}$$

The values of $W_{\max}$ and η_{II} represent an effectiveness criterion of the processes through the gas turbine components. Furthermore, they can be assumed as reference values when compared with the actual levels of mechanical output and efficiency, W_{cc} and η_{cc}, which can be reached in combined plant operation. The combined plant mechanical output is obtained by adding to the W_P term the steam cycle work, which accounts, of course, for the steam production in the HRSG.

In calculations, the lower heating value, LHV, of the fuel and the corresponding combustion heat are directly derived from the thermal balance of the combustor, by evaluating the heat of formation of the chemical species (Svhela and McBride, 1974). The fuel exergetic value is calculated in standard conditions, by accounting for the standard exergy of elementary species included in fuel gas mixture (Kotas, 1985).

Thermal NO Formation Model

The calculations for the prediction of thermal nitrogen monoxide are based on the reactions considered in the well-known Zeldovich mechanism (Zeldovich et al., 1947; Lefevbre, 1983; Warnatz, 1990).

The reaction development takes place in accordance with the chemical kinetics laws and is, therefore, characterized by a number of coefficients (k_{af}, . . . , k_{cf}, . . . , k_{cr}) for the

Downloaded 02 Jun 2010 to 171.66.16.122. Redistribution subject to ASME license or copyright; see http://www.asme.org/terms/Terms_Use.cfm

forward and reverse processes. This leads to the relationship for the evaluation of the rate of NO formation:

$$\frac{d\mathrm{NO}}{d\tau} = 2\, r_a \frac{1-\left(\frac{[\mathrm{NO}]}{[\mathrm{NO}]_{eq}}\right)^2}{1+\frac{[\mathrm{NO}]}{[\mathrm{NO}]_{eq}} r_0} \tag{17}$$

where

$$r_a = k_{af}\,[\mathrm{O}]_{eq}[\mathrm{N_2}]_{eq}$$

$$r_b = k_{br}\,[\mathrm{NO}]_{eq}[\mathrm{O}]_{eq}$$

$$r_c = k_{cr}\,[\mathrm{NO}]_{eq}[\mathrm{H}]_{eq} \tag{18}$$

$$r_0 = \frac{r_a}{r_b + r_c}$$

Equation (17) summarizes the dependence of the rate of thermal NO formation on the local concentration, [NO], versus that possible in chemical equilibrium conditions $[\mathrm{NO}]_{eq}$. A further influence is, of course, exerted by the speed of the fundamental reactions (*a–c*) that have been considered, since each "*k*" coefficient responds to the Arrhenius law:

$$k = A\, T^n \exp(-E_A/RT) \tag{19}$$

T is the "local" gas temperature in the combustor. The values of the A coefficients and the n exponents and of the E_A energy of activation are derived from experimental correlations (Glassman, 1987; Heywood, 1987).

Despite the well-known limits of this simplified approach, the mechanism considered is strongly affected by the combustion development. Therefore, it is necessary to evaluate the local values of the gas temperature and of the equilibrium concentrations $[\,.\,.]_{eq}$, as functions of the fuel/air ratio in each combustor zone.

The model proposed by the authors follows the development of the process by assuming the time τ as a free variable within an interval, τ_r, which can be considered as the gas residence time after the primary combustion process. The interval τ_r is then subdivided into three fractions, τ', τ'', and τ_d, which respectively correspond to:

- The permanence of the combustion gases in the typical conditions of the primary combustion, without further air supply. Therefore numerical computation starts with gases considered at the maximum temperature level and with a composition depending on the fuel to air ratio adopted for the primary combustion. If water or steam injection occurs, the amount is supposed to be progressively provided within the τ' interval.
- The secondary combustion phase, characterized by an air supply (which is hypothesized to occur in a time $0.5\,\tau''$) and by the permanence of the gases in conditions that allow a complete oxidation and elimination of unburned fractions.
- The dilution process, with a linear rate of increase for both air and other species produced by any previous combustion.

The rate of thermal NO formation is thus evaluated in the time interval $(0, \tau_r)$ and its value is updated in accordance with local thermochemical conditions. Really, it has to be pointed out that a correspondence can be established between each gas location inside the combustor and any instant, τ. As a consequence, the evolution of thermodynamic conditions must be followed for both reactants and combustion products as a function of time. It should also be remembered that the model must include a number of situations, such as reheat or the presence of steam mixed with the air and water injection.

In the following, the method for thermal NO prediction is therefore described for a general case, by including all of the above-listed occurrences. Particular conditions, according to the schemes of Figs. 1 and 2, can then be easily derived. Therefore the generic combustion process is represented by the "i" subscript. Quantities with "$i-1$" will, of course, disappear when dealing with the first combustion. The evaluation of the mass of the several fluid species that participate to the process at any instant is performed as follows, by referring to the unit of air mass entering the compressor.

Gas Mixture Entering the Combustor. The mass of mixture entering the combustion chamber (i.e., air and products of any previous combustion and eventually injected steam) can be represented by the nondimensional fraction:

$$Z_i = Y_i(1 + X_{wi}) + Y_{i-1} F_{i-1} \tag{20}$$

Air. The fraction of air available for the combustion process contained in this mixture is given by:

$$Y_i^* = Y_i - Y_{i-1}\,\Phi_{i-1} \tag{21}$$

The local amounts of air, $y_i(\tau)$, and of gas mixture, $z_i(\tau)$, which participate to the several phases of the process are then determined as follows.

1 Primary Combustion. The fraction of primary air, Y_i', is evaluated according to the equivalence ratio established for this phase, Φ_i':

$$Y_i' = Y_i^* \frac{\Phi_i}{\Phi_i'} \tag{22}$$

and the related local values are given by:

$$y_i(\tau) = Y_i' \quad (0 \le \tau \le {}' \tau_i) \tag{23}$$

2 Secondary Combustion. If the secondary air mass fraction for this phase is fixed (according to an assigned Y_i''/Y_i^* ratio) the value of $y_i(\tau)$ is supposed to increase linearly from Y_i' to Y_i'' in the time interval $(\tau_i' < \tau \le \tau_i' + 0.5\tau_i'')$. A constant value is next maintained:

$$y_i(\tau) = Y_i'' \quad (\tau_i + 0.5\tau_i'' < \tau \le \tau_i'') \tag{24}$$

3 Dilution. As said above, in this phase a linear increase of air mass is considered in the time interval τ_d until the final value, Y_i^*, has been reached.

The evaluation of the $z_i(\tau)$ fractions is carried out according to the relationship:

$$z_i(\tau) = y_i(\tau) \frac{Z_i}{Y_i^*} \quad (0 < \tau \le \tau_r) \tag{25}$$

Fuel.

$$f_i(\tau) = F_i\, Y_i^* \quad (0 < \tau \le \tau_r) \tag{26}$$

Steam or Water Injected. Since steam injected upstream of the combustion chamber is already considered in the $z_i(\tau)$ fractions, a further amount, $x_{wi}(\tau)$, is introduced as to represent the water or steam injected directly into the combustor. For this amount, a linear rise is assumed during the time interval τ'.

Figure 3 summarizes the conditions described above for the rate of increase of the fractions of reactants and fuel.

The evaluation of the single amounts of fluid present at each instant allows calculation of gas composition and of local properties. In fact, the total mass of gases is:

$$M_{gi}(\tau) = z_i(\tau) + x_{wi}(\tau) + f_i(\tau) \tag{27}$$

and the corresponding enthalpy level:

$$M_{gi}(\tau) h_{gi}(\tau) = z_i(\tau) h_{mi} + x_{wi}(\tau) h_{wi} + f_i(\tau) h_{fi} \tag{28}$$

Besides, the local value of equivalence ratio, ϕ, can be derived from the amounts of air and fuel that have been introduced up to the time instant τ:

$$\phi_i(\tau) = \frac{Y_i}{y_i(\tau)}\,\Phi_i \tag{29}$$

Downloaded 02 Jun 2010 to 171.66.16.122. Redistribution subject to ASME license or copyright; see http://www.asme.org/terms/Terms_Use.cfm

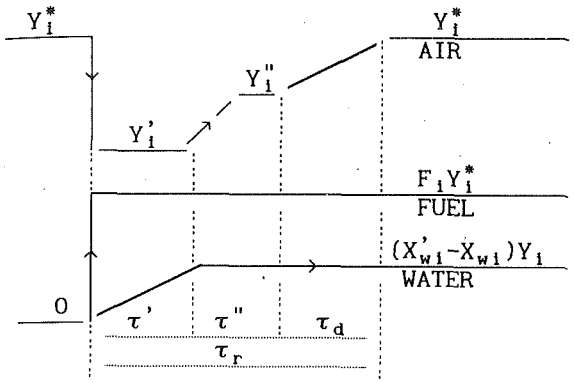


Fig. 3 Qualitative sketch of the changes in air, water, and fuel amounts within the residence time

Thermodynamic calculations are performed according to the relationship:

$$h_{gi}=f\ (p_i,\ T_{gi}(\tau),\ \phi_i(\tau)) \tag{30}$$

which allows, through an inverse process, the evaluation of the local gas temperature, $T_{gi}(\tau)$. Both typical equivalence ratio and gas temperature behavior are shown in Fig. 4(*a*, *b*) as functions of time, for a given combustion pressure level. In fact, it has to be borne in mind that the energy level h_{gi} is strongly affected by both thermodynamic conditions of gas mixture entering the combustor and gas composition. Thus, the inlet enthalpy value, h_{mi}, is also influenced by any previously occurring combustion and steam injection as well.

The thermodynamic model therefore allows estimation of thermal NO development, through the local equilibrium composition and gas temperature, which must be introduced in the computational schema for numerical integration of Eq. (17). Furthermore, the method permits analysis of the influence of several operating parameters of either gas turbine plant or, more specifically, of the combustion chamber.

Emission Indices. The instantaneous values of $d\mathrm{NO}/d\tau$ are provided by Eq. (17) in mole/(cm^{3}s). A typical pattern of this parameter is shown in Fig. 4(*c*). In the case of reheat cycles, the time variation of moles of NO in the exhaust can be estimated, by accounting both for further amounts of NO induced by the thermal mechanism in the second combustor and for those arising from previous combustion processes and introduced in the combustor together with the secondary or dilution air. The local NO concentration, [NO], can therefore be obtained.

Figure 4(*d*) illustrates a trend evaluated for [NO] within the residence time. The increase that can be observed in the NO formation rate at the beginning of the secondary combustion phase (Fig. 4*c*) is a consequence of the greater oxygen and nitrogen content. The following decrease in NO concentration is obviously due to both the lower temperature and to the air dilution effects (Fig. 4*d*).

The final values of [NO] at the end of the numerical calculation over the whole process can be used to estimate the usual emission indices (Kretschmer and Odgers, 1989):

- The wet or dry thermal NO concentration [ppm];
- The whole amount of NO produced per kg of either air or fuel, EINO_a [$g_{\mathrm{NO}}/\mathrm{kg}_{\mathrm{air}}$] and $\mathrm{EINO}_f = \mathrm{EINO}_a/F$[$g_{\mathrm{NO}}/\mathrm{kg}_{\mathrm{fuel}}$].
- The emission index, EINO_W [g_{NO}/kWh], is of particular interest. This relates the global amount of thermal NO (or, in general, of total $\mathrm{NO_x}$) to the unit of mechanical output of a power plant. Hence its behavior can be quite different from those of the other indices and can highlight the benefits of devices which improve work capacity or reduce specific fuel consumption. A similar emission index, based on the exhaust composition, has been employed for carbon dioxide, EICO_{2W}, expressed in [$\mathrm{kg}_{\mathrm{co2}}$/kWh].

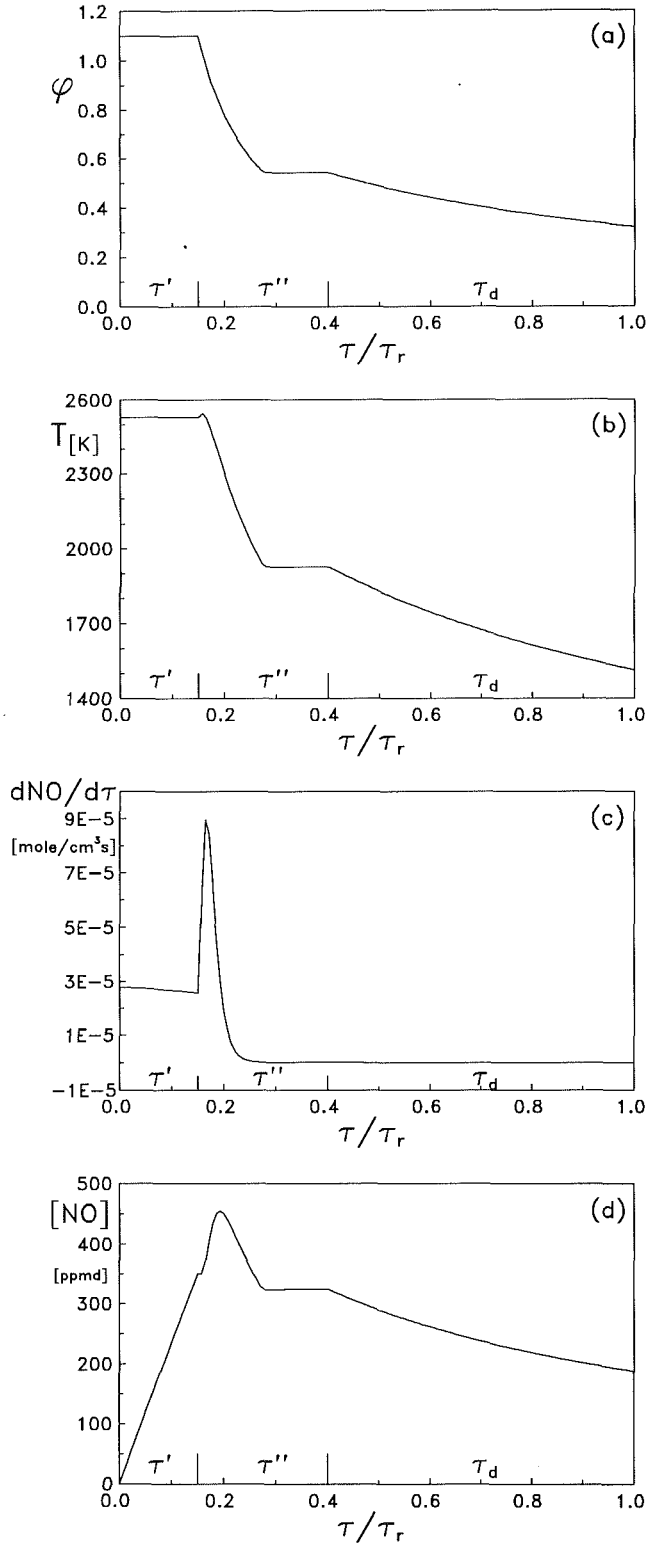


Fig. 4 Typical trend estimated for equivalence ratio, gas temperature, and NO formation rate and concentration

Fuel $\mathrm{NO_x}$

A further contribution to $\mathrm{NO_x}$ formation is given by the nitrogenous species, like ammonia, contained in fuel, which undergo a direct conversion into nitrogen oxides, named "fuel $\mathrm{NO_x}$." This particular $\mathrm{NO_x}$ formation occurs according to chemical mechanisms different from those of thermal NO (Folsom et al., 1980).

Downloaded 02 Jun 2010 to 171.66.16.122. Redistribution subject to ASME license or copyright; see http://www.asme.org/terms/Terms_Use.cfm

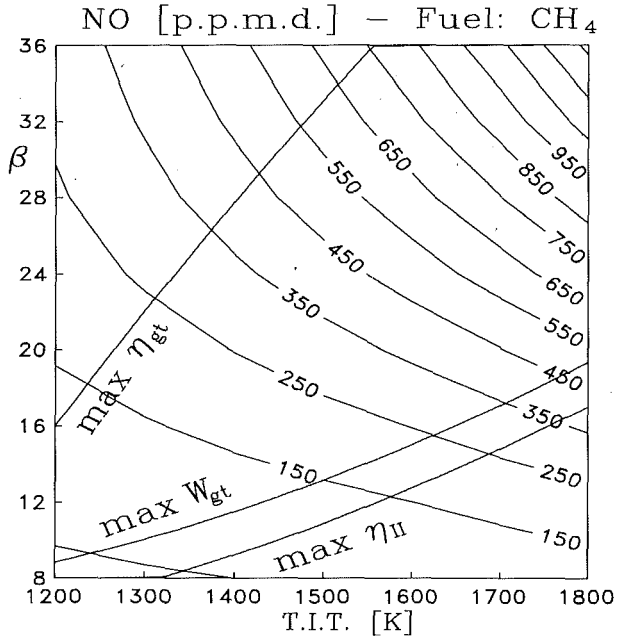


Fig. 5 Qualitative trend of thermal NO emission as a function of gas turbine cycle parameters

The relative weight of this contribution is more significant for those fuels, such as low LHV coal-derived gases, which manifest good behavior from the point of view of thermal NO. In particular these fuels may be characterized by ammonia content.

The examples presented in the following include the fuel NO_x prediction through the estimation of the degree of conversion of ammonia into nitrogen oxides. The latter parameter was derived from experimental data available in the literature (Sato et al., 1990) as a function of the initial NH_3 concentration in the fuel and of the equivalence ratios assumed for both primary combustion, ϕ_1, and for the whole process. All emission indices are then corrected for the presence of fuel NO_x.

Performance and Emission Analysis

An example of both performance and emission analysis through the computational model is reported in Fig. 5. The typical behavior of the NO concentration in the exhaust is presented as a function of pressure ratio and T. I. T. for simple Brayton cycle gas turbines. Three lines are superimposed, on the emission index contours that indicate the optimum values of cycle pressure ratio, β, which maximize first and second law efficiencies or mechanical output.

These patterns clearly indicate that pursuing the objective of maximum in η_{gt} efficiency could lead to dramatically increased emission levels. A slower rise can be observed in the pressure ratio range, which optimizes work or second law efficiency. This range is usually of interest also for the best operation of combined cycle plants (Fontana and Tuccillo, 1990). In the case of combination with a steam bottoming plant, also the $EINO_W$ index would be decreased due to the higher mechanical output obtained.

These results were obtained by the authors (Bozza et al., 1991) for fixed values of the parameters influencing thermal NO formation and represent a qualitative sketch of the rise in this emission as a consequence of any allowable increase in turbine inlet temperature. Of course this indicates the importance of the actions that should be taken in order to reduce emission to acceptable levels, by means of either a more effective dry combustor design (Aoyama and Mandai, 1984; Kreitmeier et al., 1991) or water injection (Fitts et al., 1990).

Comparison of Heavy Duty and Aeroderivative Gas Turbines.

Table 1(*a*) Air and fuel composition

TABLE 1.a	CH_4	C_6H_6	CO	H_2	CO_2	H_2O	N_2	A_r	O_2
Air	---	---	---	---	0.03	0.9	77.35	0.92	20.8
CH_4	100	---	---	---	---	---	---	---	---
G1	7.2	---	57.3	28.3	3.0	---	4.20	---	---
G2	4.4	0.5	16.6	21.4	11.5	11.2	34.40	---	---
G3	2.5	---	18.3	6.9	12.9	3.0	56.40	---	---

Table 1(*b*) Fuel data

TABLE 1.b	F_{st} /	LHV kJ/kg	ξ_{0f} kJ/kg
CH_4	0.0578	49856	52145
G1	0.2555	14284	14117
G2	0.5230	6582	6728
G3	1.1285	3221	3293

Table 2

TABLE 2	Gas Turbine LM 1600				Gas Turbine MS 7001F			
Fuel	CH_4	G1	G2	G3	CH_4	G1	G2	G3
$F_{\%}$	1.64	5.72	13.43	29.97	1.95	6.81	16.22	37.11
Φ	0.284	0.224	0.257	0.266	0.337	0.266	0.310	0.329
W_{gt}	307.4	321.4	389.0	490.7	340.7	355.4	435.8	559.2
η_{gt}	.3828	.3932	.4402	.5083	.3577	.3655	.4083	.4679
W_P	290.0	266.2	277.7	282.0	320.1	289.7	301.4	300.9
η_P	.3612	.3257	.3143	.2922	.3361	.2980	.2824	.2518
η_{II}	.5766	.5903	.5617	.5470	.5942	.6080	.5805	.5648
M_{cl}	.1188	.1252	.1472	.1840	.1030	.1078	.1201	.1418
T_{ex}	756.8	761.9	759.1	759.5	860.1	866.3	868.4	875.0
W_{cc}	417.5	400.3	422.1	445.5	515.9	494.8	530.8	571.9
η_{cc}	.5200	.4897	.4777	.4615	.5416	.5090	.4973	.4785

Table 3

TABLE 3	Gas Turbine LM 1600				Gas Turbine MS 7001F			
Fuel	CH_4	G1	G2	G3	CH_4	G1	G2	G3
I_c	5.23	5.75	5.51	5.56	3.86	4.28	4.14	4.23
I_t	6.78	7.22	7.72	8.22	5.01	5.34	5.49	5.63
I_b	28.54	24.14	24.57	23.44	29.81	25.56	26.15	25.36
I_{tg}	40.54	37.11	37.80	37.22	38.68	35.19	35.79	35.22
I_{ch}	1.80	3.86	6.03	8.08	1.90	4.01	6.16	8.30

Tables 2-4 present a comparison of a typical heavy duty gas turbine (GE MS7001F) with an aeroderivative engine (GE LM 1600) whose operating parameters would lead to significant differences in both performance and emission indices:

Gas turbine	Pressure ratio	Turbine inlet temperature
GE LM 1600	$\beta = 22$	T. I. T. = 1513.7 K
GE MS 7001F	$\beta = 13.5$	T. I. T. = 1533 K

Downloaded 02 Jun 2010 to 171.66.16.122. Redistribution subject to ASME license or copyright; see http://www.asme.org/terms/Terms_Use.cfm

Table 4

TABLE 4	Gas Turbine LM 1600				Gas Turbine MS 7001 F			
Fuel	CH_4	G1	G2	G3	CH_4	G1	G2	G3
T'_{max}	2530	2680	2307	2048	2464	2624	2260	2012
$[NO]_{th}$	165.2	957.1	13.93	0.51	78.47	616.3	7.371	0.28
$[NO_x]_f$	---	71.29	144.3	232.5	---	87.34	174.6	276.
$EINO_f$	10.07	17.43	.1139	.0022	4.007	9.443	.0505	.001
$EINO_W$	2.049	13.49	.1982	.0083	.8767	7.986	.0979	.005
$EINOx_W$	2.049	15.13	2.425	3.936	.8735	9.577	2.634	4.60
$EICO2_W$	603.9	1190	1285	2150	653.3	1307	1447	2510
$EINOx^{cc}_W$	1.423	10.06	1.596	2.492	.5439	5.607	1.496	2.42
$EICO^{cc}_{2W}$	419.5	791.1	845.8	1361	406.6	765.3	821.7	1321

Compressor and turbine polytropic efficiencies were assumed, respectively, to be 0.85 and 0.88.

The examples also compare the influence of fuel burned. For both cases four fuels were examined: methane and three different coal derived fuels, G1–G3 (De la Mora et al., 1985; Nakata et al., 1990), whose composition is reported in Table 1.a.

The pressure ratios of the two gas turbines (the T. I. T. being essentially the same) led, as expected, to higher efficiency levels for the LM 1600, while the heavy duty turbine presents better values for specific power and second law efficiency, that make possible a more favorable use in combined plants (Table 2).

As regards the influence of the fuel burned, the most interesting feature of the employment of low-Btu fuels (like G2 and G3) is the noticeable increase in gas turbine work, W_{gt}, due to the large fuel-to-air ratio, F, which must be adopted to reach the required turbine inlet temperature. The related η_{gt} efficiency would result considerably higher. The net plant mechanical output, W_p, would, however, be reduced, as a consequence of the increased fuel compression work. Therefore, the level of plant first-law efficiency, η_P, is clearly lower in the case of coal-derived gases.

Slighter differences appear in second law efficiency comparison between natural and coal derived gases, thus confirming the possibility of achieving satisfactory performance levels using integrated coal gasification combined plants (Pechti et al., 1988; Tuccillo et al., 1990). It should also be remembered that IGCC plants allow the increased costs and energy losses arising from the gasification process to be compensated.

The results of the second-law analysis are summarized in Table 3 and indicate the irreversibility losses, which led to the η_{II} level reached according to the fuel burned. Coal gases reduce the combustion loss, I_b, owing to a lower entropy increase related to the change in gas composition. In general, a smaller overall exergy destruction, I_{gt}, occurs in the gas turbine process with coal derived fuels. On the contrary, a more significant loss is associated, as has already been stated, with the chemical contribution, to the total exergy flow at the gas turbine discharge, I_{ch}.

For thermal NO evaluation, a fixed set of values was assumed for the combustion chamber parameters of both engines, in order to perform comparisons based only on the differences in thermodynamic cycles:

- Equivalence ratio: $\Phi' = 1.1$
- Residence time: $\tau_r = 7$ ms
- Fraction of τ' time: $\tau'/\tau_r = 0.15$
- Fraction of τ'' time: $\tau''/\tau_r = 0.25$
- Fraction of secondary air: $Y''/Y^* = 0.3$

The thermal NO level appears to be higher for the aeroderivative engine, due to the increased inlet temperature of the combustor. The low LHV fuels (i.e., G2 and G3 in Table 1) present quite negligible emission levels as regards thermal nitrogen oxides. This is due to the lower temperature levels inside the combustor and, regarding the thermal NO formation mechanism, to a more favorable composition of fuel and exhaust. G1 gas, which is a typical medium LHV coal-derived fuel, could result in an increase in thermal NO with respect to natural gas, owing to a larger hydrogen/carbon ratio causing a higher temperature level in the combustor, T'_{max} (Table 4).

Also of interest is the possible increase in NO_x emission, which could occur due to the presence of ammonia in the fuel. The fuel NO_x formation was calculated by assuming a 1000 ppm ammonia content for all coal-derived fuels; this leads to a more significant production for plants fired with poor fuels. In this case, in fact, the combustor is supplied at a high fuel rate, increasing consequently the ammonia, which is converted into nitrogen oxides. This kind of formation is more important in the heavy-duty engine, which requires a higher equivalence ratio.

Thus, if an accurate process to eliminate ammonia has not been carried out, the overall NO_x emission level (represented by the $EINO_{xW}$ index in Table 4) becomes more relevant for fueling using very low Btu gases, than is the case for the use of methane or hydrocarbons.

As previously discussed, combined cycle operation may have significant advantages if adopted for gas turbines fired with coal-derived fuels. Results refer to dual pressure steam bottoming cycles (10/0.6 MPa for MS 7001F; 8.5/0.6 MPa for LM 1600). The high-pressure superheated steam temperature was assumed to be 813 K. Of course the latter value was reduced in the case of the LM 1600 exhaust temperature, according to a minimum approach temperature difference of 30 K.

The increase in specific power, W_{cc} in Table 2, is more evident for low Btu gas fueling, since a higher steam production is possible in the HRSG as a consequence of the greater exhaust gas flow produced by coal derived fuels. The efficiency level, η_{cc}, undergoes more significant improvements in the case of coal gases, thus confirming the comments on the second law analysis. It can be clearly noted that the differences in power plant first-law efficiency between methane and coal gas cycles appear to be strongly reduced when gas–steam cycles are considered. Of course, these values do not account for previous losses that occurred in the coal gasification process.

The benefits of combined plant operation are also evident in terms of emission indices, which undergo considerable decreases ($EINO_{x_{W_{cc}}}$ and $EICO_{2_{W_{cc}}}$ in Table 4). It should be observed, for example, that the NO_x emission index for *G2* firing in combined plants may become lower than the corresponding one in the case of a simple Brayton cycle engine with methane, even considering fuel NO_x production. Also, the CO_2 emission index achieves levels close to those of single-cycle gas turbines fired with conventional fuels.

Analysis of Different Plant Configurations. The base configuration of the GE LM 1600 was next compared with a number of different solutions (Fig. 2), such as those listed below:

1 Base two-shaft configuration, with operating parameters as indicated by the manufacturer.

2 Steam injected configuration (STIG). Three steam rates (per unit of air flow) were considered, respectively: injected downstream of the compressor (M_{w1}), into the combustor (M'_{w1}), and upstream of the power turbine (M_{w2}). The thermodynamic conditions of these fractions, in accordance with the manufacturer's data, are the following:

$M_{w1} = 5.50$ percent; $p_{w1} = 3.45$ MPa; $T_{w1} = 683$ K

$M'_{w1} = 1.60$ percent; $p'_{w1} = 3.45$ MPa; $T'_{w1} = 683$ K

$M_{w2} = 6.33$ percent; $p_{w2} = 1.31$ MPa; $T_{w2} = 661$ K

Downloaded 02 Jun 2010 to 171.66.16.122. Redistribution subject to ASME license or copyright; see http://www.asme.org/terms/Terms_Use.cfm

3-4 Water injection into the combustion chamber with two different water fractions, referred to the air flow, equal to 1.6 and 5 percent, respectively, with a temperature of 350 K and a pressure of 3.47 MPa.

5 Intercooled compression, without steam or water injection. Intercooling is considered after the low pressure compressor ($\beta_{c1} = 2.53$).

6 Similar to configuration (5) but with a regenerative heat exchanger upstream of the combustor. It should be noted that a regenerative cycle would not be possible for the base configuration without an intercooled compression.

7 Configuration with reheat upstream of the power turbine. The expansion ratio of the gas generator turbine is evaluated in accordance with mechanical equilibrium conditions.

The above-listed solutions refer to already-existing configurations or, because of the two-shaft arrangement of this engine, to ones that are quite easily obtainable. In some cases some components should undergo modifications in order to adapt their characteristics to the new operating conditions (for example, the high-pressure compressor in cases (5) and (6) and the power turbine in case 7).

Further configurations were next examined, by referring to optimized data for the cycle parameters. Such data would permit maximum first-law efficiencies but would also entail carrying out extensive modifications to either the whole power plant or to single components:

8 Reheat scheme with an optimized expansion ratio $\beta_{t1} = 1.6$. The total pressure ratio was assumed to be equal to that of the base engine and thus the work provided by the first turbine, T_1, would not be sufficient for the gas generator. Significant modifications to the whole engine arrangement would therefore be required.

9 Reheat and intercooled compression. In this case too, the total pressure ratio was fixed at its initial value but the ratios for both the C_1 compressor and the T_2 turbine in Fig. 2 were optimized ($\beta_{c1} = 2.15$ and $\beta_{t1} = 1.48$, respectively).

10 The scheme examined is identical to the previous one but in addition the total cycle pressure ratio was optimized. An optimal value of $\beta = 77.8$ was found (for the same T. I. T.) and the partial pressure ratios were established as follows: $\beta_{c1} = 4.76$, $\beta_{t1} = 2.51$.

In all cases only methane-fired conditions were analyzed and constant values were assumed for some parameters, which influence, as described above, the development of the formation process for thermal NO. The values established are the same as for the preceding examples and it must be remembered that the above conditions could be maintained for the different engine configurations, only by modifying the combustion chamber design, according to the changes in both volume flow rate and thermodynamic conditions.

Tables 5 and 6 summarize the comparison among the several configurations, in terms of performance parameters and pollutant emission (as regards only thermal NO and CO_2). Table 5 confirms the effectiveness of a number of solutions, such as the STIG one or those with multiple compressions or expansions, from the point of view of the increase in specific power. The STIG configuration also presents a high level of first-law efficiency, because of the partial utilization of the exergy contents in the exhaust flow through the HRSG. The irreversibility losses in this device explain the lower value for the second low efficiency. From the point of view of first law efficiency, configurations (5), with intercooled compressor, and (6), which also adopts a regenerative cycle, would appear to be quite satisfactory solutions. In these two cases, some difficulties could arise from the modifications required for plant design and operation, due to the necessity of adopting intercooling and regenerative heat exchangers.

Reheat (cases (7) and (8)) seems to present acceptable efficiency levels only for case (8), which involves relevant variations in the turbine and compressor matching with respect to the base configuration. It should also be observed that such solutions present the highest levels for the second-law efficiency η_{II}, but a significant part of the exhaust exergy could be dissipated in the heat recovery device, due to the overly high discharge temperature levels T_{ex}.

Table 5

TBL 5	Base	STIG	H_2O_L	H_2O_L	Int.	Int+ Reg.	Re- heat	Re- heat	Int+ Reh.	Int+ Reh.
cnf	1	2	3	4	5	6	7	8	9	10
ϕ	.284	.326	.311	.369	.344	.307	.479	.363	.407	.425
W_P	290	399	311	354	373	368	382	350	420	516
η_P	.361	.432	.354	.339	.383	.424	.281	.340	.364	.429
η_{II}	.577	.466	.556	.524	.556	.554	.616	.584	.574	.554
T_{ex}	757	733	757	758	754	756	1108	867	858	734

Table 6

TABLE 6	Base	STIG	H_2O_L	H_2O_L	Int.	Int+ Reg.	Re- heat	Re- heat	Int+ Reh.	Int+ Reh.
config	1	2	3	4	5	6	7	8	9	10
T'_{max1}	2530	2379	2530	2530	2445	2502	2530	2530	2463	2535
T'_{max2}	---	---	---	---	---	---	2255	2476	2421	2397
[NO]	165	10.3	40.7	16.4	70.0	127	158	227	124	264
$EINO_f$	10.1	.542	2.25	.763	3.50	7.15	5.56	10.7	5.18	10.6
$EINO_W$	2.05	.092	.469	.165	.670	1.24	1.45	2.31	1.05	1.81
$EICO_{2W}$	604	614	635	704	575	517	805	650	612	522

Configurations (9) and (10) would present significant increases in both specific power and thermal efficiency, but would involve considerable difficulties due to the completely different choices made for the cycle parameters. Less relevant advantages are shown by these schemes in terms of second law efficiencies. Really, case (10) would lead to increased irreversibility losses with respect to the base configuration.

The results in Table 6 confirm that a more reliable comparison of the several engine configurations should be performed by also controlling the emission indices. In fact, some interesting solutions from the point of view of performance level would appear to be less favorable in terms of pollutants. The most evident example is given by case (10), which presents higher levels for both NO dry concentration and emission index $EINO_f$. All configurations present an improvement in the emission index referred to mechanical power, $EINO_W$, although some of them, like (8) and (10), produce an increased NO concentration.

It should also be highlighted that many solutions, despite the decrease in NO production, induce a large production of carbon dioxide, as demonstrated by the $EICO_{2W}$ index. This can be detected in all water or steam-injected schemes or in some with postcombustors, due to the increased values of the total equivalence ratio.

A good compromise between satisfactory performance and limited pollutant emission is represented by configuration (5), with intercooled compression. Besides the increase in mechanical work and efficiency, this configuration produces a reduction in NO production, because of the lower temperature level in the combustion chamber (as demonstrated by the T_{max} value). Also an improvement in the $EICO_{2W}$ index can be observed, since the effects of the higher equivalence ratio are compensated for by the increase in mechanical work. Furthermore, this configuration seems to be one of the most easily obtainable from the base one.

All the above considerations about thermal NO production can be explained, from an overall point of view, by the results presented in Table 6. This shows the maximum temperature values in the first and second combustion for each configu-

Downloaded 02 Jun 2010 to 171.66.16.122. Redistribution subject to ASME license or copyright; see http://www.asme.org/terms/Terms_Use.cfm

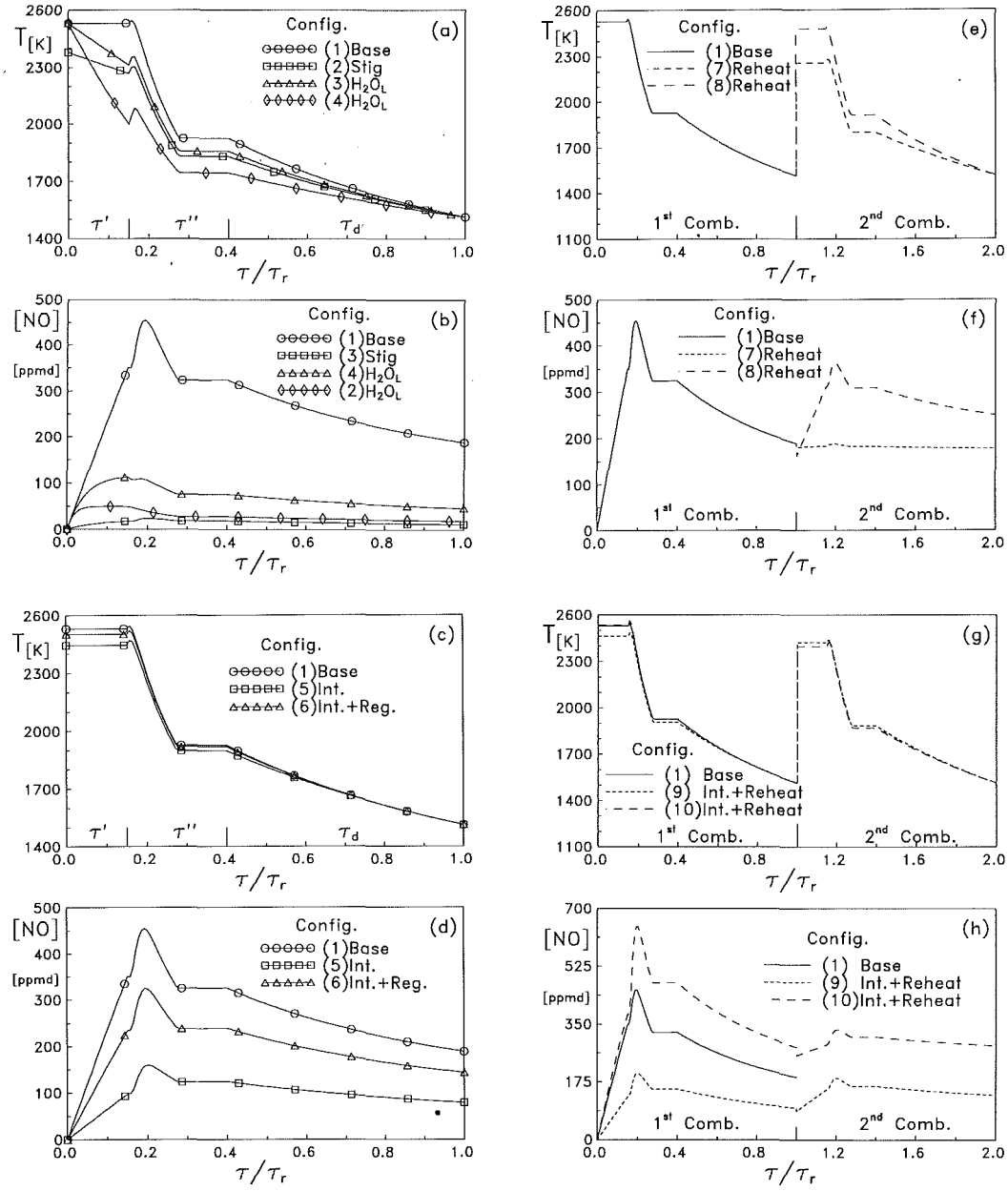


Fig. 6 Comparison of combustion temperature and NO concentration patterns for the different plant configuration examined

ration. The emission index estimation was performed by applying the model described in the previous sections, whose detailed results are displayed, for the base configuration, in Fig. 4.

Figure 6 allows examination of the different trends of combustion gas temperature and NO concentration arising from the operating parameters of the engine configurations examined. The main influences are certainly exerted by the maximum gas temperature, which is a consequence of the cycle parameters adopted, and the gas composition which also strongly affects NO formation. The final values of [NO] in Fig. 6 differ from those in Table 6, which account for the further dilution with the cooling air.

In particular, all configurations with steam or water injection produce a strong reduction in NO rate of formation, because of the sudden temperature decrease during the time interval τ' (Figs. 6*a* and 6*b*). This influence is strengthened by the effect of gas composition, related to the higher equivalence ratio (Table 5), which is required in these cases in order to reach the same T. I. T. Figures 6(*e–h*) show that reduced thermal NO production occurs during the second combustion. In fact, combustion gases again reach a high temperature level but with lower oxygen availability. Finally, Figs. 6(*c*, *d*) confirm the favorable effect of the intercooled compression on thermal NO limitation.

As discussed above, in all cases the most significant parameters for the NO formation mechanism were held constant, thus hypothesizing that a new combustor was designed to suit each engine configuration. The same combustion chamber, employed for the different cases would, of course, operate under strongly different conditions in terms of residence times, air dilution laws, etc.

The effects of the most significant parameters for combustor operation should be, therefore, analyzed also by more accurate models. As previously stated, an optimized choice of these parameters will involve an adequate fluid-dynamic design of the combustion chamber, in order to achieve the most effective conditions of fuel injection law and air supply.

Downloaded 02 Jun 2010 to 171.66.16.122. Redistribution subject to ASME license or copyright; see http://www.asme.org/terms/Terms_Use.cfm

Conclusion

The thermodynamic model proposed by the authors for gas turbine cycle analysis, including thermal and fuel NO_x evaluation, allows different solutions for gas turbine design and operation to be investigated.

The possibility of firing conventional and coal-derived fuels has been analyzed on the basis of both performance and emission features. This allowed the general advantages related to the use of medium or low Btu gases to be confirmed, in terms of increase in mechanical output and satisfactory combined plant operation. On the other hand the possibility of more relevant thermal NO_x production for some coal-derived fuels has been highlighted, together with the considerable effects of ammonia, which can be converted to fuel NO_x.

Similarly, another set of examples presented in this paper allowed the comparison of several gas turbine plant configurations obtainable from a basic aeroderivative engine. Each of these solutions was analyzed by highlighting the efficiency of the thermodynamic processes taking place in the component parts and also accounting for engine behavior from the point of view of pollutant emission.

The widely employed systems of water or steam injection for NO_x reduction present well-known benefits but, on the other hand, create problems related to demineralized water consumption and, in some cases, to a decrease in thermodynamic efficiency or to larger exergy losses.

On the other hand, some solutions, like those with reheat, which seem to be interesting from the point of view of improvements in mechanical output and efficiency, present larger rates of carbon dioxide production and higher values of some emission indices.

The analysis has allowed some satisfactory compromises between the objectives of performance improvement and emission limitations to be identified. For example, the scheme with an intercooled compressor seems to satisfy both conditions with reduced difficulties in terms of manufacturing and operation.

The possibility of controlling both classical performance parameters and emission indices will allow the authors to extend their analysis to the optimization of gas turbine operating parameters and to the choice of the best configuration.

Finally, it must be noted that the thermodynamic model for NO_x prediction is a tool for a fast analysis of the influence exerted by numerous physical quantities. Hence information can be derived for introduction into more accurate computational models in order to find the optimal conditions for fuel and air supply and for water or steam injection laws.

Acknowledgments

The research is supported by the financial contribution of the Italian Government and National Research Council (M.U.R.S.T. and C.N.R. funds).

References

Aoyama, K., and Mandai, S., 1984, "Development of a Dry Low NO_x Combustor for a 120-MW Gas Turbine," ASME JOURNAL OF ENGINEERING FOR GAS TURBINES AND POWER, Vol. 106, pp. 795–800.

Bejan, A., 1988, *Advanced Engineering Thermodynamics*, Wiley, New York.

Bozza, F., Fontana, G., and Tuccillo, R., 1991, "Prestazioni ed Emissioni Inquinanti di Impianti Motori Alimentati a Gas di Carbone," *Proc. of 5th Conference on "Gruppi Combinati; Prospettive Tecniche ed Economiche,"* pp. 395–417, Pitagora, Bologna.

Bozza, F., and Tuccillo, R., 1992, "Performance Upgrading of Aero-Derivative Gas Turbines," presented at "Flowers 92" Symposium, Florence, June.

Cerri, G., and Arsuffi, G., 1988, "Steam Injected Gas Turbine Integrated With a Self-Production Demineralized Water Thermal Plant," ASME JOURNAL OF ENGINEERING FOR GAS TURBINES AND POWER, Vol. 110, pp. 8–16.

De la Mora, J. A., et al., 1985, "Evaluation of the British Gas Corporation/Lurgi Slagging Gasifier in Gasification-Combined-Cycle Power Generation: Final Report," EPRI AP-3980, Palo Alto, CA.

El Masri, M. A., 1986, "On Thermodynamics of Gas-Turbine Cycles: Part 3—Thermodynamic Potential and Limitations of Cooled Reheat Gas-Turbine Combined Cycles," ASME JOURNAL OF ENGINEERING FOR GAS TURBINES AND POWER, Vol. 108, pp. 160–170.

El Masri, M. A., 1987, "Exergy Analysis of Combined Cycles: Part 1—Air Cooled Brayton-Cycle Gas Turbine," ASME JOURNAL OF ENGINEERING FOR GAS TURBINES AND POWER, Vol. 109, pp. 228–236.

El Masri, M. A., 1988, "A Modified High-Efficiency Recuperated Gas Turbine Cycle," ASME JOURNAL OF ENGINEERING FOR GAS TURBINES AND POWER, Vol. 110, pp. 233–241.

Fitts, D. O., Symonds, R. A., and Western, E. R., 1990, "Combustion System Performance of Water Injected MS7001E Gas Turbine Operating at a NO_x Emission Level of 25 ppmd," ASME Paper No. 90-GT-71.

Folsom, B. A., Courtney, C. W., and Heap, M. P., 1980, "The Effects of LBG Composition and Combustor Characteristics on Fuel NO_x Formation," ASME JOURNAL OF ENGINEERING FOR GAS TURBINES AND POWER, Vol. 102, pp. 459–467.

Fontana, G., and Tuccillo, R., 1990, "Optimization of Coal Gasification Combined Cycles," *Proceedings of ASME Cogen-Turbo IV*, pp. 57–65.

Glarborg, P., Miller, J. A., and Kee, R. J., 1986, "Kinetic Modeling and Sensitivity Analysis of Nitrogen Oxide Formation in Well-Stirred Reactors," *Combustion and Flame*, Vol. 65, pp. 177–202.

Glassman, I., 1987, *Combustion*, Academic Press, New York.

Heywood, J. B., 1987, *Internal Combustion Engine Fundamentals*, McGraw-Hill, New York.

Hung, W. S. Y., 1975a, "An Experimentally Verified NO_x Emission Model for Gas Turbine Combustors," ASME Paper No. 75-GT-71.

Hung, W. S. Y., 1975b, "A Diffusion Limited Model That Accurately Predicts the NO_x Emissions from Gas Turbine Combustors Including the Use of Nitrogen Containing Fuels," ASME Paper No. 75-Pwr-11.

Kreitmeier, F., Frutschi, U. H., and Vogel, M., 1991, "Optimized NO_x Reduction for GT and CC Power Plants Based on an Economic Evaluation," *Proceedings of ASME-IGTI COGEN TURBO V*, pp. 509–516.

Kretschmer, D., and Odgers, J., 1989, "The Effects of Hydrocarbon Fuels Upon Exhaust Pollutants in Gas Turbine Combustors," ASME Paper No. 89-GT-268.

Kotas, T. J., 1985, *The Exergy Method of Thermal Plant Analysis*, Butterworths, United Kingdom.

Larson, E. D., and Williams, R. H., 1987, "Steam Injected Gas Turbines," ASME JOURNAL OF ENGINEERING FOR GAS TURBINES AND POWER, Vol. 109, pp. 55–63.

Lefebvre, A. H., 1983, *Gas Turbine Combustion*, Hemisphere Publ. Co.

Lugand, P., and Pariett, C., 1991, "Combined Cycle Plants With Frame 9F Gas Turbines," ASME JOURNAL OF ENGINEERING FOR GAS TURBINES AND POWER, Vol. 113, pp. 475–481.

Manfrida, G., and Stecco, S. S., 1982, "Exergy Loss Modeling of Power Plants and Industrial Processes," *Proc. of 17th IECEC Conference*, IEEE Paper 829004.

McGuirk, J. J., 1990, "Subsonic Combustor Flow Model," von Karman Institute for Fluid Dynamics Lecture Series 1990-02.

Meier, J. G., Hung, W. S. Y., and Sood, V. M., 1986, "Development and Application of Industrial Gas Turbines for Medium-Btu Gaseous Fuels," ASME JOURNAL OF ENGINEERING FOR GAS TURBINES AND POWER, Vol. 108, pp. 182–190.

Moran, M. J., 1982, *Availability Analysis: A Guide to Efficient Energy Use*, Prentice-Hall, NJ.

Nakata, T., et al., 1990, "Experimental Evaluation of a Low NO_x LBG Combustor Using Bypass Air," ASME Paper No. 90-GT-380.

Odgers, J., and Kretschmer, D., 1985, "The Prediction of Thermal NO_x in Gas Turbines," ASME Paper No. 85-IGT-126.

Pechti, P., Staudinger, G., and Lehner, J., 1988, "Effect of Coal Gasification Reactor Exit Temperature on Combined Cycle Efficiency," *Proceedings of ASME Cogen-Turbo II*, pp. 165–174.

Sato, M., et al., 1990, "Coal Gaseous Fueled, Low Fuel-NO_x Gas Turbine Combustor," ASME Paper No. 90-GT-381.

Singh, R., 1990a, "Combustion in the Gas Turbine," von Karman Institute for Fluid Dynamics Lecture Series 1990-02.

Singh, R., 1990b, "Pollutants," von Karman Institute Lecture Series 1990-02.

Svhela, S. A., and McBride, B. J., 1974, "Fortran IV Computer Program for Calculation of Thermodynamic and Transport Properties of Complex Chemical Systems," NASA TND-7056.

Tuccillo, R., Fontana, G., and Jannelli, E., 1990, "Coal-Derived Gas Utilization in Combined Gas-Steam Cycle Power Plants," ASME Paper No. 90-GT-366.

Warnatz, J., 1990, "Chemistry of Combustion Processes," von Karman Institute for Fluid Dynamics Lecture Series 1990-02.

Zeldovich, Y. B., Sadovnikov, P. Y., and Frank-Kamenetskik, D. A., 1947, "Oxidation of Nitrogen in Combustion," Academy of Science of SR, Institute of Chemical Physics, Moscow–Leningrad, translated by M. Shelef.

Downloaded 02 Jun 2010 to 171.66.16.122. Redistribution subject to ASME license or copyright; see http://www.asme.org/terms/Terms_Use.cfm

The Effectiveness of Heat Transfer From Flue Gases to Ammonia-Water Mixtures

I. Kuštrin

M. Tuma

Faculty of Mechanical Engineering,
University of Ljubljana,
61000 Ljubljana, Slovenia

The paper deals with the theoretical comparison of the heat transfer process from the exhaust gases of a gas turbine to pure water or to an ammonia-water mixture in the single-pressure, nonreheat, heat recovery boiler. The main difference is the variable-temperature boiling of the mixture, which improves the match of the temperature profiles in comparison to the match obtained by the use of pure water. The result is smaller loss of energy and exergy. Thermal and exergetic efficiencies are improved, which means better use of the primary heat source, i.e., the fuel of the gas turbine. At the end of the paper the usefulness of the ammonia-water mixture at higher inlet (above 500°C) and outlet (above 180°C) gas temperatures is analyzed. The main advantages of the mixture disappear under such conditions.

Introduction

There are always losses of exergy in the process of heat transfer from flue gases to working fluid. These losses are the result of the temperature difference between the two streams and of the remaining heat content of the gases leaving the utilizer.

During the process the temperature of the heating gases decreases while the temperature of the heated fluid increases. The temperature profiles of the two streams do not match because of different heat capacities and because of the intermediate phase change of the working fluid. The match of temperature profiles can be improved by the use of a multipressure boiler or by implementation of the supercritical cycle. A third possibility is the use of a fluid that has variable-temperature boiling, such as binary or multicomponent fluid mixtures.

The paper deals with the third alternative and analyzes the efficiency of heat transfer from flue gases to water or to an ammonia-water mixture in the single-pressure utilizer. Such a simple heat recovery boiler is not used by ammonia-water power cycles of commercial interest, such as Kalina Cycle System 6 for combined cycle applications (Kalina and Leibowitz, 1987) and the Kalina Cycle System 5 for coal fired applications (Kalina, 1989). The pressure and the ammonia mass fraction in the mixture are varied at realistic and constant boundary conditions. A mathematical model is used to calculate the thermal and exergetic efficiency of the heat transfer process.

The mathematical model used is similar to the model presented by El-Sayed and Tribus (1985). In this paper only the results for one pressure and concentration were stated. The paper shows the thermal and exergetic efficiencies of the heat transfer process as a function of pressure and concentration in the form of three-dimensional diagrams, which gives a very good overview of the computational area.

The optimum pressure and concentration are chosen with regard to the lowest allowable exit temperature of the gases and the highest possible exergetic efficiency of the utilizer. The results are compared to those obtained by the use of pure water at optimum pressure for the highest possible exergetic efficiency.

Thermodynamic Properties of Gases

For the analysis the specific enthalpies and exergies of gases must be known as a function of temperature and composition. The generalized diagram (*e-h*, *t-h*) for specific enthalpy and exergy published by Rant (1962) and Oprešnik and Opara (1977) was used for the estimation of these. The assumptions for estimating the values from the diagram were:

- composition: 75 vol. % of air, 4.5 vol. % of water
- temperature of ambient 15°C
- gas density 1.282 kg/m^3 at 0°C and 101325 Pa

Thermodynamic Properties of Water and Ammonia

For computing specific enthalpies, entropies, and volumes of water and ammonia the equations from Keenan and Keyes (1936) and Reynolds (1980) were used. They were built into the computer program. The program computes the values for specific enthalpy, entropy, and volume for temperatures from 0 to 800°C and pressures from 0.0006 to 100 MPa for water and temperatures from −73 to 800°C and pressures from 0.009 to 100 MPa for ammonia. The computed values were compared to values published by Schmidt and Grigull (1979) for water and Haar and Gallagher (1978) for ammonia. The differences are so small (±1 percent) that they can be easily ignored.

Contributed by the International Gas Turbine Institute for publication in the JOURNAL OF ENGINEERING FOR GAS TURBINES AND POWER. Manuscript received by the International Gas Turbine Institute February 22, 1992. Associate Technical Editor: L. S. Langston.

Copyright © 1994 by ASME
Downloaded 02 Jun 2010 to 171.66.16.122. Redistribution subject to ASME license or copyright; see http://www.asme.org/terms/Terms_Use.cfm

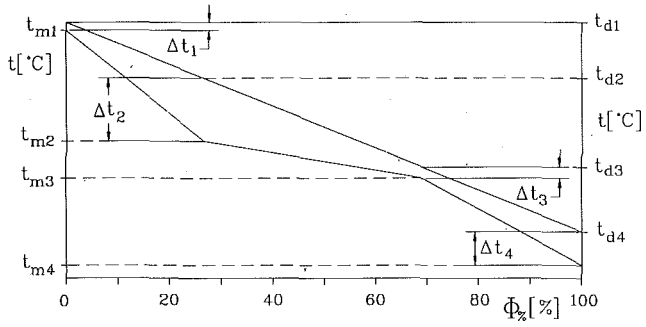


Fig. 1 Temperature profiles of the flue gases and the working fluid

Thermodynamic Properties of Ammonia-Water Mixtures

For estimating the thermodynamic properties of ammonia-water mixtures the mathematical model described by Kuštrin (1991) was used. The model was built in the computer program that computes the values for thermodynamic properties of the mixture for pressures from 0.1 to 11 MPa and ammonia mass fractions from 0 to 1. The program has two options:

- computing the values for thermodynamic properties of the mixture at vapor-liquid equilibria from the data for p, ξ_l or p, ξ_v or p, t,
- computing the values for thermodynamic properties of the mixture from the data for p, t, and ξ.

Thermal Boundary Conditions for the Analysis

In order to compare the efficiency of heat transfer from the flue gases to water or an ammonia-water mixture, both processes must be observed at the same thermal boundary conditions (Fig. 1):

- temperature of the flue gases entering the utilizer: $t_{d1} = 500°C$
- temperature of the working fluid entering the utilizer: $t_{m4} = 25°C$
- temperature difference between the flue gases and the working fluid at the beginning of boiling: $\Delta t_3 = 22$ K
- temperature difference between the flue gases and the working fluid at the end of superheating: $\Delta t_1 = 15$ K
- mass flow of the flue gases: $\dot{m}_d = 1$ kg/s

Because of variable-temperature condensation it is quite realistic to assume that the mixture's temperature at the end of condensation (t_{m4}) is not considerably higher than the inlet temperature of the cooling water (t_{ok}). The heat rejection system presented by Kalina (1984) was assumed.

If the working fluid is pure water, then it is not realistic to assume the same inlet temperature (t_{m4}), although this was done in order to compare the two fluids under the same conditions. It must, however, be realized that it is a better, although not realistic, starting point for pure water and that it will result in better thermal and exergetic efficiencies than expected. The temperature of the incoming gases is 500°C, so they are not preheated before entering the utilizer.

Mathematical Model for the Analysis of the Utilizer

The basis for the analysis of the heat transfer process is the determination of the temperature profiles of the fluid gases and the working fluid (Fig. 1).

Assuming that the working fluid is heated, vaporized, and superheated at the same pressure, the computer program was used to determine the thermodynamic properties of the mixture at the inlet (h_{m4}, s_{m4}, v_{m4}) and outlet (h_{m1}, s_{m1}, v_{m1}) of the utilizer and under ambient conditions (h_{mok}, s_{mok}, v_{mok}). The values were computed from the data for pressure, temperature, and ammonia mass fraction. From the data for pressure and ammonia mass fraction in the liquid phase the thermodynamic properties of mixture in bubble (t_{m3}, h_{m3}, s_{m3}, v_{m3}) and dew (t_{m2}, h_{m2}, s_{m2}, v_{m2}) points were computed. These values were the basis for estimating the specific exergies in the same points by the equation:

$$e_{mi} = h_{mi} - h_{mok} - T_{ok}(s_{mi} - s_{mok}). \tag{1}$$

The gas temperature at the point where boiling begins is:

$$t_{d3} = t_{m3} + \Delta t_3. \tag{2}$$

Specific enthalpies of the fluid gases h_{d1} and h_{d3} are determined by the (e-h, t-h) diagram.

In the next step the mass flow of the working fluid that can be vaporized and superheated to t_{m1} by the stream of flue gases is calculated:

$$\dot{m}_m = \dot{m}_d(h_{d1} - h_{d3})/(h_{m1} - h_{m3}). \tag{3}$$

Then the enthalpies h_{d2} in h_{d4} are:

$$h_{d2} = h_{d1} - \dot{m}_m(h_{m1} - h_{m2}), \tag{4}$$

$$h_{d4} = h_{d3} - \dot{m}_m(h_{m3} - h_{m4}) \tag{5}$$

and the values for t_{d2} and t_{d4} are read from the diagram.

Specific exergies of gases e_{d1}, e_{d2}, e_{d3}, e_{d4}, and e_{dok} and enthalpy h_{dok} are also read from the diagram at the corresponding temperatures.

The thermal and exergetic efficiencies can now be calculated:

$$\eta_k = \dot{m}_m(h_{m1} - h_{m4})/(\dot{m}_d(h_{d1} - h_{dok})), \tag{6}$$

$$\zeta_k = \dot{m}_m(e_{m1} - e_{m4})/(\dot{m}_d(e_{d1} - e_{dok})). \tag{7}$$

The losses of exergy are:

$$\zeta_{iz} = 1 - \zeta_k. \tag{8}$$

Losses of exergy in the utilizer are the sum of losses from the temperature difference between the two streams and losses because of the heat of the exiting gases.

The losses because of exiting gases can be calculated by the equation:

$$\zeta_{izd} = \frac{e_{d4} - e_{dok}}{e_{d1} - e_{dok}}. \tag{9}$$

The remaining losses are the consequence of the temperature difference:

$$\zeta_{izpt} = \zeta_{iz} - \zeta_{izd}. \tag{10}$$

Nomenclature

e = specific exergy, J/kg
h = specific enthalpy, J/kg
$\dot{m}$ = mass flow, kg/s
p = pressure, Pa
s = specific entropy, J/kgK
T = temperature, K
t = temperature, °C
v = specific volume, m^3/kg
x = dryness of vapor
ζ = exergetic efficiency
η = thermal efficiency
ξ = mass fraction

Subscripts

d = flue gases
iz = loss
k = utilizer
l = liquid
m = working fluid, mixture
ok = ambient
pt = heat tranfser
v = vapor

Downloaded 02 Jun 2010 to 171.66.16.122. Redistribution subject to ASME license or copyright; see http://www.asme.org/terms/Terms_Use.cfm

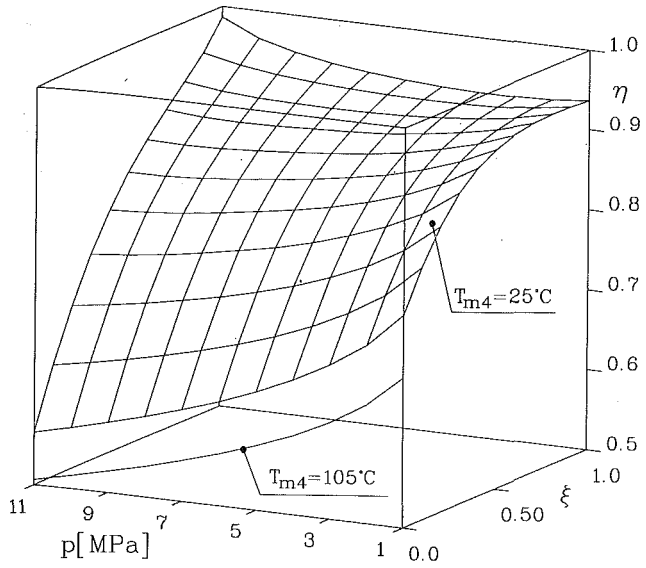


Fig. 2 Thermal efficiency of the utilizer

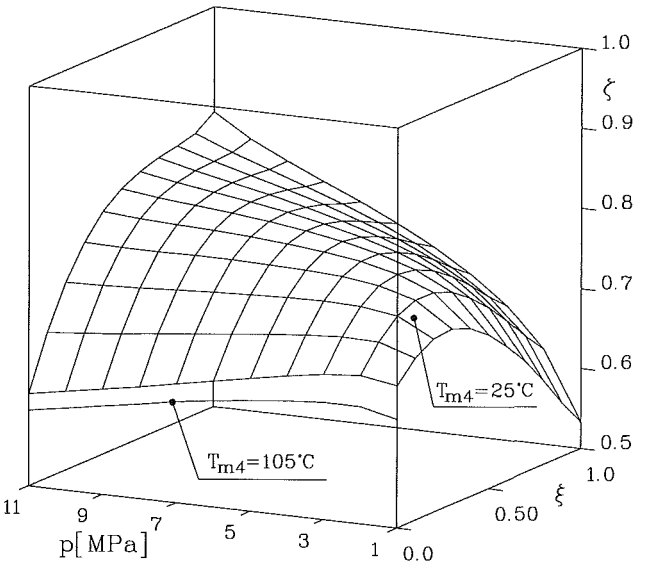


Fig. 3 Exergetic efficiency of the utilizer

Computer Program for the Analysis of the Utilizer

The previously described mathematical model was built into the computer program that computes, for pressures from 1 to 11 MPa, for ammonia mass fractions from 0 to 1, and for given thermal boundary conditions: the thermal and exergetic efficiencies, losses of exergy, outlet gas temperatures, and transferred heat. The computed values are written to corresponding files. These values were drawn in the form of two and three-dimensional diagrams by the software package ACAD 10.

Results of the Mathematical Model

Figure 2 shows the dependence of thermal efficiency of the utilizer on pressure and composition of the working fluid at the given boundary conditions.

At all pressures the utilizer fed by pure ammonia has higher thermal efficiency in comparison to those fed by a mixture or pure water. Note that at the lowest pressure and ammonia mass fraction 1, the thermal efficiency is very high (over 0.92) while the exergetic efficiency, as shown later, is the lowest

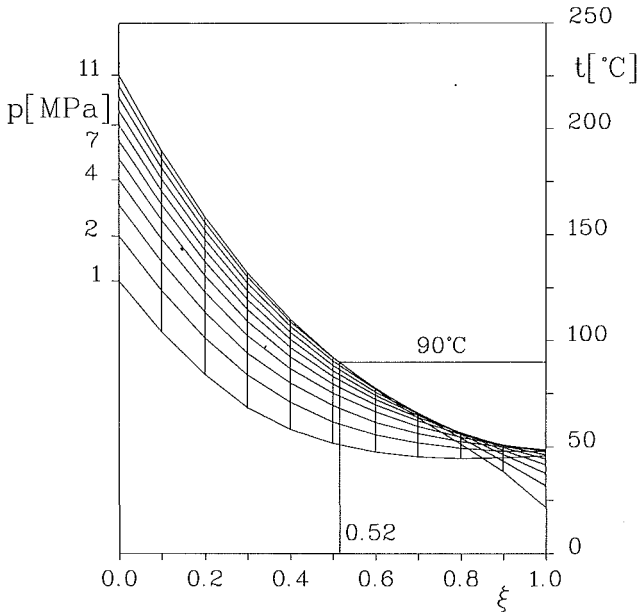


Fig. 4 Determination of the allowable ammonia mass fraction with regard to the temperature of the exiting gases

possible (0.533). Once again, an evaluation of thermodynamic processes only from the energetic point of view failed (Rant, 1962).

There is also a line for pure water entering the utilizer with t_{m4} = 105°C drawn in Fig. 2. It is placed lower than the line at t_{m4} = 25°C.

The lowest exergetic efficiency is at the lowest pressure (1 MPa) and using pure ammonia (Fig. 3), while the highest exergetic efficiency is achieved also with the use of pure ammonia but at the highest pressure (11 MPa). At lower pressures, there exist maxima of exergetic efficiency at intermediate ammonia mass fractions. If the pressure increases, the maxima approach higher ammonia mass fractions, i.e., pure ammonia. In the case of pure water the maximum is at a pressure of 2 MPa.

There is also a line in the case of pure water entering the utilizer with t_{m4} = 105°C drawn in Fig. 3. It is placed lower than the line at t_{m4} = 25°C.

Determination of the Working Ammonia Mass Fraction and Corresponding Thermal and Exergetic Heat Exchanger Efficiencies

In order to maintain good efficiency it would be best to choose pure ammonia at 11 MPa, but there are some limitations that prevent such a choice. One of them is the temperature of the exiting gases.

Say, for example, that the temperature of the exiting gases should not fall beyond 90°C. The limit of 90°C crosses the line of exit temperatures for a pressure of 11 MPa at 0.52 ammonia mass fraction (Fig. 4). A pressure of 11 MPa is chosen because for almost all concentrations the exergetic efficiency at this pressure achieves its highest value. If the chosen ammonia mass fraction is subjected to the mathematical model for calculating efficiencies, the resulting thermal efficiency is 0.844 and exergetic efficiency 0.824.

Comparison of Usefulness of Pure Water and Mixture

The mixture is examined at determined ammonia mass fraction 0.52 and a pressure of 11 MPa, while pure water is examined at 2.1 MPa pressure. These values are chosen for the

Downloaded 02 Jun 2010 to 171.66.16.122. Redistribution subject to ASME license or copyright; see http://www.asme.org/terms/Terms_Use.cfm

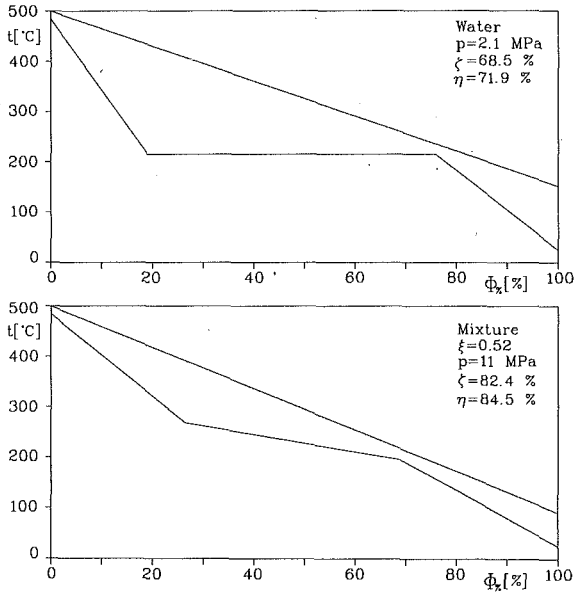


Fig. 5 Temperature profiles of the flue gases and water at optimum pressure and of the flue gases and mixture at the allowable ammonia mass fraction

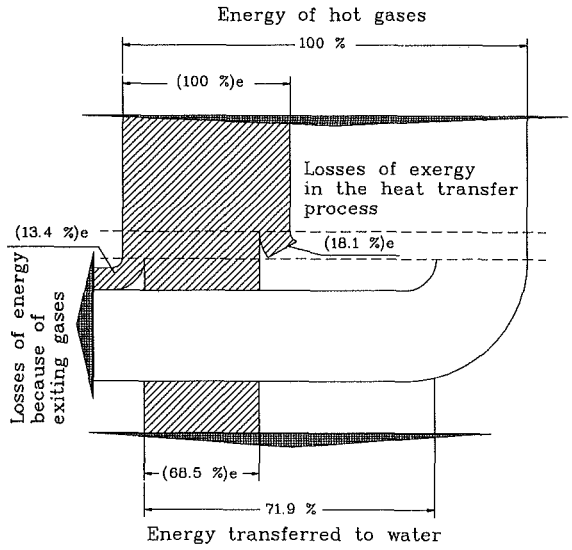


Fig. 6 Rant's diagram for an utilizer fed by pure water

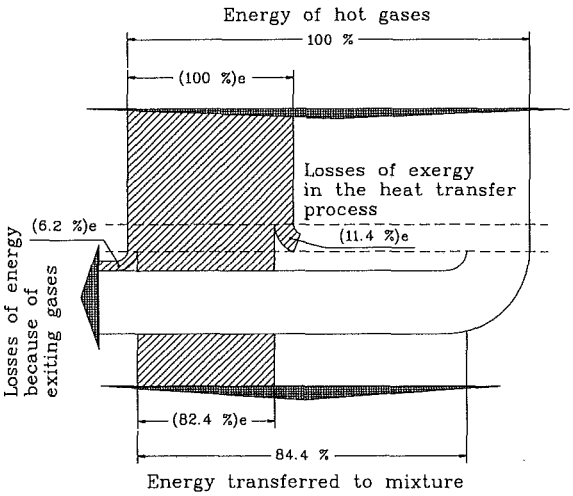


Fig. 7 Rant's diagram for an utilizer fed by mixture ξ = 0.52

Table 1 Comparison of usefulness of pure water and ammonia-water mixture ξ = 0.52

Comparison	Water	Mixture
Exergetical efficiency of utilizer	68.5 %	82.4 %
Losses of exergy in utilizer because of temperature difference	18.1 %	11.4 %
Losses of exergy in utilizer because of exiting-gases-heat	13.4 %	6.1 %
Thermal efficiency of utilizer	71.9 %	84.5 %
Specific exergy of exiting working fluid	148 (kJ/kg)/(kg/s)$_d$	186
Temperature of exiting gases	151° C	90 °C

highest possible exergetic efficiency of the utilizer at the given thermal boundary conditions.

The temperature profiles of the flue gases and water at optimum pressure and of the flue gases and mixture at the allowed ammonia mass fraction are drawn on Fig. 5. The values are calculated by the mathematical model presented earlier.

Figures 6 and 7 show Rant's diagrams for the process of heat transfer in the utilizer under the same conditions as for Fig. 5. In the process of heat transfer from the flue gases to the mixture, 11.4 percent of incoming exergy is transformed irreversibly to anergy (useless energy), while 6.2 percent leaves with the exiting gases. The rest of the exergy (82.4 percent) is available in energy (84.4 percent) transferred to the mixture.

In the case of pure water, the losses of exergy are greater in the process of heat transfer (poorer match of temperature profiles) and through the exiting gases (higher exit temperature of gases). Only 71.9 percent of incoming energy and 68.5 percent of incoming exergy is transferred to the water.

A detailed comparison is given in Table 1.

Usefulness of Ammonia-Water Mixture at Higher Inlet and Outlet Temperatures of Hot Gases

At temperatures over 800°C the optimum ammonia mass fraction is so low that the process using the binary mixture is equivalent to that of pure water. In practice it means that the use of a mixture is justified only in cases where there is no preheating of gases entering the utilizer.

In boilers where the fuel is coal, combustion temperatures are always higher than 800°C, which means that ammonia-water and similar mixtures do not give better results than pure water in boilers fired by coal.

In most cases there are limitations on the temperature of the exhaust gases. If there is sulfur in the exhaust gases then they should not be cooled below 180°C because the sulfur compounds would cause corrosion of the equipment. The line in Fig. 8 is drawn for an ammonia-water mixture at a pressure of 11 MPa because for almost all mass fractions at this pressure the highest exergetic efficiencies are achieved.

If the lowest allowed exit temperature of the flue gases rises from 90 to 180°C, the working mass fraction falls from 0.52 to 0.13, which is very close to pure water, and the use of the mixture is hardly justified. These results confirm the facts stated by El-Sayed and Tribus (1985).

Conclusions

The process of heat transfer from flue gases to water and ammonia-water mixture in the single pressure, nonreheat, heat recovery boiler was analyzed. Although the ammonia-water

Downloaded 02 Jun 2010 to 171.66.16.122. Redistribution subject to ASME license or copyright; see http://www.asme.org/terms/Terms_Use.cfm

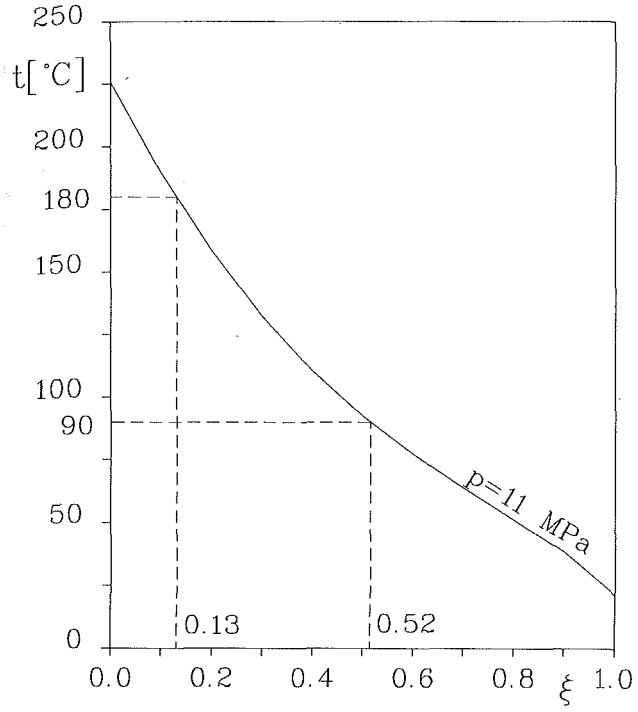


Fig. 8 Working ammonia mass fractions with regard to the lowest allowable temperature of exiting gases

power cycles such as the Kalina Cycle System 6 for combined cycle applications and the Kalina Cycle System 5 for coal-fired applications do not use such a simple heat recovery boiler, the results of the analysis are not to be neglected:

At given thermal boundary conditions, an utilizer fed by an ammonia–water mixture has better thermal and exergetic efficiency, smaller losses because of the heat content of the exiting gases (lower exit temperature), and smaller losses of exergy in the process of heat transfer (better match of temperature profiles) than a utilizer fed by pure water.

By raising the temperature of the exhaust gases temperature (sulfur content) the allowable ammonia mass fraction is minimized. At an exit temperature of 180°C, the allowable mass fraction is only 0.13, which is very close to pure water and the use of mixture is hardly justified.

The fuel used in gas turbine cycles usually has a very small sulfur content, which allows low temperatures of exiting gases. The temperature of the flue gases entering the utilizer should be about 500°C. The optimum ammonia mass fraction at these temperatures is approximately 0.5. In such cases, the bottoming cycle using an ammonia–water mixture has higher thermal and exergetic efficiency than a cycle using pure water.

The last two conclusions are not applicable to the Kalina Cycle Systems 5 and 6, where the advantage conferred by the use of an ammonia–water mixture remains at flue gas inlet temperatures above 800°C and despite any minimum temperature limitation to avoid acid condensation in the flue gas.

Power cycles using a binary or multicomponent mixture as a working fluid will become even more interesting with the improvement and reduction of price of devices for cleaning exhaust gases, use of new materials for the equipment of power systems and with the development of new components for mixtures having similar or even better thermodynamic and physical properties than ammonia.

References

El-Sayed, Y. M., and Tribus, M., 1985, "A Theoretical Comparison of the Rankine and Kalina Cycles," *Analysis of Energy Systems: Design and Operation*, ASME, New York.

Haar, L., and Gallagher, J., 1978, "Thermodynamic Properties of Ammonia," *Journal of Physical and Chemical Reference Data*, Vol. 7, No. 3, pp. 635–792.

Kalina, A. I., 1984, "Combined-Cycle System With Novel Bottoming Cycle," ASME JOURNAL OF ENGINEERING FOR GAS TURBINES AND POWER, Vol. 106, pp. 737–742.

Kalina, A. I., and Leibowitz, H. M., 1987, "Applying Kalina Technology to a Bottoming Cycle for Utility Combined Cycles," ASME Paper 87-GT-35.

Kalina, A. I., 1989, "The Kalina Cycle Technology Applied to Direct-Fired Power Plants," ASME Paper No. 89-JPGC/Pwr-24.

Keenan, J., and Keyes, R., 1936, *Thermodynamic Properties of Steam*, Wiley, New York.

Kuštrin, I., 1991, "Binary Mixtures in Turbine Power Cycles," Master's Thesis [Slovene text], Faculty of Mechanical Engineering, University of Ljubljana, Ljubljana, Slovenia.

Oprešnik, M., and Opara, M., 1973, "Thermodynamic Tables and Diagrams" [Slovene text], Faculty of Mechanical Engineering, University of Ljubljana, Ljubljana.

Rant, Z., 1962, "Thermodynamics" [Slovene text], Faculty of Mechanical Engineering, University of Ljubljana, Ljubljana.

Reynolds, W., 1980, "Thermodynamic Properties in S.I.," Stanford University.

Schmidt, E., and Grigull, U., 1979, *Properties of Water and Steam in SI Units*, Springer-Verlag, Berlin.

Downloaded 02 Jun 2010 to 171.66.16.122. Redistribution subject to ASME license or copyright; see http://www.asme.org/terms/Terms_Use.cfm

Development of Gas Turbine Steam Injection Water Recovery (SIWR) System

H. B. Nguyen

A. den Otter

NOVA Corporation of Alberta,
Edmonton, Alberta, Canada

This paper describes and discusses a "closed-loop" steam injection water recovery (SIWR) cycle that was developed for steam-injected gas turbine applications. This process is needed to support gas turbine steam injection especially in areas where water cannot be wasted and complex water treatment is discouraged. The development of the SIWR was initiated by NOVA in an effort to reduce the environmental impact of operating gas turbines and to find suitable solutions for its expanding gas transmission system to meet future air emission restrictions. While turbine steam injection provides many benefits, it has not been considered for remote, less supported environments such as gas transmission applications due to its high water consumption. The SIWR process can alleviate this problem regardless of the amount of injection required. The paper also covers conceptual designs of a prototype SIWR system on a small gas turbine unit. However, because of relatively high costs, it is generally believed that the system is more attractive to larger size turbines and especially when it is used in conjunction with cogeneration or combined cycle applications.

Introduction

NOVA is a widely held company operating internationally from headquarters in Calgary, Alberta, Canada. NOVA has built its future on pipelines and the manufacturing and marketing of chemicals and plastics processed primarily from Alberta natural resources. NOVA owns and operates a 10,500 mile natural gas transportation system in Alberta. The NOVA system carried more than 13 percent of the gas produced annually in Canada and the United States, including more than 75 percent of marketed Canadian production. In 1990, it carried a record 2.89 trillion cubic feet of gas.

Background and Needs

Entering the 1990s, NOVA, as well as other gas turbine users, must find ways to reduce atmospheric pollution by tightening air emissions from equipment in their systems. With the more stringent amendments to the Clean Air Act in the United States in 1990 and environmental legislation under consideration in Canada, it is likely that NOVA will have to reduce air emissions from both existing and new facilities. In response, NOVA is actively working with gas turbine manufacturers to find ways to reduce both NO_x and CO_2 emissions. Consequently, demand for natural gas is steadily increasing throughout North America since it is a relatively clean and low-priced fossil fuel. As a result, the NOVA's Alberta Gas Transmission (AGTD) system is also faced with major facility expansion in this decade to meet customer needs. Therefore, reduced NO_x, reduced CO_2, and increased compression power for higher system throughput are seen as major business needs of AGTD in the 1990s. The Division is aware that it is important to combine and coordinate efforts to achieve all the above objectives since an attempt to achieve one objective may cause adverse effects on the other two. The question remaining is whether AGTD can find an effective approach that satisfies all these needs.

Several potential solutions were considered for application in the AGTD system.

(1) Low NO_x Combustor Technologies. This approach refers to any new advanced combustor design with the purpose of reducing thermal NO_x formation in the combustion process. While low-NO_x combustors have been applied to industrial gas turbines before, they are still in the development stage for aeroderivative gas turbines. Many gas turbine manufacturers insist that low-NO_x combustors will be available on their equipment by 1995 and will reduce NO_x emission to the 25–42 ppm range. Little information on the actual shape, size, and retrofitability is publicized. Once available and proven, low NO_x combustion appears to be the most economical solution if reducing NO_x emissions is the only concern.

(2) Selective Catalytic Reduction. This is a post-combustion exhaust gas clean up process, which requires injecting ammonia into the exhaust gas stream before running it through a catalyst bed. Existing SCR installations have indicated that while this process has the potential to remove over 90 percent of NO_x in the exhaust gas, it is perceived as one with substantial operating problems. Controlling ammonia injection in the SCR

Contributed by the International Gas Turbine Institute and presented at the 37th International Gas Turbine and Aeroengine Congress and Exposition, Cologne, Germany, June 1–4, 1992. Manuscript received by the International Gas Turbine Institute February 4, 1992. Paper No. 92-GT-87. Associate Technical Editor: L. S. Langston.

Copyright © 1994 by ASME
Downloaded 02 Jun 2010 to 171.66.16.122. Redistribution subject to ASME license or copyright; see http://www.asme.org/terms/Terms_Use.cfm

process is also a major concern, especially when it is used in an application with high thermal turndown ratio such as in a gas transmission system. Early SCR systems are limited to gas turbine systems with exhaust heat recovery since the catalysts were only effective below 400°C. However, some new catalyst, developed lately using zeolite catalytic coatings on honeycomb ceramic structures can handle operating temperature above 540°C. This mean SCR application is now possible on simple cycle gas turbines.

(3) Water Injection. Water injection appears to be one of the oldest NO_x control technology for gas turbines. While it is an effective and proven method in reducing NO_x to about 42 ppm it also results in a minor power enhancement and thermal efficiency reduction to this equipment. Water injection requires large quantities of high-purity feed water. If the purity is reduced even temporarily, the gas turbine is susceptible to damage.

(4) Steam Injection. Steam injection is similar to water injection except that the water is boiled before injection. As the water is vaporized, most of the water contaminants are retained, concentrated, and blown down from the boiler. Generally speaking, water acceptable for high-pressure boiler feed water will generate steam of satisfactory quality for steam injection. This water quality is more tolerable for the industry. While steam injection has been a well-proven NO_x reduction technology, it can also be used to provide incremental power, as required, at any particular location an the system, thereby delaying the addition of new compressor units.

With the introduction of steam injection on high compression ratio aeroderivative gas turbines in the past 10 years, many gas turbines have achieved 10 to 15 percent efficiency improvement. The development of steam injection is still an ongoing process as some manufacturers have considered more massive steam injection techniques as well as intercooled steam injection. The latter is expected to achieve thermal efficiencies in the 50 percent range or a 30 percent efficiency improvement over the basic simple cycle turbine.

For a gas transmission pipeline, compressor units must be large enough to handled all forecasted operating conditions including peaking conditions, which may occur less than 10 percent of the operating time. For baseload conditions, gas turbines operate at partial power output only. This situation prevents gas turbines from operating at their best fuel efficiency most of the time. With a steam injected gas turbine, the peaking condition can be handled with the incremental power of high ratio steam injection while the baseload condition can be handled with low ratio steam injection. Thus, steam injection can be used to help gas turbines operate at higher efficiency levels and at reduced NO_x emissions.

Normally, steam is produced from a waste heat recovery boiler and for many gas turbines, only a portion of the steam produced can be injected into the turbine. The remaining steam can be used for other purposes such as cogeneration or combined cycle.

(5) Cogeneration/Combined Cycle. Since cogeneration/combined cycle produces power from exhaust gas energy, it does not create extra NO_x and CO_2. Cogeneration is therefore considered the most favored air emission reduction option. In many parts of the world, cogeneration/combined cycle must be incorporated into new major gas turbine installations to meet emission restrictions.

(6) Engine Uprate. Upgrading gas turbines is one option that has become more popular recently. An uprate increases power output as well as reducing specific fuel consumption of an existing unit with minimal alterations to its installation. Most turbine uprates provide a 10 to 30 percent increase in power output. This makes the engine uprate the most attractive solution to meet modest increases in power demands. In many cases, the turbine uprate also includes a thermal uprate, which involves an increased firing temperature. For this reason, an engine uprate often results in an increase in NO_x emissions. Turbine uprate is, unfortunately, not always available from turbine manufacturers since it requires a thorough engineering review of equipment design, performance and in many cases, it involves internal component modifications.

(7) Electric Drivers. Another option for AGTD to consider in reducing NO_x and CO_2 emissions, is to replace natural gas fueled turbines with electric drivers. This completely eliminates CO_2 and NO_x emissions from the compressor equipment of the gas transmission company. However, because most of the power and any incremental power used is produced from coal-fired equipment in this part of the country, utility companies would consequentially produce the same amount of NO_x and nearly twice the level of CO_2 as was emitted by gas turbines for the required power. Therefore replacing natural gas fueled gas turbines with electric drivers does not reduce the overall emission level unless the power is produced from less polluting sources.

A quick review of the potential solutions indicates that steam injection and cogeneration are the only two methods that can help AGTD achieve all stated objectives. These two methods also compliment each other since they share many major components such as the water treatment system, steam boiler, steam condenser, etc. They can also provide a flexible operation since they share the same steam production. The major drawback of steam injection is the long-term requirement in having large quantities of good quality feed water. This disadvantage is particularly severe for AGTD's gas compression facilities as they are primarily located in dry, remote areas. For example, in order to support steam injection on a General Electric LM2500 unit, two truckloads of clean water supply are required every hour or up to 200,000 cubic meters of water per year. This water requirement not only makes steam injection impractical but also may cause further environmental problems where water is scarce. For this reason, even though steam injection is very promising, it can not be applied unless the water supply problem is resolved. This is the main reason for development of a water recovery system that eliminates water supply problems for the steam injection process. In order to achieve sufficient water recovery, all steam injected into the gas turbine must be condensed and separated from the exhaust gas, treated, and reused.

Technical Considerations

While steam injection is a proven technology, water recovery from turbine exhaust gas has not been demonstrated in a field installation. Therefore, it is important to investigate a steam injection water recovery (SIWR) system that leads to a prototype field installation and a demonstration program. The purpose of the prototype and demonstration program is to prove the concept and to evaluate the performance and reliability of a closed-loop SIWR mechanical drive gas turbine on the AGTD system.

AGTD operates many different gas turbines. Of all the gas turbines in operation, the Solar Saturn appears to be best suited to the steam injection water recovery demonstration program. First, AGTD operates many of these units and the demonstration unit's size is such that it can be tested with minimum cost and impact on the operation of our pipeline system. Second, work by Solar in 1980 indicates substantial amounts of steam can be injected at different locations on the Saturn gas turbine. This allows the demonstration program to prove steam injection reduces NO_x emissions and enhances performance. Third, Solar Turbines has agreed to cooperate with NOVA and provide engineering support to this demonstration program.

Downloaded 02 Jun 2010 to 171.66.16.122. Redistribution subject to ASME license or copyright; see http://www.asme.org/terms/Terms_Use.cfm

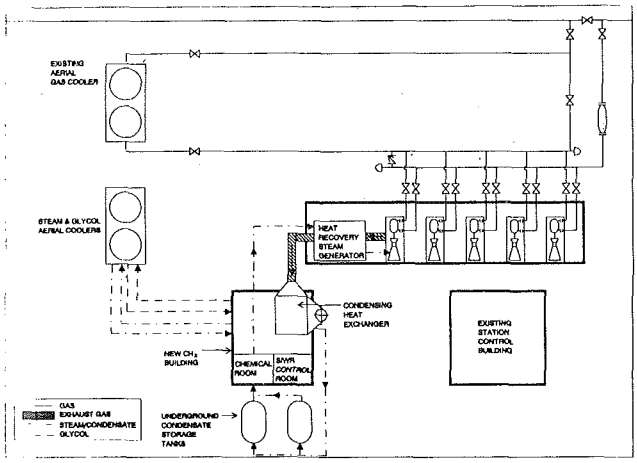


Fig. 1 Beaver creek compressor station site plan

The Beaver Creek Compressor Station was chosen for the prototype SIWR installation and demonstration program. This 20 year old station is located 150 km northwest of Edmonton, Alberta, Canada. The station was designed for automatic operation with remote monitoring from a control center in Edmonton. This station was chosen since it has 5 turbine units in parallel and the prototype SIWR system will pose minimal interference to the system operation during its demonstration period. Increased power output of the SIWR will be immediately used to substitute the compression power that is otherwise produced by another unit in the station (Fig. 1).

The successful operation of a steam injected gas turbine on the NOVA pipeline system will depend on the ability to recover and recycle the injected steam. To our knowledge there are no systems installed on a gas turbine where the primary purpose is to recover water, but equipment does exist to recover latent energy from the exhaust of gas turbines and other combustion equipment. Using this equipment to recover water from turbine exhaust gas is an extension of its application in latent energy recovery. The water recovery concept involves reducing the exhaust temperature to the level that sufficient water is condensed to support the process.

The water recovery application requires lowering the gas turbine exhaust temperature below the acid vapor and water vapor dewpoints. Unless the equipment used in the process is protected against corrosion the water recovery application will expose the equipment to both acid and cold end corrosion.

Condensate samples from 2 gas turbines were collected and analyzed. The water recovered is cleaner than most water sources but still contained some products of combustion. It will require little treatment to neutralize these dissolved, acidic, combustion products (Table 1).

The sample was taken from a non-steam injected gas turbine. The exhaust gas NO_x levels will be substantially reduced in a steam injected gas turbine. This will reduce the NO_x anions in the exhaust gas condensate and thus reduce its acidity. This will result in even less water treatment to neutralize the recovered condensate.

Boilers require alkaline boiler water and gas turbine manufacturers also have stringent requirements regarding the steam injected to the gas turbine (Table 2).

In addition, the water treatment system must also protect the boiler and other related equipment during long periods of standby operation. Verification of the water treatment subsystem is an important part of the demonstration.

One of the most critical concerns is whether water can be recovered in sufficient amounts to support the cycle needs. Water recovery takes place when the exhaust gas is cooled to its water vapor dewpoint (WVDP). Per the attached graph, the WVDP is a function of the amount of water contained in the exhaust (Fig. 2).

Table 1 Analysis of water recovered from solar Mars exhaust

	* DISSOLVED *	TOTAL
CATIONS:	PPM	PPM
Sodium (CaCO3)	2.0	2.0
Calcium (CaCO3)	1.0	1.1
Magnesium (CaCO3)	<0.5	<0.5
Potassium (K)		.0.1
Ammonia (CaCO3)	1.6	
ANIONS:	PPM	PPM
Sulfur (S)	1.1	1.1
Chloride (CaCO3)	1.1	
Sulfate (CaCO3)	2.4	
Nitrate (CaCO3)	3.1	
Nitrite (NO2)	4.0	
OTHERS:	PPM	PPM
Acidity (CaCO3) - Free Mineral	8.	3.8
pH Units		*63.*
Conductivity (micromhos/cm.)		0.2
Turbidity - Nephelometric Units (NTU)		
Notes: Passes through 0.45 Micron filter		

Table 2 Typical steam or water quality required for turbine injection

Contaminants	Limit	Test Method
Total matter, ppm Max	5	ASTM D1888
Dissolved matter, ppm, Max	3	ASTM D1888
pH(1)	6.0 - 8.0	ASTM D1293
Conductivity, micromhos/cm at 25°C, max (1)	0.05 - 0.1	ASTM D1125
Sodium + potassium, ppm, max	0.1	ASTM D1428
Silicon dioxide, ppm, max	0.1	ASTM D859
Chlorides, ppm, max	0.5	ASTM D512
Sulfates, ppm, max	0.5	ASTM D516
Notes: (1) pH and/or conductivity shall be measured when water is free of carbon dioxide.		

Courtesy of General Electric Company.

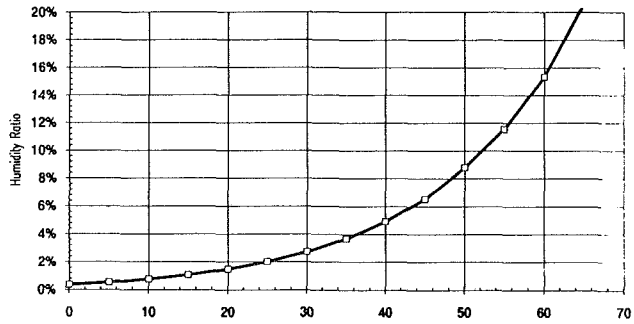


Fig. 2 Turbine exhaust gas dew points

The exhaust of a "dry" natural gas fueled turbine contains a substantial amount of water due to relative humidity in the intake air and water produced from combustion of hydrogen in the fuel.

$$CH_4 + 2O_2 \Rightarrow CO_2 + 2H_2O$$

From the above combustion equation, each mole of methane produces 2 moles of water. Each mole of methane weighs 16.043 g and each mole of water weighs 18.016 g. The result is that burning 16.043 g of methane produces 36.032 g of water or 2.246 times the mass of methane burned.

The exhaust of a steam injected unit contains the water vapor that originates from the air intake and the combustion process plus the steam injected into the engine. If the exhaust gas of a steam injected unit is cooled to the WVDP temperature of a "dry" gas turbine, all the injected steam can be recovered. In order to support steam injection process without water

Downloaded 02 Jun 2010 to 171.66.16.122. Redistribution subject to ASME license or copyright; see http://www.asme.org/terms/Terms_Use.cfm

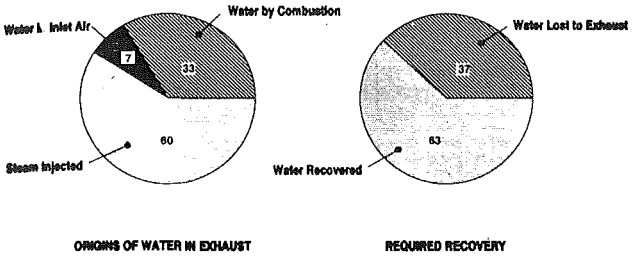


Fig. 3 Water vapor mass balance—solar saturn

supply from external sources the recovery amount must be approximately 5 percent more than the injected amount to compensate for the water loss in the steam production process; see Fig. 3.

Typically, the exhaust gas of steam injected turbines must be cooled to the 30°C–40°C range to meet the recovery requirement. This dew point temperature varies with the design parameters of the turbine. Generally speaking, turbines with low air mass flow per unit power output have higher exhaust gas dewpoint temperatures and thus require smaller condensing heat exchangers per kW output.

Any surface of the condensing heat exchanger that is in contact with the exhaust gas must be protected from corrosion. The best material for this service was found to be DuPont Teflon. Teflon has excellent corrosion resistance and has been used to protect chemical plant piping from acid attack. In the CHX exchanger, the tubes are covered with a 0.38-mm-thick extrustion of DuPont Teflon over the outside diameter. The shell is protected with Teflon 1.5 mm thick. This type of equipment has been used as a low-temperature economizer to recover both sensible and latent heat from the exhaust of many boilers.

While factory testing of this type of heat exchanger indicates that it can withstand 370°C inlet air for 30 minutes without apparent damage, the maximum continuous operating temperature is limited to 260°C. For this reason the unit is well suited for installation downstream of a waste heat recovery steam boiler.

As the condensing heat exchanger must cool exhaust gas to the 30°C to 40°C range it can use either air or water as a cooling medium. Applications in the proximity of large water bodies such as platform installations may find water-cooled systems the most attractive.

The Prototype SIWR System Design

The SIWR system consists of several individual pieces of equipment supplied by different manufacturers. It is important to establish design parameters for each item and ensure that their designs are adhered to. A simplified system diagram is provided (Fig. 4) to facilitate discussion.

Exhaust gas from the gas turbine goes through a diverter valve to the boiler, where its temperature is reduced from 480°C to 210°C. From the boiler, the flue gas goes to the CHX where it is further cooled to a 30°C dew point. From the CHX exhaust gas is vented through a fiberglass stack. The recovered water from the CHX unit goes to fiberglass underground storage tanks. The water is then pumped to a water treatment section where it is deaerated and chemicals added to reduced corrosion. From the deaerator, the water is pumped to the boiler to produce superheated steam. Steam from the boiler is sent to the gas turbine and the surplus steam is sent to the excess steam condenser. The condenser water from this unit is returned to the deaerator to conserve water. The CHX is cooled with a closed-loop glycol system. The glycol is cooled with an aerial fin-fan heat exchanger.

Gas Turbine

The gas turbine is a Solar Saturn T1300, with an added

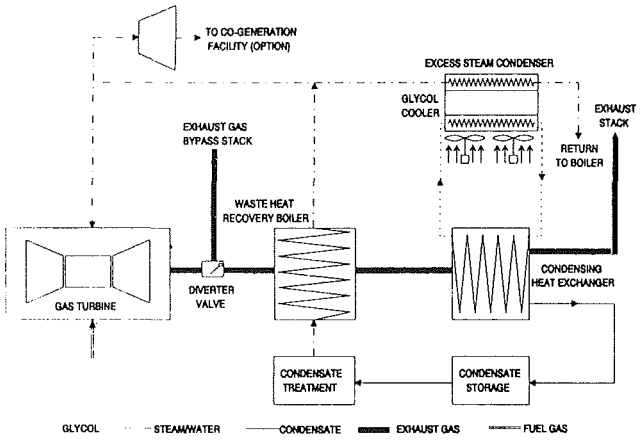


Fig. 4 Turbine steam injection water recovery system diagram

steam manifold. The unit will generally run with a 4 to 1 steam to fuel ratio, which is equal to a 6 percent steam to air ratio. Solar indicates that the Saturn can accept a higher steam ratio but this capability is not yet fully developed. Under certain site conditions, the steam to fuel ratio will be temporarily reduced below 4 to 1 for the following reasons:

1 To conserve water during extended warm weather periods.
2 To prevent axial compressor stall during low ambient temperatures.
3 To reserve steam for cogeneration if this is needed at a later date.

Gas Diverter Valve

The gas diverter is a single blade design with a pressurized double seal. The single blade design is used since it is the simplest and well proven in industry. Seal air is used to pressure the space between the double seals to ensure the seals are not leaking when the boiler is isolated from exhaust gas. If the seal is leaking, the seal air pressure will not be maintained and the gas turbine will be shut down to protect the isolated boiler from overheating.

Boiler

The type of boiler selected for this proposal is a modified single pass boiler with no steam drum. This type of boiler contains a single tube, which passes through the exhaust gas. It is considered to be safer than the conventional drum type boiler as it has minimal steam inventory. It was selected since it receives special consideration by local boiler authorities on operating attendance. This consideration is important since all AGTD high-pressure natural gas compression facilities have been designed for remotely monitored, unmanned operation. These facilities have been operated as such for the past 20 years with an excellent track record.

The water is heated to saturation temperature and then 83 percent vaporized (Fig. 5). This 83 percent quality steam is passed through a separator to remove liquids. The steam is then superheated 30°C to ensure dry steam is produced for turbine injection. The separated water, which contains all of the inlet impurities, is returned to the deaerator after being analyzed for pH and conductivity. Due to the vaporization of pure water, this remaining water will have a total dissolved solids (TDS) level of five times the inlet water rate; it will also contain corrosion inhibitor chemicals.

There are three important factors that must be considered when sizing the boiler:

1 Produce steam of sufficient pressure for injection
2 Reduce the exhaust gas below 250°C to protect the Teflon in the CHX.

Downloaded 02 Jun 2010 to 171.66.16.122. Redistribution subject to ASME license or copyright; see http://www.asme.org/terms/Terms_Use.cfm

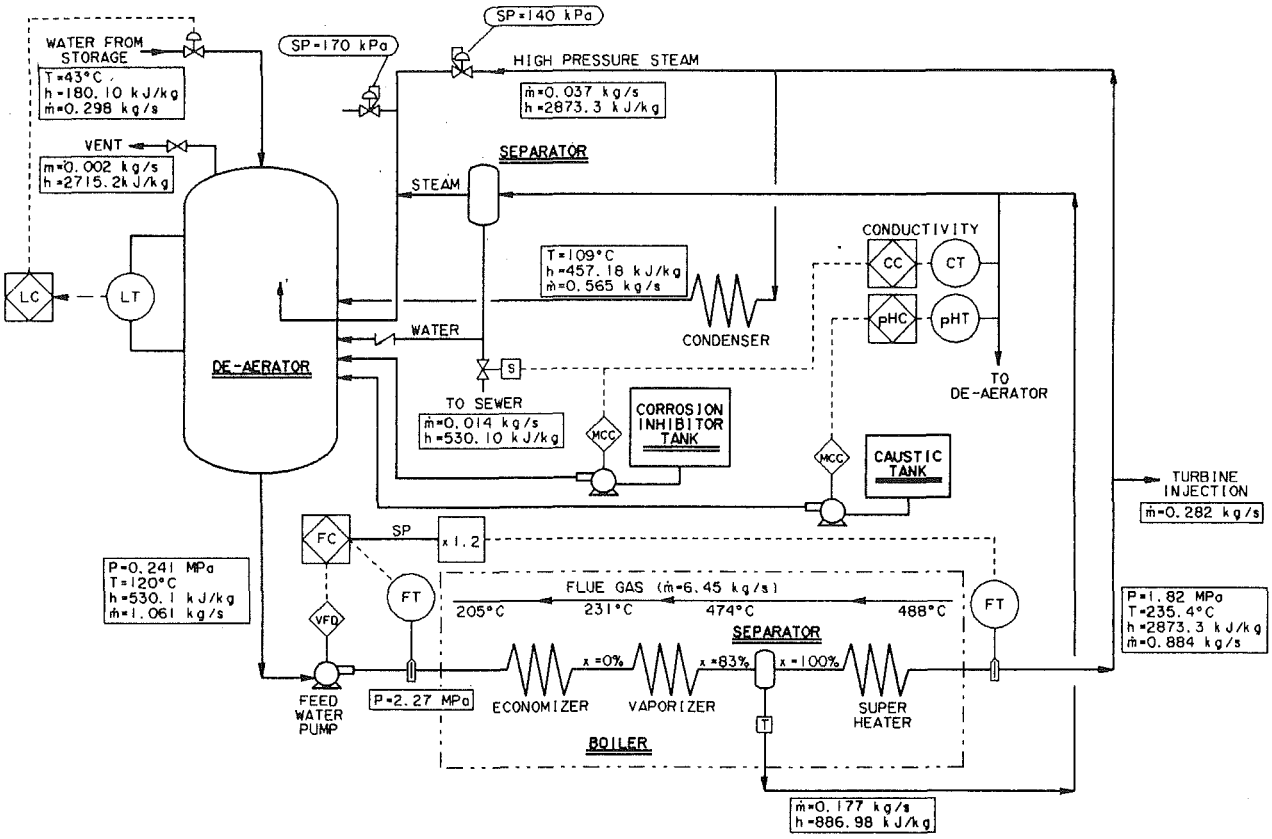


Fig. 5 Boiler mass balance and control schematic

3 Work with the whole amount of exhaust gas since water can not be recovered from any portion of exhaust gas which does not go through the boiler and the CHX.

This resulted in a 3200 kg/h, 1750 kPa boiler being selected.

This boiler produces approximately 2.5 times the amount of steam required for injection. This surplus steam must be condensed so the water can be re-used. A cogeneration facility could have been incorporated; however, this technology is already proven and need not be demonstrated at this point.

The boiler feed water flow is controlled at 120 percent of the boiler steam production.

Condensing Heat Exchanger (CHX)

The CHX is designed to remove heat from the exhaust gas to reduce its dewpoint below 31.4°C. It accomplishes this by passing the exhaust gas downward past cooled Teflon coated tubes. At the end of the cooling section the gas turns 180 deg and continues up the stack. The water is removed in the 180 deg turn.

It was originally proposed to use direct air to exhaust gas CHX because of the cold climate installation. It was later found more cost effective to use a water-cooled CHX in conjunction with an external water to air cooler. This decreased the overall project cost by 5 percent, reduced the total power consumption from 100 kW to 60 kW, and lowered the exhaust gas pressure drop from 870 Pa to 350 Pa through the CHX. Pure water cannot be used due to its high freezing point; adding 50 percent ethylene glycol reduces the freezing point sufficiently.

The CHX unit contains seven modules; each module consists of 336 1 in. diameter, 96-in.-long tubes. It is sized to reduce the moisture content in the Solar Saturn gas turbine exhaust from approximately 8 to 3 percent. To achieve this requirement, 1.97 MW of sensible and latent heat must be removed from the exhaust gas. This is done by circulating 55.6 kg/s of 50 percent ethylene glycol solution at 21.1°C. The glycol is heated to 45.5°C in the CHX (Fig. 6).

The graph shows the the performance of the CHX after each of its seven modules. The water recovery and temperature change phenomena in the CHX are of a complex nature; they require extensive knowledge of heat transfer to explain, is beyond the scope of this paper. The CHX will be automatically isolated if either the exhaust gas temperature to the CHX unit exceeds 250°C, or the CHX outlet gas temperature exceeds 120°C. This will protect both the Teflon extrusions and the fiberglass exhaust stack from high temperature.

Glycol Cooler

The hot glycol from the CHX unit is pumped through an aerial fin-fan heat exchanger. The glycol cooler is designed to cool 55.6 kg/s of 50 percent ethylene glycol solution from 46°C to 21°C when the ambient temperature is 13°C. It is a single aerial heat exchanger with two variable speed 18.75 kW fans. It is expected the rate of water recovery will exceed the steam injection water requirements when the ambient temperature is below 13°C. If this condition is prolonged, such as in winter, the water storage facility will not be able to contain all the water. For this reason the glycol cooler fans will be controlled with input from the water level in the storage tank.

When the ambient temperature exceeds 13°C, water from the tank will be used to supplement water recovery. If the ambient temperature rises above 21°C for prolonged periods or the water tank level goes below 25 percent, the system will automatically shut down to preserve water.

The 13°C design point was selected because the average monthly temperature only exceeds it in July (Fig. 7).

The hot glycol could have been used in other low grade heating applications, for example, heating buildings or greenhouses.

Glycol Pump

The glycol pump is a single-stage centrifugal unit driven by

Downloaded 02 Jun 2010 to 171.66.16.122. Redistribution subject to ASME license or copyright; see http://www.asme.org/terms/Terms_Use.cfm

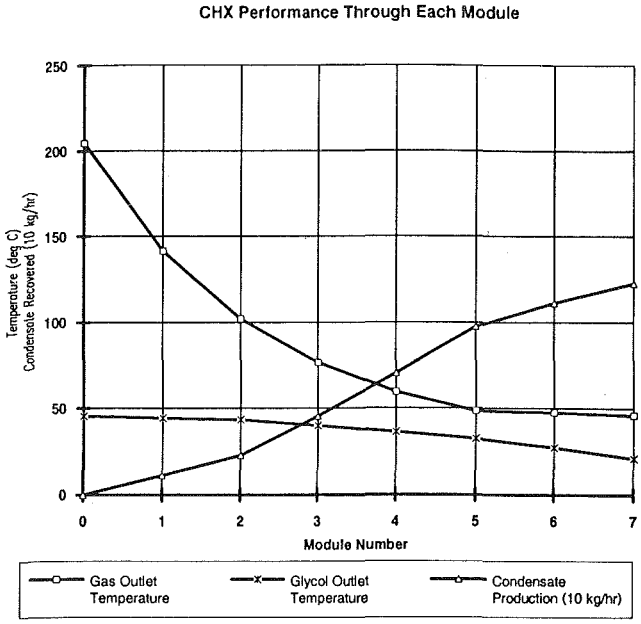


Fig. 6 CHX performance through each module

an 18.75 kW electric motor. It draws suction from the CHX and passes it to the cooler. The pump is designed for operation between 20 kg/s and 60 kg/s. A thermal expansion tank is provided upstream of the tank to compensate for fluctuations of glycol temperature.

Excess Steam Condenser

The surplus steam produced in the boiler must be condensed to recover its water. This steam can also be used for cogeneration as long as the condensate is returned.

The excess steam condenser is a single pass finned coil bank installed above the glycol coils in the glycol cooler. This arrangement was selected since it reduces the possibility of freezing the coil and has minimal effect on condenser performance due to the high temperature of steam. The condensate of the surplus steam condenser is controlled at 125°C to reduce flash steam. Normally subcooling water in the presence of steam causes water hammer. However, due to the small diameter of tubes in the condenser, it is expected that water hammer will be minimal. If water hammer is a problem, a standard steam trap will be installed and the flash steam will be handled elsewhere.

The surplus steam condenser is sized to condense the full boiler capacity at design conditions (13°C ambient temperature). If the temperature is lower, the fans for the glycol cooler will also run slower and the air into the steam condenser many be slightly warmer. As this happens, the capacity of the excess steam condenser decreases and steam may be vented. This steam can be vented to the CHX for water recovery. Fortunately, during cold weather operation, when the excess steam condenser is least effective, the system has the best ability to make up water from the exhaust gas. The excess steam condenser is unlikely to run for long periods at 0.88 kg/s since this does not permit steam injection.

Water Treatment Design

Corrosion in boilers is a serious problem; in order to minimize the capital expense and simplify equipment procurement, carbon steel materials are used instead of more corrosion resistant alloy materials. As a result, the water needs be treated to reduce corrosion. A water treatment chemical company was consulted to design a system for this application. The factors they considered are:

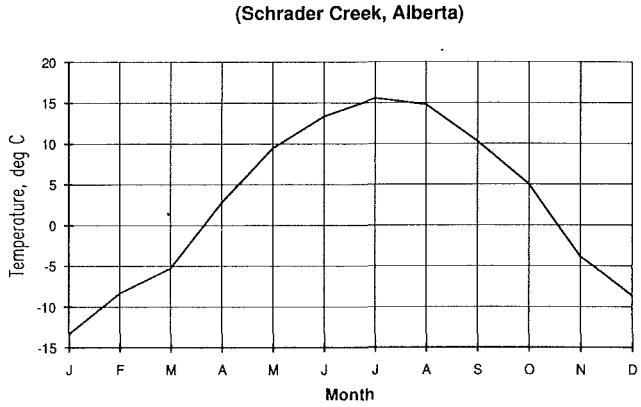


Fig. 7 Average monthly temperature in central Alberta

(*a*) The treatment has to control corrosion in the water, steam, and condensate systems during operation and shutdown since the boiler will be stopped and started frequently in gas transmission applications. The corrosion control during shutdown is a major concern since down-time corrosion has a significant effect on steam system maintenance.
(*b*) The treatment must be designed for minimal operator intervention since the site may be left unattended for up to 5 days.
(*c*) The treatment must be forgiving of over or under doses.
(*d*) The solution must be simple to implement.
(*e*) The treatment chemicals must be environmentally friendly to allow many alternatives for blowdown disposal.
(*f*) The blowdown must be minimal to reduce the makeup and disposal of blowdown.
(*g*) The treatment must work with the CHX condensate.
(*h*) The normal requirements exists for anti-foam agents and sludge conditioning.

The proposed water treatment chemical program is as follows:

1 Water is first mechanically deaerated; this removes the CO_2, O_2, and N_2. This will improve the pH somewhat while not increasing the TDS. Mechanical deaeration is done by heating the water to saturation. Normally this is done by having the raw water contact low-pressure steam in a specially designed vessel.
2 Caustic (NaOH) is added to the deaerator to increase the water pH level to 10. Corrosion inhibitors are most effective with a pH of 10 or 11. Adding caustic unfortunately also increases the TDS and thus the blowdown.
3 A combination corrosion inhibitor/sludge conditioner is also added to the deaerator. The corrosion inhibitor works by passivating the metal. Only a small percentage of corrosion inhibitor is vaporized to provide condensate system corrosion control.
4 The recycle water pH and conductivity is analyzed after the separator. If the pH is low, caustic is added to the deaerator; if the conductivity is above 7000 micromhos the recycle water from the separator is diverted to the sewer. Corrosion inhibitor is added to the deaerator during the blowdown to make up for chemicals lost in the blowdown.
5 The supply of feedwater to the boiler is 20 percent more than the boiler can vaporize. This surplus water is separated from the steam after the boiler vaporization section and recycled to the deaerator. This water contains all the TDS and most of the water treatment chemicals.

Deaerator

The purpose of the deaerator is to: remove dissolved gases, absorb low-pressure steam, allow a place for chemical addition

Downloaded 02 Jun 2010 to 171.66.16.122. Redistribution subject to ASME license or copyright; see http://www.asme.org/terms/Terms_Use.cfm

and residence time, and finally provide a reservoir for the boiler feed water pump to draw from. The deaertor receives water from the excess steam condenser, the boiler recycle, steam traps, sample coolers, and sends it through the boiler feed water pump to the boiler. The water level in the deaerator is maintained by adding condensate from the underground storage tank. Steam from the boiler discharge is added to maintain a deaerator pressure of 20 PSI and a small amount of steam is purged to remove O_2, CO_2, and other previously dissolved gases.

The energy balance of the deaerator indicates that most of the steam required for deaeration and purging comes from the 20 percent boiler recycle. Sufficient cold water from the storage tank has to be added to condense this. If all the steam produced is recycled through the excess steam condenser then there will be a surplus of low-pressure steam in the deaerator. A valve near the deaerator will open to discharge this steam. The deaerator air vent and the surplus steam valve can be discharged into the CHX for water recovery.

Storage Tank and Piping

The water from the CHX water recovery unit is routed to underground fiberglass storage tanks through plastic piping. The plastic piping and fiberglass tanks are used due to their superior corrosion resistance. The tank is installed underground so the water can drain from the CHX without pumping and also to protect the condensate from freezing.

The storage tanks are provided to accommodate the fluctuations of water recovery performance under different ambient temperatures. They store water to allow steam injection to continue when the ambient temperature is above 13°C.

To determine the storage tank size, a computer model was used to simulate the equipment operation. The wet bulb and dry bulb temperatures from Environment Canada 1989 temperature surveys were entered along with tank level and water recovery to determine whether the system could operate. It was determined that increasing the tank above 40,000 liters does not increase the operating time significantly. The tanks will be filled with clean water for the initial start-up.

Instrumentation

The SIWR facility will be controlled by an Allan-Bradley programmable logic controller (PLC) model 5/15. This PLC will sequence the start-up and shut-down of the system in addition to providing analog controls while operating.

In order to provide safe operation and to protect the equipment, there are three levels of shutdown.

The first level is triggered when any measured variable deviates sufficiently from its expected value. It delays closing the diverter valve for 5 minutes while the chemical injection pump is operated. This allows maximum corrosion protection for the equipment while it is shutdown.

The second level of shutdown is triggered when the deviation from set-point gets larger than the first level. It closes the diverter valve immediately. Only certain variables can trigger this second level; they include pressures and temperatures, but do not include minor problems such as analyzer failures or low condensate tank level.

The third level of shutdown is triggered when the diverter valve either fails to close within 30 seconds or it leaks. It shuts down the gas turbine immediately. This shutdown is in operation whether the CHX is operating or not.

There are only two control interfaces between the existing turbine controller and the SIWR controller:

1 The turbine controller will give a start-up permissive to the SIWR when the operating status of the turbine is normal.
2 The SIWR system will shut down the gas turbine if the diverter valve fails.

Conclusions

Through all the design considerations discussed earlier, we can draw the following conclusions:

1 It is practical to recover all the steam injected to a gas turbine by cooling its exhaust gas to a certain temperature. Ambient air or large water bodies can be used as a cooling medium.

2 The size of the water recovery system is primarily dependent on the air and fuel mass flows of the turbine rather than the size, the power rating, or the amount of steam injected into the turbine. Water recovery is, therefore, more attractive for the new generation of gas turbines, which have high specific output, and for units with high ratio steam injection.

3 The recovered condensate is slightly acidic as it is contaminated with products of combustion. However, it is still of higher quality than most water supply sources and requires little treatment to bring it to boiler feed water quality.

4 As the SIWR system favors lower exhaust gas temperatures, it is best to have this system downstream of a waste heat recovery boiler. This boiler can produce a lot more steam than that is normally required for steam injection. This surplus steam can be used for other purposes such as cogeneration to reduce overall exhaust emissions, increase power output and provide flexible operation at different loading and ambient temperature conditions. Since SIWR and cogeneration share the same steam production system and its operating costs, it is more cost attractive when both systems are used in conjunction.

5 A significant amount of energy could be recovered from the condenser while condensing the exhaust gas. This energy is available in convenient forms such as clean hot air or hot glycol. Further study could be made to find a use for this energy.

Notes

TEFLON is a trademark of E.I. DuPont. CHX is a trademark of Condensing Heat Exchanger Corporation.

References

Alberta Department of Energy, 1990, "A Discussion Paper on the Potential for Reducing CO_2 Emissions in Alberta," 1988-2005, Executive Summary, Sept.

Belanger, R., 1990, "Boiler Water Treatment Program on Gas Turbine Steam Injection System for Nova Corporation," Dearborn Chemical Company Ltd. Report.

Federal/Provincial Long Range Transport of Air Pollutants Steering Committee, "Management Plan for Nitrogen Oxides (NO_x) and Volatile Organic Compounds (VOCs)," Canada, 1st ed., Mar.

Heaphy, J., Carbonara, J., and Joseph, J., 1991, "Condensing Heat Exchanger Demonstration Project," Electric Power Research Institute Report, May.

Keller, S. C., and Studniarz, J. J., 1987, "Aeroderivative Gas Turbines Can Meet Stringent NO_x Control Requirements," General Electric Company.

Kolp, D. A., Gagnon, S. R., and Rosenbluth, M. J., 1990, "Water Treatment and Moisture Separation in Steam-Injected Gas Turbines," ASME Paper No. 90-GT-372.

Nguygen, H. B., 1991, "Gas Turbine Steam Injection Water Recovery (SIWR) System," Canadian Gas Association Report, Banff, Alberta, Oct.

Sailer, E. D., 1989, "NO_x Abatement With Steam Injection on Aircraft Derivative Gas Turbines," American Cogeneration Association Report, Scottsdale, AZ, Mar.

Smith, K. O., 1989, "Gas Turbine NO_x Emissions Control Technologies," presented at the Turbomachinery Technology Seminar, Solar Turbines Inc.

Solar Turbine Inc., 1980, "Investigation of the Effect of Steam and Water Injection on Performance and Emissions of a GSC 1200 Saturn Engine."

Thames, J. M.; and Coleman, R. P., 1989, "Preliminary Performance Estimates for a GE Steam Injected LM1600 Gas Turbine," ASME Paper No. 89-GT-97.

Downloaded 02 Jun 2010 to 171.66.16.122. Redistribution subject to ASME license or copyright; see http://www.asme.org/terms/Terms_Use.cfm

Infrared Signature Suppression for Marine Gas Turbines: Comparison of Sea Trial and Model Test Results for the DRES Ball IRSS System

A. M. Birk
Queen's University,
Kingston, Ontario, Canada

D. VanDam
W. R. Davis Engineering Limited,
Ottawa, Ontario, Canada

Sea Trials have recently been underway for Canada's new City Class Patrol Frigate (CPF). These trials provided the first opportunity to measure the performance of the new DRES Ball Infrared Signature Suppression (IRSS) system installed on a ship. Prior to these trials 1/4-scale hot flow model test and computer simulation performance results were available. The CPF DRES Ball IRSS systems are installed on the exhaust uptakes of the GE LM2500 main gas turbines. The DRES Ball provides both metal surface cooling for all view angles and plume cooling. The DRES Ball significantly reduces the IR signature of the LM2500 exhaust. This paper presents a comparison between the 1/4-scale hot flow model test results with the full-scale sea trial results. Performance variables included in the comparison are: metal surface temperatures, back pressure, plume temperature distribution, and surface static pressures. Because of the confidential nature of the DRES Ball system performance, all classified data have been nondimensionalized so that only relative comparisons can be made between the full-scale and 1/4-scale data. The results show that the full-scale system performs better than the 1/4-scale model because of Reynolds number effects. The plume temperature, surface temperatures, and back pressure were all lower (better) than in the 1/4-scale model tests. One of the original concerns with the installation was that relative wind would degrade the performance of the DRES Ball onboard a ship. The wind effect was found to be benign during the trials.

Introduction

The DRES Ball IR signature suppression (IRSS) system for marine gas turbines was developed for Canadian Navy ships and is based on a concept originating from the Defense Research Establishment Suffield (DRES). The system was described by Birk and Davis (1988) and is shown in Fig. 1. The system consists of a film-cooled outer duct, a film-cooled optically blocked center body, and a film-cooled diffuser.

The objective of the DRES Ball is to reduce the temperature of the visible metal surfaces of the exhaust ducting and also to reduce the temperaure of the exhaust plume. The DRES Ball device cools the visible metal for all view angles and therefore is believed to be unique in the world for marine applications. The DRES Ball device also effectively cools the core of the plume because of the presence of the center body. Previously conducted 1/4-scale hot flow model tests have shown that the device can reduce the IR signature of the exhaust system in the 3–5 μm waveband by 95–99 percent.

The film cooling of the various surfaces is facilitated by introducing ambient air at the various gaps that are located along the axis of the device. The gaps are created by a series of overlapping ring sections that make up the device, as illustrated in Fig. 1.

The DRES Ball device is located in the ship's stack and replaces the top section of the exhaust uptakes. The design of such installations requires attention to a number of factors such as cooling air supply, engine flow conditions, back pressure and weight limitations, etc. These various items are discussed further by Birk and Davis (1988).

The DRES Ball system for CPF has been designed to be fan assisted, which means that the center body and outer duct can be provided with pressurized air if desired. This is illustrated in Fig. 1, which shows the plenum surrounding the outer body. When the DRES Ball device is designed to be fan assisted (it can be designed for purely passive operation without fans) the

Contributed by the International Gas Turbine Institute and presented at the 37th International Gas Turbine and Aeroengine Congress and Exposition, Cologne, Germany, June 1–4, 1992. Manuscript received by the International Gas Turbine Institute February 21, 1992. Paper No. 92-GT-310. Associate Technical Editor: L. S. Langston.

Copyright © 1994 by ASME
Downloaded 02 Jun 2010 to 171.66.16.122. Redistribution subject to ASME license or copyright; see http://www.asme.org/terms/Terms_Use.cfm

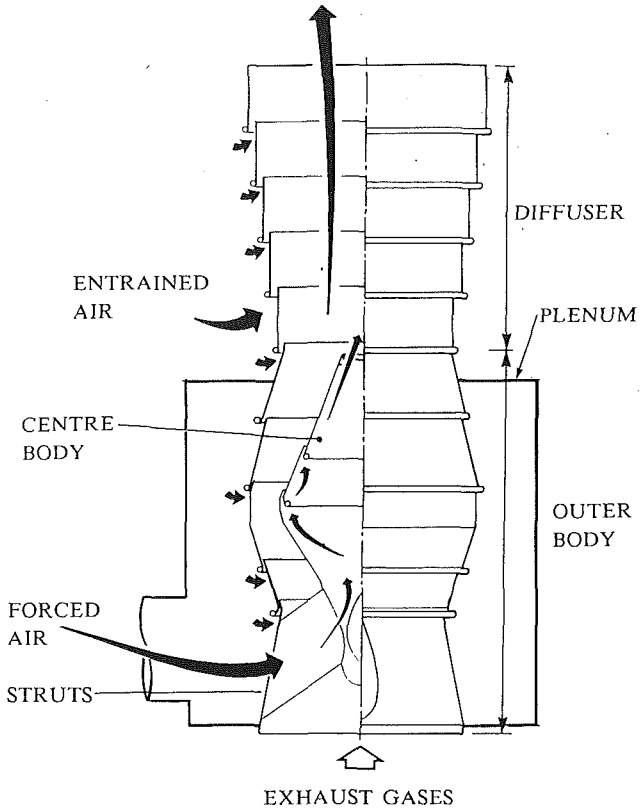


Fig. 1 DRES ball device

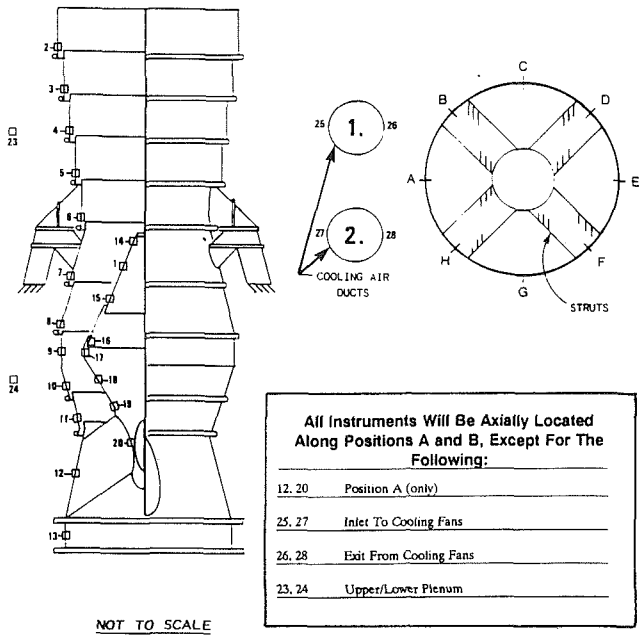


Fig. 2 Static pressure tap locations

device can effectively be turned off by turning the fans off. However, when the fans are off, the DRES Ball still provides significant IR suppression with reduced back pressure, as will be shown later in this paper.

Dimensional Analysis and Scale Effects

As described by Birk and VanDam (1989) the DRES Ball device is basically a complicated ejector. The performance of the system is measured in terms of its pumping ability and this depends on the pressure distribution in the device. These pressures are a function of the device geometry and the flow Reynolds and Mach number as shown below:

$$C_p = C_p(\text{Re, M, } T_s/T_p, \text{ geometry}) \quad (1)$$

where

C_p = pressure coefficient = $2\Delta P/\rho U^2$
Re = flow Reynolds number = $\rho UD/\mu$
M = Mach number = U/a
T_p = primary fluid (exhaust gas) absolute temperature
T_s = secondary fluid (cooling air) absolute temperature
U = inlet velocity
D = inlet diameter
ρ = inlet fluid density
μ = inlet fluid viscosity
a = speed of sound

Previous testing of the DRES Ball system involved 1/4-scale models under hot flow conditions. The simulated engine flow and the cooling air flow temperatures were matched to those of the full-scale systems and therefore no temperature effects needed to be accounted for. The flow velocities were the same as the full-scale system and therefore the Mach numbers were also matched. However, this leaves the Reynolds number for the model tests low by approximately the scale factor (i.e., model flow Re was 1/4 that of the full-scale system).

The model scale Re based on the inlet diameter is approximately 3×10^5 and the full-scale Re is 1.2×10^6. It was assumed that this is sufficiently high to allow the test to be conducted with small Re effects. An analysis of the Reynolds number effects was carried out and the following conclusions were drawn:

(*i*) The skin friction effects in the full-scale device would be less than in the model because of reduced relative roughness of the ducting surface. This would result in increased air entrainment (i.e., improved film cooling of surfaces and a cooler plume) and a lower back pressure.

(*ii*) The lip thickness (see for example Mukherjee, 1976) effect on the film cooling effectiveness would be reduced and the film cooling would be improved. This is because the ratio of the metal thickness to the cooling gap dimension is smaller in the full-scale device.

(*iii*) The film cooling effectiveness increases with increasing Reynolds number, over the range of Reynolds numbers considered here.

(*iv*) The boundary layer effects on the center body support struts would result in lower drag losses and therefore a lower back pressure for the full scale device.

The factors listed above lead the designers to conclude that the full-scale DRES Ball device would perform superior to the 1/4-scale models. The results about to be presented document this.

Sea Trial Instrumentation

The sea trial instrumentation was designed to measure the basic operating characteristics of the system, including:

(*i*) metal surface temperatures
(*ii*) plume temperature and velocity profile
(*iii*) surface pressures
(*iv*) back pressure

Figures 2 and 3 show the location of the surface pressure transducers and thermocouples. As can be seen from the figure, each ring on the device was fitted with a number of thermocouples and surface pressure taps. Two stationary flow rakes were used at the inlet and exit of the device.

A fixed rake was installed at the entrance and the exit of

Downloaded 02 Jun 2010 to 171.66.16.122. Redistribution subject to ASME license or copyright; see http://www.asme.org/terms/Terms_Use.cfm

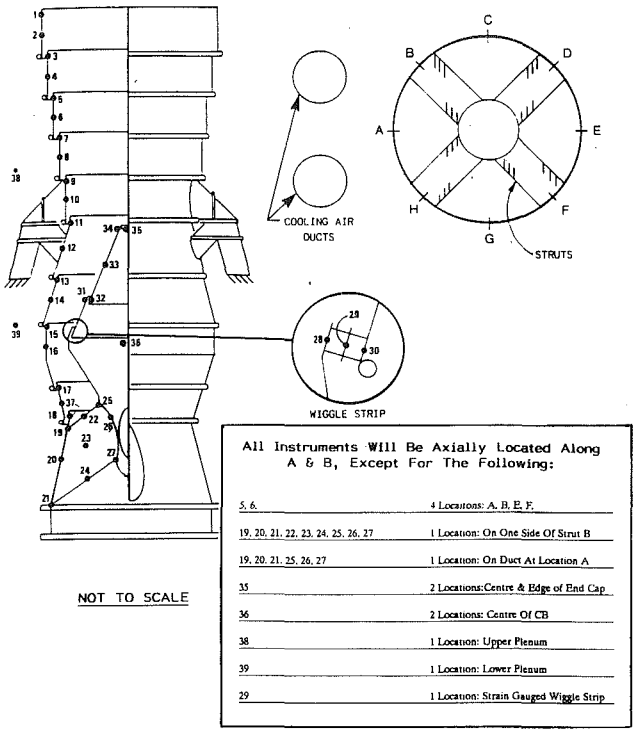


Fig. 3 Surface thermocouple locations

the device to measure pressures (total and static at the entrance and just total at the exit) and temperatures. The exit rake consisted of four diagonal rakes with eight transducers each (32 total). The probes were located at centers of equal areas. The inlet rake consisted of a single diagonal with eight probes. The exit rake had many more instrument positions because of the distorted flow profiles at the device exit.

Surface temperatures are of interest because the main purpose of the device is to decrease the temperature of visible metal surfaces. Plume temperature and velocity profiles are of interest because they can be used to determine the IR signature of the plume. Surface pressures are of interest because they establish how well the flow is distributed in the device and allow for detailed comparison with the design calculations. Back pressure is a critical item because of the adverse effects on the performance of the engine.

Test Matrix

The test matrix for the sea trials is shown in Table 1. As can be seen from the table, tests were performed at various engine power settings with and without the cooling fans on. During the tests the ship performed various maneuvers, which resulted in significant ship roll. The roll had no appreciable effect on the DRES Ball performance. In addition the ship sailed at various angles to the wind and this showed that wind had no adverse effects on the device performance.

Sea Trial Results

The sea trial results are presented in the form of normalized plots of metal temperature, plume temperature, surface pressures, and back pressure. For the purposes of presenting the results the following variables are defined:

BP = design back pressure at full power
T_{pl} = design average plume temperature at full power
T_s = design average surface temperature at full power
V_{pl} = design plume average exit velocity at full power

Table 1 Engine power and cooling fan condition for test designations

TEST	ENGINE POWER (%, APPROXIMATE)	# OF COOLING FANS ON
*A	100	2
*B	100	2
C	90	2
D	75	2
E	50	2
F	25	2
G	IDLE	2
H	100	0
I	50	2
J	50	1
K	50	0
L	25	0
M	IDLE	0

All of the results about to be presented will be referenced to these variables. The design plume and surface temperatures are confidential and therefore cannot be quoted here. The design back pressure was 2000 Pa total pressure measured at the device inlet. The design plume exit velocity was 45 m/s.

Table 2 presents a summary of the trial results. Plume temperatures shown are mass-averaged values. Several interesting things can be observed from the data of Table 2.

(*i*) As the engine power decreases, the back pressure of the DRES Ball device drops rapidly because the volume flow rate through the device decreases. The plume temperature also drops because of the decreased exhaust gas temperature.

(*ii*) When the cooling fans are on for low engine power levels there is basically no back pressure imposed on the engines (i.e., the DRES Ball with the forced cooling air flow acts as an ejector pump for the exhaust uptake).

(*iii*) When the cooling fans are off the back pressure of the DRES Ball device drops significantly (at full power the drop in back pressure is 600 Pa (2.4 in. of water)) because of the reduced volume flow rate through the device. The plume temperature rises with the fans off but not anywhere near the unsuppressed plume temperature. This is an important advantage of the fan-assisted DRES Ball. In other words, the back pressure penalty is only present when IR suppression is needed and the cooling fans are on. Under normal operation the fans would be off and the back pressure would be reduced. However, as will be discussed later the DRES Ball continues to provide significant IR suppression even with the fans off.

Viewed Metal Temperatures

The DRES Ball IRSS system cools the exhaust uptake metal for all view angles. When a viewer looks down into the device (i.e., 90 deg down from the horizontal) they will see the inside of the diffuser section and the downstream end of the center body optical block. For angles less than 90 deg down from the horizontal the viewer will see primarily the inside of the diffuser. For a small range of view angles the viewer will see some parts of the outer duct.

During the trials the DRES Ball was instrumented with surface thermocouples as described earlier. Similar instrumen-

Downloaded 02 Jun 2010 to 171.66.16.122. Redistribution subject to ASME license or copyright; see http://www.asme.org/terms/Terms_Use.cfm

Table 2 Summary of test results

Test	Ambient Temp. (°C)	Exhaust Mass Flow (kg/s)	Exhaust Gas Temp. (°C)	Plume Temp. $\left(\frac{T - T_a}{T_{pl} - T_a}\right)$	Total Back Pressure (Pa)
A	16	73.8	446	1.00	BP + 100
B	15	71.8	450	0.96	BP + 130
C	15	66.4	436	1.02	BP + 50
D	16	60.6	418	0.92	BP - 405
E	17	56.0	402	0.87	BP - 570
F	16	49.0	355	0.62	BP - 1165
G	18	22.6	300	0.34	BP - 1960
H	16	75.6	429	1.31	BP - 500
I	22	47.3	408	0.95	BP - 640
J	23	57.9	397	1.13	BP - 920
K	21	57.7	398	1.12	BP - 1040
L	16	48.4	347	1.08	BP - 1295
M	17	43.6	331	0.98	BP - 1480

T = measured plume mass average temperature (°C)
T_a = ambient temperature (°C)
T_{pl} = contract plume average Temperature (°C)
BP = contract Back Pressure (Pa)

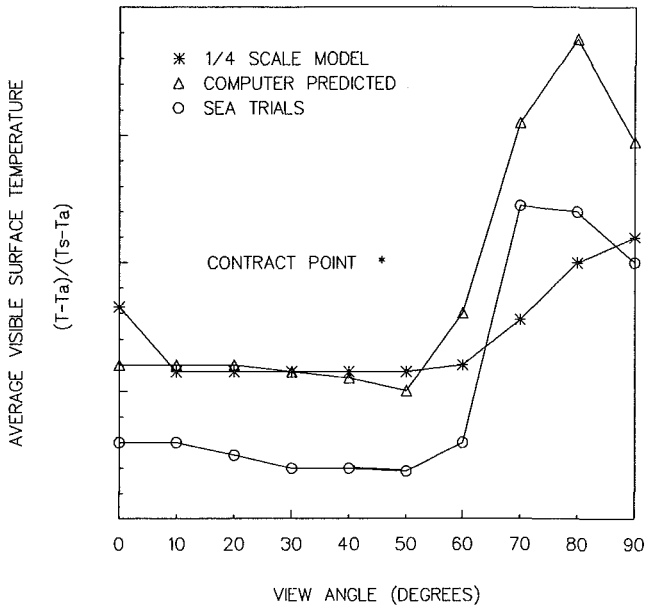


Fig. 4 Comparison of average visible surface temperature with view angle

tation was used on all of the 1/4-scale hot flow model tests. Viewed metal temperatures were predicted using film cooling correlations as described by Birk and VanDam (1989). Figure 4 presents a comparison between the measured surface temperatures from the sea trials, from the 1/4-scale hot flow model tests and the predicted surface temperatures from the film cooling correlations. The area-averaged surface temperature is shown as a function of view angle relative to horizontal. The temperature is normalized with respect to the ambient temperature and the design temperature (i.e., the desired surface temperature, which is classified).

As can be seen from the figure, the sea trials temperatures are generally lower (better) than both the predicted and the model test temperatures. The highest measured temperatures are around the 70 to 80 deg view angles where the warmest parts of the center body and outer duct are partially in view. The normalized maximum sea trial temperature exceeds the normalized design temperature by about 20 percent for view angles greater than about 67 deg. However, the contract specified view angle was 45 deg (i.e., the surface temperature specification was for this point only) and at this view angle the device performance is much better than the contract requires. In other words the visible metal is much cooler than the contract requires while still meeting all of the design constraints such as back pressure, weight, etc.

As stated above, the trials temperatures are higher than the model results for view angles around 70 to 80 deg. This is most likely due to the center body temperature, which may be slightly warmer in the trials. This will be discussed further when the device surface pressure distribution is reviewed.

It is also interesting to note that for the 1/4-scale model the last ring in the diffuser is warmer than the rest of the diffuser. This is seen in the sudden increase in viewed temperature at the 0 deg view angle. This indicates that the film cooling on the last diffuser ring was degraded. However, this is not seen as strongly in the trials results. It is possible that the full-scale diffuser is performing better in terms of providing film cooling for the last ring surface. This will also be discussed further when the pressure distribution in the device is reviewed.

Plume Temperature

The plume temperature distribution for the DRES Ball shows a characteristic saddle shape because of the presence of the center body. The center body wake results in an area of lower velocity and lower temperature downstream of the center body.

Figure 5 shows a comparison between the model test and sea trials plume temperature distribution for the full engine power case with both the cooling fans on. The plume is gen-

Downloaded 02 Jun 2010 to 171.66.16.122. Redistribution subject to ASME license or copyright; see http://www.asme.org/terms/Terms_Use.cfm

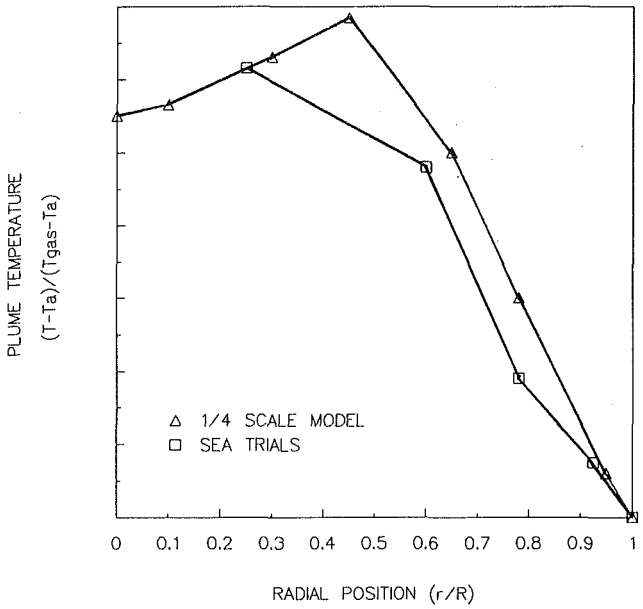


Fig. 5 Plume temperature profile

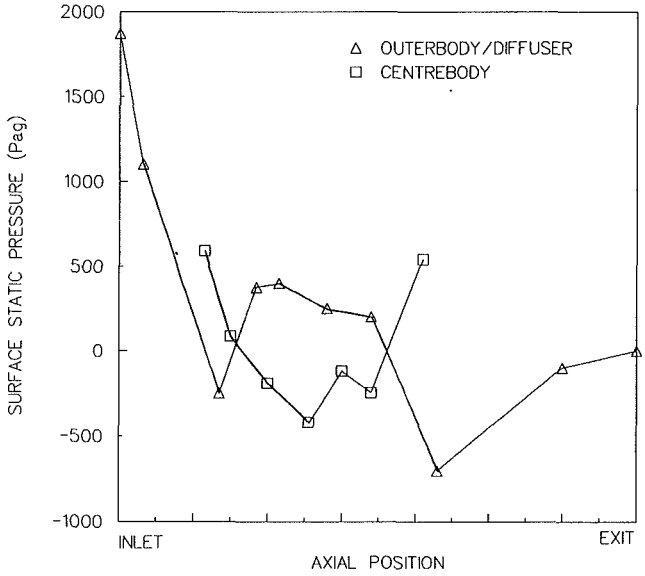


Fig. 7 Static pressure distribution, 100 percent power, fans/on

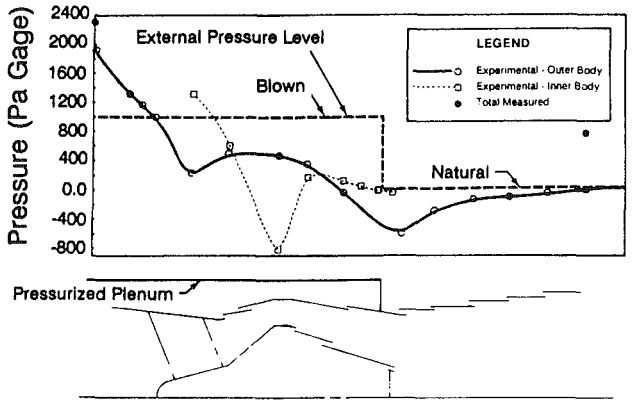


Fig. 6 DRES ball pressure distribution (fan-assisted design)

erally cooler for the trial results except that there appears to be a trend toward a warmer plume core. Unfortunately a plume center temperature was not obtained during the trials and therefore this warmer core trend cannot be confirmed. However, this will be discussed later when the center body pressure distribution is discussed.

Back Pressure and Internal Pressure Distribution

Back pressures and flow channel pressure distributions from the 1/4-scale hot flow model tests of the DRES Ball system were previously shown by Birk and Davis (1989) and are shown here again for reference in Fig. 6. These pressures were also measured in the full-scale sea trials and these are shown in Fig. 7.

Unfortunately as a result of painting by the ship yard and soot from the engine exhaust some of the static pressure taps were obstructed and therefore some of the pressure data were suspect. The data shown in Fig. 7 are averages of the measured pressures with some obviously bad data removed.

The pressures shown are for the full engine power case with cooling air fans on. When the two pressure distributions are compared, it is seen that the diffuser pressure recovery in the trial data is better than that from the model tests (i.e., 700 Pa versus 600 Pa). This results in more cooling air being drawn into the diffuser section of the device and improved metal temperatures and plume temperature. This probably explains the improvement in the top diffuser ring temperature as discussed earlier.

The outer duct pressures are very similar except at the station where the center body support struts are located. At this position the trial data show much lower pressures. This would result in increased cooling air flow at the first outer duct cooling air gaps. A possible reason for the lower pressures follows with the discussion of center body pressures.

The center body surface pressures are significantly different. The trial data show the pressures to be higher generally than those from the model tests. This would mean a reduced cooling air flow from the center body and therefore less core cooling of the plume. This appears to be the case shown by the trends in Fig. 5 where the plume temperatures are compared. This pressure distribution may also explain the increase in the viewed temperature for view angles between 70 and 80 deg as shown earlier in Fig. 4.

It is possible that a small axial displacement of the center body could change the annular flow passage and result in the observed pressure changes on the center body and outer duct. This is being investigated further for future installations to ensure that an optimum placement is achieved. Flow separation in the diffusing flow channel could also cause the above to occur.

Effects of Fan

The DRES Ball system installed in the CPF is a fan-boosted design where the center body and outer duct cooling air flows can be augmented with a fan. This type of design allows for variable performance of the device depending on the level of IR suppression required. When the fans are off the cooling air flow to the center body and outer duct is reduced and therefore surface temperatures in those regions are higher. The plume temperature is also higher when the fans are off. As a result the IR suppression is reduced with the main benefit being that the back pressure on the engines is also reduced.

It should be noted that the CPF DRES Ball device was designed with a fan because of the design limits set on available space and minimum plume velocity, for a given set of performance targets (i.e., plume temperature and maximum back pressure). DRES Balls have been designed and built without fans for the full operating range. These no-fan DRES Balls

Downloaded 02 Jun 2010 to 171.66.16.122. Redistribution subject to ASME license or copyright; see http://www.asme.org/terms/Terms_Use.cfm

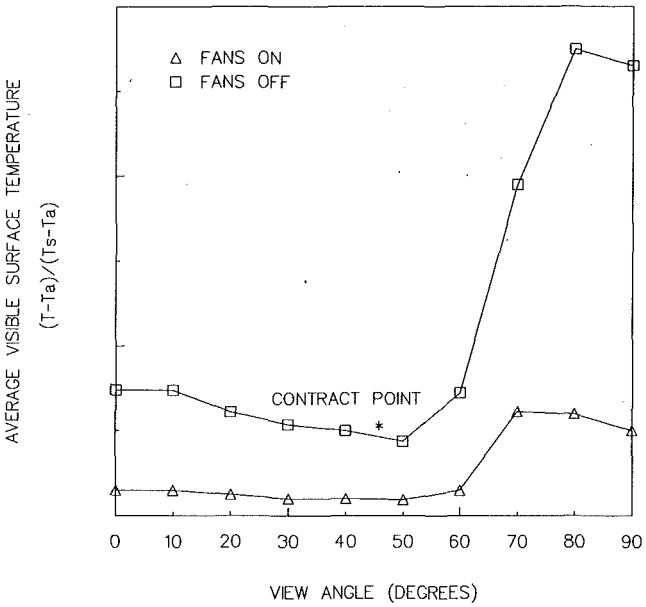


Fig. 8 Variation of average visible surface temperature with view angle

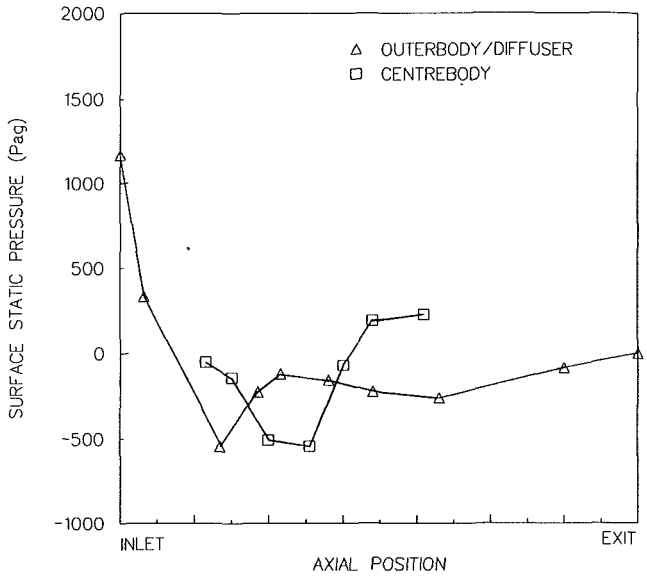


Fig. 9 Static pressure distribution, 95 percent power, fans off

are generally slightly larger and the back pressures are slightly higher than the fan powered designs.

Figure 8 compares the normalized surface temperature as a function of view angle for the cases when the cooling fans are on and off. As can be seen, the temperatures are significantly higher when the fans are off. However, it is interesting to note that the device actually meets the design target with the fans off as indicated by the contract point on the graph. In other words, this fan-assisted design for the DRES Ball continues to provide significant IR suppression even when the fans are off.

Figure 9 shows the surface pressure results for the case with the fans off at near full engine power (≈95 percent power). As can be seen from the fans-off pressure distributions the pressure recovery in the diffuser section is not nearly as strong as when the fans are on. This explains the much lower surface temperatures in the diffuser for the fans-on case. The energetic boundary layer flows provided by the fan probably retards separation in the diffuser to provide the better pressure recovery.

It should be noted that in the fans-off case the pressures at all the measured surface locations are subatmospheric and therefore air is always flowing into the device through the cooling air gaps (i.e., there are no locations where hot gases are leaving the DRES Ball device). This is an important point because with some fan-powered IR suppression devices hot gases leak out to heat stack spaces when the fans are off and this can lead to significant IR signatures from the heated stack.

Table 3 presents a comparison of the back pressures for the various test cases with fans on and off. As can be seen from the table, the back pressures are generally lower when the fans are off, except for the lowest engine power case (idle) where with the fans on the DRES Ball device actually becomes an ejector pump for the exhaust system. The most important point is for the 100 percent engine power where we see that with the fans off there is a very significant drop in the system back pressure.

Final Results

The design performance goals were specified at specific ambient and engine flow conditions (i.e., 15°C, full power) and therefore it was necessary to translate the trials results to these

Table 3 Back pressure summary for fans on and fans off cases

Engine Power %	Back Pressure (Pa)		Change (Pa)
	Fans-On	Fans Off	
100 *	BP + 115	BP - 500	- 615
50	BP - 570	BP - 1040	- 470
25	BP - 1165	BP - 1295	- 130
Idle	BP - 1960	BP - 1480	+ 480

* full power fans-on is the design point.

BP = design back pressure at 100% engine power
= 2000 Pa (≈8 inches of water)

reference conditions. This was done using the IRSCOOL computer code that was used to design the DRES Ball system. This code is basically a perfect mixer model as used for ejector analysis with allowance for streamline curvature, multiple stages of air injection and various coefficients for friction losses, gap losses, strut drag losses, and momentum correction.

The formal acceptance criteria for the equipment allowed some tolerances on the various performance values. This was allowed for CPF because this DRES Ball installation was to be the first full-scale system in the world and obviously there was some uncertainty associated with the system's exact performance.

Table 4 presents the results of this translation process. It should be noted that the contract specifications were for the fans-on case only and that the exhaust flow conditions for the LM2500 were assumed to be identical for fans-on and fans-off for comparison purposes. As can be seen from the table, the DRES Ball system performance came very close to the design targets.

Conclusions

The first shipboard DRES Ball IR signature suppression system has been successfully trialed and the results show the system to be even more effective than the 1/4-scale models that were previously tested under hot flow conditions.

The CPF DRES Ball system was designed with fan assist for cooling the center body and outer body sections. Trials

Downloaded 02 Jun 2010 to 171.66.16.122. Redistribution subject to ASME license or copyright; see http://www.asme.org/terms/Terms_Use.cfm

Table 4 DRES Ball performance at contract standard conditions

Fans	Approx. Engine Power (%)	Ambient Temp. (°C)	Exhaust Mass Flow (kg/s)	Exhaust Gas Temp. (°C)	Plume Temp. $\left(\frac{T - T_a}{T_{pl} - T_a}\right)$	Total Back Pressure (Pa)
ON	100	15	73.3	446	0.98	BP+115
ON	50	15	53.2	380	0.76	BP-920
ON	Idle	15	37.8	343	0.56	BP-1500
OFF	100	15	73.3	446	1.40	BP-750
OFF	50	15	53.2	380	1.18	BP-1350
OFF	Idle	15	37.8	343	1.07	BP-1700

results show that even when the fans are off the device provides significant IR suppression at a much lower back pressure penalty.

The DRES Ball system has been under development in Canada since the late 1970s. Over the years there has been a great deal of debate as to whether systems like the DRES Ball are effective or even necessary. Some experts believe that full overhead protection is not necessary. Some experts claim that with today's IR seeker and imager technologies devices like the DRES Ball system are ineffective. At the same time other experts claim that devices such as the DRES Ball combined with modern IR decoys are an effective counter measure against modern anti-ship IR guided missiles. Only time will tell who is correct.

References

Birk, A. M., and Davis, W. R., 1988, "Suppression of the Infrared Signatures of Marine Gas Turbines," ASME JOURNAL OF ENGINEERING FOR GAS TURBINES AND POWER, Vol. 111, pp. 123–129.

Birk, A. M., and VanDam, D., 1989, "Marine Gas Turbine Infrared Suppression: Aerothermal Design Considerations," ASME Paper No. 89-GT-240.

Mukherjee, D. K., 1976, "Film Cooling With Injection Through Slots," ASME JOURNAL OF ENGINEERING FOR POWER, Vol. 98.

Downloaded 02 Jun 2010 to 171.66.16.122. Redistribution subject to ASME license or copyright; see http://www.asme.org/terms/Terms_Use.cfm

TEMPER—A Gas-Path Analysis Tool for Commercial Jet Engines

D. L. Doel
Data Analysis Technology,
GE Aircraft Engines,
Evendale, OH 45215

Almost from the inception of the gas turbine engine, airlines and engine manufacturers have sought an effective technique to determine the health of the gas-path components (fan, compressors, combustor, turbines) based on available gas-path measurements. The potential of such tools to save money by anticipating the need for overhaul and providing help in work scope definition is substantial, provided they produce reliable results. This paper describes a modern gas-path analysis tool (GE's TEMPER[1] program), discusses the benefits and problems experienced by current TEMPER users, and suggests promising research areas that may lead to an improved algorithm.

Introduction

As a result of several factors, the performance of a gas turbine engine gradually deteriorates with time. This deterioration increases the internal operating temperature of the engine and reduces its fuel economy. When the internal temperature reaches a specified limit, the engine must be removed for overhaul. Depending on the cost of fuel and the available temperature margin of the engine, it may be cost effective to overhaul an engine before it reaches its temperature limit. Gas-path analysis is used by airlines to evaluate the performance of an engine and its components. The results may be included in the process to determine overhaul work scope.

Gas-path analysis can be performed using data acquired during routine service on-wing. Gas-path analysis is also accomplished using test cell data obtained during an acceptance[2] or in-bound run. The on-wing analysis has access to data at some fixed interval. This permits an examination of each new reading in relation to prior readings from the same engine. Deterioration can be recognized as the change in performance from when the engine was new. The objectives of the on-wing analysis are to decide when an engine should be removed for overhaul and what the overhaul work scope should be.

Gas-path analysis based on test cell data is, of necessity, a snapshot evaluation. The engine's and component's performance levels must be inferred from one or more readings that are obtained at a fixed instant in time. Usually, the test cell analysis is based upon an out-bound acceptance run. If the engine satisfies its acceptance limits, there is little interest in the results of the analysis. When the engine fails the acceptance requirement, the data are reviewed to try to determine the minimal rework to correct the problem. Occasionally, an engine removed from service will be run in a test cell to help to define its required work scope.

Most modern gas-path analysis programs use statistical techniques to estimate sensor error. This is desirable because of the limited amount of gas-path instrumentation and the inaccuracy of the available data. The older algorithms did not estimate sensor error. Thus, measurement error was interpreted as component performance by these algorithms. This often produced bizarre results (e.g., an extremely high turbine efficiency coupled with an equally low compressor efficiency). Urban (1980) and Volponi (1982) showed that weighted least-squares techniques could be used to reduce the sensitivity to measurement error. Following their lead, modern test cell and on-wing gas-path analysis programs use weighted least-squares or a closely related algorithm.

Mathematical Basis of Gas Path Analysis

To evaluate engine component performance correctly, sensor error must be considered in the analysis. Weighted least-squares facilitates the determination of engine state in the presence of sensor error. Weighted least-squares is based on a model of the measurement process of the form:

$$\mathbf{z} = h(\mathbf{x}) + \nu \tag{1}$$

The elements of this equation are:

$\mathbf{z}$ is the measurement vector consisting of the independent[3] measurements upon which the analysis is based (e.g., core speed, fuel flow). Note that $\mathbf{z}$ has dimension "p."

$\mathbf{x}$ is the state vector incorporating those characteristics of the engine expected to vary with time (e.g., compressor efficiency, HP turbine flow function). Other attributes, not

[1]For Turbine Engine Module Performance Estimation Routine.

[2]Jet engines are normally tested after overhaul to assure that performance and mechanical requirements are satisfied prior to return to service. This test is known as an acceptance test.

Contributed by the International Gas Turbine Institute and presented at the 37th International Gas Turbine and Aeroengine Congress and Exposition, Cologne, Germany, June 1-4, 1992. Manuscript received by the International Gas Turbine Institute September 28, 1991. Paper No. 92-GT-315. Associate Technical Editor: L. S. Langston.

[3]Some of the measurements are used to specify the operating condition of the engine. These include inlet pressure and temperature, fan speed, humidity, and the variable geometry position variables. The measurements are not available to the analysis. The remaining measurements are the independent measurements.

Copyright © 1994 by ASME
Downloaded 02 Jun 2010 to 171.66.16.122. Redistribution subject to ASME license or copyright; see http://www.asme.org/terms/Terms_Use.cfm

expected to change with time, such as nozzle area, are excluded from $\mathbf{x}$. Note that $\mathbf{x}$ has dimension "n."

$h(\mathbf{x})$ is the $p \times n$ matrix representing the nonlinear effect of the state variables upon the measurements. With no measurement error, $\mathbf{z} = h(\mathbf{x})$ should be precisely true.[4] In the jet engine condition monitoring example, $h(\mathbf{x})$ is a cycle model.

ν is the vector composed of the random element of measurement error. Measurement bias is to be included in the model.[5]

For the weighted least-squares analysis to succeed, it must be possible to determine the state vector, $\mathbf{x}$, from the available measurements. This requires the dimension of the measurement vector to equal or exceed that of the state vector. Further, it must be possible to choose a subset of $\mathbf{z}$ that yields a unique solution[6] for $\mathbf{x}$. That is, the engine state must be *observable* from the available measurements.

To avoid difficulties associated with nonlinear optimization, the nonlinear model, $h(\mathbf{x})$, is replaced by a linear approximation, $\mathbf{Hx}$. The resulting approximation to Eq. (1) is:

$$\mathbf{z} = \mathbf{Hx} + \nu \tag{2}$$

Several assumptions are made to simplify the mathematics. The measurement error is assumed to be Gaussian, with zero mean. $\mathbf{R}$ is defined to be the covariance matrix of the measurement error:

$$\mathbf{R} = E(\nu\nu^T) \tag{3}$$

where E is the expected value operator. The diagonal elements of $\mathbf{R}$ represent the variances of the measurement errors. The off-diagonal elements represent covariance between measurements. Usually, the off-diagonal elements are assumed to be zero.[7]

The state variables, $\mathbf{x}$, are also assumed to be Gaussian. Without loss of generality, their mean can be taken to be zero.[8] $\mathbf{M}$ is defined to be the covariance matrix for the state vector:

$$\mathbf{M} = E(\mathbf{x}\mathbf{x}^T) \tag{4}$$

Some off-diagonal elements of $\mathbf{M}$ are expected to be nonzero. For example, any mechanism that changes the flow capacity of the fan is almost certain to produce an effect on fan efficiency. However, most off-diagonal elements of $\mathbf{M}$ are assumed to be zero.[9]

The measurement error, ν, is assumed to be statistically independent of the engine state, $\mathbf{x}$:

$$E(\mathbf{x}\nu^T) = 0$$

With these assumptions, the objective of the weighted least-squares analysis is to determine a "best estimate" of the state of the system given a set of measurements, $\mathbf{z}$. The matrices $\mathbf{M}$ and $\mathbf{R}$, with the assumptions above, allow definition of a Bayesian probability model for the system. A probability density function can be defined for the likelihood that the set of measurements, $\mathbf{z}$, originated from an initial state vector, $\mathbf{x}$. The designation for this probability density function is $P(\mathbf{x}|\mathbf{z})$. It can be shown (Gelb, 1974) that $P(\mathbf{x}|\mathbf{z})$ is a decreasing monotonic function of the quadratic form J, where:

$$J = 1/2\{\mathbf{x}^T\mathbf{M}^{-1}\mathbf{x} + (\mathbf{z} - \mathbf{Hx})^T\mathbf{R}^{-1}(\mathbf{z} - \mathbf{Hx})\} \tag{5}$$

Minimizing J with respect to $\mathbf{x}$ will yield the state vector estimate with highest conditional probability. The minimum J is found by requiring that dJ be zero for arbitrary $d\mathbf{x}^T$. Solving this for the optimal solution, $\mathbf{x}_o$, yields:

$$\mathbf{x}_o = (\mathbf{M}^{-1} + \mathbf{H}^T\mathbf{R}^{-1}\mathbf{H})^{-1}\mathbf{H}^T\mathbf{R}^{-1}\mathbf{z} \tag{6}$$

Corresponding to the estimate of the engine state, $\mathbf{x}_o$ is an estimate of the true measurements, $\mathbf{z}_o$. This is computed using Eq. (2):

$$\mathbf{z}_o = \mathbf{Hx}_o$$

This is combined with Eq. (6) to compute the estimated measurement error, ν_o:

$$\nu_o = [\mathbf{I} - \mathbf{H}(\mathbf{M}^{-1} + \mathbf{H}^T\mathbf{R}^{-1}\mathbf{H})^{-1}\mathbf{H}^T\mathbf{R}^{-1}]\mathbf{z} \tag{7}$$

The corresponding solution residual, J_o, is obtained by substituting $\mathbf{x}_o$ into Eq. (5). It can be shown that the expected value for J_o is $p/2$ where p is the number of independent measurements (Bryson and Ho, 1975). The actual value of J_o will vary depending upon the ability of the model to fit the observed data. As J_o increases, it becomes less likely that the assumed statistical model (expressed by the engine model, $\mathbf{H}$, and the covariance matrices, $\mathbf{M}$ and $\mathbf{R}$) is correct for the particular data sample. When J_o is much larger than $p/2$, it is reasonable to assume that at least one of the statistical assumptions is incorrect.

Properties of the Gas Path Algorithm

The weighted least-squares solution is the expected value for the engine state, given the measurement vector. That is:

$$\mathbf{x}_o = E(\mathbf{x}|\mathbf{z})$$

It can be shown that $\mathbf{x}_o$ is both the maximum-likelihood and the minimum-variance estimate for $\mathbf{x}$ (Bryson and Ho, 1975). Thus an estimate that properly accounts for measurement error is superior to any estimate that does not acknowledge its presence.

Equations (6) and (7) define the estimate for the state of the engine and the measurement errors as a function of the three matrices: $\mathbf{H}$, $\mathbf{R}$, and $\mathbf{M}$. These matrices define the effect of state variables on the measurements, the expected magnitude of sensor errors, and the expected variation of state variables, respectively. The matrices are available before taking any data.[10] They are independent of the analysis results. Therefore, the state and measurement error estimates are *linear* functions of the input measurement vector, $\mathbf{z}$.

Consequently, it is possible to predict the response of the weighted least squares algorithm to a specific input. For example, one can input the measurement vector associated with a 1 percent deterioration in the high-pressure turbine efficiency (with no other deviation present). The weighted least-squares solution for this input will, in general, underestimate the change

[4]There are errors in the model. Jet engine cycle models enforce the conservation of mass and energy. The modeling of loss is empirically derived. The models are mainly one dimensional. Multidimensional effects are considered only in special circumstances, and then only approximately. For this and many other reasons, the models themselves are a source of error.

[5]In a practical sense, ν will include, in addition to the random measurement errors, the influence of any state variables not included in the state vector, $\mathbf{x}$, and any random imperfections in the model.

[6]This requirement can be strengthened in practice to require that the matrix, h, be well conditioned. If this is not the case, the errors in the state variables can become unacceptably large.

[7]It is not unreasonable for there to be a nonzero correlation between measurement errors. This could occur with pressure measurements if several were measured against barometer (gage pressure) and then the same barometric pressure were added to all.

[8]This can be achieved by defining $\mathbf{x}$ and $\mathbf{z}$ as deviations from a nominal condition. Thus $\mathbf{z}$ is not the raw measurement value, but is instead the deviation of the measurement from a nominal reference condition, and $\mathbf{x}$ represents the deviation of the state variables from that same nominal point.

[9]There could be some correlation as a result of temporal effects; that is, different engine components tend to deteriorate with time and thus their deviation from nominal is positively correlated. This effect is ignored.

[10]In the classic Kalman filter, the $\mathbf{M}$ matrix is updated after each reading is obtained to reflect the increased certainty of the engine state. This update is entirely predictable, and does not depend on the data that were acquired. Furthermore, the $\mathbf{M}$ matrix approaches a steady-state value as the number of readings gets large, reflecting the reduction in the initial uncertainty of the engine state.

Downloaded 02 Jun 2010 to 171.66.16.122. Redistribution subject to ASME license or copyright; see http://www.asme.org/terms/Terms_Use.cfm

in turbine efficiency.[11] Some of the efficiency change will be attributed to other engine components and to measurement error. This behavior occurs because a solution with small changes to several elements is more probable than a solution with the entire deviation attributed to a single element (the turbine efficiency).

The amount of the underestimate depends on the relative magnitude of the elements of the **M** and **R** matrices. If the element of **M** corresponding to high-pressure turbine efficiency is increased while all other variances are held fixed, the solution will more closely agree with the input. However, as the response to a turbine-efficiency problem is improved, the fidelity of the solution to other problems (e.g., compressor-efficiency deterioration, fuel-flow measurement error) is reduced. Thus, the elements of **M** and **R** define the sensitivity of the algorithm to various problems that occur in an engine.

Since the algorithm is linear in **z**, the solution error is proportional to the measurement deviation. If the turbine-efficiency deviation is doubled, the solution error also will be doubled (the percent error remains fixed). Hence, the weighted least-squares algorithm provides better results when measurement deviations are small. This is unfortunate since the most interesting cases are those for which the performance of the engine is far from nominal. To address this limitation of the weighted least-squares algorithm, TEMPER includes a special feature known as "fault logic." The fault logic is used to search for large deviations in component performance, or for large measurement errors, whenever the solution residual is large.

The solution residual, J_o, provides the mechanism for recognizing that a specific case is far from nominal conditions.

The expected value for this residual is $p/2$, where p represents the number of independent measurements. TEMPER assumes that J_o follows the Chi-Squared distribution.[12] Figure 1 shows the expected value and the 95 percent confidence limit for the residual, based on the assumption that J_o obeys the Chi-Squared distribution. The TEMPER fault logic is invoked whenever the residual exceeds the 95 percent limit.

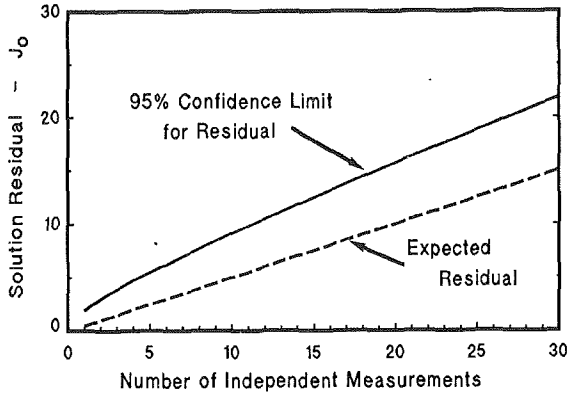


Fig. 1 Weighted least-squares solution residual

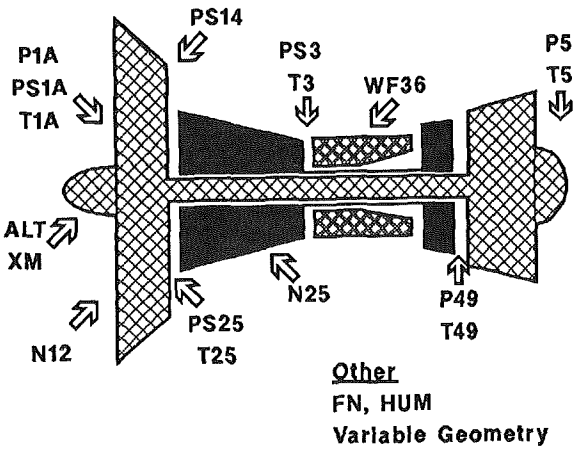


Fig. 2 Typical sensors for gas path analysis

Acceptance Test Gas Path Analysis

After overhaul, a jet engine must pass an acceptance test. The test evaluates the thrust level and EGT[13] margin of the engine, and may verify the engine's fuel economy as well. The sensors available for this run are a combination of built-in instrumentation used during revenue service and special sensors available in the test cell (Fig. 2). Usually, sensors are single-element probes, subject to significant profile error and to normal measurement noise. Therefore, the weighted least-squares algorithm is well suited to the analysis of the test cell data.

The acceptance test consists of a series of discrete readings at a range of power levels. The readings recorded at the highest power levels are compared to performance requirements to evaluate the overhaul. If the engine fails to achieve desired performance, the readings at high power are analyzed to identify the origin of the problem. The data to be analyzed are acquired at a specific instant in time. Consequently, the analysis is a snapshot evaluation of the performance of the engine and its modules.

The original, deterministic algorithms sought the absolute performance of the engine and its modules. They attempted to identify a faulted module by comparing its performance to an absolute standard. There are several difficulties associated with this approach:

Measurement noise distorts the analysis of the performance of the modules.

Measurement bias produces consistent errors in the assessment of modular performance.

Changes to parasitic flows, or other elements not included in the analysis, distort the absolute performance levels for the modules.

The use of an absolute performance standard may lead to unprofitable maintenance by encouraging performance gains that will quickly be lost in service (such as excessively tight clearances in seals and rotating components).

The weighted least-squares approach reduces problems associated with measurement noise, but does not address the other difficulties. These other problems are solved by seeking a relative assessment of performance in place of the absolute analysis. Thus, TEMPER seeks to learn how a deficient engine's modules differ from those of an accepted engine. This is accomplished by comparing data from the specific engine to model derived from similarly overhauled engines. The effect of consistent measurement bias is eliminated by this approach. Unrealistic component improvement goals are also avoided by evaluating performance relative to overhauled engines.

Figure 3 shows a flow chart of the basic Test Cell TEMPER algorithm. The core of the software is an aero-thermodynamic engine cycle model. This cycle model predicts the performance of the engine as a function of environmental variables and engine power level. The model used in TEMPER also accounts for deviation of the variable geometry (e.g., variable stators) from nominal control schedules.

[11] As long as no correlation between state variables or measurement errors is present, the solution response is constrained to lie between 0 and 1. With state variable correlation present, it is possible that the solution will overestimate the deterioration in a particular state variable. It is also possible, with correlation, that the estimate will err in the direction of the change.

[12] Actually, $2J_o$ is assumed to obey the Chi-Squared distribution with p degrees of freedom. We are not aware of a proof for this assertion.

[13] EGT stands for "Exhaust Gas Temperature." It represents a temperature that is measured at the inlet or discharge of the turbine, which is used to assure that the engine hot section is not operated above its metal temperature limit.

Downloaded 02 Jun 2010 to 171.66.16.122. Redistribution subject to ASME license or copyright; see http://www.asme.org/terms/Terms_Use.cfm

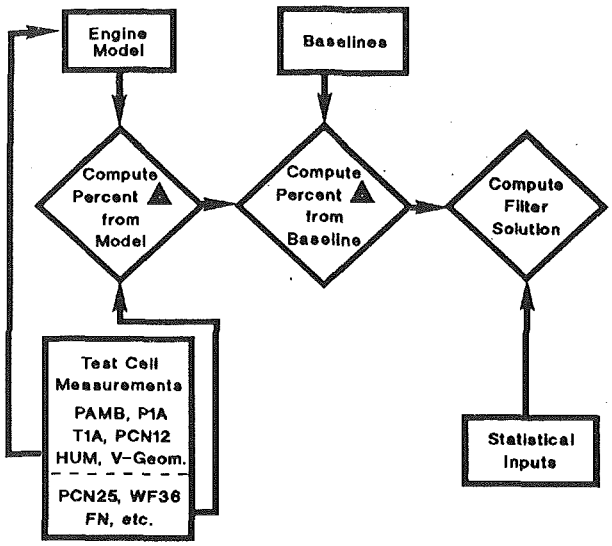


Fig. 3 Basic test cell TEMPER flow chart

Table 1 Typical jet engine measurements for gas path analysis

Parameter	Description	Availability
P1A	Inlet Total Pressure*	Test Cell
PS1A	Inlet Static Pressure (Used for Air Flow)	Test Cell
T1A	Inlet Total Temperature (Also Total Air Temperature)*	Both
ALT	Pressure Altitude*	On Wing
XM	Aircraft Mach Number*	On Wing
HUM	Ambient Humidity (Water to Air Ratio)*	Test Cell
N12	Fan Rotor Speed*	Both
PS14	Fan Discharge Static Pressure (Sometimes Total Pressure)	Both
PS25	High Pressure Compressor Inlet Static Pressure	Both
T25	High Pressure Compressor Inlet Total Temperature	Both
N25	Core Rotor Speed	Both
VSV	Variable Stator Vane Position*	Both
VBV	Variable Bypass Valve Position*	Both
PS3	High Pressure Compressor Discharge Static Pressure	Both
T3	High Pressure Compressor Discharge Total Temperature	Both
WF36	Fuel Flow	Both
TCC	Turbine Clearance Control Position*	Both
P49	High Pressure Turbine Discharge Total Pressure	Both
T49	High Pressure Turbine Discharge Total Temperature	Both
P5	Low Pressure Turbine Discharge Total Pressure	Test Cell
T5	Low Pressure Turbine Discharge Total Temperature	Both
FN	Net Thrust	Test Cell

* Parameters used to specify engine operating condition for engine model

Several of the available measurements are used to specify the operating point of the engine (Table 1). These include inlet pressure and temperature, humidity, fan speed (to specify engine power level), and variable-geometry settings. These measurements are known as "setting parameters." The remaining independent measurements form the basis for the gas-path analysis. The cycle model predicts the independent measurements.

The first step in the analysis is to calculate the difference between the independent measurements and the cycle-deck predictions. These differences may be a result of component performance deterioration, measurement noise or measurement bias. The cycle model represents the performance expected from a new production engine. Therefore, it represents a performance level higher than most overhauled engines. Measurement *base lines*[14] are used to adjust the cycle deck so that it represents the performance exhibited by a typical overhauled engine (including measurement bias). Thus, the next step in the analysis (Fig. 3) is to adjust the measurement-to-cycle-deck differences for the base lines.

After the base-line adjustment is made, the modified measurement-to-cycle-deck differences represent two elements. They are:

module performance differences due to variation in the overhaul process;
measurement noise.

At this point, the weighted least-squares analysis is performed. The analysis estimates the deviation of the performance of the modules from that of an average overhauled engine. It also estimates the magnitude of the measurement noise.

There are several factors that contribute to error in the basic weighted least-squares analysis. The weighted least-squares analysis is likely to underestimate any pure fault (either measurement error or module performance deviation). The remaining deviation is attributed to other measurement errors and module performance changes. The size of the error is proportional to the size of the actual performance fault.

Another source of error is change to system elements not included in the weighted least-squares analysis. For instance, a change in a turbine cooling flow is indistinguishable from a turbine performance fault (affecting both efficiency and flow function). The TEMPER analysis includes consideration of the turbine performance parameters, but does not estimate turbine cooling flow. Any change in turbine cooling flow will be interpreted as if it were a change to the turbine performance parameters.

Measurement error in the setting parameters is not evaluated by the gas-path analysis. These errors will be interpreted as module performance change, or as noise in the independent measurements.

There is no algorithmic way to eliminate these problems. As the number of redundant sensors is increased, the fidelity of the weighted least-squares solution is improved. The addition of new sensors to distinguish between turbine performance and cooling flow would permit estimation of additional system elements. This would reduce the tendency to mislabel deteriorated system elements. Redundant setting-parameter sensors can be used to include setting-parameter errors in the analysis. These improvements call for additional sensors. However, large gains are unlikely due to the penalties associated with the additional sensors.[15]

TEMPER Fault Logic

Although the problems enumerated above cannot be avoided in all instances, there is a strategy to eliminate an important subset of these problems. It is often possible to identify a single cause for a large deviation from normal behavior. For instance, sensors often exhibit sudden large shifts as a result of some failure mechanism.[16] Foreign object damage or some other mechanism may produce a large shift in a single component, with little effect on the others.

When a large shift in a measurement error or module performance occurs, the statistical assumptions of the weighted least squares analysis are violated. Consequently, the solution residual is very large. When this occurs, it is possible to modify the algorithm to seek a single cause for the large residual. In TEMPER, this alternate strategy is employed whenever the solution residual exceeds the 95 percent confidence limit.

[14]This terminology is unfortunate. The term "base line" suggests different meanings to different people. In some cases it is treated as being synonymous with an a priori estimate. In other situations, it is interpreted to be the standard against which performance is to be measured. In this latter case, an engine that is better than the base line has been overhauled to exceed the performance requirement. The confusion leads to misunderstanding of the algorithm results. In some instances, it can even cause incorrect determination of the base lines.

[15]These penalties include cost, weight, reliability, and even performance. While some increase in the number of sensors may be desirable, it is likely that the number needed to eliminate all problems with the weighted least-squares algorithm would not be cost effective.

[16]An example might be a leak in a pressure line.

Downloaded 02 Jun 2010 to 171.66.16.122. Redistribution subject to ASME license or copyright; see http://www.asme.org/terms/Terms_Use.cfm

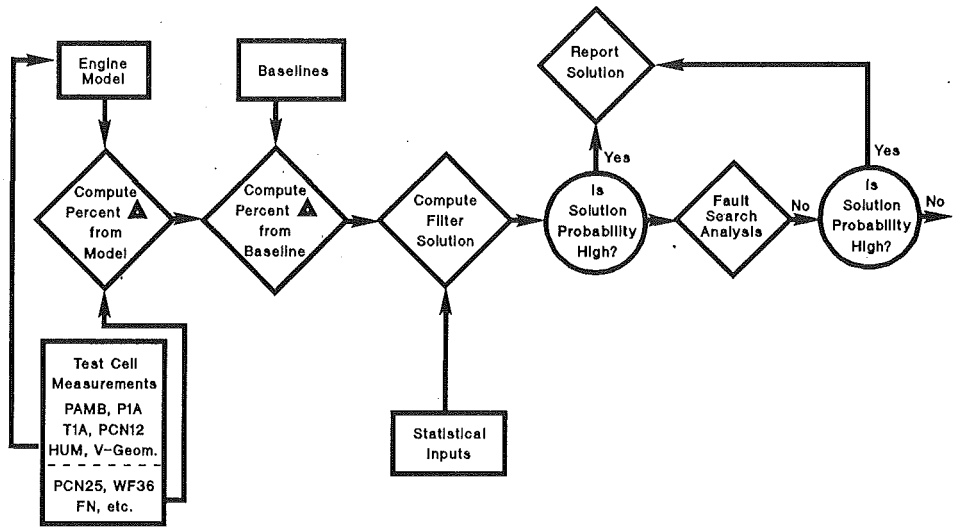


Fig. 4 Test cell TEMPER flow chart including fault logic

When the fault logic is invoked, a special weighted least-squares analysis is performed to evaluate each possible hardware fault or sensor error. When a particular sensor error is to be evaluated, its standard deviation is increased by a factor of 100. If the large residual of the original solution is due to error in that sensor, the new analysis will return a much lower solution residual. If some other mechanism is at fault, the solution residual will remain nearly unchanged.

A similar technique is applied to seek a large shift in a hardware module. A weighted least-squares analysis is performed for each module, with the module's standard deviation increased by a factor of 100. If the performance of the specific module being considered is far from nominal, the solution residual will be returned to the normal range. For hardware modules, it is possible to evaluate a change to efficiency only, to flow capacity only, or a change to both.

The fault search can evaluate system changes not included in the basic gas-path analysis. For instance, a large error in a setting parameter can be detected by adding the setting parameter to a special weighted least-squares analysis[17] (with a large standard deviation). If the setting parameter has a large error, this analysis will produce a much lower solution residual. Similarly, a special analysis can be performed to evaluate the possibility that the large residual resulted from a large shift in one of the cooling flows. Any reasonable mechanism for the residual can be evaluated in this way.

The TEMPER fault search performs a weighted least-squares analysis for each candidate explanation for the large solution residual. Often, one or more of the solutions will yield a residual that is in the normal range. When this occurs, the best solution[18] is presented in place of the no-fault result. In many situations, no single explanation will account for a large solution residual. Nevertheless, this feature allows TEMPER to analyze an important fraction of highly deteriorated engines. These successes are far more critical than those associated with normal engines. Figure 4 shows a modified flow chart for Test Cell TEMPER including the fault search.

[17]Note that the setting-parameter error is evaluated in the same way as a hardware fault. Thus, it is introduced into the analysis in the same way that a state variable would be added, i.e., as an additional element in $\mathbf{x}$. The $\mathbf{H}$ matrix must be augmented to include the effect of the setting-parameter error on the measurement deviations.

[18]Actually, the selection of a best solution is done using a probability derived from the solution residual. This probability accounts for the degrees of freedom that are associated with the solution residual. It adds a bias toward simpler explanations for the observed deviation.

On-Wing Gas Path Analysis

Gas-path measurements are taken regularly during revenue service. Data are acquired at steady-state cruise, either once per flight or at a regular interval (e.g., every four flight hours). The data are analyzed to detect sudden shifts or slope changes that may indicate a problem.

Some airlines purchase expanded instrumentation for their engines to permit analysis of module health based on the cruise data. They hope to use the analysis results to isolate problems identified by trend charts. They also hope to use the data to help define the work scope when the engine is removed for overhaul.

The sensor data are similar to those in the test cell (Table 1) except that inlet static pressure and thrust are not available. The loss of information from these sensors is partly offset by the ability to analyze data obtained at regular intervals over a long period. The time-history element of the data opens the possibility of distinguishing faults based on the timing of their occurrence. Suppose the fuel-flow sensor develops an error and, later, the EGT sensor shifts in the same direction. The knowledge that these events occurred at different times rules out the possibility that they resulted from a common cause. Without this temporal knowledge, it would be tempting to seek a common cause for the two events.

A snapshot analysis does not provide this memory capability. Some mechanism is needed to carry the solution forward from point to point if the fuel flow shift and the later EGT shift are to be recognized as separate events. The classis means of implementing this memory feature is the Kalman Filter (Sorenson, 1985). On-Wing TEMPER, while not using the Kalman filter directly, mimics the approach in many ways. Specifically, smoothed analysis results for module deterioration and sensor error (called "running base lines") provide an a priori estimate for the analysis of new data. Exponential smoothing is used to smooth the module deterioration and sensor error analysis results (Bowerman and O'Connell, 1979). Exponential smoothing gradually substitutes the new results for the old, using the formula:

$$\chi_i = \chi_{i-1} + \alpha(x_i - \chi_{i-1}) \tag{8}$$

where:

χ_i represents the smoothed value at the ith time step.
x_i represents the unsmoothed value of the parameter at the ith time step.
α is the smoothing coefficient (typically $0.02 \leq \alpha \leq 0.2$).

Downloaded 02 Jun 2010 to 171.66.16.122. Redistribution subject to ASME license or copyright; see http://www.asme.org/terms/Terms_Use.cfm

Figure 5 illustrates the result of applying exponential smoothing to a step increase in a parameter.

The only significant way that On-Wing TEMPER is structurally different from Test Cell TEMPER is in the processing of the a priori estimates (Fig. 6). The initial base line for On-Wing TEMPER is derived from the observed performance of newly installed production engines.[19] This fleet-wide base line is used for the initial processing of an engine's data. However, the first ten valid readings for an engine are used to modify the fleet base line for the specific engine.[20] After this specific base line is established for the engine, it is used to reprocess the initial readings. The a priori estimate for each new reading is equal to the running base line from the previous reading.

There is a subtle change in the interpretation of the fault logic in On-Wing TEMPER. In Test Cell TEMPER, the solution residual represents the difference between the reading being analyzed and a fixed reference. In On-Wing TEMPER, the residual is a measure of the deviation of the current reading from the recent past for the engine. A large residual in On-Wing TEMPER is, therefore, an indication of a step change in the data since the last readings. There is a change of emphasis from comparing an engine to a similar class of engines, to comparing an engine to itself. This change increases confidence in the assumptions upon which the fault logic is based.

When the fault logic in On-Wing TEMPER identifies a bias shift or a step change to the performance of one of the modules, an alternate process is used to update the running base lines. If a measurement fault is identified, the base line for that measurement's bias is changed to agree precisely with the result from the fault solution. The exponential smoothing process is not applied to that measurement. All other measurements and module performance parameters are treated in the usual way (with exponential smoothing). Similarly, if the fault logic indicates a step change to the performance of one of the engine modules, exponential smoothing is not used for that module performance parameter. Instead, the full change indicated by the fault logic is applied. This approach is taken to reflect the increased certainty associated with a fault solution. It also avoids the need to apply the fault logic repeatedly until the step change has been fully assimilated by the exponential smoothing.

The fault logic may choose a setting parameter or some hardware fault (e.g., cooling flow) for which there is no running base line. The available base lines are updated when this occurs. The special fault is enunciated but no special base line is created. The underlying assumption is that these faults require special maintenance action on the part of the user.

Several specific problems must be addressed when analyzing data acquired during revenue service. Occasionally, readings do not yield a solution with a small residual. Such readings may indicate that the data were taken under unfavorable conditions, or that there was a temporary problem in the data system. If the high residual can be eliminated through use of the fault logic, then a single cause is identified, and the problem may be considered resolved. However, there are instances where the fault logic fails to give a low residual. When this occurs,

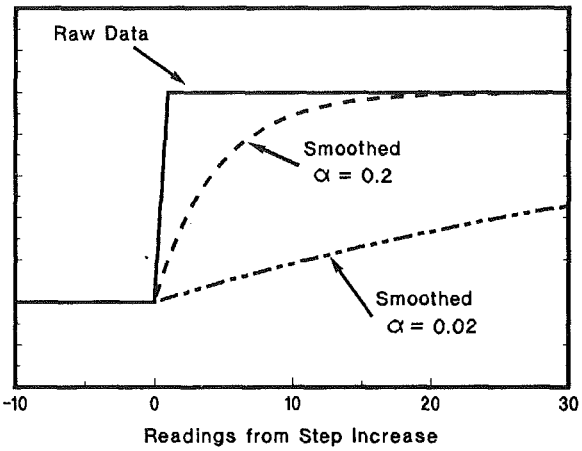


Fig. 5 Exponential smoothing of a step increase in a parameter

On-Wing TEMPER does not update the running base lines. This practice avoids spurious drift associated with data system problems.

Service experience has indicated that additional precautions are needed to avoid running-base-line drift associated with data system problems. Occasionally, a spike in one or more measurements has been seen for a single reading. In some cases, the fault logic found a feasible solution to the tainted reading that reduced the residual to an acceptable level. When the problem was spurious, the following reading had a problem of approximately the same magnitude with opposite sign (because of the running base line shift). Usually, the fault logic identified the same fault and returned to the pre-spike condition. Occasionally, the second analysis identified a fault different from the first. This can occur if the two faults have similar signatures with small differences leading to the choice of one or the other. To avoid this problem, On-Wing TEMPER now requires corroboration of a fault from a second reading before any running base line changes are implemented.

Another situation requiring special attention is maintenance to the engine while it is installed on wing. Sensors might be changed or some repair procedures (such as water washes) can be performed without removal of the engine. When this occurs, it is desirable to ensure that the gas-path analysis properly interpret any performance changes. To meet this requirement, On-Wing TEMPER allows input of maintenance codes to indicate that certain types of maintenance occurred after the last reading. When maintenance codes are supplied, TEMPER performs a reduced fault search, seeking evidence of a performance change in the repaired item. If the residual for a relevant fault solution is substantially lower than for the no-fault case, the fault solution is used.

Sensor failures are common occurrences in regular service. These failures may be recognized by the data system. TEMPER also tests to confirm whether the sensor is within a reasonable range before using it in an analysis. When a sensor is unavailable for a particular reading, its average (base line) value is used. The standard deviation corresponding to that sensor is increased by a large amount (multiplied by 200) to eliminate the influence of that sensor on the solution. On-Wing TEMPER requires that a sufficient complement of sensors be available to perform modular diagnosis. If too many sensors are unavailable, the modular diagnosis is aborted. The requirements for the performance of a fault search are even more stringent.

When a sensor that was inoperative for a time is repaired, On-Wing TEMPER reintroduces it to the analysis gradually. This gradual return is achieved by scaling the measurement's standard deviation for the first few readings after its repair (Fig. 7). The larger standard deviation limits the impact of the

[19]Before revenue service data are available, the On-Wing TEMPER base lines are derived from the flight test for the aircraft. These original base lines often do not adequately represent the performance of engines in service. Often these differences can be traced to the use of different sensors in the flight test. The flight-test engines may not be typical of the performance of later production engines. Thus a sample of newly installed engines is often preferable to the flight-test base lines.

[20]The fleet base line is expressed in terms of deviations from the engine-cycle model for the independent measurements. The so-called "running baselines" are expressed as smoothed averages for the module performance and sensor-error results. Thus, the running base lines are applied after the fleet base lines have first been applied. The running base lines are, therefore, a smoothed estimate of the deviation of the engine's performance from a new production engine.

Downloaded 02 Jun 2010 to 171.66.16.122. Redistribution subject to ASME license or copyright; see http://www.asme.org/terms/Terms_Use.cfm

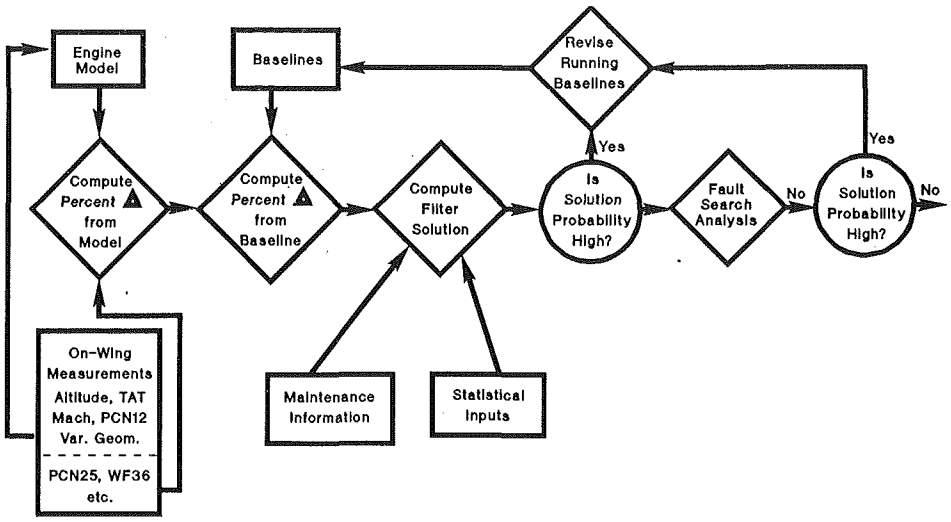


Fig. 6 On-wing TEMPER flow chart

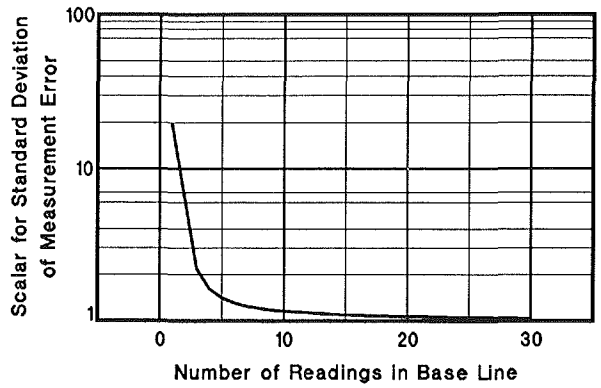


Fig. 7 Scaler applied to measurement standard/deviations

sensor on the analysis, and causes its bias to be chosen consistent with the current assessment of engine performance. The scaler is based on the Student t-distribution[21] (Burington and May, 1953).

Suggestions for Improvement

TEMPER and other comparable algorithms for gas-path analysis represent a clear improvement over the previous, deterministic approaches. Nevertheless, there are still significant problems associated with gas-path analysis of jet engines. To understand these problems, it is important to recognize that the success of the algorithm for engines that meet their performance requirements is of little interest. It is only when an engine fails to achieve its performance requirements that users look to gas-path analysis for help. In this latter case, they hope to obtain a clear indication of the repairs needed to restore the engine to acceptable performance levels.

Often, TEMPER successfully identifies the problem(s). There are a number of success stories where the TEMPER analysis identified a faulted module that either had not been repaired or had been repaired improperly. There have been On-Wing Temper analyses that detected a performance shift and successfully isolated the source of the problem. Unfortunately, there are also several examples where the gas-path analysis result has been incorrect, leading to expensive and fruitless repairs. One frequently encountered example is where TEMPER identifies a module just repaired as deficient. Only rarely does this result prove to be correct.

Some of the problem can be attributed to the difficulty of interpreting the TEMPER results (Doel, 1991). The information is presented in terms that are more familiar to the gas-turbine-engine performance engineer than to the mechanic. The analysis includes assumptions (such as the constancy of cooling and leakage flows) that are not apparent to the mechanic. Overhaul decisions can be guided by information not included in the gas-path analysis (e.g., module age, repair history, borescope results). In these circumstances, the correct solution may not be discovered until the proper experts examine the data.

There are also circumstances where no amount of review can uncover the difficulty. Sometimes, the measurements point to problems that clearly are not present. Some engines defy all analysis, even detailed tear-down inspections of the individual modules. Sometimes the only solution seems to be to scatter the modules to other engines to eliminate the "curse."

Two experimental improvements have been developed for Test Cell TEMPER. Both are still in the evaluation stage. The first allows simultaneous analysis of the two readings[22] normally acquired in the acceptance run. This strategy assumes that the module performance deviations (efficiency and flow capacity) are identical for both power settings. The measurement errors are allowed to differ for the two readings. Several authors have suggested that the simultaneous analysis of multiple readings increases the information available to the analysis (e.g., Stamatis et al., 1989). However, it is likely that the efficiency and flow capacity also change with significant changes to operating condition. The take-off and maximum-continuous operating conditions are close aerodynamically. Hence these changes should be small. The generation of a single result will eliminate inconsistencies between the two readings. It also should improve the analysis of highly deteriorated engines when the fault logic is invoked.

The second experimental change allows use of a deterioration model to improve the a priori estimates. The expected variation

[21]The scale factor represents the effective increase in the standard deviation of the t-distribution based on the small number of samples from which it is derived. The scale factor is equal to the ratio of the 95 percent confidence range for the given number of degrees of freedom (number of samples minus one) to the corresponding range for the normal distribution (infinite degrees of freedom). The value of 20 for the first reading was chosen arbitrarily (there is no value corresponding to zero degrees of freedom).

[22]These readings correspond to the take-off and maximum-continuous power settings. Maximum-continuous thrust is typically about 10 percent below take-off.

Downloaded 02 Jun 2010 to 171.66.16.122. Redistribution subject to ASME license or copyright; see http://www.asme.org/terms/Terms_Use.cfm

of efficiency and flow capacity versus module age[23] is specified in the input. This information is used to alter the predicted values for the independent measurements so the deviations to be analyzed should be smaller. The associated standard deviations are also allowed to vary with age, to reflect the increased uncertainty in the performance of older modules. The use of a deterioration model requires generation of new base lines (that represent the performance of zero-age modules). The basic statistical inputs should also be tightened, since the scatter due to module age should now be smaller.

Both improvements are in "Beta Test." The simultaneous two-point analysis is almost certain to improve the ability to interpret test-cell data. The introduction of a deterioration model is less sure to help because of the large amount of additional information which needs to be identified. Neither improvement is likely to be revolutionary.

One possible way of improving the results would be to take advantage of the digital electronic controls on newer gas turbine engines. These controls offer doubly or triply redundant sensors in place of the single probes of earlier engines. The key to achieving the potential associated with the new controls would be to provide the *individual* sensor values to the gas-path analysis. Having the individual measurements available would increase the amount of redundant information. This should permit choosing statistical inputs that would lessen the tendency to underestimate hardware degradation. Unfortunately, the current practice is to combine the sensor values in the control. Only the average[24] is provided to the ground software.

Another possible vehicle for improvement would be to emphasize the decisions to be made, rather than focusing on the determination of the gas path state (Doel, 1991). This change of emphasis should encourage the algorithm designers to express results in terms the mechanic understands. It also should encourage optimization of the maintenance decisions, instead of module-performance determination. Finally, an emphasis on decisions would encourage consideration of all the information (the gas-path data is only a part) that is relevant to the problem.

There are emerging technologies that could foster improvements to gas-path analysis. Expert-systems techniques offer the possibility of integrating qualitative and quantitative elements of the maintenance decision process (Doel, 1990). Developments in fuzzy logic could offer useful methods to express the uncertainty of the gas-path analysis so that the user receives the appropriate message. Neural networks might offer an alternative to model-based algorithms for fault identification.

It is important to pursue these improvements. With the new engine designs employing features such as counterrotating and variable-area turbines or "unducted fans," improvements may be needed even to retain the status quo.

Summary

Jet-engine gas-path analysis is used to interpret data acquired from overhaul acceptance tests and from aircraft during routine service. The goal is to isolate performance deficiencies to the faulted modules so that repair can be successfully accomplished. The analysis results are of little interest unless performance is deficient. When this occurs, gas-path analysis results can generate important savings for the user, if they are correct.

Achieving correct diagnosis is difficult, because of the limited instrumentation. Most sensors are single-element probes that do not adequately sample the gas stream. To be effective, a gas-path analysis algorithm must consider sensor error. Modern algorithms use weighted least-squares or a similar approach to simultaneously estimate module state and sensor error. These algorithms are a clear improvement over earlier approaches, but their reliability still falls short of user requirements.

Some improvement could be realized if the results were more clearly communicated to the users. Often, inappropriate maintenance is initiated because the mechanic misinterprets the results of the algorithm. If other information such as maintenance history and borescope inspection results were integrated with the gas-path analysis results, better recommendations would be likely. The use of emerging technologies such as expert systems, fuzzy logic, and neural networks might generate further gains.

[23]Age is normally expressed as either flight hours or cycles, but more sophisticated indices are permitted.

[24]This situation is more unfortunate than suggested. The value provided to the ground software may be an average of the two or three available probes, or it may be the result of a single probe. The software in the control compares the individual values to each other and to an engine model. The output given to the ground software depends on the outcome of this comparison. In the extreme, it is possible the ground software will receive only the output of the on-board engine model.

References

Bowerman, B. L., and O'Connell, R. T., 1979, *Time Series and Forecasting*, Duxbury Press.

Bryson, A. E., Jr., and Ho, Y. C., 1975, *Applied Optimal Control*, Hemisphere Publishing Corporation, Washington, DC.

Burington, R. S., and May, D. C., 1953, *Handbook of Probability and Statistics With Tables*, Handbook Publishers.

Doel, D. L., 1990, "The Role for Expert Systems in Commercial Gas Turbine Engine Monitoring," ASME Paper No. 90-GT-374.

Doel, D. L., 1991, "A Philosophy for Integrated Monitoring System Design," *Proceedings of the Sixteenth International Symposium on Aircraft Integrated Monitoring Systems*, University of the Armed Forces, Munich, Germany, Sept. 18.

Gelb, A., ed., 1974, *Applied Optimal Estimation*, The M.I.T. Press, Cambridge, MA.

Sorenson, H. W., ed., 1985, *Kalman Filtering: Theory and Application*, IEEE Press, NY.

Stamatis, A., Mathioudakis, K., Berios, G., and Papailiou, K., 1989, "Jet Engine Fault Detection With Differential Gas Path Analysis at Discrete Operating Points," *Proceedings of the Ninth International Symposium on Air Breathing Engines (ISABE)*, Athens, Greece, Sept.

Urban, L. A., 1980, "Gas Path Analysis—A Tool for Engine Condition Monitoring," presented at the 33rd Annual International Air Safety Seminar, Christchurch, New Zealand, Sept. 15–18.

Volponi, A. J., 1982, "Gas Path Analysis—An Approach to Engine Diagnostics," presented at the 35th Symposium of the Mechanical Failures Prevention Group, Gaithersburg, MD, Apr. 20–22.

Downloaded 02 Jun 2010 to 171.66.16.122. Redistribution subject to ASME license or copyright; see http://www.asme.org/terms/Terms_Use.cfm

Integration of Turbo-Expander and Turbo-Ramjet Engines in Hypersonic Vehicles

B. Zellner

W. Sterr

O. Herrmann

DASA-MBB,
Munich, Federal Republic of Germany

Turbo-expander-ramjet and turbo-ramjet are two engine concepts considered for hypersonic aircraft designs with a flight regime between Mach 0 and 7. To establish any performance or integration aspects for these two combined-cycle engine types, an extended study of a variety of influence parameters is necessary, because the interaction between aircraft and propulsion system is even stronger than on conventional aircraft. In fact, the propulsion system is very sensitive to intake and nozzle/afterbody design at these high speeds. This paper presents the engine configurations chosen for comparison and describes the computer program used for the propulsion system performance simulation, including all relevant integration aspects. Furthermore, some results of propulsion system performance for a generic hypersonic aircraft and a typical ascent profile will be compared to indicate the special characteristics of the engines. Finally, some thoughts concerning the suitability and relevant technological requirements of the two engine types—seen from an aircraft manufacturer's view—are included. The paper includes the results of two diploma theses, written by W. Sterr [1] and B. Zellner [2] at the Technical University of Munich, supervised by Prof. H. Rick (LFA) and O. Herrmann (MBB).

1 Introduction

High Mach number aircraft considered for commercial transport aircraft, as well as for the first stages of two stage to orbit space transport systems, have been studied extensively in recent times. The aircraft types our studies are based on may be characterized by a maximum required Mach number of 5 to 7 and by the need of an extended range cruise capability to be achieved by ramjet engines with subsonic combustion. These aircraft types are described in detail in the literature [3, 4].

In addition to ramjet engines for the high-speed regime, accelerators are required to reach the minimum speed from which ramjets can operate efficiently. Subsonic cruise segments for flying over populated regions should not be excluded from our simulation. Our study—concentrated on air-breathing engines with turbomachinery—led mainly to two candidates, i.e., dual-mode turbo-ramjet and turbo-expander. Since the accelerator engines are *not* in use most of the mission, weight and dimensions are considered to be even more important than minimized fuel consumption.

The accelerator engines have to be designed to meet critical requirements given by the flight trajectory, especially for the ascent part, by the mission constraints and integration aspects. Figure 1 represents a typical ascent trajectory chosen as a basis for this study. The trajectory is influenced mostly by the needs

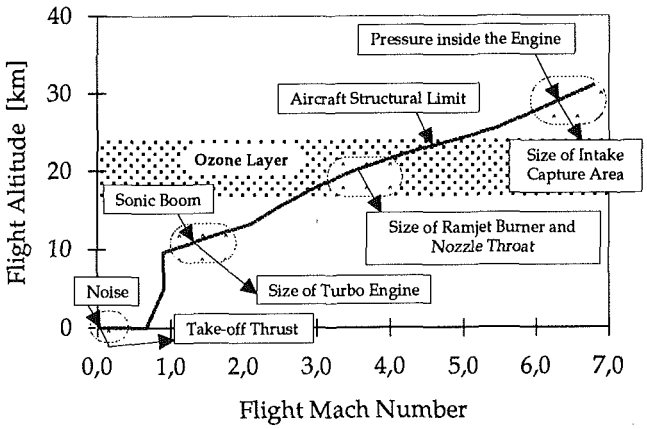


Fig. 1 Ascent trajectory showing critical parameters

and limitations of the aircraft itself and only marginally by the engine characteristics. For example, an acceptable altitude for passing to supersonic flight has to be chosen for sonic boom reasons and a constant dynamic pressure region is required by the structural limitations of the aircraft. In the hypersonic regime, a segment is defined by the maximum allowable pressure inside the intake and the ramjet engines. On the other hand, the trajectory and required thrust at critical points define the design and the size of the engines.

Four critical regions were found:

- The take-off condition, where a minimum static thrust at acceptable noise levels has to be reached.

Contributed by the International Gas Turbine Institute and presented at the 37th International Gas Turbine and Aeroengine Congress and Exposition, Cologne, Germany, June 1-4, 1992. Manuscript received by the International Gas Turbine Institute February 21, 1992. Paper No. 92-GT-204. Associate Technical Editor: L. S. Langston.

Copyright © 1994 by ASME
Downloaded 02 Jun 2010 to 171.66.16.122. Redistribution subject to ASME license or copyright; see http://www.asme.org/terms/Terms_Use.cfm

- The low supersonic regime, where aircraft and installation drag rise to a high level, but engine thrust is still low at low dynamic pressures. The resulting small value of thrust minus drag is the design criterion for the size of the turbo engines.
- The third is the transition from turbo to ramjet operation at low hypersonic speeds. Here the thrust of the turbo engine decreases as temperature is limited within the engines while ramjet thrust is still low since burner and nozzle throat areas limit the mass flow capability of the propulsion system.
- The fourth condition is close to the maximum flight Mach number, where the required thrust for acceleration or cruise defines the size of the intake capture area.

On this basis, the use of a fixed ascent trajectory and a constant minimum design thrust at 10 km altitude and M = 1.2 was thought to be adequate for the comparison of turbo-expander and turbo-ramjet engines.

2 Propulsion Systems for Hypersonic Aircraft

Propulsion systems for hypersonic "cruise" aircraft need an acceptable specific impulse for the total acceleration phase between take-off and maximum Mach number. For the cruise phase itself, the specific range of the aircraft must be optimized.

Figure 2 shows typical values of specific impulse for the three basic engine types: turbojets, ramjets, and rockets including variants, such as turbo-expander engines and supersonic burning ramjets. No single concept, except the rocket engine with its very low specific impulse, can cover the whole Mach number range; therefore a combination of two or even three engine types becomes necessary. In this study a ramjet engine, which is not discussed within this paper, is combined with two different turbo engines.

The first type is a conventional turbojet or turbofan engine with extremely low bypass ratio ("leaky" turbojet) with afterburner, capable of reaching a maximum Mach number of at least 3.5

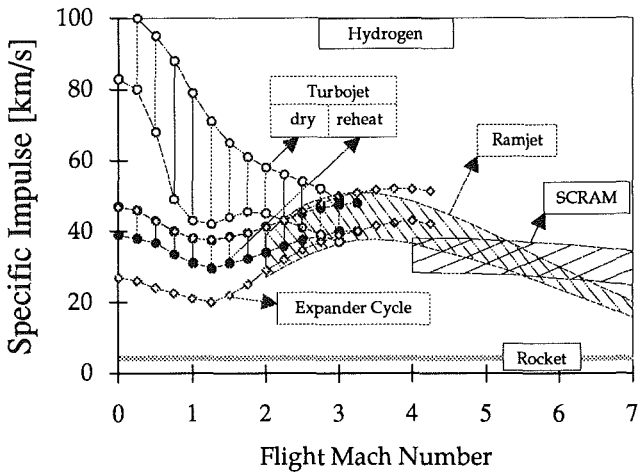


Fig. 2 Fundamental propulsion concepts and their combinations

The second type is an expander-type turbo engine, where the air-breathing compressor is driven by a turbine powered with hydrogen fuel, which is heated in a heat exchanger. This engine is also equipped with an afterburning device.

Characteristics of both engine types are included in Fig. 2. The turbo engine is shown in its two operation modes, i.e., with and without afterburning (dry). For the expander type engine only the reheated mode is feasible. This engine may be operable to even higher transition Mach numbers (M > 4) than the turbojet type.

In principle there are two different ways of combining turbo and ramjet engines. The first is coaxial, where the ramjet airflow is led through an annular duct, wrapped around the turbo part, to a common afterburner/ramjet burner (tandem concept) or into a wrapped-around ramjet burner (wrapped-around concept). The other way of combining is the parallel concept: The airflow is parted either in the supersonic or subsonic part of the air intake, often designated as an over-and-under or side-by-side arrangement. Various concepts of this second kind are investigated in [3].

Figure 3(*b*) depicts the arrangement, chosen for the study of turbo and turbo-expander engines. It offers the possibility to run turbo and ramjet engines simultaneously. From previous studies this feature was found to be advantageous, reducing spillage and nozzle/afterbody drag. In addition, simultaneous operation of the ramjet supports the turbo thrust in the critical low supersonic and transition regimes, enabling the reduction of turbo engine size and weight.

The installation chosen for the engines is the belly type configuration, as shown in Fig. 3(*b*). The forebody is used for precompression of the airflow and the aircraft tail represents a single expansion ramp for the nozzle exhaust [5, 6].

One of the other possibilities is shown in Fig. 3(*a*) with the engines arranged above and below the aircraft's wings. In both cases the maximum diameter of the turbo engine is one of the important parameters. It defines the number of engines to be arranged below the fuselage (for the belly type) but also determines the drag of the turbo parts during hypersonic flight (for the wing arrangement).

3 Computerized Synthesis of an Integrated Propulsion System

3.1 Integration of the Turbo Part Into the Total System. The aerodynamic integration of engines into a total propulsion system is of extreme importance for hypersonic aircraft. Mass flow handling, installation effects, wave and friction drag have more influence on engine performance and fuel consumption than in conventional aircraft. Thrust and drag components have to be precisely balanced, especially at high speeds where the resulting net thrust is only a small difference between large absolute values.

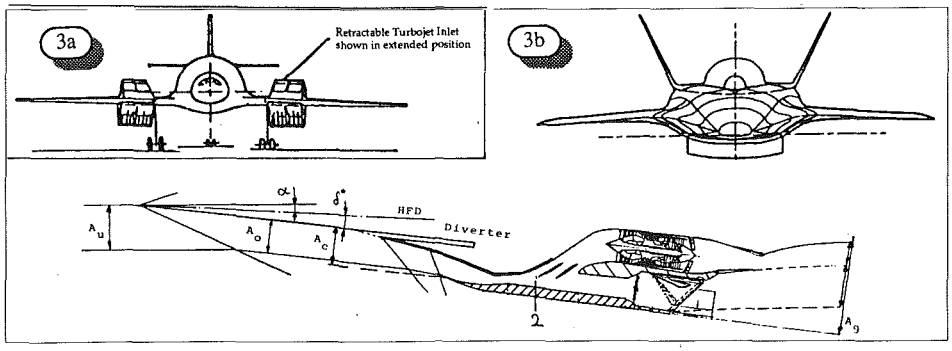


Fig. 3 Configurations of combined-cycle propulsion systems

Downloaded 02 Jun 2010 to 171.66.16.122. Redistribution subject to ASME license or copyright; see http://www.asme.org/terms/Terms_Use.cfm

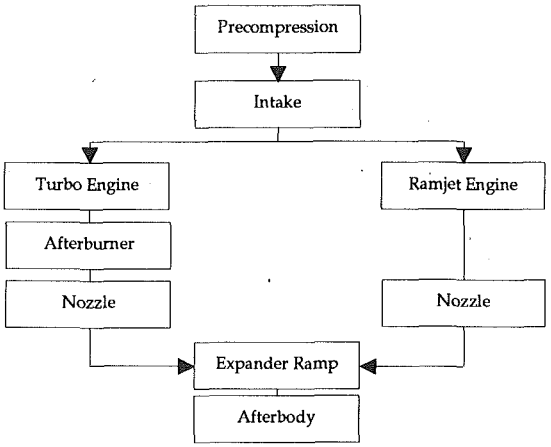


Fig. 4 Integration of the turbo part into the total propulsion system

A schematic view of this integration is shown in Fig. 4. Performance of the propulsion system is so sensitive to intake and nozzle/afterbody influences that bench tests of the engine would not sufficiently reproduce the whole propulsion system performance. Major attention must therefore be given to a theoretical simulation program of the whole system right from the beginning.

Since it would be totally insufficient to compare the uninstalled performance of the two engine types, they have been compared installed by including their specific installation aspects (real intake and pressure recovery, etc.).

3.2 Description of the Synthesis Program. For the computer simulation of the hypersonic engine, we used a modular synthesis program, comprising several subroutines for the relevant engine components.

The program starts with a turbo engine design part. The engine is configured by setting all design parameters, e.g., altitude, Mach number, engine mass flow, technological requirements, and geometry.

Off-design points of turbo engine and ramjets are computed by subroutines of the synthesis program. Both the turbo and ramjet engine program contain a chemical analysis program designed by Gordon McBride [7], which also includes real gas effects at high temperatures for calculating afterburner, ramjet, and nozzle processes.

The above-mentioned engine programs are linked to other subroutines, which take into account all additional effects, such as precompression, characteristics of variable intake, different intake operation modes—diverter open/closed, with/without bypass, with/without spillage or bleed—thrust nozzle characteristics, and afterbody drag. For this study, precompression and inlet characteristics given by Morris and Brewer [3] were used.

Figure 5 shows the flow chart for the synthesis program. There are three possible operation modes:

(*a*) separate turbo engine operation mode
(*b*) simultaneous operation of turbo and ramjet engine
(*c*) separate ramjet engine operation mode

After input of various data—turbo and ramjet data, intake data, nozzle data, atmosphere data—and selection of the desired operation point and mode, the gas dynamic condition in front of the engine entry plane within the intake (plane 2, see Fig. 3) is determined by calculation of the precompression and the flow in the intake. Afterward the engine program is selected, depending on the operation mode.

During this computation, numerous internal checks are carried out to see whether the engine itself and each component of the total propulsion system stay within their physical limits

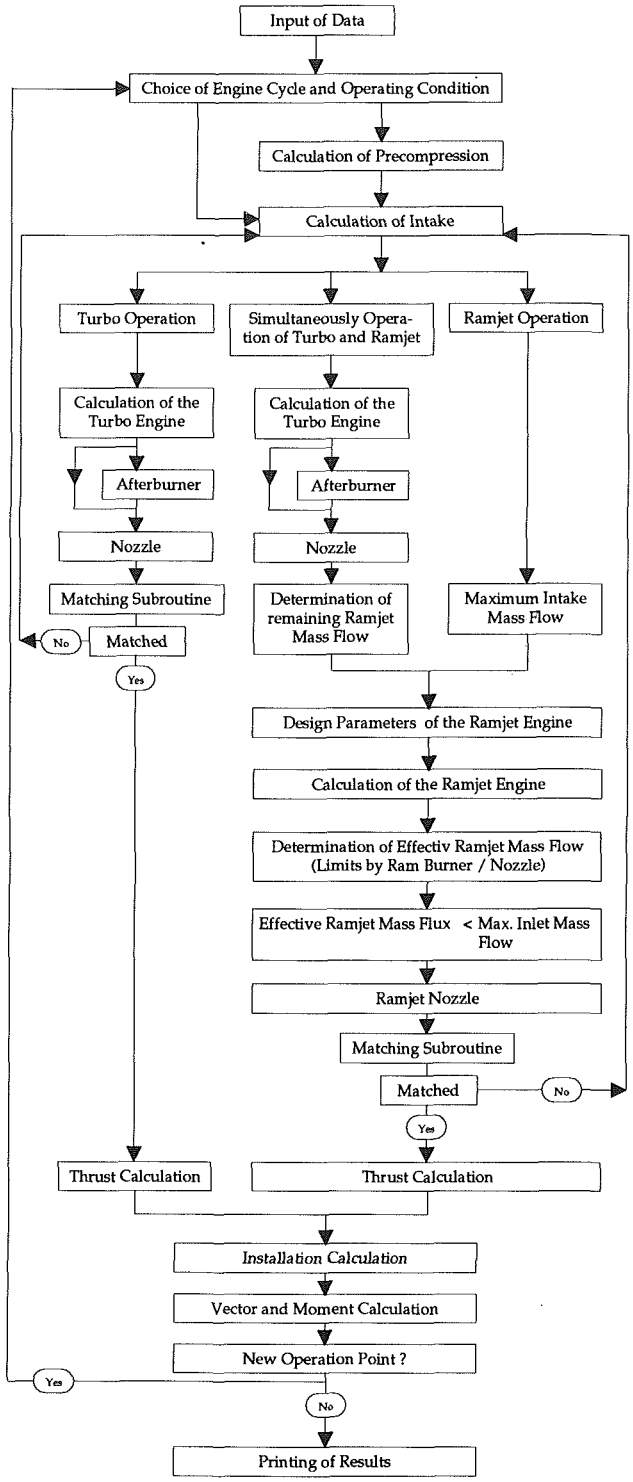


Fig. 5 Flow chart of the synthesis program

like maximum nozzle throat area or maximum Mach number within the ramduct.

If, for example, the maximum air flow supplied from the intake cannot be fully ingested by the engine or by a limited nozzle throat area, the remaining flow will have to be bypassed or will cause spillage in front of the intake, resulting in additional drag.

The synthesis program computes other operating points in additional loops, before all relevant data of the examined operation mode are finally listed.

3.3 Some Examples for Considered Installation Effects.

Downloaded 02 Jun 2010 to 171.66.16.122. Redistribution subject to ASME license or copyright; see http://www.asme.org/terms/Terms_Use.cfm

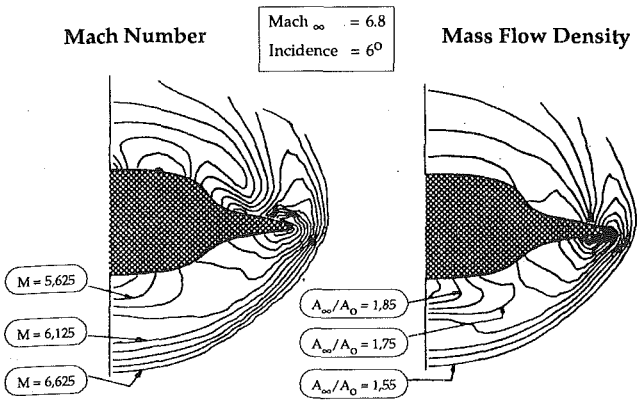


Fig. 6 Mach number and mass flow density at intake entry plane

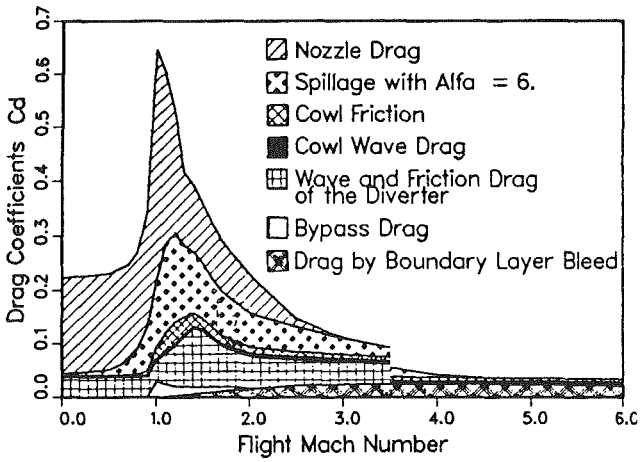


Fig. 7 Drag coefficients of intake and nozzle as a function of flight Mach number

Very important for the integrated propulsion system is the above-mentioned precompression, which is a function of forebody design, strongly increasing with incidence and Mach number. This effect results from the shock system at the forebody, which compresses the air flow in front of the intake. In the high Mach number regime the thrust is mainly defined by the mass flow through the intake capture area, so that ramjet thrust increases nearly proportional to the amount of precompression.

Figure 6 presents the results of an Euler calculation (method Dr. Eberle, MBB—EUFLEX) with isolines of Mach number and mass flow density factors (A_∞/A_0) and the contour of the capture area as indicated [5, 8]. The Mach numbers at the intake entry plane are lowered and the mass flow density is increased significantly compared to the free stream of the air. At high Mach numbers in turbo operation (M $\geq$ 3) this effect also reduces the mismatch between intake mass flow capacity and turbo engine demand.

Figure 7 presents drag coefficients according to Morris and Brewer [3] and shows how the single drag components contribute to the total drag. At Mach numbers below three (M $\leq$ 3) the nozzle drag (since the nozzle design point is near the maximum flight Mach number), the spillage drag (since the engine can ingest only a part of the intake flow), and the wave and friction drag of the diverter are the main parts of the drag coefficients. The installation drag coefficients show their maximum at transonic and low supersonic speeds.

4 Turbojet Engine

4.1 Turbo Engine in Over-and-Under Configuration. The synthesized turbojet in the over-and-under configuration, described above in Section 2, is a two-shaft engine with a very low bypass ratio for cooling purposes, an afterburner, and a convergent–divergent nozzle. The characterizing parameters of the engine, illustrated in Fig. 8, do not show extremely demanding technological requirements. The design point of the turbo engine in this configuration for a hypersonic vehicle was set at a Mach number of 1.2 at an altitude of 10 km, where thrust minus drag reaches a minimum. At that point, the bypass ratio is about $\mu = 0.15$, but it varies up to $\mu = 0.32$ with higher flight Mach numbers. The total pressure ratio decreases from $\pi \approx 12$ in the design point to $\pi \leq 2$ near the maximum Mach number of the turbo engine (M $\approx$ 3.5), limited by temperature at the compressor exit ($T_{max} = 1000$ K).

Engine Characteristics			Turbojet
Design point	(DP)	M = 1.2 , Altitude =10 km	
Net thrust	(DP)	F_n	210 kN
Max. dry thrust (sea level, static, uninstalled)		F_n	220 kN
Bypass ratio	(DP)	μ	0,15
Pressure ratio: Fan	(DP)	π_{Fan}	4 (3-stage)
Total	(DP)	π_{total}	12 (9-stage)
Max. compressor exit temperature		T_{s8}	1000 K
Max. turbine inlet temperature		T_{s4} (SOT)	1800 K
High pressure turbine		-	1-stage
Low pressure turbine		-	1-stage
Fan diameter		$\varnothing_{Fan}$	1,60 m
Transition Mach number		-	3.3 - 3.8
Geometrical capture area per engine		A_C	4 m² [1]

[1] At turbo operation $A_c = 3.15$ m² would be enough to receive a net thrust of 210 kN (DP), but with regard to a simultaneous operation of turbojet and ramjet A_c was set to 4 m² (increase of ramjet thrust!).

Fig. 8 Design parameters of the turbo and the turbo-expander engine

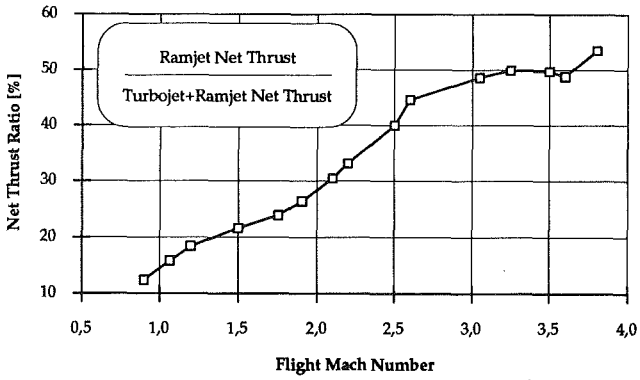


Fig. 9 Net thrust ratio between turbojet and ramjet in simultaneous mode

The stochiometric level of the afterburner and the relevant nozzle throat area are controlled for maximum thrust during the supersonic acceleration phase. During subsonic climb, acceleration, and cruise phases, dry operation is advantageous due to the extremely high specific impulse and will be indispensable at low flight levels for noise limitations.

4.2 Some Aspects of Simultaneous Engine Operation. Since the size of intake capture area results from ramjet characteristics close to the maximum flight Mach number, the intake mass flow capacity during turbo operation can be matched better by simultaneous operation of turbo and ramjet engines. The simultaneous operation of the ramjet not only supports total thrust, but reduces spillage drag and afterbody drag especially in the low supersonic range and therefore permits the reduction of turbo engine size.

Figure 9 presents the ratio between ramjet net thrust and total net thrust of a simultaneous turbo and ramjet calculation

Downloaded 02 Jun 2010 to 171.66.16.122. Redistribution subject to ASME license or copyright; see http://www.asme.org/terms/Terms_Use.cfm

(ascent trajectory, see Fig. 1). Here the ramjet is already working from flight Mach number M ≥ 0.9. Compared to a turbo engine in separate mode, the turbo engine in this simultaneous mode is about 13 percent smaller in fan diameter for the same total thrust. The ramjet net thrust-part at Mach 1.2 (design point of the turbo engine) is about 19 percent, and increases to more than 50 percent at the transition point (M ≈ 3.5).

One additional advantage of the simultaneous mode is the possibility to reach higher Mach numbers with almost conventional turbo engines, since thrust reduction by throttling down the turbo engine at high Mach numbers is compensated for by ramjet thrust. The higher the transition Mach number, the smaller the necessary dimensions of the ramjet burner and maximum nozzle throat area can be. Another advantage of the simultaneous mode may result from the continuous transition to the separate ramjet mode.

4.3 Performance Calculation. Figure 10 shows thrust and drag of a turbo-ramjet engine, calculated along the above-mentioned flight trajectory (see Fig. 1) including a cruise phase at Mach 4.5.

From take-off to Mach 0.9, the engine works without afterburner, between Mach 0.95 and 3.5 in simultaneous mode, ramjet and turbojet (max reheat), and at higher Mach numbers (transition Mach number 3.5) only in ramjet operation. The boundary layer is diverted from the intake during turbo operation, but not during separate ramjet operation. This causes a step in thrust at Mach 3.5 mainly due to reduced pressure recovery and mass flow.

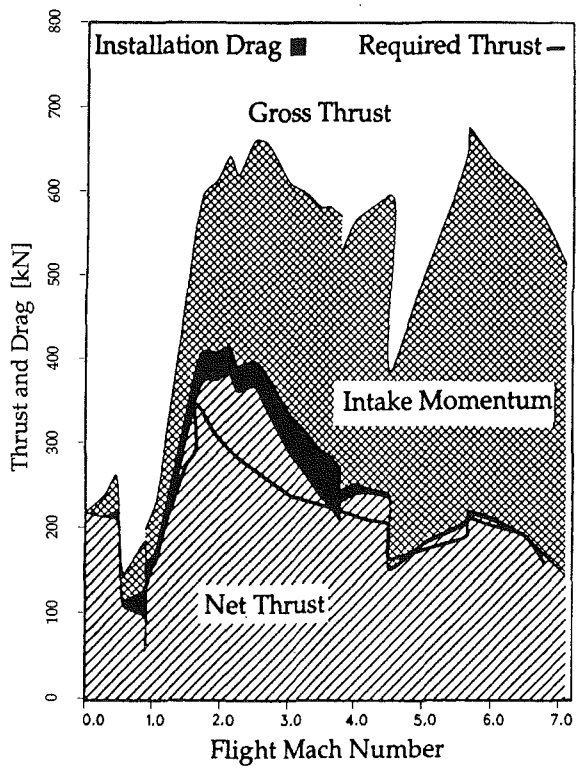


Fig. 10 Performance calculation of a turbo-ramjet cycle on a typical ascent profile

The behavior of gross thrust, intake momentum, installation losses, and the resulting net thrust is shown in Fig. 10. With increasing Mach number the ratio between gross and net thrust rises considerably.

5 Turbo-Expander Engine

5.1 Turbo-Expander-Cycle Engine History and the Chosen Configuration. From 1956–1958 an expander-cycle-engine (Model 304) was developed by Pratt & Whitney [9] for a high-altitude aircraft, the Lockheed CL 400 (flight Mach number 2.5, altitude 33 km, range 4000 km).

The main development efforts were:

- safe operation at high altitudes
- high thrust/weight ratios
- low specific fuel consumption

Liquid hydrogen was used as fuel, typical for this type of engine, as will be shown later. Figure 11 shows the schematic of this engine (Pratt & Whitney 304 "Suntan"). In this engine, heated hydrogen alone was used in the turbine to drive the compressor. The turbine had 18 stages with low diameter and very high peripheral speed, driving the fan through a reduction gear.

The hydrogen gas flow to the turbine is heated in a heat exchanger, located behind the primary burner, where a part of the hydrogen exhausting from the turbine is burned with the air flow exiting the compressor. In the afterburner, the flow is reheated by injecting and burning the remaining hydrogen.

Figure 11 compares the configuration chosen for this study with the Pratt & Whitney 304 "Suntan" engine. As can be seen, both engines have the same components and configuration. For our performance calculations the design parameters of the engine components were changed with respect to the boundary condition, described in the first paragraph of this section.

5.2 Design Criteria for Turbo-Expander Engines and Differences to Turbojet Engines. The main difference between a turbojet and a turbo-expander engine is the powering of the turbine to drive the fan. In a conventional turbojet engine nearly the whole compressor flow and fuel flow is used to drive the compressor. In a turbo-expander engine the turbine flow is the fuel mass flow. So the hydrogen flow provides the energy to compress the air flow, which is about 30 times higher in mass.

Figure 12 shows the relationship between total pressure ratio and isentropic specific enthalpy for air–kerosene exhaust (fuel–

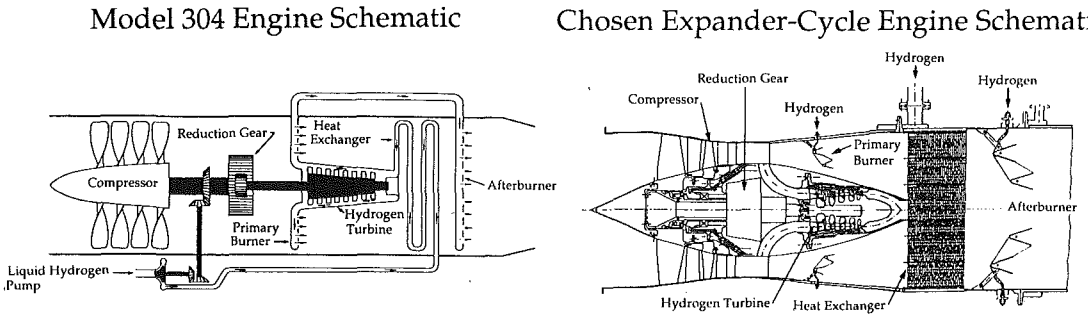


Fig. 11 Schematic diagram of both a historical and a simulated configuration

Downloaded 02 Jun 2010 to 171.66.16.122. Redistribution subject to ASME license or copyright; see http://www.asme.org/terms/Terms_Use.cfm

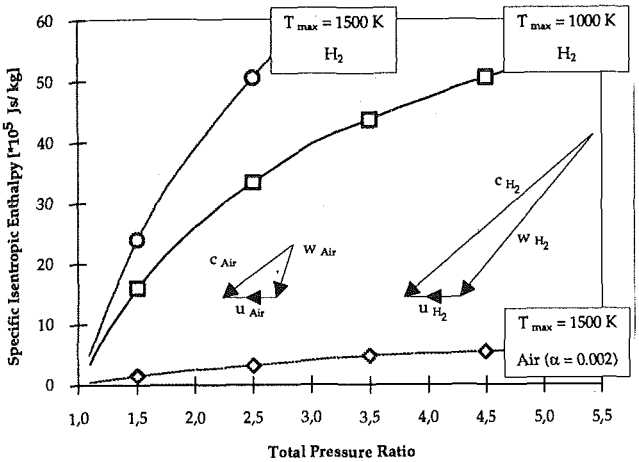


Fig. 12 Relation between pressure ratio and isentropic specific enthalpy for air-exhaust and H_2

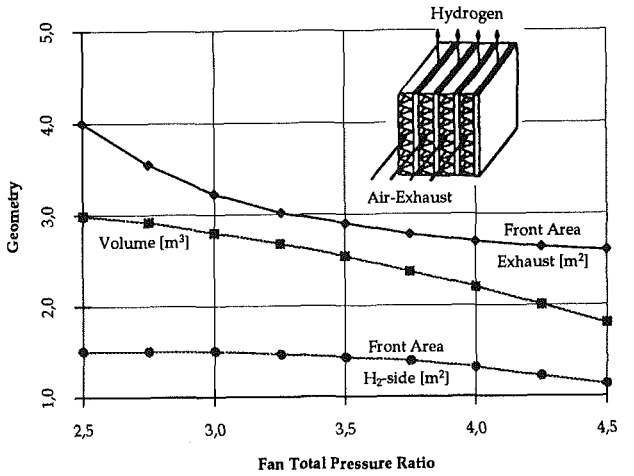


Fig. 13 Heat exchanger design for several fan pressure ratios

air ratio $\alpha = 0.002$) and gaseous hydrogen at several temperatures. The isentropic specific enthalpy is energy per mass flow. For a constant total pressure ratio, it is possible to obtain a much higher isentropic specific enthalpy by driving a turbine with hydrogen. This is the result of the very high specific heat capacity of hydrogen in comparison to air–kerosene exhaust. So the low hydrogen turbine mass flow is partially compensated for by the high energy content of this medium even at moderate turbine entry temperatures (see Fig. 12).

The high gas constant of hydrogen—compared to air–kerosene exhaust—leads to a high sonic velocity. At a comparable Mach number, the absolute velocity at the guide vanes is about three times higher for hydrogen turbines. The peripheral speed of the hydrogen turbine is low, compared to the absolute inlet speed of the hydrogen. This leads to small changes in the velocity vectors in the relative system and therefore to small pressure ratios per turbine stage. In Fig. 12 typical velocity triangles of air-exhaust and hydrogen turbines are depicted (c denotes absolute velocity at the guide vanes, u, peripheral speed, w, velocity in the relative system).

In order to reduce the number of turbine stages in hydrogen turbines, the peripheral speed must be as high as possible. This can be achieved using a reduction gear or a tip turbine. Nevertheless, the number of stages of hydrogen turbines will always be higher than in conventional turbines, since the maximum tensile strength of the turbine rotor defines the peripheral speed.

A very sophisticated component of the turbo-expander-cycle engine is the hydrogen heat exchanger. In order to achieve a proper engine concept, weight and volume of the heat exchanger, in particular the surface at the exhaust side of the primary burner, have to be as small as possible

Engine Characteristics		Engine A	Engine B	Engine C
Design point	(DP)	Mach =1.2 , altitude = 10 km		
Net thrust	(DP)	~ 161 kN	~ 183 kN	~ 200 kN
Compressor: Number of stages		2	2	3
Pressure ratio π		2,5	3,5	4,5
Turbine: Number of stages		3	5	6
Entrance temperature (DP)		1000 K	1000 K	1000 K
max. peripheral speed		550 m/s	550 m/s	550 m/s
Reduction gear: max. power		44 MW	63 MW	78 MW
Heat-exchanger: Volume		3.0 m³	2,5 m³	1,8 m³
Area H_2- side		1,5 m²	1,4 m²	1,2 m²
Area air-exhaust - side		4,0 m²	2,9 m²	2,5 m²
Geometrical capture area		3,0 m²	3,0 m²	3,0 m²
Transition Mach number		> 4,0	> 4,0	> 4,0

Fig. 14 Design parameters of three expander-cycle engines

The pressure losses at the air-exhaust side (primary burner exit) and on the hydrogen side have to be small in order to achieve acceptable efficiency. Figure 13 presents the results of a heat-exchanger calculation (according to [10]) for several fan pressure ratios at a constant engine size and a constant pressure loss for the air-exhaust side (≈ 11 percent) of the heat exchanger.

The design of the heat exchanger of an expander-cycle engine is critical due to the differential temperatures and pressures ($\Delta T_{max} \approx 1100$ K, $\Delta p_{max} \approx 200$ bar at a fan pressure ratio of $\pi = 4.5$) as well as the design of a reduction gear, if used, due to the high power transfer (≈ 8.9 MW in the 304 "Suntan" and ≈ 78 MW for the "study engine" with compression ratio $\pi = 4.5$).

Figure 14 shows the main design parameters of the three expander-cycle engines considered for performance calculation. Due to the small density of the air at lower compressor pressure ratios, the heat exchanger is heavier and of a higher volume leading to an increased engine diameter.

5.3 Comparison of Turbo-Expander-Cycle Engines With Various Pressure Ratios. Figure 15 presents a comparison of a turbo-expander-cycle engine with pressure ratios of $\pi = 2.5$ and 4.5. The pressure losses at the air-exhaust side of the heat exchanger were kept to about 11 percent for both designs. The engine diameter of the 2.5 compression ratio design is larger because of the large heat exchanger cross section, whereas the integration of the heat exchanger is possible within the fan diameter envelope at higher pressure ratios, like $\pi = 4.5$.

On the other hand, the increase of pressure ratio π leads to a higher number of turbine and compressor stages and a more complex and heavy reduction gear. A trade-off between the engine integration aspects, powerplant total weight and size, development risk, etc., is necessary to optimize this kind of propulsion system.

5.4 Performance Calculation. Figure 16 shows the net installed thrust along a typical trajectory (see Fig. 1), for the three selected engines. Up to a flight Mach number of 3.5, the thrust level is determined by the compressor pressure ratio. Beyond Mach 3.5 the difference is negligible since the engine control reduces the fan pressure ratio with increasing flight Mach number, and engine operation becomes similar to a ramjet.

6 Aspects Concerning Turbojet and Turbo-Expander Engines

The capability to reach high flight Mach numbers and the

Downloaded 02 Jun 2010 to 171.66.16.122. Redistribution subject to ASME license or copyright; see http://www.asme.org/terms/Terms_Use.cfm

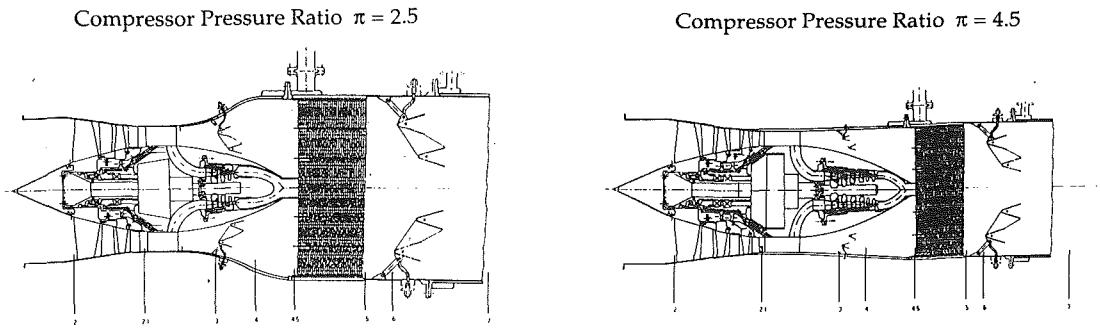


Fig. 15 Turbo-expander-cycle engines with various fan pressure ratios (π = 2.5 and π = 4.5)

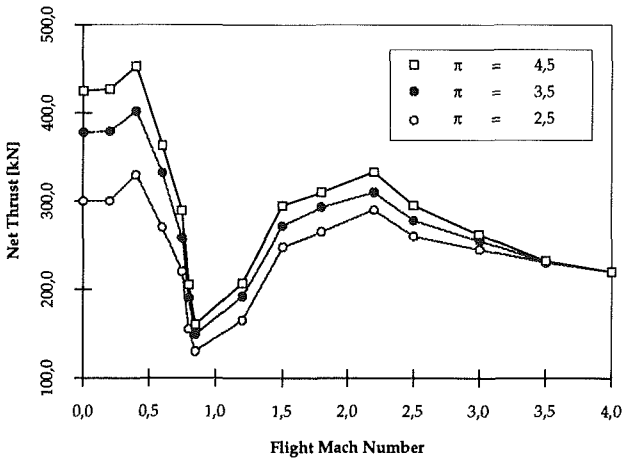


Fig. 16 Net thrust at the chosen ascent profile

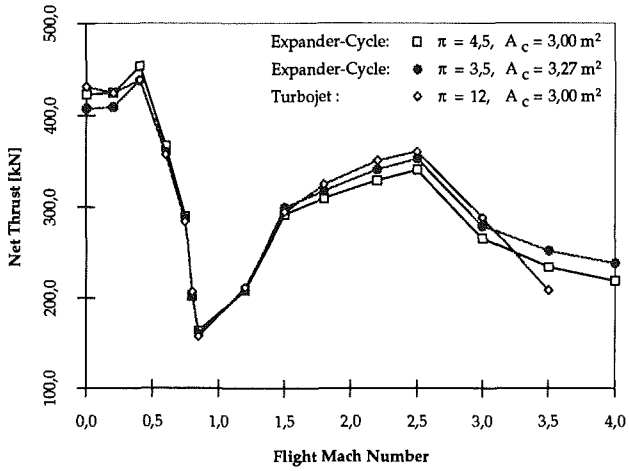


Fig. 17 Net thrust of two expander-cycle engines and a turbojet at the chosen ascent profile

adaptability to the mission flight profile are two of the most important criteria that must be considered when studying turbo engines for hypersonic aircraft.

Due to its low overall compressor pressure ratio, the expander-cycle engine has a thrust level, which may be sufficient up to a flight Mach number of about 4.5, leading to compact ramjet engines. Compared to the expander-cycle engine, the conventional turbojet has a much steeper decrease in net thrust beyond a flight Mach number of about 3.0, since this engine type is limited by high compressor exit temperatures, as can be seen in Fig. 17.

In Fig. 17 thrust values of three engines are plotted, all sized to the same installed net thrust of 200 kN at the design point.

Engine Characteristics		Turbojet	Turbo-Expander
Operational range		o	+
Flexibility to subsonic operation		+	-
Noise		o	-
Specific impulse at	max. thrust	+	+/o
	part power	++	-
Diameter		o	o/-
Weight		o	o
Development cost		+	-
-ilities		+	-
Safety aspects		+	-

Fig. 18 Valuation of various characteristics of both engine types

Two expander-cycle engines with π = 3.5 and 4.5 are compared to a "leaky" turbojet, quite similar to the turbojet of paragraph 4.1 (without simultaneous operation of turbojet and ramjet; reduced capture area). It is obvious that the thrust characteristics below Mach 3 are quite similar. The lower pressure ratio (π = 3.5) leads to a lower specific thrust at low speeds, demanding an increased intake size (A_c) and fan diameter (air flow). In addition, this engine shows inferior specific fuel consumption. The fuel consumption of the high-pressure expander-cycle engine proved to be nearly as good as the turbojet.

The dimensions of the high pressure ratio expander and the turbojet engine, in both cases defined by the fan diameter, are comparable. Lower compression ratios increase the envelope of the heat exchanger above the fan size considerably, making the integration of the engine more difficult.

When we first considered the weight of the engines, it was found that the expander-cycle engines had a similar, or even higher weight, than the conventional turbojet, in contrast to the previous assumptions. The saved weight of the high-pressure section of the conventional turbojet is at least compensated for by the additional weight of the heat exchanger and the reduction gear. These results, however, are only valid for the chosen design and mission demands. In the case of single stage to orbit accelerators, configured as low compressor ratio, tip turbine driven expander-cycle engines, or even supported by hydrogen-oxygen combustion, often designated as air turbo rockets, the pure engine weight can be reduced drastically.

In the expander-cycle, fuel mass flow and engine speed (rpm) are closely coupled. Therefore "dry" operation is not possible. The conventional turbojet engine has a high mission flexibility, enabling lower noise levels, and drastically improved specific fuel consumption during subsonic acceleration, climb and cruise in dry operation, because high engine speeds are obtainable without any afterburning fuel flow.

Downloaded 02 Jun 2010 to 171.66.16.122. Redistribution subject to ASME license or copyright; see http://www.asme.org/terms/Terms_Use.cfm

Figure 18 presents an evaluation of various characteristics of both engine types, seen from the aircraft manufacturer's view, and valid for mission and integration requirements as described in the first paragraph of this section.

7 Conclusion

The study of expander-cycle and conventional turbojet engines combined with ramjet engines for hypersonic aircraft with definite cruise capability led to the conclusion that the conventional turbojet cycle is more suitable than the expander type.

At comparable fuel consumption and engine diameter a reduction in engine weight could not be realized for the expander engine. In addition, it is anticipated that the expected high development risk and cost for the unconventional components such as the heat exchanger, high-power hydrogen turbine, and reduction gear, will not pay off. The high safety risk of the heat exchanger, the high noise level at take-off and subsonic flight, and low mission flexibility are further arguments, which were taken into consideration.

The main effort with respect to the turbo engine development should be on mass reduction. Improvements in aero- or thermodynamics are considered to be of lower importance.

References

1 Sterr, W., "Auslegung und Berechnung eines Turbo-Expander-Cycle-Triebwerks mit Wasserstoff-Wärmetauscher für ein Hyperschallflugzeug," Diplomarbeit, Lehrstuhl für Flugantriebe, Technische Universität München, Germany, 1989.

2 Zellner, B., "Synthese eines Turbo-Staustrahl-Kombinationsantriebs für Hyperschallflugzeuge," Diplomarbeit, Lehrstuhl für Flugantriebe, Technische Universität München, Germany, 1989.

3 Morris, R. E., and Brewer, G. D., "Hypersonic Cruise Aircraft Propulsion Integration Study, Vol. 5. I, II," Lockheed-California Company Burbank, California, Contract NAS1-15057, NASA Contractor Report CR-158926-1, 1979.

4 Künkler, H., and Kuczera, H., "Turbo-Ramjet Propulsion System Concepts for Future European Space Transport (Sänger)," Paper No. IAF-87-265, 1987.

5 Herrmann, O., "Integration of Turbo-Ramjet Engines for Hypersonic Aircraft," AGARD-FDP Symposium, Fort Worth, TX, 1991.

6 Herrmann, O., "Propulsion Aspects of Hypersonic Turbo-Ramjet-Engines With Special Emphasis on Nozzle/Aftbody Integration," ASME Paper No. 91-GT-XXX, 1991.

7 Gordon, S., and McBride, B. J., "Computer Program for Calculation of Complex Chemical Equilibrium Compositions, Rocket Performance, Incident and Reflected Shocks, and Chapment-Jouguet Detonations," NASA Lewis Research Center, National Aeronautics and Space Administration, Washington, DC, 1971.

8 Bissinger, N. C., "BMFT-Förderkonzept Hyperschalltechnologie 1b—Technologiebereich, Einlauf—Modellbau und Erprobung (E4)," 2. Zwischenbericht, MBB, Ottobrunn, 1991.

9 Mulready, R. C., "Liquid Hydrogen Engines," Pratt & Whitney Aircraft Group, 1979.

10 Kays, W. M., and London, A. L., "Hochleistungs-wärmeübertrager," Akademie Verlag, Berlin, Germany, 1973.

Downloaded 02 Jun 2010 to 171.66.16.122. Redistribution subject to ASME license or copyright; see http://www.asme.org/terms/Terms_Use.cfm

Flow Separation in Shock Wave Boundary Layer Interactions

A. Hamed
Department of Aerospace Engineering and Engineering Mechanics, University of Cincinnati, Cincinnati, OH 45221

A. Kumar
Theoretical Flow Physics Branch, NASA Langley Research Center, Hampton, VA 23665-5225

This work presents an assessment of the experimental data on separated flow in shock wave turbulent boundary layer interactions at hypersonic and supersonic speeds. The data base consists of selected configurations where the only characteristic length in the iteration is the incoming boundary layer thickness. It consists of two-dimensional and axisymmetric interactions in compression corners or cylinder-flares, and externally generated oblique shock interactions with boundary layers over flat plates or cylindrical surfaces. The conditions leading to flow separation and the empirical correlations for incipient separation are reviewed. The effects of Mach number, Reynolds number, surface cooling, and the methods of detecting separation are discussed.

Introduction

Shock boundary layer interactions are usually the cause of flow separation at hypersonic and supersonic speeds. In addition to increasing the drag and the aerodynamic heating on the aircrafts and missiles, they adversely affect the inlet and control surface performance. The conditions leading to flow separation and the subsequent changes in the flow have been the subject of extensive research efforts over the past 30 years. The results of these investigations have been compiled and discussed in several excellent reviews [1–4]. However, in spite of these efforts, the combined influence of viscous–inviscid interactions, turbulence, and compressibility on the resulting complex flow fields is not fully understood at high speeds. Owen [5] discussed the problems associated with the experimental measurements of flows at hypersonic speeds, and the inadequacy of existing experimental techniques in shock boundary layer interactions involving separation, time-dependent flow reversal, and high levels of turbulence.

The focus of the present work is the assessment of the experimental data on separated flow in shock wave turbulent boundary layer interactions at hypersonic speeds. The data base will consist mainly of two-dimensional and axisymmetric interactions of shock wave and turbulent boundary layer. Only two configurations will be considered, namely compression corner or cylinder-flare, and externally generated oblique shock interactions with boundary layers over flat plates or cylindrical surfaces. Interactions in forward or backward steps will not be included. The choice is based on the absence of any characteristic length, with the exception of the incoming boundary layer thickness, in the two configurations shown in Fig. 1.

Incipient Separation

The conditions for incipient separation due to shock boundary layer interactions in two-dimensional hypersonic flow have been determined experimentally by a number of investigators [6–11]. The Mach number in these experiments ranged between 6 and 13 and the Reynolds number based on the boundary layer thickness before the interaction was in the range of 10^5–10^6. The results indicated that the resistance to separation increased with the Mach number and decreased with the Reynolds number [7–11]. Since the boundary layer thickness on a full-scale model is usually much larger than that on a smaller wind tunnel model, the effect of the Reynolds number on the shock boundary layer interactions and flow separation need to be understood, if the experimental data is to be used in practical applications. For this reason, incipient separation data for supersonic two-dimensional flow [12–18] are included in the present survey, since it covers a wider range of Reynolds number [$10^4 < Re_\delta < 10^7$].

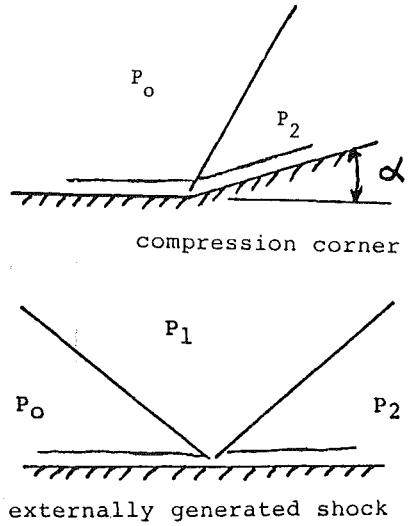


Fig. 1 Flow configurations

Contributed by the International Gas Turbine Institute and presented at the 37th International Gas Turbine and Aeroengine Congress and Exposition, Cologne, Germany, June 1–4, 1992. Manuscript received by the International Gas Turbine Institute February 21, 1992. Paper No. 92-GT-205. Associate Technical Editor: L. S. Langston.

Copyright © 1994 by ASME
Downloaded 02 Jun 2010 to 171.66.16.122. Redistribution subject to ASME license or copyright; see http://www.asme.org/terms/Terms_Use.cfm

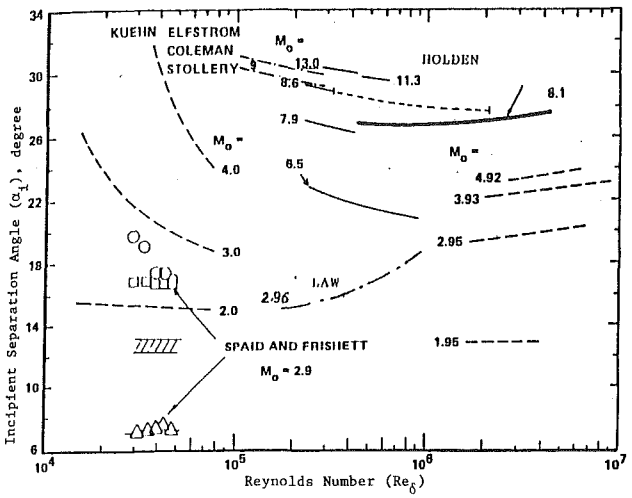


Fig. 2 Wedge angle to induce incipient separation

The experimentally determined [6–20] incipient separation conditions in hypersonic and supersonic flows are presented in Fig. 2. One can see the variation in the incipient separation angle in a compression corner with the Reynolds number for different values of Mach number. The Reynolds number in the figure is based on free-stream conditions and the incoming boundary layer thickness before the interaction. Such a plot was first used by Kuehn [12] to present his experimental results and later appeared in other references, with a continuously expanding incipient separation data base. Some of the incipient separation data in Fig. 2 were obtained in the interaction of an impinging externally generated oblique shock with the turbulent boundary layer on a flat plate. In these cases, an equivalent angle is defined that would produce the same overall pressure ratio. Holden [6, 10], Kuehn [12], and Settles et al. [18] demonstrated the equivalence between the separation data in the compression corner and this configuration, when correlated in terms of the overall pressure ratio across the incident and reflected shock.

Effect of Mach Number. The incipient separation angle increased with the Mach number for both supersonic and hypersonic flows. This influence decreases however with increasing Mach number and is very weak in hypersonic flow above Mach eight.

Effect of Reynolds Number. Kuehn [12] conducted one of the earliest experimental investigations to study the Mach and Reynolds number effects on incipient separation in shock wave turbulent boundary layer interactions. His results indicated that the flow resistance to separation increased with the Mach number ($2 < M < 4$) and decreased with the Reynolds number. The supersonic data reported earlier by Drougge [13] and later by Sterrett and Emery [14] and by Kessler [15] exhibited the same Mach and Reynolds number effects on incipient flow separation. The experimental results of Roshko and Thomke [16] over a range of Reynolds number that was at least an order of magnitude higher showed a trend reversal with a moderate increase in the resistance to separation with Re, but the Mach number effect did not change. An increase in the boundary layer resistance to separation with the Reynolds number was also reported by Law [17] for M = 2.96. Settles et al. [18] presented incipient separation results in which the incipient separation angle was practically independent of the Reynolds number.

Different explanations have been advanced to explain the difference in the Reynolds number trends in the experimentally measured transition. Elfstrom [7] related the trend reversal of the Reynolds number to the changes in the wake component of the boundary layer, and was able to predict it analytically using a simple two-layer model. Hankey and Holden [3] offered another explanation based on the nonequilibrium development of the turbulent boundary layers in some of the experiments. Bushnell et al. [19] demonstrated that the nonequilibrium effects due to the favorable pressure gradient on the tunnel walls can persist at distances up to one hundred times the boundary layer thickness downstream of the nozzle exit. Roshko and Thomke [16] and Settles et al. [18], however, reported the same incipient separation trends with the Reynolds number on tunnel walls and on axisymmetric models, which contradicts the argument that the tunnel wall boundary layers are fuller [20, 21] and therefore harder to separate. Bushnell et al. [19] demonstrated also that downstream of transition, the turbulent boundary layer velocity profile power exponent N first decreases until the boundary layer becomes fully developed, then increases with the Reynolds number as shown in Fig. 3. Based on this, Hankey and Holden [3] explained that Kuehn's measurements were obtained in the range where as a result of boundary layer relaxation, the profiles became less full, hence the decrease in resistance to separation with the Reynolds number. The Roshko and Thomke [16] data, on the other hand, were in the range where N increased with Re_δ. Holden also explained the trend reversal between the experimental measurements reported in two of his studies [6, 10] in terms of the effect of nonequilibrium on the skin friction variation with the Reynolds number. Holden [10] also pointed out the difficulty of attempting to induce transition prematurely in hypersonic flows. He mentioned the possibility of a transitional rather than a fully turbulent boundary layer in the interaction zone when the boundary layer was tripped as in Kuehn's experiments.

Effect of Surface Cooling. All of the hypersonic incipient separation experiments [6–10] with the exception of [11], involved surface cooling. The experimental results of Holden [10] and Elfstrom [7] indicate that cooling increases the boundary layer resistance to separation at hypersonic speeds. Favorable effects of wall cooling on both the incipient separation angle and separation length were also measured in supersonic flows by Spaid and Frishett [26] and Gulbran et al. [20]. A nearly linear trend of increasing incipient separation angle with decreasing wall temperature was reported by Spaid and Frishett [26].

End Effects. Few of the surveyed experiments used fences to reduce end effects, but only Holden [6, 10] verified the diminished end effects on the measurement at the center through varying the model width in the absence of fences. According to experimental evidence, very moderate bleeding (2–4 percent of the boundary layer, mass flow) can control flow separation

Nomenclature

C_f = friction coefficient
L_s = separation length
M = Mach number
N = boundary layer velocity profile exponent
p = pressure
Re = Reynolds number
x = streamwise coordinate
α = ramp angle
δ = boundary layer thickness
θ = momentum thickness

Subscripts

i = incipient separation
o = upstream of shock
s = separation

Downloaded 02 Jun 2010 to 171.66.16.122. Redistribution subject to ASME license or copyright; see http://www.asme.org/terms/Terms_Use.cfm

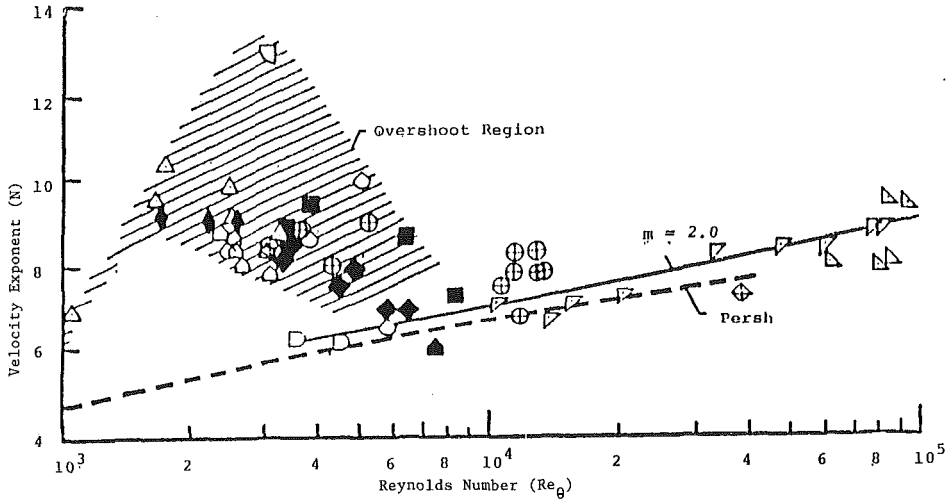


Fig. 3 Variation of velocity exponent with Reynolds number for flat plates, cones, and hollow cylinders [19]

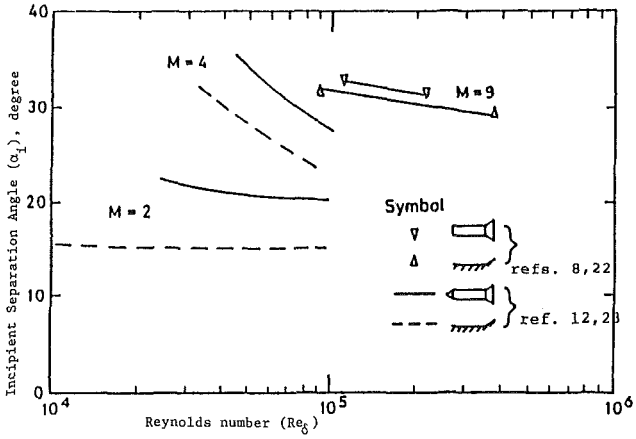


Fig. 4 Comparison of incipient separation results for compression corner and cylinder-flare

in shock boundary layer interaction. Delery [2] discussed this phenomenon and explained the cause for the strong influence of removing a small amount of the flow in the separation zone on controlling separation. The end effects might therefore play a significant role in flow separation. Coleman and Stollary [22], Kuehn [23], and Rose et al. [24] obtained incipient separation data in axisymmetric configurations. Coleman and Stollery [22] obtained incipient separation data in a cylinder-flare axisymmetric configuration to assess the end effects in their compression corner incipient separation results [8]. They determined that the incipient separation angles differed only by one degree in a cylinder-flare model from the equivalent wedge compression corner at M = 9. The surface pressure distributions near the corner were also identical in the two geometries under the same flow condition. Their results are shown in Fig. 4 together with Kuehn's data [12, 23], which exhibit larger differences between the axisymmetric and two-dimensional data at M = 2 and 4.

Incipient Separation Detection Methods. Several methods have been used by the different investigators to identify the conditions for incipient separation in shock wave turbulent boundary layer interactions. The experimentally measured surface pressures [7, 9, 12–14, 16–18, 23–24], temperatures [8], and skin friction [6, 10] have been used in conjunction with different criteria to detect flow separation. Incipient separation conditions have also been deduced from shadowgraphs and schlieren [7–10, 25, 26] pictures as well as from surface oil flow visualization [17] and powder deposition techniques [26]. Law [17], Apples and Richards [25], and Spaid and Frishett [26] determined the incipient separation conditions in their experiments using different methods, and demonstrated that experimentally determined incipient separation angles in a compression corner can be dependent on the method of detection.

Different criteria have been used in detecting separation from the surface pressure measurements. Kuehn [12] identified separation with the appearance of three inflection points in the measured surface pressure distribution in the compression corner experiments. Coleman and Stollary [8] and Drougge [13] also used the first appearance of a kink in the surface pressure distribution as the criterion for incipient separation. This criterion is not suitable in the case of externally generated incident shock, since Green [27] found that this change in the pressure distribution occurred only when a relatively large separation region was formed.

Another separation criterion is based on the variation of the measured surface pressure near the corner with the corner angle. This criterion was used by Roshko and Thomke [16] and by Elfstrom [7] who identified separation angle with the inflection in the pressure versus corner angle plot. The disappearance of the overshoots in the surface pressure distribution was suggested by Elfstrom [7] as a criterion for incipient separation in hypersonic flows.

Coleman and Stollary [8] used the measured surface heat transfer distributions to detect separation in their experiments. They identified the separation angle with the conditions when the heat transfer rate started to increase just ahead of the hinge line of the compression corner. Experimental evidence of this increase in the heat transfer was also reported by other investigators including Holden [10], Holloway et al. [28], and Gadd et al. [29].

Due to the unsteady characteristics in the separation zone, Holden [6, 10] used the surface shear measurements instead of pressure, to detect separation. Incipient separation was identified with the condition where the time average of surface shear was zero at one point. This approach has not been used by many other investigators because of the difficulties associated with the accurate measurement of the extremely small wall shear stress values near separation.

Shadowgraph and schlieren pictures have been used to detect separation due to shock turbulent boundary layer interactions in supersonic and hypersonic flows. The change in the shock wave angle in the schlieren picture due to the formation of a

Downloaded 02 Jun 2010 to 171.66.16.122. Redistribution subject to ASME license or copyright; see http://www.asme.org/terms/Terms_Use.cfm

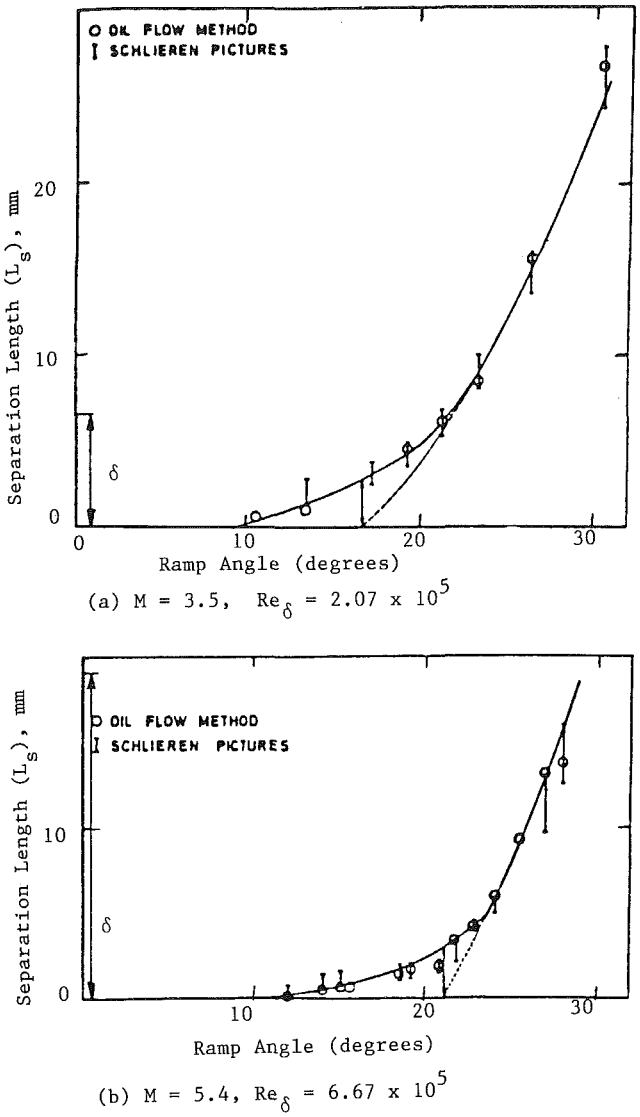


Fig. 5 Separation distance as function of wedge angle [25]

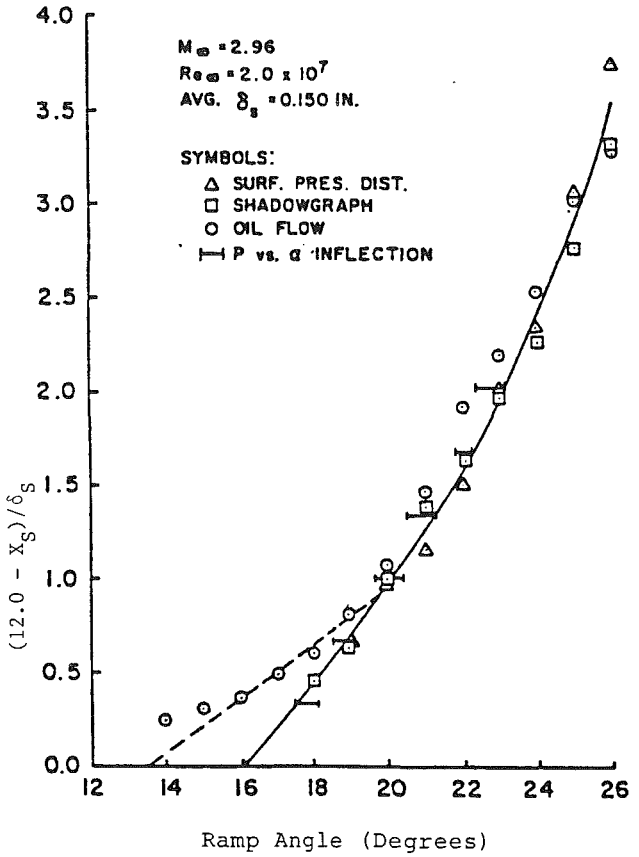


Fig. 6 Variation of separation distance with compression ramp angle [17]

double shock system was used by Drougge [13] and Sterrett and Emery [14] as the criteria for incipient separation in a compression corner. Another method that was extensively used by a number of investigators [7–10, 25, 26] was based on measuring the separation length from the schlieren pictures. The separation length has also been determined from the surface pressure distribution, in which case the separation and reattachment points are identified with the first and third inflection points.

Surface oil flow visualization has also been used to detect flow separation [25, 26]. In this method the liquid is applied to the surface before the test and the flow separation is identified by the liquid line where the oil has accumulated. Because the liquid line thickness is comparable to that of the separation bubble, the effect of their interaction can be a source of error. Apples and Richards [25] studied this phenomenon by running some of the tests for much larger times, in which case the accumulated oil was entrained into the separation region and filled the separation bubble. In order not to disturb the separation bubble for a small separated region, the same authors demonstrated that the interaction can be minimized by applying a very small quantity of oil ahead of the expected separation region. They also used high-speed schlieren pictures to study the effect of the flow unsteadiness in the separated regions, which was negligible in their experiment. Since liquid accumulation can also result from the balance between the wind and buoyancy forces, Spaid and Frishett [26] used a powder deposition technique to verify their oil flow results. The two methods were in agreement within the liquid line reading uncertainty.

In principle, the distance L_s between the separation and reattachment points is measured at different shock strengths. Plots of the measured separation length versus the corner angle are then used to extrapolate the angle of incipient separation α_1, corresponding to $L_s = 0$. Coleman and Stollary [8] based their results on a linear interpolation, while others [17, 25] used more than two separation data points for their extrapolation. One source of error in this detection method is the uncertainty in locating the separation point from the schlieren photographs. By including measurements for small separations with $L_s/\delta < 5.0$, Apples and Richards [25] demonstrated that the L_s–α_I curve is nonlinear and showed that the extrapolation of data with relatively large separation regions may overestimate α_I by as much as 10 deg at M = 5.4 as shown in Fig. 5.

Effect of Detection Method on Separation Results. More than one method has been used to detect separation by Roshko and Thomke [16], Law [17], Apples and Richards [25], Spaid and Frishett [26], and Rose et al. [24]. Roshko and Thomke [16] obtained consistent results for the incipient separation angle using orifice dams and the inflection in the curve for the variation in the pressure near the corner with α. Law [17] investigated the effect of the experimental method used in the determination of the separation length on the incipient separation angle, as determined from the extrapolation of $L_s - \alpha$ curve to zero L_s. Figure 6 shows a comparison of the separation point location, as determined from four different procedures under different test conditions (M = 2.96, α = 14–26 deg). In the first procedure, the separation point was identified with

Downloaded 02 Jun 2010 to 171.66.16.122. Redistribution subject to ASME license or copyright; see http://www.asme.org/terms/Terms_Use.cfm

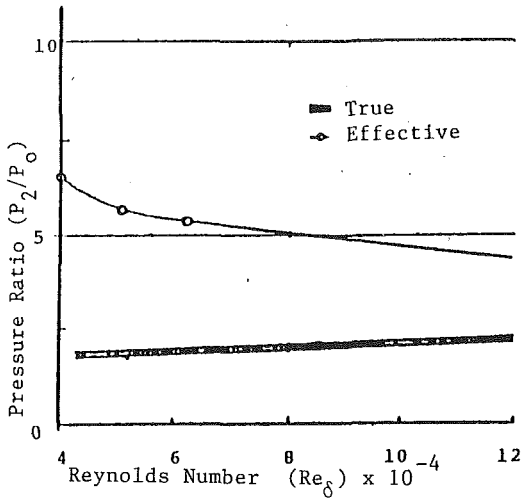


Fig. 7 Difference between "true" and "effective" incipient separation [24]

the first inflection point in the surface pressure distribution; in the second, it was determined from the shadowgraph; in the third, it was assumed at the oil accumulation line; and in the fourth method, the separation point was associated with the axial location, where there was an inflection point in the p versus α curve. Figure 5 shows that the separation lengths detected by all four methods are in agreement for large separated region. For small separation regions comparable with the boundary layer thickness, the oil flow predicts larger separated regions. It is clear from the figure that this difference translates into overpredicted incipient separation angles based on the surface pressure and shadowgraph data.

Delery and Marvin [1] distinguished between "true" incipient separation, corresponding to the first appearance of a separation bubble, and "effective" incipient separation, when the separation bubble starts to produce significant changes in the flow field. The first, which can be detected by surface flow visualization techniques, can be present without affecting the surface pressure according to Holden [10], Kuehn [12], and Settles et al. [18]. Figure 7 shows the difference between the "true" and "effective" incipient separation according to Rose et al. [24]. Holden [6] also distinguished between techniques for detecting the first appearance of reverse flow and other "pragmatic" methods, since each detects a different phenomenon. The former techniques such as oil flow measurements, and measurements of surface shear and heat transfer, were used to detect the presence of separation in the sublayer. On the other hand, observing the inflection in the pressure distribution and the first appearance of a separation shock are pragmatic indicators of boundary layer separation. Hankey and Holden [3] suggested that turbulent boundary layer separation is a two-stage process. The first separation is in the laminar sublayer with a laminar recirculation region at the base of the turbulent boundary layer. Next, a turbulent recirculation region is formed that increases rapidly with the interaction strength. This explains the abrupt change in the upstream influence that was observed by Holden [10] and by Elfstrom [7] when a turbulent boundary layer separated over a highly cooled surface in hypersonic flow. More gradual separation was reported by Roshko and Thomke [16], Settles et al. [18], and Spaid and Frishett [26] for turbulent boundary layers in supersonic flows over adiabatic surfaces. In the latter case, the laminar sublayer had a greater influence on the development of separation with the increased interaction strength, as opposed to the weaker influence of the relatively thin laminar sublayer in the former case.

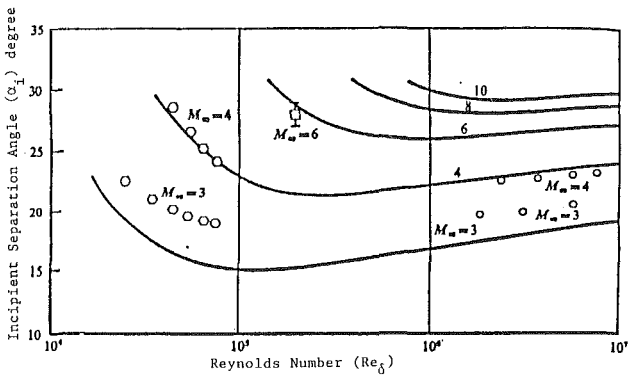


Fig. 8 Predicted incipient separation for adiabatic wall conditions: experiment: ⬡, Kuehn; □, Gray and Rhudy; ⬡, Thomke and Roshko

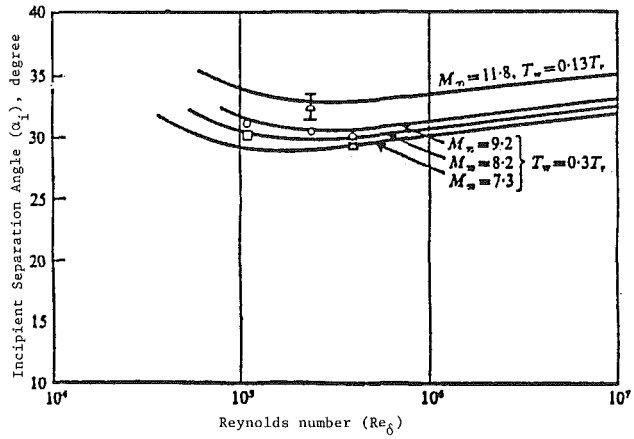


Fig. 9 Predicted incipient separation for nonadiabatic wall conditions: experiment: ⌓, Apples and Richards; ○, □, △, Elfstrom

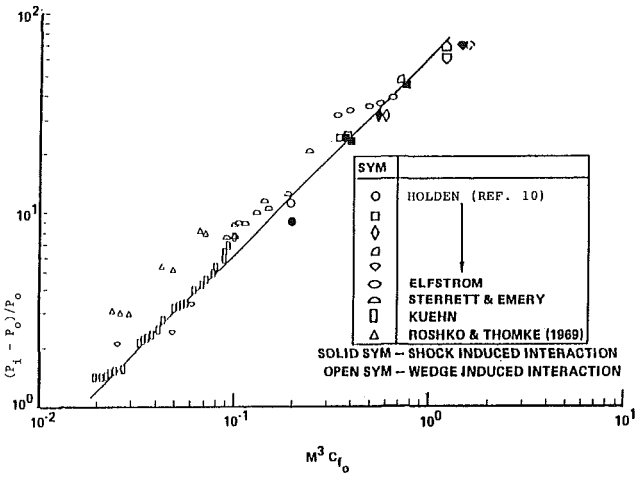


Fig. 10 Correlation of incipient separation conditions for shock turbulent boundary layer interaction [10]

Incipient Separation Correlations. Kessler [15], Elfstrom [7], and Hankey and Holden [3] proposed different correlations for the condition of incipient separation. Elfstrom [7] demonstrated that Kessler's correlation severely overpredicted the separation trends at high Mach numbers ($6.05 \leq M \leq 11.8$).

Elfstrom [7] proposed a simple model to predict the wedge angle at incipient separation. This theory is based on the inviscid rotational analysis of the supersonic outer portion of

Downloaded 02 Jun 2010 to 171.66.16.122. Redistribution subject to ASME license or copyright; see http://www.asme.org/terms/Terms_Use.cfm

the boundary layer in the shock interaction region proposed by Roshko and Thomke [16]. Using the wake profile with the appropriate compressibility transformation, Elfstrom [7] determined the incipient separation angle based on the conjecture that the laminar sublayer separates when it encounters a normal shock. His model prediction and the experimental results of Kuehn [12], Gray and Rhudy [11], and Roshko and Thomke [16] are given in Fig. 8, which shows good agreement for Mach numbers in the range of 3 to 6. He also compared his model prediction for incipient separation angle with the cooled flow data at higher Mach numbers with good success (Fig. 9). One can see from Figs. 8 and 9 that his model predicts the trend reversal in incipient separation at high Reynolds numbers over a wide range of Mach numbers and wall temperatures.

Holden [10] suggested a correlation for the pressure ratio inducing separation in the form

$$\frac{P_i - P_o}{P_o} \propto C_{f_o} \, M_o^3.$$

The experimental results from different sources are shown with the above correlation in Fig. 10. Holden based his correlation on viewing the separation mechanism in terms of the balance between the inertial and viscous forces at the wall. He arrived at this conclusion from the consistent pressure ratios in the shock and wedge induced separation in his experiments. The agreement between the experimental results of the two geometries in a large number of experimental studies is evident in Fig. 10.

Acknowledgments

This work was supported by NASA Langley Research Center Contract NAS1-18458.

References

1 Delery, J., and Marvin, J. G., "Shock-Wave Boundary Layer Interactions," AGARD-AG-280, Feb. 1986.

2 Delery, J., "Shock Boundary Layer Interaction and Its Control," *Progress in Aerospace Sciences*, Vol. 22, 1985, pp. 209–280.

3 Hankey, W. L., and Holden, M. S., "Two-Dimensional Shock-Wave Boundary Layer Interactions in High Speed Flows," AGARD-AG-203, June 1975.

4 Green, J. E., "Interactions Between Shock Waves and Turbulent Boundary Layers," *Progress in Aerospace Sciences*, Vol. 11, 1970, pp. 235–340.

5 Owen, F. K., "Measurements of Hypersonic Flow Fields," AGARD-FDP-VKI Special Course, Aerothermodynamics of Hypersonic Vehicles, May–June 1988.

6 Holden, M. S., "Shock Wave-Turbulent Boundary Layer Interactions in Hypersonic Flow," AIAA Paper No. 77-45, 1975.

7 Elfstrom, G. M., "Turbulent Hypersonic Flow at a Wedge-Compression Corner," *Journal of Fluid Mechanics*, Vol. 53, Part 1, 1972, pp. 113–127.

8 Coleman, G. T., and Stollary, J. L., "Heat Transfer From Hypersonic Turbulent Flow at a Wedge Compression Corner," *Journal of Fluid Mechanics*, Vol. 56, Part 4, 1972, pp. 741–752.

9 Batham, J. P., "An Experimental Study of Turbulent Separating and Reattaching Flows at a High Mach Number," *Journal of Fluid Mechanics*, Vol. 52, Part 3, Apr. 1972, pp. 425–437.

10 Holden, M. S., "Shock Wave-Turbulent Boundary Layer Interaction in Hypersonic Flow," AIAA Paper No. 72-74, 1972.

11 Gray, K. D., and Rhudy, R. W., "Investigation of Flat Plate Aspect Ratio Effects on Ramp Induced Adiabatic Boundary Layer Separation at Supersonic and Hypersonic Speeds," Final Report AEDC-TR-70-235, 1971.

12 Kuehn, D. M., "Experimental Investigation of the Pressure Rise Required for the Incipient Separation of Turbulent Boundary Layers in Two-Dimensional Supersonic Flow," NASA MEMO 1-21-59A, Feb. 1959.

13 Drougge, G., "An Experimental Investigation of the Influence of Strong Adverse Pressure Gradients on Turbulent Boundary Layers at Supersonic Speeds," FFA Report 47, 1953.

14 Sterrett, J. P., and Emery, J. C., "Experimental Separation Studies for Two Dimensional Wedges and Curved Surfaces at Mach Numbers of 4.8 to 6.2," NASA TN D-1014, 1962.

15 Kessler, W. C., "Supersonic Turbulent Boundary Layer Interaction With an Expansion Fan and a Compression Corner," MDC E0264, Dec. 1970.

16 Roshko, A., and Thomke, G. J., "Supersonic Turbulent Boundary Layer Interaction With a Compression Corner at Very High Reynolds Number," *Proceedings of the 1969 Symposium on Viscous Interaction Phenomena in Supersonic and Hypersonic Flows*, University of Dayton Press, 1964, pp. 109–133.

17 Law, H. C., "Supersonic Turbulent Boundary Layer Separation Measurements at Reynolds Numbers of 10^7 to 10^8," *AIAA Journal*, Vol. 12, No. 6, 1974, pp. 794–797.

18 Settles, G. S., Bogdonoff, S. M., and Vas, I. E, "Incipient Separation of a Supersonic Turbulent Boundary-Layer at Moderate to High Reynolds Numbers," *AIAA Journal*, Vol. 14, No. 1, 1976, pp. 50–56.

19 Bushnell, D. M., Johnson, C. B., Harvey, W. D., and Feller, W. V., "Comparison of Prediction Methods and Studies of Relaxation in Hypersonic Turbulent Boundary Layers," *Turbulent Boundary Layer Conference Proceedings*, NASA Langley Research Center, Dec. 1968.

20 Gulbran, C. E., Redeker, E., Miller, D. S., and Strack, S. L., "Heating in Regions of Interfering Flow Fields, Part III: Two Dimensional Interaction Caused by Plane Shocks Impinging on Flat Plate Boundary Layers," AFFDL-TR-65-49, Mar. 1967.

21 Fernholz, H. H., and Finley, P. J., "A Critical Compilation of Compressible Turbulent Boundary Layer Data," AGARDograph No. 223, June 1977.

22 Coleman, G. T., and Stollary, J. L., "Incipient Separation of Axially Symmetric Hypersonic Turbulent Boundary Layers," *AIAA Journal*, Vol. 12, 1974, pp. 119–120.

23 Kuehn, D. M., "Turbulent Boundary Layer Separation Induced by Flares on Cylinders at Zero Angle of Attack," NASA TR 117, 1961.

24 Rose, W. C., Page, R. J., and Childs, M. E., "Incipient Separation Pressure Rise for a Mach 3.8 Turbulent Boundary Layer," *AIAA Journal*, Vol. 11, No. 5, 1973, pp. 761–763.

25 Apples, C., and Richards, B. E., "Incipient Separation of a Compressible Turbulent Boundary Layer," AGARD CP-168, *Flow Separation*, May 1975.

26 Spaid, F. W., and Frishett, J. C., "Incipient Separation of a Supersonic, Turbulent Boundary Layer, Including Effects of Heat Transfer," *AIAA Journal*, Vol. 10, No. 7, July 1977, pp. 915–922.

27 Green, J. W., "Reflection of an Oblique Shock Wave by a Turbulent Boundary Layer," *Journal of Fluid Mechanics*, Vol. 40, Part 1, 1970, pp. 81–95.

28 Holloway, P. F., Sterrett, J. R., and Greekmore, H. S., "An Investigation of Heat Transfer Within Regions of Separated Flow at a Mach Number of 6.0," NASA TND-3074, 1965.

29 Gadd, G. E., Cope, W. F., and Attridge, L. L., "Heat Transfer and Skin-Friction Measurements at a Mach Number of 2.44 for a Turbulent Boundary Layer on a Flat Surface and in Regions of Separated Flow," R&M No. 3148, British Aeronautical Research Council, 1960.

Downloaded 02 Jun 2010 to 171.66.16.122. Redistribution subject to ASME license or copyright; see http://www.asme.org/terms/Terms_Use.cfm

Air-Breathing Hypersonic Cruise: Prospects for Mach 4–7 Waverider Aircraft

I. M. Blankson
Hypersonics Research Division,
National Aeronautics and Space Administration,
Washington, DC 20546

There is currently a renewal of world-wide interest in hypersonic flight. Vehicle concepts being considered range from cruise missiles to SSTO and TSTO vehicles. The new characteristics of these vehicles are that they will be powered by air-breathing engines and have long residence times in the air-breathing corridor. In the Mach 4–7 regime, waverider aircraft are being considered as candidates for both long-range and short-range cruise missions, as hypersonic missiles, and as high-L/D highly maneuverable vehicles. This paper will discuss the potential for near-term and far-term application of air-breathing engines to the above-mentioned waverider vehicle concepts and missions. In particular, the cruise mission is discussed in detail and attempts are made to compare and contrast it with the accelerator mission. Past criticisms levied against waveriders alleging low volumetric efficiency, lack of engine/airframe integration studies, poor off-design performance, poor take-off and landing capability, have been shown by ongoing research to be unfounded. A discussion is presented of some of the technical challenges and ongoing research aimed at realizing such vehicles: from turboramjet and scramjet technology development, propulsion-airframe integration effects on vehicle performance, aeroservothermoelastic systems analysis, hypersonic stability and control with aeroservothermoelastic and propulsion effects, etc. A unique and very strong aspect of hypersonic vehicle design is the integration and interaction of the propulsion system, aerodynamics, aerodynamic heating, stability and control, and materials and structures. This first-order multidisciplinary situation demands the ability to integrate highly coupled and interacting elements in a fundamental and optimal fashion to achieve the desired performance. Some crucial technology needs are found in propulsion-airframe integration and its role in configuration definition, hypersonic boundary-layer transition and its impact on vehicle gross-weight and mission success, scramjet combustor mixing length and its impact on engine weight and, CFD (turbulence modeling, transition modeling, etc) as a principal tool for the design of hypersonic vehicles. Key technology implications in thermal management, structures, materials, and flight control systems will also be briefly discussed. It is concluded that most of the technology requirements in the Mach 4–7 regime are relatively conventional, making cited applications near-term, yet offering very significant advancements in aircraft technology.

I Introduction

Following nearly 15 years of relative inactivity, several countries have initiated research and technology programs to develop various types of aero/spacecraft. Their ultimate goal is direct, reliable, and easy access to space [1]. In Europe, Russia, Japan, India, etc., hypersonic programs are directed toward vehicles such as Hermes, Sanger, Hotol, Hope, Hyperplane, etc. Concepts for hypersonic vehicles powered by air-breathing engines are also evolving as part of these programs. In the U.S., the National Aerospace Plane (NASP) program is developing the key technologies required for the successful operation of air-breathing hypersonic aerospace vehicles. The general goal of the NASP program is the construction and testing of an experimental, fully reusable vehicle, designated the X-30, that will be used as a manned demonstrator for hypersonic flight. The vehicle will use hydrogen-fueled, air-breathing ramjet/scramjet engines and will be capable of horizontal takeoff and landing. It will be designed to expand the envelope of high-speed flight in and beyond the atmosphere to the point that access to low earth orbit can be achieved. The uniqueness of NASP lies in its highly integrated scramjet, special structures and materials requirements, absence of suborbital stages, and inherent payload return capability. NASP addresses SSTO (single-stage-to-orbit) as well as aspects

Contributed by the International Gas Turbine Institute and presented at the 37th International Gas Turbine and Aeroengine Congress and Exposition, Cologne, Germany, June 1–4, 1992. Manuscript received by the International Gas Turbine Institute March 5, 1992. Paper No. 92-GT-437. Associate Technical Editor: L. S. Langston.

Copyright © 1994 by ASME
Downloaded 02 Jun 2010 to 171.66.16.122. Redistribution subject to ASME license or copyright; see http://www.asme.org/terms/Terms_Use.cfm

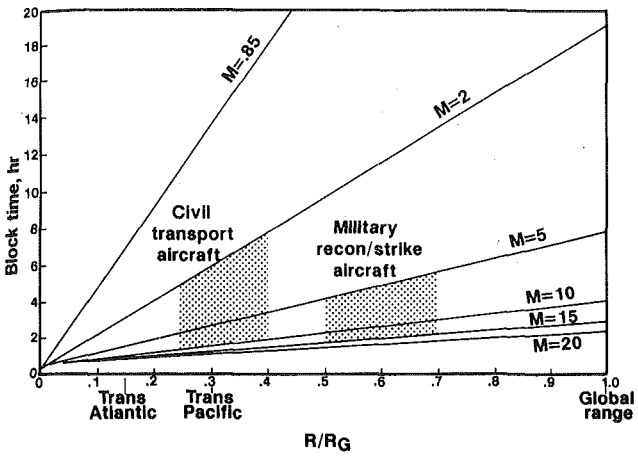


Fig. 1 Block time for long distance travel

of several accelerator/interceptor applications, but does not adequately address the technology aspects unique to cruise applications. For either class of vehicle, however, a tradeoff between engine thrust-to-weight ratio and specific fuel consumption is necessary.

In this paper, the prospects for air-breathing hypersonic vehicles, especially hydrocarbon-fueled Mach 4–7 waverider aircraft, are examined. Prospects for generic air-breathing hypersonic vehicles (Mach 5–25) were previously discussed in Refs. [2 and 3]. Figure 1 shows flight block time as a function of global range fraction for several cruise Mach numbers. The shaded regions indicate the global range fractions and Mach numbers believed to be of primary interest for future high-speed civil transport aircraft and military reconnaissance/strike aircraft. Cruise Mach numbers of 2 to 3 for civil aircraft, which are consistent with Concorde and current operational military aircraft, would reduce the block time for transpacific flights from about 14 hours to about 4–6 hours. Mach 5–6 military aircraft could provide worldwide coverage in about 4 hours. Mach numbers greater than about 10–15 provide an insignificant improvement in block time for both civil and military aircraft. Much greater distances are required for these higher speeds to pay off in block time. The Earth simply isn't big enough to warrant aircraft that cruise faster than about Mach 10–15.

As already noted, most national and international hypersonic activities are focused on transatmospheric flight with the goal of constructing air-breathing single-stage-to-orbit second generation shuttles or two-stage transports that incorporate an air-breathing first stage. An obvious intermediate regime, and perhaps spin-off technology from the above concepts, is the development of extremely high-speed civilian and military vehicles designed for sustained flight in the range of Mach 4–25. At the high end of this anticipated air-breathing flight corridor, sustained orbital flight at Mach 25 is now routine. At the low end, the speed record for air-breathing vehicles stands at Mach 5.2, held by a ramjet-powered Martin Marietta ASALM missile that disobeyed a fuel shut-down signal. The cruise application, specifically for Mach 4–7, is the focused topic of this paper. The purpose in addressing this application separately is that there are technologies that are specific to Mach 4–7 cruise. There are also technologies that are common to cruise and other hypersonic missions. These are discussed in this paper. The paper offers an in-depth investigation of the most pertinent technology issues associated with hypersonic cruise and also addresses issues associated with one class of vehicles that is fundamentally suited for hypersonic cruise waveriders. A summary of the status of waverider technology for air-breathing missions is provided so that the extremely important technologies that must be developed for the benefit of the entire hypersonic vehicle development community are stressed with a perspective of applicability to real missions. Also, some of the technologies for waveriders are actually specific to waveriders, and must be addressed in the context of a waverider discussion. Because air-breathing hypersonic vehicles are multidisciplinary systems, brief discussions about the technical areas that impact the design of such vehicles are presented.

Mach 4–7 is an attractive segment of hypersonics as it offers a combination of very high-speed capability and use of relatively conventional technologies. This range of speeds offers dramatic reductions in travel time compared to subsonic or even supersonic speeds as shown in Fig. 1. This range of speeds may also be very competitive (depending on mission) with higher speeds of Mach 8 to 12 over distances up to 12,000 nmi (or half the way around the earth). Such speed capability has a number of useful applications including first stage of a two-stage-to-orbit vehicle, interceptor, recce, and transports.

Although the need for high-speed travel has remained roughly constant over time (perhaps increasing with the advent of integrated global socio-economic ties), the availability or maturity of technologies for the Mach 4 to 7 range has been progressing. In the past few years several key enabling technologies have matured to significant levels. These technologies include high-temperature hydrocarbon fuels, high-temperature materials, practical combined cycle engines (e.g., turboramjets and scramjets), and highly efficient vehicle/aerodynamic shapes.

One element of the latter, which is a key driver in the overall concept of a Mach 4 to 7 vehicle, is the advent of modern efficient waverider concepts. These concepts have the potential of excellent levels of performance in at least three key areas of L/D, volumetric efficiency, and stability and control. Although the shape of candidate Mach 4 to 7 waverider vehicle concepts are relatively simple, they are nonetheless the result of extensive analytical optimizations involving highly nonlinear relationships. These concepts have only recently matured as a result of advances in (1) analytical techniques that account for viscous effects on rather complex aerodynamic shapes, (2) computational resources (e.g., low cost workstations), (3) efficient linking of CAD and analytical systems, (4) recent subsonic, supersonic and hypersonic wind-tunnel tests of basic nonintegrated cone-derived shapes, and (5) propulsion integration technologies that apply to candidate waverider shapes. As a result of the aforementioned factors and technical progress to date, the viability of near-term development of a Mach 4 to 7 waverider vehicle appears to be quite high. Achievement of this, however, is contingent upon continued successful research and development in several pertinent areas.

Hypersonic vehicles will operate at flight conditions very different from those experienced by subsonic or low supersonic vehicles. Our experience with wind tunnel facilities, computational capacity, and flight research has provided the framework for the low speed area. This is not the case for air-breathing hypersonic flight, where verification and development through experiment will not be possible in ground facilities, current or in the foreseeable future. The problems of hypersonic flight are primarily associated with the high stagnation temperatures/enthalpies associated with very high speeds. These higher temperatures result in high heat transfer to the vehicles, changes in the gas characteristics around the vehicles, and changes in the chemical constituents of air, which can directly affect the classical combustion phenomena. For air-breathing hypersonic vehicles the severe operational environment, the need totally or partially to integrate the propulsion system with the airframe, the ultimate disciplinary coupling of the vehicle subsystems, and the long residence times in an environment at high levels of aerodynamic heating and dynamic pressure introduce technical and sociological problems that will be with us for a long time to come. It will be seen in

Downloaded 02 Jun 2010 to 171.66.16.122. Redistribution subject to ASME license or copyright; see http://www.asme.org/terms/Terms_Use.cfm

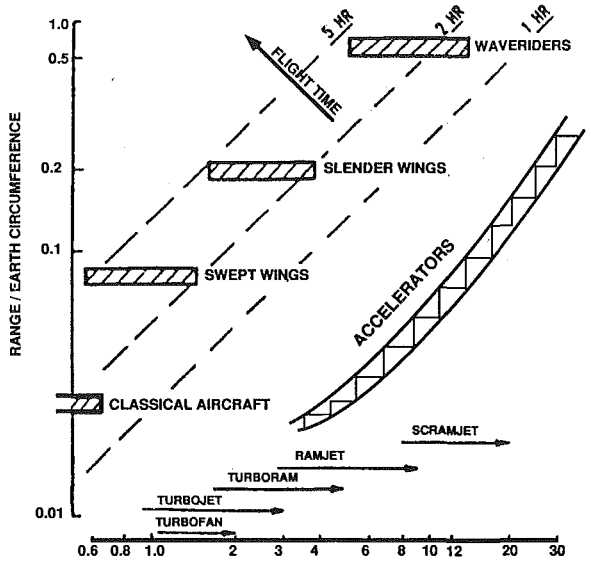


Fig. 2 Classification of aircraft shapes and engine cycles

this paper that in the Mach 4–7 range most of the needed technologies are conventional or near maturity making applications in this range short-term.

II Projected Applications

Kuchemann [4] classifies the progression of cruising aircraft configurations in terms of: classical straight wing aircraft, swept wings, slender wings, and waverider aircraft. His classification is based on a sound interpretation of the Breguet range equation. This classification of aircraft shapes is shown in Fig. 2 [5]. The progression of optimum "cruising" engines as a function of flight speed is also shown. For classical and swept-wing aircraft, the means for providing volume, lift, propulsion, and control are distinct; they do not typically interact. As flight speed increases, the situation changes dramatically, leading to a completely different aircraft design philosophy. Many examples of classical, swept, and slender wing aircraft already exist. For the waverider class, flat-top waverider principles were used in the design of the half-million pound XB-70 Valkyrie. This aircraft achieved an L/D of about 7 at Mach 3 in test flights in the mid-1960s. The XB-70 program demonstrated the high L/D potential and the practical applicability of waverider concepts to full-scale cruise aircraft.

With the rekindled interest in hypersonics, a large spectrum of military and civilian applications of both hydrogen-fueled and hydrocarbon-fueled air-breathing aircraft are being considered. Some of these applications are accelerator/interceptor aircraft, advanced reconnaissance aircraft, strategic cruise aircraft and missiles, highly maneuverable interceptor aircraft and missiles, long-range hypersonic hydrogen-fueled commercial transports, single-stage to orbit vehicles (SSTO), and the first stage of two-stage-to-orbit vehicles (TSTO). Detailed studies of possible missions for Mach 4–7 aircraft have been presented in many references (e.g., [6]).

As previously indicated, the primary applications for hypersonic air-breathing propulsion include single-stage-to-orbit (SSTO), air-breathing launch vehicles, long-range cruise vehicles, and hypersonic missiles. While many of the research topics associated with these missions are similar, some very fundamental differences exist. The SSTO mission is an acceleration-type mission, which covers a very wide Mach number range, requiring a large movement of variable geometry to accommodate low speed, ramjet, and scramjet cycles in the same engine hardware. A turboaccelerator as a low-speed accelerator option affects the nature of the variable geometry

Table 1 Requirements and drivers for cruise and accelerator (SSTO) vehicles

Cruiser	Accelerator
• Mach number to 8	• Mach numbers to orbital speeds
• Lift-to-drag ratio (wave drag reduction/trim drag/thrust vectoring)	• Performance across entire Mach range.
• Fuel fraction (volumetric efficiency)	• Thrust minus drag
• Isp	• Fuel fraction (volumetric efficiency)
• Compression process not as critical	• Isp
• Aerodynamic efficiency critical. Specific fuel consumption (SFC) very important	• Inlet capture area high (i.e. mass capture per unit drag)
• Design optimized for cruise Mach number	• Aerodynamic efficiency not critical. (T-D) is critical.
• Inlet capture area low to moderate	• Only hydrogen fuel acceptable - slush hydrogen for higher density
• Endothermic hydrocarbon fuels.	• Heat load critical - transient. Very high peak heating
• Large time integrated heat load	• Fineness ratio not as critical. Vehicle may operate at significant angles of attack
• Large fineness ratio , significant aeroelasticity problems	• New, high specific strength materials are needed with active cooling
• From a thermal management standpoint, present materials adequate (i.e. hot integral structure) but vehicle may be heavy.	• High Mach engine operation critical/ essentially unknown
• Fatigue/ multiple re-use/cyclical reliability	• Air-breathing limitations at extremely high Mach number/high altitude combinations may force the use of rocket propulsion or LOX augmentation to achieve orbit

requirement and perhaps suggests an over/under turbojet/scramjet propulsion system similar to that which might be employed in a long-range cruise vehicle. The SSTO mission also introduces unique problems at high Mach numbers, which include forebody/inlet and viscous interactions as well as nozzle frozen chemistry effects. The long-range cruise missions share the variable geometry requirements of the SSTO mission but without the complexity of very high Mach number limitations. However, high aerodynamic and propulsion efficiencies are required at cruise Mach numbers, leading to different solutions to the aerodynamic shape (such as waverider configurations) and the propulsion/aircraft integration. In addition, smaller vehicles designed for interceptor missions may require dense hydrocarbon fuels and thus share fuels and combustor research topics with hypersonic missiles. If it uses rocket boost to hypersonic speeds, the missile mission provides a potential propulsion system simplification by allowing a near point design scramjet engine. The resulting fixed-geometry design allows more geometric freedom, making square-to-circular engine designs possible, which would improve structural efficiency. A focus on SSTO includes most research topics such as variable geometry requirements, large integrated forebody and aftbody surfaces, and high Mach number inlet viscous and nozzle chemistry effects. Low-speed geometry problems include turbojet/scramjet installations typical of cruise vehicles if low-speed accelerator cycles are expanded to include turbojets. A topic not covered by SSTO research, except possibly by technology transfer, is integrated propulsion systems for high efficiency cruise at speeds of Mach 4–8, which may use hydrocarbon (possibly endothermic) fuels. This will be the focus of this paper. We will explore the status of thermal management systems and detailed structural analysis capability, the readiness of endothermic fuels for these applications, the degree or level to which air-frame-propulsion integration should be pushed, and also outline some of the major differences between cruise and SSTO aircraft. Accelerators are essentially driven by thrust minus drag, Isp, fuel fraction, and efficient flight for Mach 0–25. Cruise vehicles are driven by lift-to-drag ratio, Isp, volumetric efficiency, and a design optimized for the cruise Mach number. Some of these requirements and drivers for cruise and accelerators are presented in Table 1. It should be emphasized that major shortcomings in ground-test capability exist for both missions.

For turboramjet systems questions concerning whether tandem or over/under arrangements are optimum need to be resolved in addition to fuel issues. Aerodynamic design of inlets, nozzles, and the thermal analysis of these components will be a major activity. For advanced hypersonic airplane configurations, the external geometry is highly three dimensional and the flowfields possess strong complex wave systems (Fig. 3). The flows are dominated by viscous effects; shock/

Downloaded 02 Jun 2010 to 171.66.16.122. Redistribution subject to ASME license or copyright; see http://www.asme.org/terms/Terms_Use.cfm

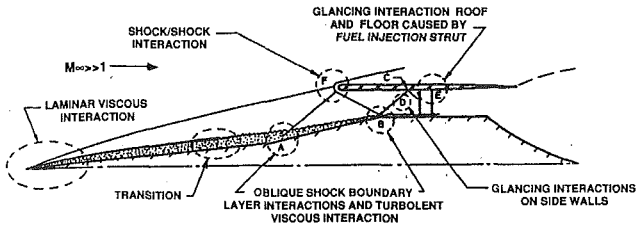


Fig. 3 Regions of shock-wave boundary-layer interaction

boundary layer interactions occur; the boundary layers will be laminar, transitional, and turbulent. For vehicles with air-breathing propulsion, the external and propulsion system flowfields are strongly coupled. Also, real-gas effects may affect the combustor and nozzle flows and, above about Mach 10, the forebody flowfield. A key feature of any hypersonic flight vehicle is that its technology and the methodologies employed are *specific* to the application or mission. Familiar examples, even though they are supersonic examples, are the F-15, the Concorde, and the SR-71. All are supersonic aircraft but their shapes are different because of their different missions and operational requirements. This configuration-mission coupling will be even more pronounced for hypersonic aircraft. This feature for the "confined flowfield configuration (waverider)," which is considered best-suited to a high-speed cruise mission, is addressed further in the following sections.

III What Are Waveriders?

A waverider is a supersonic or hypersonic vehicle that has an attached shock all along its leading edge. Because of this, the vehicle appears to be riding on top of its shock wave—hence the term waverider. Since the shock wave is attached at the leading edge in the cruise condition the upper and lower surfaces have independent flowfields and thus can be designed separately. This is in contrast to a more conventional hypersonic vehicle, where the shock wave is usually detached from the leading edge. The aerodynamic advantage of the waverider is that the high pressure behind the shock wave under the vehicle does not "leak" around the leading edge to the top surface; the flowfield over the bottom surface is contained, and the high pressure is preserved.

Waveriders are generated from known flowfields established by basic shapes, such as wedges, cones and power-law bodies, different from that of the waverider itself. For example, the waverider concept was first introduced by Nonweiler [7] in 1959, who generated a caret-shaped waverider from the two-dimensional flowfield behind a planar oblique shock wave associated with a wedge. Cone-derived waveriders including viscous effects were analyzed in [8, 9], and a generalized approach based on arbitrary three-dimensional shocks is outlined in [10]. The essence of the idea is that an inverse procedure could be used in a straightforward way to deduce nonlinear large-disturbance supersonic and hypersonic flowfields, and the relatively complex three-dimensional finite-span configurations from which they arise. It offered prospects for rational design in this strongly nonlinear regime by using a method giving configurations with exactly predictable properties developed from use of basic simple known flowfields. Excellent and authoritative surveys of waverider research have been given by Townend [11], Roe [12], and Schindel [13].

The recent "1st International Symposium on Hypersonic Waveriders" [14] provided many excellent papers. Results of the symposium are also summarized and assessed in [15]. Development of waverider configurations with anhedral/dihedral, advances in synergistic propulsion-airframe integration methodology, waveriders with high volumetric efficiency, and ingenious extensions of the inverse design method were a few of the significant results presented. Procedures to alleviate the leading edge heating problem without incurring lift and drag penalties were outlined. *The progress noted at the symposium indicates that an air-breathing, passively cooled waverider vehicle using hydrocarbon fuel could be built within a decade.* This could be a small cruise vehicle operating in the Mach 4–7 range at an altitude of around 100 kft. It would be used as a flight test vehicle. Multidisciplinary optimization of such a vehicle will still be a challenge, though. The required technologies, however, are relatively conventional.

Past criticisms levied against waveriders—alleged low volumetric efficiency, lack of engine/airframe integration studies, poor off-design performance, poor take-off and landing capability—were shown to be unfounded. With this in mind, the following section addresses the technologies associated with air-breathing hypersonic waverider development, and also addresses several of the key technology issues related to almost all air-breathing hypersonic vehicles.

IV Mach 4–7 Waverider Technologies

As indicated earlier in Section II, Kuchemann [4] describes how air-breathing aircraft can be classified into three categories according to their shape: wing-body (or swept), slender-wing, and waverider aircraft. An understanding of one class does not necessarily allow one to design an effective vehicle in another. In this section, the potential for waverider aircraft in the Mach 4–7 range is briefly examined. Development of operational aircraft capable of extended and efficient operation above Mach 4 will require a substantial leap in aerodynamic design philosophy and concepts, not a mere evolutionary progression from the supersonic cruise aircraft which have been evolving over the past four decades. The waverider is a true aircraft concept which satisfies this need. It offers the methodology for rational design in this strongly nonlinear regime (hypersonic) by using a method giving configurations with exactly predictable properties developed from use of basic simple known flowfields. Also, the means for producing lift, volume and propulsion are highly integrated. Some of the advantages of the waverider class are [15]:

- No lateral flow spillage
  - Attached leading edge shock
- Volume generates all-positive lift
- Clean blended shapes produce low drag (i.e., efficient lift)
- Balance achieved between viscous and inviscid losses
  - Product of waverider optimization code
- Synergistic propulsion integration
  - Forebody precompression of inlet flow
  - Natural base area for nozzle integration

Several significant technologies pertinent to the Mach 4–7 range are currently being pursued outside of the ongoing SSTO and TSTO programs, including turbomachinery-based combined-cycle systems, hydrocarbon fuels (possibly endothermic), advanced aerodynamic concepts, advanced analytical methods, thermal management systems, certain high-temperature materials, and vehicle/pilot interface systems. Applications under consideration include long-range cruise vehicles, missiles, interceptors, and the first stage of a two-stage-to-orbit mission. These are very different missions, which will lead to significantly different vehicles.

For waveriders to become viable aircraft for these applications, certain challenges must be met. Some key challenges are summarized below:

- Using volume efficiently
  - Volumetric efficiency
  - Conformal tankage
- Structural efficiency
  - Large wetted area and compound curves
  - Can be simplified without reducing performance

Downloaded 02 Jun 2010 to 171.66.16.122. Redistribution subject to ASME license or copyright; see http://www.asme.org/terms/Terms_Use.cfm

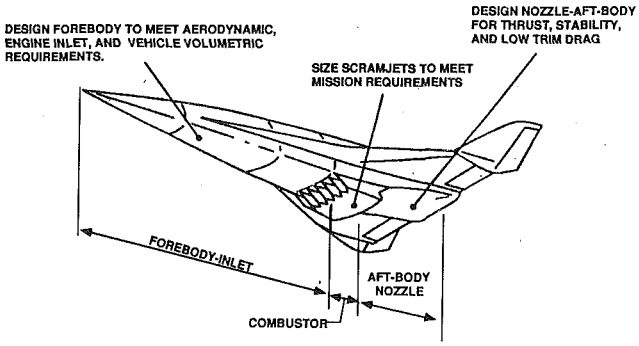


Fig. 4 Design features for efficient engine airframe integration

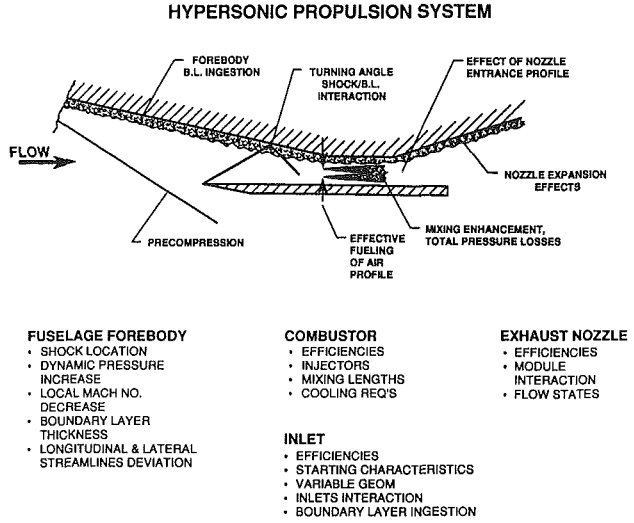


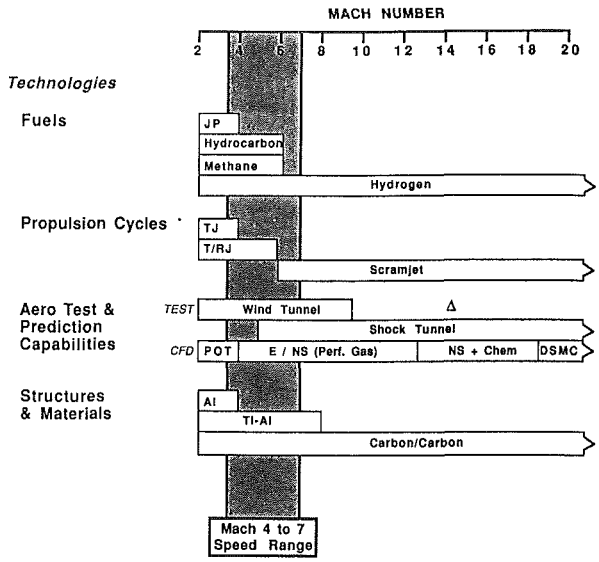
Fig. 5 Scramjet engine technical issues

- Propulsion integration
  - Propulsion interactions
  - Combined aeropropulsion optimization
- Stability and control
- Transonic drag
  - Synergistic low and high-speed nozzle design
  - External burning
- Multidisciplinary optimization

Of these, propulsion is a major enabling technology for Mach 4–7 vehicles. Various combined-cycle systems have been studied and will continue to be studied and developed for this speed range [5]. Subjects of study include engine cycles, fuels, thermal management, and propulsion integration. The combination of a turbojet and ramjet appears a prime candidate for the Mach 4–6 range, with operation above Mach 6 probably requiring a scramjet. The development of hydrocarbon-fueled scramjet technologies with dual mode combustor ramjet/scramjet engine cycles have allowed consideration of high-speed hydrocarbon fueled vehicles. Also, work on endothermic hydrocarbon fuels has shown potential for extending the heat sink capacity of these fuels.

Propulsion system integration is another key challenge. This includes the design and functional interaction of the inlet, engine, nozzle, and related airframe components such as the forebody. The most fundamental aspect of this area is whether the propulsion system is mounted as a distinct module or it is highly integrated with the airframe. Figures 4 and 5 capture the basic elements of a hypersonic air-breathing propulsion system and emphasize that the propulsion system is an integral part of the vehicle, not just an add-on package.

Table 2 Technologies applicable to hypersonic Mach range



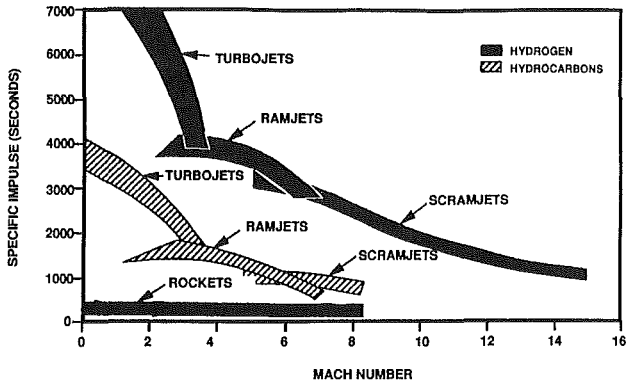


Fig. 6 Specific impulse for various propulsion devices

The Mach 4–7 range, the area of primary interest, offers significant speed advantages over supersonic speeds with only a modest increase in technology requirements. Relevant technologies are relatively conventional and lower cost compared to technology requirements for higher speeds. Table 2 summarizes some of the technologies applicable to the Mach 4–7 range of interest. It is intended to develop the waverider using these technologies and tools.

IV.1 Air-Breathing Propulsion. The potential performance of conventional engine cycles using hydrogen fuel is shown in Fig. 6. The corresponding performance for hydrocarbon fuels is also shown. As flight speed increases, the turbo-accelerator engine class is supplanted first by the subsonic combustion ramjet and secondly by the supersonic combustion ramjet. Consequently, for a hypersonic flight vehicle operating at a maximum speed above Mach 7, a multimode propulsion system is required. Given the limitations of materials, such an engine system might operate as a turbo-accelerator to speeds of the order of Mach 4, then transition to subsonic ramjet operation to about Mach 6, and then operate as a supersonic combustion engine for speeds to and above Mach 7. Figure 6 offers a simple comparison of various engine cycles based on fuel specific impulse (I_{sp}) *and is therefore appropriate to assess cruise flight performance where the Breguet equation is used to compare ranges*. However, as noted in [5], for acceleration missions the performance of an engine must be compared on

Downloaded 02 Jun 2010 to 171.66.16.122. Redistribution subject to ASME license or copyright; see http://www.asme.org/terms/Terms_Use.cfm

the basis of both its specific impulse and its corresponding thrust-to-weight ratio.

Scramjet propulsion is one of the driving technologies that must be developed to make the hypersonic air-breather a reality. Encouraging results have been obtained to date through both experimental and computational efforts. However, scramjet-related test capability has been constrained by a combination of available power, facility size, structural and thermal limits of hardware, and the few practical techniques for heating test gases to the high temperature required for high-speed flight simulation. To prove scramjet operability and performance, high Mach number data obtained in facilities with reasonable test durations in relatively clean, undissociated test flows, and large scales is required. Tests with vitiated air must consider the effects of vitiation on inlet aerodynamics and reaction kinetics in the combustor and thrust nozzle. Despite these limitations, current programs have advanced the state of scramjet feasibility to the point where a Mach 4–7 scramjet engine can be realized with acceptable risk.

Various combined-cycle engines have been studied as potential candidates for use in the Mach 4–7 regime [5]. These systems are based on hydrocarbon fuels or a combination of hydrocarbon and hydrogen fuel. The dual-mode turboramjet appears to be the engine of choice for hypersonic vehicles in the flight regime. Fuel heat sink capacity and ramburner temperature issues indicate that a switch to the scramjet mode at around Mach 6 is desirable. The storability of hydrocarbon fuels, the advances being made with endothermics, and the existing logistics infrastructure make these fuels essentially the only choice up to about Mach 6. The volumetric inefficiency of hydrogen makes it an unlikely choice for hypersonic cruise aircraft in the Mach 4–6 range. However, hydrogen is still an excellent candidate for Mach 6–8 scramjets because of the heat sink capacity and the very high values of heat of combustion.

The mechanical packaging of the turbojet/fan and ramjet engines essentially takes on one of three forms. These configurations are referred to as "the over-and-under, the wrap-around, and the tandem," depending upon the method of integration of the core turbomachinery and the ramjet flowpaths [6, 16a]. Each has advantages and disadvantages. The actual selection of a particular arrangement depends on a number of important design issues, such as propulsion-airframe integration (in particular the degree to which the integration should be taken). Trade studies are currently being pursued within programs by the Air Force and NASA Lewis. Candidate existing turbojet engines have been identified for the Mach 4–7 application. The turbojet's weight becomes a liability during operation of the ramjet; hence, future investments should be made to develop a more advanced lightweight turbomachine.

Cooling a Mach 4–7 hypersonic aircraft is a key technical challenge. Analyses and development of fuel/thermal management systems for such hypersonic vehicles have been under way for some time. Excellent research is progressing in this area, with significant systems simulation for representative trajectories. The recent detailed work by Bergholz and Hitch [16a] and Petley [16b] for example, illustrate the integrated nature of thermal balance for these vehicles. For the waveriders under consideration, the airframe would most likely be built primarily with hot structures. Since these vehicles have large wetted surface area, the thermal management problem may take on a different dimension if extensive areas have to be actively cooled. Research efforts for advanced fuels and heat exchangers are continuing.

IV.2 Aero/Aerothermodynamics. Some of the major phenomena associated with waveriders include:

- Airframe/propulsion integration
- Aerodynamic heating, especially leading edges and nose
- Viscous interaction effects
- High altitude effects (Knudsen effects)
- Off-design performance
- Stability and control, etc.

A database must be developed and methods must be established for the full integration of air-breathing propulsion systems into super/hypersonic vehicles. Current programs are conducting aerothermodynamics research in the definition of the forebody flowfield and boundary layer development, *three-dimensional inlet design* and inlet location and angle-of-attack effects, nozzle exhaust flowfield, afterburning, thrust vector changes, and nonaxisymmetric nozzle effects on the vehicle afterbody. The relationship between airframe/propulsion integration effects and the stability and control and performance of such vehicles is a primary product of this research. Wind tunnel simulation techniques, powered and unpowered cold gas test techniques, and validated or proven CFD results will be used in developing ground-to-flight scaling procedures.

Ongoing research in the areas of boundary layer transition physics and modeling, turbulence physics and modeling, real gas effects, and rarefied flows will have applications to waverider aircraft. Boundary layer transition strongly dominates the design of a scramjet engine inlet, affects the overall drag from all vehicle components, influences the choice and selection of materials, affects combustor mixing efficiency, controls the heat loads a vehicle must sustain, and may determine overall mission success or failure. The calculation and prediction of this condition at hypersonic speeds are currently based on empirical correlations that use existing data and the wide safety margins required force excessive vehicle weight and performance compromises. These correlations cannot be generalized in any meaningful way. A sustained effort is necessary to develop a general design code formulation for boundary layer transition and high-speed mixing phenomena. This requires the "quiet tunnels" capabilities, major efforts in theoretical studies, significant advances in nonintrusive diagnostic instrumentation, and the conduct of several carefully constructed flight research experiments.

Methods for the control of forebody boundary layer flows are currently being studied. This includes especially viscous induced crossflow effects. It is well known that hypersonic boundary layers can be thick, and represent a substantial fraction of the shock layer that exists between a hypersonic shock and the generating surface. Because there is no apparent means to bleed off the boundary layer that will form on the surface of a hypersonic vehicle, a hypersonic engine system must be designed to operate with this thick incoming boundary layer. The control of the boundary layer thickness, and whether the boundary layer is laminar or turbulent, will have a profound impact on the performance of a hypersonic engine, especially under varying flight conditions. Another boundary layer issue is limiting the boundary layer displacement thickness. This is important not only for providing as uniform an inlet flowfield as possible to the engine, but also to avoid undesirable coupling between vehicle attitude and engine performance. Because the hypersonic boundary layer thickness scales in inverse proportion to the surface angle of obliquity, changes in angle of attack can translate into unity-order changes in ingested mass flow, and therefore thrust, if the boundary layer approaching the engine is thick.

Another improvement to inlet flowfield boundary layer stratification can be sought by limiting crossflow and three-dimensional boundary layer effects. One of the problems observed in computational solutions over proposed hypersonic vehicle configurations is a flow leakage from the upper surface down to the lower surface, leading to dramatic thickening of the forebody boundary layer. Elimination of such leakage is a characteristic of the waverider design. In addition, the generally flat undersurfaces of the waverider should further limit undesirable three-dimensional thickening of the forebody boundary layer. Improvements in boundary layer displacement

Downloaded 02 Jun 2010 to 171.66.16.122. Redistribution subject to ASME license or copyright; see http://www.asme.org/terms/Terms_Use.cfm

thickness and flowfield stratification should therefore be realized with a waverider configuration, and this should be a principal area of investigation. The boundary layer problem described above is not only significant for propulsion considerations, it is important in determining the pressure distribution over a waverider and optimizing its configuration. Since a laminar boundary layer grows as the free-stream Mach number squared, the boundary layer thicknesses can be very large on a hypersonic vehicle flying at high speeds at high altitudes. This in turn leads to massive viscous interaction with the external inviscid flowfield, which markedly increases the pressure over the surface near the leading edge, and results in an increase in skin friction and heat transfer. These thick boundary layers also change the effective geometry of the configuration by adding to its thickness. Viscous interaction effects can be particularly important on slender vehicles, of which waveriders are included. Viscous interaction effects have recently been studied [17].

Previously, for missiles and entry vehicles, the structure could attain very high temperatures but, since the rate of transfer to the interior is usually slow, payloads and crew quarters never attain high temperatures before the mission is over. However, waveriders may operate in a severe heating environment for relatively long durations, providing adequate time for interior temperatures to reach specific design limits. Aerodynamic heating to leading edges, nose region or surface area over a critical component is also a very important design consideration. Typically, stagnation point heating is the most critical of this type and is often easier to calculate than heating to other portions of the vehicle. For waveriders, critical internal components will most likely be close to a hot vehicle skin at many locations on the vehicle and the critical heating areas will be configuration dependent.

Leading edge heating protection of waveriders is an enabling technology that is currently being addressed. If, at the design condition, the shock wave remains attached to the sharp swept leading edge on the compression surface, then disturbances cannot propagate upstream of this shock. Thus the upper and lower surfaces of the waverider will be independent of each other and each may be designed separately. This is a basic property of waveriders. Some blunting of leading edges will, however, be required to avoid excessive local temperatures. How sharp the leading edge has to be to satisfy the above "independence" property has not been established. Previous work by Squire [18] on this subject showed that for delta wings, substantial lack of sensitivity existed. Even when the shock standoff distance was appreciable this independence persisted. Lead edge bluntness effects on caret wings were considered by Collingbourne and Peckham [19]. Estimates were made of the simultaneous decrease in lift and increase in drag for given nose bluntness. Their conclusions emphasize the importance of designing for the smallest possible leading edge radii.

From a practical point of view, the leading edge must be able to withstand large aerodynamic and aerothermal loads. Thus the structure must be designed to have the desired mechanical strength and also be able to cope with the aerodynamic heating in such a way that the lead edge geometry is preserved, the shock remains attached, and the wing structure is protected from excessive heat. Note that the waverider is a vehicle for which the integrity of its geometry determines aerodynamic performance so that the use of conventional ablative coatings are ruled out. These would lead to significant changes in shape of the leading edge with subsequent adverse effects on performance. Various passive and active methods of cooling sharp leading edges have been proposed. Carbon–carbon composite materials appear to be a good choice. A passive cooling method was proposed by Nonweiler [20a]. In this method, the wing structure is capped with a sharp leading edge made of a highly conductive material and the heat is radiated away from both sides of the cap. Preliminary estimates and experiments have confirmed the feasibility of this method. A practical design based on this method needs to be developed and evaluated although previous analysis and experiment have verified its feasibility. A recent study [20b] also concludes that radiative cooling would be sufficient for the present applications.

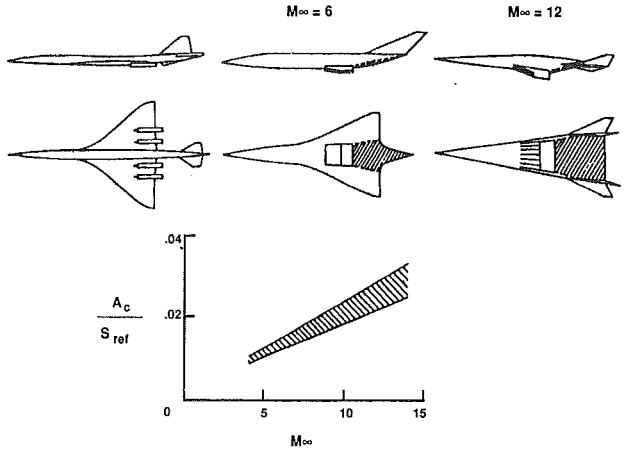


Fig. 7 Required inlet capture

IV.3 Airframe/Propulsion Integration. Propulsion/Airframe Integration (PAI) may be defined as that aspect of the design process that addresses external features that directly influence or are influenced by the propulsion system. For hypersonic air-breathing vehicles, designing the airframe separately from the engine is neither desirable nor simple, and the concept of aerodynamic efficiency needs a new meaning. In fact, part of the external surface of the vehicle may contribute solely to the creation of lift and bounding volume, while another part affects the airflow through the engine. Also, the jet exhaust may be deflected from the direction of flight and consequently will participate in the creation of both thrust and lift. The dependent variables in the aircraft design process influenced by PAI are aerodynamic drag, lift, propulsive thrust, volume, structural weight, and stability and control. The independent variables that influence the above performance parameters include forebody design, inlet design, engine module location, nozzle design, and the aircraft external configurational shape. Other issues that must be addressed include controls effectiveness, forebody-inlet interactions, inlet spillage effects, exhaust-plume interactions and boundary layer transition, which was discussed earlier.

The selection of the optimum airplane shape, in particular the lifting surfaces and the deflection of the reaction jet, reduces to the problem of finding the shapes corresponding to minimum fuel-flow rate and satisfying other necessary requirements in the desired flight regime. Propulsion-airframe integration is the dominant consideration. It appears that the state of the art in high Mach number vehicle integration is represented by the 25-year-old supersonic SR-71 design. Hence a void exists in the availability of hypersonic powered configuration data and also experimental and computational methods for evaluating installed vehicle performance.

A common feature of hypersonic aircraft is the necessity to integrate the propulsion system with the vehicle airframe carefully to obtain optimum overall performance. As shown in Fig. 7 [21], the size of the propulsion system relative to aircraft size increases rapidly with increasing flight Mach numbers, and the forces generated by the propulsion system become large when compared with aerodynamic forces. Mutual interactions between these large forces are advantageous when the propulsion system is properly integrated with the vehicle airframe. Thus, the engine-airframe integration process represents a major design challenge to maximize the performance

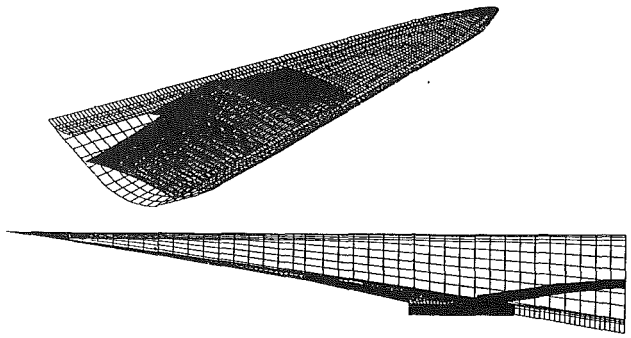
Downloaded 02 Jun 2010 to 171.66.16.122. Redistribution subject to ASME license or copyright; see http://www.asme.org/terms/Terms_Use.cfm

of hypersonic air-breathing vehicles. For hypersonic air-breathers, it becomes increasingly difficult to separate the airframe from the engine. A part of the external surface of the airplane may be associated only with the creation of lift force and bounding volume, while part will be associated with airflow through the engine. The jet exhaust, in general, may be deflected from the direction of flight, and consequently will participate in the creation of both thrust and lift.

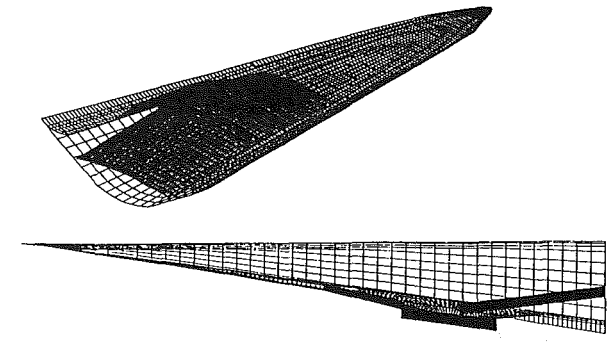
The highly integrated aircraft concepts depicted in Fig. 4 are attractive because they provide both maximum inlet capture area and maximum nozzle expansion area while maintaining minimum cowl drag. However, the full benefits of these concepts can only be realized when the vehicle propulsion system is properly integrated early in the design process. Interactive constraints that must be considered in the design of highly integrated hypersonic systems are shown in Fig. 4. The size and number of the engines must be sufficient to meet mission requirements. The scramjet inlet must be located within the forebody compression field to obtain maximum performance. An effective precompression tends to reduce the physical dimensions of the inlet. Reduction in inlet dimensions tends to reduce engine weight and cowl drag. If the precompressed flow at the inlet face can also be made uniform, the increased complexity in inlet design required for efficient operation in widely varying flows can also be alleviated. However, the available shock-layer capture area decreases with Mach number so that the inlet must capture most of the flow between the body and the bow shock across the entire fuselage span. The engine size and the flowfield requirements are not the only considerations necessary for a good forebody design. Aerodynamic (including boundary layer transition), structural, and internal volume requirements are other constraints that must be incorporated early in the design process to achieve an optimum configuration. Scramjet nozzle design, for example, is primarily governed by thrust and stability requirements. Thus, the location of the scramjet, orientation of the thrust vector, and the resulting trim penalties must be examined across the entire flight envelope. The strong interaction between the nozzle exhaust and the nonuniform flows surrounding the vehicle afterbody and external cowl must also be accounted for in the evaluation of nozzle performance.

This *integration and interaction* of the propulsion system, aerodynamics, aerodynamic heating, stability and control, materials and structures, fuels, thermal management, energy availability, missions, trajectories, etc., are unique and very important aspects of hypersonic vehicle design. This extremely interactive nature of air-breathing hypersonic vehicles requires a special in-depth multidisciplinary effort beyond typical "systems studies." It calls for development of new analytical tools whose validity and/or accuracy are critical. It also requires the development and application of optimization techniques to analyze large interacting systems with extreme uncertainties and disturbances. Work along these lines is being conducted in ongoing programs. Trajectory optimization is an example of an integration issue. It requires a trade-off between dynamic pressure requirements for propulsion and heating and pressure loads. Also, for vehicles designed specifically for cruise, the acceleration and deceleration phases of the cruise mission can be significant relative to the cruise phase. Optimization of the vehicle design must hence be based on total mission considerations rather than on cruising flight alone. Cross-discipline interactions, mostly nonlinear, will generally have to be included in the optimization scheme. More will be said about this later, as they pertain to Mach 4–7 waveriders.

Forebody performance is one of the big unknowns in the aerodynamics of the vehicle classes under consideration. Typical shapes produce complex and difficult to analyze flows whereas waveriders offer more predictable flows. As indicated earlier, most effective integrated design concepts use the forebody as part of the inlet compression surface. Although



Integrated waverider/scramjet configuration with cowl parallel to freestream. Perspective view (top). Side view (bottom).



Integrated M = 10 waverider/scramjet configuration with cowl carved from conical flowfield. Perspective view (top). Side view (bottom).

Fig. 8 Integrated waverider scramjet configurations

the geometric shape of the forebody may appear relatively simple, it will have a significant effect on vehicle aerodynamics, aerothermodynamic, and propulsive performance. The forebody must provide the desired mass flow to the inlet as well as minimize inlet flow distortion. Thus forebody shaping is a critical study area, as is the sensitivity of forebody performance to geometric changes. The problem is further complicated by the fact that the flowfields of practical interest for hypersonic aircraft design are predominantly three dimensional, but relatively few simple reference configurations and flowfields are available as either starting points or for purposes of comparison. However, the waverider class of vehicles provides the link between supersonic aircraft and spacecraft and may be used to make systematic studies of integrated designs. Propulsion-Airframe integration studies on waveriders are being conducted by several research institutions and in industry. At the University of Maryland, a novel forward-marching approach is used to develop inlets and nozzle as an integral part of the waverider generation process. In other words the engine and nozzle are not just add-ons after the fact. An example of the type of results obtainable with the Maryland code is shown in Fig. 8. At NASA Ames a research program has been initiated to investigate first, the aerothermal field, and second, the optimization of integrated waveriders [23]. Some preliminary results of temperature distributions and optimization are shown in Figs. 9 and 10.

Significant adverse ground effects occur during the takeoff maneuver for propulsion systems mounted on the bottom of the fuselage [24]. Current waverider designs may have this feature if the level of integration is pushed to the limit. With power off the usual increase in lift is observed as the ground plane is approached. With power on, however, the highly overexpanded nozzles create a venturi effect resulting in large losses in lift and changes in pitching moment. At high thrust levels, a strong suckdown effect could adversely affect takeoff performance. The magnitude of this effect can be ade-

Downloaded 02 Jun 2010 to 171.66.16.122. Redistribution subject to ASME license or copyright; see http://www.asme.org/terms/Terms_Use.cfm

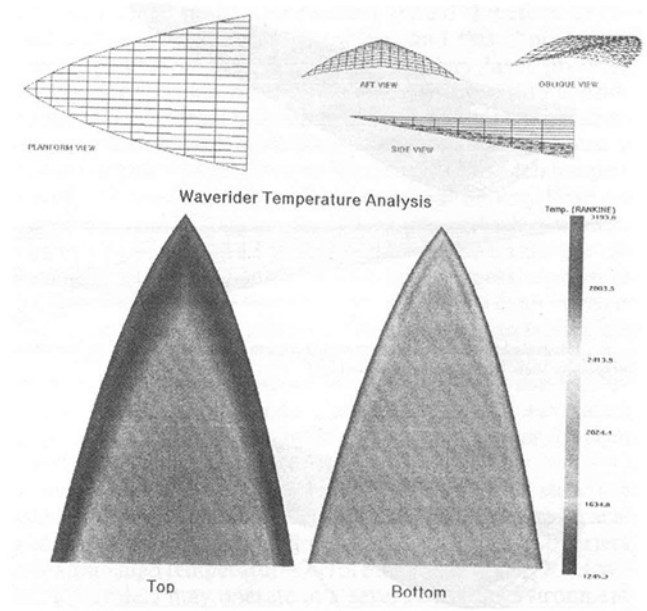


Fig. 9 Waverider optimization—temperature analysis

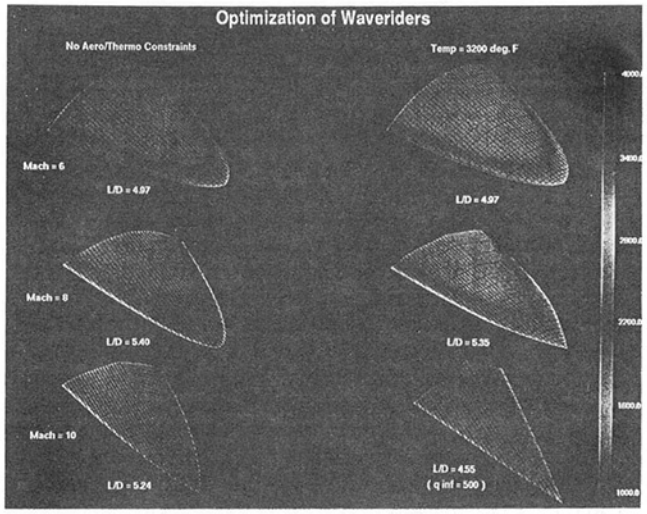


Fig. 10 Optimized waveriders

quately assessed experimentally for a given configuration; however, the experimental approach must include operating inlets to generate realistic values. Neither model nor facility sizes are serious limitations in this speed regime. The degree of exhaust simulation required to address this problem is unknown at this time. The ability to control or alleviate the adverse effects on a given configuration is nonexistent. Numerical techniques have not been successfully applied to build an empirical approach. Therefore, a reliable numerical approach coupled with a substantial parametric experimental program could be of tremendous value in eliminating this particular performance limiter. The influence of large overexpanded nozzles again becomes a dominant integration parameter at transonic speeds. The nozzles tend to separate quickly downstream of the combustor exit, creating a huge increase in base drag and potentially drastic changes in pitching moment, which compound the problem. It does not appear feasible to eliminate this effect with external nozzle contouring alone.

Installed performance is defined here as the integrated forces on a configuration with operating propulsion system. It is a complete vehicle value rather than the traditional propulsion estimate. An accurate quantitative estimate of this parameter (including off-design sensitivities across the speed range) is critical to the success of any air-breathing hypersonic vehicle. The maximum sensitivity and/or uncertainty in performance for hypersonic vehicles occurs at three sets of conditions, namely: (1) takeoff (and landing as well, if powered), (2) transonic ascent, and (3) hypersonic powered flight beyond Mach 5.

IV.4 Structures Materials/Structural Dynamics. Hypersonic vehicles demand unprecedented *structural mass fractions* under the most severe thermal and acoustic environments to meet all of the currently envisioned goals. To design such structures, advanced materials with high specific strength and stiffness, high-temperature capability, resistance to thermal shock and thermal cycling, compatibility with hydrogen and LOX, good thermal conductivity, ductility, and resistance to oxidation must be developed. They must be readily fabricated into complex shapes, and have good fatigue/fracture characteristics and known *and* predictable failure mechanisms. The loads used to design such structures must be known with exacting precision so every bit of structural weight saving can be extracted for the airframe and propulsion systems. Advanced instrumentation must be developed to measure temperature, high-frequency pressures, heat fluxes, and strains at extremely high temperatures. Advanced structural concepts that can be hot, insulated, or cooled depending on the structural application must be designed, fabricated, and tested to show viability for actual applications and to demonstrate all other disciplines required in the analysis, fabrication, and testing of such structures. Materials issues and availability for the SSTO class of vehicles have been discussed in [25].

Advanced high-temperature composites are required for lightweight hot structures for hypersonic vehicles. Thin-gage, light-alloy metal-matrix composites offer significant potential for reducing the weight of airframe and engine components that will operate at 600–1500°F on hypersonic vehicles. Research is required to develop these materials with high specific properties in thin gages; to develop processing and joining technology to enable fabrication of complex hot structural components; and to develop life prediction methodology to assure safety of flight. Similarly, carbon–carbon and ceramic-matrix composites are required for structural components that will operate at 1500–3000°F. Higher strengths in thin gages and improved damage tolerance are key technology needs for these materials. Extensive testing and analysis are required to establish the durability of materials and hot structures under the hostile service environment conditions expected for hypersonic flight vehicles.

Large regions of the airframe of advanced hypersonic vehicles will reach very high temperatures as a result of aerodynamic heating. Depending on the particular vehicle, mission, and location on the vehicle, these temperatures can exceed 3000°F. For temperatures below this level, carbon–carbon composites are candidate materials because of their desirable combination of low weight and high-temperature strength and modulus. They are attractive even at lower temperatures because of their engineering properties. At temperatures above about 1400°F even the most advanced engineering materials begin to decrease in specific strength and modulus relative to carbon–carbon composites.

Accurate loads are required if optimum weight structures are to be obtained. For hypersonic vehicles acoustic loads from the boundary layer as well as combustion and plume dynamics are design drivers, and little is known about such loads for hypersonic-speeds and scramjet propulsion systems. Local aerothermal loads are known to be design drivers from experience with such high speed vehicles as the YF-12, X-15, and shuttle. A data base for generic detailed areas such as cowl lips, wing-cove junctions, and deflected ramps/control sur-

Downloaded 02 Jun 2010 to 171.66.16.122. Redistribution subject to ASME license or copyright; see http://www.asme.org/terms/Terms_Use.cfm

faces is needed to provide the structural analyst a starting point for his design and for assessment and validation of CFD codes. In addition, validated codes for the structural response to such loads are required as well as test apparatus and techniques to validate proposed structural concepts. No data exist for fluctuating pressure loads associated with combustion, plume dynamics, or plume-boundary interaction at high Mach numbers. Validated prediction methods for high-frequency boundary layer loads, validated prediction methods for high frequency boundary layer loads, and validated integrated-flow-thermal-structural analysis capability are also needed.

Mach 4–7 cruise aircraft will be exposed to maximum temperatures of 1000°F to 1400°F for long durations at a time. Higher temperatures will occur in localized regions such as wing and cowl leading edges due to shock interaction phenomena. Hot structures concepts are adequate and will be used because they are relatively simple compared to actively and passively cooled structures. Although experience with hot airframe structures is limited, their use leads to lighter vehicles. The SR-71/YF-12 (to about 600°F) and the X-15 (to around 1200°F) are the only reusable vehicles that have flown with hot structures [26]. Carbon–carbon, ceramic, and ceramic-matrix structures are slowly emerging, constrained by material properties and fabrication techniques. Structural concepts and materials selection are mission dependent. As indicated in Table 2, the Mach 4–7 range shows a heavy reliance on advanced titanium alloys, which are commercially available to 1100°F, and also the promising titanium–aluminide intermetallics, which are a subject of much current development work. These are lower in density than the titanium alloys but possess a higher use temperature range from 1500°F to 1800°F.

For hypersonic airplanes, structural dynamic and aeroelastic areas of concern include vibration characteristics (with interactions between structure, control system, and fuel), propellant dynamics (fuel sloshing), lifting surface and panel flutter, control surface buzz, high intensity noise generated by engine and external aerodynamics, and so on. Details of some of these issues are outlined in [27]. The high speeds, elevated temperatures, and unconventional geometries and structural designs that are characteristic of hypersonic vehicles introduce considerable complexity compared with conventional aircraft. Figure 11 illustrates the effect of aerodynamic heating on flutter characteristics of a generic hypersonic vehicle. These calculations were based on the finite-element method and show that the frequencies were reduced by changes in material properties (decrease in stiffness), but were increased by thermal stress effects (increase in stiffness). Thus natural vibration characteristics are complicated by the fact that, for hypersonic configurations, the effects of aerodynamic heating on structural stiffness has to be considered. Furthermore, a hypersonic airplane may have a relatively high ratio of gross weight to empty weight because of the high fuel fraction. Thus the vibration characteristics may change considerably as fuel is consumed, leading to complications in the design of the flight control system. The possibility of very low structural weight fraction also implies significant flexibility in the vehicle structure. Elastic deformations of the structure produced by aerodynamic loading will affect the loading and thus change the aerodynamic stability derivatives of the airplane. These considerations are complicated by high temperature and thermal gradient effects on the structural stiffness. The design of the flight control system will be impacted. The influence of fuselage flexibility is illustrated in the vehicle vibrational mode shapes shown in Fig. 12 for a generic hypersonic shape. These calculations were performed for both carbon–carbon and titanium–aluminide structures [27]. Results for titanium–aluminide are presented in the figure. Frequencies ranged from 3 to 9 Hz. The dominant flutter mechanism found was a coalescence of modes 2 and 3, the fundamental wing-bending mode and a highly coupled wing-bending/second fuselage-bending mode, respectively. The

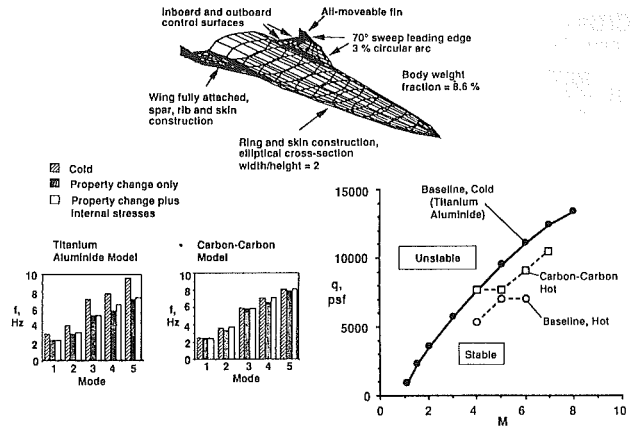


Fig. 11 Effects of aerodynamic heating on flutter

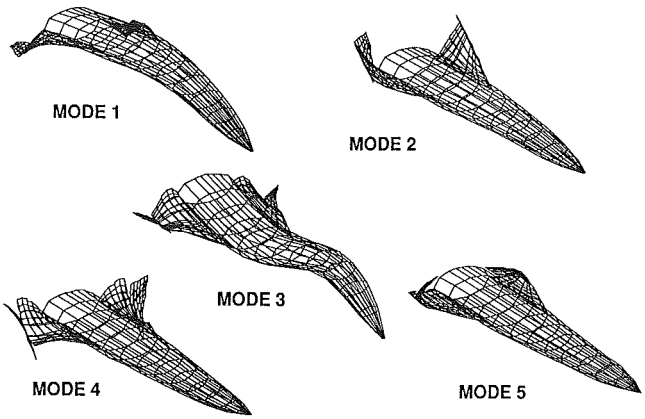
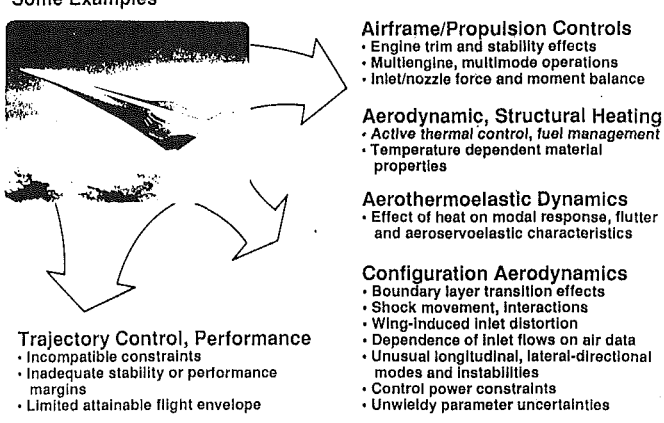


Fig. 12 Mode shapes of generic hypersonic configuration

visual appearance and overall character of these modes did not change with material and temperature. However, significant differences occur in both frequencies and amplitudes between hot and cold. The first and third elastic modes exhibit significant fuselage motion. The interaction of these mode shapes (especially the forebody) with the flow into the intakes, and hence overall propulsion system is only very recently being addressed.

IV.5 Flight Systems. Hypersonic vehicles will require unprecedented precision to maintain nominal trajectories and local flight conditions so that maximum performance can be achieved from the aero/propulsive system. Mission objectives will be threatened by atmospheric disturbances, modeling uncertainties, weak coupling between disciplines and nonexistent, off-nominal performance margins. Onboard flight systems will be required to solve these issues while providing the flexibility and safety for manned operations. The development of manned aerospacecraft will provide a whole new philosophy for flight qualifying and testing research vehicles. Flight system technologies will require significant research breakthroughs in understanding, approaches, algorithms, and equipment to enable the safe and accurate flight of aerospace vehicles. Current work in these areas is being conducted for the NASP program [28, 29]. This work appears directly applicable to the Mach 4–7 waverider. A flight test simulator for cruise aircraft in this range would be extremely useful. Current research areas for flight systems are: (1) multidisciplinary modeling/controls integration, (2) guidance, navigation, and trajectory optimization and (3) pilot-vehicle interfaces. Multidisciplinary modeling of hypersonic waveriders combined with advanced control theory will increase vehicle performance and reduce the likelihood

Downloaded 02 Jun 2010 to 171.66.16.122. Redistribution subject to ASME license or copyright; see http://www.asme.org/terms/Terms_Use.cfm



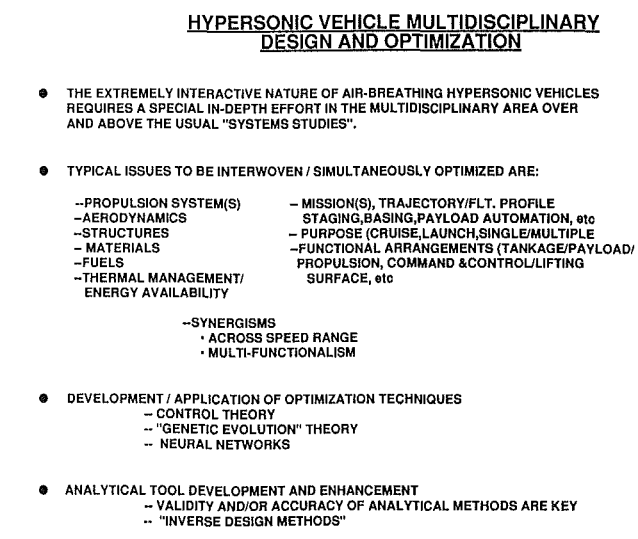


Fig. 13 Multidisciplinary design and optimization

of redesign after flight test. Disciplines that are closely linked and require control system solutions include: structural dynamics, aeroelasticity, flight mechanics, flying qualities, propulsion, and thermal balance. Design methodologies to simultaneously optimize performance of multiple, interacting control systems need development. Historically, piloted aerospacecraft have either had rapidly traversed hypersonic regimes or have been automatically controlled. Hence, appropriate design criteria for flying qualities do not exist. The desired information and/or display formats that would enable a pilot to fly effectively in hypersonic regimes have not been determined. Since direct view windows are especially a liability for hypersonic vehicles in cost, weight and effectiveness, alternative viewing schemes must be evaluated. Manned cockpit aids such as fault-diagnosing tools and replanners for accommodating failures and major disturbances are desired.

A unique and very strong aspect of hypersonic vehicle design is the integration and interaction of the propulsion system, aerodynamics, and aerodynamic heating, stability and control, and materials and structures. The technical problems faced by the designer are multidisciplinary to first order, so that their proper resolution requires the ability to integrate highly coupled and interacting elements in a fundamental and optimal fashion to achieve the desired performance. The degree of coupling intensifies with increasing Mach number. This is the real problem with hypersonic vehicle design. Obviously for some applications it will be necessary to have satisfactory low-speed, transonic, supersonic speed, and hypersonic cruise Mach number performance simultaneously built into the design. Figure 13 gives a summary of some of the more important cross-discipline interactions as well as a description of the multidisciplinary optimization issues. The optimization process is generally assumed to be numerical and methods must be available for analyzing forebody/inlet interactions, complete internal flows (inlet, combustor, and nozzle), and nozzle/aftbody interactions, etc. The validity and/or accuracy of analytical methods is the most important factor of the optimization process. There must be parametric sensitivities to achieve an optimum and the realism/accuracy in determining these sensitivities limits the degree of optimization. Therefore, demonstration of confidence in numerical methods (i.e., code calibration/validation) is a *critical* element of optimization and demonstration efforts should initially be designed and conducted for conditions of maximum sensitivity, rather than the areas of greatest physical uncertainty (the current overriding criterion of priority).

V Summary and Conclusions

The Mach 4–7 range offers significant speed advantages over supersonic speeds and requires only a modest increase in technological capability. Relevant technologies are relatively conventional with lower cost as compared to technology requirements for higher speeds. The author's assessment leads him to believe that an operational hydrocarbon-fueled Mach 4–7 cruise waverider airplane can be built within a decade using conventional materials. The major investment should be in propulsion/airframe integration. Operation beyond about Mach 6 will be in the scramjet mode to limit combustor temperatures. Development of a usable ramburner insulation will require increased attention. Procedures to alleviate the leading edge heating problem without incurring lift and drag penalties are available and will need to be extensively tested. Since the real problem of hypersonic vehicle design is the integration and interaction of the power plant, heat transfer, aerodynamics, stability and control and materials and structures, then multidisciplinary optimization will still be a challenge. If such a waverider aircraft can be successfully realized and demonstrated in flight, it will represent an extremely high return-on-investment for both fundamental and applied slender-body air-breathing hypersonics in addition to demonstrating long-duration hypersonic cruise.

Acknowledgments

The author would like to thank Mr. Paul Hagseth (General Dynamics, Ft. Worth, Texas) and Mr. Peter Kutschenreuter (General Electric, Cincinnati, Ohio) for useful suggestions concerning this paper. The help of Mr. Ed Nielsen (WJ Schafer Associates) is also gratefully acknowledged.

References

1 Kors, D. L., "Design Considerations for Combined Air-Breathing-Rocket Propulsion Systems," *Hypersonic Combined Cycle Propulsion*, AGARD CP No. 479, Paper No. 12, May–June 1990.

2 Beach, H. L., and Blankson, I. M., "Prospects for Future Hypersonic Air-Breathing Vehicles," presented at the 10th International Symposium on Air-Breathing Engines (ISABE), Nottingham, United Kingdom, Sept. 1991.

3 Beach, H. L., and Blankson, I. M., "Prospects for Future Hypersonic Air-Breathing Vehicles," AIAA Paper No. 91-5009, 1991.

4 Kuchemann, D., *The Aerodynamic Design of Aircraft*, Pergamon Press, NY, 1978.

5 Curran, E. T., Leingang, J. L., and Donaldson, W. A., "A Review of High Speed Propulsion Systems," presented at the Eighth International Symposium on Air-Breathing Engines, Cincinnati, OH, June 15–19, 1987.

6 Hagseth, P. E., and Beuerlein, D. L., "Mach 4–7 Vehicle Applications," presented at the USAF Hypersonics Conference, Washington, DC, 1990.

7 Nonweiler, T. R. F., "Aerodynamic Problems of Manned Space Vehicles," *Journal of the Royal Aeronautical Society*, Vol. 63, 1959, pp. 521–528.

8 Bowcutt, K. G., Anderson, J. D., Jr., and Capriotti, D. P., "Viscous Optimized Hypersonic Waveriders," AIAA Paper No. 87-0272, 1987.

Downloaded 02 Jun 2010 to 171.66.16.122. Redistribution subject to ASME license or copyright; see http://www.asme.org/terms/Terms_Use.cfm

9 Bowcutt, K. G., Anderson, J. D., Jr., and Capriotti, D. P., "Numerical Optimization of Conical Flow Waverider Including Detailed Viscous Effects," in: *Aerodynamics of Hypersonic Lifting Vehicles*, AGARD-CPP-428, Mar. 1987, pp. 27/1-27/23.

10 Sobieczky, H., et al., "Hypersonic Waverider Design From Given Shock Waves," *Proceedings of the 1st International Waverider Symposium*, University of Maryland, College Park, MD, Oct. 17-19, 1990.

11 Townend, L. H., "Research and Design for Lifting Reentry," *Progress in Aerospace Sciences*, Vol. 18, 1979, pp. 1-80.

12 Roe, P. L., "Theory of Waveriders," in: *Aerodynamic Problems of Hypersonic Vehicles*, K. Enkenhus, J. F. Wendt, and R. C. Pankhurst, eds., AGARD LS-42, 1972.

13 Schindel, L. H., "Tactical Missile Aerodynamics," *AIAA Progress in Astronautics and Aerodynamics*, Vol. 104, M. S. Hemsch and J. N. Nielsen, eds., AIAA, New York, 1986.

14 *Proceedings of the 1st International Waverider Symposium*, J. D. Anderson, Jr., M. J. Lewis, S. Corda, and I. M. Blankson, eds., University of Maryland, College Park, MD, Oct. 17-19, 1990.

15 Blankson, I. M., "Hypersonic Waveriders: State of the Concept," AIAA Paper No. 91-0529, 1991.

16a Bergholz, R. F., and Hitch, B. D., "Thermal Management Systems for High Mach Air-Breathing Propulsion," AIAA Paper No. 92-0515, 1992.

16b Petley, D., and Jones, S., "Thermal Management for a Mach 5 Cruise Aircraft Using Endothermic Fuel," AIAA/AHS/ASEE Paper No. 90-3284, 1990.

17 Chang, J., "A Study of Viscous Interaction Effects on Hypersonic Waveriders," NASA CR-189587, Jan. 1992.

18 Squire, L. C., "The Independence of Upper and Lower Wing Flows at Supersonic Speeds," *The Aeronautical Journal*, Oct. 1976, pp. 452-456.

19 Collingbourne, J. R., and Peckham, D. H., "The Lift and Drag Characteristics of Caret Wings at Mach Numbers between 5 and 10," ARC C.P. No. 930, Feb. 1966.

20a Nonweiler, T. R. F., "The Waverider Wing in Retrospect and Prospect: A Personalized View," *Proceedings of the 1st International Waverider Symposium*, University of Maryland, College Park, MD, Oct. 17-19, 1990.

20b Vanmol, D. O., and Anderson, J. D. Jr., "Heat Transfer Characteristics of Hypersonic Waveriders With Emphasis on Leading Edge Effects," NASA CR-189586.

21a Edwards, C. L. W., "A Forebody Design Technique for Highly-Integrated Bottom-Mounted Scramjets With Application to a Hypersonic Research Airplane," NASA TND-8369, Dec. 1976.

21b Small, W. J., Weidner, J. P., and Johnston, P. J., "Scramjet Nozzle Design and Analysis as Applied to a Highly Integrated Hypersonic Research Airplane," NASA TND-8334, 1976.

22 O'Neill, M. K. L., and Lewis, M. J., "Scramjet Integration on a Waverider," *Proceedings of the 1st International Waverider Symposium*, University of Maryland, College Park, MD, Oct. 17-19, 1990.

23 Kidwell, G., and Bowles, G., NASA Ames Research Center, Moffett Field, CA, Private Communication.

24 Whitehead, A., "NASP Aerodynamics," AIAA Paper No. 89-5013, 1989.

25 Ronald, T. M. F., "Materials for Hypersonic Engines," *Hypersonic Combined Cycle Propulsion*, AGARD-CP-479, Paper 36, Madrid, Spain, May-June 1990.

26 DeAngelis, V. M., "Summary of Hot Structures Workshop and Current Test Plans," presented at Section 27: Workshop on Correlation of Hot Structures Test Data With Analysis, NASA Ames-Dryden Flight Research Center, Nov. 15-17, 1988.

27 Cazier, F. W., Doggett, R. V., Ricketts, R. H., "Structural Dynamics and Aeroelastic Considerations for Hypersonic Vehicles," AIAA Paper No. 91-1255, 1991.

28 Morrell, F. R., NASA Langley Research Center, Hampton, VA, Private Communication.

29 Petersen, K. L., NASA Dryden Flight Research Facility, Edwards, CA, Private Communication.

Downloaded 02 Jun 2010 to 171.66.16.122. Redistribution subject to ASME license or copyright; see http://www.asme.org/terms/Terms_Use.cfm

Numerical Simulation of the Flow Field Around Supersonic Air-Intakes

G. Freskos[1]
CERFACS,
42 av. Coriolis,
31057 Toulouse, France

O. Penanhoat
SNECMA Villaroche Center,
77550 Moissy-Cramayel, France

The demand for efficiency in today's and in future civil aircraft is such that experimental studies alone do not suffice to optimize aircraft aerodynamics. In this context, much effort has been spent in the past decade to develop numerical methods capable of reproducing the phenomena that occur in the engine flow field. This paper presents some studies in Computational Fluid Dynamics related to supersonic inlets. Two approaches are considered. First, there is a need for a code capable of calculating in a cost-efficient way the entire flow field around a two-dimensional or three-dimensional inlet, e.g., to perform parametric studies. To this effect, a computing method based on grid construction by mesh generator dedicated to inlet shapes and on the discretization of the unsteady Euler equations with an explicit upwind scheme was developed. The treatment of complex geometries led us to adopt a multiblock grid approach. Therefore particular attention was paid to the treatment of the boundary conditions between the different domains. Second, there is a need for a code that can capture local phenomena in order to get a better understanding of inlet behavior (shock/shock, shock/boundary layer interactions, etc.). To this effect a two-dimensional turbulent Navier–Stokes code is used. The two-equation k–ϵ *turbulence model included in the program seems to be one of the most successful models for calculating flow realistically. Correction of the near-wall influence extends its capability to complex flow configurations, e.g., those with separated zones.*

1 Introduction

Efficient, reliable numerical tools are and will be increasingly more helpful in designing aerodynamic air intakes for high-speed aircraft. Their use can help cut down the time and cost of experimental tests and get a better understanding of several underlying phenomena. Two codes are presented here, together with a review of relevant numerical issues.

Let us first recall some major problems that are encountered when dealing with supersonic air-intakes: In such a realistic problem, the flow is viscous with a flow regime that is either laminar or turbulent, many shocks (normal or oblique) are generated, and shock–shock or shock–boundary layer interactions are frequent; the flow field (and the thermal fluxes) in the vicinity of the cowl lip is a problem in and by itself. Also, the complete geometry may be difficult to handle because of its complexity. Other problems would certainly require special attention: For instance, real gas and chemistry effects should be taken into account when reaching the hypersonic regime, a case not treated in this paper.

In this framework, we first present the Euler code FLU3M capable of solving two-dimensional and three-dimensional problems, then a two-dimensional Navier–Stokes code with a k–ϵ turbulence model.

FLU3M is well suited for supersonic flow calculation. As in all Euler codes, it neglects important phenomena that occur in supersonic intakes, but it provides a quick first estimate of the solution and enables computations with a great number of points. It also permits validating a numerical scheme for convective fluxes. We added to the initial code a few developments concerning boundary conditions; we chose here to focus on the multidomain approach technique, which shows itself to be useful in the calculation of complete intake configurations. Therefore we present more particularly a new block matching condition, which we implemented in the code.

The Navier–Stokes code solves the compressible Reynolds-averaged Navier–Stokes equations in two-dimensional configurations. This code naturally requires more mesh points due to the necessary refinement in boundary layers but is also more representative of physical reality. A three-dimensional extension is planned. The recently implemented numerical TVD scheme will be more detailed, and consequences of the upwinding needed for the convective part on the description of high shear zones will be discussed.

After a few words upon mesh generation, we present the results obtained with the Euler code on a three-dimensional Mach 1.865 intake configuration and with the Navier–Stokes code on the two-dimensional Mach 7.4 Nasa P8 intake test case.

[1]Present address: Institut für Strahlantriebe, RWTH Aachen, Templergraben 55, 52056 Aachen, Germany.

Contributed by the International Gas Turbine Institute and presented at the 37th International Gas Turbine and Aeroengine Congress and Exposition, Cologne, Germany, June 1–4, 1992. Manuscript received by the International Gas Turbine Institute February 21, 1992. Paper No. 92-GT-206. Associate Technical Editor: L. S. Langston.

Copyright © 1994 by ASME
Downloaded 02 Jun 2010 to 171.66.16.122. Redistribution subject to ASME license or copyright; see http://www.asme.org/terms/Terms_Use.cfm

2 Presentation of the Three-Dimensional Euler Code FLU3M

2.1 General Features. FLU3M can handle three-dimensional supersonic flows with strong discontinuities of a nonviscous perfect gas (Guillen and Dormieux, 1989). Its discretization uses the finite volume method with a multidomain approach on a structured grid. The numerical scheme is upwind TVD of MUSCL type. More specifically, flux calculation is upwinded by the flux splitting of Van Leer (1982) or Roe (1982). TVD type slope limiters are applied in order to capture better shocks, choosing between Van Albada (Van Leer, 1974), Van Leer (1977), Minmod, and Superbee (Roe, 1985) limiters. Second-order accuracy in space is achieved thanks to the MUSCL approach (Van Leer, 1977). Stationary solutions are deduced as the limits of pseudo-instationary calculations that can be performed explicitly or implicitly using the Chakravarty formulation (1988). Only explicit calculations were tested here, with Van Leer solver and Van Leer or Minmod limiters. More details on similar concepts are given in the Navier–Stokes code scheme presentation. Boundary conditions were handled using compatibility relations for subsonic entrance and exit conditions (Viviand and Veuillot, 1978). Supersonic conditions pose no problem since, deduced from characteristics theory, all or nothing must be imposed. Wall boundary conditions are treated by flux correction. Finally, the code uses a plane processor that saves memory and has a modular structure, which permits a great flexibility (e.g., when introducing new boundary conditions).

2.2 Reliable Block Matching Conditions for a Flexible Multidomain Approach. When solving a problem in fluid dynamics through the finite volume or finite difference methods, structured grids offer the advantage of simplicity over unstructured ones and make calculation management easier. Another advantage is the narrowing of array bandwidth in implicit treatments. There are two drawbacks however in using structured grids; one is lack of flexibility when meshing complex shapes (significant mesh distortion may occur); the other comes into play if there are zones with steep gradients that require a fine local mesh scale; the grid then has to be very fine in regions where it is useless, and therefore is wasteful in terms of mesh points. A classical and simple remedy is given by the multidomain approach. But there are various degrees of flexibility, starting with splitting the full computational domain into several subdomains using patching structured grids. We shall here consider the multidomain approach authorizing the maximum freedom:

- Strong grid scale discontinuity is permitted from one grid block to the next.
- Two blocks may be just in contact or overlapping as much as necessary.
- No coincidence of nodes is required (or patched grids).

A reliable block matching condition is a prerequisite to achieve this goal, as the qualities of the multidomain approach depend entirely on the block matching condition. This has been one of the priorities in the development of FLU3M. A few matching conditions were already available (Dormieux et al., 1990; Guillen and Dormieux, 1989). But they were satisfactory in restrictive situations (those requiring a small overlapping or continuity of grid slope and grid step through coupling interfaces). Looking for more flexibility, we decided to introduce a new and unique matching condition.

Before turning to the solution we devised, let us define a principle of validity for a block matching condition, quite simple and close to existing analysis (Freskos et al., 1991; Chesshire and Henshaw, 1990): Considering that in a region where two blocks are in contact or overlapping, the solution sought will be calculated in the best case (when the exact solution is very regular) at the order 0 (h^p) where p is the precision of the numerical scheme, and h the scale of the coarsest mesh, the coupling condition will be satisfactory if it respects this order. Moreover, between two possible treatments respecting this order, the one most respecting the scheme should be chosen. (For example, if flux splitting can be preserved, it should.) In this way, coupling regions will be transparent for the scheme.

Motivated by this idea we proceeded in the following way: Let us call "interface nodes," the nodes located in block matching regions where the scheme cannot be applied normally because a neighboring node is missing, as opposed to "current nodes." The goal is to treat the evolution of the solution on the former as well as on the latter. As was already done in the initial treatment (ONERA) fictitious nodes are introduced to replace the missing neighbors. Here coordinates of fictitious nodes are perfectly extrapolated from real nodes so that no discontinuity of slope or step will appear inside each grid block. Lastly, fictitious nodes are interpolated from the field values in the adjacent domain, at the order required. Then the exact numerical scheme can be applied to the interface nodes.

2.3 Practical Implementation in FLU3M. For each time step, the evolution of the unknown function U at a current node referenced by its block number n and its three indices (i, j, k) is deduced from the values of its four immediate neighbors in each direction, with the accuracy $O(h^2)$ in space for the flux calculation and $O(Dt^2)$ in time for the evolution calculation by an explicit approach. This may be written:

$$U(n, i, j, k, t+Dt) = S[U(n, i+\alpha, j+\beta, k+\gamma), \alpha=1, 2; \beta=1, 2; \gamma=1, 2] \quad (1)$$

where $S(\ )$ symbolizes that we call the numerical scheme. In fact this scheme can be broken down into three steps:

(a) On each cell (centered on a grid node) the slopes are evaluated by the MUSCL and TVD approach and primitive variables are then deduced at the order $O(h^2)$ on the internal side of the cell interfaces.

(b) Using the evaluation of primitive variables on each side of a cell interface, the flux splitting gives the final flux still at the order $O(h^2)$.

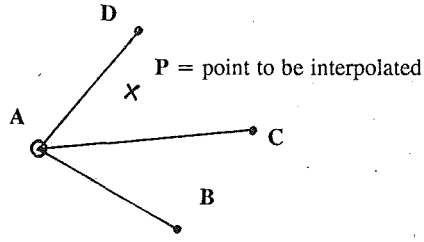
(c) The integration of fluxes on each cell is realized, which gives the evolution of the solution on the nodes.

Let us now consider that the block boundary ($i = i\max$) is a coupling interface; we can see that the scheme cannot be applied directly on nodes ($i\max - 1, j, k$) and ($i\max, j, k$) because one or two nodes are missing. If we wanted to respect the scheme perfectly, we would introduce two ranges of fictitious nodes corresponding to indices ($i\max + 1, j, k$) and ($i\max + 2, j, k$). An interpolation on this fictitious node, at the order $O(h^2)$ is then sufficient to apply the scheme without losing any accuracy in the flux calculation and so in the evolution of the solution on the interface nodes. This is verified if the exact solution is regular enough, but it is no longer true in the vicinity of a shock as will be pointed out below.

To avoid too many points, only the ($i\max + 1, j, k$) range of points was introduced enabling ($i\max - 1, j, k$) points to be treated fully by the scheme whereas the ($i\max, j, k$) points require a special treatment: On the external side of the cell interface situated between a ($i\max, j, k$) point and the corresponding ($i\max + 1, j, k$) fictitious point, the solution is evaluated with the mean value of the solution on ($i\max, j, k$) and ($i\max + 1, j, k$) points. On the internal side, the solution is evaluated in accordance with step (a) of the scheme. The flux is then derived with a second-order accuracy thanks to step (b); step (c) is then normally applied.

Let us briefly sum up the interpolation technique for a point P: An automatic research of the first neighbor of P over all the other domains is done. Among the eight tetrahedra that have this first neighbor as vertex, the one containing P is determined. Finally, using the notations of the figure below and i designating one component of the solution, we have:

Downloaded 02 Jun 2010 to 171.66.16.122. Redistribution subject to ASME license or copyright; see http://www.asme.org/terms/Terms_Use.cfm



$$U_i(P) = U_i(A) + \{ (\underline{AP}[\underline{AB}, \underline{AC}, AD]^T)^{-1} \} \cdot \begin{bmatrix} U_i(B) - U_i(A) \\ U_i(C) - U_i(A) \\ U_i(D) - U_i(A) \end{bmatrix} \quad (2)$$

giving a second-order interpolation, keeping in memory the three-component vector contained in braces.

In conclusion, such a block matching condition is easy to implement and respects the scheme as best as possible. We believe such is not the case for the block coupling condition that uses compatibility relations (Viviand and Veuillot, 1978; Cambier et al., 1985), which seems to handle interface points and current points differently.

It should also be pointed out that this analysis of the incidence of the coupling condition on the accuracy of the calculation should be examined in detail where strong discontinuities due to shock are present. In fact, the accuracy of the scheme drops to one in these regions. Suffice it to say here that our coupling condition in shock regions generally did not affect the solution behavior in our calculations.

3 Presentation of a Navier–Stokes Code

3.1 Numerical Treatment. The unsteady Reynolds-averaged Navier–Stokes equations are solved. The conservation laws are expressed using a finite volume technique on a curvilinear coordinate system. In order to simplify the analysis presented here, a simple Cartesian system is used where the axis x (respectively y) coincides with the i (respectively j) direction.

A domain decomposition approach could also be used (Freskos et al., 1991) but a limited use of the possibilities offered by the multiblock technique was made in the results presented at the end of this paper.

The viscous terms of the governing equations are centrally discretized. Turbulent phenomena are considered by means of the Jones–Launder low Reynolds number k–ϵ turbulence model.

In the present study we are mainly concerned with the discretization of the convective terms. A successful treatment of the latter is needed to correctly capture steep gradient phenomena connected to their nonlinearity.

The two-dimensional unsteady inviscid flow equations are written in vector form as follows:

$$\frac{\partial U}{\partial t} + \frac{\partial F}{\partial x} + \frac{\partial G}{\partial y} = 0. \quad (3)$$

The numerical treatment of the above system of equations is based on the so-called Total Variation Diminishing approach (TVD) (Yee, 1989).

Equation (3) can take the following discretized form:

$$\frac{U_i^{n+1} - U_i^n}{\Delta t} + \frac{\tilde{F}_{i+(1/2),j} - \tilde{F}_{i-(1/2),j}}{\Delta x} + \frac{\tilde{G}_{i,j+(1/2)} - \tilde{G}_{i,j-(1/2)}}{\Delta y} = 0 \quad (4)$$

The numerical convective flux $\tilde{F}$ at $(i+1/2, j)$ will be expressed according to Yee's unified formulation (flux difference splitting):

$$\tilde{F}_{i+(1/2),j} = \frac{1}{2} \left(F(U^R_{i+(1/2),j}) + F(U^L_{i+(1/2),j}) + \hat{R}_{i+(1/2),j} \Phi_{i+(1/2),j} \right) \quad (5)$$

where MUSCL interpolation is assumed. The same analysis also applies to the $(i, j+1/2)$ interfaces for approximating the $\tilde{G}$ fluxes.

Based on scalar considerations and for a fully upwind scheme, the left and right states for the conservative variables are approximated as follows:

$$U^R_{i+(1/2),j} = U_{i+1,j} - \frac{1}{2} g_{i+1,j}$$

$$U^L_{i+(1/2),j} = U_{i,j} + \frac{1}{2} g_{i,j} \quad (6)$$

where g is the slope limiter function. The behavior of the solution as a function of various limiters can be studied. For the present calculations Roe's Minmod and Van Leer (Van Leer, 1974) limiters were mainly retained. The expression for the latter is:

$$g^l_i = \frac{\Delta^l_{i+(1/2),j} \Delta^l_{i-(1/2),j} + |\Delta^l_{i+(1/2),j} \Delta^l_{i-(1/2),j}|}{\Delta^l_{i+(1/2),j} - \Delta^l_{i-(1/2),j}} \quad (7)$$

where

$$\Delta_{i+(1/2),j} = U_{i+1,j} - U_{i,j}$$

Many authors prefer to impose the limiters on the characteristic variables. In our approach limiting was exclusively applied to the conservative variables.

The components of the dissipation term $\Phi_{i+1/2,j}$ in Eq. (5) are expressed as follows:

$$\tilde{\delta}^l_{i+(1/2),j} = -\psi(\hat{a}^l_{i+(1/2),j}) \hat{\alpha}^l_{i+(1/2),j}$$
$$\hat{\alpha}_{i+(1/2),j} = \hat{R}^{-1}_{i+(1/2),j} (U^R_{i+(1/2),j} - U^L_{i+(1/2),j}) \quad (8)$$

where $a^l_{i+(1/2),j}$ are the eigenvalues and $\hat{R}$ is the right eigenvector matrix of the Jacobian A^x of the flux vector F. They are computed at some symmetric average between $U^R_{i+(1/2),j}$ and $U^L_{i+(1/2),j}$. Here Roe's average state between $U^R_{i+(1/2),j}$ and $U^L_{i+(1/2),j}$ has been chosen (Roe, 1982). ψ is an entropy function introduced in order to enforce the entropy condition. It is destined for regions where the eigenvalues of the Jacobian A^x tend to zero (shock waves or contact discontinuities). It eliminates expansion shocks and ensures a smooth transition from supersonic to subsonic flow. The choice of ψ is very important for viscous flow computations. Indeed, low numerical viscosity in boundary layer regions and stabilization of convective terms are simultaneously required. Harten (1984) proposed the following expression for ψ, where a parameter δ adjusts the correction introduced by ψ:

$$\psi(\hat{a}^l_{i+(1/2),j}) = \begin{cases} |\hat{a}^l_{i+(1/2),j}|, & |\hat{a}^l_{i+(1/2),j}| > \delta \\ \dfrac{\hat{a}^{l2}_{i+(1/2),j} + \delta^2}{2\delta}, & |\hat{a}^l_{i+(1/2),j}| \le \delta \end{cases} \quad (9)$$

Furthermore δ can be evaluated locally (Montagne et al., 1988) as:

$$\delta = \delta_1 (|u| + |v| + |c|) \quad (10)$$

In this way ψ can be switched on by choosing δ_1 large enough in regions where this is necessary (shock capturing), whereas it can be set equal to some small value in zones where it can provoke unwanted effects (boundary layers) (Lafon, 1990).

Difficulties encountered in adjusting this parameter for viscous flow computations are discussed below.

3.2 Implicit Option. An implicit updating is used for the purpose of convergence acceleration by overcoming the severe

Downloaded 02 Jun 2010 to 171.66.16.122. Redistribution subject to ASME license or copyright; see http://www.asme.org/terms/Terms_Use.cfm

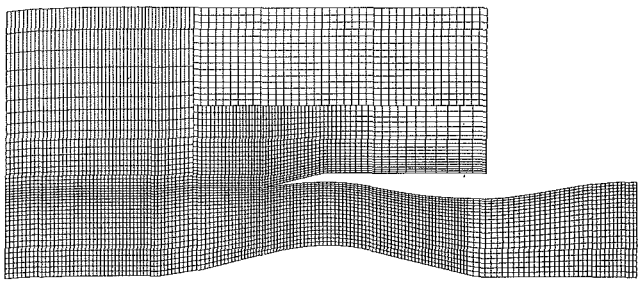


Fig. 1 Five-domain grid for the two-dimensional Mach 1.865 intake

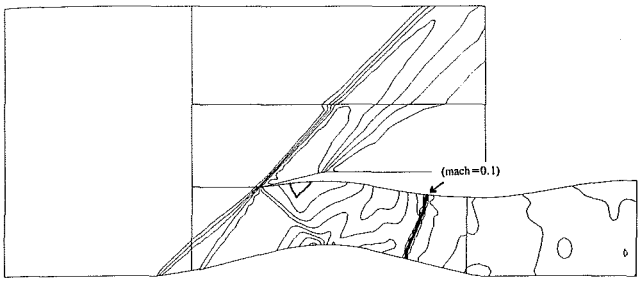


Fig. 2 Isomach lines for the two-dimensional Mach 1.865 intake with counterpressure = 0.83 (step = 0.1)

time step limitations due to an explicit method applied to high Reynolds number flows.

The implicit approximation is derived from series expansion of the fluxes. If linearization is introduced, the following expression can be deduced:

$$\frac{\delta U^n_{i,j}}{\delta t}+\frac{1}{2}\frac{\delta t}{\delta x}[(-A^x_{i-1,j}-\Omega^x_{i-(1/2),j})\,\delta U^n_{i-1,j}$$
$$+(\Omega^x_{i-(1/2),j}+\Omega^x_{i+(1/2),j})\,\delta U^n_{i,j}+(A^x_{i+1,j}-\Omega^x_{i+(1/2),j})\,\delta U^n_{i+1,j}]$$
$$+\frac{1}{2}\frac{\delta t}{\delta y}[(-A^y_{i,j-1}-\Omega^y_{i,j-(1/2)})\,\delta U^n_{i,j-1}$$
$$+(\Omega^y_{i,j-(1/2)}+\Omega^y_{i,j+(1/2)})\delta U^n_{i,j}+(A^y_{i,j+1}-\Omega^y_{i,j+(1/2)})\,\delta U^n_{i,j+1}]$$
$$=-\frac{\delta t}{\delta x}(\tilde{F}^n_{i+(1/2),j}-\hat{F}^n_{i+(1/2),j})-\frac{\delta t}{\delta y}(\tilde{G}^n_{i,j+(1/2)}-\tilde{G}^n_{i,j-(1/2)}) \quad (11)$$

In the implicit part, first-order accuracy is used, and we can therefore write:

$$U^R_{i+(1/2),j}=U_{i+1,j},\quad U^L_{i+(1/2),j}=U_{i,j}$$
$$A^x_{i,j}=A^x(U_{i,j})$$

For steady-state computations the accuracy of the converged solution will depend on the order of the approximation used in the explicit part.

The matrix Ω^x (and in the same way for Ω^y) is given by the following expression:

$$\Omega^x_{i+(1/2),j}=\hat{R}_{i+(1/2),j}\mathrm{diag}[\psi(\hat{a}^l_{i+(1/2),j})]\hat{R}^{-1}_{i+(1/2),j} \quad (12)$$

For steady-state applications the matrix Ω^x is simplified to

$$\Omega^x_{i+(1/2),j}=\max_l(\psi(\hat{a}^l_{i+(1/2),j}))I$$

In the implicit part the quantities computed at $i+1/2, j$ are approximated as the mean values of the same quantities between cells (i,j) and $(i+1,j)$.

Approximate factorization technique is used for solving the above system (11). Two block-tridiagonal matrices are inverted at each time step.

The source terms present in the two additional equations of the Jones–Launder low turbulent Reynolds number k–ϵ model are also included in the implicit part. A special treatment enhances the robustness of the numerical approach (Freskos and Vandromme, 1991).

4 Mesh Generation

Several meshing tools were developed or exploited in order to deal with various two-dimensional or three-dimensional air-intake configurations. In all the cases, we took advantage of the multidomain option. The mesh generators we developed were devoted to two-dimensional supersonic air-intakes for Euler and Navier–Stokes calculations. The domain decomposition used is given in Fig. 1: The first domain is located upstream, the second domain with global refinement covers the sensitive region of the entrance section, the cowl lip, and the stabilized normal shock. The third domain constitutes the major part of the diffuser. The fourth domain allows, if needed, a local refinement above the cowl lip, avoiding its vertical spreading; the fifth and last domain, which is coarser, partly contains the cowl shock.

In case of unexpected behavior at interfaces crossed by strong shocks, the possibility of merging second and third domains and satisfying node coincidence was preserved.

In three-dimensional calculations the interest of a dedicated mesh generator decreases because too many parameters appear in the geometric definition. Thus in the three-dimensional air-intake test presented here, we used the surface mesh generator Catiamesh and the three-dimensional mesh generator Mesh-3D (Jacquotte, 1988). However a dedicated two-dimensional mesh generator enabled calculations on a two-dimensional projection of the intake as shown in Fig. 2.

5 Euler Results

Our purpose was to calculate the Euler flow for a three-dimensional supersonic intake configuration. As in a supersonic regime the flow around the intake has no incidence on the flow upstream of a vertical plane containing the cowl lip and therefore on the internal flow inside the cowl, we opted to restrict the calculation domain up to that vertical plane. Internal aerodynamic performance could then be deduced. A perspective view of the three-dimensional intake using the superficial mesh is given in Fig. 3(*a*); the design of the external cowl edge was beyond the scope of this study. Up to about the middle of the cowl, the three-dimensional shape can be obtained by translating the two-dimensional shape in the third direction, and is therefore quasi-two-dimensional. The second half of the cowl is actually three-dimensional with a cross section evolving from rectangular to circular, as shown by the cross-sectional meshes in Fig. 3(*b*).

The free-stream Mach number (Mach) was set to 1.865, which corresponds to adaptation; incidence and sideslip were set to zero. We could therefore reduce the calculation domain using the geometric symmetry plane. Last, we considered that the wing on one side or sideplates on the opposite side allowed us to neglect spillage at the cowl entrance.

Based on this hypothesis and on the quasi-two-dimensional structure of the first half of the cowl, a two-dimensional calculation was first carried out on a transverse section of that first half, supplemented by a two-dimensional design for the end of the cowl. We also added, only for the two-dimensional calculations, a reasonable external cowl edge. This two-dimensional calculation enabled us to verify the validity of the shape and the possibility of stabilizing a normal shock just behind the narrow section of the cowl. Furthermore, so long as a normal shock can be stabilized inside the first half of the cowl, the flow rate coefficient (ϵ = captured flow section/front section) and the pressure recovery coefficient (n = mean total pressure at the cowl exit/free-stream total pressure) should be exactly equal in a two-dimensional or three-dimensional calculation for the same position of the normal shock.

Downloaded 02 Jun 2010 to 171.66.16.122. Redistribution subject to ASME license or copyright; see http://www.asme.org/terms/Terms_Use.cfm

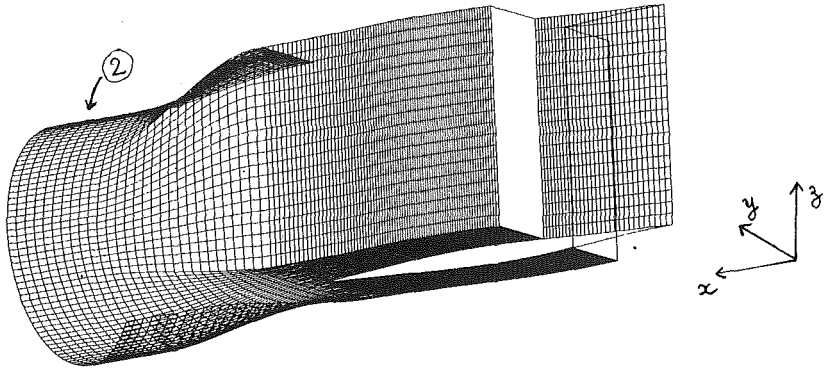


Fig. 3(*a*)

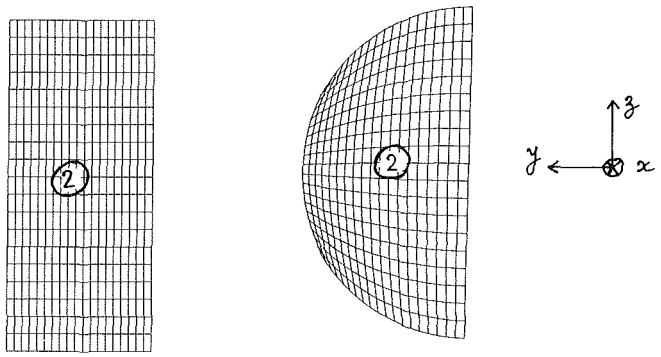


Fig. 3(*b*)

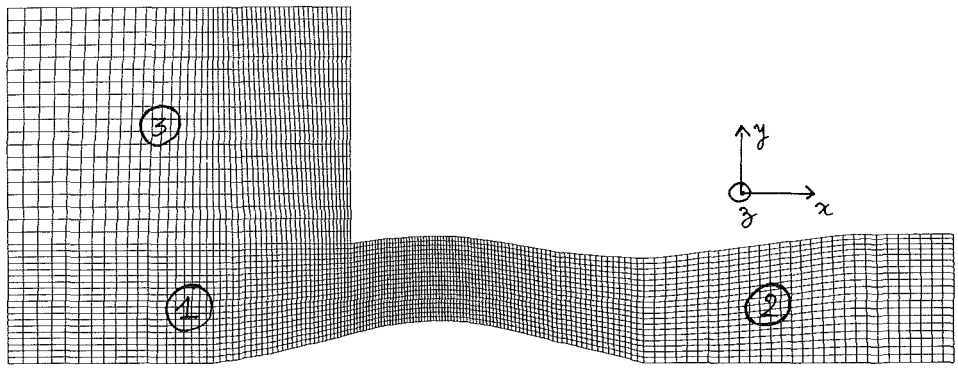


Fig. 3(*c*)

Fig. 3 Computational mesh for the three-dimensional Mach 1.865 intake

In the two-dimensional calculation, we obtained a stationary solution by imposing a counterpressure (*pe/pi*0 = cowl exit static pressure/free-stream total pressure) in the range [0.6–0.83]. The normal shock was always well stabilized inside the diffuser. The corresponding pressure recovery coefficient n was varied in the range [0.76–0.93]. Mass conservation along the cowl was achieved with a 4 percent maximum variation close to the normal shock and so ϵ was approximately equal to one. The two-dimensional isomach results using the Van Leer limiter and for a counterpressure equal to 0.83 are shown in Fig. 2; with *pe/pi*0 = 0.833 the normal shock goes out of the diffuser. We should remark that a few perturbations of the total pressure were apparently generated at the cowl lip. They could be significantly reduced using a Minmod limiter instead of a Van Leer limiter, but the choice of one of these two limiters did not affect isomach results.

Based on the two-dimensional calculation, the three-dimensional calculation could be carried out with confidence. We realized a three-domain mesh, which is presented in Fig. 3; Fig. 3(*c*) shows a two-dimensional X-projection of a transverse section mesh and pinpoints where each domain is located. Approximately 50,000 points were necessary. A few different shapes for the second domain were tested until a satisfactory calculation could be executed with a supersonic exit condition at the end of the diffuser. An increasing counterpressure was then imposed and we reached a counterpressure of 0.75 with a stabilized normal shock. For this value ϵ was equal to one (with the same 4 percent accuracy as in the two-dimensional case), which is normal since no spillage is permitted and we had $n = 0.92$. This value is clearly inside the two-dimensional calculation range. Isomach results are given in perspective view in Fig. 4(*a*); Fig. 4(*b*) shows a two-dimensional X-projection of isomach lines and we verify that in the first part of the diffuser the flow is the same as for the two-dimensional calculation.

The three-dimensional effect was due here only to the second

Downloaded 02 Jun 2010 to 171.66.16.122. Redistribution subject to ASME license or copyright; see http://www.asme.org/terms/Terms_Use.cfm

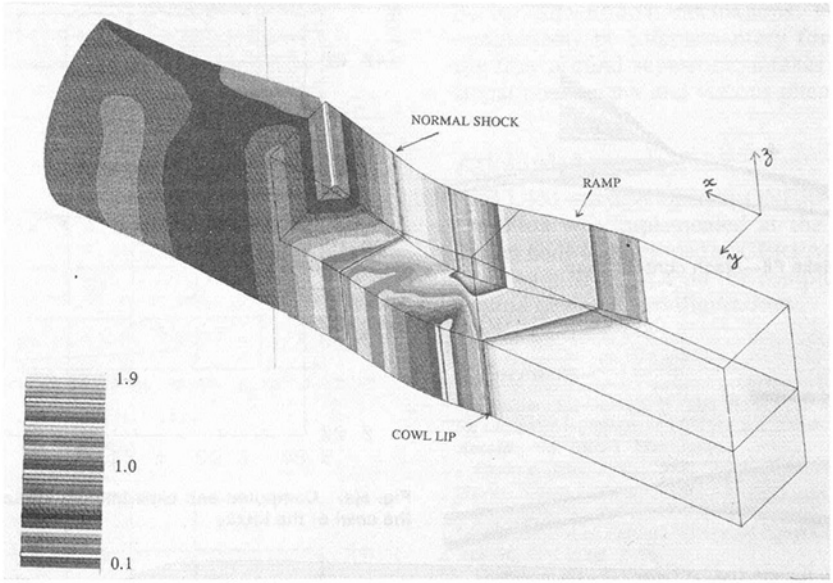


Fig. 4(*a*) Isomach repartition for the three-dimensional Mach 1.865 air-intake

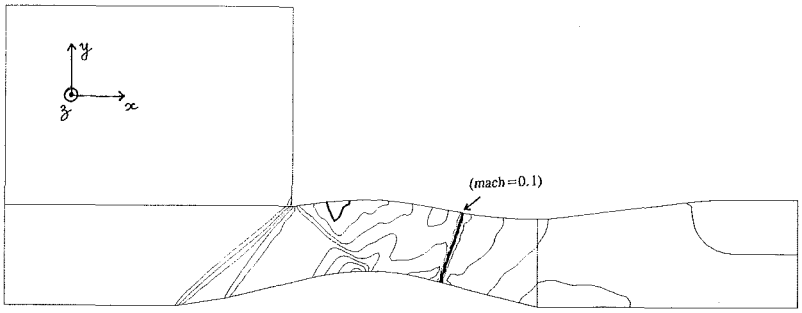


Fig. 4(*b*) Isomach lines of a two-dimensional-*z* projection of a section for the three-dimensional Mach 1.865 intake (step = 0.1)

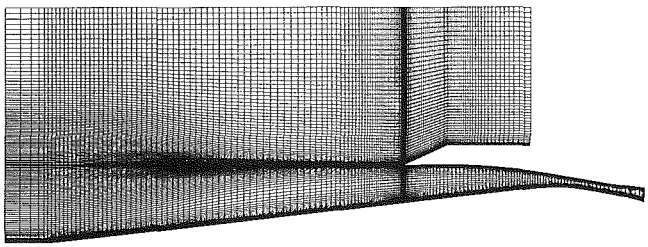


Fig. 5 Air-intake P8—computational domain (2 blocks)

domain shape. As proved by the computation, the numerical scheme can handle a three-dimensional calculation where mesh distortion (see the circular cross section, Fig. 3(*b*)) is tolerated although its incidence on the solution accuracy should be evaluated. This calculation constitutes a first important step in the numerical simulation of supersonic intake flows. The multidomain approach should be now exploited fully to avoid mesh distortion, spillage should be introduced, and finally the external flow has to be computed.

6 Navier–Stokes Results

The flow around the P8 air-intake (Vernon et al., 1973) provides a rather challenging problem for the validation of our approach. The prescribed free-stream Mach number is fixed at 7.4 and the Reynolds number is equal to 8.86×10^6/m. The total temperature (T_i) is equal to 811 K. Since low-temperature regions are present in the flow, a modification of Sutherland's law has been introduced (Inria, 1990) for temperatures lower than 120 K:

$$\mu(T<120\text{ K})=\mu(120\text{ K})\,\frac{T}{120} \tag{13}$$

In the following, preliminary viscous results are presented. The turbulent character of the flow is taken into account through the Jones–Launder k–ϵ model. Laminar to turbulent regime transition is considered as dictated by the experimental observations (Vernon et al., 1973): on the wedge at $x/x_{\text{ref}}=1.909$ and on the cowl at $x/x_{\text{ref}}=5.837$. The reference length is the cowl height $x_{\text{ref}}=18.33$ cm. An adiabatic wall condition is assumed.

On Fig. 5 the grid is presented. It is made of two blocks containing 179×79 and 159×69 points. As it has been a posteriori confirmed, it is fine enough in the boundary layer of the flow.

Among other interesting aspects, our study has been concerned with the influence of the parameter δ_1 on the computed results. On $i+1/2,j$ interfaces δ_{1x} has been set equal to 0.1. On $i,j+1/2$ interfaces (corresponding to the ones where viscous flux exchange is mainly taking place) δ_{1y} was also equal to 0.1 with the exception of the eigenvalue v where it has been switched to 0.5. This high value helps in stabilizing the numerical scheme and is necessary in order to overcome problems emerging from the insufficient domain discretization at the cowl lip.

A thick boundary layer is deduced, especially on the cowl

Downloaded 02 Jun 2010 to 171.66.16.122. Redistribution subject to ASME license or copyright; see http://www.asme.org/terms/Terms_Use.cfm

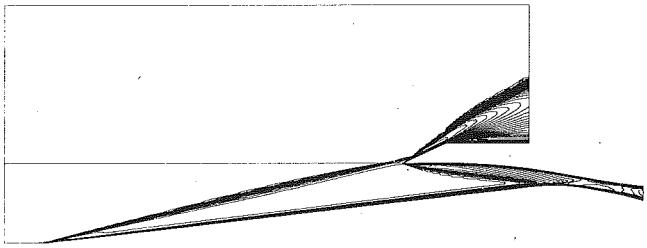


Fig. 6(*a*) Air-intake P8—Mach contour lines

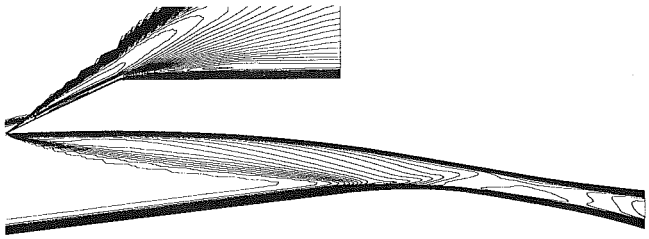


Fig. 6(*b*) Mach contour lines—diffuser part

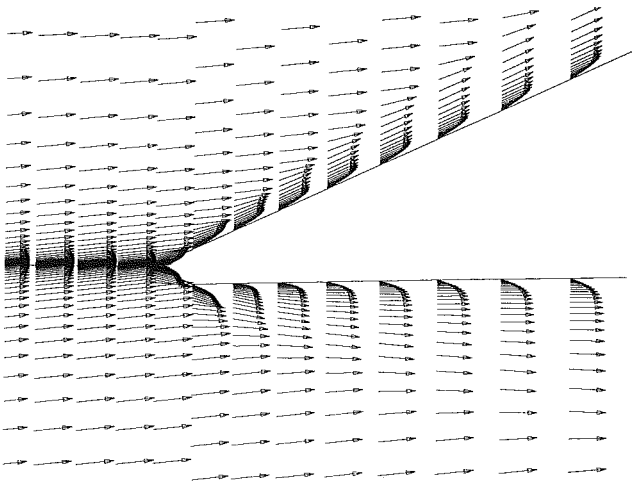


Fig. 7(*a*) Velocity vectors around the cowl lip

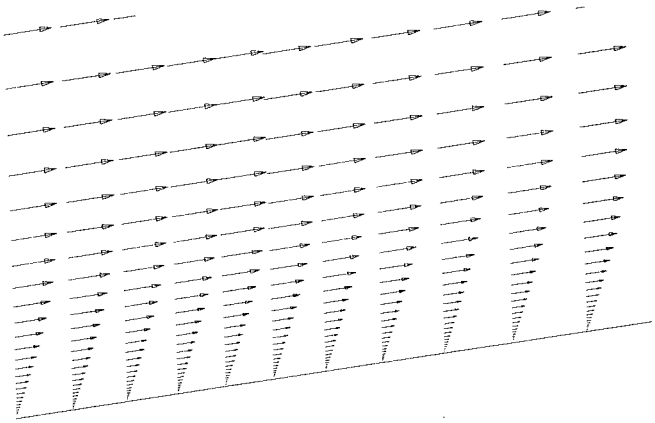


Fig. 7(*b*) Velocity vectors on the ramp

surface. The scheme proves to be very dissipative as it was a posteriori verified, as a consequence of the value of δ_1 in regions where the laminar and turbulent viscosity should have been sufficient for stabilizing the numerical algorithm.

In an attempt to reduce the dissipation terms introduced by the important value of δ_{1y} it has been set equal to 0.1 for all

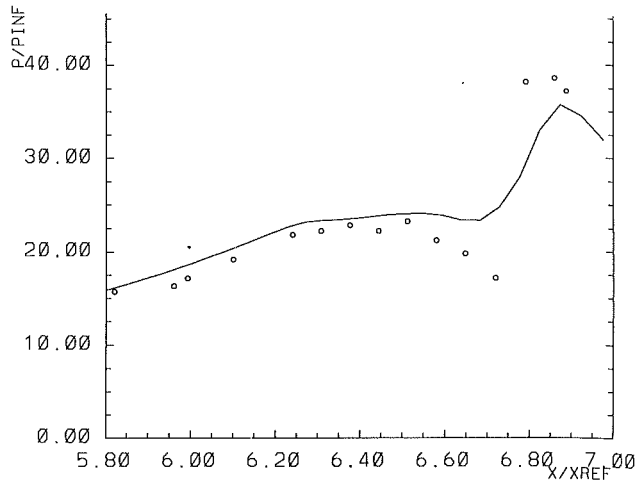


Fig. 8(*a*) Computed and experimental static pressure distribution on the cowl of the intake

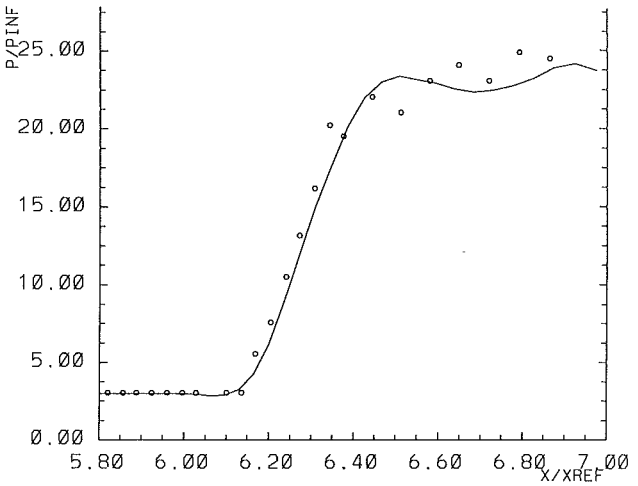


Fig. 8(*b*) Computed and experimental static pressure distribution on the ramp

eigenvalues along $i, j+1/2$ interfaces. Consequently, it was necessary to adjust δ_{1x} to some higher value (0.4).

On Fig. 6 the isomach contours around the intake geometry are presented. The modified values of δ_1 and the grid of Fig. 5 were used for this computation. The slope limiter was the Minmod one. Figure 7 presents the velocity vectors at the region of the cowl lip and on the wedge (at the diffuser's inflow section). The boundary layer discretization seems satisfactory. The first grid points are close enough to the solid boundaries ($y^+ = 1.$). As can be seen from Fig. 7(*a*), even at the cowl lip where the boundary layer is very thin, an important number of points refines the boundary layer region.

More quantitative indications concerning the quality of the presented results are provided from Fig. 8. The static pressure distributions along the diffuser ramp and the cowl are given. Computed and experimental results are in good agreement. It should be noted that an Euler calculation fails, in general, to give the correct pressure distribution, due to phenomena connected to shock-boundary layer interactions.

On Fig. 9, pitot pressure profiles at two stations downstream of the shock reflection on the ramp are represented. Comparisons with experimental results on specified diffuser sections will be very useful.

These preliminary results, previously exposed, are quite encouraging for a more detailed exploitation of the computed flow field. More particularly, the influence of the parameter

Downloaded 02 Jun 2010 to 171.66.16.122. Redistribution subject to ASME license or copyright; see http://www.asme.org/terms/Terms_Use.cfm

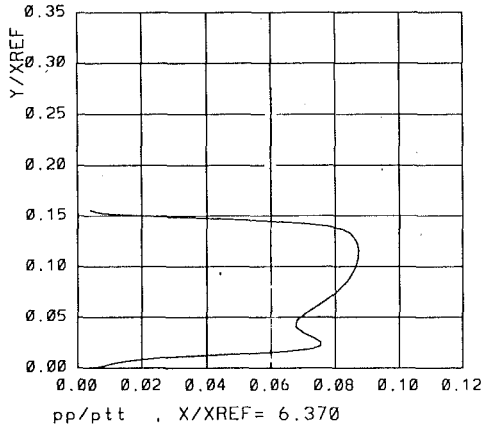


Fig. 9(*a*)

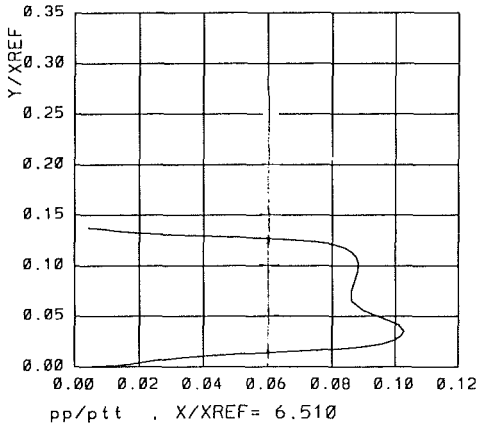


Fig. 9(*b*)

Fig. 9 Pitot pressure profiles

δ_1 must be more thoroughly examined. Also, compressibility effects should be introduced, at least at the upstream high Mach number zones. Close to the diffuser exit, the model performs better. Nevertheless, significant improvements with the k–ϵ turbulence modeling are obtained compared to simple laminar Navier–Stokes computation.

7 Conclusion

The two codes we presented proved to be reliable for the treated situations. A robust block matching condition was described and tested, mainly in two-dimensional calculations, for the Euler code. Its three-dimensional ability was demonstrated on a realistic configuration. A performant numerical scheme for the convective terms together with an implicit method in the Navier–Stokes code were presented and validated by two-dimensional calculations. Finally the two codes will undoubtedly be complementary for numerical simulation of the flow around supersonic intakes where both three-dimensional phenomena and viscous phenomena take place.

Acknowledgments

FLU3M was developed by ONERA. The new block matching condition was implemented at the SNECMA. The Navier–Stokes code is developed at CERFACS in a collaboration program with SNECMA on the computation of supersonic flow around air-intake configurations.

References

Cambier, L., Dusson, F., and Veuillot, J. P., 1985, "Multi-domain Method for the Euler Equations: Application to Subdomains With Overlapping," *Rech. Aerosp.*, No. 1985-3, May–June.

Chakravarthy, S. R., 1988, "High Resolution Upwind Formulations for the Navier–Stokes Equations," VKI Lecture.

Chesshire, G., and Henshaw, W. D., 1990, "Composite Overlapping Meshes for the Solution of Partial Differential Equations," *J. of Computational Physics*, Vol. 90, No. 1, pp. 1–64.

Dormieux, M., Guillen, Ph., and Abgrall, R., 1990, "Numerical Simulation of Transverse Jet Flows by a Nonreactive Two Species Multidomain Euler Flow Solver," *AIAA Journal*.

Freskos, G., and Vandromme, D., 1991, "An Implicit Treatment of Two Equations Turbulence Models for High Speed Flow Computations," presented at the 7th International Conference on Numerical Methods in Laminar and Turbulent Flows, Stanford, CA.

Freskos, G., Vandromme, D., and Ha Minh, H., 1991, "A Flexible Domain Decomposition Technique for Real Flow Computations," presented at the 4th International Symposium on Computational Fluid Dynamics, Sept., Davis, CA.

Guillen, Ph., and Dormieux, M., 1989, "Design of a 3D Multidomain Euler Code," presented at the Int. Seminar on Supercomputing, Boston, MA.

Harten, A., 1984, "On a Class of High Resolution Total-Variation-Stable Finite-Difference Schemes," *SIAM J. Num. Anal.*, Vol. 21, pp. 1–23.

Inria and Gamni-Smai, 1990, "Workshop on Hypersonic Flows for Re-entry Problems, Part I," Antibes, Jan.

Jacquotte, O. P., 1988, "Methode de Maillage Multidomaine," *Rapport technique de synthese*, 3/3519 AY Janv 88, ONERA.

Lafon, A., 1990, "Calcul d'Écoulements Visqueux Hypersoniques," C.E.R.T.-O.N.E.R.A., rapport technique OA 32/5005.22, Mar.

Montagne, J. L., Yee, H. C., Klopfer, G. H., and Vinokur, M., 1988, "Hypersonic Blunt Body Computations Including Real Gas Effects," NASA TM100074.

ROE, P. L., 1982, "Approximate Riemann Solvers, Parameter Vectors and Difference Schemes," *Journal of Computational Physics*, Vol. 43, pp. 357–372.

ROE, P. L., 1985, "Some Contributions to the Modeling of Discontinuous Flows," *Lecture in Applied Mathematics*, Vol. 22.

Van Leer, B., 1974, "Towards the Ultimate Conservative Difference Scheme. II. Monotony and Conservation Combined in a Second-Order Scheme," *Journal of Computational Physics*, Vol. 14, pp. 361–370.

Van Leer, B., 1977, "V a Second Order Sequel to Godunov Method," *Journal of Computational Physics*, Vol. 23, pp. 276–299.

Van Leer, B., 1982, "Flux Vector Splitting of the Euler Equations," Icase report 82-30.

Vernon Gnos, A., Watson, E. C., Seebaugh, W. R., Sanator, R. J., and Decarlo, J. P., 1973, "Investigation of Flow Fields Within Large Scale Hypersonic Inlet Models," NASA TN D-7150.

Viviand, H., and Veuillot, J. P., 1978, "Methodes Pseudo-instationnaires Pour le Calcul d'Écoulements Transsoniques," publication ONERA (English translation ESA TT 561).

Yee, H. C., 1989, "A Class of High-Resolution Explicit and Implicit Shock-Capturing Methods," VKI lecture series, 1989-04.

Downloaded 02 Jun 2010 to 171.66.16.122. Redistribution subject to ASME license or copyright; see http://www.asme.org/terms/Terms_Use.cfm

Thrust Vectoring/Reversing Tactics in Air-to-Air Combat

C. W. Boppe

R. P. Martorella

Grumman Corporation,
Bethpage, NY 11714

Considerable effort is now under way to develop technologies for enhancing fighter maneuvering limits. This has in part been motivated by the capabilities of advanced air-to-air missiles. One approach to enhanced combat effectiveness involves flight envelope expansion and improved controllability via engine thrust-vectoring and thrust-reversing. The complexity of fighter combat, however, makes it difficult to perform engineering analyses for assessing potential technological enhancements and risks. This paper describes a digital simulation that has been used to identify benefits associated with improved maneuverability. The Navy/Grumman F-14 aircraft provides the flight characteristics database. Combat tactics are developed as part of the solution process and are based solely on characteristics of the combatants and weapons employed. Head-on and codirectional neutral start combat engagements are used to illustrate study results.

Introduction

Technological advances that improve performance can change the outcome of air-to-air combat. Sometimes performance advantages can be quite small if complemented by pilot skills; history reveals that in other cases, a performance advantage can be negated by improved tactics (Shaw, 1985). Determination of new technology benefits is hindered by the complex way in which elements interact and the nonlinear manner in which these features combine to characterize a complete system that has a clear advantage.

For fighters, advances in the airframe, engine, weapon, and pilot capabilities all have a beneficial effect. Engine thrust vectoring has received considerable attention during the past decade. Simpler, lighter weight, and more reliable mechanization makes vectoring a viable option for the aircraft designer. Thrust vectoring technology provides several potential combat advantages:

- Expanded trimmed envelope (pitch and yaw).
- Augmented normal acceleration to increase turn rate.
- Attitude (pointing) dynamic response improvement.

These benefits will be offset by penalties associated with weight, control system complexity, mechanical complexity, maintenance, additional failure modes, etc.

One approach to assessing thrust vectoring benefit/penalty trades might involve manned simulation and flight test programs. There are many good reasons to take this tack, but the facilities and equipment involved are extraordinarily expensive and time consuming to use. Beyond this, the expense of manned simulation and flight test programs will constrain the options and variables examined. This constraint may limit the important hands-on learning time needed to identify key combat offensive and defensive tactics. The upfront resolution of flight safety issues also might be compromised. In view of this, there are advantages to performing analytical investigations prior to initiating programs that involve pilots. There also are engineering advantages to assessing technologies prior to incorporating the pilot's effect on the overall system.

Grumman has initiated a program to evaluate the impact of engine thrust vectoring on F-14 combat effectiveness. An analytical approach has been taken to take advantage of the ability of digital computers to process large amounts of data efficiently and simulate complex dynamic engagements. This can be important for tactics optimization because often what may appear as a performance advantage that should translate into an exchange ratio benefit results in a negligible impact because a defender can develop a tactic or maneuver that foils the attacker's technology and strategy. Using computers and differential game theory, engineering analysis can be used to explore tens of thousands of combat engagements made up of millions of pilot maneuver decisions. The results can be processed statistically to derive optimum offensive and defensive strategies that will be a function only of the aircraft and weapon system characteristics. Developing all this information via manned simulation or flight test programs could prove to be impractical.

A second facet of this analytical approach is that developed tactics are based on combatant characteristics only. No prejudgment as to what is a good or bad tactic is required. Judgments of this type would be based on combat experience derived from technologies that are different from the ones currently of interest; and, as such, the reasoning is improperly influenced or contaminated.

Discussion

This section describes the flight dynamics computer simulation that has been structured to capture the highly nonlinear

Contributed by the International Gas Turbine Institute and presented at the 37th International Gas Turbine and Aeroengine Congress and Exposition, Cologne, Germany, June 1–4, 1992. Manuscript received by the International Gas Turbine Institute March 13, 1992. Paper No. 92-GT-362. Associate Technical Editor: L. S. Langston.

Copyright © 1994 by ASME
Downloaded 02 Jun 2010 to 171.66.16.122. Redistribution subject to ASME license or copyright; see http://www.asme.org/terms/Terms_Use.cfm

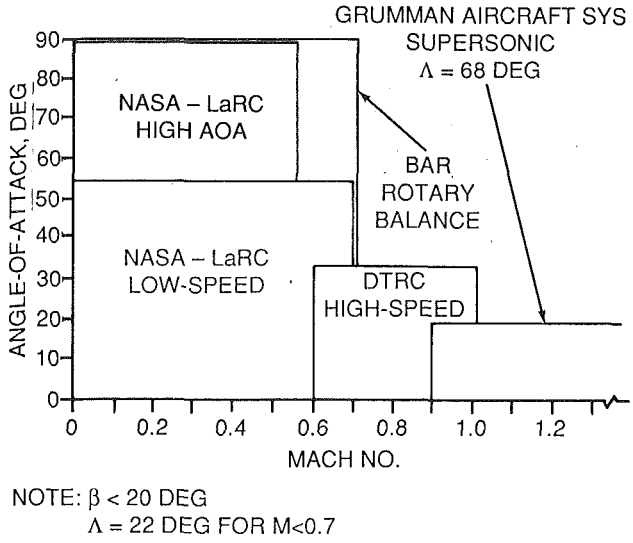


Fig. 1 F-14 aircraft experimental database

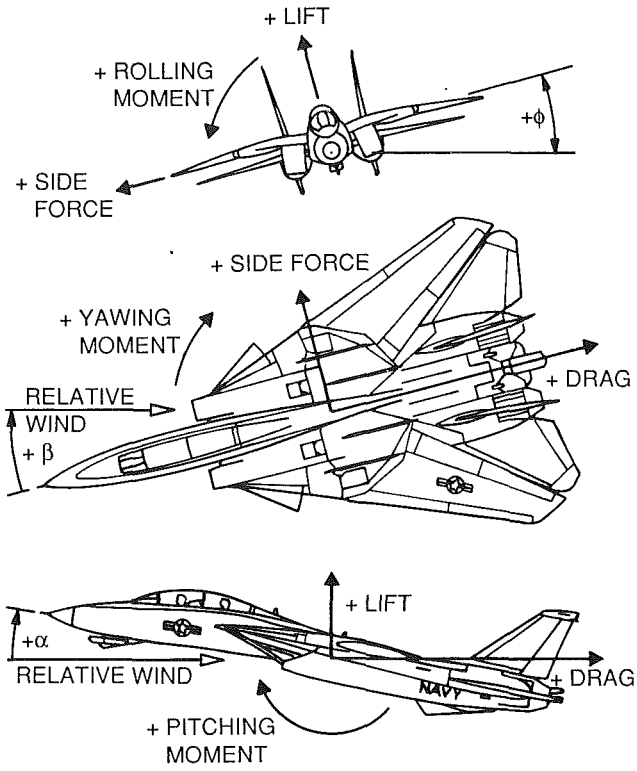


Fig. 2 Navy/Grumman F-14 configuration

dynamics that characterize fighter combat wherein the combatants operate at the edges of the vehicle flight envelope. In addition, considerations employed to conserve computing resources are identified. Details of the aircraft, weapon, and combat optimization models employed are then described. This is followed by a summary of key results.

Aircraft and Database. The Navy/Grumman F-14 was selected for this study in part because of the availability of good quality high-angle-of-attack (AOA) experimental data. Aerodynamic data (Fig. 1) for incidence angles up to 90 deg and sideslip angles to 20 deg were generated by NASA for simulation programs performed using Langley Research Center's Differential Maneuvering Simulator. These data were generated because the F-14 was by many measures the first U.S. high-AOA fighter to go into production.

F-14 airframe stability characteristics are considered to be very good. In addition, the vehicle's maximum pitch rate and pitch acceleration are extremely high—the result of large horizontal tail surfaces (Fig. 2) sized to facilitate turns at supersonic speeds where the aircraft is excessively stable. A high level of nose-down pitch power (-75 deg/s @ $\alpha = 0$ deg to -300 deg/s @ $\alpha = 85$ deg) for recovery during high-incidence maneuvers is inherent in the basic design.

Because F-14s have been used for some time in developing combat tactics at the Fighter Weapons School (TOPGUN) in Miramar, CA, there is a field experience base for relating both current and new tactics with the basic aircraft characteristics. During the mid-1980s the NAVY used the F-14 to conduct a flight test manuevering program (see Lacey, 1983, and Sappington and Thompson, 1984) where panels were positioned to deflect engine exhaust for yawing forces at low-speed, high-incidence conditions. Beyond this, the X-31 Program has focused attention on thrust-vectoring technology, as has the YF-22. As a result, Naval Air Systems Command technologists

Nomenclature

S = reference area
M = Mach number
h = altitude
α, AOA = angle-of-attack
β = angle-of-sideslip
μ = bank angle
R = range
ω = angle off
$\Delta\chi$ = relative heading angle
q = dynamic pressure
σ = bearing angle
λ = elevation angle
γ = flight path angle
X = down-range location
Y = cross-range location
χ = velocity vector bearing angle
V = velocity vector magnitude
T = net thrust
m = aircraft mass
D = trimmed drag
L = trimmed lift
μ = wind axis roll angle
F_γ = total applied normal force
Fx = total applied lateral force
τ = time constant
c = mean aerodynamic chord
$CL_{\max}$ = maximum lift coefficient
$C_{M_{\alpha_T}}$ = $dCM/d\alpha$ at $CL_{\max}$
$C_{N_{\beta_T}}$ = $dCN/d\beta$ at $CL_{\max}$
δ = nozzle deflection angle
ζ = damping ratio
ω_n = damped natural frequency
q, p, r = aircraft rotational rates about pitch, yaw, and roll axes
b = wing span
Λ = wing sweep-back angle
Lx = longitudinal thrust application point
FRL = fuselage reference line
TOPCAT = tactics optimization and combat analysis technique
BAR = Birhle applied research
LaRC = Langley Research Center (NASA)
DTRC = David Taylor Research Center
MAX A/B = maximum afterburner thrust setting
IRT = intermediate thrust setting
LOS = Line-of-sight

Downloaded 02 Jun 2010 to 171.66.16.122. Redistribution subject to ASME license or copyright; see http://www.asme.org/terms/Terms_Use.cfm

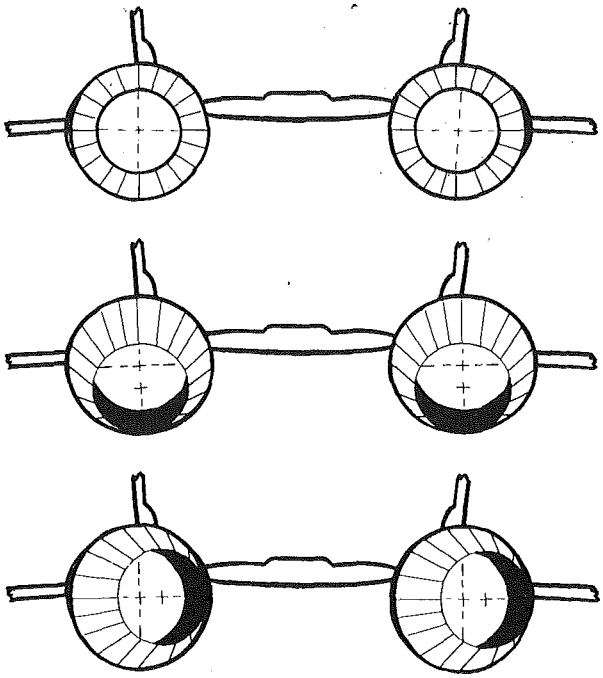


Fig. 3 Thrust vectoring options modeled

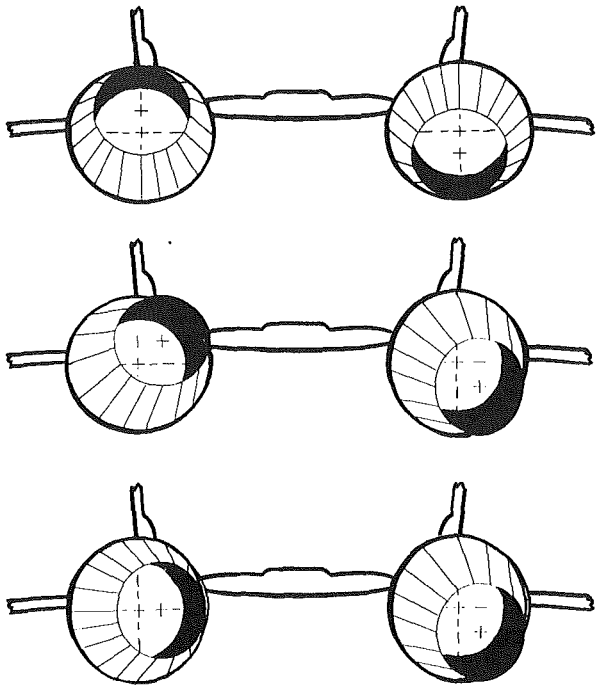


Fig. 4 Thrust vectoring options deferred

have recently expressed interest in identifying the impact of multi-axis thrust vectoring on F-14 combat characteristics.

Thrust Vectoring Options Modeled. A practical vectoring angle of 12 deg has been selected for deflections in all directions. Figure 3 identifies the thrust-vectoring options modeled in this study.

It is recognized that additional options exist; for example, coupled roll-yaw maneuvers are possible as well as coupled pitch-roll-yaw maneuvers (Fig. 4). The F-14 twin engine, widely spaced, axisymmetric nozzles are separated by 2.8 m, making it possible to add thrust vectoring roll control to the pitch and yaw control enhancement that would not be possible with a single engine aircraft. These options will be deferred for a later investigation.

In the combat tactics optimization model to be described, only maximum performance climbs, dives, and turns are commanded in order to position the aircraft in an end-game state where final pointing adjustments are made consistent with launching a weapon. Reduced performance maneuvers that are less than the maximum are not considered in this study, save for the option of performing a left and right sustained turn. For this option the bank angle and engine thrust setting are selected to maintain both altitude and speed.

The Blue aircraft (with thrust vectoring and reversing) will benefit in several ways when control commands are executed. First, when aircraft pitch and yaw angles have not yet reached the commanded level, thrust axis gimbaling is set to augment achievable rates, i.e., the vectoring is implemented so the aircraft can reach a commanded orientation sooner than would be possible with conventional aerodynamic effectors. Second, when the commanded pitch or yaw angle is greater than that which can be trimmed with the control surfaces, nozzle gimbaling is used to command a higher pitch/yaw limit that is a function of the dynamic pressure, thrust force, and nozzle gimbal angle limits. Finally, thrust vectoring generates a higher commanded normal force level, the result of the thrust vector component in the normal direction. This last benefit can be secured only at flight conditions when the aircraft structural limit has not been exceeded.

Potential benefits listed above will be effective providing that tactics developed do not accentuate attendant penalties. One thrust vectoring penalty that should be apparent is that the vectoring component used in the normal direction reduces thrust available in the axial direction. This increases deceleration rates during maximum performance maneuvers. But more important, higher trimmed pitch angles generate extraordinarily higher drag levels, the result of aircraft drag polar characteristics at very high incidence. As a result, the thrust vectoring Blue aircraft will bleed off speed much faster than its red opponent when vectoring is used; this places a premium on achieving a kill before the higher performance vehicle reaches stall speed, forcing it to dive. The dive option will extend combat time to the extent that the aircraft altitude has not reached "0."

Tactics Optimization Mechanics. Tactics and trajectories identified in this study were derived using a modified form of a Grumman-developed analytical tool called Tactics Optimization and Combat Analysis Technique (TOPCAT) (Falco et al., 1974; Falco and Carpenter, 1982); development was completed during the mid-70s under contract to the U.S. Air Force. The TOPCAT formulation takes advantage of differential game theory, stochastic learning processes, and optimal control theory. In past applications, this tool has been used to quantify the relative zones of advantage between two combatants using a statistical approach, but for this study emphasis will be on identification of specific tactics and the resulting trajectories. In particular, the computer simulation is required to identify aircraft state parameters during extreme combat maneuvering.

Toward this end, two aircraft models were developed. The first, or Red aircraft, has the flight characteristics of a standard F-14 and the maneuvering options are consistent with current F-14 flying qualities and combat tactics. The second aircraft, designated Blue, is a standard F-14 augmented with twin engine thrust vectoring/reversing as an enhancement for pitch and yaw control.

A gaming space is required to implement the mathematical process, so both the Blue and Red F-14s are positioned at the center of 30 km spheres that are discretized into a large number of three-dimensional regions for computational purposes (see Fig. 5). As the aircraft "fly" along their respective trajectories, the spherical regions move with them. For this study, the following space segmentation was effected:

Downloaded 02 Jun 2010 to 171.66.16.122. Redistribution subject to ASME license or copyright; see http://www.asme.org/terms/Terms_Use.cfm

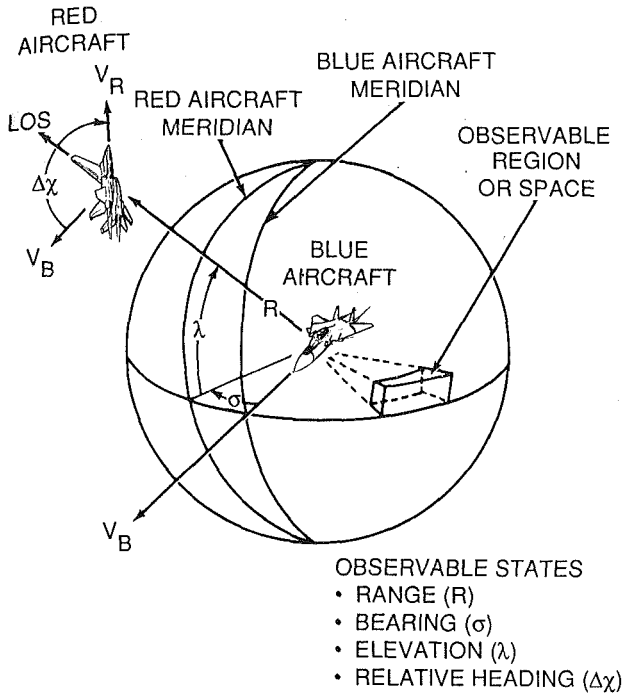


Fig. 5 *Discretization of observable space*

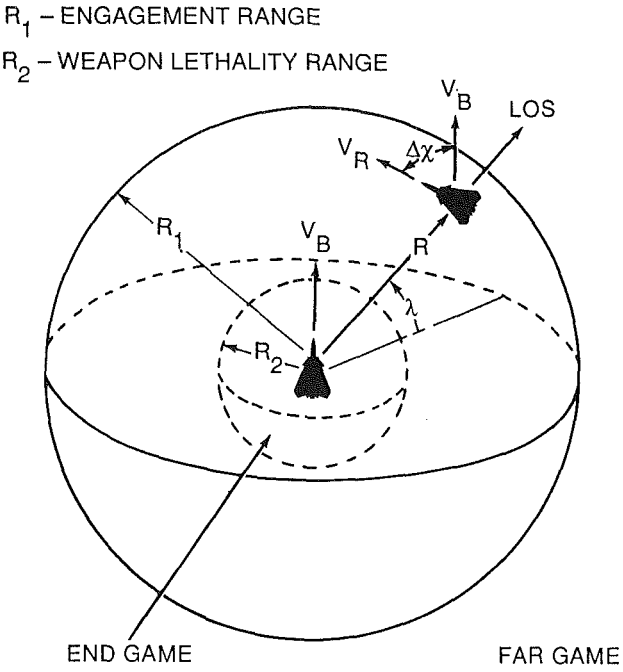


Fig. 6 **Combatant far and end-game regions**

- Range (km) — 0/0.5/1.0/2.0/3.0/5.0/10.0/20.0/30.0
- Bearing (deg) — 0/15/45/90/135/165/180/195/225/270/315/345/360
- Elevation (deg) — 90/45/15/0/−15/−45/−90.

These regions in the space about each combatant can be thought of as observable states. In other words, during a combat engagement, each pilot will observe his opponent at some position in space outside the canopy. In addition, the pilot will identify a relative heading of the target aircraft. This heading information adds another dimension to the problem that also must be discretized. That has been done as follows: Heading (deg) – 0/90/180/270/360. Thus, 8 range bins combine with 12 bearing, 6 elevation, and 4 heading bins to form 2304 observable spaces (or regions). By propagating a large number of trajectories, the best maneuver decision in each observable region can be derived for both the Blue and Red combatants.

Figure 6 illustrates another important aspect of the computational space. At any point in time, the relative states of the combatants will place each in a specific observable region. During the engagement, each combatant is given the opportunity to make a new maneuver decision when the adversary crosses over into a different observable region. This maneuvering trajectory propagation continues until one aircraft is maneuvered into the weapon launch acceptable region (LAR) of the other. At this point in time, transition into a near-field or end-game scenario might be effected with fine-tuning the controls for tracking and launch. For this study, the primary interest is thrust-vectoring impact on overall far-game maneuvering and positioning. As a result, one combatant transitioning into the end-game mode is equated with a kill or win. This end-game or kill-point along the trajectory is declared when:

- The target aircraft is within weapon LAR (i.e., between min/max weapon ranges).
- The attacking aircraft maximum turning rate is 20 percent greater than the LOS rate.
- The angle between the attacking aircraft boresight axis and LOS is less than 25 deg.

Instead of an exhaustive study that addresses all possible combat engagement scenarios, the present effort focuses on codirectional and head-on engagements where the Blue and Red aircraft begin combat maneuvering side-by-side separated by 300 m. In this manner, no aircraft has a starting position advantage. Both aircraft have tracking angles initiated at 90 deg for the side-by-side head on, and codirectional cases. Trajectories are displayed in a reference coordinate system labeled with "Down Range," "Cross-Range," and "Altitude."

Weapon Model. The aircraft aerodynamic characteristics and control options available to the pilot will have a first-order effect on fight mechanics and ultimately the tactics used to achieve favorable outcomes in aerial combat. But the weapon used also will have an important effect on this process, so it too must be modeled in some manner. For the present investigation, a state-of-the art, short-range, IR seeker, air-to-air missile has been selected. Interest in this weapon for close-range aerial combat is reinforced by the absence of gun kills in the recent Gulf War.

Propagating the weapon's trajectory, simulating the weapon end-game, and computing kill probabilities based on warhead characteristics are beyond the scope of this study. Instead, because combat kills will to a large extent be determined by which combatant achieves a firing position first, the key facet of the weapon model becomes the LAR. For this study, the minimum and maximum launch ranges are required. These ranges are modeled as a function of three variables:

- The angle between the target velocity vector and the LOS to the interceptor (ω).
- Missile Mach number at launch (M_L).
- Target Mach number at launch (M_T).

The relation used is:

$$R_{\min} = a_0 + a_1\omega + a_2\omega^2 \quad (1)$$

$$R_{\max} = [b_0 + b_1\omega + b_2\omega^2]\ (1.0 + 0.5\ (M_L - M_T)) \quad (2)$$

where the "a" and "b" coefficients are selected to fit weapon characteristics. One set of coefficients is used when the angle between the target velocity vector and the LOS is between 0 and 90 deg and another set is used for angles from 90 to 180 deg.

Downloaded 02 Jun 2010 to 171.66.16.122. Redistribution subject to ASME license or copyright; see http://www.asme.org/terms/Terms_Use.cfm

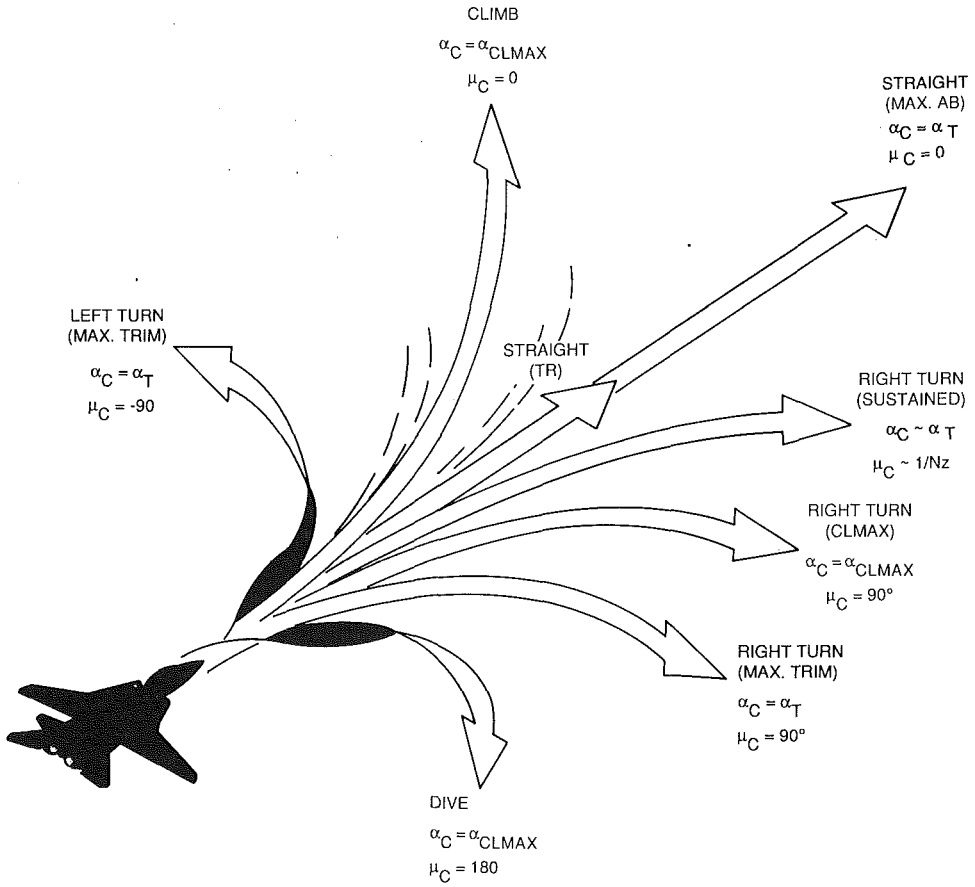


Fig. 7 Blue aircraft maneuver command options

Maneuvering Options. During aerial combat the pilot makes maneuvering decisions as time progresses. This sequence of climbs, dives, and turns is aimed at maximizing win or survivability probability. Trajectory point decisions translate into commands to the aircraft flight control system; these commands will be a function of the control technology level inherent in the vehicle design. Control system commands will next transition into aircraft kinematics that are derived from airframe and control system models.

It should be apparent that the Red and Blue aircraft will have different maneuvering options available. The Blue aircraft will have 10 options (Fig. 7). The maximum afterburner power level is selected for seven of the maneuver choices. Left and right sustained turns set thrust (and bank angle) to levels required for maintaining altitude and speed. The "straight" option with thrust-reversing sets power to half that available with maximum afterburner, but the force is applied in the opposite direction. An AOA command is derived from the aircraft trimmed life-drag characteristics that is consistent with the thrust available at the trajectory point Mach number and altitude.

The Red aircraft or standard F-14 is also modeled with a total of 10 maneuver options. The only difference between these options and those of the Blue aircraft is that the "straight" option with thrust-reversing is now replaced with IRT thrust. As with the Blue aircraft, all maximum performance options are affected with a maximum afterburner power setting.

Each maneuver command option for Red and Blue results in a unique set of thrust, incidence, roll, and yaw commands for the aforementioned dynamics modeling. For the "straight" option, however, the aircraft is trimmed at the flight path angle at that point in time and the angle is held constant until the next time step.

Aircraft Model. Combat maneuvering typically occurs at the limits of aircraft performance and controllability. This demands a mathematical model with an inherent nonlinear formulation to capture true flight mechanics. A full 6-DOF simulation would be desirable, but the tactics optimization phases of this effort required 120-s trajectories that numbered in the tens-of-thousands for each combination of aircraft, weapon, and control parameters investigated. For this reason, it becomes important to find a viable alternative to 6-DOF that will generate pertinent physics but without the need for modeling specific control deflections and solving the angular rate equations.

In view of satisfactory results generated during an X-29 tactics study, the present effort will take advantage of two established resource-saving schemes. First, the aircraft kinematics are simulated using a three-dimensional point mass representation that is complemented with a first-order lag approximation for pitch and yaw attitude dynamics and a similar approximation for roll rate response. Second, performance data (trimmed lift, drag, net thrust, etc.) is curve fit to avoid time consuming multi-argument table look-up algorithms. This requires some work up front but saves considerable resources over the course of the study.

Using a Cartesian coordinate system, the Blue and Red aircraft positions are computed by integrating the differential equations listed below:

$$\dot{X} = V \cos\gamma \cos\chi \tag{3}$$

$$\dot{Y} = V \cos\gamma \sin\chi \tag{4}$$

$$\dot{h} = V \sin\gamma \tag{5}$$

Velocity vector magnitude and orientation are obtained by integration of the following wind-axis differential equations:

Downloaded 02 Jun 2010 to 171.66.16.122. Redistribution subject to ASME license or copyright; see http://www.asme.org/terms/Terms_Use.cfm

$$m\dot{V} = T - D - mg \sin \gamma \tag{6}$$

$$mV\dot{\gamma} = F_\gamma \cos \mu - F_x \sin \mu - mg \cos \gamma \tag{7}$$

$$mV\dot{X} \cos \gamma = F_x \cos \mu + F_\gamma \sin \mu \tag{8}$$

Aircraft longitudinal response characteristics are modeled using a first-order transfer function for AOA:

$$\alpha/\alpha_c = \frac{1}{\tau_p s + 1} \tag{9}$$

Lateral-directional dynamics are modeled in a similar manner where:

$$r/r_c = \frac{1}{\tau_r s + 1} \tag{10}$$

Finally, roll response is modeled using:

$$p/p_c = \frac{1}{\tau_r s + 1} \tag{11}$$

The relations listed above are suitable for the Red aircraft independent of the maneuver option selected and the Blue aircraft when the maneuver option selected is "straight." But the Blue aircraft with thrust vectoring requires model upgrades to simulate maximum performance turns and thrust reversing properly.

Taking the simplest case first, thrust reversing is modeled by assuming that 50 percent of the net forward thrust available is achieved in the aft direction, i.e.,

$$T_{tr} = -0.5 \times T_{\text{net}} \tag{12}$$

Turns involving pitch and yaw require additional effort. First, thrust vectoring will affect trimmed attitudes. To model this, the aerodynamic and propulsive forces and moments are balanced beyond the point of maximum aerodynamic trim:

$$M_A = M_T \tag{13}$$

$$M_A = N_T \tag{14}$$

where

$$M_A = qScC_{M_{\alpha_T}} \Delta\alpha_{TV} \tag{15}$$

$$M_T = LxT \sin \delta_{T_P} \tag{16}$$

$$N_A = qSb\ C_{N_{\beta_T}} \Delta\beta_{TV} \tag{17}$$

$$N_T = LxT \sin \delta_{T_y} \tag{18}$$

This results in increments to trimmed incidence and sideslip that effectively expand the trimmed flight envelope.

$$\Delta\alpha_{TV} = \frac{Lx \cdot T \cdot \sin \delta_{T_P}}{qSc\ C_{M_{\alpha_T}}} \tag{19}$$

and

$$\Delta\beta_{TV} = \frac{Lx \cdot T \cdot \sin \delta_{T_y}}{qSb\ C_{N_{\beta_T}}} \tag{20}$$

This envelope (α, β) expansion is used during the simulated combat engagement to attain maximum maneuverability or pointing where $CL_{\max}$ has been attained providing that the aircraft structural limit has not been exceeded.

Thrust vectoring also will have an effect on the time constants described earlier. The pitch time constant due to vectoring thrust has been approximated by:

$$\tau_{p_{TV}} = \frac{2\zeta_P}{\omega_{N_P}} \left[\frac{\dot{q}_{\max}\ (\text{AERO})}{\dot{q}_{max}\ (\text{AERO}) + \dot{q}_{TV}} \right]^{1/2} \tag{21}$$

Similarly, the yaw time constant due to vectoring thrust has been approximated by:

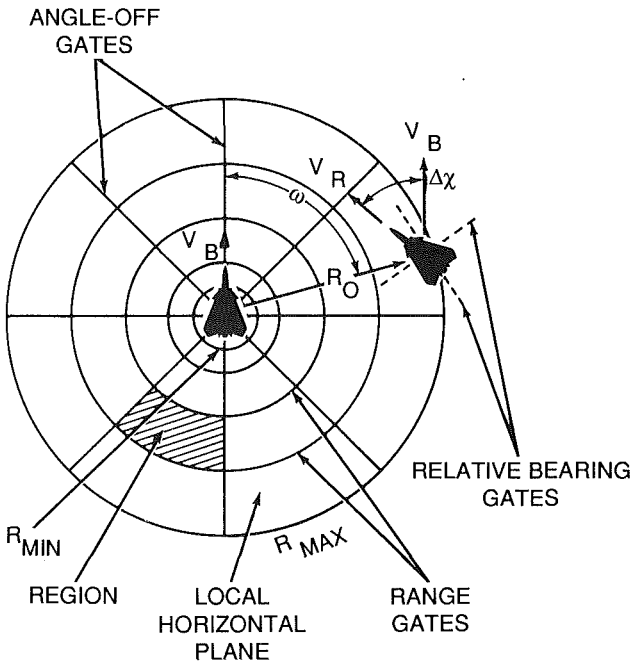


Fig. 8 Sample space discretization

$$\tau r_{TV} = \frac{2\zeta_{DR}}{\omega_{N_{DR}}} \left[\frac{\dot{r}_{\max}\ (\text{AERO})}{\dot{r}_{\max}\ \text{AERO}) + \dot{r}_{TV}} \right]^{1/2} \tag{22}$$

Key characteristics that make up the remainder of the aircraft model are listed below along with their functional dependence:

Aircraft model characteristic	A function of:
1 Trimmed lift	AOA and Mach
2 Engine thrust	Altitude and Mach
3 Trimmed drag	AOA and Mach
4 Max trimmed α	Mach
5 Max lift α	Mach

Game Theory Maneuver Strategy Development. A large number of trajectories must be simulated to develop optimum defensive and offensive strategies for the Red and Blue combatants. To accomplish this, a reference or sampling space must be defined. Discretization of this sampling space provides a basis for aircraft relative starting positions. Three-dimensional aerial combat can be initiated with any combination of range, angle off, elevation, and relative heading. For this simulation optimization process all possible starting scenarios are collapsed into a local horizontal plane. Range effectively becomes downrange and elevation no longer has any meaning.

Discretization of the sample or initial state space is affected by setting range, angle off, and relative bearing boundaries (see Fig. 8). For the present investigation the following sample space breakdown has been used:

- Down range (km) = 0/0.25/0.50/1.0/2.0/3.0/5.0/10.0.
- Angle off (deg) = 0/30/60/90/120/150/180/210/240/270/300/330/360.
- Relative heading (deg) = −45/45/135/225/315.

This yields 7 range, 12 angle off, and 4 relative heading bins for a total of 336 sample space regions. Symmetry about the vertical plane makes it possible to consider only angle-off values from 0 to 180 deg. Each of the remaining 168 regions requires about 100 trajectories to develop useful tactics. Each

Downloaded 02 Jun 2010 to 171.66.16.122. Redistribution subject to ASME license or copyright; see http://www.asme.org/terms/Terms_Use.cfm

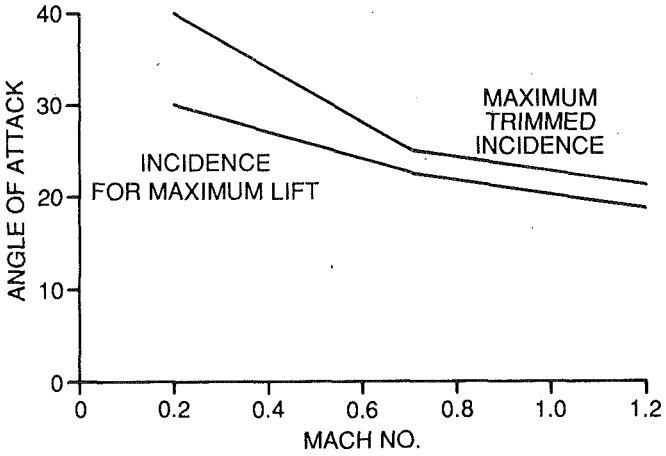


Fig. 9 F-14 high angle-of attack characteristics

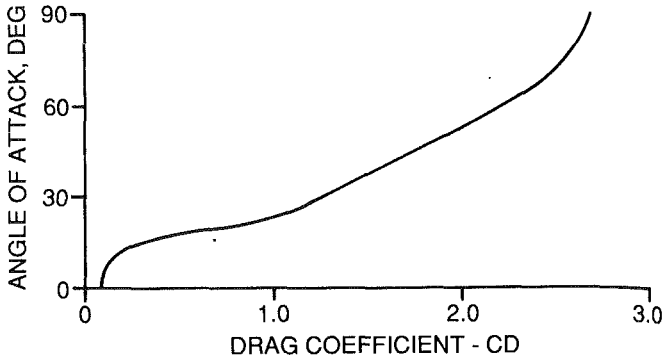


Fig. 10 F-14 low-speed drag characteristics

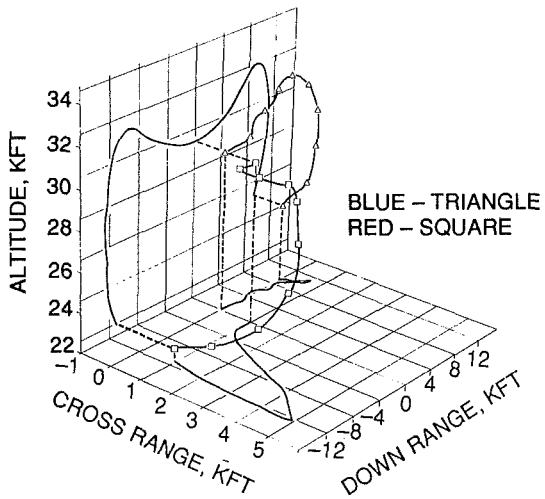


Fig. 11 Head-on start combat trajectories

trajectory is propagated for a maximum of 120 flight seconds. This step is simplified if a supercomputer is available and for this study a Cray Y-MP was used. The 16,800 trajectory, "Learning Phase" of this effort required approximately two hours of computing for each case of interest.

To begin the process, each combatant is assigned a strategy table, the dimensions of which are the number of observable state regions by the number of control options. For the Red and Blue aircraft this table is 2304 by 10. The tables are initialized by setting all control choices in all observable regions equal to the reciprocal of the number of control choices. In other words, at the beginning of the process, all control choices have the same probability of being selected.

A random number generator picks the relative initial condition from within the sampling space. As the aircraft paths pass through contingency or observable state regions, a control option is selected at random and the aircraft is propagated forward in time. Each control choice in each observable region is saved and at the end of the trajectory a reinforcement (reward/penalize) strategy is affected. The table below summarizes the strategy elements when both the Red and Blue aircraft are aggressive:

No.	Event Description	Reinforcement Policy Blue	Red
1	Kill by Blue	Reward	Penalize
2	Kill by Red	Penalize	Reward
3	Blue stalls	Penalize	NA
4	Red stalls	NA	Penalize
5	Blue ground impact	Penalize	NA
6	Red ground impact	NA	Penalize

Thus if Event No. 1 occurs, all control choices made by Blue in the appropriate contingency spaces along the trajectory are incremented in the Blue strategy table. At the same time control choices made by Red are decremented in respective observable regions for the Red strategy table. After a very large number of trajectories, a preferred control choice evolves in each of the aircraft's observable regions that maximizes the combatant's goals.

Tactics Optimization. Initial tactics optimization analyses generated surprising results. The Blue aircraft with thrust vectoring lost every engagement. In this initial modeling the difficulty was tracked back to the lift and drag characteristics of the basic aircraft and the control options made available. To understand this better, F-14 angles for maximum lift and trim have been sketched in Fig. 9. It can be seen that the clean airframe incidence angles achievable are quite high, particularly at low speeds. The maximum trimmed AOA is attained with the stick in the full-back position. At these extreme incidence conditions the drag forces are relatively high, as can be seen in Fig. 10. But depending on the conditions, thrust vectoring adds an additional 5 to 15 deg of trimmed AOA (Eq. (19)). This can effectively double drag levels that are already very high.

Examination of the initial trajectories that permitted only maximum performance climbs, dives, and turns revealed that the Blue thrust vectoring aircraft lost speed at a much faster rate than the conventional Red aircraft without thrust vectoring. On average, the Blue aircraft reached stall speed before turning could be completed to affect a kill. When stall was reached, the command to dive (to gain speed) forced the Blue aircraft into a compromised position of which the Red aircraft could always take advantage.

This problem is not related to deficiencies in thrust vectoring technology, but rather it points out an error in the initial formulation of control choices. For this reason the maneuver control choices were augmented. Results presented in this paper reflect control choices that include sustained turns and maximum lift turns in addition to maximum trimmed AOA turns. This now makes it possible for the Blue thrust vectoring aircraft to use the vectoring capabilities sparingly (if that is required to achieve a win).

Combat Trajectory Characteristics. In using a Differential Game Theory tool for investigating tactics and trajectories it is important to recognize that there is no simple closed-form optimum solution that is attainable. The statistical method produces a result that represents some "average best" and as such it becomes important to check out a number of trajectories in the starting set region to ensure that any one is not an

Downloaded 02 Jun 2010 to 171.66.16.122. Redistribution subject to ASME license or copyright; see http://www.asme.org/terms/Terms_Use.cfm

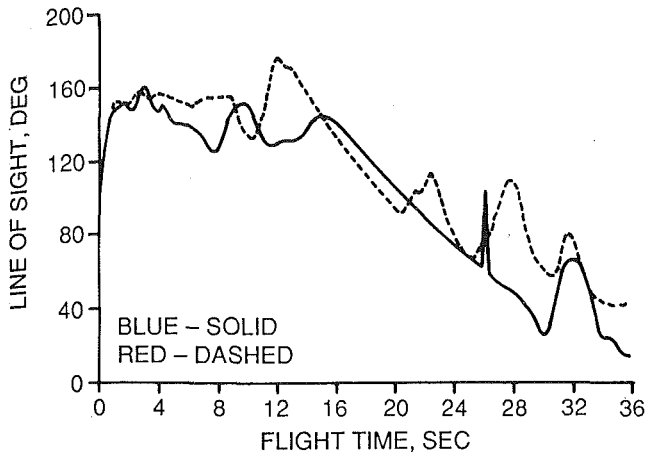


Fig. 12 Blue/red aircraft line-of-sight characteristics for head-on start combat maneuvering

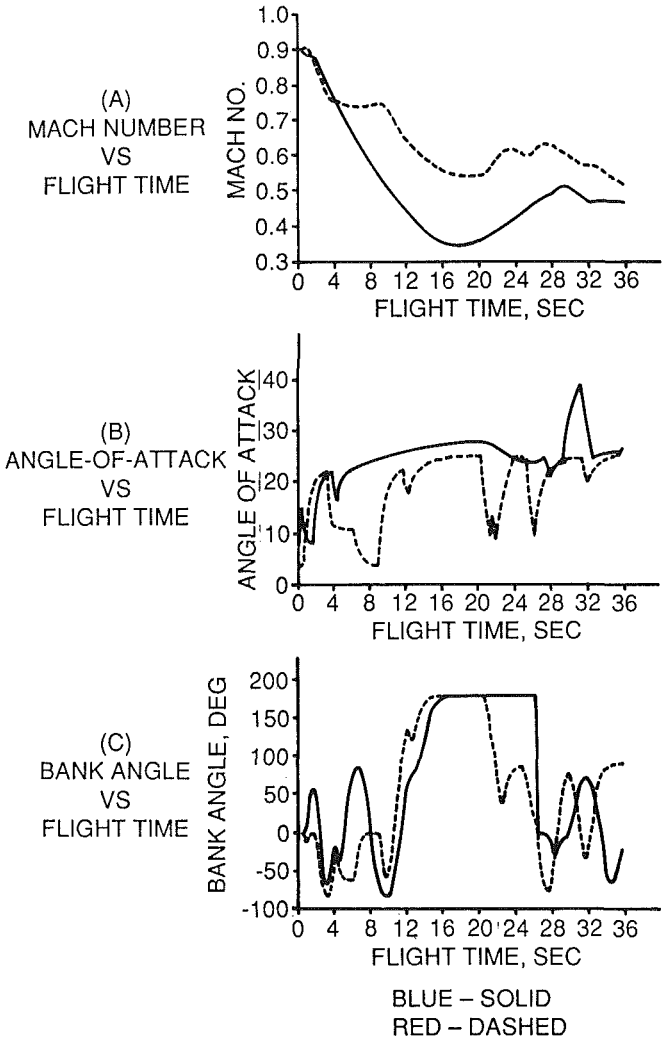


Fig. 13 Mach number and pitch/roll response for head-on start combat maneuvering

anomaly. This has been done, but given the size constraints of this paper, only two trajectories can be selected to illustrate typical characteristics.

Figure 11 shows the three-dimensional trajectory that results when the combatants start head-on at M = 0.9 and 30K ft. Traces on the back and horizontal planes serve as an aid to

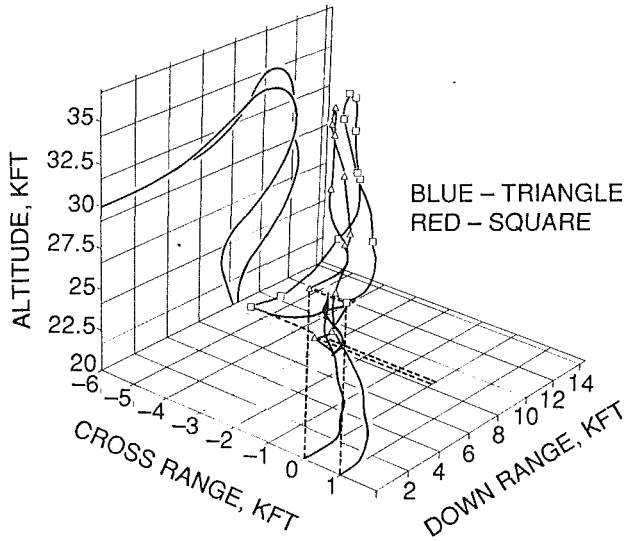


Fig. 14 Codirectional start combat trajectories

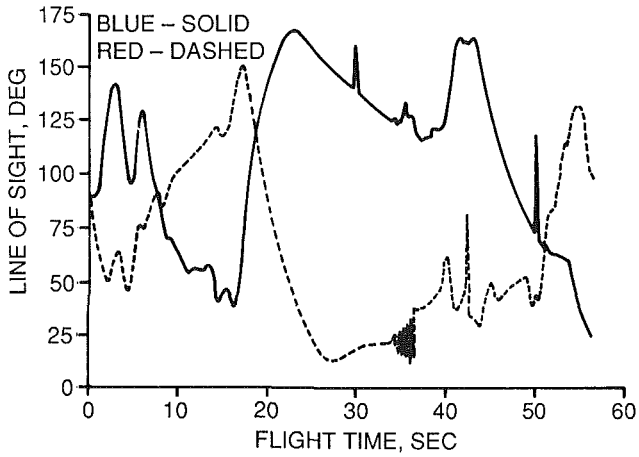


Fig. 15 Blue/red aircraft line-of-sight characteristics for codirectional start combat maneuvering

visualizing the trajectories. This engagement results in Blue gaining an advantage over Red in 35 s. It can be seen that both aircraft start by climbing; this is followed by turning and diving. LOS, Mach number, and pitch/roll characteristics during this combat sequence can be found in Figs. 12 and 13. From these figures it can be seen that the Blue aircraft does not use thrust vectoring to expand pitch attitude capabilities until about 30 s into the combat sequence. When vectoring is implemented, the result is to close the LOS angle for a win.

An interesting facet of this simulation is that one of the combatants can act defensively. In this mode, the Red, or less capable fighter, can satisfy a goal of survivability by reaching "out of range" or by avoiding being fired upon within the 120 s time limit imposed. When the "Red-Defensive" option was exercised, the Blue aircraft thrust-vectoring and thrust-reversing benefit identified during mutually offensive combat did not register for head-on start engagements.

Similar high AOA tactics can be identified when the combatants start side-by-side going in the same direction (Figs. 14–16). Blue achieves an advantage over Red in 56 s. In this case, the Blue aircraft uses thrust-vectoring to expand aircraft pitch limits near the 3, 6, and 38 s points along the trajectory. Once again, the final application of vectoring appears to initiate a trend of rapid closure of the LOS angle.

Unlike the head-on start case, the "Red-Defensive" option did not guarantee survivability, i.e., for side-by-side codirec-

Downloaded 02 Jun 2010 to 171.66.16.122. Redistribution subject to ASME license or copyright; see http://www.asme.org/terms/Terms_Use.cfm

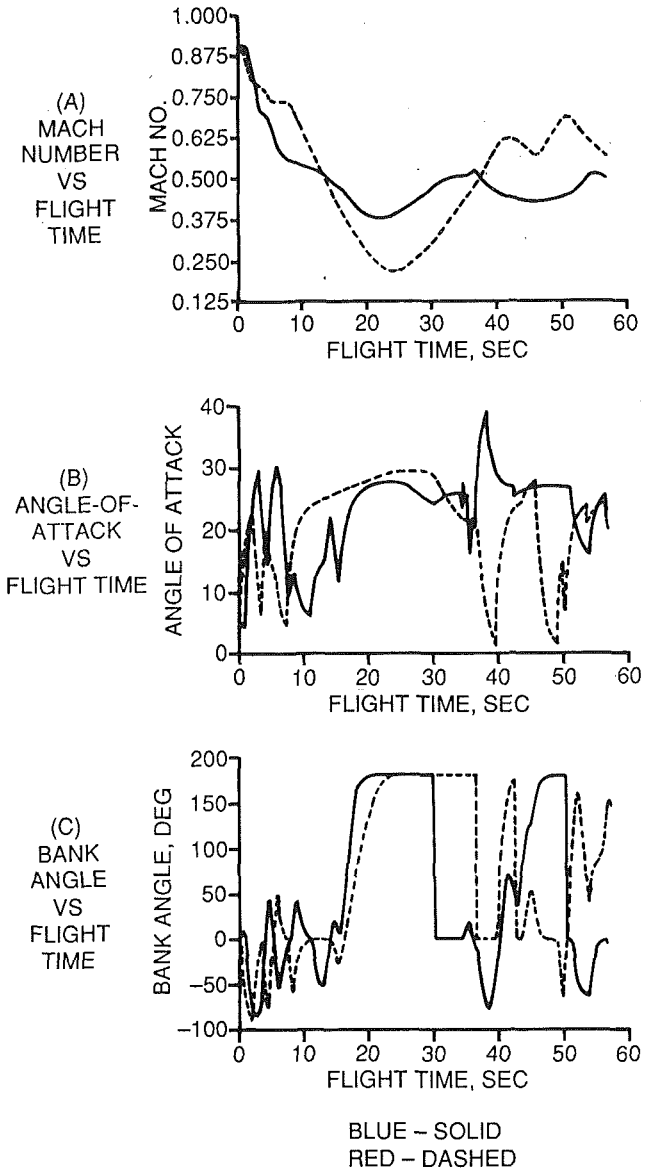


Fig. 16 Mach number and pitch/roll response for codirectional start combat maneuvering

tional start engagements, the less capable Red aircraft could not escape the more capable attacking or offensive aircraft.

Concluding Remarks

This paper describes a digital simulation performed to identify the potential benefits and risks associated with implementation of engine thrust-vectoring in air-to-air combat. A key feature of the study is that the tactics developed were dependent only on the characteristics of the combatants and weapons. There were no prejudgments as to what is a good or bad tactic.

One of the most interesting observations was that thrust-vectoring and thrust-reversing capabilities were used very sparingly during the simulated combat engagements. This is explained by the fact that high AOA flight and reversed thrust come with an attendant loss of speed. This speed loss is sufficiently large to prevent line-of-sight closure before the attacking aircraft stalls, or is forced to dive.

It also should be apparent that higher trimmed incidence angles for the thrust vectoring combatant (39 deg for cases included herein) increases the potential for loss of control in the event of an engine thrust or flight control failure. This can be attributed to the fact that existing fighter aircraft have better flight and handling characteristics below about 20 deg AOA than above this level (Schaefer, 1982). In view of this, a failure modes study is an appropriate complement to the study just described.

Finally, the results and conclusions are based on the aircraft and simulation code modeling assumptions and limits described earlier. Additional characteristics of thrust vectoring and reversing are expected when the model is enhanced for the deferred options identified in Fig. 3. Beyond this, different insights might be gained by including the representation of end-game manuevering in the overall simulation.

Acknowledgments

The authors would like to acknowledge the efforts of Charles Giannetto and his team for setting up and performing an X-29 combat effectiveness study during the mid-1980s. This modeling formed the tactics optimization basis for the study described herein, but no unclassified references exist to convey proper credit.

References

Beaufrere, H., 1991, Grumman Corporation, Private Communication.

Etkin, 1959, *Dynamics of Flight*, Wiley, New York.

Falco, M., et al., 1974, "The Analysis of Tactics and System Capability in Aerial Dogfight Game Models," AFOSR F44620-72-C-0032.

Falco, M., and Carpenter, G., 1982, "The Assessment of Aircraft Combat Effectiveness Using a New Computational Method," AGARD CP-319, pp. 22-1, 22-11.

Lacey, D., 1983, "Jet Engine Thrust Turning by the Use of Small Externally Mounted Vanes," DTNSRDC Report DTNSRDC-82/080.

Lacey, D., 1990, DTRC, Private Communication.

Sappington, J. W., and Thompson, R. L., 1984, "F-14A Yaw Vane Technology Demonstration Program," DTNSRDC Report DTNSRDC/ASED-84/08.

Schaefer, F., 1982, "F-14A High Angle-of-Attack Investigation With Asymmetric Thrust and Stores," *Proceedings of the 13th Annual Symposium of the Society of Flight Test Engineers.*

Downloaded 02 Jun 2010 to 171.66.16.122. Redistribution subject to ASME license or copyright; see http://www.asme.org/terms/Terms_Use.cfm

Transient Phenomena in Compressor Stations During Surge

K. K. Botros
NOVA HUSKY Research Corporation,
Calgary, Alberta, Canada
T2E 7K7

Transient phenomena are generally inherent in the operation of compressor stations: These are either fast or slow transients. A model describing the governing equation for the gas dynamics, control system, compressor and turbine shaft inertias has been developed. The effect of these inertias is manifested by an example of a compressor station operating near the surge control line. Another example deals with a station that has a cooler placed in the recycle path. This alters the rate at which the compressor shaft decelerates upon shutdown and may cause backward spinning depending on the relative magnitude of the shaft inertia with respect to the cooler volume. Backward spinning of compressor shaft has detrimental effects on dry seals and is undesirable. It was found that by keeping the recycle valve closed upon shutdown, the rate of shaft deceleration will be reduced.

Introduction

The mathematical modeling of the gas dynamic behavior of a compressor/turbine set in natural gas compressor station involves solution of different equations describing both the gas dynamics in the piping and compressor elements as well as those describing the associated station and unit controls. Both sets of equations are necessary for any accurate simulation of unsteady and transient phenomena in compressor stations. These transient phenomena are generally inherent in the system as the gas flow is never steady and the operation of the station necessitates changes in the setpoints and operation modes in order to meet certain demands.

A model describing the governing equations for the gas dynamics and the control system has been developed [1]. In this model, all conservation equations for one-dimensional unsteady compressible fluid flow in all piping elements were written and solved to handle both slow and rapid transients. The governing equation for the turbomachinery considered a dual-shaft gas turbine/compressor arrangement (see Fig. 1), which responds to any perturbation in a quasi-steady manner. In this formulation neither the gas generator, nor the power turbine/gas compressor shafts inertias were taken into account. Obviously in rapid transients such as those occurring during compressor startup and shutdown, and also during compressor surge protection, neglecting these inertias can lead to inaccurate simulation results.

In this paper, the governing equations for the turbomachinery, including shaft inertias, are described. The effect of these inertias is manifested by an example of a compressor station operating near the surge control line with the surge control in effect. Comparison with field measurements shows that better agreement is obtained when shaft inertias are included in the simulation. Another example deals with a high-head (enthalpy) unit station, which necessitated a large cooler in the recycle path. When such a unit is shut down, the high capacitance (volume) of the cooler may cause a higher rate of compressor deceleration, which may result in shaft spinning in the opposite direction. This may damage the compressor dry seals and therefore should be avoided. The effects of shaft inertia and its relative magnitude to the cooler volume are assessed numerically following unit shutdown. The phenomenon also involves unstable surge cycles.

The last topic discussed in this paper is the effect of placing these coolers in the recycle path on unit surge protection. The concern was that the large capacitance associated with the coolers may sustain the high discharge pressure for a while, causing the unit to surge even with a high-response recycle valve.

Governing Equations for the Turbomachinery With Shaft Inertia

The mathematical models describing the gas flow dynamics in various piping elements have been presented in detail in [1].

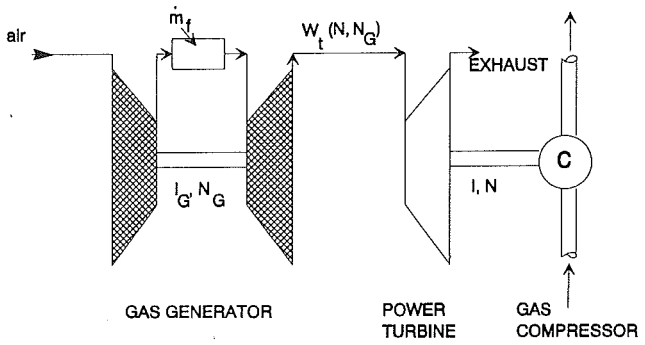


Fig. 1 Schematic of a dual-shaft compression system

Contributed by the International Gas Turbine Institute and presented at the 37th International Gas Turbine and Aeroengine Congress and Exposition, Cologne, Germany, June 1-4, 1992. Manuscript received by the International Gas Turbine Institute January 28, 1992. Paper No. 92-GT-24. Associate Technical Editor: L. S. Langston.

Copyright © 1994 by ASME
Downloaded 02 Jun 2010 to 171.66.16.122. Redistribution subject to ASME license or copyright; see http://www.asme.org/terms/Terms_Use.cfm

These models comprise large systems of nonlinear hyperbolic partial differential equations mainly to describe the one-dimensional, compressible, and unsteady flow in pipes, together with nonlinear algebraic equations describing the quasi-steady flow through valves, constrictions, capacitance and resistive elements. The control system mathematical description consists of mixed algebraic and ordinary differential equations with some inequalities representing controller's limits. Solution of the above two systems of equations is performed in a stepwise and sequential manner so as to close the feedback loop of information transferred between the two systems. Linearization techniques adapted depend on the type of transients considered, e.g., slow or rapid.

The compressor system is assumed to respond to any perturbation in a quasi-steady manner. Linearization via first-order Taylor expansion with Jacobians evaluated at time ($n \cdot \Delta t$) is applied to the governing equations. This furnishes the relationship between the perturbed quantities of the gas flow on both sides of the gas compressor.

The dual shaft gas turbine/compressor arrangement shown in Fig. 1 is considered here, where the gas generator speed (N_G) is different from that of the power turbine and compressor speed (N). The governing equation of gas flow through the centrifugal compressor can be approximated by the polytropic process [1, 2], i.e.:

Continuity

$$F_1 = \dot{m}_1 - \dot{m}_2 = 0 \tag{1}$$

Polytropic Pressure Ratio

$$F_2 = \frac{P_1}{\rho_1^n} - \frac{P_2}{\rho_2^n} = 0 \tag{2}$$

Polytropic Head (Energy)

$$F_3 = \frac{Z_a R T_1}{(n-1)/n}\left[(P_2/P_1)^{\frac{n-1}{n}} - 1 \right] - H_P(Q_a, N) = 0 \tag{3}$$

where the polytropic head (H_P) for the compressor is a function of the actual inlet flow to the compressor (Q_a) and the compressor speed (N). Subscripts 1, 2 here refer to suction and discharge locations. A quadratic polynomial function was used alongside the affinity laws to determine $H_P(Q_a, N)$ and also for the compressor polytropic efficiency $\eta_P(Q_a, N)$ [2].

For constant-speed compressors,the above three equations are sufficient to determine the relationship between the flow parameters upstream of the compressor [ρ_1, $\dot{m}_1$, P_1] to that downstream of the compressor [ρ_2, $\dot{m}_2$, P_2]. For variable speed compressors, two other equations are necessary, one relating the power turbine gas energy rate (W_t) to the fuel rate ($\dot{m}_f$) and the other the machine matching equation between power turbine output power and the compressor power. In both equations, both gas generator and power turbine/compressor shafts inertias come into play [3], viz.:

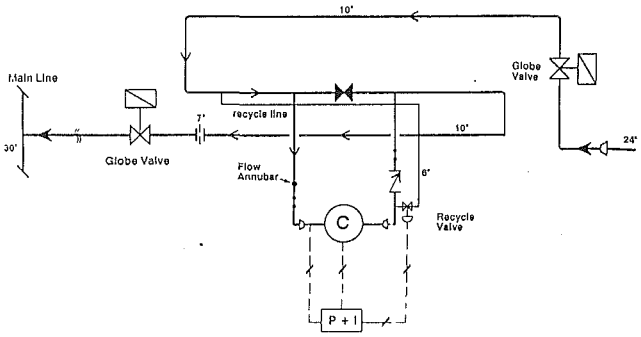


Fig. 2 Schematic of a single unit compressor stations

$$F_4 = W_t(N, N_G) + I_G \cdot N_G \cdot \frac{dN_G}{dt} - \dot{m}_f(t) \cdot \mathrm{LHV} \cdot \eta_t(N, N_G) = 0 \tag{4}$$

and

$$F_5 = \frac{H_P(Q_a, N) \cdot \dot{m}_1}{\eta_p(Q_a, N)} + I \cdot N \cdot \frac{dN}{dt} - \eta_m W_t(N, N_G) = 0 \tag{5}$$

where I_G and I are gas generator and power turbine/compressor shaft inertias, respectively. The coefficient η_t is the thermal efficiency of converting the heat energy into net gas energy produced by the power turbine, while the coefficient η_m is an efficiency relating the net output power taken by the gas compressor to the input power provided by the power turbine. The latter includes coupling, friction, and transmission efficiencies between the power turbine and the gas compressor. Linearization of the above five equations and rearranging to eliminate ΔN and ΔN_G will reveal the formal transfer matrix for the compressor in the form:

$$\begin{bmatrix} \text{Transfer Matrix} \\ 3 \times 6 \end{bmatrix} \begin{bmatrix} \delta U_1 \\ \delta U_2 \end{bmatrix} = [\text{RHS}]$$

$$U_1 = [\rho_1, \dot{m}_1, P_1],\ U_2 = [\rho_2, \dot{m}_2, P_2]$$

In the above formulation, both the power turbine output power (W_t), and the overall thermal efficiency (η_t) are functions of the air temperature and pressure, gas generator speed (N_G), and power turbine speed (N). Affinity laws similar to those developed for the gas compressor were used and are referenced in [1].

Compressor Surge Protection—Case Study

This example involves field measurements of a single unit compressor station in the gas transmission system of NOVA Corporation of Alberta. The layout of the station is shown schematically in Fig. 2. The objective was to assess the effec-

Nomenclature

Cg = valve coefficient
F = function
H_p = polytropic head
H_o = compressor head at zero flow
H_{SS} = steady-state compressor head
I = compressor/power turbine inertia
I_G = gas generator rotor inertia
LHV = Low Heating Value of the fuel
$\dot{m}$ = mass flow rate
$\dot{m}_f$ = gas fuel rate
n = polytropic exponent
N = compressor speed
N_G = gas generator speed
P = pressure
P_r = pressure ratio
Q_a = actual flow rate through compressor
r = compressor eye radius
R = gas constant
R_o = impeller outer radius
T_f = frictional torque
T_1 = compressor gas temperature
W_t = ower turbine gas power
Z_a = average compressibility factor
β = parameter of the cubic characteristic of the compressor
η_m = mechanical efficiency
η_p = polytropic efficiency
η_t = gas turbine thermal efficiency
ρ = density
τ = time constant
ϕ = parameter of the cubic characteristic of the compressor
ω = compressor speed, rad/s

Downloaded 02 Jun 2010 to 171.66.16.122. Redistribution subject to ASME license or copyright; see http://www.asme.org/terms/Terms_Use.cfm

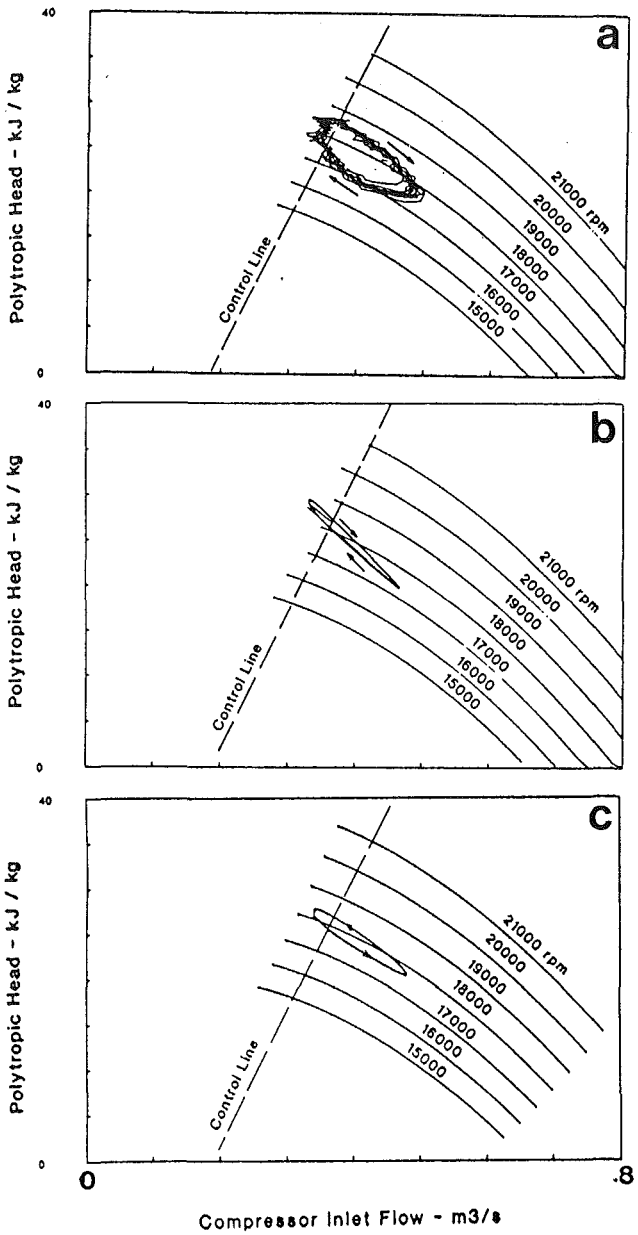


Fig. 3 Surge protection cycle for the system shown in Fig. 2: (*a*) measurements, (*b*) simulation results without shaft inertia, (*c*) simulation results with shaft inertia

tiveness of the surge protection control system as the field personnel indicated that the recycle valve tends to oscillate violently (from 0 to 50 percent open) when the compressor operates close to the surge control line. Field measurements involving both suction and discharge pressures and temperatures, flow rate through the compressor by means of the annubar shown, and the delivered flow using the orifice meter were taken during a surge protection process. This process was effected via throttling the flow by means of both suction and discharge globe valves shown in Fig. 2. Comparison between field measurements and a previous simulation reported in [1], which did not include compressor shaft inertias, has confirmed that the surge control system is shown to be unstable, as is evident in Figs. 3(*a*) and 3(*b*) (measurements and simulation, respectively). Although the oscillation cycle time, flow, and pressures seem to be in good agreement, the lack of the inertia terms in this simulation manifests itself by the difference in the character of the oscillation cycle on the compressor performance map. Note that the simulation results show a rather

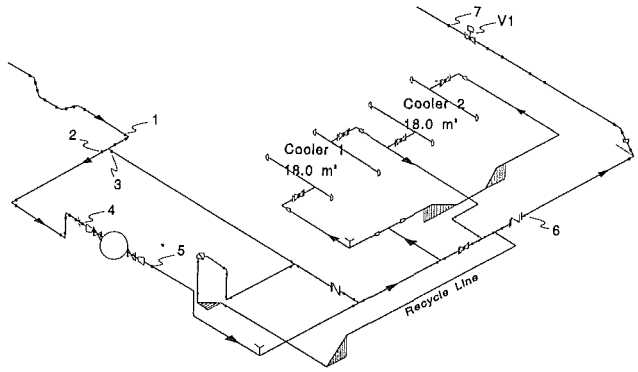


Fig. 4 Schematic of part of a compressor station with two coolers in the recycle path

narrower cycle, the axis of which exhibits higher oscillations of the compressor speed (i.e., higher slope) than that obtained from field measurements.

The simulation was repeated but with the inclusion of the inertia terms in both Eqs. (4) and (5). These inertias were taken as 0.175 kg•m^2 for each shaft. The results are shown in Fig. 3(*c*). Obviously, the inclusion of the shaft inertias in this fast transient example has resulted in a better agreement. The fact that the oscillation cycle is not as open as the one shown from measurement is attributed to the constant gas fuel rate ($\dot{m}_f$) assumed in the simulation, which, of course, is not likely to be the case in the field during this surge protection. Additionally, the slope of the axis is lower in this case indicating lower oscillating speed, which is a natural result of including the inertia of the compressor shaft.

Compressor Deceleration During Shutdown

After-coolers are commonly used in natural gas compressor stations to maintain the discharge gas temperature below a certain limit dictated by the pipe stresses and pipeline coating materials. In high-pressure units, these coolers may be required to be located within the recycle path to allow a longer warmup period during startup and also to permit recycling of cooler gas during either idling or compressor surge protection. With such an arrangement, the presence of large capacitances (volumes) associated with these coolers, downstream of the compressor unit, and upstream of the unit check valve (see Fig. 4) may cause fast deceleration of the compressor shaft even to backward spinning upon shutting the unit down. Backward spinning of the compressor shaft has very detrimental effects on the compressor dry seals and, therefore, is not desirable.

An example of this configuration is taken from NOVA's gas transmission system. A schematic of a portion of the station is shown in Fig. 4. The compressor/gas turbine unit is ISO rated at 22,110 kW and the compressor performance map is shown in Fig. 5. Two coolers are configured for this unit capable of limiting the discharge temperature to 35°C. The associated volume per cooler is approximately 18.0 m^3. The concern with this configuration is the backward spinning of the compressor upon shutting it down as the compressor shaft is equipped with dry seals. In order to study this phenomenon, a steady-state condition was first achieved numerically by imposing the following boundary conditions: P_1 = 4776 kPa, P_7 = 6261 kPa, T_1 = 16°C (subscripts refer to locations identified in Fig. 4). The steady-state (S.S.) operating point is shown on the compressor performance map in Fig. 5, at a compressor speed of 5500 rpm.

Upon shutdown, the gas fuel rate ($\dot{m}_f$) will immediately be cut off and hence deceleration of the gas generator shaft will take place as a result of the deficiency in the power provided to its air compressor by the first-stage turbine (Fig. 1). Al-

Downloaded 02 Jun 2010 to 171.66.16.122. Redistribution subject to ASME license or copyright; see http://www.asme.org/terms/Terms_Use.cfm

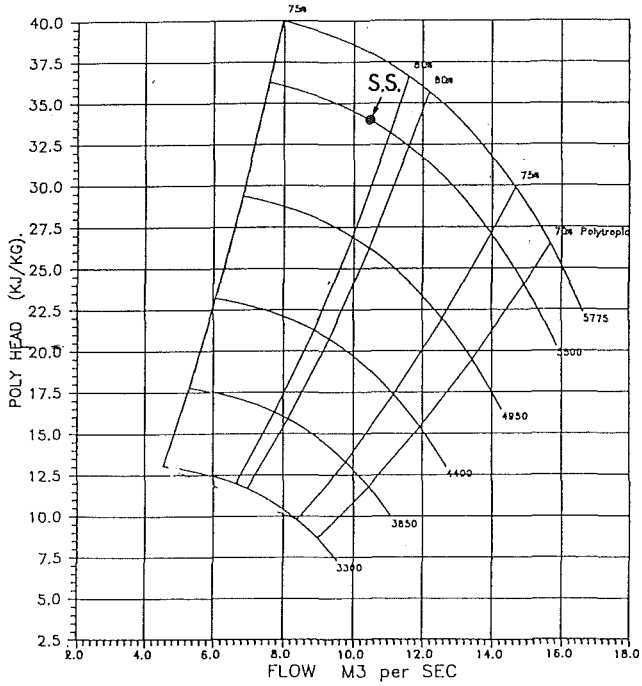


Fig. 5 Compressor performance characteristics for the station shown in Fig. 4 (s.s. is a steady-state operation point)

though in reality, warm air will continue to flow through the power turbine blades, we will assume for simplicity that the flow of such air will be stopped completely upon shutdown hence setting (W_t) to zero momentarily. Equation (5) will therefore reduce to the following deceleration equation:

$$I\frac{dN}{dt} = -\left[\frac{H_p(Q_a, N)\cdot|\dot{m}_1|}{N\cdot\eta_p(Q_a,N)} + T_f\right] \tag{6}$$

where T_f is the frictional torque, assumed to be 3.5 percent of the fluid torque. Note that the absolute value of $|\dot{m}_1|$ was taken in the above equation. This is because, if the flow through the compressor is positive, the energy required to compress this mass from the low pressure side to the high-pressure side will be taken from the compressor/power turbine rotor kinetic energy. On the other hand, when ($\dot{m}_1$) is negative, indicating compressor surge, the energy loss associated with flowing gas from the high-pressure side to the low-pressure will be consumed by the compressor/power turbine rotor deceleration. Therefore, in both cases, the rotor will decelerate whether ($\dot{m}_1$) is positive or negative. The actual degree of deceleration depends on the value of $\dot{m}_1$.

Therefore, in order to model this phenomenon, the complete steady characteristic of the compressor beyond the surge point and into the negative flow is required. At a given flow, however, the actual head (or pressure difference or pressure ratio) may differ from this characteristic. This is a consequence of the compressor surge, should it occur. Determination of this characteristic by measurements is possible [4–6]; however, it requires the compressor to undergo surge cycles for extended period of time. A physically realistic and commonly used representation of this characteristics is that of a simple cubic [7] as shown in Fig. 6, where:

$$H_{SS} = H_o + \beta\left[1 + \frac{3}{2}\left(\frac{Q_a}{\phi} - 1\right) - \frac{1}{2}\left(\frac{Q_a}{\phi} - 1\right)^3\right] \tag{7}$$

where H_o, β, and ϕ are parameters identified in Fig. 6. Here, ϕ is half of the actual flow through the compressor at the surge point corresponding to the compressor rotating speed, and H_o is the compressor head at zero flow.

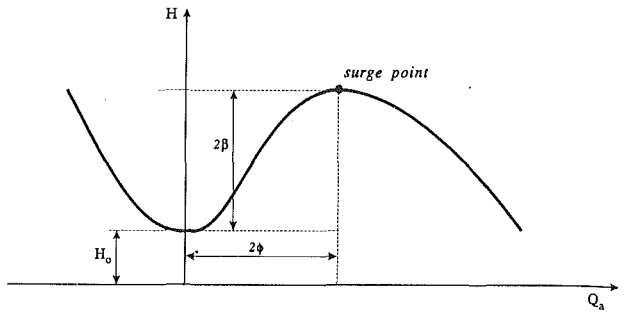


Fig. 6 Steady characteristic cubic model for the compressor to the left of the surge point

For a single-stage compressor such as the one under consideration, and assuming no losses in the compressor impeller nor in the diffuser section, H_o can be determined from

$$H_o = \frac{Z_a R T_1}{(n-1)/n}\left[(P_r)^{\frac{n-1}{n}} - 1\right], \tag{8}$$

$$P_r = 1 + \frac{1}{2}\frac{\rho_1}{P_1}\omega^2[R_o^2 - r^2] \tag{9}$$

where:

ω = compressor speed, rad/s
R_o = impeller outer radius
r = compressor eye radius

Equations (8) and (9) above are used in conjunction with the compressor affinity laws to determine the full compressor characteristics to the left of the compressor surge point.

During the surge cycle, Greitzer's model [8], which was developed for axial flow compressors and was extended to centrifugal compressors [9], was used with a varying time constant τ. This model relates the actual head across the compressor (H) (or pressure difference) with that denoting the steady-state characteristic (H_{SS}), viz.:

$$\tau\frac{dH}{dt} = (H_{SS} - H) \tag{10}$$

This equation describes, in general terms, the compressor response to departures from steady-state operation. As it turned out in our analysis, the results obtained in the present study had relatively small sensitivity to the value of τ.

The station depicted in Fig. 4 was modeled using the above consideration. Anechoic conditions were imposed at locations 1 and 7 during the simulation, until the unit check valve closes at which time zero flow is imposed at location 6. In the present case, the compressor/power turbine has a combined inertia of 250 kg m^2, impeller outer diameter = 0.96 m, and compressor inlet eye diameter = 0.56 m. The recycle valve in this station is Fisher 16″ × 24″ FBT WHISPER III A3, linear characteristics, maximum Cg = 89,391. Four cases were examined in this example problem of unit shutdown. These are:

Case *i*: no cooler, recycle valve opens in 1.0 s
Case *ii*: no cooler, recycle valve does not open
Case *iii*: with coolers, recycle valve opens in 1.0 s
Case *iv*: with coolers, recycle valve does not open

The results for each case are presented in indicative Figs. 7–10, respectively, showing the results of the simulation for a period of 25 s immediately after the unit shutdown. Case (*i*) represents a normal compressor station installation with no cooler, and the recycle valve is commanded to open immediately after the unit is signaled to shutdown. Figure 7(*a*) shows that the compressor undergoes few surge cycles (3–5 cycles) before it restores its positive flow permitted by opening the recycle valve. After the unit check valve closes, the unit dis-

Downloaded 02 Jun 2010 to 171.66.16.122. Redistribution subject to ASME license or copyright; see http://www.asme.org/terms/Terms_Use.cfm

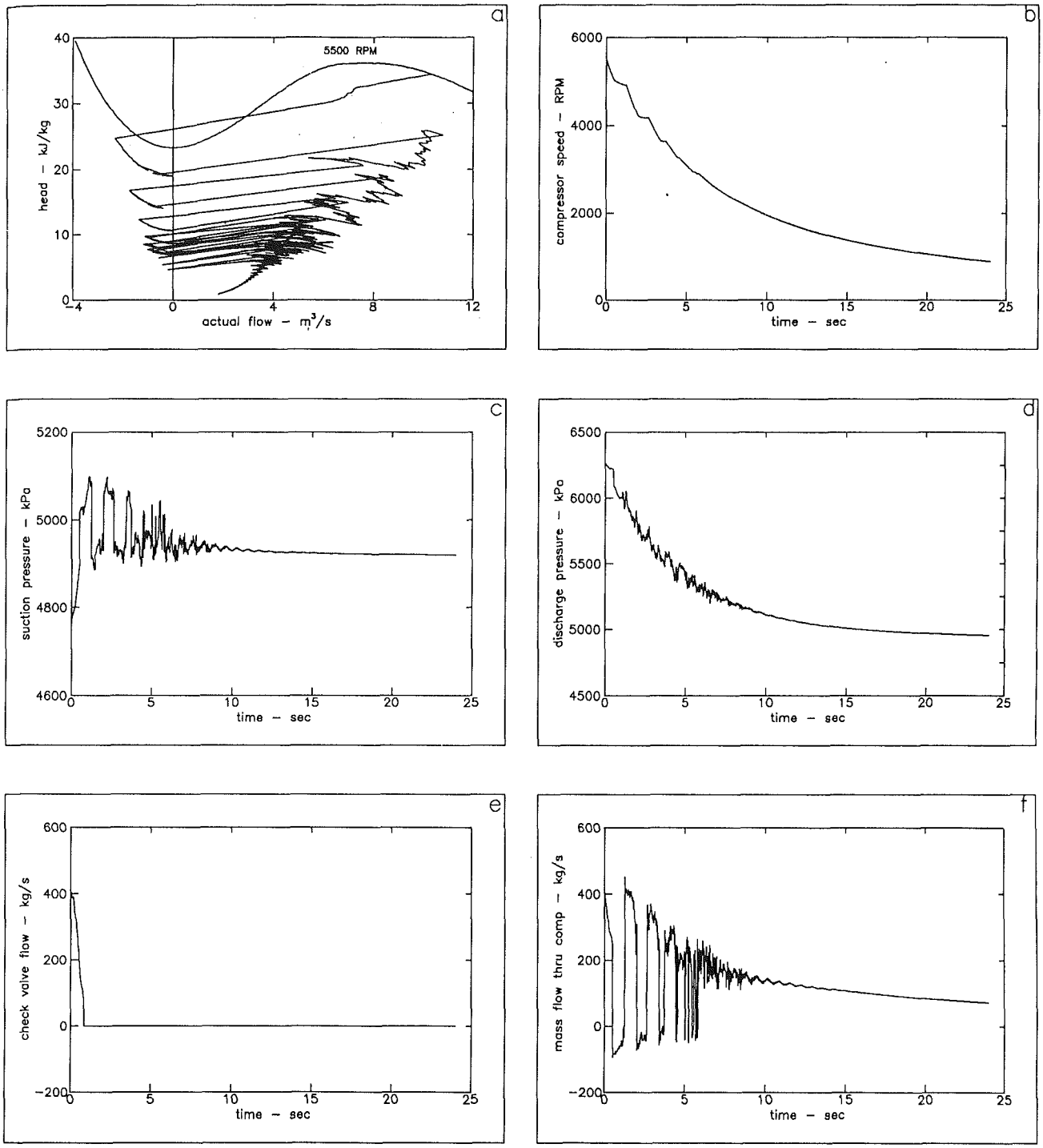


Fig. 7 Simulation results of compressor shutdown *without* coolers and recycle valve opens in 1.0 s (case *i*)

charge pressure quickly depletes almost to the suction side in 10 s. The compressor decelerates from an initial speed of 5500 rpm to 2000 rpm in this period, followed by a very slow deceleration (due to the low head) down to a speed of approximately 1000 rpm after 25 s. The compressor obviously will continue to decelerate due to friction and fluid windage till final stop.

In case (*ii*), the recycle valve was assumed closed, allowing pressure equalization to take place only through the compressor itself (i.e., negative flow through the compressor). The results of this case are shown in indicative Fig. 8. Here, the discharge pressure does not deplete as quickly as in case (*i*), which is rather expected since the recycle valve did not open after shutdown. What is interesting here, however, is that since the flow through the compressor remained negative, the rate of compressor deceleration was much lower than when the recycle valve opened, allowing positive flow (Case *i*). This is due to the fact that at the same head, negative flow through the compressor is always less than the positive flow (see Fig. 6). As a result, and with the aid of Eq. (6), the fluid torque responsible for compressor deceleration will be lower in this case of negative flow. Although in both cases (*i*) and (*ii*), the compressor did not spin backward, it appears that keeping the recycle valve closed after unit shutdown can reduce the de-

Downloaded 02 Jun 2010 to 171.66.16.122. Redistribution subject to ASME license or copyright; see http://www.asme.org/terms/Terms_Use.cfm

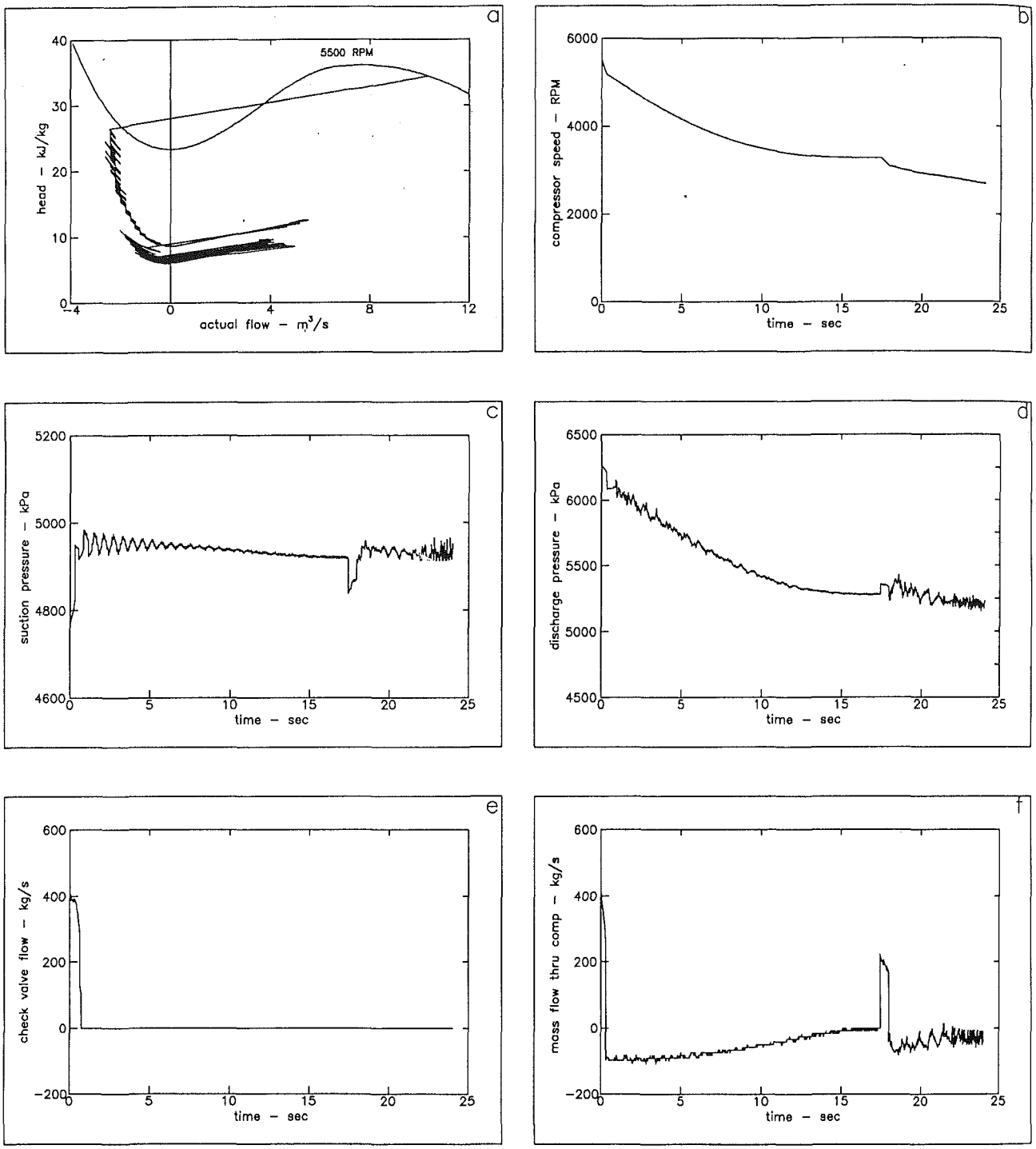


Fig. 8 Simulation results of compressor shutdown *without* cooler and recycle valve closed (case *ii*)

celeration rate of the compressor shaft and hence may prevent it from backward spinning. That is, for units with dry seals keeping the recycle valve closed after unit shutdown has an advantage. The only drawback in this case is the negative flow through the compressor and its side effects on compressor blades and thrust bearings.

Cases (*iii*) and (*iv*) are similar to (*i*) and (*ii*) above, respectively, but with coolers, i.e., with extra capacitance in the recycle path. Results for case (*iii*) are very close to those for case (*i*). The discharge pressure in case (*iii*) is depleted almost in the same time as in case (*i*) due to the capability of the recycle valve to equalize the pressure even with the presence of the extra capacitance posed by the coolers. As a result, the deceleration rate is much the same for these two cases (*i* and *iii*). More rattling disturbances are evident in this case, however, after the first three surge cycles. This is perhaps due to the presences of the capacitance and its inherent instability problem [10]. However, in case (*iv*), a faster rate of compressor deceleration is exhibited with this case as compared to case (*ii*) without cooler (compare Figs. 8*b* and 10*b*). Clearly, the presence of the cooler volume and the fact that pressure equalization has to be established only through compressor path, results in faster deceleration rate of the compressor shaft. Again, in cases (*iii*) and (*iv*), it is demonstrated that closing

Downloaded 02 Jun 2010 to 171.66.16.122. Redistribution subject to ASME license or copyright; see http://www.asme.org/terms/Terms_Use.cfm

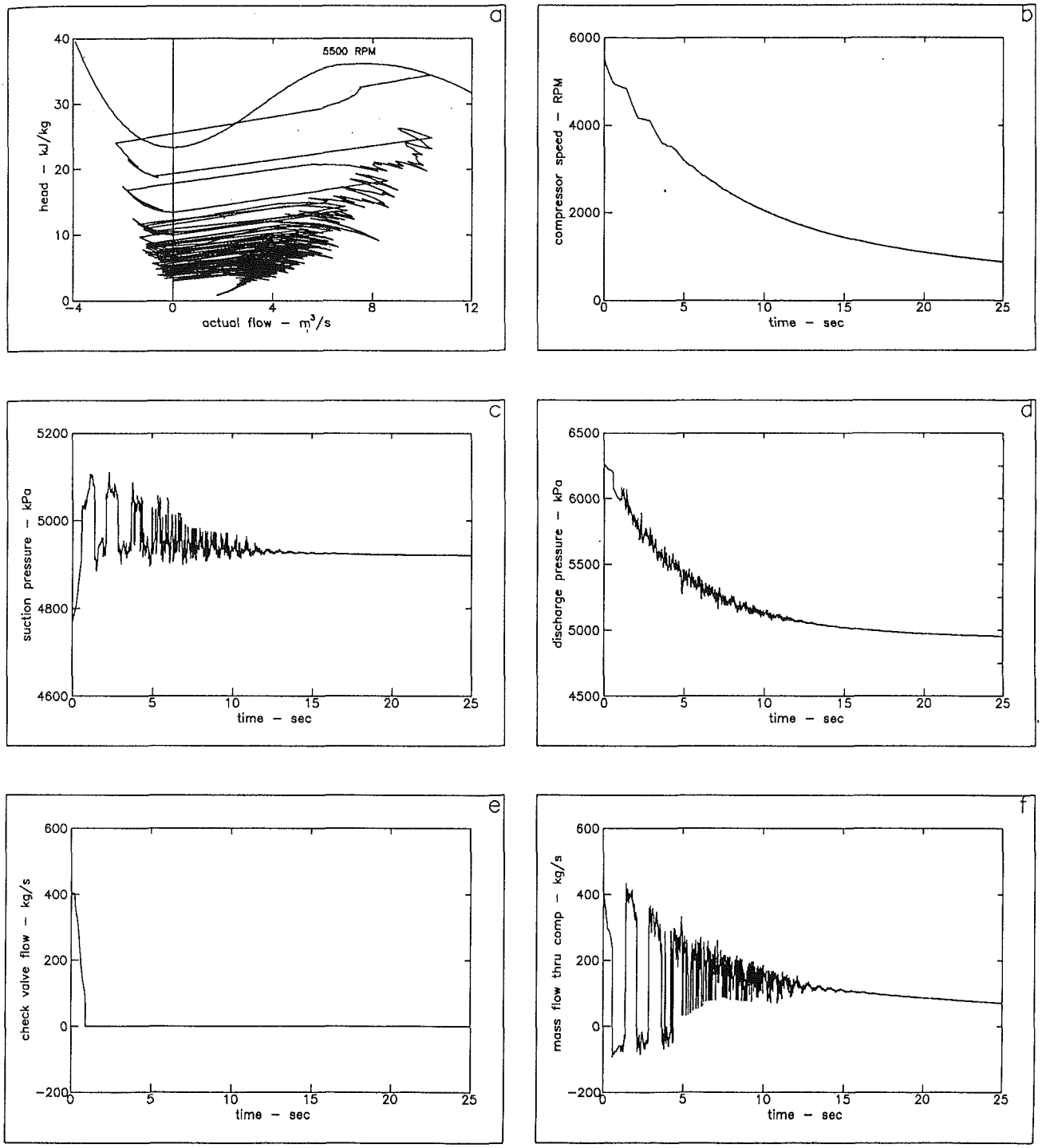


Fig. 9 Simulation results of compressor shutdown *with* coolers and recycle valves opens in 1.0 s (case *iii*)

the recycle valve after shutdown has an advantage over opening it insofar as decreasing the rate of deceleration and reducing the chance for backward spinning of compressor shaft.

Effects of Recycle Coolers on Compressor Surge

Another concern associated with placing an after-cooler within the recycle path is the possibility of impairing the surge protection control system if the unit is suddenly hit with a severe disturbance that can cause the unit to go into deep surge. The same compressor station considered in the previous example is analyzed here and the problem posed is that of a typical surge control scenario. The compressor was assumed to be operating at a S.S. point at a maximum speed of 5775 rpm. A discharge valve (V1 shown in Fig. 4) is suddenly closed (hypothetically) in 2.0 s so as to simulate a violent disturbance causing a stop in the delivery flow. The control system is designed such that the recycle valve can open to full position in 1.0 s (as before). Results of a normal case without cooler (similar to case *i* in the previous example) are shown in indicative Figs. 11. Here the surge control system seems to have protected the unit for this violent disturbance and prevented it from going into surge, as shown in Fig. 11(*a*). Figures 11(*b*) and 11(*c*) show the corresponding mass flow rates at four points

Downloaded 02 Jun 2010 to 171.66.16.122. Redistribution subject to ASME license or copyright; see http://www.asme.org/terms/Terms_Use.cfm

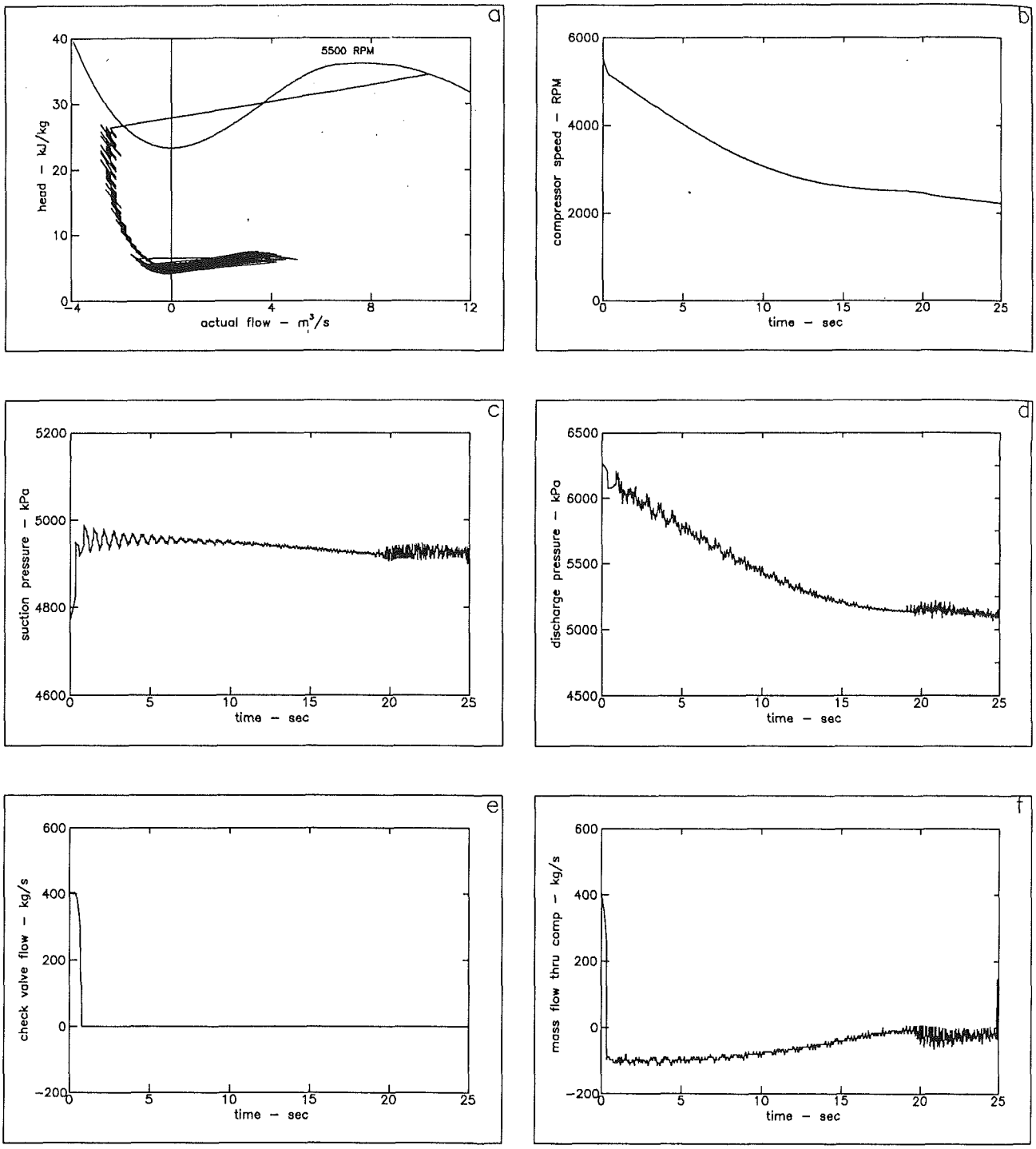


Fig. 10 Simulation results of compressor shutdown *with* coolers and recycle valves closed (case *iv*)

identified on the schematic of Fig. 4. It is shown that after the unit check valve closes ($\dot{m}_6 = 0$), the compressor flow ($\dot{m}_2$) is maintained positive by the recycle flow ($\dot{m}_3$). Notice also in Fig. 11(*b*) that the main line flow ($\dot{m}_1$) tend to decrease with time as a result of gas expansion [11].

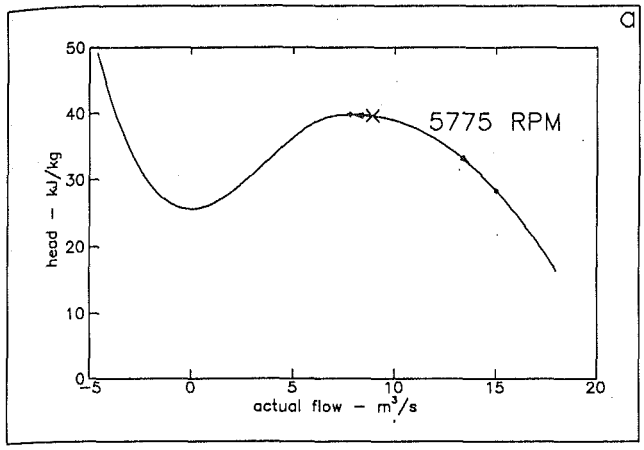
When the coolers were introduced and the same disturbance is effected (a case similar to case *iii* in the previous example), the cooler capacitance seemed to cause the unit to undergo one surge cycle (Fig. 12*a*) before the surge protection system restored the compressor to a stable operation. Figure 12(*b*) shows that the compressor flow was negative for a period of 1.2 s before stable operation was restored to a positive flow.

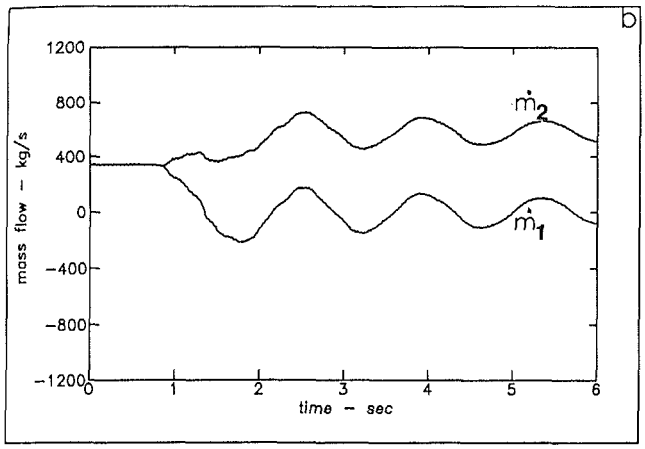
Summarizing, it was concluded that in the above particular station, placing a cooler (with the given capacitance) in the recycle path of a compressor unit (with a given shaft inertia) will not cause the unit to spin backward upon shutdown. The only drawback is that the unit may surge for one or more cycles if hit with a very violent disturbance for which the given recycle valve of 1.0 s response time may not be able to protect the unit from surging.

Concluding Remarks

1 Inclusion of shaft inertias in the dynamic simulation of

Downloaded 02 Jun 2010 to 171.66.16.122. Redistribution subject to ASME license or copyright; see http://www.asme.org/terms/Terms_Use.cfm





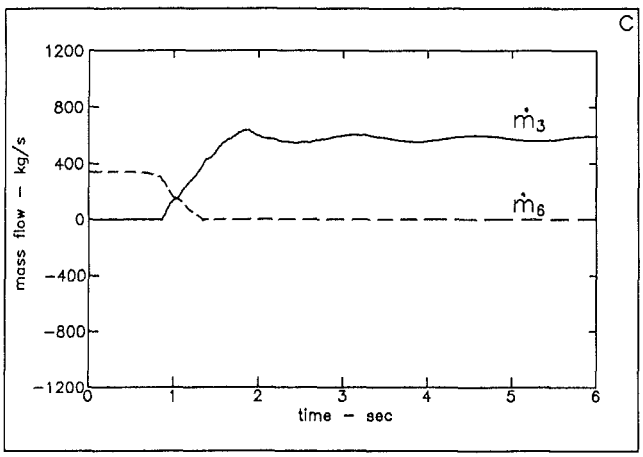
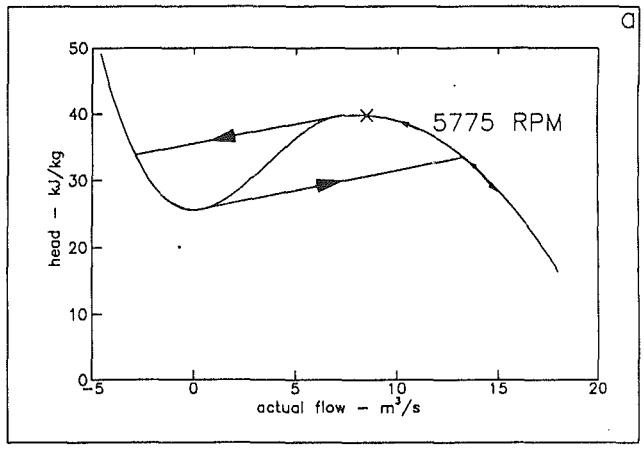
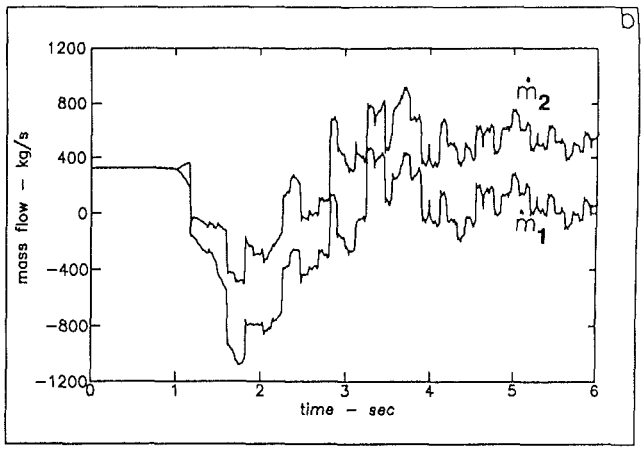


Fig. 11 Simulation results of compressor surge protection for the station shown in Fig. 4 without coolers





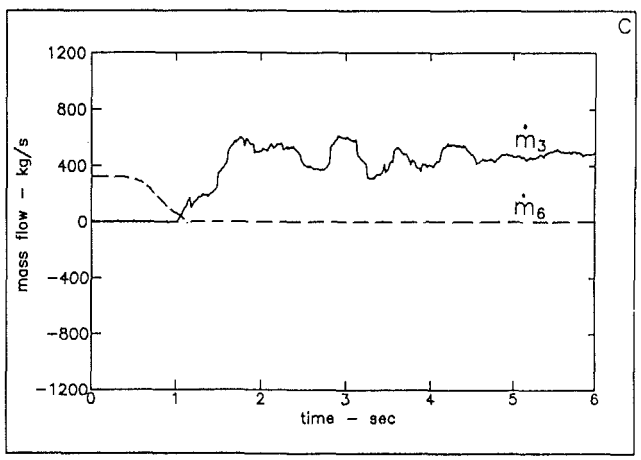


Fig. 12 Simulation results of compressor surge protection for the station shown in Fig. 4 with coolers

compressor station operation is necessary in cases where fast transients are expected. Examples are compressor surge protection and unit shutdown.

2 In certain cases, placing a cooler within the recycle path of a compressor unit may not cause the compressor to spin backward upon shutdown. Determination of the possibility of compressor backward spinning is case specific and depends, among other parameters, on the magnitude of the unit inertia as well as the cooler's volume.

3 If compressor deceleration upon shutdown is a critical design problem, keeping the recycle valve closed upon shutdown in the control philosophy will result in decreasing the rate of deceleration. However, pressure equalization across the unit will only take place through the compressor, resulting in negative flow and hence loading the compressor thrust bearings.

4 Placing the coolers in a compressor recycle path may cause the unit to undergo few surge cycles if hit with severe disturbances, even with a fast response recycle valve.

Acknowledgments

The work presented here is part of a research project spon-

Downloaded 02 Jun 2010 to 171.66.16.122. Redistribution subject to ASME license or copyright; see http://www.asme.org/terms/Terms_Use.cfm

sored by NOVA Corporation of Alberta and the permission to publish it is hereby acknowledged.

References

1 Botros, K. K., Campbell, P. J., and Mah, D. B., "Dynamic Simulation of Compressor Station Operation Including Centrifugal Compressor and Gas Turbine," ASME JOURNAL OF ENGINEERING FOR GAS TURBINES AND POWER, Vol. 113, 1991, pp. 300–311.

2 Schultz, J. M., "The Polytropic Analysis of Centrifugal Compressors," ASME JOURNAL OF ENGINEERING FOR POWER, Vol. 84, 1962, pp. 69–82.

3 Stanley, R.A., and Bohannan, W. R., "Dynamic Simulation of Centrifugal Compressor Systems," *Proceedings of the 6th Turbomachinery Symposium*, Texas A &M University, 1977.

4 Koff, S. G., and Greitzer, E. M., "Axisymmetrically Stalled Flow Performance for Multistage Axial Compressors," ASME *Journal of Turbomachinery*, Vol. 108, 1986, pp. 216–223.

5 Wachter, J., and Rohne, K. H., "Centrifugal Compressor Surge Behaviour," ASME Paper No. 84-GT-91, 1984.

6 Toyama, K., Runstadler, P. W., Jr., and Dean, R. C., Jr., "An Experimental Study of Surge in Centrifugal Compressors," ASME *Journal of Fluids Engineering*, Vol. 99, 1977, pp. 115–131.

7 Moore, F. K., and Greitzer, E. M., "A Theory of Post-stall Transients in Axial Compression Systems: Part I—Development of Equations," ASME JOURNAL OF ENGINEERING FOR GAS TURBINES AND POWER, Vol. 108, 1986, pp. 68–76.

8 Greitzer, E. M., "Surge and Rotating Stall in Axial Flow Compressors," ASME JOURNAL OF ENGINEERING FOR POWER, Vol. 98, 1976, pp. 190–198.

9 Hansen, K. E., Jørgensen, P., and Larsen, P. S., "Experimental and Theoretical Study of Surge in a Small Centrifugal Compressor," ASME *Journal of Fluids Engineering*, Vol. 103, 1981, pp. 391–395.

10 Epstein, A. H., Ffowcs Williams, J. E., and Greitzer, E. M., "Active Suppression of Compressor Instabilities," AIAA Paper No. 1914, 1986.

11 Botros, K. K., "Thermodynamic Aspects of Gas Recycling During Compressor Surge Control," presented at the Pipeline Engineering Symposium of the 13th Annual Energy-Sources Technology Conference, ASME, New Orleans, LA, Jan. 14–18, 1990.

Downloaded 02 Jun 2010 to 171.66.16.122. Redistribution subject to ASME license or copyright; see http://www.asme.org/terms/Terms_Use.cfm

Foothills Decompression/ Recompression Facilities—Unique Power Recovery Application in Gas Pipelines

S. R. Kitt
Foothills Pipe Lines Ltd.,
Calgary, Alberta, Canada

B. D. Rose
AMOCO Canada Petroleum Company Ltd.,
Calgary, Alberta, Canada

Foothills Pipe Lines Ltd. is the Canadian sponsor of the Alaska Natural Gas Transportation System (ANGTS), a pipeline project selected in Canada and the United States as the means for transporting Alaskan gas reserves to the lower 48 United States. Currently, certain Prebuild portions of the ANGTS are in operation delivering Canadian gas to U.S. markets. A recent system expansion of the Eastern Leg Prebuild to accommodate increased Canadian gas exports entailed the construction of Decompression/Recompression facilities at Empress, Alberta to enable high-pressure operation of the Foothills pipeline while maintaining gas stripping at existing low-pressure extraction plants. The general process of the Decompression/Recompression facilities involves the expansion of high-pressure pipeline gas to conditions acceptable to the low-pressure extraction plants, then the recompression of the residue gas for return to the pipeline at original pressure. By directing the inlet gas through turbo expanders coupled to brake compressors, a substantial portion of the expansion energy is captured and used in providing the first stage of gas recompression. Including supplemental conventional compression, the Decompression/Recompression facilities are capable of providing approximately 37 MW (50,000 HP) for continuous gas recompression. Although power recovery with turbo expanders is relatively common in the gas processing industry, such an application for gas recompression in large gas pipelines is unique. This technical paper describes the Foothills Decompression/Recompression facilities with their utilization of turbo expanders for pipeline recompression service, emphasizing the process design as well as the characteristics of the rotating equipment.

I Introduction

The ANGTS Prebuild. Foothills Pipe Lines Ltd. ("Foothills") is the Canadian sponsor of the Alaska Natural Gas Transportation System ("ANGTS"), a trans-North American pipeline project selected by both Canadian and United States governments and regulatory agencies in the late 1970s as the most effective and environmentally sound means of transporting Alaska natural gas volumes to markets in the lower United States. When completed, the ANGTS project will comprise approximately 7693 kilometers of large-diameter, high-pressure pipeline divided geographically into four major segments (Fig. 1); namely the Alaskan segment (1200 kilometers); the Canadian segment (3273 kilometers); the U.S. Western Leg, extending 1398 kilometers to the San Francisco area; and the U.S. Eastern Leg, extending 1818 kilometers to the Chicago area. Provision is also made in the ANGTS project for connecting Canadian gas supplies in the Mackenzie Delta region of the Canada Arctic via the Dempster Lateral, or alternatively via the recently proposed Mackenzie Valley Pipeline.

Although the original plans for completing construction of the ANGTS to connect Prudhoe Bay gas supplies by the latter half of the 1980s did not materialize due to market and economic conditions, certain southern portions of the ANGTS in Canada and the U.S. were "prebuilt" in the early 1980s and are operational today, delivering Alberta gas volumes to California and U.S. midwestern markets. The ANGTS Prebuild as existent today comprises two legs, viz., the Western and Eastern Legs, and approximately 2430 Kilometers of pipeline, which in total constitutes approximately one third of the ultimate ANGTS project length. The Western Leg Prebuild extends from Caroline, Alberta to Stanfield, Oregon and consists of approximately 470 kilometers of ANGTS pipeline "loops," which are integrated operationally with existing facilities of operating sponsor companies. The Eastern Leg Prebuild likewise commences at Caroline, Alberta and extends as one con-

Contributed by the International Gas Turbine Institute and presented at the 37th International Gas Turbine and Aeroengine Congress and Exposition, Cologne, Germany, June 1–4, 1992. Manuscript received by the International Gas Turbine Institute January 28, 1992. Paper No. 92-GT-26. Associate Technical Editor: L. S. Langston.

Copyright © 1994 by ASME
Downloaded 02 Jun 2010 to 171.66.16.122. Redistribution subject to ASME license or copyright; see http://www.asme.org/terms/Terms_Use.cfm

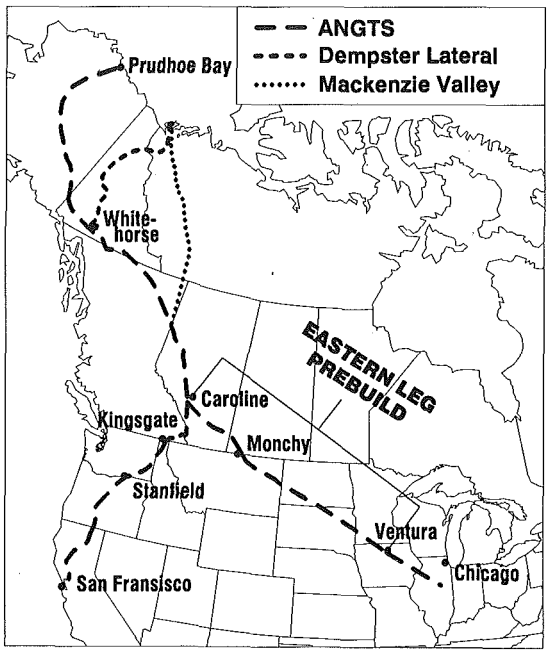


Fig. 1 The Alaska natural gas transportation system

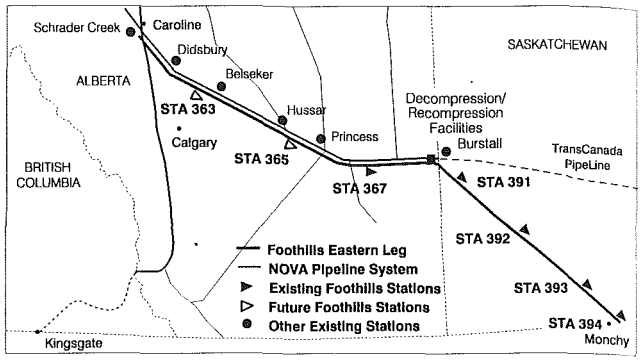


Fig. 2 System map—eastern delivery leg

tinuous pipeline approximately 1960 kilometers to Ventura, Iowa. Both the Western Leg and Eastern Leg prebuilt portions of ANGTS have now surpassed their 10th anniversaries of operation, and plans are well advanced toward their further expansion. The first stage of expansion on the Eastern Leg has already been completed, while the second is currently in progress. Expansion plans for the Western Leg anticipate completion for November 1993 service.

Foothills Eastern Leg Prebuild Expansion. The Decompression/Recompression facilities that are the subject of this paper are located along and are related to the expansion of the Foothills Eastern Leg Prebuild segment of the ANGTS in Canada. The Foothills Eastern Leg Prebuild pipeline originates at a point near Caroline in Alberta and extends in a southeasterly direction across the provinces of Alberta and Saskatchewan to a point of interconnection with Northern Border Pipeline Company on the Canada/U.S. border near Monchy, Saskatchewan. The Foothills system as currently configured comprises 637 kilometers of 1067 O.D. (42 in.) pipeline with maximum allowable operating pressure of 8690 kPa (1260 psig), five compressor stations of which one is located in Alberta and four in Saskatchewan, and the Decompression/Recompression facilities at Empress near the Alberta/Saskatchewan border (Fig. 2). The Decompression/Recompression facilities, constructed and placed into service in November 1990, provide a link between the high-pressure Foothills pipeline and low-pressure liquids extraction plants located in the Empress area. The Decompression/Recompression facilities proved to be an optimum solution to engineering problems associated with Eastern Leg System expansion requirements for accommodating larger Canadian natural gas export volumes.

The Decompression/Recompression facilities constitute a power recovery application that is unique in large-diameter, high-pressure gas pipelines. The objective of this paper is to provide a description of these facilities, including their purpose, the general process design, and the peculiar characteristics of the rotating equipment. The idea of the Decompression/Recompression facilities was first conceived during 1988, then developed into a definitive facilities application, which was submitted to the Canadian National Energy Board for approval in the spring of 1989. Upon receipt of Board approval on June 30, 1989, the project entered its final design and construction stages, with construction completed in November 1990. As Amoco Canada Petroleum Company Ltd. ("Amoco") was operator of the adjacent extraction plant to which the Decompression/Recompression facilities were to be connected, Foothills selected Amoco both as operator of its facilities and as project manager for their design and construction.

II Why Decompression/Recompression Facilities

Pre-expansion Configuration and Empress Plants. The high-pressure Foothills pipeline in Alberta parallels the existing NOVA Corporation of Alberta ("NOVA") pipeline system throughout its length from Caroline to Empress near the Alberta/Saskatchewan border (Fig. 2). In its pre-expansion configuration (i.e., prior to the construction of the Decompression/Recompression Facilities at Empress in 1990), the Foothills pipeline was operationally integrated with the multiline, lower

Nomenclature

ANGTS = Alaska Natural Gas Transportation System
ESD = Emergency Shutdown Valve
FC = Flow Controller
hp = horsepower
JT Valve = Joule Thompson Valve
kPa = kilopascals (gage)
kV = thousands of volts
kW = kilowatts
m^3/d = gas flow rate in cubic meters per day at a pressure and temperature base of 101.325 kPa (absolute) and 15°C
MMBtu/h = millions of Btu's per hour
MMCFD = gas flow rate in millions of cubic feet per day at a pressure and temperature base of 14.73 psia and 60°F
M.A.O.P. = Maximum Allowable Operating Pressure
MW = megawatts
O.D. = outside diameter
PC = pressure controller
PDC = Pressure Differential Controller
P_{in} = inlet pressure
P_{out} = outlet pressure
rpm = revolutions per minute
RTD = Resistance Temperature Device
TC = Temperature Controller
T_{in} = inlet temperature

Downloaded 02 Jun 2010 to 171.66.16.122. Redistribution subject to ASME license or copyright; see http://www.asme.org/terms/Terms_Use.cfm

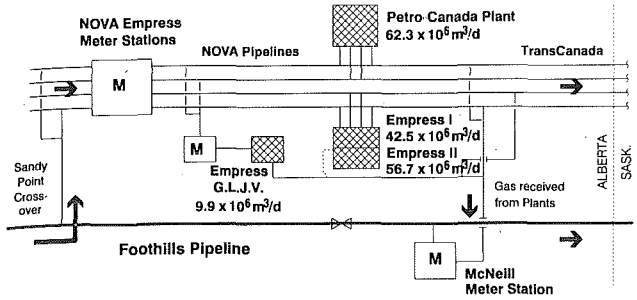


Fig. 3 Extraction plants in the Empress area

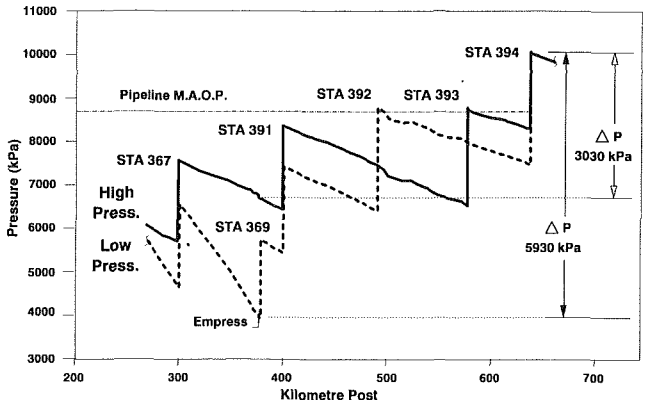


Fig. 4 Foothills eastern leg prebuild steady-state hydraulic pressure profile; Monchy flow 38.2 × $10^6 m^3/d$

pressure NOVA system, with both pipelines delivering gas as one entity to Empress for measurement and distribution to extraction plants prior to removal from the province (Fig. 3).

The maximum allowable operating pressure of the NOVA pipeline system in the segment Caroline to Empress ranges from 5700 kPa to 6450 kPa (826 psig to 935 psig) depending upon location, whereas the corresponding pressure of the Foothills pipeline is 8690 kPa (1260 psig). At Empress, the maximum allowable operating pressure of the extraction plants is approximately 4480 kPa (650 psig), while normal delivery pressure of the combined Foothills/NOVA pipeline was 4200 kPa (610 psig). The operational integration of the Foothills and NOVA systems, coupled with the low-pressure delivery requirements at Empress, resulted in the Foothills system being seriously constrained hydraulically.

Downstream of Empress, the Foothills system received processed gas from the immediate downstream side of the Empress extraction plants at a nominal pressure of 4000 kPa (580 psig). The gas was then compressed by three of the four compressor stations in Saskatchewan (either of Sta 392 or Sta 393 would normally be on standby) for transmission and delivery to Northern Border at Monchy at a pressure of 8690 kPa (1260 psig). Consequently, the pre-expansion operation required compression not only to overcome pressure losses associated with pipeline flow, but also a fixed static pressure differential of 4690 kPa (680 psig). With planned system expansion for accommodating increased Canadian exports through Monchy, this static pressure differential would have been exacerbated if the then existing Low-Pressure, Integrated regime was preserved, since the delivery pressure at Monchy was to be increased to 9890 kPa (1435 psig), the maximum operating pressure of the downstream Northern Border pipeline. The preservation of the Low-Pressure, Integrated mode of operation for expansion, therefore, raised some serious concerns in regard to system operational stability under compressor station outages and the resultant pressure and flow transients that would be initiated thereby. System operational stability therefore became a significant factor in the expansion design selection process.

Interconnecting Facilities at Empress. Additional to the pipeline hydraulic constraint and operational stability factors, the pre-expansion regime in the Empress area also constituted a rather complex interconnetion of pipeline and extraction plant facilities, whose operations directly affected one another. The Foothills and NOVA pipelines were directly interconnected upstream of the extraction plants at the Sandy Point crossover. Downstream of the extraction plants, the NOVA pipeline interconnected with the TransCanada PipeLines Limited ("TransCanada") pipeline as well as the Foothills pipeline. The TransCanada pipeline itself has a large compressor station located in the immediate proximity of the extraction plants; i.e., approximately 3 km downstream near the town of Burstall, Saskatchewan (Fig. 2). Similarly Foothills has a compressor station located on its pipeline approximately 22 km downstream of the extraction plants. Finally the four extraction plants themselves straddle the NOVA pipeline. This complex network of pipelines, compressor stations, and extraction plants posed some potentially serious operational difficulties, as compressor upsets on either the downstream TransCanada or Foothills systems would directly and immediately affect the operation of all interconnecting facilities. The interdependence of operations, therefore, was also an important consideration in the selection of a system design for the Foothills pipeline expansion.

Expansion Design. System expansion design alternatives in a broad sense were essentially limited to two:

1 Low-Pressure, Integrated Expansion option entailing retention of the prevalent operating regime wherein the Foothills/NOVA system in Alberta remained integrated operationally while delivering gas to Empress at low pressure.
2 High-Pressure, Segregated Expansion option, involving expansion through segregating the Foothills pipeline from the NOVA pipeline in Alberta, operating the Foothills pipeline and delivering gas to Empress at high pressure, and installing Decompression/Recompression facilities at Empress in order to maintain gas stripping by the low-pressure extraction plants.

Design analysis included an evaluation of the steady-state hydraulic pressure profiles for the two alternatives, illustrated in Fig. 4, from which the superiority of the High-Pressure, Segregated option was immediately apparent. Transient analyses of both expansion configurations were also performed using an off-line, hydraulic transient simulator to examine the flow and pressure transients that would be experienced as a result of compressor unit outages, with special attention given to system operational stability. The hydraulic profile for the Low-Pressure expansion option especially indicated that operational stability under transients may be a serious concern for this alternative. Transient analysis indeed confirmed this suspicion, with the result that an additional spare compressor unit had to be included at the proposed new Sta 369 located immediately downstream of the extraction plants.

Transient analysis for the High-Pressure expansion alternative indicated a relatively stable operation under station outages without the need for any additional spare compressor units. The operation under transients of the High-Pressure alternative was shown to be at least equivalent, and probably superior, to the Low-Pressure alternative in terms of stability, as illustrated in Fig. 5. For a full description of the transient comparative analysis for the two expansion alternatives, the reader is referred to Kitt and Sampath (1990).

As a result of the extensive engineering, operations, and economic analyses performed for the alternative expansion

Downloaded 02 Jun 2010 to 171.66.16.122. Redistribution subject to ASME license or copyright; see http://www.asme.org/terms/Terms_Use.cfm

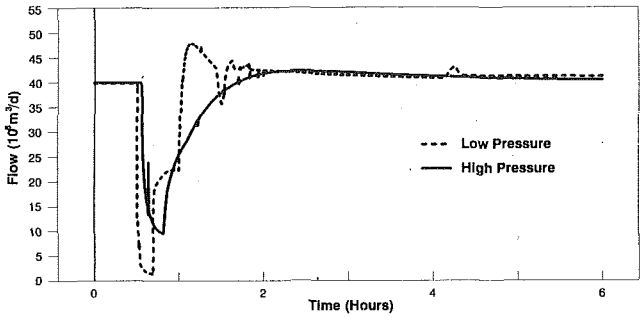


Fig. 5 Flow transient at McNeill: low versus high pressure; STA 369/391 outage

configurations, the High-Pressure Segregated option entailing construction of the Decompression/Recompression facilities at Empress was selected as the optimum manner of system expansion. This alternative offered the following significant advantages:

1 The segregation of the Foothills pipeline from NOVA enabled the Foothills system to be operated at or near its design M.A.O.P.
2 The high arrival pressure at Empress greatly unconstrained the downstream pipeline capacity.
3 Concerns about pipeline operational instability due to flow and pressure transients were alleviated.
4 Transient effects on interconnecting facilities at Empress would be minimized as the Foothills pipeline would be effectively isolated.
5 The capital costs were significantly lower.

III Decomp/Recomp Facilities Design

Purpose. The purpose of the Decompression/Recompression facilities is to provide the link that would enable the Foothills pipeline to be operated at high pressure in the Empress area, while allowing the existing, low-pressure extraction plants at Empress to continue stripping those gas volumes transported by Foothills in their traditional manner. Accordingly, the function of the facilities is to decompress (expand) and condition the high-pressure pipeline gas to pressure and temperature conditions acceptable to the extraction plant, then to recompress and condition the processed residue gas to pressure (usually original inlet) and temperature conditions acceptable to the pipeline. The general process of decompression/recompression entails first the expansion of the gas from pipeline operating pressure to plant operating pressure by routing the high-pressure inlet gas through turbo-expanders/brake compressors, by which a substantial portion of the expansion energy is recovered for use in recompressing extracted residue gas partly back to original pipeline pressure. Supplemental compression facilities are then used to compress the residue gas from the brake compressor discharge conditions back to original pipeline pressure.

Location. The Decompression/Recompression Facilities are located adjacent to the Empress II extraction plant, approximately 1.6 kilometers distant from the Foothills pipeline right-of-way. The decision to locate the Facilities at this site was made based on the following factors:

- Proximity to the Foothills mainline.
- Availability of plant processing capacity.
- Opportunity for the sharing of existing facilities and utilities such as fire and cooling water, instrument air, glycol, emergency power supply, control center, office, etc.
- Suitability for common operation with the extraction plant.

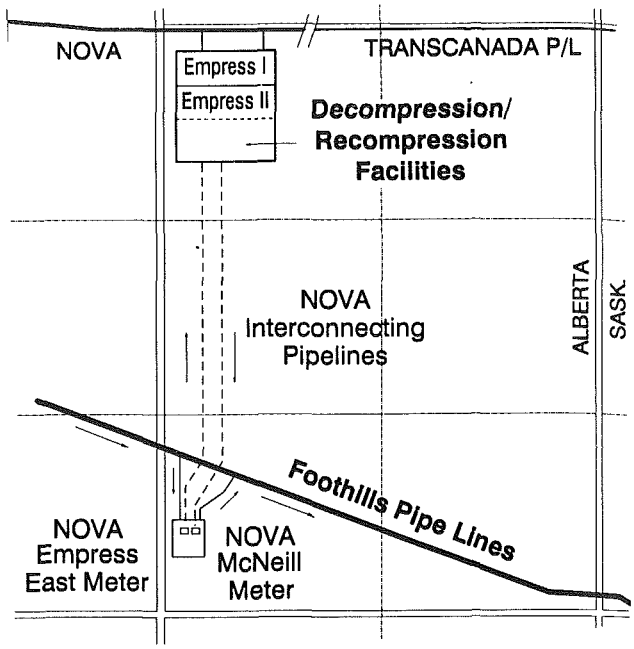


Fig. 6 Location of Decompression/Recompression facilities

The Empress II extraction plant was in these respects the most suitable site for location of the Decompression/Recompression Facilities. The general location of the Decompression/Recompression facilities relative to the Empress extraction plants and the Foothills pipeline is illustrated in Fig. 6.

Design Considerations. As the Decompression/Recompression facilities were to be the interface between the higher operating pressure Foothills pipeline and the lower operating pressure Empress II extraction plant, the design of the facilities had therefore to conform to the requirements and constraints of both the pipeline and the extraction plant. Considerations used for the design of the facilities included the following:

- Initial design capacity of 40.4×10^6 m^3/d (1425 MMCFD) of pipeline inlet gas and 38.2×10^6 m^3/d (1350 MMCFD) of processed outlet gas.
- Capability of accommodating a relatively broad range of inlet and outlet volumes in accordance with projected seasonal flows in the Foothills pipeline.
- Easy expansion capability for a future, ultimate pipeline volume of up to approximately 59.5×10^6 m^3/d (2100 MMCFD).
- Capability of delivering gas to and receiving gas from the extraction plant at 4240 kPa (615 psig).
- Capability of being generally neutral to the pipeline under normal operation; i.e., the return pressure to the pipeline after recompression to be generally equal to the inlet pressure from the pipeline under normal pipeline operation.
- Capability of continuous operation under minor pipeline transient conditions, and of being isolated temporarily from the pipeline under severe transient conditions.
- Capability of controlling the temperature of the inlet gas to the extraction plant to the range 5–10°C (40–50°F).
- Capability of cooling the gas stream returning to the pipeline to 30°C (86°F) on an average July day.

Process Description. The general process of decompression and recompression at the facilities is illustrated in the simplified process flow diagram provided as Fig. 7, which reflects the original design conditions of the existing facilities

Downloaded 02 Jun 2010 to 171.66.16.122. Redistribution subject to ASME license or copyright; see http://www.asme.org/terms/Terms_Use.cfm

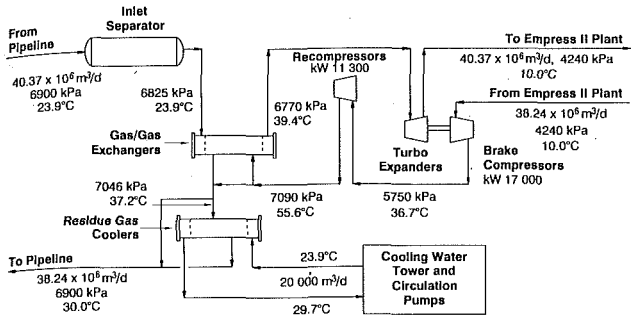


Fig. 7 Facilities flow diagram—design operation

under average July flowing conditions. Gas from the pipeline is received at the facilities at pressure and temperature conditions prevalent in the pipeline, namely 6900 kPa (1000 psig) and 23.9°C (75°F). After separation of entrained liquids and any solid particles in the inlet separator, the scrubbed gas is preheated to 39.4°C (103°F) in shell and tube heat exchangers prior to being routed to the turbo-expanders for expansion (decompression), the heating medium in this exchange being the hot recompressed gas en route back to the pipeline. The heating of the inlet gas is controlled by regulating the supply of the hot recompressed gas to the exchangers. The preheated inlet gas is then expanded in the turbo expanders to pressure and temperature conditions acceptable to the Empress II extraction plant, namely 4240 kPa (615 psig) and 10°C (50°F), respectively. Thereafter, the expanded and conditioned gas is supplied to the inlet of the extraction plant where it is commingled with incoming volumes delivered by NOVA. After processing by the extraction plant, the residue gas stream is returned to the pipeline at original plant inlet conditions. The portion of the low-pressure residue gas destined for Monchy is returned to the Decomp/Recomp facilities for recompression and cooling prior to delivery to the Foothills pipeline, while the remainder is returned to NOVA for delivery to the TransCanada pipeline.

The first stage of recompression at the facilities is provided by the brake compressors, which are direct coupled to the turbo expanders, by which the gas pressure is boosted to 5750 kPa (834 psig). Approximately 55 percent of the pressure energy released during the expansion of the inlet gas is thus recovered in the expander/brake compressors. Supplemental compression, which is provided by electric motor driven recompressors, is then used to pressure the residue gas back to the original pipeline pressure. The hot, fully compressed gas is cooled first in the gas to gas exchangers where its heat energy is used to preheat the inlet gas. Additional cooling of the gas stream to temperatures acceptable to the pipeline is subsequently achieved in the water cooled residue gas coolers prior to the gas being returned to the pipeline.

Process Alternatives. One alternative process scheme was identified and examined during the initial project development stage. This option entailed an alternate turbo-expander arrangement wherein the electric driven recompressors would provide the first stage of gas recompression while the brake compressors would provide the second and final stage of recompression. With this scheme, although capital and operating costs were similar to the process arrangement ultimately adopted, significantly more control problems were anticipated. That is, with the fixed speed recompressors boosting to the downstream variable speed brake compressors, the brake compressors would see a relatively constant suction pressure from the recompressors, and would provide boost based on the speed at which they were operating, the operating speed being variable depending upon inlet flow conditions. Consequently, the resultant variable head from the brake compressors would make it difficult to control and maintain constant pipeline pressure under variable flow rate conditions. The selected scheme, on the other hand, has the brake compressors providing a variable suction pressure to downstream fixed speed recompressors. Through the use of variable pitch guide vanes on the recompressors, the recompressor discharge pressure can be controlled more accurately while high compression efficiencies are maintained.

Table 1 Major equipment details

EQUIPMENT	SPECIFICATION
Turbo Expander/Brake Compressors	10 925 kW (14 650 HP) maximum each
Recompressors	8 200 kW (11 000 HP) each Fixed speed electric drive. Centrifugal compressors with inlet guide vanes.
Gas/Gas Exchangers	Shell and tube construction. Two shells per train. Design duty 11.09 MW (37.8 MMBTU/hr.)
Residue Gas Coolers	Shell and tube construction. Two shells per train. Design duty 3.26 MW (11.1 MMBTU/hr.)
Inlet Separator	Size: 1 975 mm x 3 048 mm Flow capacity 59.49 x 10^6m^3/d (2 100 MMCFD) Filtration capability - 98% of 5 microns and higher particle sizes.
Switch Gear	15 KV switch gear.
ESD Valves	36 inch full port ball valves with EIM actuators.
Cooling Water Tower	Capacity of 29.31 MW (100 MMBTU/hr.)

Facilities Configuration and Equipment. The current configuration of the facilities comprises two parallel and identical equipment trains and certain additional equipment common to both the existing trains as well as a future third train. Each of the currently installed equipment trains at the facilities comprises the following major equipment items:

- Two gas to gas shell and tube type heat exchangers arranged in parallel.
- One turbo-expander/brake compressor unit.
- One electric drive recompressor unit.
- Two shell and tube residue gas coolers arranged in parallel.

The installed equipment items that are common to both the existing equipment trains as well as the future third equipment train include the inlet separator, cooling water tower and circulation pump, major isolation valves, and communications and control equipment.

All the common equipment items have been sized to service the requirements of an ultimate three equipment train configuration of the facilities. All utilities required for the operation of the facilities including cooling water supply, waste water disposal, flare systems, glycol, nitrogen, instrument air, and emergency power are supplied from the excess capacity available at the adjacent Empress II extraction plant. Electrical power to operate the recompressors is likewise available from TransAlta Utilities via two existing transformers located at the Empress II extraction plant.

Summary specifications of the major equipment items as currently installed at the facilities are provided in Table 1.

(*a*) *Gas/Gas Exchangers.* The gas/gas exchangers comprise two shell and tube heat exchangers arranged in parallel

Downloaded 02 Jun 2010 to 171.66.16.122. Redistribution subject to ASME license or copyright; see http://www.asme.org/terms/Terms_Use.cfm

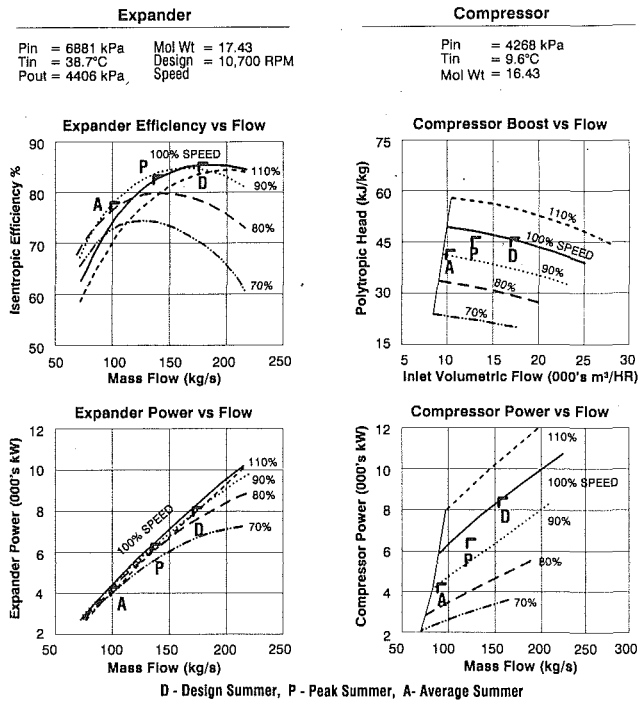


Fig. 8 Turbo-expander/compressor performance

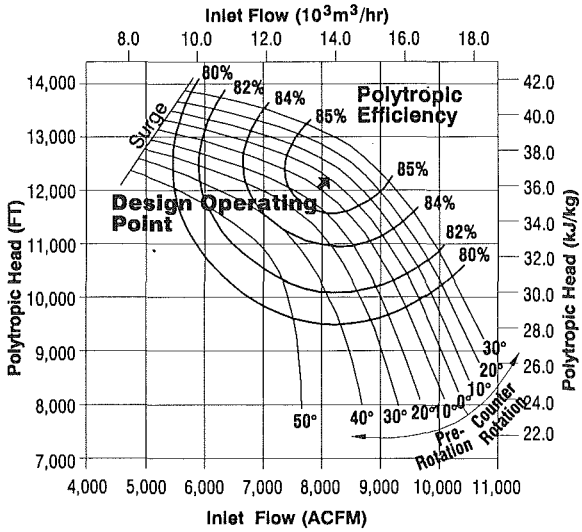


Fig. 9 Recompressor performance curve

for each equipment train, and serve the dual function of preheating the relatively cold inlet gas entering the turbo-expanders, and partially cooling the hot residue gas returning to the pipeline. The inlet gas, which flows on the shell side of the shell and tube exchangers, is preheated by the hot recompressed gas flowing on the tube side of the exchangers such that its minimum temperature after expansion and associated cooling is approximately 10°C (50°F) at inlet to the Empress II plant. This minimum temperature is required in order to maintain the gas at or near extraction plant design conditions as it is further cooled in the extraction process. Residue gas by-pass control is provided to allow for control in preheating the inlet gas stream.

(*b*) *Turbo-Expanders/Brake Compressors.* The turbo-expander/brake compressor units, which provide the first stage of gas recompression, comprise radial inlet/axial outlet expanders direct coupled to axial inlet/radial outlet brake compressors. The radial inlet turbo-expanders are equipped with actuator-controlled guide vanes for control of gas flow through the equipment, the guide vane assembly being designed to provide control over a range of 0 to 130 percent of the design flow. Each turbo-expander, under design conditions of 6900 kPa (1000 psig) suction pressure and 4240 kPa (615 psig) discharge pressures, respectively, and a flow rate of $20.18 \times 10^6 m^3/d$ (712.5 MMCFD), will generate approximately 8480 kW (11,100 hp) of recompression power at an isentropic efficiency of 86 percent and a speed of approximately 11,000 rpm. At the future inlet pressure of 7930 kPa (1150 psig), each machine will be capable of producing 10,925 kW (14,650 hp) at a speed of 13,000 rpm.

The direct coupled centrifugal brake compressors are designed to operate at a polytropic efficiency of 75 percent and will boost $19.12 \times 10^6 m^3/d$ (675 MMCFD) of gas from 4240 kPa (615 psig) to 5750 kPa (834 psig). At corresponding future conditions the brake compressors will boost the same volume of gas from 4240 kPa (615 psig) to 6170 kPa (895 psig). The relationship of expander and brake compressor performance over a range of flow rates and shaft rpm's is illustrated in Fig. 8.

(*c*) *Electric Drive Recompressors.* The recompressor units, which provide the second stage of residue gas recompression, are fixed-speed axial inlet/radial outlet centrifugal compressors driven by electric induction motors rated at 8200 kW (11,000 hp). The centrifugal compressors are equipped with actuator operated inlet guide vanes for control of inlet flow, thereby providing operational flexibility while maintaining high compressor efficiencies. Speed increasing gears serve to increase the 1800 rpm speed of the electric motors to the 10,700 rpm speed required by the compressors.

At design conditions, each recompressor will take suction from the brake compressor in the equipment train and will boost $19.12 \times 10^6 m^3/d$ (675 MMSCFD) of residue gas from 5750 kPa (834 psig) to 7090 kPa (1028 psig) at a polytropic efficiency of 85 percent. For future conditions when a third recompressor train is to be added, it is anticipated that the recompressors will be required to operate at higher head. Accordingly provision was made to increase the compressor speed to 11,000 rpm by change-out of the speed increasing gears, while the electric motors were sized with sufficient capacity to accommodate any associated increase in power requirements. Figure 9 indicates the range of performance for which the recompressors were designed.

(*d*) *Residue Gas Coolers.* The function of the residue gas coolers is to provide supplementary cooling of the partially cooled recompressed gas leaving the gas/gas exchangers prior to re-entry into the pipeline. The gas coolers, which are of shell and tube construction, comprise two shells arranged in parallel per equipment train. The cooling medium is water, which is cooled with ambient air in a water cooling tower. The cooling water travels on the tube side of the exchanger while the residue gas travels on the shell side. The combined design duty of the two shells in each equipment train is 3.26 MW (11.1 MMBtu/h). Temperature-controlled bypass of the residue gas through the coolers is provided to regulate the gas temperature at the outlet of the coolers.

The cooling tower, which provides the cooling water for the residue gas coolers as well as the water cooled electric motors driving the recompressors and the lube oil heat exchangers, is a single cell induced draft crossflow type, with design rating of 29.31 MW (100 MMBtu/h). An electric motor driven centrifugal pump with a design capacity of 851.8 m^3/h (3750 USGPM) was provided for circulating the cooling water.

IV Control System Design

Since the Decompression/Recompression facility design requirements included the ability to accommodate a broad range

Downloaded 02 Jun 2010 to 171.66.16.122. Redistribution subject to ASME license or copyright; see http://www.asme.org/terms/Terms_Use.cfm

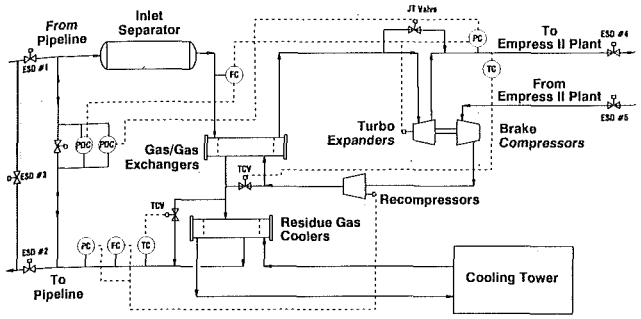


Fig. 10 Facilities control schematic

of gas inlet and outlet volume flow rates as well as variations in pipeline pressures and temperatures, special control features were incorporated into the Control System design. The concepts involved are illustrated in the Facilities Control Schematic shown in Fig. 10.

The essential basis of the control system philosophy is the requirement that the operation of the Decompression/Recompression facilities be "neutral" to the operation of the pipeline; i.e., that gas be returned to the pipeline at approximately the same pressure as it was received from the pipeline. Thus, it was imperative that the facilities have the ability to respond to normal changes in the pipeline operations (e.g., discharge pressure set point changes of upstream or downstream compressor stations or changes in flow nominations), as well as to transient surges in the pipeline resulting from unscheduled compressor station outages. One added complication to the facilities controls system design is the fact that a volume discontinuity occurs at the facilities; that is, the flow volume entering the facilities is generally greater than the flow leaving the facilities. This situation exists because the inlet of the facilities accommodates volumes destined for both Monchy via the Foothills pipeline and eastern Canadian/U.S. markets via the TransCanada pipeline, whereas the outlet of the facilities accommodates only those volumes destined for Monchy. Further, the volumes into and out of the facilities are to a large extent unrelated, and are subject to periodic change depending on nominations.

The facilities control system therefore has the following design requirements:

- control of inlet/outlet flows;
- control of inlet/outlet pressures;
- control of inlet gas preheating;
- control of outlet gas cooling;
- control of expander by-pass;
- control of brake compressor recycle;
- control of recompressor recycle;
- control of full facilities recycle; and
- control of facilities isolation from the pipeline.

Control of the discharge volume from the Facilities is effected by regulating the set point pressure for the pressure controller (PC) on the downstream side of the recompressors. This set point is provided by the Gas Control Centre for the Foothills pipeline, based primarily on the nomination volumes at Monchy. The pressure controller, in a cascaded arrangement with the flow controller (FC), regulates the guide vanes of the recompressors, and thereby effects changes in flow through the recompressors and hence flow from the extraction plant. The portion of the extraction plant residue flow not drawn into the Facilities automatically flows into the NOVA system for delivery to the TransCanada system.

While the Facilities discharge pressure and flow are regulated using the pressure set point provided by pipeline Gas Control on the basis of the downstream pipeline system requirements, the flow into the Facilities is regulated on the basis of the requirement for equal pressures at the Facilities inlet and outlet. Two parallel differential pressure controllers (PDCs) monitor the pressure difference across the two-way bypass valve in the piping connecting the Facilities inlet and outlet sides. When pressure differences greater than the preset tolerance are detected, the first PDC will activate the flow controller (FC) downstream of the inlet separator to regulate the guide vanes on the turbo-expanders and thereby adjust the flow into the Facilities. The direction of the pressure differential across the bypass valve will determine the control exercised on the turbo-expander guide vanes. When the inlet pressure is higher than the Facilities discharge pressure, the guide vanes will be opened further to allow more flow into the Facilities and thereby reduce the inlet pressure. The reverse of this action ensues when the discharge pressure is higher than the inlet pressure. To protect against excessive pressures developing at the inlet to the extraction plant, the pressure controller downstream of the turbo-expanders would exercise override control on the expander guide vanes. The second parallel PDC across the bypass valve controls the position of the Joule Thompson (JT) valve. This valve, which would normally be closed, would open only when pressure equalization is not possible by control of the expander guide vanes alone or when the expanders are not operating. Under unusual circumstances, when pressure equalization across the Facilities inlet and outlet is not possible through the exercise of control on the expanders and the JT valve, the first PDC will act to open the normally closed two-way bypass valve to establish this equalization.

Control of the inlet gas heating is achieved using the temperature controller (TC) located in the piping upstream of the inlet to the extraction plant. This controller regulates the flow of hot compressed residue gas to the gas-to-gas exchangers depending on the observed temperature of the gas feeding the extraction plant. A similar control is exercised by the temperature controller located at the outlet of the Facilities for the flow of the partially cooled residue gas into the residue gas coolers.

The Facilities can be effectively isolated from the pipeline by closing the ESD (Emergency Shut Down) valves 1 and 2 and opening ESD valve 3. A similar isolation from the extraction plant is possible by closing ESD valves 4 and 5. In addition to these valves, pressure relief valves located at the inlet and outlet as well as in the piping to the inlet of the extraction plant protect the Facilities from transient pressure surges.

V Turbo-Expander Design Features

The turbo-expanders/brake compressors utilized in the decompression/recompression process are central and critical to performance and efficiency of the facilities. The simultaneous requirements of high-volume, high-pressure, noncryogenic, and high-efficiency service resulted in units of unique design. The turbo-expanders, manufactured by Mafi-Trench Corporation of Santa Maria, California, are the highest shaft horsepower and the highest power per unit volume (i.e., "power density") of any expanders manufactured to date. Some of the unique design features incorporated in the turbo-expander design are described below.

Bearings. Initially, vendors' standard fixed-pad journal bearings were designed and manufactured for the turbo-expander. Analysis confirmed that these bearings would operate acceptably for most conditions, but may be marginal at certain conditions. Mafi-Trench designed tilting-pad journal bearings, which would fit into the same envelope as the original bearings, and constructed these in parallel with the fixed pad bearings so that both could be mechanically tested. The tilting-pad bearings proved to be superior and were used in the final shipped assembly.

Downloaded 02 Jun 2010 to 171.66.16.122. Redistribution subject to ASME license or copyright; see http://www.asme.org/terms/Terms_Use.cfm

Variable Inlet Guide Vanes. The actuator-controlled guide vanes were contructed of hardened, ground, and lapped 400 series stainless steel. All parts were specially coated to reduce sliding friction and eliminate galling. The guide vanes pivot to control the flow angle and flow area, thus allowing them to be used like a control valve while continuing to direct the gas into the impeller in an efficient manner.

Turbo-Expander Impeller Design. Typical gas processing turbo-expander impellers are manufactured from high-strength aluminum alloys, which are ideal because of their high strength-to-weight ratios. The high "power density" of the turbo-expanders for the Decompression/Recompression facilities resulted in the selection of Type 403 stainless steel for the expander impellers. Type 403 steel was selected because of its high fatigue strength and superior internal damping, which features are needed to avoid fatigue failure at high power densities. Finite Element stress and modal analyses were performed to confirm adequacy of mechanical design before actual manufacture of the impellers commenced.

The turbo-expander packages were purchased as self-contained units complete with lube oil surge tank, pumps, filters, coolers, and associated instrumentation mounted on two skids. Each expander/brake compressor unit was mounted on one skid, while the associated lube oil system and control panel was mounted on a second skid. The turbo-expanders were also extensively tested prior to shipping to confirm mechanical and aerodynamic performance.

VI Recompressor Design Features

The electric driven recompressors were purchased as a complete package including motor, gear, lube oil system and compressor from IMO Industries Inc., Delaval Turbine Division in Trenton, NJ. Some of the design features incorporated in the recompressor train design are discussed below.

Recompressors. The recompressors were manufactured to Amoco specification, which included requirements of API-617, 5th ed. Specific features of the compressor units included variable inlet guide vanes, dry gas seals, vibration probes, bearing RTD's, and other instrumentation. In addition, lateral and torsional critical analysis were done on the rotating assembly. The compressors also underwent mechanical and PCT-10 performance testing prior to shipping. The lube oil system was designed to Amoco specifications which included requirements of API-614, 2nd ed. Components of the lube oil system include PD pumps, filters, coolers, overhead tank, and surge tank. The piping and tanks are of stainless steel construction to eliminate corrosion products forming in the lube oil system, and to reduce startup problems associated with scale from carbon steel plugging filters.

Variable Inlet Guide Vanes. The guide vanes provided with the compressors are specialized flow diversion devices located on the inlet to the compressor wheel. As the compressors are axial inlet machines, the guide vanes serve to "direct" the gas in either the direction of rotation of the compressor impeller (counterrotation), at 90 deg to the impeller, or in a direction opposite to the rotation of the impeller (pre-rotation). The guide vanes, which are equipped with pneumatic controllers, serve to control flow through the compressors. The use of throttling valves on the inlet of the recompressor was initially considered as an alternative to the guide vanes; however, there is a penalty in efficiency with this form of control. Application of continuous control of guide vanes has proven to be a very effective means for controlling gas flow out of the facilities.

Speed Increasing Gear. The speed increasing gear in the recompressor train was supplied by Lufkin Industries Inc., and was manufactured to Amoco specification, which includes the requirement of API 613, 3rd ed. The gears are equipped with vibration probes and RTD's, and are designed for a ratio of 5.956:1, which allows the speed to be increased from 1800 rpm provided by the electric motor to 10,700 rpm required by the compressor. The gears, which are 98.4 percent efficient, were shop tested at full speed/part load to confirm operability. The gear cases were also designed to accept gears of different ratio to allow a speed of 11,000 rpm when future higher head conditions for the recompressors may be required.

Electric Motor. The electric motors included in the recompressor packages were 8200 kW (11,000 hp), 13.2 kV induction motors manufactured by Westinghouse Motor Company Canada Ltd., Hamilton, Ontario. The motors were designed to Amoco specification, which includes the requirements of API-541-1987. The motors were tested by the superposition dual frequency method in the shop and achieved the guaranteed efficiency of 96.8 percent.

The compressors and gears were tested as a unit at IMO's shop and shipped to site, while the motors were tested separately at Westinghouse's test facility in Round Rock, Texas, and shipped to site later. The compressor skids were designed to accept the installation of the motors separately on site upon their subsequent delivery.

Compressor/Driver Selection. A number of options for the compressor/driver combinations were available for the Decompression/Recompression facilities. These options included:

- gas turbine driven centrifugal compressors;
- variable speed electric driven centrifugal;
- fixed speed induction electric driven centrifugal;
- fixed speed synchronous electric driven centrifugal; and
- combinations of the above.

In selecting the compressor/driver combination for the Decompression/Recompression facilities the following factors were considered:

(*a*) The compressor driver combination should be compatible with the two train turbo expander units, and synchronized with the operating characteristics of the brake compressors.

(*b*) The Empress Plants have a very reliable electric power supply of more than adequate capacity.

(*c*) Amoco has experience in operating both electric driven fixed speed and turbine driven centrifugal compressors downstream of brake compressors.

(*d*) In excess of 75 MW (100,000 hp) of synchronous electric motor driven compressors were currently being operated at the Empress Plants.

(*e*) Capital and operating costs for the selected driver option should be optimal.

(*f*) The initial two trains should have sufficient operational flexibility to accommodate a future third train.

Based on previous Amoco experience, it was believed that recompressor capacity should match the turbo-expander capacity and this, in keeping with the equipment train concept, led to the decision to match the brake compressor and recompressor flow capacities. To match brake compressor throughput over a range of conditions, a variable speed recompressor either electrically or turbine driven offered the most flexibility, although based on the previous experience at Empress, it was believed that constant speed recompressors with variable guide valves would also provide adequate flexibility on throughput. Given that the electric power supply was reliable and of more than adequate size, the issue of driver type was then resolved primarily on the basis of economics. Constant speed electric drivers were of lesser capital cost than equivalent, variable speed drivers or turbines; however, the operating cost savings of the variable speed drivers were not sufficient to pay out the incremental capital cost. On this basis, constant-speed electric

Downloaded 02 Jun 2010 to 171.66.16.122. Redistribution subject to ASME license or copyright; see http://www.asme.org/terms/Terms_Use.cfm

driven recompressors with variable guide vanes that matched individual brake compressor performance were chosen.

There were two options available for the electric drives: synchronous or induction motors. The decision was driven by the economic trade-off of higher capital and lower operating costs for the synchronous motors. The payout of the higher capital was calculated to be greater than 3 years. Amoco's experience also indicated that additional costs would be incurred for couplings and torsional analysis on the synchronous motors. Given the large synchronous load operating at Empress, which controlled the power factor to unity, and the sufficient power supply and transformer capacity, which would allow the induction motors to start without reduced voltage starting equipment, the decision was made to purchase the induction motors for the Decompression/Recompression facilities.

VII Startup Operating Experience

Startup problems experienced were minor in nature, with the most notable being the compressor couplings running too hot. The coupling guards were modified to allow more air flow through the couplings and this problem was thereby resolved. Other than the coupling problem and the normal control system debugging and tuning, the facility startup went smoothly. Much of the startup success can be attributed to the extensive shop testing of the expander, compressor, and lube oil systems that was done, and to the fact that plant operations staff were involved throughout the design and construction stages.

In the first year of operation, the facilities have demonstrated that the design performance can be met and that equipment efficiencies meet or exceed manufacturer's predictions. Field testing has confirmed that the expanders are operating at design efficiency, while the brake compressors are operating at 3 percent greater than design efficiency. The recompressors are also meeting design efficiency, but it has been demonstrated that the guide vanes have not given the degree of flexibility that was predicted. Some piping modifications have also been made to allow cooling of the brake compressor discharge gas as pipe stress and temperature limitations for the brake compressor wheels were being encroached on. This problem was experienced because of lower than design flow through the brake compressor/recompressor side of the plant, and the resultant excessive recycling of gas to prevent surge conditions.

Although not unanticipated, noise levels in and around the facilities have proven excessive. Noise was recognized as a problem during design but due to the difficulty in predicting noise levels and the effectiveness of mitigative measures, it was decided to complete the facilities with few noise control measures. After startup, noise level surveys were performed and a scheme of selective insulation on the piping for noise control was undertaken. This scheme provided for cost-effective noise control with no impact on the actual operation of the facilities.

Equipment vibration levels are being monitored continuously and have been within design requirements. Piping vibration in some parts of the facilities was a concern initially; however, vibration studies have subsequently shown that vibration and pipe stress levels are safe.

The facilities are currently being expanded by the addition of a third expander, the third set of gas-to-gas exchangers, and the third set of residue gas coolers to accommodate additional volumes of gas scheduled for service in November 1992.

Acknowledgments

The authors wish to acknowledge the engineering staff of Mafi-Trench Corporation for their valued assistance in the preparation of the turbo expander technical material included in this paper. In addition, Sam Sampath of Sampath Consulting Ltd., and Albin Zubot, Amoco Canada Plant Manager, Empress Extraction Plant are acknowledged for their welcome contributions toward the preparation and review of this paper.

References

Kitt, S. R., and Sampath, S., 1990, "Foothills Decompression/Recompression Facilities, A Unique Approach to Pipeline Expansion," presented at 22nd Annual Meeting of PSIG, Baltimore, MD.

Downloaded 02 Jun 2010 to 171.66.16.122. Redistribution subject to ASME license or copyright; see http://www.asme.org/terms/Terms_Use.cfm

Axial Inlet Conversion to a Centrifugal Compressor With Magnetic Bearings

T. Novecosky
NOVA Corporation of Alberta,
Edmonton, Alberta, Canada

NOVA's Alberta Gas Transmission Division transports natural gas via pipeline throughout the province of Alberta, Canada, exporting it to eastern Canada, United States, and British Columbia. There is a continuing effort to operate the facilities and pipeline at the highest possible efficiency. One area being addressed to improve efficiency is compression of the gas. By improving compressor efficiency, fuel consumption and hence operating costs can be reduced. One method of improving compressor efficiency is by converting the compressor to an axial inlet configuration, a conversion that has been carried out more frequently in the past years. Concurrently, conventional hydrodynamic bearings have been replaced with magnetic bearings on many centrifugal compressors. This paper discusses the design and installation for converting a radial overhung unit to an axial inlet configuration, having both magnetic bearings and a thrust reducer. The thrust reducer is required to reduce axial compressor shaft loads, to a level that allows the practical installation of magnetic bearings within the space limitations of the compressor (Bear and Gibson, 1992).

Introduction

NOVA is a widely held company operating internationally from headquarters in Calgary, Alberta, Canada. NOVA has built its future on pipelines and the manufacturing and marketing of chemicals and plastics processed primarily from Alberta natural resources. NOVA owns and operates a 10,500 mile natural gas transportation system in Alberta. The NOVA system carries more than 13 percent of the gas produced annually in Canada and the United States, including more than 75 percent of marketed Canadian production. In 1990, it carried a record 2.89 trillion cubic feet of gas.

Conversions to an axial inlet configuration on overhung compressors began in 1987 within NOVA. To date four Cooper RF30 compressors have been converted using conversion kits supplied by the manufacturer. Each retrofit was successful, resulting in increased compressor adiabatic efficiency. As a result, fuel costs and hence operating costs have been reduced. This has provided the justification for similar compressors to be converted.

Discussion

At NOVA's Beiseker Compressor Station there are two Cooper RF30 overhung centrifugal gas compressors (Units 1 and 2), which operate in parallel, each driven by a Coberra 1533/RT48 Turbine package (see Fig. 1). The Unit 1 compressor has conventional hydrodynamic bearings and dry seals. The Unit 2 compressor is unique in that it has magnetic bearings and dry seals. This presented NOVA with the opportunity to convert the first overhung compressor with magnetic bearings (see Fig. 2) to an axial inlet configuration (see Fig. 3).

Conversion of Unit 2 required significant modifications to both the suction piping and the compressor:

Piping Modifications

1 Reroute suction piping from the side of the compressor to the compressor door (see Fig. 1).

Compressor Modifications

1 Replace the existing door with one having a 30-in.-dia

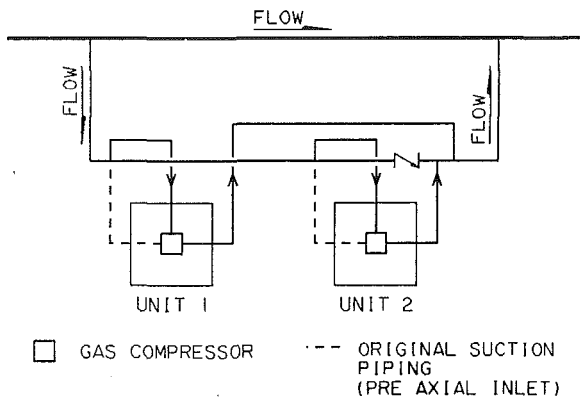


Fig. 1 Beiseker Compressor Station plot plan

Contributed by the International Gas Turbine Institute and presented at the 37th International Gas Turbine and Aeroengine Congress and Exposition, Cologne, Germany, June 1-4, 1992. Manuscript received by the International Gas Turbine Institute January 28, 1992. Paper No. 92-GT-25. Associated Technical Editor: L. S. Langston.

Copyright © 1994 by ASME
Downloaded 02 Jun 2010 to 171.66.16.122. Redistribution subject to ASME license or copyright; see http://www.asme.org/terms/Terms_Use.cfm

hole to accommodate the rerouted suction piping (see Fig. 3, Item A).

2 Install an inlet extension to duct flow the intake flange to the compressor wheel (impeller) (see Fig. 3, Item B).

3 Modify the inlet diffuser to accept the inlet extension (see Fig. 3, Item C).

As a result of installing an inlet extension, modifications to the support tube assembly were required. A new support tube flange was machined to mate to the inlet extension hub (see Fig. 3) and the length of the support tube needed to be shortened. In addition, the external connections for the buffer supply gas and seal leakage gas, used only to operate the thrust reducer, could no longer be directly mounted to the support tube flange outside the compressor door (see Fig. 2). Access to the new support tube flange from outside the compressor could only be obtained through two of the five inlet extension struts (see Figs. 3 and 4).

Design Concept of Inlet Extension. In converting to an axial inlet configuration NOVA was responsible for the piping

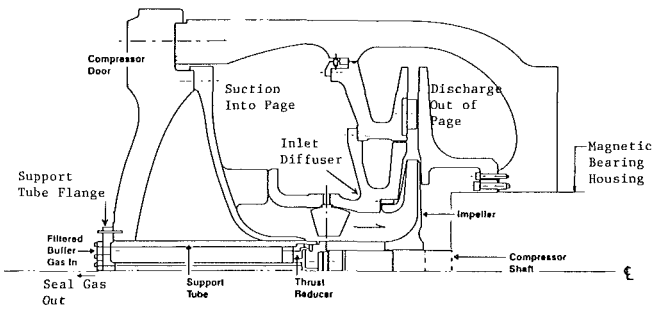


Fig. 2 Conventional overhung compressor cross section with magnetic bearings

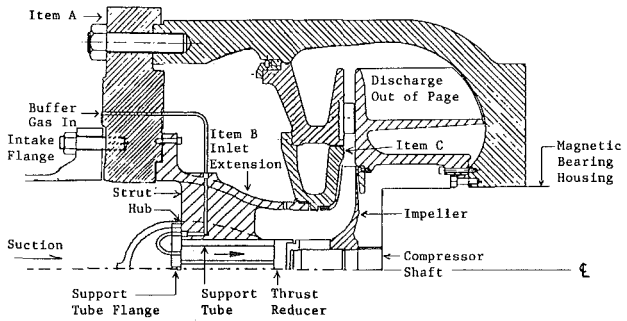


Fig. 3 Magnetic bearing overhung compressor cross section converted to axial inlet

modifications. Cooper Energy Services provided the conversion kit, which included a new door, modified inlet diffuser and accessories. Following discussions with Cooper Energy Services it was decided NOVA would provide the inlet extension. The following discusses the design of the inlet extension in detail.

Originally the support tube and thrust reducer were supported by the compressor door (see Fig. 2). In converting to an axial inlet, this support was lost, therefore necessitating an alternate arrangement. After review, the inlet extension was the most logical device to use to provide this support. The inlet extension consists of a center hub, held in position by five airfoil-shaped struts, which are mounted to an outer wall (see Fig. 4). The struts were designed as airfoils to minimize the drag by having the proper balance between friction drag and form drag. Two of the struts, each 72 deg from top dead center (TDC), have a 0.5-in. hole for buffer supply gas and seal leakage gas. If the struts are too thick, they could restrict the flow and reduce operating efficiency. The cross-sectional area (A_1) along the length of the inlet extension must not be less than the cross-sectional area at the inlet of the compressor wheel (A_2). This would also result in a flow restriction.

After review of various NACA (National Advisory Committee for Aeronautics) strut profiles, the NACA 0012 profile was chosen. At a length of 11.5 in., its greatest thickness was 1.5 in., resulting in a wall thickness of 0.5 in. at the strut holes, which was ample to withstand all stresses during operation.

The hub consists of a machined face and a 9-in.-dia hole. The support tube fits into the hole and is fixed with a series of bolts. A nose cone is screwed onto the hub to direct inflowing gas around the hub. The nose cone has four pressure equalizing holes, which eliminate stress due to hydrostatic pressure on the walls during operation. To aid in the nose cone installation, a hex head was made to attach the installation tool to the cone.

To eliminate circumferential stresses on the outer wall, caused by inlet pressure, six pressure-equalizing holes were spaced equally on the downstream end of the inlet extension. The holes were sized so their total cross-sectional area was greater than the cross-sectional area of the compressor vent line. This prevents the outer wall from collapsing during compressor depressurization.

Material Selection. In reviewing inlet extensions supplied by Cooper Energy Services, NOVA felt the design would be much lighter and thinner if a stronger material was used. With a lighter casting, machining the end faces would be faster and handling the inlet extension simpler. When installing the conversion kit the cost of upgrading the overhead crane for a heavier inlet extension would be eliminated.

During operation the inlet extension would be subject to high stress and fatigue conditions. American Petroleum In-

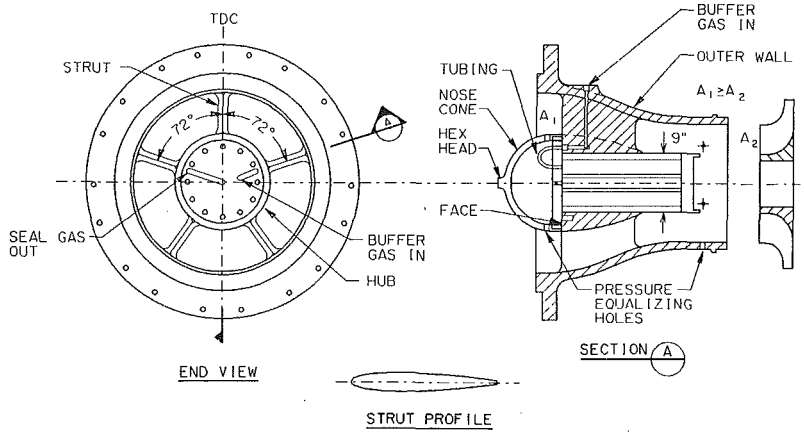


Fig. 4 Inlet extension

Downloaded 02 Jun 2010 to 171.66.16.122. Redistribution subject to ASME license or copyright; see http://www.asme.org/terms/Terms_Use.cfm

Table 1 Material properties

TENSILE PROPERTIES				
Property	UTS(psi)	Yield (PSI)	Elong.%	Reduction in area %
Required	85,000	60,000	18.00	35.00
Obtained	104,298	82,251	26.00	60.00
IMPACT PROPERTIES (Test Temperature minus 50°F.)				
Required		Single Test min. 13 ft/lb	Average min. 20 ft/lb	
Obtained		I 72, II 80, III 71	Average 74	
OTHER PROPERTIES - HARDNESS				
Maximum		BHN = 237		
Obtained		BHN = 207		

stitute (API) Standard 617 recommends various materials for diaphragms and vanes for this application. NOVA consulted a metallurgist, specialized in the field of castings, and decided a stronger material could be used for a minimal price increase. This was the first NOVA inlet extension design and damage could result from failure. The recommended choice was ASTM A148 Grade 8560.

To withstand these operating conditions the material requirements were high toughness, ductility, and yield strength, and at the same time, good machinability. By obtaining high toughness (see Table 1—Impact Properties) and high ductility (see Table 1—Elongation and Reduction in Area) crack propagation would be reduced to a minimum, providing good resistance to fatigue cracking. With high yield strength, a thinner wall could be designed to withstand the high forces this area is subject to during normal operating and surge conditions.

To obtain a material with these characteristics the following were required:

1 A chemistry with good hardenability and low carbon content.
2 Heat treatment practice and quenching severity to ensure desired microstructure.
3 Establishment of an internal an external inspection standard detailing radiographic and magnetic particle acceptance criteria.

To ensure these requirements were met before pouring the casting, the material was checked for correct chemical composition by conducting a spectrographic analysis. Tensile and impact properties were also checked following heat treatment. Shown in Table 1 are the properties required and obtained.

Stress Analysis. During operation of the compressor, the struts and nose cone were subject to drag forces (F_{STRUT}, F_{CONE}) caused by inflowing gas (see Fig. 5). A force existed ($F_{P1/P2}$) toward the shaft, caused by the pressure differential ($P_1 - P_2$) across the thrust reducer, acting at the inlet flange face. These forces produced stresses that needed to be analyzed to provide a design that met all operating conditions.

Due to the complexity of the shape being analyzed, the cost and time required to perform a finite element analysis were not justified. Instead, the outer wall and struts were modeled and analyzed as a cantilever beam extending from a wall without the support of the hub. After reviewing the shear and moment diagrams, it was evident the maximum shear and normal stresses existed along the trailing edge of the strut, adjacent to the outer wall (see Fig. 5, Location A). These calculated stresses were low when compared to allowable stresses. One additional condition analyzed was blockage of the pressure equalizing holes. The maximum hoop stress on the outer wall was well below allowable limits.

Installation. Installation of the conversion kit consisted of two main steps. The first step was to assemble the new door, inlet extension, and short spool piece as one (see Fig. 3). The short spool piece acts as a counterweight to the inlet extension during installation. The large diameter end of the inlet extension was bolted to the compressor door while the opposite end

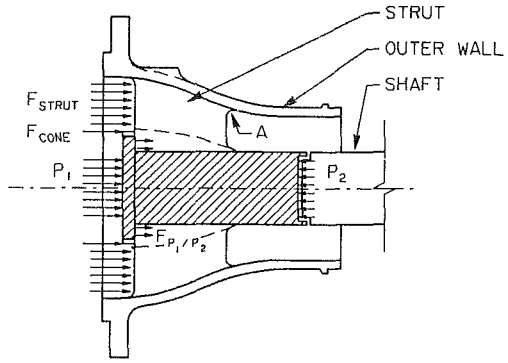


Fig. 5 Forces acting on inlet extension

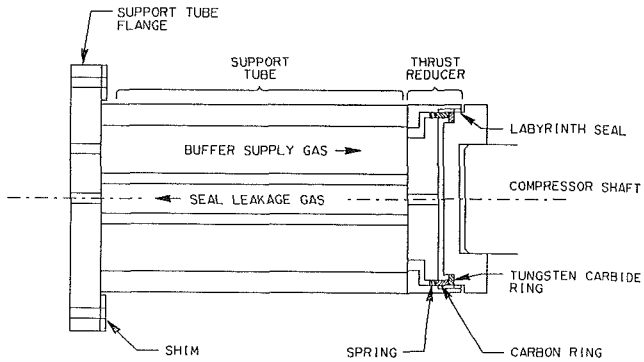


Fig. 6 Support tube and thrust reducer

was a friction fit next to the inlet diffuser. This assembly was bolted to the compressor casing.

The second step was the installation of the support tube and thrust reducer. There were two main objectives during this installation. The first objective was to ensure the carbon ring within the thrust reducer (see Fig. 6), which mates to the tungsten carbide ring, would be compressed to half its total travel. The second objective was to align the centerline of the thrust reducer with the centerline of the levitated compressor shaft (shaft position during operation). To ensure correct axial positioning of the carbon ring a shim was installed just behind the support tube flange. The thickness of the shim was calculated based on how much the compressor walls grew and the amount the carbon ring was to be compressed during operation.

To align the thrust reducer and shaft centerlines, the radial magnetic bearing located nearest the thrust reducer was utilized. Throughout the alignment procedure the magnetic bearings must be energized to keep the rotor levitated. This avoids damaging the thrust reducer labyrinth seal and maintains the shaft centerline. A specially designed tool was used to place the support tube and thrust reducer assembly into the inlet extension hub. The support tube flange was attached with studs.

To match centerlines, the shaft was moved vertically using the radial magnetic bearing. Clearances between the labyrinth seal and shaft were determined. If all clearances were within acceptable tolerance the thrust reducer was aligned. If not, the thrust reducer required adjustment. Once all clearances were checked and confirmed within tolerance, the assembly was considered aligned and the shaft was then lowered.

Tubing for the buffer supply and seal leakage gas were also connected (see Fig. 4). The nose cone was screwed onto the hub using a specially designed tool attached to the hex head. The installation was then complete.

This installation procedure was discussed in general terms. A more detailed procedure has been written for field installation.

Downloaded 02 Jun 2010 to 171.66.16.122. Redistribution subject to ASME license or copyright; see http://www.asme.org/terms/Terms_Use.cfm

Conclusion

Overall, the conversion of an overhung centrifugal compressor with magnetic bearings to an axial inlet configuration was successful in meeting all objectives. To date, compressor Units 1 and 2 have been running without any problems. Due to difficulty in obtaining proper pipeline conditions, pre- and post-compressor efficiencies could not be quantified.

The following areas were recognized and noted:

1 On future units the strust should be designed thicker, thus making the drilling of the buffer supply gas and the seal leakage gas holes a less precise procedure.
2 The nose cone should be designed to profile more closely a bullet nose, producing better aerodynamics and possibly resulting in higher adiabatic efficiency.
3 The material properties for the inlet extension were better than expected resulting in a stronger and more durable material.
4 Installation of the support tube and thrust reducer required the design of new installation tools.

Based on the success of this conversion and the continuing application of magnetic bearings within NOVA, future conversions are being considered.

Acknowledgments

I would like to thank Mr. Robert Peterson, Senior Technologist, Clayton Bear, P. Eng., and Mr. Vaclav Kulle, P. Eng., who jointly developed the original concept and design of the inlet extension.

I would like to thank Mr. Martin Ishkanian who provided valuable input in developing the material for the inlet extension.

References

Bear, C., and Gibson, S., 1992, "Applications Using Dry Gas Seals to Control Axial Shaft Loads in Centrifugal Compressors," ASME Paper No. 92-GT-104.

Downloaded 02 Jun 2010 to 171.66.16.122. Redistribution subject to ASME license or copyright; see http://www.asme.org/terms/Terms_Use.cfm

K. Mathioudakis

A. Stamatis

Laboratory of Thermal Turbomachines,
National Technical University of Athens,
Athens, Greece

Compressor Fault Identification From Overall Performance Data Based on Adaptive Stage Stacking

In the present paper a method for the identification of faulty stages in a multistage compressor is presented. The values of overall compressor parameters, namely mass flow rate, pressure ratio, and efficiency, at different operating points are the input data to the method. Employing these data, the method gives the location and the number of faulty stages, as well as the amount of deviation from intact condition performance. It is shown that the kind of fault that has caused stage performance deterioration can be identified. Features of the method, such as generality of applicability, input data requirement, and reliability of the findings, are discussed.

1 Introduction

The ongoing effort of research in the area of engine condition monitoring has provided gas turbine users with a number of techniques for engine condition assessment and fault diagnosis. In particular, methods based on aerothermodynamic measurement data have been developed. A common feature of such methods is that they can provide in one way or another a global picture of the engine condition and identify the engine component suffering from a particular problem: One can state that techniques based on aerothermodynamic data can show which component is malfunctioning and what kind of problem is present (this second piece of information being very much dependent on experience on particular engines rather than generalized rules).

The compressor, being a critical component of a gas turbine, and particularly susceptible to environmental hazards, has received particular attention in recent studies. Some compressor faults constitute routine events in gas turbine field operation, and it is therefore vital to have the ability to handle them, in order to ensure efficient and reliable engine operation. A commonly encountered such problem is compressor fouling, while erosion, corrosion, foreign object damage, and tip clearance deterioration are other types of problems frequently encountered in field operation of both industrial gas turbines and jet engines.

In order to identify the existence of such problems and investigate their effect on overall engine performance, techniques for simulating compressor overall performance from stage data have been employed by different investigators, as for example Batcho et al. (1987), Aker and Saravanamuttoo (1989), Muir et al. (1989), and Tabakoff et al. (1990). The approach followed in these works is a "direct" one: A certain kind of stage characteristic alteration is assumed to be caused by a fault and the overall compressor performance is synthesized. The deviations caused by the presence of different kinds of faults can then lead to identification of a problem from overall performance data.

Such approaches are very valuable when the impact of faults on engine operation is analyzed. When the engine operator has a set of performance data from a faulty engine in hand, however, his interest is to reach a conclusion about the kind of fault as quickly and as reliably as possible.

The method introduced in the present paper tackles this problem. The overall performance data are used as an input and the modification of performance and localization of faulty stages is directly derived (as opposed to trying different faults scenarios in order to match the data in hand). The technique is thus of the "inverse" type, as far as performance prediction is considered. A technique of this kind has been used by Massardo (1991), for fault diagnosis. Since Massardo restricted himself to a linear semi-analytical method of solution of the problem, the only fault he considered was fouling of a single stage of a multistage compressor. Such a fault, however, even though possible, does not cover the majority of practically encountered cases of fouling, which appears distributed in a number of stages of the compressor. Neither can it cover cases of other faults extending through several compressor stages.

The method proposed in this paper employs optimization techniques, along the same principles as the overall engine performance adaptive modeling introduced by the present authors (Stamatis et al., 1989). The "stage-stacking" technique for multistage compressor performance prediction is employed as a basic tool (this method was developed a while ago and descriptions can be found in a number of sources, e.g., Robbins and Dugan, 1965). It is coupled to suitably formulated fault models and numerical optimization schemes. Existing empirical background is employed in order to give the technique as general features as possible and applicability to faults that are realistic according to the experience accumulated by various investigators.

Contributed by the International Gas Turbine Institute and presented at the 37th International Gas Turbine and Aeroengine Congress and Exposition, Cologne, Germany, June 1-4, 1992. Manuscript received by the International Gas Turbine Institute September 28, 1992. Paper No. 92-GT-28. Associate Technical Editor: L. S. Langston.

Copyright © 1994 by ASME
Downloaded 02 Jun 2010 to 171.66.16.122. Redistribution subject to ASME license or copyright; see http://www.asme.org/terms/Terms_Use.cfm

We start by describing the theoretical and empirical background employed for the formulation of the technique. The actual technique as well as application aspects follow.

2 Theoretical and Empirical Foundation

2.1 Overall Performance and Stage Data. Energy addition to the gas flowing through a multistage compressor is effected by the cumulative pressure and temperature rise of individual stages. The overall compressor performance can therefore be reconstituted by synthesizing the effects of successive stages, bearing in mind that exit conditions from a stage are inlet conditions to the one following it. A technique that has been found very effective in performing such calculation is the "stage-stacking" technique. The performance of the compressor is analyzed on a one-dimensional basis, each stage being represented by means of its nondimensional characteristic curves, namely curves relating the following nondimensional characteristic parameters of the stage: Φ, Ψ, η (or ζ).

If these parameters, as well as the inlet conditions, are known at one operating point of the compressor then the overall temperature rise, pressure ratio, and efficiency of the compressor can be calculated through the following relations:

$$\Delta T_t = \frac{1}{C_p} \sum_{i=1}^{N} \frac{\psi_i}{\eta_i} U_i^2 \tag{1.1}$$

$$PR = \prod_{j=1}^{N} \left(\frac{\Psi_i U_i^2}{C_p T_{t0} + \sum_{k=1}^{i} \left(\frac{\Psi_k}{\eta_k} \right) U_k^2} + 1 \right)^{\frac{\gamma}{\gamma - 1}} \tag{1.2}$$

$$\eta_{c,is} = \frac{PR^{\frac{\gamma-1}{\gamma}} - 1}{\frac{T_{t\text{exit}}}{T_{t0}} - 1} \tag{1.3}$$

(The relations are written here for a gas with C_p, γ constant, in order to facilitate the presentation in terms of analytical relations. In the actual implementation of the method calculations are performed by taking into account their dependence on temperature, through appropriate polynomial expressions.) These relations show that if at one particular operating point the inlet mass flow rate is known, then knowledge of the area variation along the compressor, stage exit angles, and the characteristic curves Φ–Ψ, Φ–η of each stage enables the calculation of the overall compressor pressure ratio and efficiency.

The problem we are interested in consists of determining individual stage parameters, when the overall pressure ratio and efficiency for a given mass flow are known. In general the parameters of individual stages cannot be determined, since each stage operates at a different set of Φ_i, Ψ_i, η_i and we have more unknowns than equations as long as the compressor comprises more than one stage ($N > 1$). A possibility to derive Φ_i, Ψ_i, η_i for each stage could result under one of the following circumstances: (*a*) if we had a corresponding additional number of equations, sufficient to close the problem, (*b*) the parameters Φ_i, Ψ_i, η_i for each stage are interrelated so that the number of unknowns is reduced, (*c*) combination of cases (*a*) and (*b*). This would be the case if for example pressure and temperature were measured at the exit of each individual stage, a situation that is however unrealistic for practical applications of engine monitoring.

An alternative way to solve this problem can be derived if one takes into account some empirical facts that have been observed by various researchers. Let's consider the case of occurrence of a fault. We assume that the initial stage characteristics are known. The occurrence of a fault will result in a modification of the characteristic curves of the stages influenced. For any stage we assume that this modification can be represented in a monoparametric manner:

$$\Psi(\Phi) = \Psi(\Phi) + \Delta\Psi \tag{2.1}$$

$$\eta(\Phi) = \eta(\Phi) + \Delta\eta \tag{2.2}$$

$\Delta\Psi$, $\Delta\eta$ do not depend on Φ but are related to Ψ, η through a single parameter. The assumption of this kind of modification is based on observations by various investigators (Seddigh and Saravanamuttoo, 1991; Aker and Saravanamuttoo, 1989; Tabakoff et al., 1990; Batcho et al., 1987). A translation of the Φ–Ψ, Φ–η curves on their corresponding planes is such a modification. In that case $\Delta\Psi$, $\Delta\eta$ are constant for every Φ. Of course the way we have chosen to represent the modification does not necessarily correspond to the actual way by which the alteration is happening. It could be, for example, that, while the energy addition capacity of the stage doesn't change, its swallowing capacity is reduced. If this change is in the form of plane translation, then it can be represented as a change along some arbitrarily chosen direction. We simply choose the direction to be perpendicular to the Φ axis. Different possible choices of a point-to-point transformation to represent the translation are shown in Fig. 1.

If the amounts $\Delta\Psi_i$, $\Delta\eta_i$ by which the characteristics of every stage are changed are considered as unknowns, then the problem of identifying the stage with a fault is equivalent to determining the values of these parameters for each stage. Intact stages will be associated with zero values. If we consider Eq. (1), we see that for one operating point the overall compressor pressure ratio and temperature rise are functions of the changes in the characteristics:

Nomenclature

C_p = specific heat at constant pressure
$\mathbf{g}$ = vector with geometric data, Eq. (6)
$\dot{m}$ = mass flow rate
N = number of compressor stages
PR = pressure ratio
Q = corrected mass flow rate = $m\sqrt{(T/T_{\text{ref}})}/(p/p_{\text{ref}})$
U = peripheral velocity
$\mathbf{u}$ = independent compressor parameter vector
Va = axial velocity
v = independent stage parameter
$\mathbf{x}$ = dependent stage parameter vector
$\mathbf{y}$ = dependent compressor parameter vector
Δh = enthalpy rise
ΔT_t = total temperature rise
γ = ratio of specific heats
$\zeta = \Delta h/U^2$ = temperature rise coefficient
$\eta = \Psi/\zeta$ = stage efficiency
$\eta_{c,is}$ = overall compressor isentropic efficiency
$\Phi = Va/U$ = flow coefficient
$\Psi = \Delta h_{is}/U^2$ = pressure rise coefficient

Subscripts

a = axial
is = isentropic
exit = conditions at exit of a stage
ref = reference quantity
t = total quantity
0 = conditions at engine inlet

Downloaded 02 Jun 2010 to 171.66.16.122. Redistribution subject to ASME license or copyright; see http://www.asme.org/terms/Terms_Use.cfm

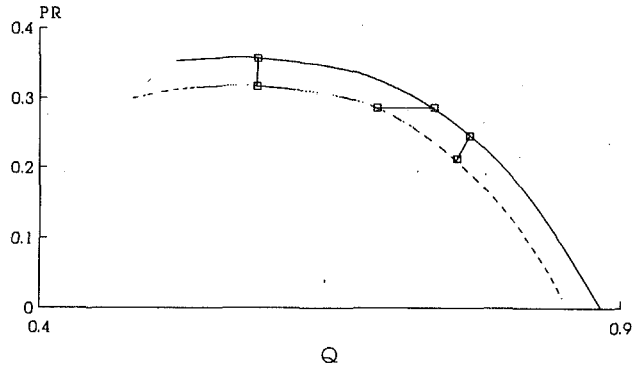


Fig. 1 Alternatives of point-to-point correspondence for expressing modification of stage characteristics

$$\Delta T_t' = \frac{1}{C_p} \sum_{i-1}^{N} \left(\frac{\Psi_i + \Delta\Psi_i}{\eta_i + \Delta\eta_i} \right) U_i^2 \tag{3.1}$$

$$PR' = \prod_{i=1}^{N} \left(\frac{(\Psi_i + \Delta\Psi_i) U_i^2}{C_p T_{t0} + \sum_{k-1}^{i} \left(\frac{\Psi_k + \Delta\Psi_k}{\eta_k + \Delta\eta_k} \right) U_k^2} + 1 \right)^{\frac{\gamma}{\gamma - 1}} \tag{3.2}$$

These equations show that if $\Delta T_t'$, PR' are known, it is not generally possible to determine $\Delta\eta_i$, $\Delta\Psi_i$ since we have $2N$ unknowns and two equations. If however $\Delta\Psi_i$, $\Delta\eta_i$ are not arbitrarily distributed along the compressor, then it may be possible to find a solution. For example, if $\Delta\Psi_i$, $\Delta\eta_i$ are the same for all the stages of the compressor, then the above two equations have two unknowns and the system can be solved for their determination. (This solution will have to be performed numerically in the general case.) If on the other hand the variation of $\Delta\Psi_i$, $\Delta\eta_i$ along the compressor can be described through a relation involving a number of M parameters, then we will have $2M$ unknowns. The only way to determine them is to formulate $2M$ equations. This can be achieved by applying Eq. (3) at M different operating points. Care should be taken in the selection of points so that the system of equations thus formulated can be solved. In general we can state that the corresponding equations will be independent. This results from the fact that, when the compressor operates at off-design conditions, the stage operating points will move differently on their Φ-Ψ characteristic, as shown qualitatively in Fig. 2. This means that the corresponding coefficients of the unknowns in Eq. (3) will be different and not multiples of the same values.

We now discuss what would be possible parametric formulations in order to cover realistic compressor fault cases.

2.2 Faults and Stage Characteristic Modifications Along the Compressor. Before examining the solution of the problem of defining stage deterioration parameters, it is useful to see how different kinds of stage characteristic modifications reflect on overall performance characteristics. The kind of modification we will consider will not be arbitrary but related to observations of faults published by other investigators.

The first fault case considered is that of compressor fouling. As discussed by Aker and Saravanamuttoo (1989) and Seddigh and Saravanamuttoo (1991), a realistic way to model fouling in a compressor is to assume a linear variation of stage performance drop at the front stages of the compressor, as indicated on Fig. 3(*a*). On the other hand, they introduced the idea that fouling is characterized by a certain proportion between stage parameter shifts.

When compressor blade erosion is considered, it is possible

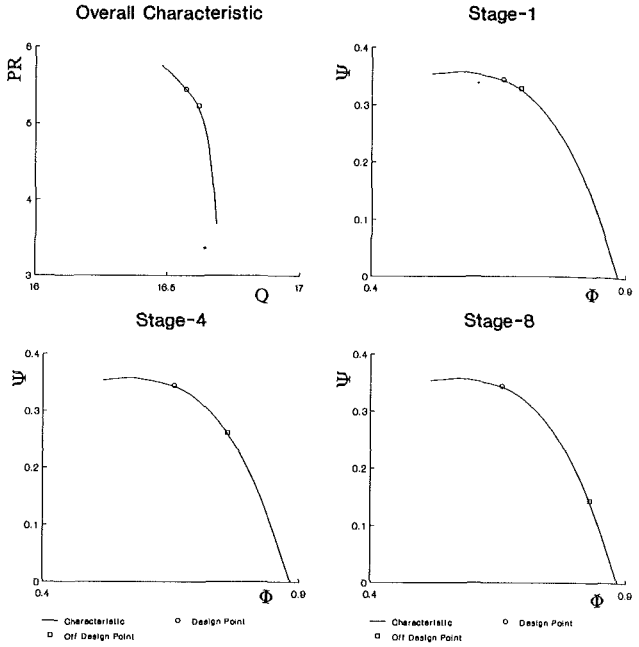


Fig. 2 Typical configuration of stage operating points for design and off-design conditions

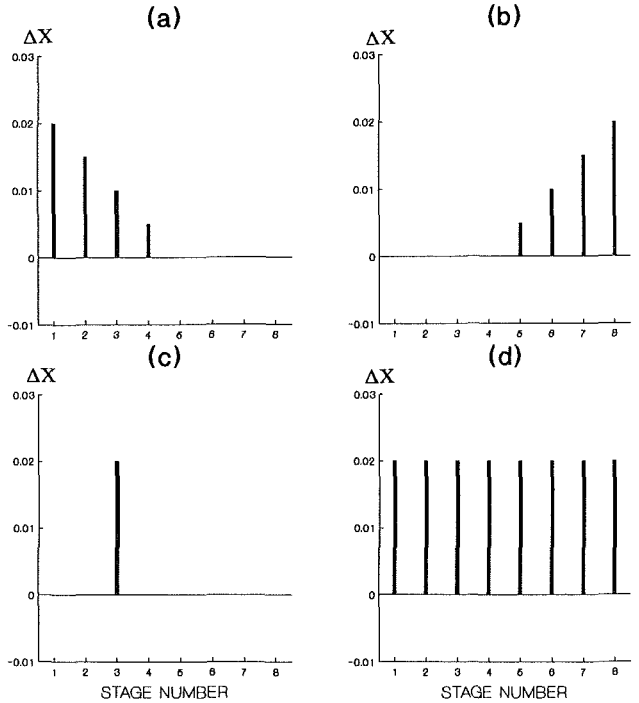
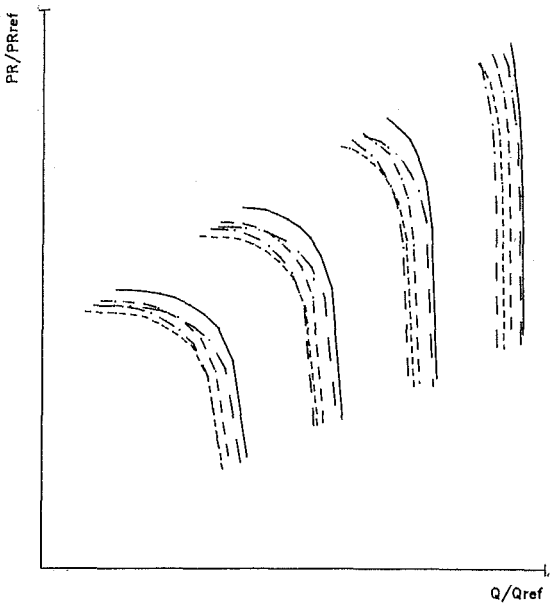


Fig. 3 Distribution of stage performance loss along the compressor for different fault cases

that the loss of performance in the stages can be more severe in the rear stages of the compressor, as for example the case reported by Batcho et al. (1987). For that case the distribution of deviations along the compressor will rather be of the form of Fig. 3(*b*).

Faults concentrated in just one or two of the compressor stages may also occur. Such is the case of a local increase of the tip clearance of one or two rotors, caused by blades rubbing into the casing at either end of the compressor shaft. Such a case has been reported by MacLeod et al. (1992), where in-

Downloaded 02 Jun 2010 to 171.66.16.122. Redistribution subject to ASME license or copyright; see http://www.asme.org/terms/Terms_Use.cfm



——Intact,------uniform degradation,— —stages 1-4 fouled,
— —stage-3 fault,– – – –stages 5-8 eroded

Fig. 4 Effect of different compressor faults on overall compressor map

creased tip clearance at the first two compressor stages has been studied. Similarly, damage caused by the injection of a foreign object can affect some stages more than others. Such cases are represented by Fig. 3(*c*).

Finally, we can have the case of a uniform distribution along the compressor, as for example when we are talking about general engine degradation. This case can be represented by Fig. 3(*d*).

2.3 The Effect of Stage Faults on Overall Performance. The occurrence of one or another modification of the characteristics of stages of a multistage compressor, discussed above, results in an alteration of the overall compressor map. It is useful to examine how each individual case will reflect on the overall compressor map. All the calculations reported in the paper have been performed on an eight-stage compressor, with a geometry similar to the compressor of the GE J-85 jet engine. Although we did not possess data for fault cases, we chose this compressor so that the characteristics and the performance quantities we are dealing with represent a realistic data set.

In order to obtain the overall map, the stage stacking technique is used. The modified characteristics of the stages of the multistage compressor are introduced as data into the program, which thus performs a fault simulation. The way of introducing stage characteristic modifications for this fault simulation is according to the fault modeling discussed in the next section. The resulting compressor maps are shown in Fig. 4. In the same figure the healthy compressor map has been plotted, in order to indicate the kind of deviations caused in each case.

Inspection of Fig. 4 reveals a property of the modified maps, which is very significant for fault identification: Different faults produce a different change of the map as a whole. This fact lays the basis for the materialization of the method we are proposing in this paper, since it establishes the general principle that different stage faults will produce different overall compressor maps. Even though one might optimistically think that the solution of the problem has already been reached, it should be noted here that the above observation still leaves unsolved two important practical problems:

1 How could one identify the kind and the extent of a particular stage fault without having to store a large number of modified complete compressor maps?

2 Is it possible to take that decision on the basis of particular, limited in number, operating point data? Obtaining an overall map from a compressor on a gas turbine in service is something that can almost surely be considered as impossible.

We will try to see how these problems can be faced by having in hand the adaptive stage stacking technique. The general ideas have already been explained in the previous section, where particular parameters were used in order to give a physical picture of the method. We proceed in describing the generalized mathematical model, which is the basis of the computational algorithm implementing the method. This generalization is given here because the resulting formulation can be employed for any set of suitable performance parameters.

3 Adaptive Stage Stacking and Fault Identification Algorithm

The two characteristic curves of each stage interrelate the three parameters Φ, Ψ, η (or ζ) so that only one of them is independent. Defining the vector $\mathbf{v}_i$ as the vector of the dependent parameters, the characteristics can be represented by a relation

$$\mathbf{x}_i = \mathbf{x}_i(V_i), \quad i = 1, N \tag{4}$$

where y_i is the independent parameter. For example if we consider the usual form of representing stages by their Φ-Ψ, Φ-η characteristic, then

$$\begin{aligned} x_i &= [\Psi_i, \eta_i] \\ \mathbf{v}_i &= \Phi_i, \quad i = 1, N \end{aligned} \tag{5}$$

Let us consider a vector $\mathbf{u}$ as the vector that contains two independent parameters defining the operating point of the compressor (for example $\mathbf{u} = [\dot{m}, \text{rpm}]$ for a given compressor and inlet conditions). Let's also consider the vectors $\mathbf{g}_i$ containing the data relevant to the geometry of each stage. It has been stated in paragraph 2.1, that the knowledge of stage's characteristics, i.e., relation (4) along with stage geometry $\mathbf{g}_i$ leads to the calculation of the overall compressor performance parameters, as a function of the independent parameters vector $\mathbf{u}$. Including the calculated parameter in a vector $\mathbf{y}$ we may describe the whole procedure by the relation

$$\mathbf{y} = \mathbf{y}(\mathbf{x}_i(V_i); \mathbf{g}_i; \mathbf{u}), \quad i = 1, N \tag{6}$$

It can be seen that the procedure (6) is general enough to allow interchanging of the parameters defining the vectors $\mathbf{u}$ and $\mathbf{y}$. This is crucial in case one is interested in defining the operating point by the speed and pressure ratio instead of speed and mass flow, in particular in the region of the design point where the speed lines of the overall map seem to be vertical to the mass flow axis.

Returning again to Eq. (5) we can express the stage characteristics modification by the relation

$$x(V_i) = x_{i,\text{ref}}(V_i) + \Delta\mathbf{x}(V_i) \tag{7}$$

Clearly, when the stage remains healthy $\Delta x(v_i) = 0$. The relation (6) by taking into account Eq. (7) yields

$$y = y(\Delta\mathbf{x}(v); \mathbf{x}_{i,\text{ref}}(v_i), g_i, u) \tag{8}$$

Thus for given intact stage characteristics $\mathbf{x}_{i,\text{ref}}(v_i)$, $\mathbf{g}_i$ we may write

$$y = y(\Delta\mathbf{x}(v_i); u) \tag{9}$$

The above equation models the direct problem and is the generalization of Eq. (3).

The adaptive stage stacking procedure consists of calculating $\Delta x_i(V_i)$'s from Eq. (9) when overall compressor data $\mathbf{y}$, $\mathbf{u}$ are given. An obvious remark is that the amount of information needed is a function of the number of different v_i, which are

Downloaded 02 Jun 2010 to 171.66.16.122. Redistribution subject to ASME license or copyright; see http://www.asme.org/terms/Terms_Use.cfm

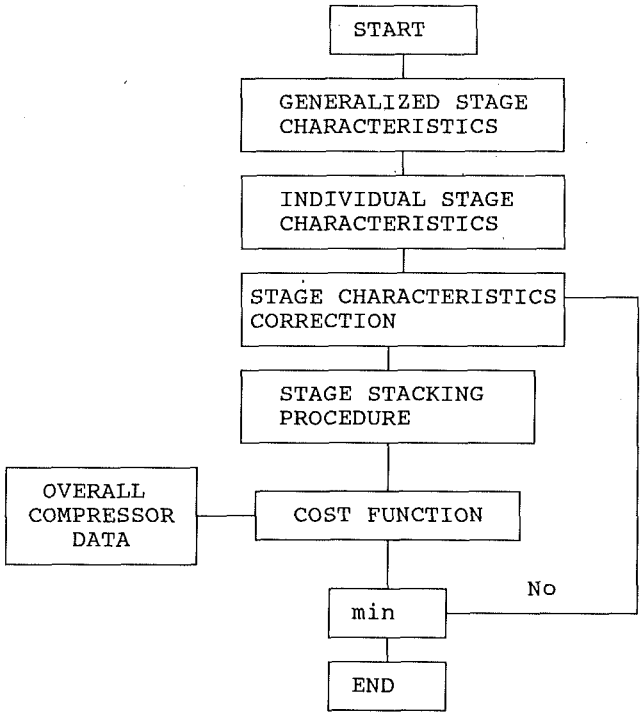


Fig. 5 Flow-chart of the adaptive stage stacking

necessary to represent the stage characteristics curves with the desired accuracy. So Eq. (9) must be considered in different operating points u_k:

$$y_1 = y(\Delta \mathbf{x}_i(v_i);\quad u_1)$$
$$\vdots \tag{10}$$
$$y_M = y(\Delta \mathbf{x}_i(v_i);\quad u_M)$$

The system (10) has no analytical solution for Δx's so the adaptive stage stacking procedure has been formulated in the following way. We formulate a *cost function* of the form

$$F = \sum_{k=1}^{M} [y(\Delta \mathbf{x}_i(v_i);\quad u_k) - y_{kg}]^T\, [y(\Delta \mathbf{x}_i(v_i),\, u_k) - y_{kg}] \tag{11}$$

where $\mathbf{y_{kg}}$ are the known values of performance parameters.

It can be seen that this function is nonnegative and its minimization leads to the solution of the system (10). This is achieved by employing a minimization method as shown in the flow chart of the procedure in Fig. 5. Δx_i are the independent variables. The minimization is performed by a numerical search algorithm in the space of the deviations Δx_i.

Practical limitations concerning the information of the overall performance, as has been already discussed in paragraph 2.3, restrict the applicability of the general case. In this general case we would have Δx_i's as many as the stages times the number of independent parameters needed to represent the stage characteristic curves. So in order to close the problem for practical reasons, some smaller classes of the general solutions have to be considered. Typical fault situations, as already has been mentioned, belong to these classes. For example, the faults considered in paragraph 2.2 can be modeled, according to the observations discussed there, as follows:

(*a*) *General degradation* (*uniform distribution along the compressor*)

$$\Delta \mathbf{x}_i(V_i) = a, \quad i = 1, N$$

(*b*) *Faulty stage j*

$$\Delta \mathbf{x}_i(V_i) = 0, \; i \neq j \quad i = 1, N$$
$$= a, \; i = j$$

(*c*) *Fouling or erosion* (*linear deterioration between stages j, k*)

$$\Delta \mathbf{x}_i(v_i) = 0, \quad i < j \text{ or } i > k$$
$$= ai + b, \quad j \le i \le k$$

where a, b, are constants. Each of the above cases leads to a minimization problem in the subdomain defined by the corresponding fault model equation.

The choice of a minimization algorithm is guided by the fact that it should be able to treat nonanalytical functions (for example $x_{i,\text{ref}}(v_i)$ are given as table look up functions), and even not smooth ones (fault models). The algorithm has been chosen to be the method of the polytope (Press et al., 1986). This method has no need of derivatives calculation and also follows the possibility to incorporate error terms in order to ensure physical meaning of the solution.

(*d*) *Unified Fault model.* The previous fault models considered should give the solution to the problem of the fault magnitude, when the location of the fault is assumed known (stage number j for the case (*b*) and j, k for the case (*c*). Although this seems to be useful, it is an obvious requirement to consider the case where both the location and even the kind of fault are not assumed a priori known. These requirements are taken into account by considering a more general model. In fact this model results when considering the model of case *c* with j, k free to take discrete values.

$$\Delta \mathbf{x}_i(v_i) = ai + b, \quad j \le i \le k,$$
$$= 0, \qquad i < k \vee i > k$$
$$1 \le j \le k \le N$$

Clearly from this model we may have all previous cases (e.g., we have case (*a*) when $j = 1$, $k = N$, $a = 0$). So the general compressor fault identification algorithm solves sequentially a limited number of minimization problems and chooses as the final solution the combination of j, k, a, b that gives the lowest minimum.

The above formulation is quite general, covering not only fault identification but also reproduction of compressor stage characteristics from overall performance data. In that case $\Delta x_i(v_i)$ expresses the inaccuracy of the initially considered curves $x_{i,\text{ref}}(v_i)$ rather than modifications due to implanted faults. It can be assumed that the nondimensional characteristic curves are the same for all the stages of the compressor, when expressed in the form of scaled parameters Φ/Φ_{ref}, Ψ/Ψ_{ref}, η/η_{ref}. This assumption has been utilized by Aker and Saravanamuttoo (1989) and Muir et al. (1989), and it was found to represent quite accurately the performance of the compressor. The minimization problem is then looking for the values of Φ_{ref}, Ψ_{ref}, η_{ref} of each stage, which make the cost function minimum.

4 Test Cases of Fault Identification

We will now describe how various faults can be identified from overall data. The data used as an input to the procedure come from direct fault simulations, the ones presented in Fig. 4. They are taken from particular operating points from these maps. For each operating point compressor speed, mass flow rate, pressure ratio, and efficiency are the input data to the procedure.

(i) Overall Compressor Degradation. If all the stages of a compressor have degraded in the same way, then the overall performance data, at one operating point at least, will provide the deterioration of each individual stage, in terms of its $\Delta\Psi$, $\Delta\eta$. What we want to show here is that using data coming from a compressor at a particular condition leads to a unique solution for $\Delta\Psi$, $\Delta\eta$. This can be demonstrated by inspecting the

Downloaded 02 Jun 2010 to 171.66.16.122. Redistribution subject to ASME license or copyright; see http://www.asme.org/terms/Terms_Use.cfm

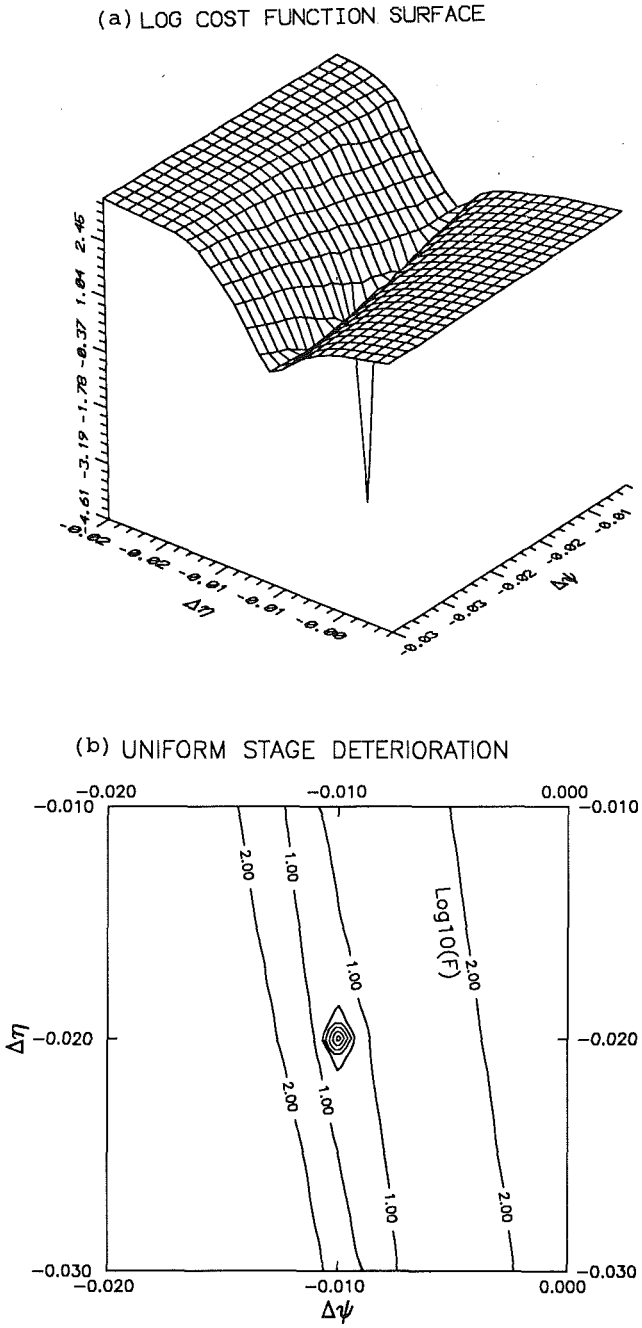


Fig. 6 Cost function variation for the case of uniform degradation: (*a*) values, (*b*) isocontours

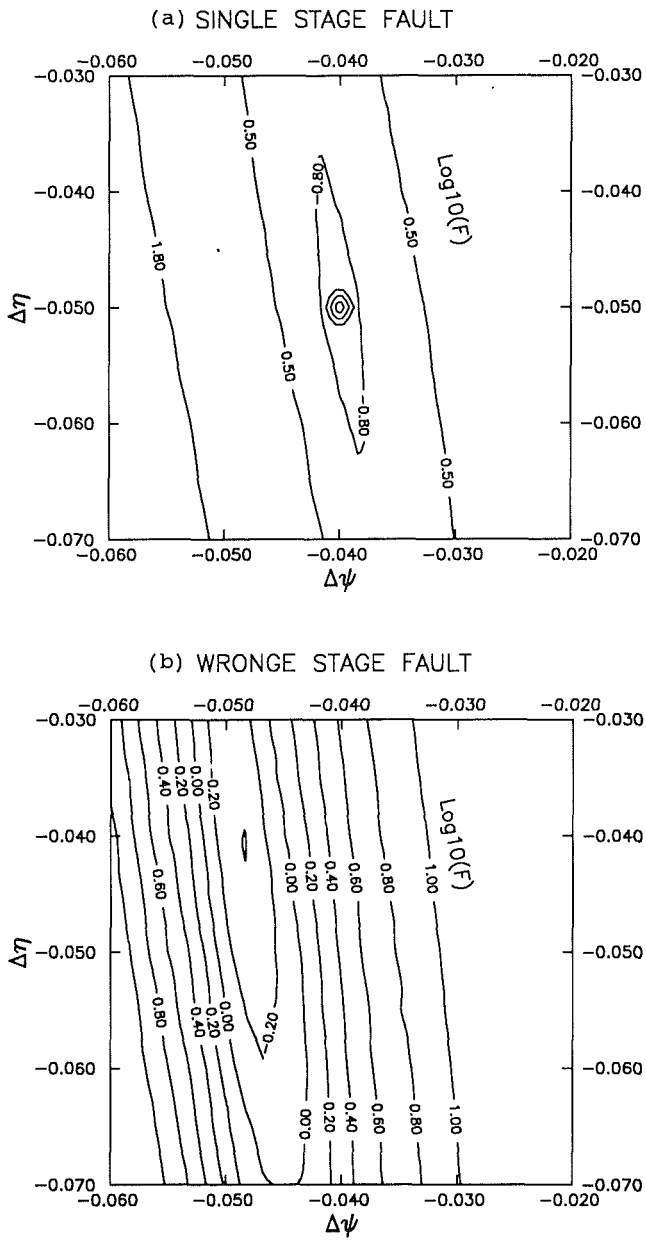


Fig. 7 Cost function isocontours assuming: (*a*) faulty stage three, (*b*) faulty stage four

cost function values in Fig. 6(*a*). This figure shows that the cost function has a unique minimum for a certain combination of $\Delta\Psi$, $\Delta\eta$. The location of the minimum can be visualized better by inspecting the cost function isocontours on the $\Delta\Psi$, $\Delta\eta$ plane, Fig. 6(*b*). The error function has been evaluated at one operating point of a compressor whose stages have undergone uniformly a drop in pressure rise by 2 percent and a drop in efficiency by 3 percent. The isocontours show that the function has a unique overall minimum at the point $(-0.02, -0.03)$ of the $(\Delta\Psi, \Delta\eta)$ plane. This means that the solution is the correct one. In practical terms, this means that introduction of a set of particular overall data will lead to the kind of stage deterioration. It must be pointed out here that the ratio $\Delta\Psi$, $\Delta\eta$ will be different if we are talking about fouling or tip clearance degradation.

(ii) Single-Stage Faults. Let us now consider the case in which only one stage of a multistage compressor has suffered a problem. The overall data come from a case of a fault in stage 3, which caused a variation $\Delta\Psi = -0.04$, $\Delta\eta = -0.05$ to that stage.

In order to identify this fault, the search algorithm is considering that every single stage can be the faulty one. Every time a stage is considered, the combination of $\Delta\Psi$, $\Delta\eta$ giving the minimum error function is determined. The faulty stage is identified as the one that gives the lowest minimum.

For the particular test case examined, we show first that a unique combination of $\Delta\Psi$, $\Delta\eta$ exists for each stage, giving a minimum error function, namely a best fit to the overall compressor data provided. This is actually happening and a particular example is shown through the error function isocontours shown in Fig. 7. It can be seen that a minimum value exists both when the actual faulty stage is considered and when another stage, a healthy one, is considered. The minimum is much

Downloaded 02 Jun 2010 to 171.66.16.122. Redistribution subject to ASME license or copyright; see http://www.asme.org/terms/Terms_Use.cfm

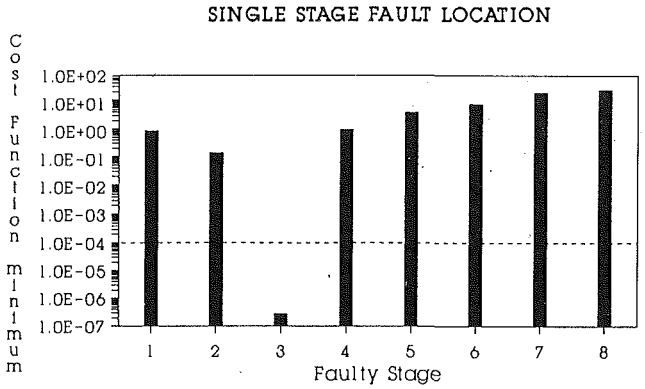


Fig. 8 Cost function minimum versus single faulty stage location

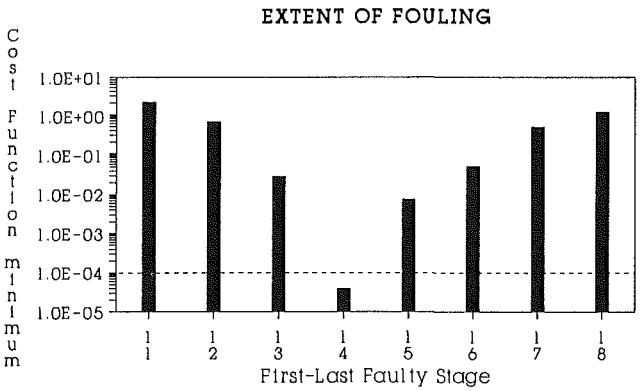


Fig. 9 Cost function minimum versus extent of fouling

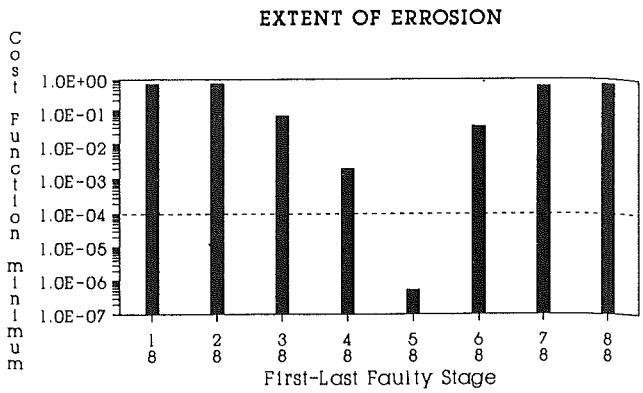


Fig. 10 Cost function minimum versus extent of erosion

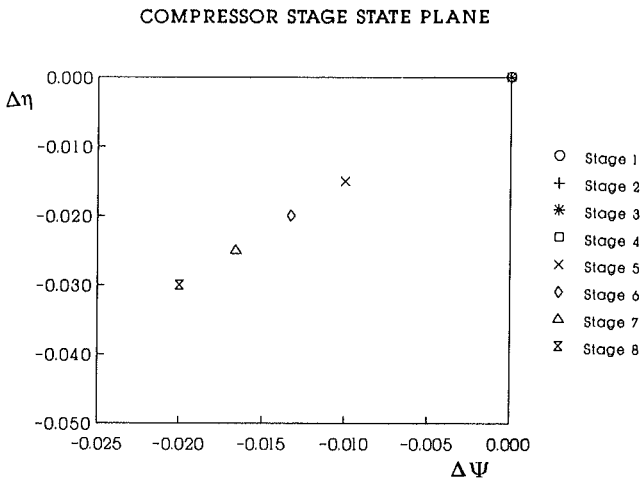


Fig. 11 Stage performance loss plane for condition assessment; the case of erosion

smaller, however, for the actual faulty stage. The minima for every stage are shown in Fig. 8. We see that the correct faulty stage exhibits the lowest minimum. This proves that the criteria set work successfully for identifying individual faulty stages.

(iii) Compressor Fouling. When this fouling model is assumed, the solution of the inverse problem consists in determining the performance drop ($\Delta\Psi$, $\Delta\eta$) of the first stage and the location of the last fouled stage (the drop of performance of the intermediate stages resulting from the linear distribution). The search in this case considers all possible fouling scenarios of the compressor, namely only stage 1 fouled, stages 1–2 fouled, etc. The minimum of the error function is determined in each case and the most probable solution is identified as the one providing the lowest minimum.

A calculation example is shown in Fig. 9, where the results of calculation with data from a compressor with fouled stages 1–4 are presented. It is shown that the combination 1–4 fouled stages gives the lowest minimum.

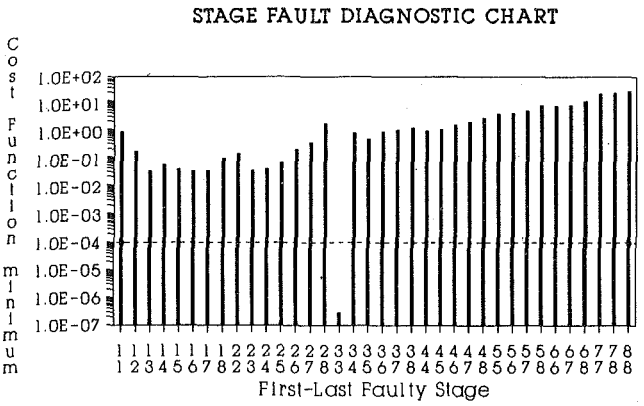
(iv) Compressor Erosion. When this model is assumed, the solution of the inverse problem consists in determining the performance drop ($\Delta\Psi$, $\Delta\eta$) of the last stage and the location of the first eroded stage (performance of the intermediate stages resulting from the linear distribution). The search in this case considers all possible erosion scenarios of the compressor, namely only stage 8 eroded, stages 7–8 eroded, etc., similar to the case of fouling. A calculation example is shown in Fig. 10. The overall data come from a compressor eroded all the way from the fifth to the last stage. It is shown that the combination 5 to 8 eroded stages is giving the lowest minimum. An additional insight to the kind of fault is provided to the operator by presenting the operating point shifts for all stages on the $\Delta\Psi$–$\Delta\eta$ plane, shown in Fig. 11.

(v) The General Problem of Stage Fault Identification. The cases examined above have as a common feature that one should be looking for a particular problem to be identified. That is, one should know in advance what the problem is. This is a realistic situation in certain particular cases. For example, fouling is a routine problem in gas turbine operation: If the user has enough experience to know that fouling is what he is concerned about, he will look for an optimum washing schedule (see, for example, Diakunchak, 1992). In this case the solution to this problem is directly obtainable from the results of the previous paragraph. This solution actually offers a means for checking whether fouling is the problem or something else has also happened. This can be checked by examining whether the ratio $\Delta\Psi/\Delta\eta$ is kept close to values denoting fouling or not.

The general problem of fault detection should be as follows: We possess data from a faulty compressor, without knowing what kind of fault we are faced with or where it is located. We want to know which stage or stages have suffered an alteration and what alteration it is. This problem can be faced by the present method by considering all possible combinations of faulty stages. In Fig. 12 the function minima for cases (*ii*) and (*iii*) above are shown in such a search. It can be seen that the solution is correctly identified in both cases.

Finally the adaptation of stage characteristics to match an overall performance is considered. In this case the generalized characteristic is assumed the same for all stages and adaptation is performed by searching the design point values for the compressor stage characteristics. A comparison of predicted map

Downloaded 02 Jun 2010 to 171.66.16.122. Redistribution subject to ASME license or copyright; see http://www.asme.org/terms/Terms_Use.cfm



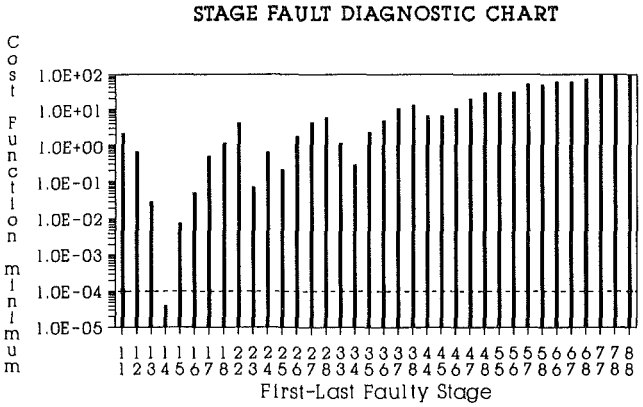


Fig. 12 *Identification of faulty stages without pre-assuming a particular fault type: (a) case of single stage fault; (b) 50 percent compressor fouling*

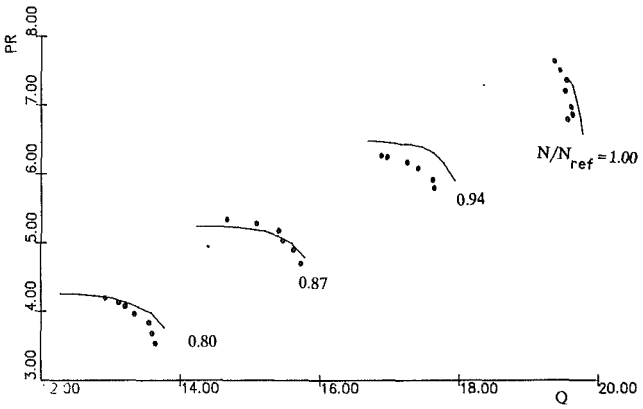


Fig. 13 **Comparison of measured performance map and map derived through adaptive stage stacking**

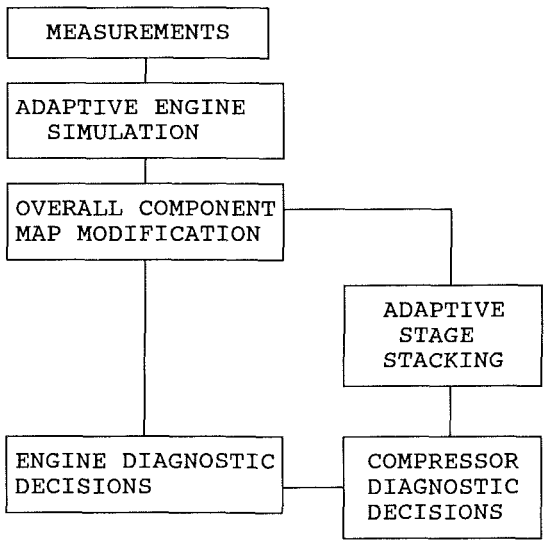


Fig. 14 **Flowchart of gas turbine monitoring incorporating adaptive stage stacking**

to measurements for the J85 compressor (obtained by Wenzel et al., 1975) is shown in Fig. 13. The capability of reproduction of the overall map is demonstrated.

5 Discussion

The method presented in the previous sections is an original powerful tool for identification of faults in compressor stages. It offers a possibility of identifying such faults by means of a computerized procedure and in this respect, it offers a fast and reliable alternative to direct methods (e.g., Aker and Saravanamuttoo, 1989; Seddigh and Saravanamuttoo, 1991; Tabakoff et al., 1990). The advantage over these methods is that: (*a*) it doesn't need assumptions about how many stages are affected by a fault and how they are affected; (*b*) it doesn't need trial and error to be performed by the operator, since this procedure is imbedded in the optimization algorithm. In any case, it has been shown that if a particular fault model is assumed, this results in an improved reliability for detection.

When a practical implementation of the method is considered, it must be taken into account that the measured data have some associated uncertainty. It should be examined then how this uncertainty will influence the final result, as to the uniqueness of the obtained solution. In this respect, the values of the cost function calculated for the different combinations will be useful as probability indicators, in interpreting the results. A threshold value for the cost function minimum will have to be chosen according to the expected uncertainties. In the results we presented above, Figs. 8, 9, 10, and 12, where the input data have been produced by simulation, such a threshold was arbitrarily chosen to the value 10^{-4}.

Concerning the procedure itself, there are several factors that influence the quality of the obtained results. Such factors are the number of operating points where data are taken, which operating points are more suitable (speeds, position with respect to operating limits), which parameters are more suitable. For example when data from a vertical speedline are used, it would be preferable to use the mass flow rate rather than the pressure ratio as matching variable. From this point of view, before the method is applied a knowledge of the form of the overall compressor map is necessary.

The results presented in the previous sections have been obtained by using the compressor efficiency and the pressure ratio as overall matching variables. For the individual stages, changes in Ψ and η are examined and are assumed to be caused in an additive manner. It must be pointed out that this is not a restrictive choice, since the formulation is general enough to allow choosing any combinations of variables of either the compressor or the stages, while changes can be applied in an additive or multiplicative manner.

The method also possesses features that make it suitable for implementation in current day monitoring systems, which are oriented to the use of expert systems (Doel, 1990). This can be seen from the fact that the results are produced as numerical values, which can easily be handled by computers, while elements that can help the decision procedure (e.g., probability indicators) are also derived. The method can also be easily integrated into existing monitoring systems. Such systems usually produce information about overall compressor condition,

Downloaded 02 Jun 2010 to 171.66.16.122. Redistribution subject to ASME license or copyright; see http://www.asme.org/terms/Terms_Use.cfm

namely input data to this method. The method can then be added as a separate module, which provides additional insight in the compressor faults. The flow chart of the integration into a monitoring system is shown in Fig. 14.

Finally, from a computational point of view, the codes have been developed in a P. C. environment. Although memory requirements are fulfilled in such an environment, computation times are still high. The authors are currently working toward reducing these times, by examining faster algorithms for the various stages of the method.

Although we have produced a set of results that proves the applicability of the methods and demonstrates its way of implementation, questions posed in this section are still to be answered. The research group of the authors is currently carrying out work in this direction.

6 Conclusions

A method of identifying faulty compressor stages from overall performance data has been presented. The method was formulated by taking into account existing observations of the way stage performances are affected by the presence of various compressor faults.

The method gives which stages have been affected and how their performance has been altered, when a fault is present. Several cases of faults were considered and the successful detection of each case was demonstrated. On the other hand, the possibility of identifying the intact compressor stage characteristics was demonstrated.

Implementation of the method in condition monitoring systems was discussed, while areas of further development were identified.

References

Aker, G. F., and Saravanamuttoo, H. I. H., 1989, "Predicting Gas Turbine Performance Degradation Due to Compressor Fouling Using Computer Simulation Techniques," ASME JOURNAL OF ENGINEERING FOR GAS TURBINES AND POWER, Vol. 111, pp. 343-350.

Batcho, R. F., Moller, J. C., Padova, C., and Dunn, M. G., 1987, "Interpretation of Gas Turbine Response Due to Dust Ingestion," ASME JOURNAL OF ENGINEERING FOR GAS TURBINES AND POWER, Vol. 109, pp. 344-351.

Diakunchak, I. S., 1992, "Performance Deterioration in Industrial Gas Turbines," ASME JOURNAL OF ENGINEERING FOR GAS TURBINES AND POWER, Vol. 114, pp. 161-168.

Doel, D., 1990, "The Role of Expert Systems in Commercial Gas Turbine Engine Monitoring," ASME Paper No. 90-GT-374.

MacLeod, J. D., Taylor, V., and Laflamme, J. C., 1992, "Implanted Component Faults and Their Effects on Gas Turbine Engine Performance," ASME JOURNAL OF ENGINEERING FOR GAS TURBINES AND POWER, Vol. 114, pp. 174-179.

Massardo, A., 1991, "An Analytical Method for the Fault Diagnosis of Axial Multistage Compressors," ASME Paper No. 91-GT-66.

Muir, D. E., Saravanamuttoo, H. I. H., and Marshall, D. J., 1989, "Health Monitoring of Variable Geometry Gas Turbines for the Canadian Navy," ASME JOURNAL OF ENGINEERING FOR GAS TURBINES AND POWER, Vol. 111, pp. 244-250.

Press, W. H., Flannery, B. P., Teukolsky, S. A., and Vetterling, W., 1986, *Numerical Recipes*, Cambridge University Press, United Kingdom.

Robbins, W. H., and Dugan, J. F., 1965, "Prediction of Off Design Performance of Multistage Compressors," in: NASA SP 36, I. H. Jonsen and R. O. Bullock, eds.

Seddigh, F., and Saravanamuttoo, H. I. H., 1991, "A Proposed Method for Assessing the Susceptibility of Axial Compressors to Fouling," ASME JOURNAL OF ENGINEERING FOR GAS TURBINES AND POWER, Vol. 113, pp. 595-601.

Stamatis, A., Mathioudakis, K., and Papailiou, K. D., 1989, "Adaptive Simulation of Gas Turbine Performance," ASME JOURNAL OF ENGINEERING FOR GAS TURBINES AND POWER, Vol. 112, pp. 168-175.

Tabakoff, W., Lakshminarasimha, A. N., and Pasin, M., 1990, "Simulation of Compressor Performance Deterioration Due to Erosion," ASME *Journal of Turbomachinery*, Vol. 112, pp. 78-83.

Wenzel, L. M., Moss, J. E., and Mehalic, C. M., 1975, "Effect of Casing Treatment on the Performance of a Multistage Compressor," NASA TM X-3175, Jan. 1975.

Downloaded 02 Jun 2010 to 171.66.16.122. Redistribution subject to ASME license or copyright; see http://www.asme.org/terms/Terms_Use.cfm

Optimizing Automated Gas Turbine Fault Detection Using Statistical Pattern Recognition

E. Loukis

K. Mathioudakis

K. Papailiou

Laboratory of Thermal Turbomachines,
National Technical University of Athens,
Athens, Greece

A method enabling the automated diagnosis of gas turbine compressor blade faults, based on the principles of statistical pattern recognition, is initially presented. The decision making is based on the derivation of spectral patterns from dynamic measurement data and then the calculation of discriminants with respect to reference spectral patterns of the faults while it takes into account their statistical properties. A method of optimizing the selection of discriminants using dynamic measurement data is also presented. A few scalar discriminants are derived, in such a way that the maximum available discrimination potential is exploited. In this way the success rate of automated decision making is further improved, while the need for intuitive discriminant selection is eliminated. The effectiveness of the proposed methods is demonstrated by application to data coming from an industrial gas turbine while extension to other aspects of fault diagnosis is discussed.

1 Introduction

Gas turbine engine condition monitoring and fault diagnosis methods have found a wide use among gas turbine users recently. At the same time their philosophy and basic features have undergone a significant change. It is recognized today that such methods no longer rely on simple observations of directly measured quantities. They have become more sophisticated and incorporate processing of some level in order to provide information of direct significance about component conditions or faults. Also economical and practical reasons led to the requirement of as little as possible empirical background from the engine user. There is a tendency to minimize the required skills of the engine operator and to have computer procedures that perform most of the "skilled" work, in order to provide the user with information that needs minimal or no interpretation, and even with hints about required action (Doel, 1990). Expert system environments, available today even for personal computers, contribute to this direction, allowing the integration of data processing and decision making.

Another practical problem recognized by engine users, in the effort to perform efficient monitoring and fault diagnosis, is associated with the restrictions in instrumenting an engine. Installing and employing a large number of measuring instruments is not only difficult and costly but also requires special care in maintaining them and avoiding false alarms. From this point of view, it is desirable to use a minimal set of instruments, with maximum fault detection capabilities. The methodologies introduced in the present paper cover needs related to the above-mentioned desired features and requirements, at the same time being suitable for computerized fault detection.

Contributed by the International Gas Turbine Institute and presented at the 37th International Gas Turbine and Aeroengine Congress and Exposition, Cologne, Germany, June 1-4, 1992. Manuscript received by the International Gas Turbine Institute January 28, 1992. Paper No. 92-GT-29. Associate Technical Editor: L. S. Langston.

It has been established today that dynamic measurements allow the identification of minor gas turbine blade faults, which would remain hidden to performance monitoring techniques. Revealing blade faults, although they may not significantly disturb overall performance, becomes important since it can prevent the sudden occurrence of catastrophic failures (a typical example being the loss of a damaged rotating blade). Loukis et al. (1991) have examined a variety of possible dynamic measurements and discussed their suitability for the detection of blade faults. On the other hand, a set of data from implanted faults on an industrial gas turbine has served as a basis for a first development of automated fault detection methods by Loukis et al. (1992).

The work presented in this paper is based on the observations and the conclusions reached in the above-mentioned works of the authors. The purpose is to derive a methodology that gives the possibility to overcome practical problems encountered in the application of fault diagnosis methods and to provide tools that allow extension of the findings from the particular set of experimental information to other situations as well. In order to achieve these targets, principles that have already been used in other technological domains are for the first time applied to data from faults in an industrial gas turbine and are adapted to particular features of such data. In particular, principles of pattern recognition that have been applied in various other domains, as for example monitoring of machine tools (Emel and Kannatey-Asihm, 1988), are employed.

2 Prior Experience in Gas Turbine Fault Identification Using Measured Patterns

The possibility of establishing fault signatures from dynamic measurement data has been demonstrated by Mathioudakis et al. (1990), from tests performed on an industrial gas turbine

Copyright © 1994 by ASME
Downloaded 02 Jun 2010 to 171.66.16.122. Redistribution subject to ASME license or copyright; see http://www.asme.org/terms/Terms_Use.cfm

and further discussed by Loukis et al. (1991, 1992). The test program included the study of various representative compressor blade faults by performing dynamic measurements with different measuring instruments. For reasons of completeness the description of the experiments is repeated here, in Appendix I. A first procedure for automated identification of faults, based on this data set, has already been described by Loukis et al. (1992). Before describing the present procedure it is useful to summarize the main points of that work. The procedure consists of two phases, the learning phase and the decision phase.

The *learning* phase includes all actions necessary to establish the background for fault identification. For each instrument the following steps are implemented:

(*a*) Measurements are performed on an engine in healthy condition as well as containing the faults of interest.

(*b*) The data sets for each fault are processed and fault indices are calculated from them by appropriate combination with data from healthy condition. Each fault index has the form of a vector $\mathbf{P}=(P_1, P_2, \ldots, P_N)$, whose components come from algebraic combinations of spectra from healthy and faulty engine at shaft rotational frequency harmonics. This vector is termed a reduced spectral difference pattern (or simply pattern).

(*c*) For each fault, a reference pattern is established using the patterns from all the data sets coming from experiments with this particular fault. The reference pattern constitutes a signature of the fault.

The *decision* phase includes all actions necessary for identifying an engine fault. The steps are:

(*a*) A data set is acquired from measurements on the engine, which has to be examined.

(*b*) A pattern is calculated, by appropriate processing of this data set and the corresponding data of healthy condition.

(*c*) The values of a discriminant are calculated for this pattern, with respect to available reference patterns of the faults, established during the learning phase.

(*d*) The diagnostic decision is made by algebraically comparing these discriminant values and classifying to the fault corresponding to the minimum distance.

An example of reference fault patterns derived and used as signatures in this procedure is shown in Fig. 1, where patterns for different instruments used and faults examined during the experimental investigation are shown.

This kind of procedure can be characterized as a "geometric" one, since the diagnostic decision is based on a minimum distance criterion from the reference patterns of the faults. The feasibility of applying this procedure has been demonstrated to be effective, with a certain degree of success for each individual instrument used as source of information.

There are, however, certain disadvantages of such a procedure for practical application in industrial environments:

(*a*) The statistical properties of the data used for establishing the signatures are not taken into account.

(*b*) The parameters used as discriminants are derived intuitively. This does not provide the possibility of improving the effectiveness of the method, unless the user has a better insight in choosing them.

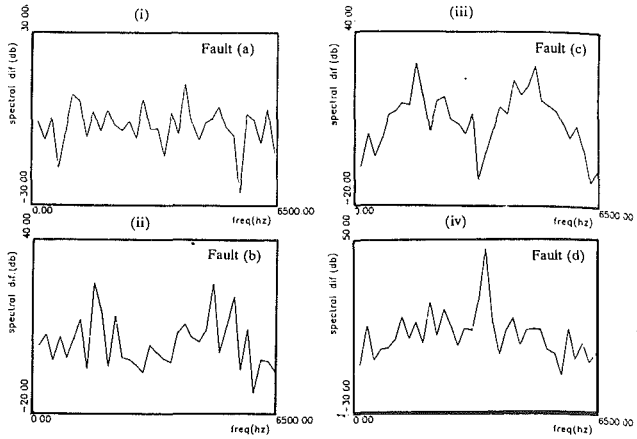


Fig. 1 Fault signatures derived from various dynamic measurements and faults: (*i*) accelerometer A5, (*ii*), (*iii*) pressure transducer PT2, (*iv*) microphone

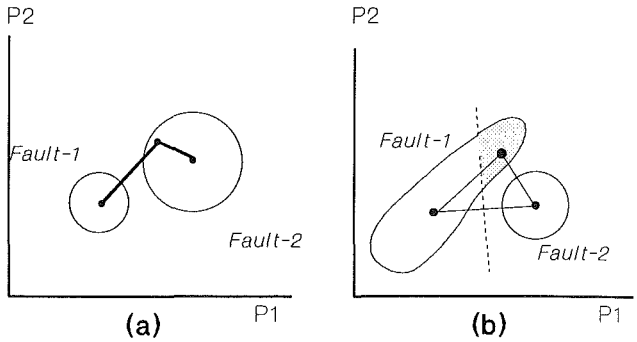


Fig. 2 Qualitative picture for effectiveness of geometric and statistical approaches: (*a*) both approaches succeed; (*b*) geometric procedure fails

(*c*) The conclusion is in a form such that it does not provide the possibility of assigning to it a level of confidence.

(*d*) Use of different discriminants does not lead always to the same conclusion for the kind of fault.

These drawbacks have the practical implication that in some cases false decisions can be made and there are no means of comparing the relative similarities of the examined case to the faults. This can be understood from the situations shown for the simplified case of two-dimensional patterns ($N=2$) in Fig. 2. In case (*a*) the regions occupied by points corresponding to patterns of each fault, in the two components P_1 and P_2 plane, are of such a shape and position, that using a geometric procedure leads for all points to a correct decision. In case (*b*), however, the regions are of such a shape and position, that some points of fault 2 can be assigned to fault 1 by a geometric procedure. Such points are for example the ones contained in the shaded region of the figure. In order to handle such situations successfully, a statistical approach to making the classification decision is required.

Nomenclature

C_i = covariance matrix for fault i, Eq. (5)

D_i = ith optimal linear discriminant

$D_{i,k}$ = discriminant i, calculated with respect to the reduced reference spectral difference pattern of fault k

N_i = the number of independent data sets available for fault i

N = number of components of reduced spectral difference patterns

M = number of faults

pr = conditional probability

$\mathbf{P}_i$ = reference spectral difference pattern for fault i

$\mathbf{X}$ = discriminant vector, Eq. (1)

$\mathbf{X}_{ij}$ = discriminant vector calculated from the jth data set of fault i

Downloaded 02 Jun 2010 to 171.66.16.122. Redistribution subject to ASME license or copyright; see http://www.asme.org/terms/Terms_Use.cfm

3 A Statistical Procedure for Fault Pattern Classification

The main feature of this procedure is that it is based not on a single discriminant calculated with respect to the available fault signatures, but on a vector $\mathbf{X}$, which has as components a number of discriminants with respect to available signatures:

$$\mathbf{X} = [D_{1.1}, D_{2.1}, \ldots, D_{K.1}, \ldots, D_{1.M}, D_{2.M}, \ldots, D_{K.M}] \tag{1}$$

where D_{ij} is the ith discriminant calculated with respect to the signature of the jth fault, for a particular data set. This vector has $K \times M$ components when K discriminants are used for M faults.

For the classification, known principles of statistical pattern recognition (e.g., Sing-Tze Bow, 1984) are employed. The procedure consists in evaluating the M conditional probabilities of having the particular vector $\mathbf{X}$, which is calculated using the data set acquired from the examined engine, if each of the faults exists. The decision is made classifying the vector to the fault that corresponds to the maximum probability, while the rest of the faults are ranked according to their relative probabilities:

$$\mathbf{x} \epsilon \text{fault-}i \text{ IF:}$$

$$pr(\mathbf{X}/\text{fault } i) = \sum_{j=1}^{M} [pr(\mathbf{X}/\text{fault } j)] \tag{2}$$

We can see that for the implementation of a statistical procedure the possibility of calculating the conditional probability functions of having a given vector $\mathbf{X}$ pr ($\mathbf{X}$/fault i) $i = 1,2. \ldots, M$, for each of the faults is required. In order to obtain this possibility, a learning phase has to be carried out. During this phase, using a number of data sets for each of the faults, the corresponding vectors $\mathbf{X}$ are derived. From these, it is selected which kind of statistical distribution function is the most appropriate for statistically modeling them and then its parameters are calculated. In our case a multidimensional normal distribution has been selected. Therefore the probability of having a given vector $\mathbf{X}$ when fault i is present is expressed by an equation of the form:

$$pr(\mathbf{X}/\text{fault } i) = \frac{1}{(2\pi)^{n/2} \|\mathbf{C}_i\|^{1/2}} e^{-(\mathbf{X}-\underline{\mathbf{X}}_i)\cdot C_i^{-1} \cdot (\mathbf{X}-\underline{\mathbf{X}}_i)^T} \tag{3}$$

where $\underline{\mathbf{X}}_i$ and C_i, $i = 1, 2, \ldots M$ are the average vector and the covariance matrix for each of the faults.

During the learning phase the average vectors $\underline{\mathbf{X}}_i$, $i = 1, 2, \ldots M$ are established for each fault by arithmetic averaging:

$$\underline{\mathbf{X}}_i = \frac{1}{N_i} \sum_{j=1}^{N_i} \mathbf{X}_{ij} \tag{4}$$

where $\mathbf{X}_{ij}$ is the vector calculated from the jth data set of the ith fault and N_i are the numbers of the independent data sets, which are available for the ith fault. Also the covariance matrices $\mathbf{C}_i$, for each fault, are evaluated through the equation:

$$\mathbf{C}_i = \frac{1}{N_i - 1} \sum_{j=1}^{N_i} (\mathbf{X}_{ij} - X_i)^T (\mathbf{X}_{ij} - X_i) \tag{5}$$

From the above we can see that for the application of the statistical procedure, a data base is required, containing for each fault not only the healthy spectra and the reference patterns $\underline{\mathbf{P}}_i$, but also the corresponding discriminant vectors $\underline{\mathbf{X}}_i$ and covariance matrices $\mathbf{C}_i$. This data base is created during the learning phase. The flow chart of both the learning and decision phases of the statistical procedure is shown in Fig. 3.

The statistical procedure has been applied to data that were acquired from a number of different instruments, during the experiments with four compressor blade faults on an industrial gas turbine described in Appendix I. Two discriminants were used, the ones described by Loukis et al. (1992), whose definitions are repeated in Appendix II. Therefore the dimension of vector $\mathbf{X}$ was $M \cdot N = 2 \times 4 = 8$. For the learning phase 16 data sets (4 data sets for each of the operating points A, B, C, D) were used. The testing was performed during the decision phase using the same data sets employed during the learning phase. The rate of success for each fault was calculated for each of the instruments. These rates of success are shown in Fig. 4. It can be seen that the rates of success are very high and reach 100 percent for almost all the cases, which is much higher compared with the corresponding results of the geometric procedure (Loukis et al., 1992).

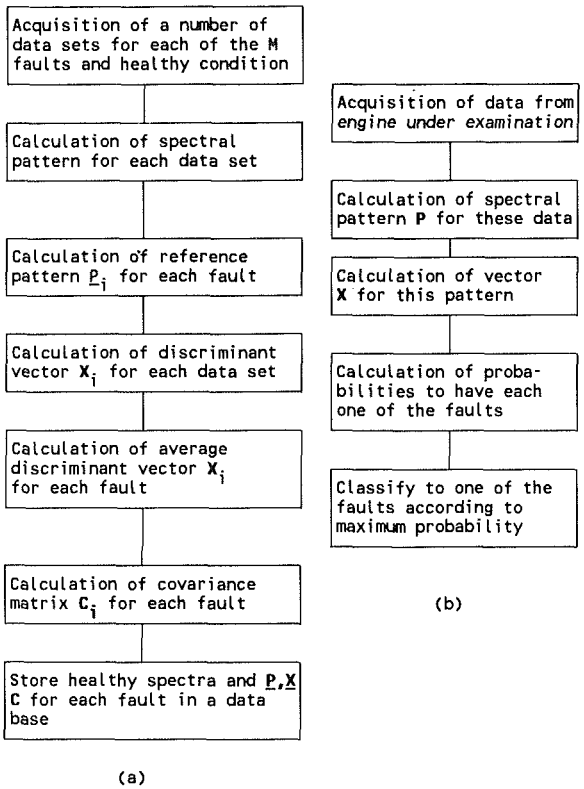


Fig. 3 Flow chart of statistical procedure: (*a*) learning phase; (*b*) decision phase

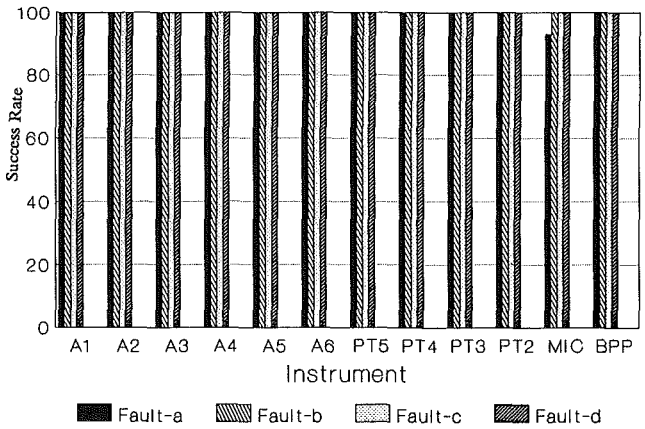


Fig. 4 Rate of success for statistical procedure for all the instruments

4 Optimal Selection of Fault Discriminants

The question posed next is whether it is possible to improve the effectiveness of a classification procedure by choosing different discriminants. In order to try to give an answer to this problem, we rely on previous experience about fault patterns.

In the work of Loukis et al. (1991) it was established that

Downloaded 02 Jun 2010 to 171.66.16.122. Redistribution subject to ASME license or copyright; see http://www.asme.org/terms/Terms_Use.cfm

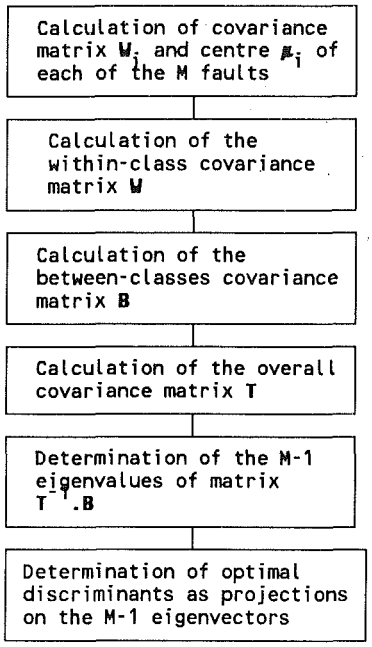


Fig. 5 Flow chart of optimal selection procedure

the diagnostic information for blade faults lies mainly in a number of discrete frequencies, which are harmonics of the shaft rotational frequency. This information is incorporated in the reduced spectral difference pattern **P**, consisting of values of a fault index calculated at these shaft harmonics. However, the information at the different shaft harmonics may not be of the same value with respect to the different faults of interest.

In order to have an efficient and reliable diagnosis, the whole of this information has to be exploited. One approach to achieving this target was the one previously mentioned, based on discriminants that are derived intuitively. This approach, however, is empirical and it is not certain that it will be successful in the general case. For this reason a systematic approach for selecting discriminants is needed, according to predefined criteria.

Establishing the methods of statistical classification of fault signatures from measurement data, enables the introduction of such criteria. From the nature of the problem two criteria are employed for the selection. If the pattern **P** coming from each data set is represented as a point in the discriminant space, the two criteria have the following form:

(*i*) Points coming from experiments with the same fault should be very close together.

(ii) The clusters of points corresponding to different faults should be far apart.

The problem of selecting the discriminants according to these criteria can be formulated mathematically using the principles of optimal linear feature selection, from pattern recognition theory (see, for example, Karagiannis and Steinhauer, 1988). According to these principles, parameters that are linear combinations of the pattern **P** components are considered as possible discriminants:

$$u = \sum_{k=1}^{N} \lambda_k P_k \tag{6}$$

The values of the linear multipliers λ_k, $k = 1, 2, \ldots, N$ are then calculated during a learning phase, by using the available data, in such a way that a quantity expressing the discrimination between the faults becomes maximum. We term such a parameter a Discrimination Potential Indicator (DPI). From these values of the linear multipliers, the optimal linear discriminant

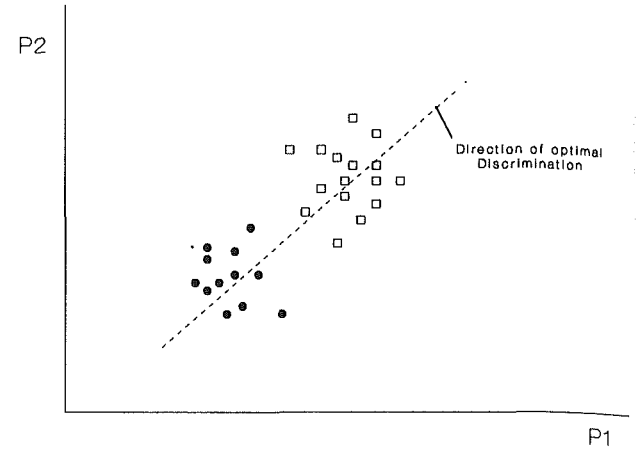


Fig. 6 Qualitative picture of the physical meaning of direction with maximum discriminability

is determined. Similarly the second, the third best, etc., discriminants can be determined.

In our case we found that a suitable DPI according to the above two criteria is the Fisher Ratio (Appendix II). It is known that when M reference patterns are available, then the maximization of the Fisher Ratio leads to $M-1$ independent linear combinations $D_1, D_2, \ldots D_{M-1}$ (their DPI values are in descending order). These linear combinations are then chosen as discriminants. The flow chart of such a procedure is shown in Fig. 5.

A qualitative picture of the underlying idea for this procedure can be given through Fig. 6. In this figure a simplified case of two-dimensional patterns ($N=2$) is presented, each pattern being represented by a single point in a two-dimensional space, with coordinates the values of the pattern components. In this space we can see two groups of points, each group corresponding to data from one particular fault. Each linear combination of pattern components corresponds to a direction in this space. From this figure we can see that different directions are characterized by different discrimination potential. For example, the directions of P_1 and P_2 are characterized by low discrimination potential and the clusters of the two faults overlap, when projected on these directions. On the contrary, we can see that there are directions, along which there is no overlapping of the clusters, one of them giving the maximum discrimination potential, as indicated on the figure.

5 Application to Experimental Data

The optimal selection procedure has been applied to the data set acquired during the experiments with the four faults on an industrial gas turbine, using a number of different instruments as described in Appendix I. The number of optimal discriminants derived was $M-1=3$. The same 16 different measurements sets were used here as well.

The points from the different experiments represented on the plane D_1–D_2 for the data from pressure transducer PT2 are shown in Fig. 7. It is observed from this figure that points from experiments with the same fault are grouped in clusters. These clusters are well separated from each other and therefore provide the possibility of making diagnostic decisions with a high confidence level.

The points from the different experiments represented on the plane D_1–D_2, for the data from accelerometer A1 are shown in Fig. 8. If we compare these results to the results of Fig. 7, it can be noticed that the clusters of points are still discrete, but (*a*) a larger scattering of the points within each cluster is observed, and (*b*) the clusters are generally closer to each other. This indicates that the discrimination on the basis of acceler-

Downloaded 02 Jun 2010 to 171.66.16.122. Redistribution subject to ASME license or copyright; see http://www.asme.org/terms/Terms_Use.cfm

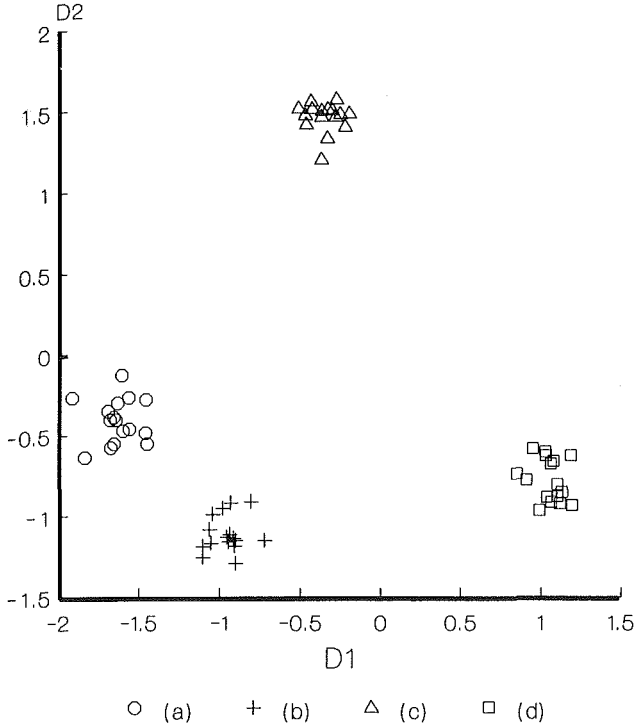


Fig. 7 Points corresponding to data from faults (*a*)-(*d*) on the plane of the discriminants D_1, D_2; measurement data from pressure transducer PT2

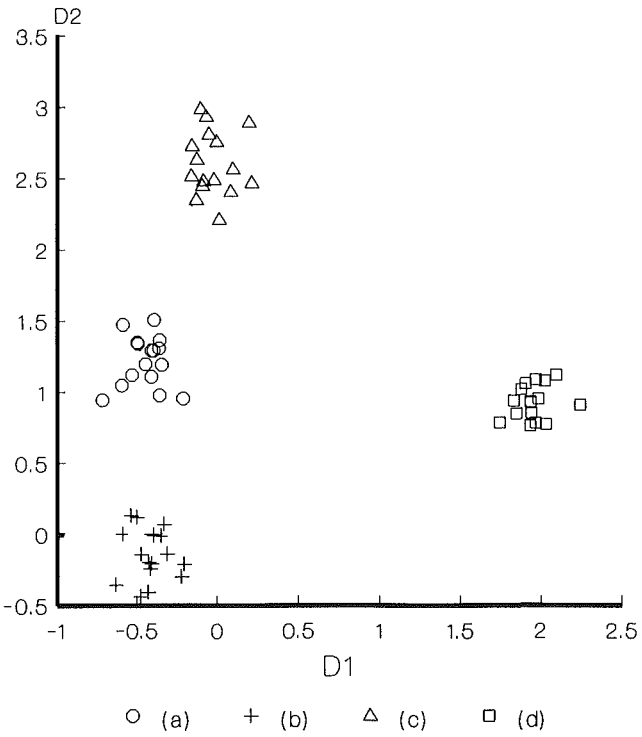


Fig. 8 Points corresponding to data from faults (*a*)-(*d*) on the plane of the discriminants D_1, D_2; measurement data from accelerometer A1

ometer data should be less effective than on the basis of pressure transducer data.

The same picture for microphone data is shown in Fig. 9 on the D_1–D_2 and D_1–D_3. It is interesting to observe here that the scattering of points in each cluster is larger than it is for the accelerometer and the pressure transducer. It can also be seen that faults *a* and *c* clusters overlap on the D_1–D_2 plane

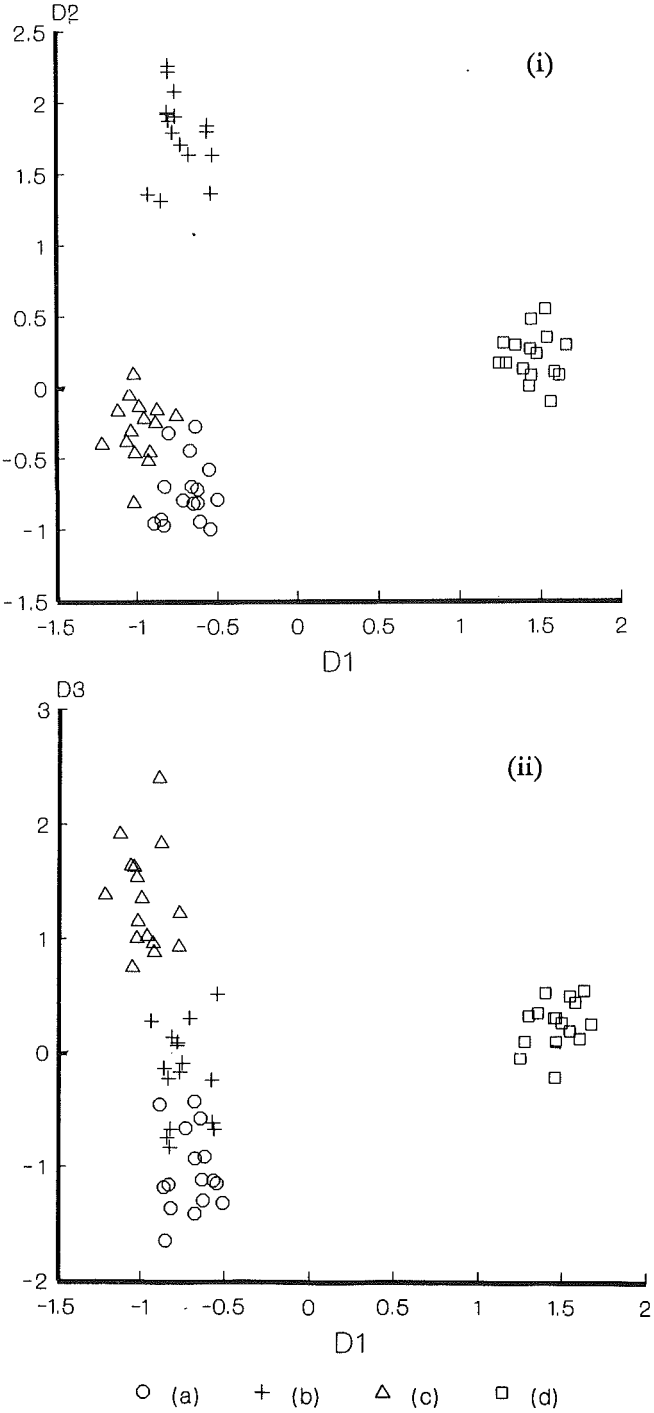


Fig. 9 Points corresponding to data from faults (*a*)-(*d*), (*i*) on the plane of the discriminants D_1, D_2, (*ii*) plane D_1, D_3; measurement data from microphone

while they are separated on the D_1–D_3 plane.A similar observation is valid for faults *a* and *b*.These observations show that if the decision is based on only two discriminants it can lead to a low success rate, while the success rate will be much higher when all three discriminants are used. On the other hand the clusters of faults *a*, *b*, *c* are close to each other but all of them well separated from the one of fault *d*. This constitutes a quantitative verification of observations based on visual inspect of fault signatures, reported by Loukis et al. (1991). (The visual inspection had shown that stator faults are easily discriminable from microphone measurements, while no visual discrimination was possible for rotor blade faults.)

Downloaded 02 Jun 2010 to 171.66.16.122. Redistribution subject to ASME license or copyright; see http://www.asme.org/terms/Terms_Use.cfm

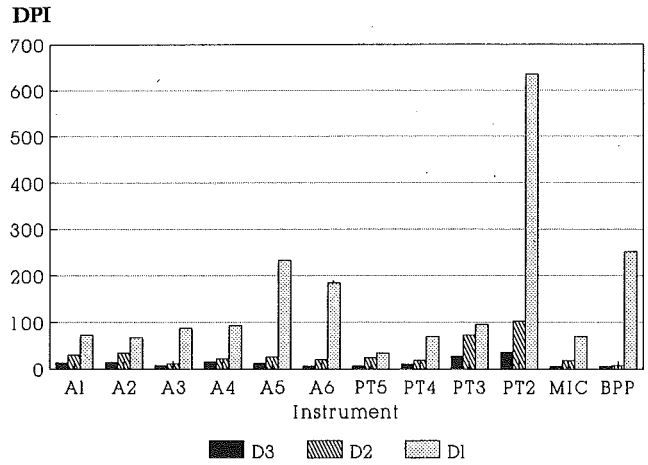


Fig. 10 DPI values for optimal discriminants D_1, D_2, D_3, for all measuring instruments

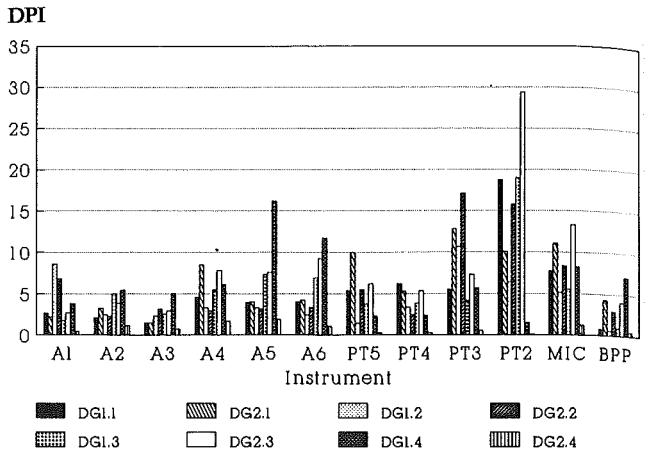


Fig. 11 DPI values for the discriminants $DG_{1,k}$, $DG_{2,k}$, calculated with respect to the four fault signatures for all instruments

An additional feature of the method is that the DPI can be used as a quantitative measure for the discrimination capability of discriminants. As an application first a quantitative assessment of the discrimination capability of the three optimal discriminants D_1, D_2, D_3 was done for all measuring instruments. The DPI values for D_1, D_2, D_3 and each measuring instrument are presented in Fig. 10. It can be observed that D_1 performs better than D_2 and D_2 better than D_3. This was expected since D_1, D_2, D_3 are by definition in descending order of DPI. On the other hand, DPI values for the discriminants of Appendix II with respect to the four fault signatures, are shown in Fig. 11. These results provide a comparative picture of the potential of the intuitively chosen discriminants. Comparison to Fig. 10 shows that the intuitive discriminants are characterized by much poorer performance than the systematically selected ones, since they exhibit much lower DPI values. This fact verifies the usefulness of the above systematic selection procedure.

The discriminants D_1, D_2, and D_3 have been used for the implementation of a statistical procedure of fault classification. This procedure has been based on a vector $\mathbf{X}$ of the form $\mathbf{X} = [D_1, D_2, D_3]$. The learning phase and the decision phase were according to Section 3. The rate of success for each fault, calculated for each of the instruments, was 100 percent for all cases. These results are a further confirmation of the improved performance achieved when systematic selection of discriminants is used.

6 Discussion

The procedures presented in the above sections possess features that make them very useful for implementation in practical industrial situations of fault diagnosis. Their most useful feature is that they incorporate data processing and decision making, while they can be implemented by a computer system.

The statistical procedure of classifying fault signatures contributes to the modern requirements mentioned in the introduction by increasing the efficiency and the reliability of diagnosis and giving the advantage of associating probabilities to the fault diagnosis. This feature makes the procedure more realistic for industrial application, in comparison with the geometric method.

The procedure of systematic discriminant selection offers the flexibility to define parameters that fulfill predefined discrimination criteria, increasing in this way the efficiency and reliability of the diagnosis as well. This systematic selection ensures that the classification procedure will be organized in accordance with the peculiarities of the specific problem, instead of a priori choosing discriminants intuitively and finding whether they are effective or not. On the other hand this procedure offers the possibility to redefine the discriminants when new data are available or new faults have to be introduced. This means that when extension of the data base to include new faults is effected, the procedure can be adapted to the new data, ensuring that discrimination capabilities will still be optimal.

Another useful product of the optimal selection procedure is the possibility to rank not only the discriminants, but also the various measuring instruments as well, according to the discrimination possibility they offer. Figure 10 can be interpreted in such a way if the values of DPI for the same discriminant are compared for the various instruments. We see that some instruments have higher DPI values than others, indicating better discrimination capabilities. Pressure transducer PT2 is characterized by the maximum DPI from all the instruments. This agrees with the conclusion reported by Loukis et al. (1991), from observations of various instrumental data, that pressure transducers are best suited for blade fault identification. The procedure above is therefore very useful in selecting the minimal and most appropriate set of instruments.

Finally, it should be mentioned that the procedure described above has been derived from one set of experiments on one engine. In order to examine generalization aspects, more data from other faults and other engines should be used.

7 Conclusions

In order to develop a sound procedure for automated gas turbine blade fault diagnosis the principles of pattern recognition theory have been employed. It was shown that when the statistical properties of fault signatures are taken into account advanced possibilities of decision making are provided.

A procedure for the systematic discriminant selection was developed. This procedure gives the possibility to select discriminants according to a priori set criteria and eliminates the need of selecting them intuitively. It was shown that this procedure further improves the decision making.

The procedure above also provides a possibility of assessing quantitatively the diagnostic effectiveness of (*a*) parameters used as discriminants, (*b*) instruments used as a source of information. Such a possibility is very useful in diagnostic systems design.

References

Carchedi, F., and Wood, G. R., 1982, "Design and Development of a 12:1 Pressure Ratio Compressor for the Ruston 6-MW Gas Turbine," ASME JOURNAL OF ENGINEERING FOR POWER, Vol. 104, pp. 823–830.

Downloaded 02 Jun 2010 to 171.66.16.122. Redistribution subject to ASME license or copyright; see http://www.asme.org/terms/Terms_Use.cfm

Doel, D., 1990, "The Role of Expert Systems in Commercial Gas Turbine Engine Monitoring," ASME Paper No. 90-GT-374,.

Emel, E., and Kannatey-Asibu, E., Jr., 1988, "Tool Failure Monitoring in Turning by Pattern Recognition Analysis of AE Signals," ASME *Journal of Engineering for Industry*, Vol. 110, pp. 137-145.

Karagiannis, G., and Steinhauer, C., 1988, "Pattern Recognition," National Technical University of Athens, Department of Mechanical Engineering, Athens.

Loukis, E., Wetta, P., Mathioudakis, K., Papathanasiou, A., and Papailiou, K., 1991, "Combination of Different Unsteady Quantity Measurements for Gas Turbine Blade Fault Diagnosis," ASME Paper No. 91-GT-201.

Loukis, E., Mathioudakis, K., and Papailiou, K. D., 1992, "A Procedure for Automated Gas Turbine Blade Fault Identification Based on Spectral Pattern Analysis," ASME JOURNAL OF ENGINEERING FOR GAS TURBINE AND POWER, Vol. 114, pp. 201-208.

Mathioudakis, K., Papathanasiou, A., Loukis, E., and Papailiou, K., 1991, "Fast Response Wall Pressure Measurement as a Means of Gas Turbine Blade Fault Identification," ASME JOURNAL OF ENGINEERING FOR GAS TURBINES AND POWER, Vol. 113, pp. 269-275.

Sing-Tze Bow, 1984, *Pattern Recognition*, Marcel Dekker Inc., New York-Basel.

APPENDIX I
Experimental Faults and Instrumentation

The present investigation was based upon dynamic measurements on an industrial gas turbine into which a number of different representative blade faults were introduced. The test engine was the Ruston Tornado, described by Charchedi and Wood (1982). The instrumentation layout and measurement conditions described by Loukis et al. (1991).

During the experiments four categories of measurements were performed simultaneously:

(*i*) Unsteady internal wall pressure, using two unsteady pressure transducers facing the first four rotors of the compressor, named PT2–PT5 respectively.

(*ii*) Casing vibration, with the accelerometers A1 to A6 mounted at the outside compressor casing.

(*iii*) Shaft displacement at compressor inlet bearings, with a Bently Nevada system (named BPP).

(*iv*) Sound pressure levels, with a double-layer microphone (named MIC).

Five experiments were performed testing the datum healthy engine and engines with the following four faults:

Fault a. Rotor fouling; all stage 2 rotor blades were coated with textured paint in order to roughen blade surface and alter their contour, in order to simulate a fault of all the blades of a rotor.

Fault b. Individual rotor blade fouling; two blades of stage 1 rotor separated by five intact blades, were coated by textured paint in order to simulate a slight individual rotor blade fault.

Fault c. Individual rotor blade twisted; a single blade of stage 1 rotor was twisted in order to simulate a severe individual rotor blade fault.

Fault d. Stator blade restaggering; three stage 1 stator blades were mistuned in order to simulate a stator fault.

All numbered references to faults and instruments in the text will correspond to the nomenclature above.

Tests were performed at four different engine loads; full load, half load, quarter load, and no load (termed operating points A, B, C, D, respectively, hereafter).

APPENDIX II
Formulas for Evaluation of Pattern Properties

Definition of Discriminants. The discriminants used for pattern classification by Loukis et al. (1992) are defined through the following relations:

$$DG_{1.k}=\sqrt{\frac{1}{N}\sum_{i=1}^{N}(P(i)-P_K(i))^2}\ \text{Euclidean distance}$$

$$DG_{2.k}=\frac{\sum_{i=1}^{N}(P(i)-Av(\mathbf{P}))(P_k(i)-Av(\mathbf{P_K}))}{\sqrt{\sum_{i=1}^{N}(P(i)-Av(\mathbf{P})^2)}\sqrt{\sum_{i=1}^{N}(\mathbf{P_K}(i)-Av(P_K)^2)}}$$

(correlation coefficient)

$$Av(\mathbf{P})=\frac{1}{N}\sum_{i=1}^{N}P(i)$$

Formulas for Optimal Linear Feature Selection. The principles we employ for optimal linear feature selection are briefly described below. Extensive descriptions can be found in textbooks (e.g., Karagiannis and Steinhauer, 1988).

The Fisher ratio expresses the classification capabilities for data if they are projected on one direction in the feature space. For a given direction, defined by its unit vector **u**, it is defined by a quotient that has as numerator the variance of the centers of the classes, if data points are projected on this direction. Its denominator is the average internal variance of the classes, if data points are projected on this direction. It is calculated, through the relation:

$$F(\mathbf{u})=\frac{\mathbf{u^T\cdot B\cdot u}}{\mathbf{u_T\cdot W\cdot u}}$$

where:

- $\mathbf{u}$ = the unit vector along the directional examined
- $\mathbf{B}$ = between-classes covariance matrix
- $\mathbf{B}=\sum_{k=1}^{M}\frac{N_k}{N}(\underline{\mu_k}-\mathbf{m})(\underline{\mu_k}-\mathbf{m})^T$
- M = number of classes
- N_k = number of available patterns of the kth class
- μ_k = mean pattern of the kth class
- N = total number of available patterns (for all the classes)
- $\underline{\mathbf{m}}$ = overall mean pattern (of all the classes)
- $\mathbf{W}$ = within-class covariance matrix, equal to the arithmetic average of the covariance matrices $\mathbf{W}_k$, $k=1, \ldots, M$, of all the classes:

$$\mathbf{W}=\sum_{k=1}^{M}\mathbf{W_k}$$

$$\mathbf{W}_k=\frac{1}{N_k},\sum_{i=1}^{N_k}(\mathbf{X}_i-\mu_k)(\mathbf{X}_i-\mu_k)^T$$

It can be shown that the sum of the within-classes covariance matrix **W** and the between-classes covariance matrix **B** gives the overall covariance matrix **T**, which takes into account the patterns of all classes, defined by the following equation:

$$\mathbf{T}=\frac{1}{N}\sum_{i=1}^{N}(\mathbf{X_i}-\mathbf{m})(\mathbf{X_i}-\mathbf{m})^T$$

It can be shown that the direction characterized by the maximum value of the above Fisher Ratio is the eigenvector of the $\mathbf{T}^{-1}\cdot\mathbf{B}$ matrix corresponding to its highest eigenvalue. Generally there are $M-1$ linearly independent directions maximizing the Fisher ratio, which are the eigenvectors of the $\mathbf{T}^{-1}\cdot\mathbf{B}$ matrix. Their Fisher ratios decrease with the corresponding eigenvalues.

Downloaded 02 Jun 2010 to 171.66.16.122. Redistribution subject to ASME license or copyright; see http://www.asme.org/terms/Terms_Use.cfm

An Infrared Pyrometry System for Monitoring Gas Turbine Blades: Development of a Computer Model and Experimental Results

M. de Lucia

C. Lanfranchi

Dipartimento di Energetica,
Università degli Studi di Firenze,
Via di Santa Marta, 3,
50139 Firenze, Italy

This work describes the development of a computer modeling system for infrared pyrometry measurement of gas turbine blade temperature. The model accurately evaluates apparent target emissivity and temperature on the basis of the radiation heat fluxes exchanged at steady-state conditions. Experimental testing conducted on gas turbine models in a controlled-temperature furnace has shown that the reliability of the target emissivity prediction effectively reduces one of the major causes of error in infrared pyrometry.

Introduction

The thermal efficiency of gas turbine engines has been steadily climbing over the past two decades. However, the tradeoff for greater efficiency has been higher and higher gas temperatures at turbine inlet and increasingly severe combinations of temperature and stress on the rotating components.

The capacity to measure temperature accurately in the turbine's rotating components has thus become an integral part of the development and monitoring phases of these machines (Schulemberg and Bals, 1987). Currently, two methods are employed: the direct contact method, utilizing sensors placed in direct contact with the moving parts, together with telemetry or slip rings, and the noncontacting method, utilizing instruments such as optical pyrometers (Beynon, 1982; Scotto and Eismeier, 1980).

Optical pyrometers measure the radiation emitted by a body according to its temperature. The two major sources of error in temperature measurement are optical contamination (Love, 1988; Kirby et al., 1986) and inaccurate evaluation of the target emissivity (Kirby et al., 1986; Benyon, 1981; Douglas, 1980). The proposed system supplies apparent emissivity and temperature values in real time with an error within 1 percent.

The theoretical basis underlying radiative heat transfer is the emission or radiance of the so-called blackbody expressed by Planck's law:

$$L_b(\lambda, T) = \frac{c_1}{\lambda^5(e^{c_2/\lambda T} - 1)} \tag{1}$$

An approximation often used to simplify the calculation of radiative heat transfer is Wien's law, whose validity is limited by the condition $(\lambda T) \ll c_2$, so that

$$L_b(\lambda, T) = \frac{c_1}{\lambda^5} e^{-c_2/\lambda T} \tag{2}$$

Real surfaces behave quite differently from ideal. Hence, the reliability of the temperature measurements is related to the degree of accuracy achieved in evaluating the emissivity parameter. The following equation:

$$\frac{dT}{T} = -\frac{\lambda T}{c_2}\frac{d\epsilon}{\epsilon} \tag{3}$$

shows that the error on the temperature caused by inaccuracy in the spectral emissivity for a given radiance temperature can be unacceptable, even when the emissivity error is slight.

A useful parameter in evaluating the transfer of radiation heat, and consequently the actual temperature, is the target apparent emissivity ϵ_a. This can be defined (Ono, 1988) as the ratio of the target exitent radiation[1] to blackbody radiance at the target temperature

$$\epsilon_a = \frac{L_{ex}(\lambda, T_t)}{L_b(\lambda, T_t)} \tag{4}$$

Hence, the knowledge of the target apparent emissivity ϵ_a, being dependent on the surrounding environment and not only on the real surface's physical properties, is critical in radiometric measurements.

Computer Modeling

Our aim in developing the computer model was to evaluate as accurately as possible the apparent emissivity in relation to the geometries, materials, and temperatures of the various components. The actual pyrometer target temperature is cal-

Contributed by the International Gas Turbine Institute and presented at the 37th International Gas Turbine and Aeroengine Congress and Exposition, Cologne, Germany, June 1–4, 1992. Manuscript received by the International Gas Turbine Institute February 4, 1992. Paper No. 92-GT-80. Associate Technical Editor: L. S. Langston.

[1]Exitent radiation = emitted + reflected radiation as defined by DeWitt and Incropera (1988). It is also called "radiosity" by Sparrow and Cess (1978), and others.

Copyright © 1994 by ASME
Downloaded 02 Jun 2010 to 171.66.16.122. Redistribution subject to ASME license or copyright; see http://www.asme.org/terms/Terms_Use.cfm

culated on the basis of the total energy transferred by radiation from the target to the surrounding bodies. The following assumptions were made:

1 Radiative heat transfer was assumed at steady-state conditions.

2 All radiances, powers, energies, and emissivities were assumed spectral, allowing evaluation at the pyrometer's constant wavelength.

3 The surfaces were assumed isothermal and gray, that is, as emitting and reflecting diffusely.

4 The surfaces were assumed to form a cavity, that is, without radiative heat transfer to the environment.

Each surface transfers heat via radiation to the other $n-1$ surfaces. The power balance of the generic surface i at steady-state conditions is

$$P_{ex_i} = P_{em_i} + P_{r_i} \tag{5}$$

with a reflected power of

$$P_{r_i} = (1-\epsilon_i) \sum_{j=1}^{n} P_{ex_{ij}} \tag{6}$$

where $P_{ex_{ij}}$ is the exitent power from surface j reaching surface i. This term can be expressed by the angle factors F_{ij}, i.e., the percentage of exitent power from j reaching i

$$F_{ij} = \frac{P_{ex_{ij}}}{P_{ex_j}} \tag{7}$$

The adimensional angle factors, related only to the geometric parameters, can be calculated according to Sparrow and Cess (1978).

Substituting radiances for the powers and using the calculated angle factors, we can rewrite the power balance, Eq. (5):

$$L_{ex_i} = L_{em_i} + \frac{(1-\epsilon_i)}{A_i} \sum_{j=1}^{n} (A_j L_{ex_j} F_{ij}) \tag{8}$$

which is a linear system of n equations in n unknowns, L_{ex_j}, with radiances L_{em_i} as its known terms. Assuming surface k as the target, we can determine the temperatures of the other $n-1$ surfaces by direct measurement or by theoretical correlations and acquire the temperature read by the pyrometer at the set emissivity. We can then calculate the target radiance by solving an n-dimensional linear system (Sparrow and Cess, 1978). It should, however, be recalled that the pyrometer temperature, due to the uncertainty of the set emissivity, can deviate notably from the target temperature. Actually, we can directly calculate the target exitent radiance L_{ex_k} with the pyrometer temperature T_{pyr}, whereas the unknown is the target's blackbody radiance L_{b_k} used to determine the actual target temperature. The kth equation of the linear system thus becomes

$$L_{b_k} = \frac{1}{\epsilon_k}\left[L_{ex_k} - \frac{(1-\epsilon_k)}{A_k} \sum_{j=1}^{n} (A_j L_{ex_j} F_{kj}) \right] \tag{9}$$

Since the other $n-1$ equations are independent of the unknown L_{b_k}, we can later solve Eq. (9) separately. The linear system reduces to a system $(n-1) \times (n-1)$ in the unknowns L_{ex_i}, $i \neq k$. The matrix of the linear system (8) $[B_{ij}]$ is defined as

$$B_{ij} = \delta_{ij} - \frac{(1-\epsilon_i)}{A_i} A_j F_{ij} \quad \begin{matrix} i, j = 1, 2, \ldots, n \\ i, j \neq k \end{matrix} \tag{10}$$

with the known term

$$C_i = \epsilon_i L_{b_i} + \frac{(1-\epsilon_i)}{A_i} A_k L_{ex_k} F_{ik} \quad \begin{matrix} i = 1, 2, \ldots, n \\ i \neq k \end{matrix} \tag{11}$$

The system may be written in matrix form

$$[B] \times [L_{ex}] = [C] \tag{12}$$

with matrix $[B]$ independent of temperature once the target has been defined. The matrix calculation is performed only once, since the geometry and physical constants of the problem are known. Having determined radiances L_{ex_i} and having substituted them in Eq. (9), we can calculate the target blackbody radiance L_{b_k} and thus the actual temperature by inverting Planck's equation. The target apparent emissivity ϵ_{ak} results

$$\epsilon_{a_k} = \frac{L_{ex_k}}{L_{b_k}} \tag{13}$$

Physical Models

Two physical models of diverse complexity were developed and tested: one, simplified, to test the data acquisition system, the sighting system, and the computer model, and one, more complex, configured to duplicate actual machine operation as closely as possible.

Simple Model. The simplified model consisted of an inconel cylinder with an emissivity of 0.83 positioned inside a cavity lined with refractory material with an emissivity of 0.3. The pyrometer target was a 4-mm circular surface in the middle of the cylinder's upper surface. The model was instrumented with 11 thermocouples: Eight were positioned on a radius 12 mm from the target center (four on the surface and four 1 mm below the surface), two were positioned at the target edge, and one was positioned on the refractory wall. The cylinder was designed with special internal cavities to obtain an isothermal upper surface even during cooling. Testing was conducted with a rhodium-coated mirror to deviate the line-of-sight by 90 deg and with no mirror.

Nomenclature

A = surface area, m^2
a = distance, m
c_1 = first radiation constant, W $\mu m^4 m^{-2} sr^{-1}$
c_2 = second radiation constant, μm K
F = angle factor
h = length, m
L = radiance, $Wm^{-2}sr^{-1}\,\mu m^{-1}$
l = length, m
P = radiant power, W μm^{-1}
s = width, m
T = temperature, K
x = spatial coordinate, m
γ = angle between perpendicular and the y axis, rad
δ_{ij} = Kronecker delta
ϵ = emissivity
λ = wavelength, μm
ρ = reflectance
φ = angular width, rad

Subscripts

a = apparent
b = blackbody conditions
em = emittent
ex = exitent
m = mirror
pyr = pyrometer
r = reflected
ref = refractory
t = target (actual)
tc = target (calculated)

Downloaded 02 Jun 2010 to 171.66.16.122. Redistribution subject to ASME license or copyright; see http://www.asme.org/terms/Terms_Use.cfm

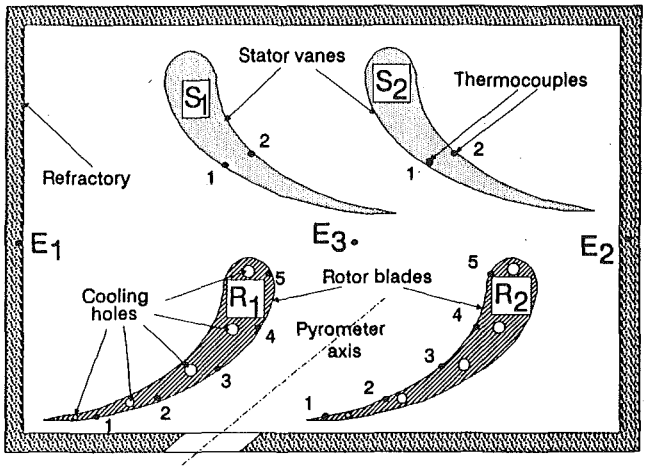


Fig. 1 Schematic of the experimental model

Only two surfaces, the cylinder and the refractory surface, were considered in modeling with constant, homogeneous properties for both. In this way, the angle factor calculation was simplified so that we could avoid having to solve the linear system. We were thus able to perform a check on how the system worked, having explicated the apparent emissivity in relation to the actual cylinder radiance L_{ex_1} and the blackbody refractory radiance L_{b_2} as

$$\epsilon_{a_1} = \frac{1}{a - b\dfrac{L_{b_2}}{L_{ex_1}}} \tag{14}$$

where 1 is the target index, 2 is the refractory index, and the constants a and b are

$$a = \frac{1}{\epsilon_1}\left[1 - (1-\epsilon_1)F_{11} - \frac{(1-\epsilon_1)(1-\epsilon_2)F_{12}F_{21}}{1-(1-\epsilon_2)F_{22}}\right]$$

$$b = \frac{\epsilon_2(1-\epsilon_1)F_{12}}{\epsilon_1[1-(1-\epsilon_2)F_{22}]}\frac{A_2}{A_1}$$

Complex Model. The complex model (Fig. 1) was comprised of a plate sustaining two stator vanes and two rotor blades placed inside a cavity formed by a refractory shield. The blades were arranged to reproduce actual machine geometric conditions as closely as possible. The blade surfaces were of oxidated inconel with an emissivity of 0.83. As in the simple model, the cavity was lined in a refractory material with an emissivity of 0.3. Five thermocouples were installed on each blade (suction side of blade $R1$ and pressure side of blade $R2$): two on each (uncooled) stator vane ($S1$ and $S2$), two on the refractory material ($E1$ and $E2$), and one in the environmental space ($E3$). The blades were cooled by an airflow from outside, which, after passing through the cooling holes, was exhausted outside through a duct. A control system was installed so that the temperature of the rotor blades could be varied separately.

In order to reproduce the actual machine layout of the sighting system, we used a mirror to deviate the line-of-sight. The mirror required constant cooling and air purging to maintain high reflectivity and low emissivity. In the sighting system, a second cooling airflow (Fig. 2) was routed over the pyrometer's jacket to the optical components prior to reaching the mirror. Since the flow of cooling air inside the controlled-temperature furnace had to be avoided, an outer jacket was attached to a vacuum pump to keep the air from reaching the target and altering the temperature distribution.

The following test equipment was selected:

(*a*) a Land high-temperature infrared pyrometer with $\lambda = 1$ μm

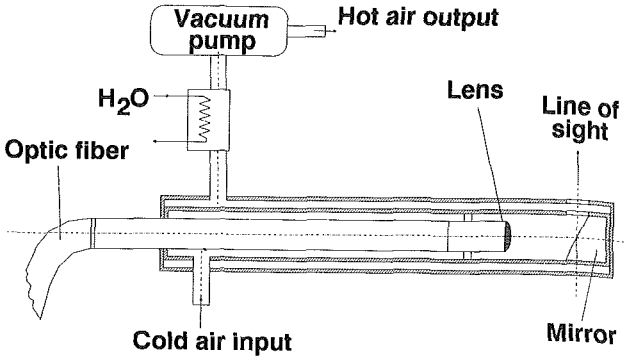


Fig. 2 Schematic of the sighting tube and cooling system

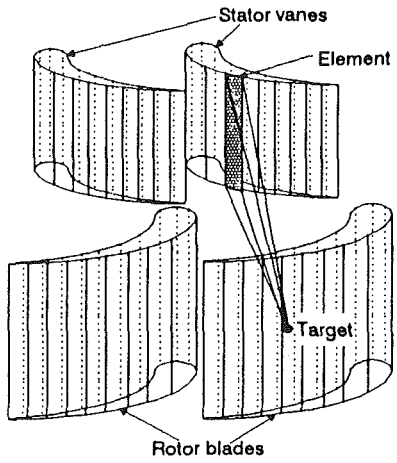


Fig. 3 Model discretization

(*b*) a support-sighting system (Fig. 2) including a mirror with a rhodium surface to provide the 90-deg deviation to the line-of-sight

(*c*) a Hewlett-Packard data acquisition system

(*d*) a dedicated personal computer for processing the data from the data acquisition system and evaluating ϵ_a in real time

(*f*) a controlled-temperature electric furnace (0–1200°C)

The blades (Fig. 3) were modeled as no-twist, two-dimensional bodies with a cross section equal to the blade midheight section and discretized with 22 connected points. A computer program was written to calculate the angle factor with finer discretization. Elementary isothermal rectangular elements were used in discretizing the blade surfaces and circular sectors and rectangles for the blade surrounding area (refractory surfaces). As the calculation of the angle factors is wholly dependent on system geometry and therefore extremely complicated, we chose an analytical method that would increase calculation accuracy and speed. The angle factor between two thin rectangular surfaces with perpendiculars parallel to the same plane (Fig. 4) can be expressed

$$F = \frac{s_1\, s_2 \cos\gamma_1 \cos\gamma_2}{2\pi A\, a}\left[(x_1 + h_1 - x_2)\tan^{-1}\left(\frac{x_1 + h_1 - x_2}{a}\right)\right.$$
$$+ (x_1 - h_2 - x_2)\tan^{-1}\left(\frac{x_1 - h_2 - x_2}{a}\right) - (x_1 - x_2)\tan^{-1}\left(\frac{x_1 - x_2}{a}\right)$$
$$\left. - (x_1 + h_1 - x_2 - h_2)\tan^{-1}\left(\frac{x_1 + h_1 - x_2 - h_2}{a}\right)\right] \tag{15}$$

while the angle factor between a thin rectangular surface and a crown sector in perpendicular planes (Fig. 5) is

Downloaded 02 Jun 2010 to 171.66.16.122. Redistribution subject to ASME license or copyright; see http://www.asme.org/terms/Terms_Use.cfm

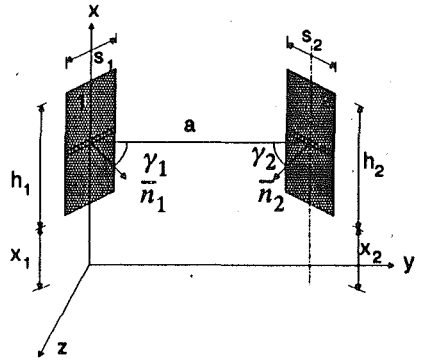


Fig. 4 Geometry for the angle factor calculation for a two-rectangle system

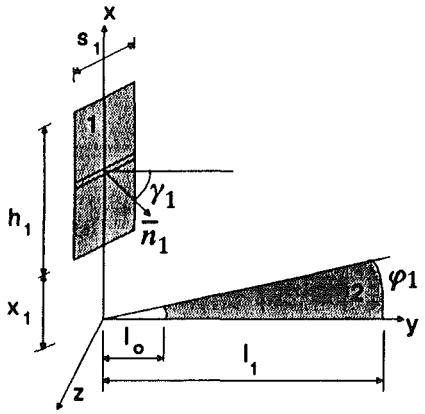


Fig. 5 Geometry for the angle factor calculation for a rectangle- and circular-sector system

$$F=\frac{s_1}{2\pi A}\left[\sin(\gamma_1+\varphi_1)-\sin(\gamma_1)\right]\left[x_1\tan^{-1}\left(\frac{l_0}{x_1}\right)-x_1\tan^{-1}\left(\frac{l_1}{x_1}\right)\right.$$
$$\left.-(x_1+h_1)\tan^{-1}\left(\frac{l_0}{x_1+h_1}\right)+(x_1+h_1)\tan^{-1}\left(\frac{l_1}{x_1+h_1}\right)\right] \quad (16)$$

Additionally, since the angle factors between elements may also be combined (Sparrow and Cess, 1978), the system for the final solution may be notably reduced to a minimum related to the number of data available. The blade temperature distribution can be derived from theoretical or experimental values, which in our case consisted of the 17 thermocouple measurements.

Experimental Results

Experimental testing was performed at furnace temperatures between 600–1000°C. The tests on the simple model designed to validate the reliability of the mathematical model and approximations were also useful in developing the mirror cooling and sighting-support systems.

Simple Model. Figure 6 shows the calculated and experimental results for a test considered among the most significant. Close agreement between the calculated and experimental temperatures is evident, with the relative error below 0.5 percent. The fact that the set emissivity was varied between 0.8–1.1 had no negative effect on the calculation of the target temperature.

Complex Model. The results were satisfactory under all test conditions, i.e., with variations in the target surface, temperature, blade cooling air flow rate, as well as with air purging. In all cases, the error was limited to within 1 percent and in many cases even fell below 0.5 percent. Although the model was designed for steady-state calculations, testing was also performed over a transient. The results were positive for slight temperature variations in time, with the error rate peaking steeply only for the more abrupt transients.

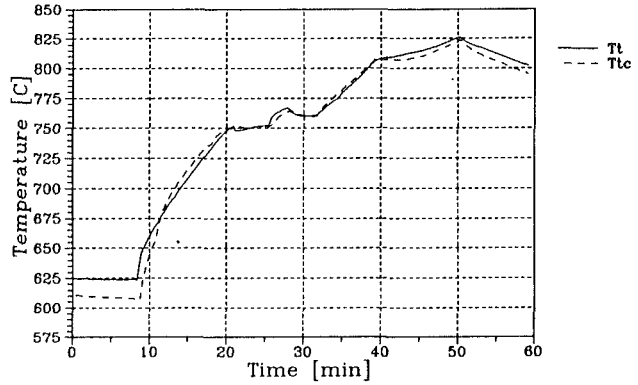


Fig. 6 Simple model: experimental (T_t) and calculated (T_{tc}) target temperatures

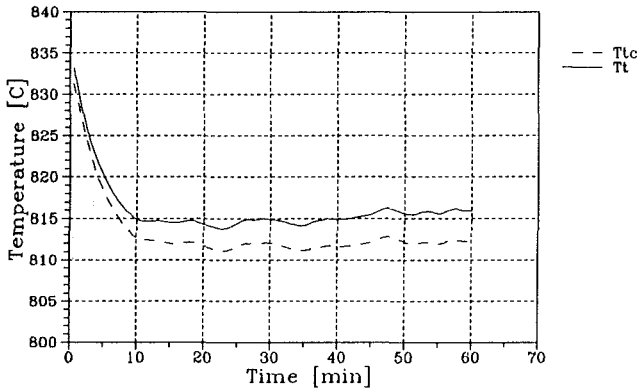


Fig. 7 Complex model: experimental (T_t) and calculated (T_{tc}) target temperatures

A deterioration in mirror performance was often encountered even during a single test period (1–2 h). This was due to the limitations of our cooling and purge systems, as well as to the high operating temperature of the mirror (100–150°C below target temperature). Mirror performance varied in relation to both operating temperature and exposure time: In high-temperature testing ($T>900$°C) mirror life was no longer than 2–3 hours, increasing only when the temperature was decreased. The normal mirror reflectance value of 0.79 ± 0.01, supplied by the manufacturer, was found to be correct only at favorable conditions, i.e., at ambient temperature and after polishing. Experimental calibration tests proved that mirror reflectance decay was nearly linear with the test temperature exposure time. Therefore, throughout testing, we assumed a constant mean mirror reflectance ρ_m of 0.76 ± 0.01, calculated averaging the actual mirror reflectance over two hours' exposure time at 750°C. This accounts for the attenuation of the reflected signal due to the deterioration in mirror performance.

The results of a test performed at 860°C are shown in Figs. 7–9. The temperature of the target (the area around thermocouple 3 on blade $R2$) was found to be 45°C cooler than the furnace, whereas the stator vanes were between 20–35°C hotter on the target. The temperature irregularity on blade $R2$ was 15°C. Figure 7 shows that the calculated and experimental target temperatures were in good agreement throughout testing, with a relative error $(T_{tc}-T_t)/T_t\cdot 100$ that tends to increase in time up to a maximum (in absolute terms) of 0.45 percent (Fig. 8). The initial transient was caused by the opening of the blade cooling air valve. (Note that values higher than the 45°C set here were used in other tests.) Figure 9 shows that the calculated apparent emissivity remained constant at 1.073.

Downloaded 02 Jun 2010 to 171.66.16.122. Redistribution subject to ASME license or copyright; see http://www.asme.org/terms/Terms_Use.cfm

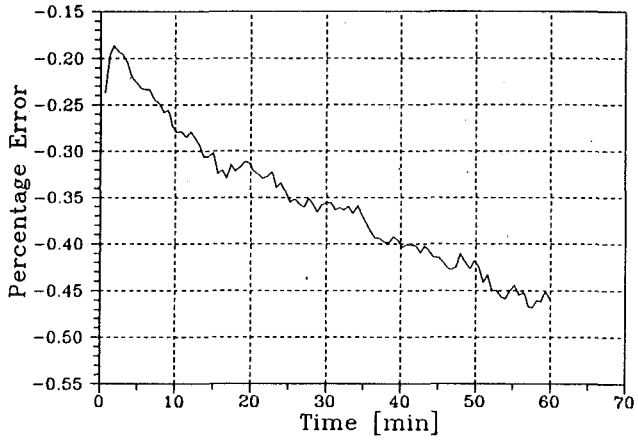


Fig. 8 Calculated target temperature error (percent)

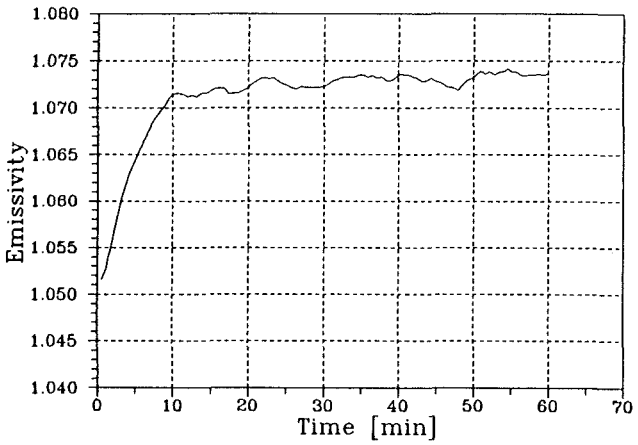


Fig. 9 Calculated target emissivity

Sensitivity and Error Analysis

The measuring error and its calculation-induced amplification were analyzed in order to validate the model's reliability. Having assumed a maximum error of 0.75 percent for each thermocouple and ±3°C for the pyrometer, we computed the maximum error of ±4°C on the calculated temperature both for the simplified and complex models—a more than acceptable error for the type of application under investigation.

Simple Model. A sensitivity analysis was performed to verify the versatility of the model. Since only two surfaces, the cylinder and the refractory surface, were considered, the calculation was appreciably simplified.

The sensitivity curves plotted in Fig. 10 show how the target temperature error depends on the refractory temperature uncertainty for various target temperatures and for a refractory-target temperature difference ($T_{ref} - T_t$) of 100°C. If the error on the refractory surface temperature is negative, the error on the calculation of the target temperature is small. Conversely, a positive refractory temperature error causes an appreciable increase in the target temperature calculation error: the lower the target temperature, the more marked the increase. Therefore, an underestimation causes a smaller error than an overestimation. The same calculations were performed for various values of the refractory-target temperature difference ($T_{ref} - T_t$) (not illustrated here). As this parameter decreases, i.e., as the system tends to isothermal conditions, the target temperature error approaches zero.

Complex Model. Since, in applying such temperature measurement systems, one of the major uncertainties is the temperature to assign to the elements used to discretize the model, we assumed in the sensitivity analysis a maximum random error of 50°C on each measured temperature, with a higher probability of underestimation (75 percent of the cases) than overestimation. Due to the assumption of random error distribution, the calculation error was extremely variable, without, however, exceeding an average of 1.5 percent. Not surprisingly, the error decreased as the number of elements used in discretization increased.

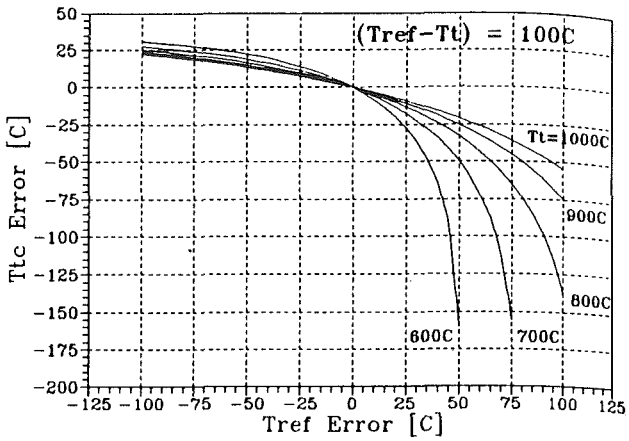


Fig. 10 Target temperature (T_t) error versus refractory surface temperature (T_{ref}) error

Conclusions

Experimental testing on models of gas turbine components has confirmed that the proposed system furnishes accurate temperature measurements at steady- or near-steady-state conditions and regardless of the emissivity set on the pyrometer. The proposed method furnishes an accurate evaluation of emissivity and thus of temperature, which in this way is univocally defined. This means that the temperature measurement can be made by an operator without special training or skills. By contrast, the sensitivity required for the discretization and calculation of the angle factors calls for more sophistication (even though this operation need only be performed once if the system geometry has not been changed in the meantime).

Obviously, the calculation accuracy is related to the degree of accuracy with which we know the parameters regarding our operating environments. The method as presented in this work has been applied to models on which it is possible to measure the temperatures of all of the surfaces surrounding the target. Hence, it must be modified before being applied to real machines in which temperatures are obtained by empiric estimates or, better still, by multiple pyrometer measurements. The target temperature can then be calculated by solving coupled sets of linear equations. This application, now under development, will be presented in a forthcoming work.

Acknowledgments

The authors are grateful to Pierluigi Nava of NuovoPignone and Francesco Carleo for their help in carrying out the experimental program and to Professor Ennio Carnevale for his invaluable support. This work was partially funded by NuovoPignone S.p.A.

References

Beynon, T. G. R., 1981, "Turbine Pyrometry—An Equipment Manufacturer's Viewpoint," ASME Paper No. 81-GT-136.

Beynon, T. G. R., 1982, "Infrared Radiation Thermometry Applied to the Development and Control of Gas Turbine Engines," *Proceedings, International*

Downloaded 02 Jun 2010 to 171.66.16.122. Redistribution subject to ASME license or copyright; see http://www.asme.org/terms/Terms_Use.cfm

Conference on Infrared Technology, Butterworth Scientific Ltd., Sevenoaks, United Kingdom, pp. 3–16.

DeWitt, P. D., and Incropera, F. P., 1988, "Physics of Thermal Radiation," *Theory and Practice of Radiation Thermometry*, P. D. DeWitt and G. Nutter, eds., Wiley, New York, pp. 21–89.

Douglas, J., 1980, "High-Speed Turbine Pyrometry in Extreme Environments," *Proceedings, New Orleans Gas Turbine Conference*, ASME, New York, pp. 335–343.

Kirby, P. J., Zachary, R. E., and Ruiz, F., 1986, "Infrared Thermometry for Control and Monitoring of Industrial Gas Turbines," ASME Paper No. 86-GT-267.

Love, T. J., 1988, "Environmental Effects on Radiation Thermometry," *Theory and Practice of Radiation Thermometry*, P.D. DeWitt and G. Nutter, eds., Wiley, New York, pp. 189–229.

Ono, A., 1988, "Methods for Reducing Emissivity Effects," *Theory and Practice of Radiation Thermometry*, P.D. DeWitt and G. Nutter, eds., Wiley, New York, pp. 565–623.

Schulemberg, T., and Bals, H., 1987, "Blade Temperature Measurements of Model V84.2 100 MW/60 Hz Gas Turbine," ASME Paper No. 87-GT-135.

Scotto, M. J., and Eismeier, M. E., 1980, "High-Speed Noncontacting Instrumentation for Jet Engine Testing," ASME JOURNAL OF ENGINEERING FOR POWER, Vol. 102, pp. 912–917.

Sparrow, E. M., and Cess, R. D., 1978, *Radiation Heat Transfer*, Hemisphere Publishing, Washington, DC, pp. 81–143.

Downloaded 02 Jun 2010 to 171.66.16.122. Redistribution subject to ASME license or copyright; see http://www.asme.org/terms/Terms_Use.cfm

Fault Signatures Obtained From Fault Implant Tests on an F404 Engine

R. W. Eustace

B. A. Woodyatt

G. L. Merrington

A. Runacres

DSTO Aeronautical Research Laboratory, Melbourne, Australia

The fault diagnostic process for gas turbine engines can be improved if data acquired by an on-board engine monitoring system (EMS) are utilized effectively. In the commercial transport field, techniques are available to extract engine condition assessment information from steady-state EMS data. In a military environment, steady-state data are not always available, and therefore it is desirable to exact at least some of the information from transient data, such as during take-off. Fault signatures are presented for an F404 engine based on fault implant tests in a sea-level-static (SLS) test cell. A comparison is then made between the fault coverage capabilities of fault diagnostic techniques based on the use of steady-state engine data with those using transient data. The important conclusions to emerge from this work are that for the range of faults examined, not only is there similar fault information contained within the transient data, but the faults can be detected with increased sensitivity using these data.

Introduction

Fault diagnosis and condition assessment of gas turbine engines are important elements of any "on-condition" maintenance program. These aspects are further emphasized when the engines involved are modular in construction. In these circumstances, the aim is to try to isolate problems to at least modular level so that the module can be replaced and the engine returned to service quickly. This contrasts with the older maintenance philosophy, whereby complete engines were removed at fixed time intervals for overhaul purposes. The benefits of an on-condition maintenance program are that components are utilized in a more cost-effective manner, engine down-time is reduced, and potential problem areas are likely to be identified early. Many current generation aircraft are fitted with engine monitoring systems (EMS), which enable a range of engine parameters to be recorded during operation. The aim of fault diagnostic work is to make use of the captured EMS data to aid maintenance personnel in detecting and isolating some of the engine-related faults. The problem is further complicated in that, for military combat aircraft, most of these data will correspond to transient engine operation. Thus, it is desirable to be able to extract the fault information from transient engine data if, and when, reliable steady-state data are unavailable.

In this paper results of a set of fault implant tests on GE-F404 engine are presented in terms of the resultant fault coverage based on transient engine data as well as steady-state data.

Contributed by the International Gas Turbine Institute and presented at the 37th International Gas Turbine and Aeroengine Congress and Exposition, Cologne, Germany, June 1-4, 1992. Manuscript received by the International Gas Turbine Institute February 6, 1992. Paper No. 92-GT-82. Associate Technical Editor: L. S. Langston.

Background

In the past, engine condition assessment has largely been based on steady-state information with minimal reference to transient performance aspects. The latter has usually been confined to monitoring the time taken to complete specific accelerations and/or decelerations because data were usually recorded manually. However, the advent of computer-based data acquisition systems has overcome many of the limitations associated with manual recording. In particular, previously derived global attributes, such as the time to complete a transient, can now be expanded to include a detailed description of the transient. Data acquisition rates of 10 to 50 Hz are common in many systems, and when compared to typical gas turbine characteristic frequencies of 5 Hz or less, sufficient information can be gleaned from the captured data to identify a range of operational type faults (Merrington, 1989; Merrington and Faragher, 1989).

Fault signatures can be constructed from an analysis of transient data. In the case of the F404 engine, the parameters used in the present investigation were limited to the parameter set normally found on the aircraft. Two approaches can be used for fault detection. One involves a direction correlation of the measured parameters (Henry, 1988; Faragher, 1989) in which a snapshot is taken in a designated capture window. Alternatively a model-based method can be used whereby parameters of the model are monitored for the effects of faults (Merrington, 1991).

Fault signatures can also be formulated from steady-state data using various techniques (Muir et al., 1988; MacLeod et al., 1992). Again the direct correlation of measured parameters is a convenient approach and furthermore, the results can be readily compared in a meaningful way with the corresponding signatures derived from transient data.

Copyright © 1994 by ASME

Downloaded 02 Jun 2010 to 171.66.16.122. Redistribution subject to ASME license or copyright; see http://www.asme.org/terms/Terms_Use.cfm

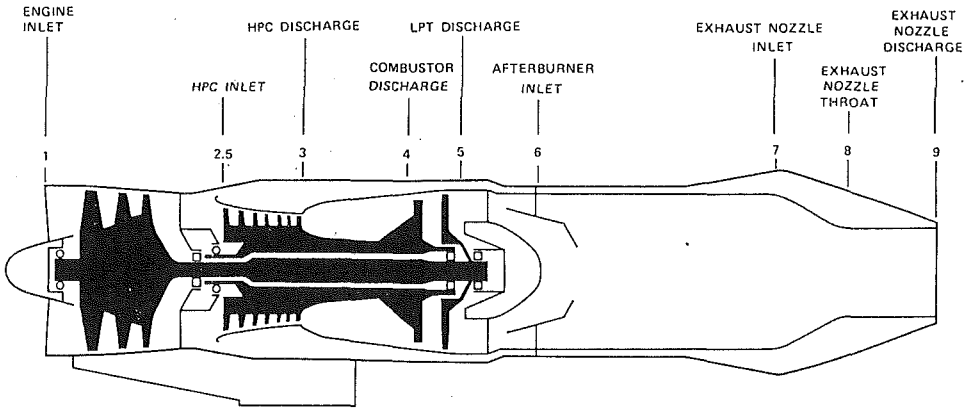


Fig. 1 F404 engine and station locations

The present investigation involves the analysis of both steady-state and transient F404 test data recorded in a sea-level-static test cell with and without implanted faults. Such a comparison of the fault coverage capability from transient versus steady-state data has not been previously reported to these authors' knowledge.

Engine Test Program

The aim of the engine test program was to implant faults in a military gas turbine engine under test cell conditions and to establish resultant fault signatures. Furthermore, these faults were to be representative of operational type faults so that meaningful comparisons could be made between the test-cell results and aircraft take-off data.

Engine. The test engine used in this study was a GE F404 engine in operational use with the RAAF fleet of F/A-18 aircraft. The F404 is a low bypass, twin spool turbofan with a mixed flow exhaust and afterburning. The major station locations are identified in the schematic diagram of Fig. 1. The engine has variable geometry in both the fan and the high-pressure compressor and a variable area exhaust nozzle. Control is via an integrated hydromechanical and electrical system. Thrust is modulated from idle to maximum afterburner through a single power lever and the control system schedules compressor rotor speed (N_H), fan and compressor geometry (FVGV and CVGV), exhaust nozzle area (A_8), and afterburner fuel flow. It also limits maximum fan rotor speed (N_L) and low-pressure turbine discharge temperature (T_5), as well as compressor minimum and maximum discharge pressure (P_{S3}). The engine is constructed in six separate modules, consisting of the fan, compressor, combustor, high-pressure turbine, low-pressure turbine, and afterburner (General Electric, 1980).

Instrumentation. Engine operational condition is continuously monitored by the airfcraft on-board In-flight Engine Condition Monitoring System (IECMS). This system consists of engine sensors, airframe-mounted signal processors, computer signal analysis, and interfacing for data recording and cockpit display (Doane and Kinley, 1983). The engine sensors comprise spool speeds and internal pressures and temperatures necessary for engine control or for pilot display. A complete list of the IECMS sensors and their primary application is given in Table 1.

Table 1 F/A-18 IECMS parameters

Parameter	Symbol	Primary Application
Engine Inlet Temperature	T_1	Engine Control
Fan Speed	N_L	Engine Control
Compressor Speed	N_H	Engine Control
Turb. Del. Temp.	T_5	Engine Control
Nozzle Area	A_8	Engine Control
Power Lever Angle	PLA	Engine Control
Main Fuel Flow	W_F	Cockpit Indication
Lube Pressure		Cockpit Indication
Comp. Discharge Pressure	P_{S3}	IECMS
Oil Tank Level		IECMS
Turb. Del. Press.	P_{T56}	IECMS
Vibration		IECMS
Anti-Ice Valve Position		IECMS

For engine performance investigative testing, such as that forming the subject of this paper, additional dedicated test

Nomenclature

A_8 = exhaust nozzle throat area
N_L = fan rotor speed
N_H = compressor rotor speed
P_S = static pressure
P_T = total pressure
T = total temperature
W_F = main engine fuel flow
σ = standard deviation

Acronyms

ARL = Aeronautical Research Laboratory
CBL = Compressor Bleed
CVG = Compressor Variable Geometry
CVGV = Compressor Variable Guide Vane
ECU = Electrical Control Unit
EMS = Engine Monitoring System
EPR = Engine Pressure Ratio
FVGV = Fan Variable Guide Vane
GE = General Electric
IECMS = In-Flight Engine Condition Monitoring System
MODAS = Mobile Data Acquisition System
RAAF = Royal Australian Air Force
SLS = Sea Level Static

Downloaded 02 Jun 2010 to 171.66.16.122. Redistribution subject to ASME license or copyright; see http://www.asme.org/terms/Terms_Use.cfm

Table 2 Additional parameters measured in the test cell

Parameter	Symbol	Signal Source
Pressures		
Inlet Total	P_0	Bellmouth Rakes
Bell Mouth Static	P_{SO}	Bellmouth Wall Taps
Fan Exit Total	P_{21}	GE 5 Point Rake
Fan Exit Static	P_{S21}	Borescope Tapping
HP Compressor Total	P_3	GE 4 Point Rake
HP Compressor Static	P_{S3}	Borescope Tapping
Temperatures		
Intake Total	T_0	Bellmouth Screen
Fan Exit Total	T_2	GE 5 Point Rake
HP Compressor Total	T_3	GE 4 Point Rake
Vane Angles		
Fan Variable Guide	FVGV	Rotary Potentiometer
Comp. Variable	CVGV	Rotary Potentiometer
Test-Cell Fuel Flow	WFTC	Turbine Flowmeter

instrumentation was fitted to the engine (Table 2). This instrumentation was designed both to supplement and to duplicate the IECMS parameters in order to enhance the performance data analysis (Streatfeild, 1988).

Data Acquisition System. The investigative test program was performed in the F404 Test Cell at Hawker de Havilland Victoria. This cell was used for the acceptance testing of all RAAF F404 engines and is equipped with an automated data acquisition and processing system. This system provides detailed steady-state analysis of the engine on test including comparison with the engine manufacturer's specification performance.

For the ARL-initiated testing, a dedicated Mobile Data Acquisition System (MODAS) was used in addition to the cell system. This provided the capability to acquire transient as well as steady-state data.

Test Procedure. To establish engine performance changes caused by the implanted faults, the same test schedules were employed in both the fault and no-fault test. The test sequence commenced with establishing the performance of the engine in the nominal, or no-fault, condition. Following this, the test schedules were repeated for each fault condition in turn. Finally the nominal performance was re-established after restoring the engine to the no-fault configuration.

The steady-state test schedule comprised running the engine at five power lever positions from idle to maximum non-afterburning power, and recording data after stabilizing on condition for 5 minutes. For transient records, the engine was stabilized at ground-idle for 5 minutes prior to executing a rapid throttle movement to maximum non-afterburning power. Data recording was commenced some seconds before the power lever movement and continued for some seconds after the maximum condition was reached.

Implanted Faults

Several faults were implanted into the F404 engine during the test program. These faults were effected by making adjustments to engine geometry and control variables. As the engine used was an RAAF operational unit, the adjustments were restricted in magnitude to be within operational limits. These faults were thus not representative of an unserviceable engine but were of sufficient magnitude to verify the effectiveness of the fault diagnostic techniques.

Several levels of each fault were implanted. However, only one level is considered here since the purpose of this study is to ascertain the relative sensitivity of detecting faults from either steady-state or transient data. The particular faults pertinent to this study are summarized here.

Compressor Variable Guide Vanes. The first three stages of the high-pressure compressor guide vanes are scheduled together as a function of corrected compressor speed and vary through approximately 50 deg to be fully open at maximum speed. Adjustments to the schedule are effected via a turnbuckle in the actuating mechanism. The fault condition consisted of biasing the CVGV four degrees closed.

Compressor Discharge Bleed. Air for aircraft environmental systems is bled from the high-pressure compressor delivery by way of an electrically actuated control valve. During the test program air was bled from the compressor via the control valve and ducted to the exhaust exit plane through a calibrated nozzle. A controlled and measured flow was thus achieved, enabling the effect of customer air bleed on the engine to be determined.

Inlet Temperature to the ECU. An engine inlet temperature (T_1) sensor delivers a signal to the Electrical Control Unit (ECU) for scheduling fan variable guide vanes, fan limiting speed, and maximum turbine delivery temperature. A biased T_1 signal was obtained by fitting a faulty ECU to the engine, which invoked the fail-safe default value of $-39°C$.

Variable Exhaust Nozzle Area. The variable exhaust nozzle of the F404 is scheduled as a function of power lever setting over most of the non-afterburning power range. Close to maximum dry power the turbine delivery and fan speed limiting schedules are encountered. At this, and higher power settings, the exhaust nozzle area is adjusted by the ECU to maintain the scheduled limits. The position of the nozzle actuators is sensed by a linear variable differential transformer (LVDT) and transmitted to the ECU. The actual nozzle area can be adjusted independently of the signal from the LVDT to create a bias error in the sensed position of the actuators. Such a bias was introduced as part of this test program to produce an error equivalent to an increase of 5 percent in the nozzle throat area.

Data Preparation

Data processing began by correcting the raw data to standard day temperature and pressure conditions. During the test program the ambient temperature did not depart from the standard day value by more than 6°C so that temperature lapse rate effects on the measured parameters would be less than 0.5 percent (Faragher, 1989). Compressor rotor speed is usually corrected to compressor inlet conditions. However, compressor inlet temperature is not available to the IECMS in the F404, and consequently fan inlet temperature was substituted.

Before the data were analyzed, filtering was applied to the time histories of both steady-state and transient data. This consisted of a median filter for removing spikes and a mean filter for reducing excess measurement noise. The level of filtering was chosen to achieve the required averaging effect without altering the form of the transient response (Figs. 2*a*, *b*). Subsequent smoothing of the transient data within the specified capture window was achieved using a fourth-order polynomial algorithm as indicated in Fig. 2(*c*).

These processed data were then analyzed for the effect of faults by plotting engine parameters against each other. The "cross-plotting" removes the temporal dependence and hence the need to synchronize the starting times of any two accel-

Downloaded 02 Jun 2010 to 171.66.16.122. Redistribution subject to ASME license or copyright; see http://www.asme.org/terms/Terms_Use.cfm

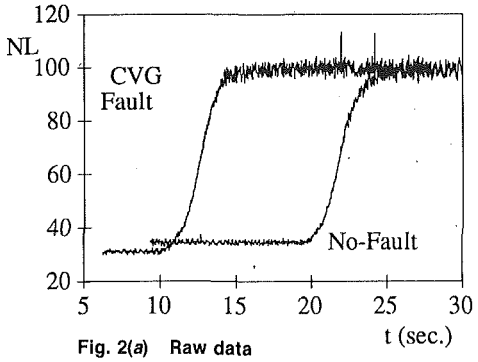


Fig. 2(*a*) Raw data

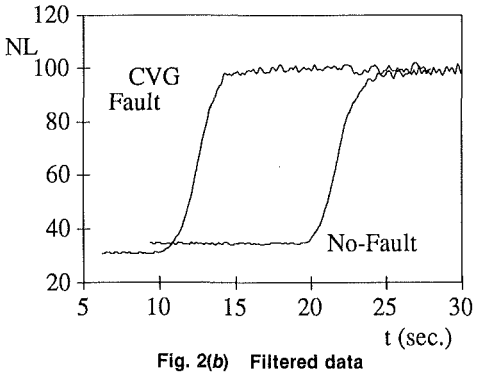


Fig. 2(*b*) Filtered data

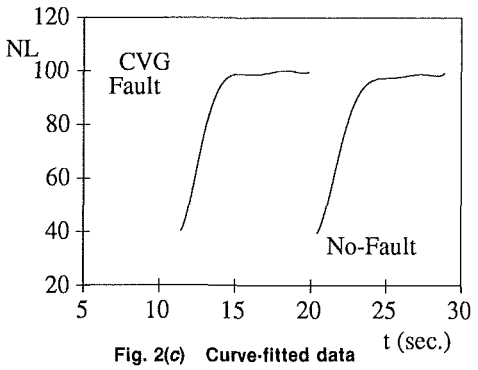


Fig. 2(*c*) Curve-fitted data

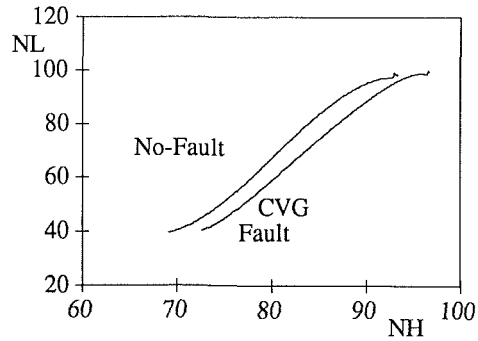


Fig. 2(*d*) Cross-plotted data

erations. As a result fault conditions are more easily detected; for example, the change in spool matching due to a compressor variable geometry fault (Fig. 2*d*).

The steady-state data recorded during the stabilized period at each power setting were averaged to produce a single value per parameter. These values were then used in cross-plots similar to the transient data. By fitting a curve through these points, steady-state performance at a designated reference point could then be found by interpolation.

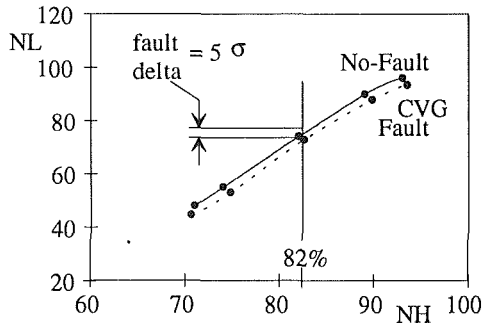


Fig. 3(*a*) Steady state data

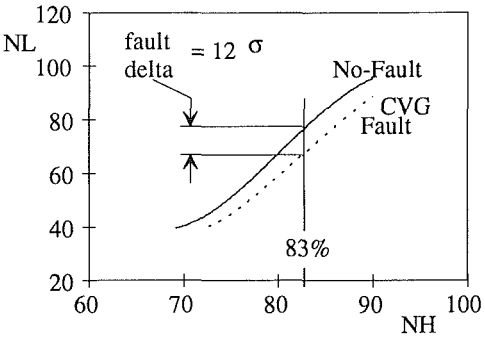


Fig. 3(*b*) Transient data

Fig. 3 Measurement of fault delta

Data Analysis

To determine whether or not a fault condition can be detected, it is necessary to determine the typical level of no-fault scatter in the measured parameters. In the case of the transient data this was done by analyzing a number of take-off records from F/A-18 airfcraft. A total of 14 take-off records taken from one engine were correlated to produce a $\pm 2\sigma$ uncertainty band. This sample does not include the effects of engine-to-engine variability and only a small effect due to performance deterioration, the records covering less than 300 hours of operation. These effects were beyond the scope of this investigation but will be considered in future work using more extensive data obtained from different engines. Unfortunately, equivalent steady-state values were not available from operational IECMS data and therefore production acceptance test records of 35 engines were used to provide this information. The data recorded for all of these engines at a number of power settings, corrected to standard day conditions, were combined and parameter correlations plotted on a single graph to determine the parameter standard deviations.

A fault delta was determined by taking the difference between the fault and no-fault parameter values at one selected reference point. For the steady-state records this was at 82 percent N_H or an EPR of 1.8, corresponding to 60 deg power lever angle in the no-fault case (Fig. 3*a*). This power setting on the F404 occurs at a point in the exhaust nozzle area schedule where the area is at the minimum value, and thus ensures nozzle geometry similarity for the data comparisons. In transient tests however, data were measured at 83 percent N_H or an EPR of 2.3 (Fig. 3*b*). These conditions were chosen to enable comparison with previous work (Faragher, 1989) and because the exhaust nozzle is also closed here during accelerations from ground idle. The difference between the steady-state and transient EPR reference conditions is the result of the change in the compressor running line during transient operation.

A normalized fault delta was computed by dividing the fault delta by the corresponding no-fault standard deviation. A fault

Downloaded 02 Jun 2010 to 171.66.16.122. Redistribution subject to ASME license or copyright; see http://www.asme.org/terms/Terms_Use.cfm

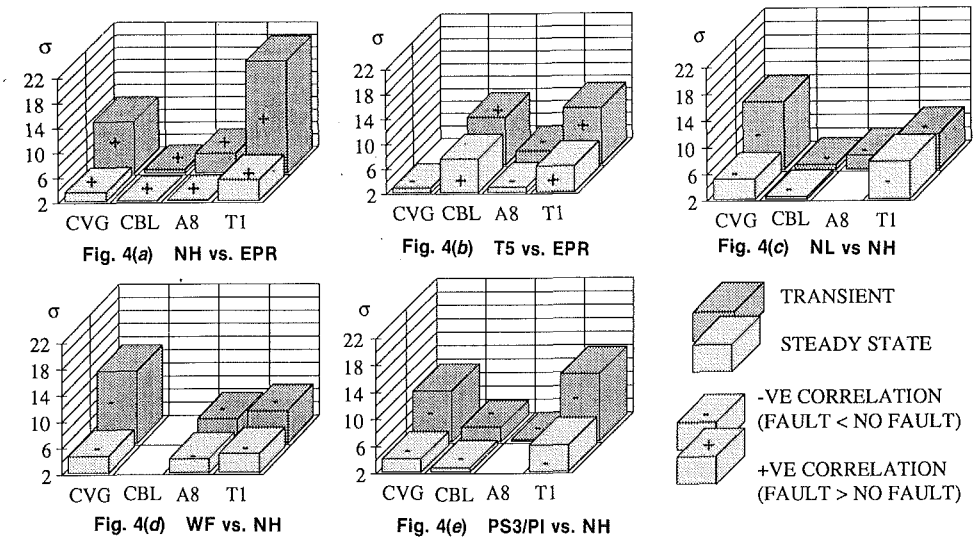


Fig. 4(*a*) NH vs. EPR

Fig. 4(*b*) T5 vs. EPR

Fig. 4(*c*) NL vs NH

Fig. 4(*d*) WF vs. NH

Fig. 4(*e*) PS3/PI vs. NH

Fig. 4 Parameter correlations

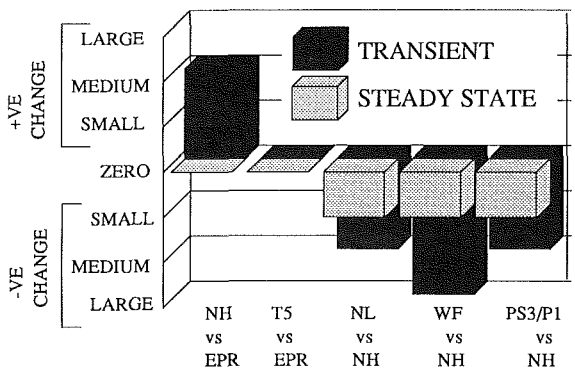


Fig. 5 A comparison of transient and steady-state fault signatures

may be deemed to be detectable if the normalized fault delta is greater than the 2σ no-fault uncertainty. This definition of detectability assumes that the engine no-fault performance closely corresponds to that of the fleet average engine. Ideally, to include all engines within the $\pm 2\sigma$ no-fault uncertainty band, and to avoid possible false fault indications, a 4σ threshold is required. However, such a definition appears to be too conservative and may mask some faults.

Results

The fault correlations derived using the foregoing analysis can then be summarized by collecting together the normalized deltas from various parameter combinations, as indicated in Fig. 4. The four implanted faults for both steady-state and transient records are identified on the horizontal plane. The bar heights represent the magnitude of the parameter change due to the fault measured in no-fault standard deviations. The horizontal base plane represents the $\pm 2\sigma$ level below which the change due to the fault is within the fleet uncertainty.

Compressor Variable Geometry. The nominal compressor variable guide vane schedule was close to the minimum (open) acceptable limit. This enabled an adjustment of sufficient magnitude to produce distinct parameter shifts from nominal. A spool match change is apparent, N_L reduced with respect to N_H (Fig. 4*c*), and the engine pressure ratio, compressor pressure ratio, and fuel flow were all reduced at constant compressor speed (Figs. 4*a*, *d*, and *e*). All of these changes are consistent with the increased throttling effect of CVGV closure on the compressor.

Compressor Discharge Bleed. This fault resulted in significant consistent parameter shifts. The main engine fuel control senses the difference between compressor delivery pressure and bleed air pressure and increases fuel flow to compensate for the effect of air bleed. No change in fuel flow with respect to compressor speed greater than the no-fault uncertainty is apparent (Fig. 4*d*), but a small spool match change is seen (Fig. 4*c*). A small loss of engine pressure ratio is indicated in Fig. 4(*a*) combined with a substantial increase in turbine delivery temperature at constant engine pressure ratio (Fig. 4*b*).

Increased Nozzle Throat Area. The 5 percent increase in the exhaust nozzle throat area also resulted in significant parameter shifts. However, the expected spool speed match change only appeared in the transient data (Fig. 4*c*). The engine pressure ratio and engine fuel flow both dropped relative to compressor spool speed (Figs. 4*a*, *d*) and turbine delivery temperature dropped with respect to engine pressure ratio.

Fan Inlet Temperature Bias. All parameter combinations clearly indicate this fault (Figs. 4*a–e*). The signatures of this fault are critically dependent on the data correction procedure. All parameters are corrected to standard ambient engine inlet conditions using the pressure and temperature measured at the fan entry. For inlet temperature, two sources are available: One is inlet screen temperature measured in the test cell by debri screen-mounted thermocouples, and the other is the T_1 transmitter to the ECU mounted in the fan inlet case. Since the T_1 transmitter is standard engine instrumentation and the signal is therefore available from operational records, this value has been used to reduce the data. The results thus predominantly reflect the effect of the large error in T_1 on parameters corrected by functions of θ_1.

Fault Signatures

Fault signatures can be obtained by collecting together the individual normalized fault deltas. The magnitude of a fault delta can be categorized as being either zero ($<2\sigma$), small (2–6σ), medium (6–12σ), or large ($>12\sigma$), and presented as a bar graph as shown in Fig. 5. It is immediately apparent from this figure that there is a similarity in the shape of the steady-state and transient signatures. That is, the normalized fault deltas in both cases have the same sense. Moreover, the transient parameter correlations are more sensitive to the fault. This same trend is evident in the unnormalized fault deltas as indicated in Table 3.

Signatures obtained from both steady-state and transient

Downloaded 02 Jun 2010 to 171.66.16.122. Redistribution subject to ASME license or copyright; see http://www.asme.org/terms/Terms_Use.cfm

Table 3 Comparison of unnormalized A_8 fault delta values

un-normalised fault delta values	N_H vs EPR (% N_H)	T_5 vs EPR (°C)	N_L vs N_H (% N_L)	W_F vs N_H (PPH)	P_{S3}/P_1 vs N_H -
Transient	1.30	-25	-2.75	-687	-0.50
Steady-State	1.22	-19	-0.07	-403	-0.22

data are shown separately for all faults in Fig. 6. This clearly shows there are significant differences between individual fault signatures.

Discussion

Comparison of the steady-state and transient fault signatures reveal three main features:

(*a*) The trends in the parameter correlation shifts for both the steady-state and transient data are similar;
(*b*) The sensitivity to correlation shift is greater during transient running; and
(*c*) Each fault produces a different signature.

The effect of a fault on the correlations is always of the same sense for both the transient and the steady-state data and is generally greater in the transient data (Fig. 4). The same effect is evident in both the normalized and unnormalized fault deltas. The only exception to this trend is the correlation between T_5 and EPR for the CVG fault.

The fault signatures derived from fault implant tests under SLS test cell conditions can be read across to the aircraft take-off environment with some confidence. This follows from the fact that the observed Mach number at lift-off for the F/A-18 (corresponding to weight-off-wheels and the termination of the IECMS take-off record) is usually of the order of 0.1. Thus the Mach number correction needed to enable strict comparisons to be made between the test cell data and the aircraft take-off results will be small. Moreover, although the performance level of the engine is affected by installation, it is felt that the actual fault deltas will be largely unchanged. The normalized values on the other hand will tend to take these factors into account.

Ideally, it would have been advantageous to have access to steady-state engine data derived from ground-runs in the aircraft to obtain no-fault parameter uncertainties equivalent to those used for the transient data. As there is no opportunity to do this in the normal RAAF operating environment, dedicated tests would be necessary. Dedicated aircraft tests, because they are expensive and time consuming, could not be justified. It was therefore convenient to substitute the production test cell data for this purpose. The resultant parameter uncertainties derived in this way are believed to be representative of the installed aircraft values.

Conclusions

This study has shown that each implanted fault can be characterized by a signature derived from the resulting parameter correlation changes. Furthermore, the signatures derived from either steady-state or transient data records have a similar form.

The observed performance changes caused by the faults have been compared to the statistical uncertainty of no-fault data, obtained from RAAF operational records in the case of transient data, and from new engine acceptance test records in the case of steady-state data. These normalized results show that

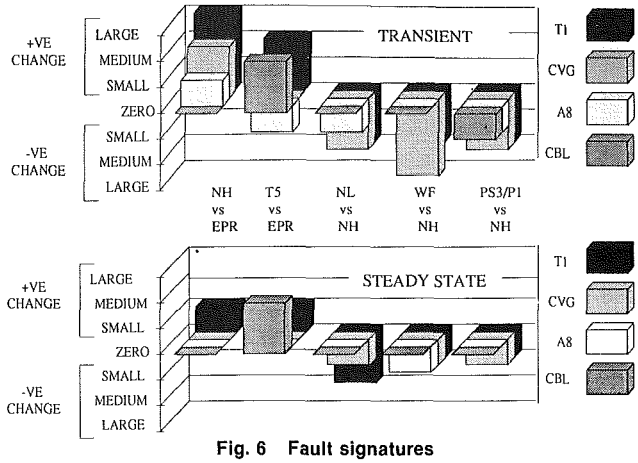


Fig. 6 Fault signatures

the transient records are more sensitive to the implanted faults. This same trend was also observed in the unnormalized fault deltas. Moreover, in both cases, the incremental changes in the parameter correlations are of the same sense for both transient and steady-state operation.

The results are encouraging for the proposed use of on-board engine condition data records to diagnose faults that result in engine performance deterioration. The effect of a fault is more easily detected from transient records; however, both transient and steady-state data sources appear to contain the same essential fault information. Further work is currently underway to study the effects of different fault magnitudes and both the effect of engine-to-engine variability and installation effects.

Acknowledgments

The authors wish to acknowledge the support of the RAAF and the contributions of ARL colleagues Mr. Andrew Vivian, Mr. Graeme Wells, and Mr. David Dyett throughout the engine test program.

References

Doane, P. M., and Kinley, W. R., 1983, "F/A-18 Inflight Engine Condition Monitoring System (IECMS)," Paper No. AIAA-83-1237.

Faragher, J. S., 1989, "F/A-18 Engine Transient Data Analysis for Engine Condition Assessment," ARL-AERO-PROP-TM-466.

General Electric, 1980, "F404 Training Guide," Aircraft Engine Group, Lynn, MA.

Henry, J. R., 1988, "CF-18/F404 Transient Performance Trending," AGARD CP No. 488, Paper No. 37, Quebec City, Canada.

MacLeod, J. D., Taylor, V., and Laflamme, J. C. G, 1992, "Implanted Component Faults and Their Effects on Gas Turbine Engine Performance," ASME Journal of Engineering for Gas Turbines and Power, Vol. 114, pp. 174–179.

Merrington, G. L., 1989, "Fault Diagnosis of Gas Turbine Engines From Transient Data," ASME Journal of Engineering for Gas Turbines and Power, Vol. 111, pp. 237–243.

Merrington, G. L., and Faragher, J. S., 1989, "Fault Diagnosis and Performance Assessment of the F404 Engine Using Transient Data," *The Australian Aeronautical Conference 1989*, The Institution of Engineers, Australian National Conference Publication, No. 89/4 Melbourne, pp. 269–275.

Merrington, G. L., 1991, "Engine Fault Diagnosis: Current Status and Future Trends," Paper No. 12B-1, Vol. 2, *Proceedings of the International Aerospace Congress*, Melbourne, pp. 399–408.

Muir, D. E., Rudnitski, D. M., and Cue, R. W., 1988, "CF-18 Engine Performance Monitoring," AGARD CP No. 488, Paper No. 7.

Streatfeild, D. K., 1988, "Development and Installation of an Instrumentation Package for the GE F404 Investigative Testing," ARL-AERO-PROP-TM 466.

Downloaded 02 Jun 2010 to 171.66.16.122. Redistribution subject to ASME license or copyright; see http://www.asme.org/terms/Terms_Use.cfm

The Effect of Compressor Rotor Tip Crops on Turboshaft Engine Performance

P. C. Frith
DSTO Aeronautical Research Laboratory,
Melbourne, Australia

The results from an experimental study into the effect of compressor rotor tip clearance changes on the steady-state performance and stability margins of a free-power turbine turboshaft engine are presented and discussed. This work was directed at the development of methods to diagnose engine condition from gas path measurements. It was found that the normal production suite of engine instrumentation was able to measure the deterioration in engine performance due to the implanted compressor degradation and the resultant deviations in the measured parameters from their respective nominal baselines do provide useful indicators of engine condition.

Introduction

Modern aircraft gas turbine engines are modular in construction and maintained on an "on-condition" basis. Recent developments in modular construction have greatly facilitated the quick and easy replacement of suspect modules and accessories. What has lagged behind is the implementation of engine health monitoring methods to initiate the original engine/module removal and to correctly isolate the fault to a specific module. To overcome this deficiency techniques are being developed at the Aeronautical Research Laboratory to diagnose engine gas path condition. The approaches taken have involved both the development of predictive aerothermodynamic models and the experimental implantation of common faults to help develop a set of fault signatures (Merrington, 1989).

The work reported here addresses the experimental portion of a study into the diagnosis of long-term deterioration in engine performance due to compressor degradation. Compressor degradation was represented by a series of rotor blade tip crops to the axial stages of a combined five-stage axial and one-stage centrifugal compressor. The tests involved crops to two single axial stages, the first and fifth, followed by simultaneous crops to all five axial stages.

The objectives of the experiments were: first, to determine the sensitivity of engine steady-state performance and stability margins to rotor tip clearance changes in the axial compressor stages; second, to determine the adequacy of the normal production set of engine instrumentation to provide a reliable indication of the resultant degradation; and third, to provide a data base against which the predictive models being developed to isolate compressor degradation can be validated.

Contributed by the International Gas Turbine Institute and presented at the 37th International Gas Turbine and Aeroengine Congress and Exposition, Cologne, Germany, June 1-4, 1992. Manuscript received by the International Gas Turbine Institute February 6, 1992. Paper No. 92-GT-83. Associate Technical Editor: L. S. Langston.

Compressor Degradation

Over the operating life of the engine, the compressor performance will degrade:

(*a*) due to the ingestion of airborne particles causing fouling, corrosion, erosion and/or foreign object damage, and

(*b*) due to engine transients and variations in flight loads causing blade tip and seal rubs.

The rate at which the compressor component and hence engine performance degrades will be dependent on the aircraft's mission profile, the severity of the operating environment, the presence or lack of inlet particle filters/separators, and the use of performance recovery procedures such as water washes, etc.

Erosion and tip rubs introduce changes to the flow path geometry of the compressor, in particular, to the blade profiles and the rotor tip clearances. A study of performance deterioration of commercial high-bypass ratio turbofan engines showed that approximately one half of the long-term deterioration of compressor performance was attributable to increased blade tip clearances (Mehalic and Ziemianski, 1980). In helicopter engines the erosion/burring of the first stage blades and blade tip clearance changes were identified as major performance loss mechanisms (Przedpelski, 1982). The sand ingestion studies of Tabakoff (1987) for a five-stage axial compressor of a helicopter engine and those of Batcho et al. (1987) for both the high and low-pressure axial compressors of two twin-spool engines showed that the severity of the resultant erosion increased toward the latter stages of the compressor. Furthermore, the compressor blade erosion was greatest at the leading edge tip corners. From the above, it was decided to represent compressor degradation by cropping the tips of the rotor blades in the axial compressor stages.

The topic of tip clearance effects in axial turbomachinery has received much attention in the literature (Sieverding, 1985). As a result, the basic mechanisms of tip clearance flows and the general effect of tip clearance changes on stage and overall

Copyright © 1994 by ASME
Downloaded 02 Jun 2010 to 171.66.16.122. Redistribution subject to ASME license or copyright; see http://www.asme.org/terms/Terms_Use.cfm

compressor performance are well understood. In this study, the tip clearance changes were introduced within an engine test rig, as distinct from a compressor rig, where the interpretation is further complicated by the matching constraints imposed by the other engine components.

As stated in the Introduction, one objective of the present work was to investigate the adequacy of the normal production set of engine instrumentation in assessing engine degradation due to tip crops. However, interstage compressor probes were also included to help validate the models being developed to predict the effect of compressor degradation on engine performance. These models go down to the individual stage level because the mechanisms of erosion, etc., produce uneven and progressive geometry changes throughout the compressor. The approach being followed revolves around the generation of a degraded compressor component map. It uses semi-empirical correlations to model the effect of degradation on the individual axial stage characteristics and combines these into the total compressor map via an axial stage-stacking method and an off-design centrifugal compressor model. The degraded compressor map is then introduced into a component based, aerothermodynamic engine model to generate the steady-state operating line characteristics.

Engine Test Rig

The tests were carried out on a Lycoming T53-L11 turboshaft engine, which was installed in the Small Engines Test House at the Aeronautical Research Laboratory. The main aerothermodynamic components of the engine are: a combined five-stage axial and one-stage centrifugal compressor, a reverse flow annular combustion chamber, a single-stage gas generator turbine, and a free-power turbine. At take-off, the engine produces a rated power of 820 kW (1100 SHP) at an output shaft speed of 6600 rpm.

The T53-L11 compressor configuration—a combined axial centrifugal—is similar to most modern helicopter engines. The main differences are the high aspect ratio blade design and the absence of variable inlet guide vanes or stator vanes. The compressor was designed to provide an overall pressure ratio of 6.2 with a mass flow of 4.9 kg/s at a spool speed of 24,600 rpm. At the design point, half the pressure rise is obtained from the five axial stages and the other half from the centrifugal stage. Essentially, this ratio holds across the entire engine operating range. Compressor interstage bleed is provided aft of the fifth-stage double row exit guide vanes. Some six percent of the compressor air is removed continuously from ground idle (50 percent) to just above flight idle (68 percent) with the bleed band fully closed at approximately 73 percent of the engine reference speed of 25,100 rpm.

The relevant first and fifth-stage rotor blade dimensions are given in Table 1. Each stage used NACA 65 series constant chord blades. The nominal tip clearances in each of the five stages were on average 0.9 mm, i.e., 1.8 percent of the first-stage blade height, and fell within the limits specified by the overhaul manual, 0.5 mm to 1.0 mm.

The only gas path parameters normally monitored on the T53 engine are engine (gas generator) speed, output shaft speed, exhaust gas temperature, and output shaft torque. Additional parameters measured in the test cell were engine fuel and air flow, as well as total temperature, total pressure, and static pressure at the compressor outlet, the axial compressor outlet, and each axial stage outlet. Also, vibration accelerometers were located at the compressor inlet housing and compressor outlet casing to monitor any vibration level changes induced by the tip crops.

All the parameters were automatically recorded on the cell's data aquisition system, a DEC LSI-11 based system. The system was set up to measure simultaneously 32 analogue signals and 8 pulse-rate signals at a sampling rate of 32 Hz. The signals from the pressure transducers and temperature thermocouples were recorded in volts and the signals from the fuel flow meters and spool speed optical tachometers were recorded as frequency counts. The results were converted to engineering units via calibration factors.

Table 1 First and fifth-stage rotor dimensions

	First stage	Fifth stage
Blade Height	48.7 mm	26.2 mm
Chord	22.7 mm	17.2 mm
Mean flow radius	101 mm	105 mm
Number of blades	26	38
Solidity	1.1	1.0

Test Procedures

Tests to establish the effect of tip crops on steady-state performance and stability margins were carried out for each crop. Initially, a comprehensive set of baseline data was obtained for the engine with its production level clearances. These tests were then repeated with the first-stage blades successively cropped by 1.5 mm, 3.5 mm, 5.5 mm, and 7.5 mm beyond the nominal tip clearance, i.e. respectively, 3, 7, 11, and 15 percent of the first-stage blade height. The first-stage blades were then replaced with new blades at the nominal tip clearance. The engine performance baseline was re-established and the tests repeated for the same magnitude crops to the fifth-stage blades, i.e., 3, 7, and 11 percent of the first-stage blade height. On completion, the engine was rebladed with new fifth-stage blades at nominal clearances and the baseline performance again checked. The final test for this report was a crop of 3 percent of the first-stage blade height to all five axial stages. Unless otherwise indicted all further references to the magnitude of the crops will be expressed as a percentage of the first-stage blade height.

The steady-state operating line was measured from ground idle to take-off power. Data were obtained at 2 percent speed increments up to 88 percent engine speed and at 1 percent speed increments thereafter. The engine was stabilized at each test point for 3 minutes prior to taking a 16 second record. For the initial baseline the water-brake load was also varied from full load to minimum load at each engine speed, subject to maximum torque and shaft speed limits. The resultant matrix of loading curves showed that the gas generator parameters at a given corrected engine speed were independent of the water-brake load applied and of the corresponding variations in output shaft speed. Consequently, for the remaining tests, full loading curves were only generated at engine speeds greater than 90 percent, i.e., in the region where engine output power was of primary interest. The loading curves also determined the sensitivity of the free-power turbine parameters affected by the load (i.e., shaft power and exhaust gas temperature) to the value of the shaft speed. This allowed discrimination between changes in shaft power and exhaust gas temperature due to shaft speed fluctuations and those due to tip crops.

The effect of the tip crops on the stability margins of the engine was assessed by carrying out a series of wave-off tests. These tests move the compressor towards surge by overfueling the engine during the acceleration transients. The tests involved a series of rapid decelerations and accelerations, which were carried out by chopping the throttle from maximum to a specified part-power position and then slamming the throttle back to maximum within a one second period. The accelerations were performed from 85, 80, 75, 68 percent (flight idle), 65, 60, and 50 percent (ground idle) engine speed. The technique used to bring about the overfueling was to pressurize the intake air pressure tube on the fuel control unit. The T53-L11 engine was deemed to be acceptable at overhaul if it was surge free at a pressurization of 20 inches of water above atmospheric. Here, the intake tube was pressurized at increments of 10 inches of water up to a maximum of 100 inches of water to help

Downloaded 02 Jun 2010 to 171.66.16.122. Redistribution subject to ASME license or copyright; see http://www.asme.org/terms/Terms_Use.cfm

discern any trend toward surge as the tip clearances were increased.

Data Analysis

Most analyses of stage and compressor performance are based on data obtained at constant corrected spool speed. On compressor component rigs for all speeds and direct coupled turboshaft engines for a single operating speed, the compressor can be moved up a constant speed line toward surge by increasing the load and hence the power turbine inlet temperature. However, for a free-power turbine engine the operation of the gas generator section is independent of the output shaft load. Hence, the compressor is constrained to run at a single compressor-turbine match point for each engine speed. Consequently, the constant-speed operating lines of the compressor characteristic could not be generated and it was appropriate to use the corrected spool speed as the independent parameter on the baseline curves.

The individual parameters were corrected to standard day conditions and plotted against corrected engine speed. Deterioration was indicated by the resultant deviation of the parameter versus speed curves from their respective baseline values at nominal tip clearance. For compressor degradation the complete operating line from ground idle to take-off power is useful whereas for assessing engine performance only the higher power levels, greater than 75 percent normal, are relevant. Consequently, in the performance assessment only the data obtained in the 88 to 98 percent engine speed range was used.

A normal power rating point of 670 kW (900 shp), i.e., the maximum continuous operating point, was chosen as the reference condition. The minimum specification engine achieved this at 94 percent engine speed and 6600 rpm output shaft speed. Data for each parameter versus engine speed plot were fitted by a linear regression fit across the 88 to 98 percent speed range. The parameter value of 94 percent speed was then calculated from the regression equation and expressed as a percentage difference from the nominal parameter value.

Experimental Results

Effect of Reblade to Nominal Tip Clearances. The results obtained from the two tests where the compressor was rebladed to nominal tip clearances after completing the first and then the fifth-stage crops were compared with the original set of parameter baselines. There were no discernible shifts from these original baselines and, consequently, the effects presented below can be attributed to the tip clearance changes and not to some other engine rebuild effect.

Effect on Engine Performance. The test results showed that the majority of the tip crops produced a significant drop in the output power of the engine. Typical deviations from the nominal engine output power versus corrected speed baseline are shown in Fig. 1. It compares the data obtained from the 7 percent crops to the first and fifth stages and the 3 percent crop to all five axial stages with the nominal tip clearance baseline. Both the single-stage crops resulted in a similar 5.5 percent drop in output power at the reference condition of 94 percent engine speed whereas the all-stage crop produced an 8.0 percent drop. The reduction in output power for the individual stage crops is summarized in Fig. 2. In both stages the first crop had little effect on the output power, less than 1 percent, but the latter crops showed a significant loss. The main difference in the results was that the loss in shaft horsepower flattened off for the last two crops of the first stage but not for the fifth stage.

Of the other overall engine parameters, the tip crops reduced the fuel flow and air flow in a similar manner to the output power but had no effect on the exhaust gas temperature. Even with the maximum 11 percent loss in power, which was obtained for the last fifth-stage crop, the corresponding change in exhaust gas temperature was an insignificant 0.6 percent (5°C). The deviations of the various parameters from their respective nominal reference condition are given in Table 2 for the two 7 percent single-stage crops and the 3 percent all-stage crop.

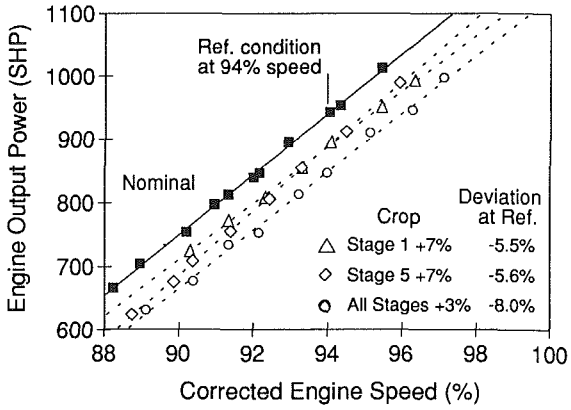


Fig. 1 Typical loss of power due to tip crops

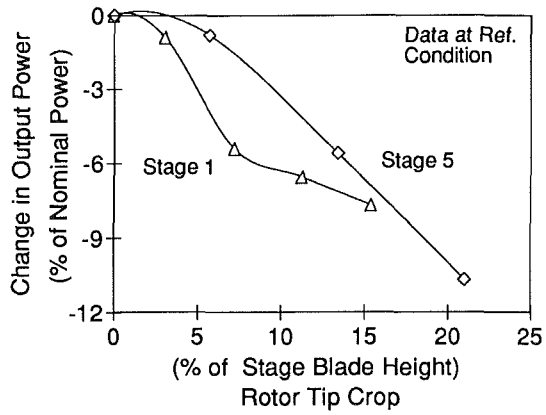


Fig. 2 Loss of power for stage 1 and stage 5 tip crops

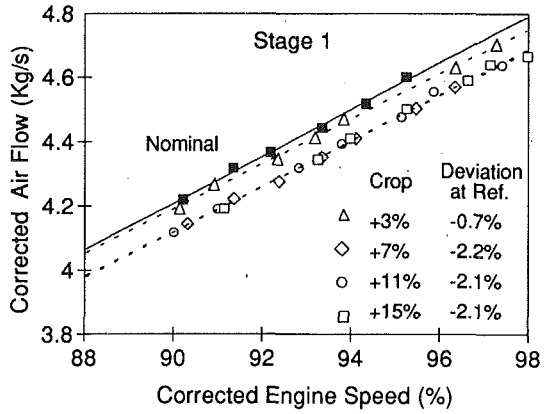
Table 2 Typical engine parameter deviations

Test Crop	Stage 1 7 percent	Stage 5 7 percent	All axial 3 percent
Parameter	Deviation from nominal value (percent)		
Output Power	−5.5	−5.6	−8.0
Exhaust gas temperature	−0.65	+0.6	+0.63
Fuel flow	−3.3	−2.8	−4.6
Air flow	−2.2	−3.6	−4.6

The reductions in air mass flow for each of the stage 1 and stage 5 crops are shown in the corrected air flow versus corrected engine speed plots of Fig. 3. Clearly, for the same size crop, there is a greater reduction in airflow for the fifth-stage crops. Again the main difference between the results for the first and fifth stage is that the data for the second, third, and fourth crops to the first stage fall on the same operating line. The flattening of the output power loss curve of Fig. 2 can be attributed to these last two crops, producing no further reduction in the engine air flow.

Effect on Compressor Performance. The test results showed that the compressor pressure ratio generated at a given corrected speed was progressively reduced as the tip crops were increased. This is illustrated in Fig. 4 for the fifth-stage crops where the last crop (11 percent) produced the maximum reduction in pressure ratio of 4.4 percent at 94 percent engine

Downloaded 02 Jun 2010 to 171.66.16.122. Redistribution subject to ASME license or copyright; see http://www.asme.org/terms/Terms_Use.cfm



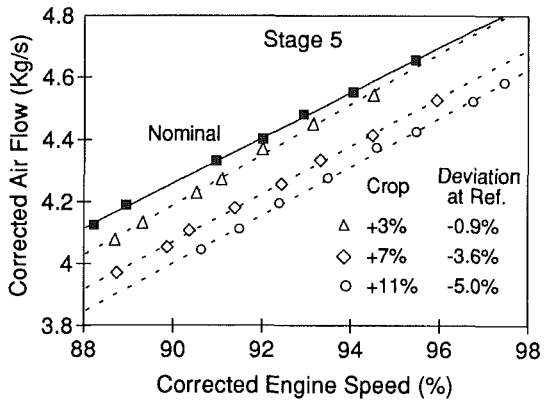


Fig. 3 Comparison of mass flow reduction for stage 1 and stage 5 tip crops

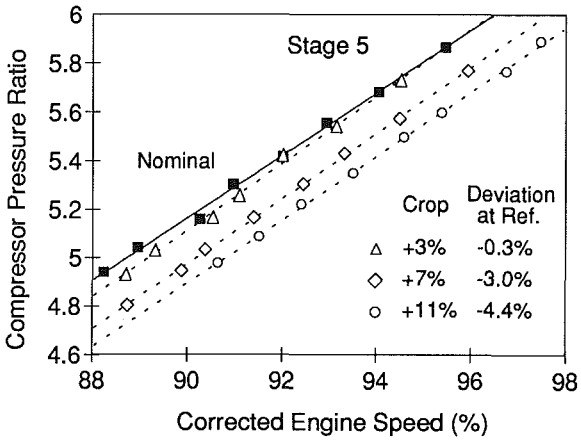


Fig. 4 Reduction in compressor pressure ratio

speed. In contrast, as shown in Fig. 5, there were no significant shifts from the nominal baseline for the corresponding compressor temperatures. Indeed, over the complete test program, the maximum deviation in the compressor temperature was −0.6 percent (3°C). A typical set of compressor parameter deviations is summarized in Table 3.

The test data from the last two fifth-stage crops and the all-stage crop when plotted on the compressor characteristic did show a significant shift of the engine operating line toward the surge line. This is illustrated in Fig. 6 where the complete operating line for the last fifth-stage crop is compared with the nominal tip clearance operating line. Also, the operating line shifts for the three typical crops are given in Table 3. The results for the first-stage crops were different in that all the

Table 3 Typical compressor parameter deviations

Test	Stage 1	Stage 5	All axial
Crop	7 percent	7 percent	3 percent
Parameter overall	Deviation from nominal value (percent)		
Pressure ratio			
total	−2.2	−3.0	−3.8
static	−1.2	−3.0	−3.6
Temperature	−0.6	−0.4	−0.3
Axial			
Pressure ratio			
total	−1.7	−2.5	−2.4
static	−2.0	−5.9	−5.7
Temperature	−0.3	+0.4	+0.3
Characteristic map			
Pressure ratio	+0.9	+2.3	+2.6

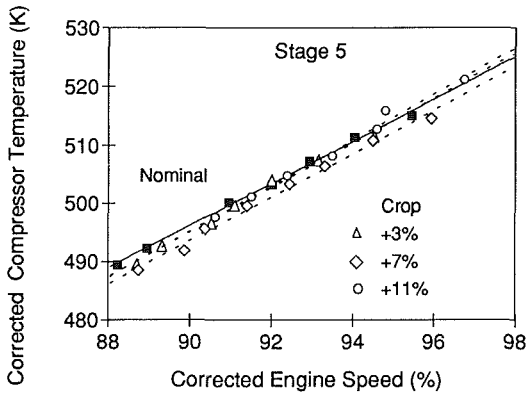


Fig. 5 No shift in compressor outlet temperature

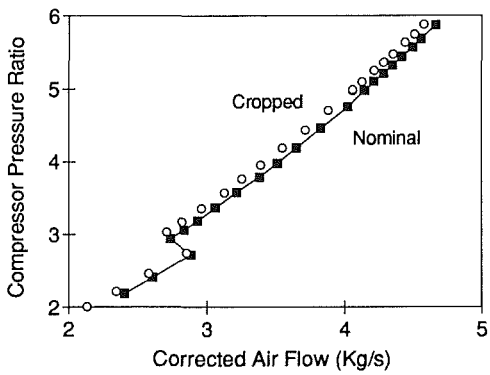


Fig. 6 Positive shift of engine operating line on compressor characteristic

stage 1 crops produced an insignificant, i.e., less than 1 percent, shift in the operating line.

Effect on Axial Compressor Stages. Of the interstage axial compressor probes, the static wall tappings provided the most sensitive and consistent response to the tip crops, and some typical results from these are shown below. Generally, the total pressure probes resulted in similar but less sensitive shifts from the nominal baselines. Again, the total temperature measurements showed no significant deviations from the nominal tip clearance baselines.

The effect of the first-stage tip crops on the ratio of the static pressure at the first stage stator to the total pressure at the engine inlet, from ground idle to take-off speed, is shown in Fig. 7. In the operating power range, 88 to 98 percent engine speed, the curves are linear and there is a monotonic departure from the nominal curve as the tip clearance is progressively increased. The shift at 94 percent engine speed for each crop is given in Table 4. In contrast, as shown in Fig. 7, a much more complex set of data curves were obtained below 88 per-

Downloaded 02 Jun 2010 to 171.66.16.122. Redistribution subject to ASME license or copyright; see http://www.asme.org/terms/Terms_Use.cfm

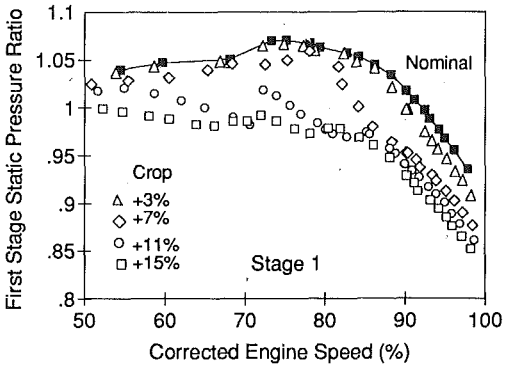


Fig. 7 Shift in first-stage static pressure ratios due to stage 1 crops

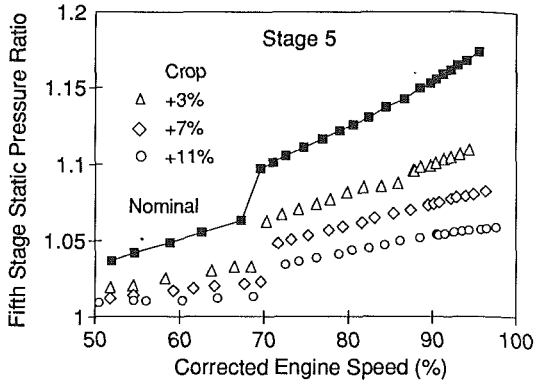


Fig. 8 Shift in fifth-stage static pressure ratios due to stage 5 crops

Table 4 First-stage static pressure ratio deviations

	Deviation from nominal value (percent)		
Crop, percent	Stage 1	Stage 5	All stage
3	−2.1	+1.7	+3.2
7	−5.94	+3.6	
11	−7.09	+4.4	
15	−8.46		

cent speed. The sharp kinks in these curves were confirmed by repeat tests.

The effect of the fifth-stage crops on the static pressure rise across the fifth stage for the entire operating range is shown in Fig. 8. The graph clearly demonstrates significant and readily measurable reductions in the stage pressure rise. The shift at 94 percent speed for each crop is given in Table 5.

As well, in a multistage compressor, the individual stage crops do affect the operating characteristics of the other stages. This is illustrated by a comparison of Figs. 7 and 9, where the nominal first-stage static pressure ratios were reduced by the first-stage crops and increased by the fifth-stage crops. The corresponding shifts at 94 percent speed are given in Table 4. In the case of the 3 percent crop to all five axial stages, the stage static pressure ratios were shifted from their respective nominal values by a positive 3.2 percent at the first stage through to a negative 4.2 percent at the fifth stage. Clearly, the interaction between the various stage crops produces a different stage ratio shift than does the same single stage crop. The above interaction can be related to moves on the individual stage characteristics as a result of the reduction in mass flow through the compressor.

Effect on Engine Stability. The wave-off tests showed that the stability of the engine was affected by the first-stage tip crops. For the nominal clearance and the initial crop (3 percent) the complete set of wave-off accelerations failed to surge the engine up to the maximum pressurization of 100 inches of water on the fuel control intake probe. For the second crop (7 percent), the accelerations from ground idle and flight idle surged the engine at pressurizations of 80 and 90 inches of water, respectively. The remaining accelerations from the higher engine speeds were surge free up to the maximum pressurization. For the third crop (11 percent), the acclerations from ground idle surged the engine at a pressurization of only 20 inches of water, those from flight idle similarly at 20 inches of water, and those from 75 percent engine speed at 40 inches of water. Again, the acclerations from the higher speeds were free of surges. For the last crop (15 percent), none of the wave-off accelerations up to the maximum probe pressurization surged the engine. This last result went against the trend established in the previous tests, that is the engine surging during accelerations from progressively higher engine speeds and lower probe pressurizations as the tip clearance was increased.

The surges induced by the accelerations were not severe enough to prevent the engine from completing its acceleration to full power. A typical set of compressor pressure-time traces obtained for surge on acceleration from 75 percent speed and flight idle are shown in Fig. 10.

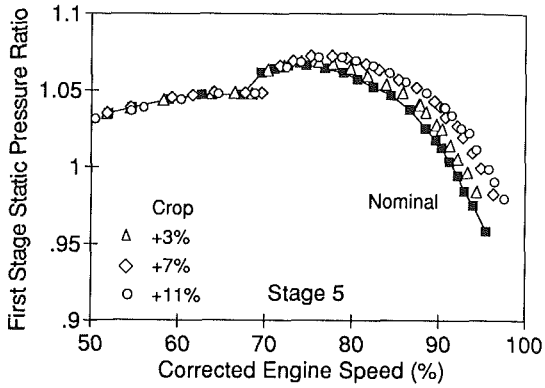


Fig. 9 Shift in first-stage static pressure ratios due to stage 5 crops

Table 5 Fifth-stage static pressure ratio deviations

	Deviation from nominal value (percent)	
Crop, percent	Stage 5	All stage
3	−4.2	−4.2
7	−7.1	
11	−9.6	

In contrast to the results for the first-stage crops, the complete set of wave-off tests for each of the three fifth-stage crops and the single all-stage crop failed to surge the engine.

Discussion

The results showed that a small tip clearance change to all five axial stages produced a greater performance loss than a very large crop to any one single stage. The effects of the initial 3 percent of first-stage blade height crop to either the first or fifth stage were only significant at the interstage level, whereas the same crop to all five stages produced near-maximum deviations from the various nominal parameter versus speed baselines. The magnitude of the deviations were second only to the largest fifth-stage crop (11 percent).

Although measured primarily to validate the stage-stacking models, the interstage static wall pressure tappings did provide the most sensitive indication of rotor tip clearance changes. Even the smallest single-stage crops produced significant reductions in the stage static pressure ratios. However, as demonstrated by the all-stage crops, the use of the resultant deviations as condition monitors will not be straightforward, since the behavior of the individual stage static pressure ratios

Downloaded 02 Jun 2010 to 171.66.16.122. Redistribution subject to ASME license or copyright; see http://www.asme.org/terms/Terms_Use.cfm

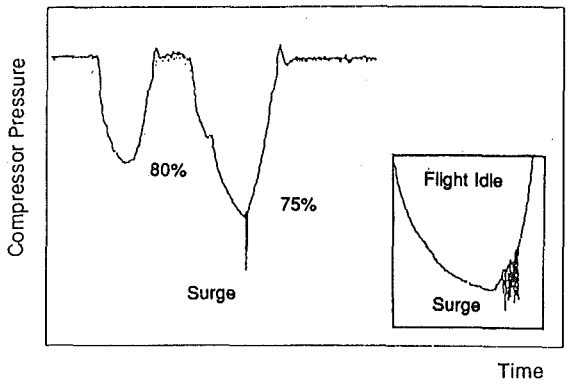


Fig. 10 Typical surges on wave-off compressor pressure-time traces

for a given stage crop was different from that obtained when combined with other stage crops. Consequently, a proper interpretation of the interstage operating line shifts will require knowledge of the individual stage characteristics and how they stack together to give the overall compressor performance. This is being pursued in the development of the predictive models, in particular, through the use of a stage-stacking technique.

On the basis of the wave-off tests, only the first-stage crops adversely affected the stability of the engine. The mildness of the resultant surges may be attributed to the fact that the automatic opening of the bleed band during the acceleration was sufficient to stabilize the engine and allow acceleration to full power. Surge on engine acceleration from low-speed regions has been attributed to discontinuities in the performance characteristics of the front stages of multistage axial compressors. The series of distinct kinks found in the low-speed region of the first stage operating curves of Fig. 7 may indicate the first-stage tip crops are producing such discontinuities in the stage characteristic and therefore more prone to surge.

From the point of view of engine health monitoring the most interesting result was the lack of sensitivity of the temperature measurements to the implanted compressor degradation. Haq and Saravanamuttoo (1991) found a similar result from measurements of compressor fouling. This has implications for the Health Indicator Test (HIT) check, which is used by many helicopter operators. The HIT check essentially establishes an exhaust gas temperature versus corrected engine speed baseline and trends the day to day deviations from it. Typically, on the T53, a shift greater than 20°C would prompt a maintenance notification and a shift greater than 30°C would result in the aircraft being grounded until troubleshooting could determine the cause. In these tests, the tip crops to the compressor rotor blades produced performance losses as great as 12 percent with a corresponding deviation in exhaust gas temperature of only 5°C. Clearly, for the compressor degradation investigated here the HIT check would not be an appropriate indicator of overall engine health.

Most aircraft turboshaft engines have a measure of output shaft horsepower, via output shaft speed and torquemeter gages, and this parameter proved to be the best indicator of overall performance loss in this investigation. In addition, air flow, fuel flow, and compressor pressure ratio, both static and total, provided a useful set of parameters to indicate performance degradation. Of these, air flow reduction was the next best measure of performance degradation. While airflow is unlikely to be measured on an operational engine, efforts should be made to include it on engine test stands that are used for intermediate or depot level maintenance testing.

The tests have produced a set of parameter deviations from the nominal baseline values, which represent fault signatures for the effect of one type of compressor degradation on engine performance. However, these signatures are not necessarily unique. For example, turbine degradation can also result in reductions of compressor pressure ratio and air flow due to the rematching of the gas generator compressor and the degraded turbine components. So while the measurements do provide an indication of degradation, there is still the problem of isolating the degradation to a specific module. Possibly, as indicated by the above results, the simplest signature for isolating cold end degradation from hot end degradation would be a significant drop in output power without a similar change in either the compressor temperature or exhaust gas temperature. In contrast, an indicator of hot end degradation would be a significant shift from the baseline variation of exhaust gas temperature versus corrected engine speed.

Conclusions

The experimental program has demonstrated the effect of rotor tip clearance changes to the axial stages of a combined axial centrifugal compressor on the steady-state performance and stability of a free-power turbine turboshaft engine.

The majority of the engine parameters were sensitive to the rotor tip crops and the resultant deviations from their respective baseline values at nominal tip clearance do provide a useful indicator of engine condition. The effects of single-stage crops were not evident until a crop greater than 3.0 percent of the first-stage blade height was made whereas the same level of crop to all five stages produced more than an 8.0 percent drop in power.

The present results show that the Health Indicator Test, commonly used in helicopter engines, is not a good indicator of overall engine condition when operating with a degraded compressor.

Acknowledgments

The author would like to thank Mr. A. Vivian, Mr. A. Godbold, Mr. D. Dyett, and Mr. G. Wells of the Aeronautical Research Laboratory for their help in developing and operating the engine test rig.

References

Batcho, P. F., Moller, J. C., Padova, C., and Dunn, M. G., 1987, "Interpretation of Gas Turbine Response Due to Dust Ingestion," ASME JOURNAL OF ENGINEERING FOR GAS TURBINES AND POWER, Vol. 109, pp. 344–352.

Haq, I., and Saravanamuttoo, H. I. H., 1991, "Detection of Axial Compressor Fouling in High Ambient Temperature Conditions," ASME Paper No. 91-GT-67.

Mehalic, C. M., and Ziemianski, J. A., 1980, "Performance Deterioration of Commercial High-Bypass Ratio Turbofan Engine," SAE Technical Paper Series 80118.

Merrington, G. L., 1989, "Fault Diagnosis of Gas Turbine Engines From Transient Data," ASME JOURNAL OF ENGINEERING FOR GAS TURBINES AND POWER, Vol. 111, pp. 237–243.

Przedpelski, Z. J., 1982, "The T700-GE-700 Engine Experience in Sand Environment," presented at the American Helicopter Society, Rotary Wing Propulsion System Specialist Meeting, VA.

Sieverding, C., 1985, "Tip Clearance Effects in Axial Turbomachines," Lecture Series 1985-05, Von Karman Institute for Fluid Dynamics, Rhode-St-Genese, Belgium.

Tabakoff, W., 1987, "Compressor Erosion and Performance Deterioration," ASME *Journal of Fluids Engineering*, Vol. 109, pp. 297–306.

Downloaded 02 Jun 2010 to 171.66.16.122. Redistribution subject to ASME license or copyright; see http://www.asme.org/terms/Terms_Use.cfm

H. R. Simmons

A. J. Smalley

Southwest Research Institute,
San Antonio, TX 78228

R. W. Frischmuth
Electric Power Research Institute,
Palo Alto, CA 94303

G. Lapini
CISE,
Segrate, Italy

G. Robinson
Westinghouse Electric Corp.,
Orlando, FL 32826

Tools for Diagnosing Case Deflections and Alignment on a Power Utility Combustion Turbine

This paper discusses development, installation, and analysis of instrumentation systems for reliably measuring casing, thermal distortion, and alignment deviation on a large combustion turbine in power utility service. A variety of redundant measurement systems were installed to document casing distortion during the cool-down period after firing. The operating principles of each measurement system are described and presented with the rationale developed for installing and locating sensors. A vertical deflection sensor used for casing bow and bearing misalignment measurement is highlighted in the paper to illustrate its potential for use in other investigations. Additional sensors used include an array of shaft proximity probes, blade tip proximity probes, thermocouples, and axial growth probes. A measurement system for casing ovalization was developed using LVDTs mounted from a thermally stabilized ring. An automated data acquisition system was developed and installed to facilitate the recording of turbine cool-down events over the complete operating season without the need for constant on-site attention. Preliminary results define the turbine cylinder bow and ovalization response during the cool-down event following normal unit operation and correlated casing distortions with thermal gradients.

Introduction

Casing Distortion is a phenomenon common to all combustion turbines due to uneven heat transfer during cool-down following fired operation (Scalzo et al., 1983). Most combustion turbine designs allow for casing distortion in establishing minimum blade tip clearances, interstage seal clearances, fits at diaphragm slots, bearing alignment, and many other internal clearances and fits. Casing distortion of some combustion turbines affects shaft centerline position relative to ground reference, which controls alignment to adjacent components. A test program that provides casing deflection and shafting alignment information on a representative turbine should be of interest both to turbine designers and to turbine operators.

This paper will present preliminary casing distortion results from a research program sponsored by the Electric Power Research Institute. The major objective was to investigate and document the causes of blade tip rubbing in the compressor section of early model Westinghouse 501 combustion turbines (Smalley and Simmons, 1988). Results from one unit at the Baltimore Gas and Electric Perryman Combustion Turbine Generating Station will be presented along with corroborating data from independent research on a similar turbine in Italy.

The uneven cooling that causes casing distortion occurs due to a number of factors; chief among these are stratification of internal air creating a thermal gradient from top to bottom, uneven distribution of air due to convection currents, and uneven or inadequately installed external insulation. Additional factors include built-in restraints due to supports and external piping. While combustion turbine design undoubtedly controls many major factors affecting casing distortion, careful control of start-up, cool-down, and turning gear procedures can play a substantial role in mitigating rub and wear damage. The manufacturer of the turbine tested recommends a procedure, using the starter motor, to enhance uniform cooling after shutdown for this purpose.

Casing rub patterns suggest that blade tip rubs are likely a result of casing distortion involving upward bowing of the entire turbine cylinder and inward ovalization along the horizontal split line. Blade tip rub patterns suggest that rotor bow deflections may also play a part. On the basis of these indications, a measurement system was designed to concentrate on defining casing distortion, journal lift, and rotor deflections. Instrumentation was specifically selected and positioned to quantify casing bow and ovalization. To measure rotor motions, proximity probes were installed at locations close to bearings, at positions outboard of the bearings, and at compressor blade tip locations midspan between bearings. Sensors were installed to record rotor and cylinder axial growth. External surface-mounted thermocouples were positioned around the case to quantify circumferential and axial temperature gradients and gradients radially outward along the flanges. In addition, internal temperatures and unit load were recorded

Contributed by the International Gas Turbine Institute and presented at the 37th International Gas Turbine and Aeroengine Congress and Exposition, Cologne, Germany, June 1–4, 1992. Manuscript received by the International Gas Turbine Institute February 20, 1992. Paper No. 92-GT-179. Associate Technical Editor: L. S. Langston.

Copyright © 1994 by ASME
Downloaded 02 Jun 2010 to 171.66.16.122. Redistribution subject to ASME license or copyright; see http://www.asme.org/terms/Terms_Use.cfm

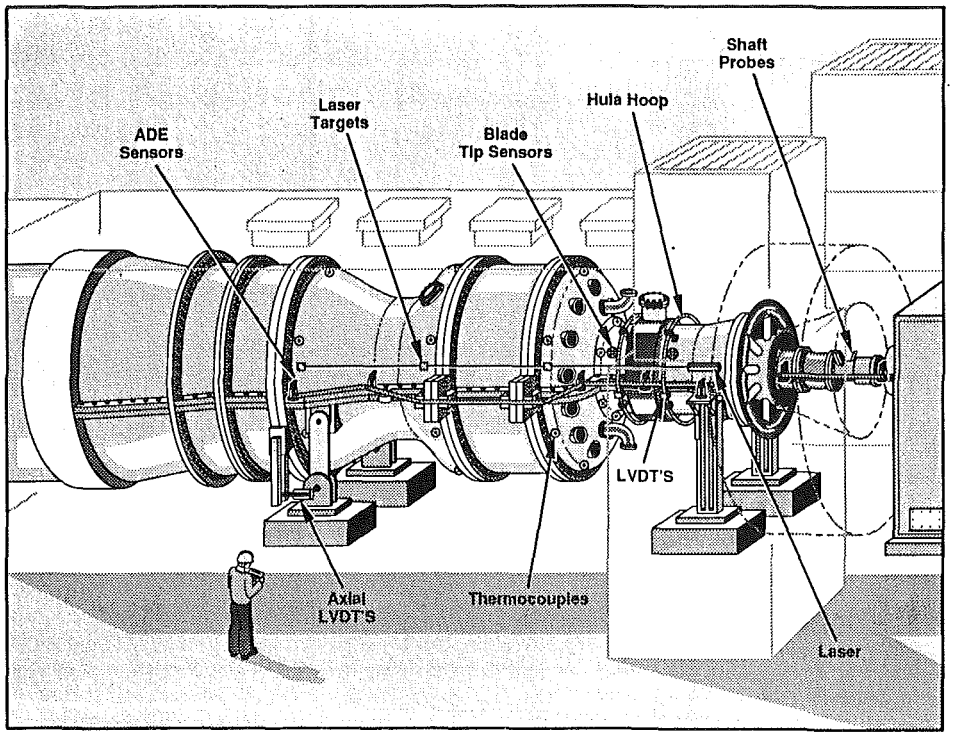


Fig. 1 Sensor locations for casing distortion measurements

to correlate casing deformations with variations in operating and environmental conditions.

A remote access data acquisition system was designed to record data continuously at predetermined intervals throughout the various operational events. Thus, normal peaking power operations could continue without specific test requests that would interfere with the utility companies' economic objectives and without the need for on-site testing personnel.

The operational status of each measurement system is described herein; all sensors have been mounted and calibrated, and operational testing has been partly completed.

Measurement Systems

The measurement systems are summarized in Fig. 1. Selection of the instrumentation and development of data acquisition techniques were based on years of experience in turbomachinery experimental programs (Simmons and Smalley, 1990). While many of the instrumentation techniques used standard transducers, some of the measurements needed special adaptations of commercially available transducers or, in one case, the development of a custom sensor. The following describes the operating principles of the measurement systems installed.

Case Bow Deflection. The primary system for measuring casing bow (banana deflection) used seven vertical displacement instruments known as ADE (Electronic Differential Altimeter) sensors. The ADE sensors (Lapini et al., 1989) were developed to measure vertical bearing and casing alignment variations in turbogenerators and are used quite extensively in Italy at power plants and on civil structures such as dams (Clapis et al., 1982). The system works by the communicating vessel principle where a number of small vessels (cups) are interconnected by horizontal channels (Fig. 2). The cups are mounted to the turbine and partially filled with a special low surface tension liquid; channels allow the levels to equalize between all cups. Each cup has a floating target and a proximity probe that produces a signal proportional to its liquid level.

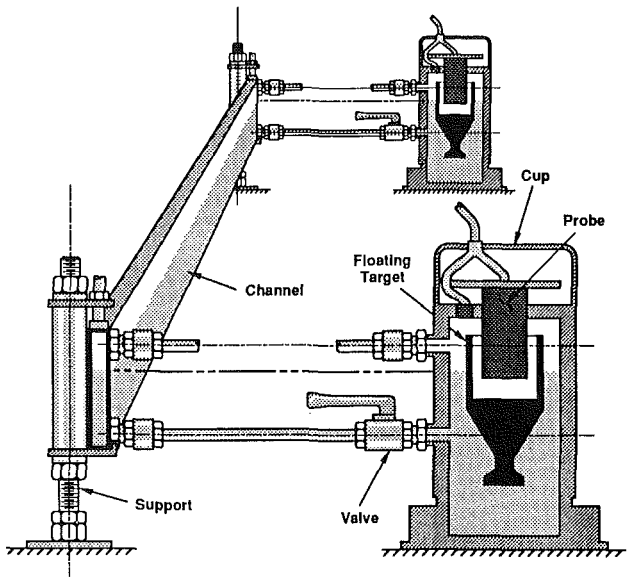


Fig. 2 Schematic of ADE sensors for vertical deflection measurements

Compensation for liquid density variation is provided by a built-in temperature sensor and appropriate electronics. The ADE sensors have a full measurement range of 5 mm (0.197 in.) with an accuracy of ±0.02 mm (0.001 in.).

Seven ADE sensors (Fig. 1) are mounted on the engine horizontal centerline near the split flange at axial locations close to the bearings, engine mounting points, midcompressor, combustor, and midturbine case. Two sensors are mounted near the bearings at the compressor end of the turbine and generator inboard side in order to detect any misalignment between these components. Zero calibration is established at the initial alignment condition when all components are at ambient temperature. Deviations from the zero calibration represent deflections of the transducers relative to one another.

Downloaded 02 Jun 2010 to 171.66.16.122. Redistribution subject to ASME license or copyright; see http://www.asme.org/terms/Terms_Use.cfm

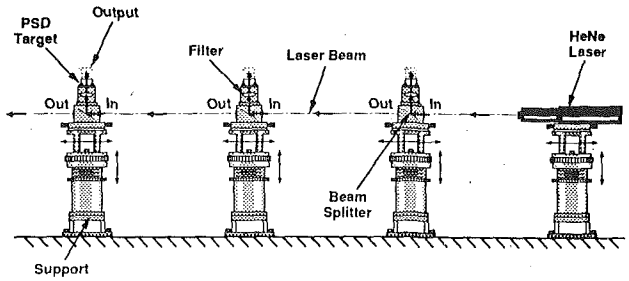


Fig. 3 Laser alignment components

To supplement the ADE vertical displacement sensors, a custom-designed laser alignment system was installed to detect deviations in both the vertical and horizontal directions at three points between the front and rear engine mounts. The system (Fig. 1) consists of a fixed 12 mW HeNe laser mounted just above the horizontal centerline on the front turbine support with targets mounted near the rear engine support and near the two large-diameter flanges at either end of the combustor case. The targets (Fig. 3) were constructed with 30/70 beam splitters and dual axis Position Sensitive Detectors (PSDs). The PSDs and amplifying electronics produce voltage signals proportional to vertical and horizontal deflections of the laser beam from the centers of each target. Micrometer-type adjustments were built into each target and laser support to provide for vertical and horizontal alignment and for target calibration. As the laser required "line-of-sight" alignment, all components had to be exactly the same distance from the turbine centerline. Past SwRI experience (Smalley, 1985) showed that shielding of the laser beam from significant convection currents is necessary to avoid noise created by beam refraction and dust particles. A low pass filter is incorporated into the electronics to reject the remaining noise. The vertical and horizontal measurement capability provided a means both for confirming the ADE sensor vertical signals and for detecting distortions along the horizontal plane.

Similar tests on combustion turbine engines indicated that special cooling techniques are required for sensors located near the hot section of the turbine (Clapis et al., 1982). An insulation and cooling water system was designed and installed to minimize high-temperature extremes of both the ADE and laser target sensors. Each sensor mount incorporated a 1-in.-thick machinable ceramic spacer to insulate the sensors from direct conduction from the hot turbine cases. Coils of 1/4-in. copper tubing, fiberglass insulation, and aluminum foil were wrapped around each sensor and its mount at locations from the combustion chamber aft in order to protect the delicate components as much as possible. Copper tubing, fiberglass, and aluminum foil were also wrapped around the interconnecting channels of the ADE system. The closed-loop cooling water system consisted of a circulating pump and a 200 gallon tank with environmentally safe ammonium phosphate solution coolant.

All seven ADE sensors installed appear to work properly; i.e., they stay within linear range during most of the test program. Initially acquired data via telephone modem indicated a leakage of fluid from the connecting channels, which was subsequently corrected. The ADE has been a most reliable system over ten months of testing after initial problems associated with the high-temperature combustion turbine environment were corrected.

The laser and two installed targets of the laser alignment system provided good operating trends during the early part of the program. A laser beam collimator measurably improved system performance at the 25-ft range and the target adjustment features provided a rugged, easily installed system.

Case Ovalization. A system for measurement of casing ovalization displacement was designed based on mounting three

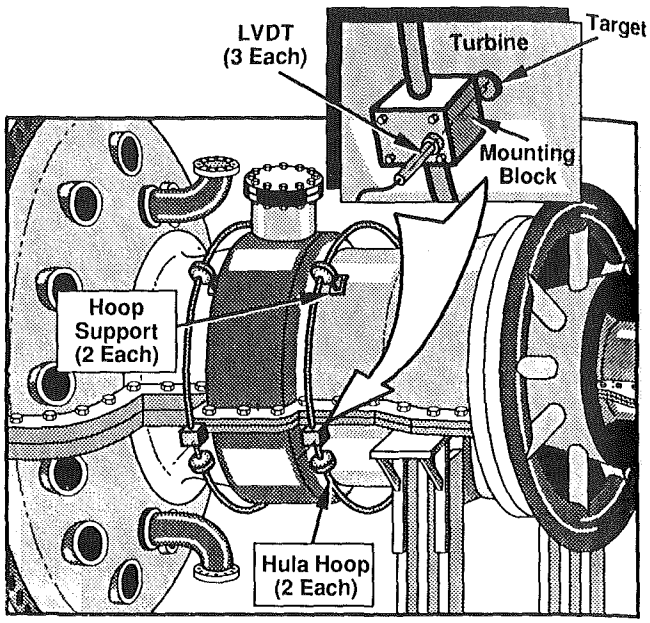


Fig. 4 Isometric of hula hoop and LVDTs for casing ovalization measurement

linear variable differential transducers (LVDTs) to thermally stabilized circular frames (hula hoops) as shown in Fig. 4. Ovalization measurements are taken at two locations on the compressor: one near the fourth stage and the other near the ninth stage (Fig. 1). Each hula hoop is mounted to the compressor case by lugs at 45 deg from top center and hangs downward to surround the case. Deflection error due to thermal distortion of the hoop, which is fabricated from a 2-in. diameter pipe, is controlled by circulating 3 gpm coolant water flow and by using fiberglass insulation and an aluminum foil radiation heat shield. The LVDTs are mounted to the hoop by adjustable brackets at 180 deg and 107 deg on both sides of the case. The spring-loaded LVDT plungers bear against adjustable casing targets, which project outside the casing insulation. The extra degrees of adjustment freedom allow the LVDT cold condition output to be set very near zero voltage. The LVDTs have a full measurement range of 2.00 in. with an accuracy of ± 0.001.

Casing radial growth and ovalization are evaluated from individual LVDT signals by Fourier analysis of the zeroth and second order:

$$X(0) = (x1 + x2 + x3 + x4 + x5)/5 \quad (1)$$

$$X(2) = [x1 \cos(45*2) + x2 \cos(107*2) + x3 \cos(180*2) + x4 \cos(253*2) + x5 \cos(315*2)]/5 \quad (2)$$

$$Y(2) = [x1 \sin(45*2) + x2 \sin(107*2) + x3 \sin(180*2) + x4 \sin(253*2) + x5 \sin(315*2)]/5$$

where:

$x2$, $x3$, $x4$ are individual LVDT measurements at $+107$, 180, and -107 deg, respectively.

$x1$ and $x5$ equal zero at the mounting points of the hula hoops.

$X(i)$, $Y(i)$ are the real and imaginary Fourier components.

Ovalization amplitudes are defined by converting from the rectangular coordinates to magnitude and phase.

Both hula hoops of the ovalization measurement system have good solid supports and sway control. All six LVDT signals look reasonable except for a few instances of plunger sticking; strong helper springs have been installed to eliminate future sticking problems. The pump and antifreeze coolant system provides adequate cooling to resist hoop thermal distortion.

Downloaded 02 Jun 2010 to 171.66.16.122. Redistribution subject to ASME license or copyright; see http://www.asme.org/terms/Terms_Use.cfm

Rotor Deflection. In order to evaluate rotor bow, journal lift-off, casing deflections, and misalignment, Bently Nevada eddy current proximity probes were installed at five locations between the generator inboard bearing and end of the turbine shaft. Probes were located (Fig. 1) to sense shaft motion at 45 deg from vertical on both turbine bearings, at the generator inboard bearing, near the coupling, and outboard of the turbine exhaust bearing. These measurements provide shaft static position and slope through the bearings, and vibration information in two orthogonal planes. Rotor bow deformation can be reasonably interpreted by subtracting shaft run-out and curve fitting the measured once-per-rev deflections. The eddy current proximity probes have a full measurement range of 0.080 in. with an accuracy of ± 0.0001.

All 10 shaft proximity probes function well, providing accurate journal position and vibration signals. A custom-designed electronic buckout box offsets probe output bias to keep signal within the analog to digital converter (ADC) range yet allow DC variations to be recorded. Probes at the coupling and at the extension from the exhaust end bearing contain significant eccentricity components that require subtraction of run-out vectors in the subsequent data analysis.

Blade Tip Clearance. Developing a system to measure clearance between the blade tips and case was a difficult and challenging task (Simmons et al., 1992). Measurements were desired at Stages 4 and 9 to provide data of the stages where most blade tip rubbing has been reported. The maximum requirements for the tip clearance probes were as follows:

Range	0.25 in.
Target size	0.3 in. wide
Velocity	1100 ft per sec
Temperature	415°F
Pressure	46 psig

Five equally spaced sensors were required to define ovalization deformations for each stage. To accomplish this, custom eddy current noncontact proximity probes were acquired from Bently Nevada Corp. The system electronics is designed with a carrier frequency about 40 times higher than used with their standard probes to accommodate the blade tip target size and velocity. A 3/4-in. probe size was used to provide a maximum range of 0.40 inches. A 1 1/2-in. hole was bored in the case to minimize signal absorption from nearby metal. The probes were fabricated with a Vespel[1] "slip over case" to fill in the void and included a threaded section for attachment to the casing brackets.

Mounting bracket design and preparation allowed all probes to be solidly installed with tips about 10 to 20 mils below the inside case surface. Experience shows that all probe signals are strong and consistent. Measurable carrier noise occurred initially but was eliminated by filters in the data acquisition electronics.

Typically, eddy current probes produce a large negative voltage spike as each blade passes (Fig. 5). The maximum pulse height represents the closest approach of the blade to the probe. Capturing the maximum pulse voltage required a peak hold detector, which functions on the principle of charging a capacitor. Additional circuitry was included to read and reset the peak hold detector after each signal pulse subsides in order to acquire clearance data as each blade passes. Blade tip proximity can be measured over a full range of 0.300 in. with an accuracy of ± 0.001.

Operating experience indicates that minimum clearance data trends are valid, but rotor vibration and blade-to-blade clearance variations on turning gear are corrupted by spikes in peak signals due to cross-talk noise between probes. The cross-talk noise problem improves above 100 rpm. Considerable effort

[1]Registered Trademark of DUPONT Corp.

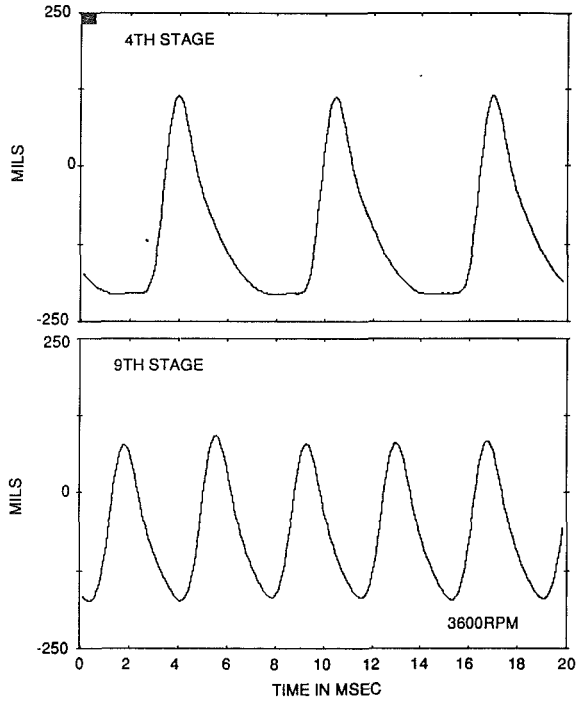


Fig. 5 Typical blade pass proximity probe signal

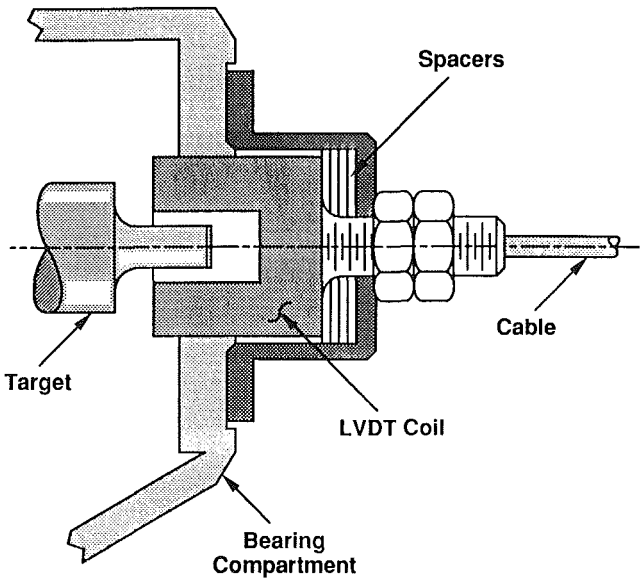


Fig. 6 Shinkawa rotor growth probe

was spent to diagnose and correct the low-speed problem; the most reliable approach found was to power only one probe at a time, which was implemented with a computer-controlled relay board.

Rotor Axial Growth. A special rotating armature LVDT (Fig. 6) was provided by Westinghouse Electric Corporation to measure rotor to cylinder relative growth. The instrument, manufactured by Shinkawa, bolts to the overspeed trip housing and can be installed without any modifications. A test target and three different sized spacers are provided for calibration. The LVDT has a full measurement range of 1.00 in. (25 mm) with an accuracy of ± 2.5 percent.

The rotor axial growth signal drifted out of range after the first several runs. The zero setting and sensitivity calibration were re-established; axial growth measurements continue to be recorded.

Downloaded 02 Jun 2010 to 171.66.16.122. Redistribution subject to ASME license or copyright; see http://www.asme.org/terms/Terms_Use.cfm

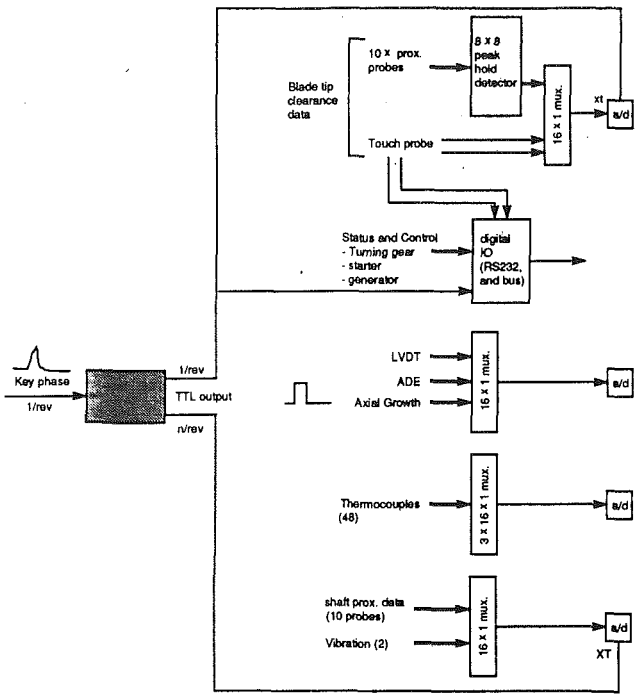


Fig. 7 Diagram of a continuous data acquisition system

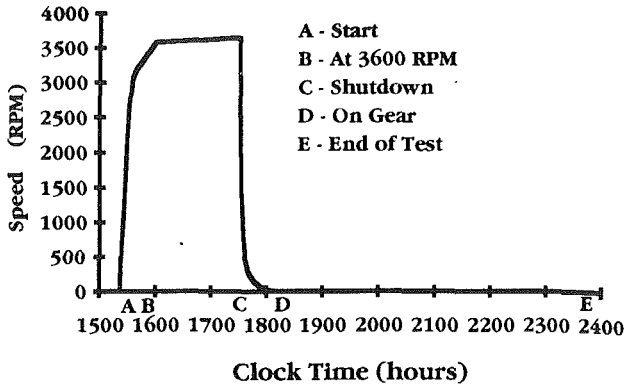


Fig. 8 Speed time history of turbine operating test

Casing Axial Growth. A standard Schavitz Model CGA1211 LVDT was mounted between the concrete pedestal supporting the rear mount link (Fig. 1) and the exhaust cylinder flange. This measurement is used as a reference indication of average cylinder temperature, and combined with the rotor axial growth measurement, the LVDTs have a full measurement range of 2.00 in. with an accuracy of ±0.001.

The case axial growth LVDT appears to continually produce reasonable data after ten months of operation.

Case Temperature. Standard type K thermocouples (TCs) were installed around the turbine to provide a measurement array for defining case temperature gradients. Four temperature measurement stations were selected (Fig. 1) on the casing; at compressor seventh stage, at combustor dome, and on the turbine case at both generator and exhaust ends. Eight thermocouples were welded to the case at each station; six equally spaced around and two on the inward side and outward side of the flange. In addition, a thermocouple was installed on each exhaust bearing support strut to define nonsymmetric radial growth.

The TCs installed on the case were calibrated with a voltage standard to adjust gain and offset on the signal acquisition board and then compared to an isolated calibrated meter at ambient conditions. A power isolation transformer was installed to eliminate any differential ground potential problem. Only one TC out of the 40 installed appears to have lost its bond to the case and was changed to an alternate location. Triple isolated amplifiers were installed to read the turbine internal thermocouples in parallel without sending false signals to the station supervisory and control system, which might result in tripping the turbine, or allowing a potentially dangerous operating condition to continue. Turbine load, discharge pressure, and exhaust temperature analog signals appear to read adequately.

Rotor Angular Position. A key phase transducer was installed at the exciter to provide a once-per-revolution shaft timing pulse from which all other signals can be related. Rotor vibration sampling pulses are generated by a phase-locked, loop-controlled frequency multiplier, so that 32 samples are taken from each regardless of turbine speed. Shaft angular position is determined from the time lag after key phase pulse and shaft speed from the time between key phase pulses.

Data Capture. Normally, power utilities operate simple cycle combustion turbines only in response to unusual peak power demand. In order that testing could be conducted without requiring the unit to operate outside its peak demand schedule, a remote data acquisition system (DAS) was developed. The DAS automatically records all data at predetermined intervals, so that the need for on-site testing personnel was eliminated.

The data acquisition system, designed to follow the data flow path presented in Fig. 7, can digitize up to 132 signals during all significant operating events; signal processing yields up to 164 parameters that are automatically stored to hard disk. Slowly varying measurements such as temperatures and case deflections are digitized using averaging algorithms to improve measurement accuracy. Rapidly varying journal and blade tip proximity probe signals are analyzed by Fourier methods to record minimum clearance and once-per-rev motion components.

The system has worked well, acquiring data at 15-minute intervals under semi-manual and automatic control since January, 1991. The software also records detailed blade tip signals twice per day and switches to recording vibration on start-up at every 25 rpm to improve resonant frequency resolution. A watch-dog timer board was installed to reset the computer if it gets hung in a loop, thus improving reliability for unattended operation.

Typically, remote modem operation requires only about two hours of connect time to retrieve one week of computer recorded data. A file is included on the remote hard disk to quickly determine the number of times per day that the turbine is operated. Records of 13 turbine starts between January and October, 1991, have been transferred back to SwRI for which data from the following sensors are available:

7 ADE level monitoring sensors
6 LVDT case ovalization sensors
1 case axial growth LVDT
1 rotor axial growth LVDT
48 thermocouples
10 shaft proximity probes
10 blade tip proximity probes
2 bearing accelerometers

Results and Observations

The preliminary results discussed below are mostly drawn from data acquired during initial operational tests in January, 1991. Records of these tests (Figs. 8–14) involved normal start-up from turning gear, operation at synchronous speed and zero load for one hour, shutdown, turning gear and end of test at midnight; these events are identified on Fig. 8 as A, B,

Downloaded 02 Jun 2010 to 171.66.16.122. Redistribution subject to ASME license or copyright; see http://www.asme.org/terms/Terms_Use.cfm

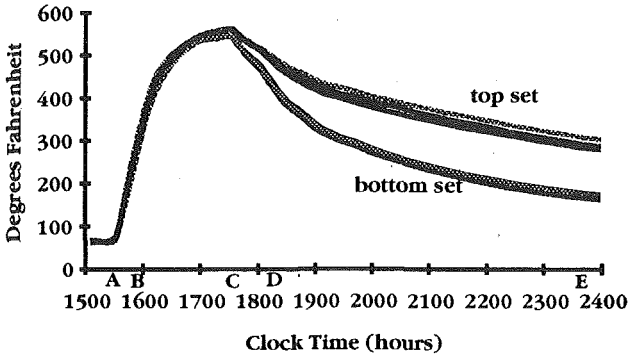


Fig. 9 Combustor dome temperature trends

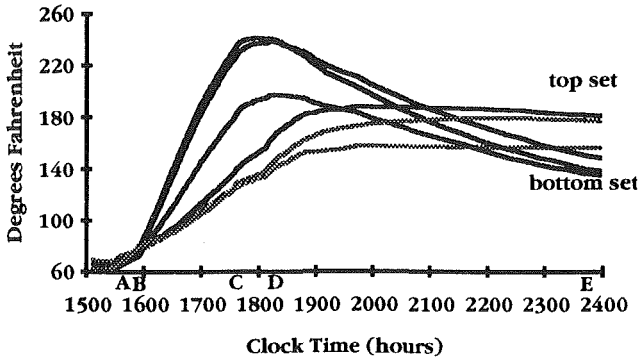


Fig. 10 Turbine section case temperature

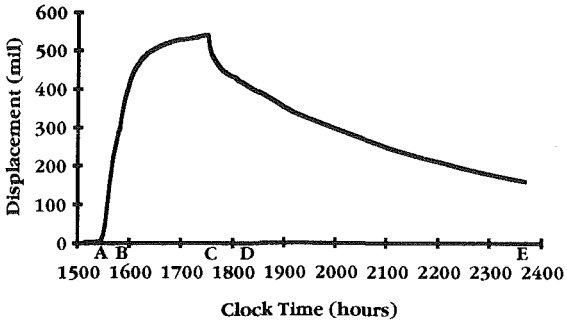


Fig. 11 Turbine case axial growth

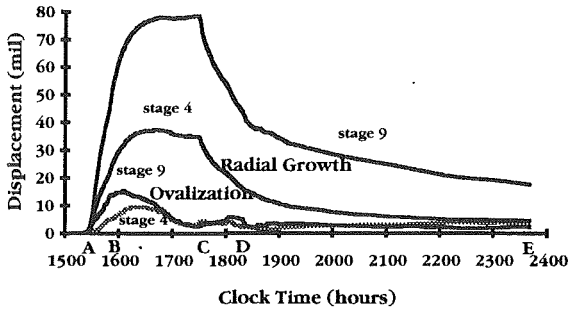


Fig. 12 Compressor radial growth and ovalization trends

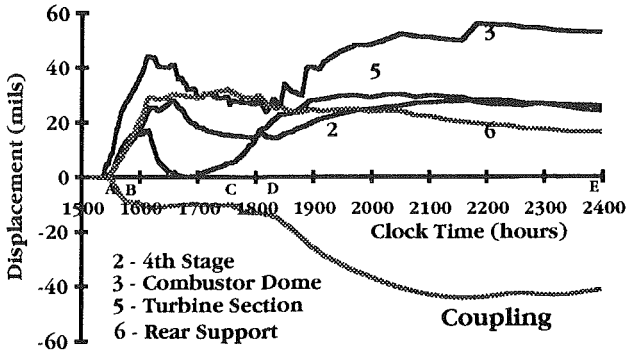


Fig. 13 Turbine casing vertical growth (ADE measurements)

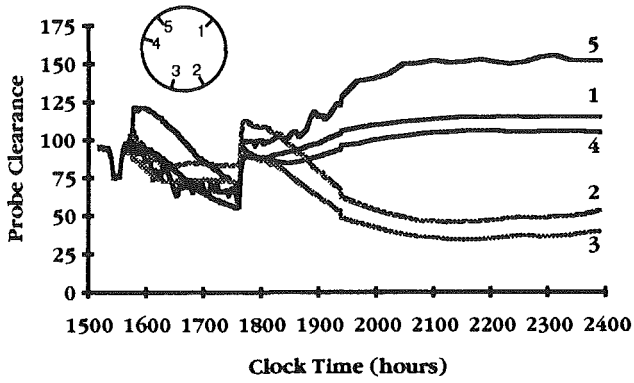


Fig. 14 Tip clearance trend

C, D, E, respectively, and marked on all related plots. As will be shown, the resulting data have sufficient accuracy to validate the instrumentation approach and to describe casing distortion mechanisms.

1 Temperature trends of equally spaced thermocouples around the combustor dome (Fig. 9) show a rapid increase and slow decline consistent with start-up, firing, and shutdown of the turbine. A temperature differential of approximately 150°F develops about 2 hours into the cool-down period after shutdown, which may be consistent with thermal stratification of air within the turbine shell.

Distribution of temperatures surrounding the external turbine case (Fig. 10) exhibits a more unusual trend. During fired operation and shortly after shutdown, the bottom case half becomes about 100 deg warmer than the top half case; after shutdown, the two case halves trend in opposite directions with the top half remaining about 40 deg hotter than the bottom at midnight when the record ended.

During fired, nonloaded operation, the turbine case grows axially about 0.53 in. (Fig. 11). This implies an average cylinder temperature of approximately 400°F, which is roughly consistent with thermocouple readings. Likewise, radial growths at the compressor cylinder (Fig. 12), of 35 and 78 mils, respectively, at fourth and ninth stages, are within 10 percent of growths based on estimated casing temperatures.

2 Casing ovalization, measured with LVDTs from an initial assumed round state (Fig. 12), indicates that the greatest out-of-round deformation (10 to 15 mils) occurs during the early part of synchronous operation when cases are heating up. Shortly after shutdown (event C), less than 5 mils oval deflection occurs during the high heat dissipation period. The small deformation levels measured suggest that for the initial cool-down conditions tested, casing ovalization does not have a strong influence on internal clearances.

3 Turbine case vertical deflection (Fig. 13) and bearing misalignment between the compressor and generator, measured with ADE sensors, show a trend that maximizes six hours after shutdown and then appears to drop off. Blade tip clearances similarly vary with time after shutdown as shown in Fig. 14, reaching a minimum at the lower probes 3 to 6 hours after start of turning gear. During the same time period, clearances near the top increased and clearances near the sides had little change, indicating that the rotor moved downward with respect

Downloaded 02 Jun 2010 to 171.66.16.122. Redistribution subject to ASME license or copyright; see http://www.asme.org/terms/Terms_Use.cfm

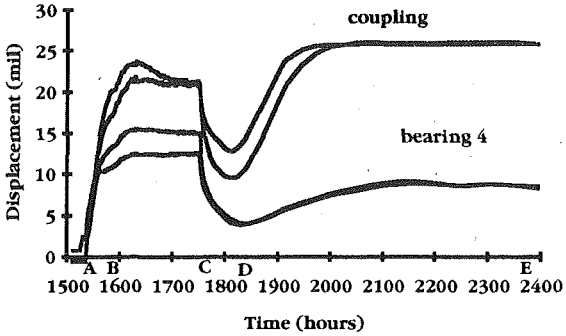


Fig. 15 Bearing and coupling static position trend

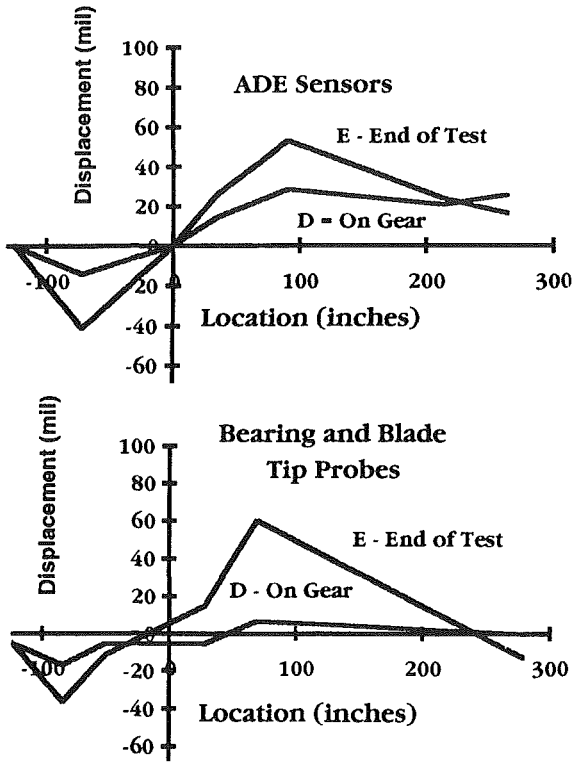


Fig. 16 Casing deflected shape due to thermal distortion

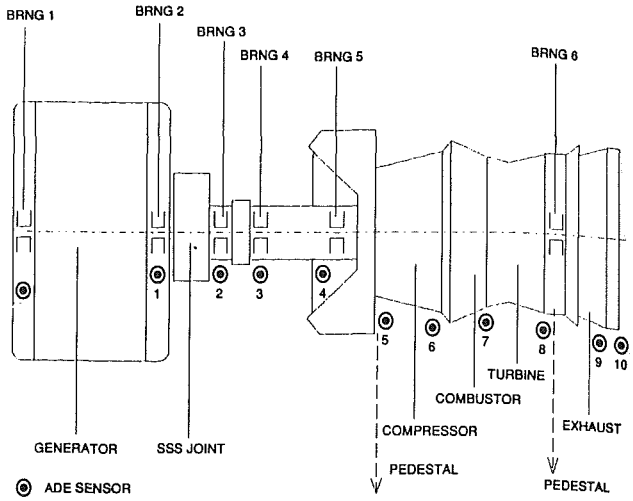


Fig. 17 ADE sensor locations for combustion turbine tests in Italy

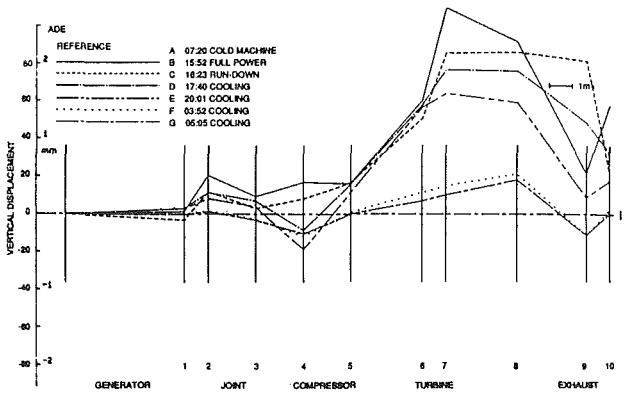


Fig. 18 Combustion turbine cylinder deflection shapes

to the case, or that the case deflects upward into the rotor (the latter is consistent with the ADE #2 readings both in magnitude and timing).

4 Static position trends of the shaft (measured with proximity probes) relative to the compressor end bearing housing and at the coupling are presented in Fig. 15. While hydrodynamic lift-off qualitatively explains shaft relative motions during start-up and shutdown, it does not explain trends observed during the cool-down period on turning gear. These trends would lead to the conclusion that thermally related deflections are key contributors.

5 The deflected casing shapes presented in Fig. 16 combine the results of all deflection sensors and provide the strongest evidence that casing bow plays the most significant role affecting minimum internal clearance. The top figure represents measurements using the ADE sensors for the events immediately after shutdown and at midnight; specific turbine locations are noted. In general, the turbine case arches upward consistent with the measured temperature differential between top and bottom case halves resulting in approximately 30 mils clearance loss at Stage 4. It is interesting to note that a reverse curvature appears at the turbine section of the case, which corresponds with the reverse temperature differential measured at that section during synchronous speed and at the beginning of the turning gear operation. The lower figure represents deflections based on proximity probe signals at bearings and blade tips for the same operating events, but assuming that the rotor remains straight and the casing deflects. The deflected shapes are quite similar for both conditions and result in reasonably close deflection levels.

6 Correlation of casing bow deflections with shaft relative deflection measurements at the coupling imply that blade tip clearance trends could be monitored by the addition of very minimal nonintrusive instrumentation. Static trends of even the present proximity probes installed near bearings would be of some value in evaluation of adverse operating conditions leading to blade rubbing.

7 Figure 17 presents casing distortion measurements on a similar design combustion turbine in power utility service in Italy. This turbine not only differed in design to accommodate 50 Hz versus 60 Hz operation, but had a clutch and long shaft between the turbine and generator. ADE sensors were also used, but they were arranged along the entire turbine/generator set. The sensors installed at positions 4 through 8 are at locations similar to those installed at Perryman Station. It is interesting to note that while the casing bow deflected shape of this turbine (Fig. 18) is similar to the BG&E turbine, it has higher deflection levels at operating conditions. This is likely due to the larger size of 50 Hz machines and the higher heat generated at 90 MW versus zero load for the test at Perryman. The data also imply that the cool-down trend is substantially different for the 50 Hz turbine, which is most likely a result of much higher turning gear speed (100 rpm) employed to force air through the turbine during this period.

Downloaded 02 Jun 2010 to 171.66.16.122. Redistribution subject to ASME license or copyright; see http://www.asme.org/terms/Terms_Use.cfm

Discussion

With recent advances in modern data acquisition system hardware and in measurement technology, meaningful data can now be obtained on elusive problems such as defining blade rub causes. Computer-controlled data acquisition systems offer the advantages of recording a large number of data channels, substantial data processing flexibility, sizable data storage capacity, and a format eminently suitable for further processing and display. Appropriate design and implementation of measurement systems can now yield a convincing self-consistent body of data, which can be used to guide operations and minimize the potential for damaging blade tip rubs. Future research will illustrate the development of such operational guidelines.

Acknowledgments

Appreciation is extended to the Electric Power Research Institute for sponsoring the research program and releasing the data for publication. Appreciation is also extended to Mr. Wayne Seifert, BG&E Plant Manager, for permitting Perryman Station to be used as the utility site host. Special thanks are offered to Messrs. Al Casalena, Tom Bietzel, Harold Iman, John Strawbridge, and many others at BG&E for their extra effort in making this project successful. SwRI would like to acknowledge Mr. David van Den Burg et al. of Bently Nevada Corp who designed the blade tip proximity probes. The authors would like to acknowledge and thank Messrs. Paul Troxler, Ralph Harris, Carl Edlund, and Steve Bird of SwRI for development of the data acquisition system.

References

Clapis, A., Possa, G., and Rossini, T., 1982, "Measurement of Vertical Bearing Alignment in Turbogenerators During Operation," CISE 1777; Presented at the "Workshop on Machine Surveillance during Operation and Intervention Thresholds," Paris, Jan. 13–14.

Harris, R. E., Simmons, H. R., Smalley, A. J., Baldwin, R. M., and Quentin, G., 1991, "Remote Condition Monitoring of a Peaking Gas Turbine," ASME Paper No. 91-GT-185.

Lapini, G. L., Vidali, P., Zippo, M., and Bernante, R., 1989, "An Automatic System for the Control of Rotor Alignment in Turbogenerators," *Proceedings, International Conference on Monitoring Surveillance and Predictive Maintenance of Plants and Structures*, pp. 799–808.

Scalzo, A. J., Howard, G. S., and Holden, P. C., 1983, "Field Test of the W501D, a 100 MW Combustion Turbine," ASME Paper No. 83-GT-174.

Simmons, H. R., and Smalley, A. J., 1990, "Effective Tools for Diagnosing Elusive Turbomachinery Dynamics Problems in the Field," ASME JOURNAL OF ENGINEERING FOR GAS TURBINE AND POWER, Vol. 112, pp. 470–477.

Simmons, H. R., Smalley, A. J., Edlund, C. E., and Frischmuth, R. W., 1992, "Monitoring Compressor Blade Tip Clearance in Combustion Turbines," *Proceedings, Electrical Power Research Institute Conference on Steam and Combustion Turbine Blading*, Orlando, FL.

Smalley, A. J., 1985, "Crankshaft Stress Reduction Through Improved Alignment Practice," American Gas Association, Project PR15-174, Arlington, VA.

Smalley, A. J., and Simmons, H. R., 1988, "Investigation of Specific Combustion Turbine and Combined-Cycle Field Problems Compressor Blade Migration," Electric Power Research Institute, AP-5887, Research Project 1802-9, Palo Alto, CA.

Downloaded 02 Jun 2010 to 171.66.16.122. Redistribution subject to ASME license or copyright; see http://www.asme.org/terms/Terms_Use.cfm

Fatigue Life Estimation Procedure for a Turbine Blade Under Transient Loads

N. S. Vyas
Department of Mechanical Engineering,
Indian Institute of Technology,
Kanpur 208 016 India

J. S. Rao
Department of Mechanical Engineering,
Indian Institute of Technology,
New Delhi 110 016 India

Fatigue analysis and consequent life prediction of turbomachine blading requires the stress load history of the blade. A blade designed for safe operation at particular constant rotor speeds may, however, incur damaging stresses during start-up and shut-down operations. During such operations the blade experiences momentary resonant stresses while passing through the criticals, which may lie in the speed range through which the rotor is accelerated. Fatigue due to these transient influences may accumulate to lead to failure. In this paper a technique for fatigue damage assessment during variable-speed operations is presented. Transient resonant stresses for a blade with nonlinear damping have been determined using a numerical procedure. A fatigue damage assessment procedure is described. The fatigue failure surface is generated on the S-N-mean stress axes and Miner's Rule is employed to estimate the accumulation of fatigue.

Introduction

Blade fatigue is a multidisciplinary problem and various aspects of the problem have been subjects of extensive research; see articles by Rao (1987), Srinivasan (1984), and Rieger (1985). Blade fatigue is influenced by the static and dynamic stress fields on the blade, fatigue properties of the blade material, loading history, and the environment of operation. Fatigue crack usually initiates in a region of high stress at some metallurgical or structural discontinuity and if critical conditions of operation are sustained, the crack may grow to lead to failure. Various factors may affect the blade behavior in several different ways to make the failure problem very specific.

The steps toward fatigue analysis can be, generally, summarized as (Rao and Vyas, 1986):

- Generating the stress loading biography.
- Definition of blade fatigue parameters under operating environment.
- Life estimation using fatigue theories.

The blade during its operation span, in addition to constant speed operation, undergoes various transient rotor operations like step-up, step-down, partial admission, etc. Attempts have been made by several researchers to obtain mathematical models for accurate determination of blade response under steady as well as transient excitations. Stress response of single rotating blades was obtained by Rao et al. (1986). Transient vibration analysis has been undertaken by Irretier (1986) and Vyas et al. (1987). Models for multiple blade systems have also been developed. Some recent works include Jones and Muszynska (1983), MacBain and Whaley (1984), and Sinha and Griffin (1984).

The problem of stress response determination is made complex by the nonlinearity of damping in the vibratory system. Energy dissipation through Coulomb, hysteretic, and viscous mechanisms of damping is a blade specific problem. Rao et al. (1986) developed an experimental technique for determination of damping properties under the overall influences of the above-described mechanisms for rotating blades and defined damping ratios in various vibratory modes as nonlinear functions of rotor speed and the vibratory strain amplitude. A numerical procedure has been developed by Rao and Vyas (1989, 1990) to account for the nonlinearity in damping for determination of resonant stresses during steady and transient rotor operations.

In this study the influence of transient resonant stresses experienced by the blade during step-up/down operations on its fatigue life is investigated. The transient resonant stress, determined for a blade with nonlinear damping using a numerical procedure in conjunction with Reissner's functional, Ritz procedure, and modal analysis, defines the alternating stress level experienced by the blade. The mean stress level is a function of the speed of rotation and the steady component of the steam/gas force. S-N and mean stress diagrams are coupled to define the fatigue failure surface for the blade under assumed conditions of operating environment. Calculations to illustrate accumulation of damage are done using Miner's rule.

Blade Vibration Model

A single free-standing blade can be considered a tapered, twisted asymmetric aerofoil cross-sectional beam mounted on a rotating disk at a stagger angle (Fig. 1*a*). The cross section

Contributed by the International Gas Turbine Institute and presented at the 37th International Gas Turbine and Aeroengine Congress and Exposition, Cologne, Germany, June 1-4, 1992. Manuscript received by the International Gas Turbine Institute February 4, 1992. Paper No. 92-GT-78. Associate Technical Editor: L. S. Langston.

Copyright © 1994 by ASME
Downloaded 02 Jun 2010 to 171.66.16.122. Redistribution subject to ASME license or copyright; see http://www.asme.org/terms/Terms_Use.cfm

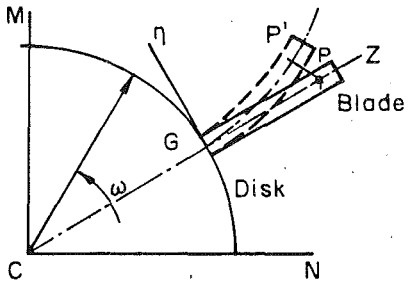


Fig. 1(*a*) Blade mounted on rotating disk

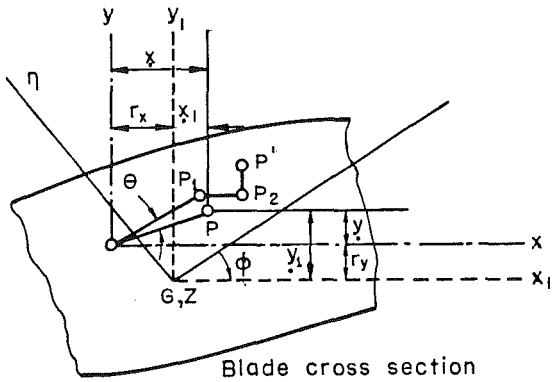


Fig. 1(*b*) Elemental displacement relations

of the blade at a height z is shown in Fig. 1(b). The centroid of the cross section is located at C, while O is the center of flexure. The kinetic energy of the blade can be shown to be (Rao et al., 1986)

$$T=\frac{1}{2}\rho\int_0^l A\{(\dot{x}+r_y\dot{\theta})^2+(\dot{y}-r_x\dot{\theta})^2\}\,dz + \frac{1}{2}\int_0^l I_{cg}\dot{\theta}^2\,dz+\frac{1}{2}\rho\omega^2\Bigg[-\int_0^l\{(x'+r_y\theta+r_y'\theta)^2 + (y'-r_x'\theta-r_x\theta')^2\}(RI_1+I_2)dz + \sin^2\phi\int_0^l A(x+r_y\theta)^2dz+\cos^2\phi\int_0^l A(y-r_x\theta)^2dz - \sin 2\phi\int_0^l A(x+r_y\theta)(y-r_x\theta)dz\Bigg] \quad (1)$$

For accurate determination of blade stress fields, Reissner's functional has been employed, which simultaneously yields good stress and displacement fields. The Reissner's functional is given by

$$I_R=\iiint_v\{\tau_{ij}\epsilon_{ij}-U^*(\tau_{ij})\}dv - \iiint_o B_iu_i\,dv+\iint_s T_iu_ids \quad (2)$$

Using beam theory and stress-strain displacement relationships, the above can be shown to be

$$I_R=\int_o^l\Bigg\{-M_y\,x''+M_x\,y''+T_\theta\,\theta'+\frac{T_\theta^2}{2C} - \frac{M_x^2I_{y1y1}+M_y^2I_{x1x1}-2M_xM_yI_{x1y1}}{2E(I_{y1y1}I_{x1x1}-I_{x1y1}^2)}\Bigg\}dz \quad (3)$$

The dynamic Reissner functional is set as

$$L=T-I_R \quad (4)$$

Using shape functions

$$x=\Sigma A_i(t)\,f_i(z)\quad M_x=\Sigma\,D_i(t)\,h_i(z)$$
$$y=\Sigma B_i(t)\,f_i(z)\quad M_y=\Sigma\,E_i(t)\,h_i(z)$$
$$\theta=\Sigma C_i(t)\,f_i(z)\quad T_\theta=\Sigma\,E_i(t)\,h_i(z) \quad (5)$$

where

$$f_i(Z)=\frac{(i+2)(i+3)}{6}Z^{i+1}-\frac{i(i+3)}{3}Z^{i+2}+\frac{i(i+1)}{6}Z^{i+3}$$

$$\bar{f}_i(Z)=Z^i-\frac{i}{i+1}Z^{i+1}$$

$$h_i(Z)=\frac{(1-Z)^i}{i+1} \quad (5a)$$

which satisfy the boundary conditions of a cantilever, Ritz process

$$\frac{\partial L}{\partial A_i}=0,\ \text{etc.} \quad (6)$$

is applied to the dynamic Reissner functional above to obtain the equations of motion

$$p^2[M]\{q\}-[K]\{q\}=0 \quad (7)$$

Nomenclature

A = area of cross section
B_i = body force distribution
a, b = coefficients in trigonometric series of forcing functions
C = torsional stiffness
E = modulus of elasticity
F_x, F_y = forcing functions
f = shape function for bending deflections
$\bar{f}$ = shape function for angular deflections
H_{mk} = mth harmonic response in the kth mode
h = shape function for bending and twisting moments
I_1 = $A_0(l-z)+1/2\,A_1(l^2-z^2)+\ldots+\frac{A_n}{n+1}(l_{n+1}-z^{n+1})$
I_2 = $1/2\,A_o(l^2-z^2)+1/3\,A_1(l^2-z^2)+\ldots+\frac{A_n}{n+2}(l^{n+1}-z^{n+1})$
I_{x1x1} = second moment of area about $x1$ $x1$ axis
I_{y1y1} = second moment of area about $y1$ $y1$ axis
I_{x1y1} = product moment of area about $x1$ $y1$ axis
I_{cg} = moment of inertia per unit length
I_R = Reissner's functional
L = Reissner's dynamic functional
l = blade length
M = moment
M_x, M_y = moments in x and y direction
m = harmonic number
N = cycles to failure
n_s = number of nozzles
p_k = natural frequency in kth mode
Q = forcing vector
R = disk radius
R_f = endurance limit modifying factor = $k_ak_bk_ck_dk_ek_f$
r_x, r_y = coordinates of the center of flexure
S_e = endurance limit for 10^3 cycles
S_e' = endurance limit for N cycles

Downloaded 02 Jun 2010 to 171.66.16.122. Redistribution subject to ASME license or copyright; see http://www.asme.org/terms/Terms_Use.cfm

Table 1 Geometric and material properties

Dist cm	A cm^2	I_{xx} cm^4	I_{yy} cm^4	I_{xy} cm^4	C x 10^{-3} $\frac{N\text{-}m^2}{rad}$	r_x cm	r_y cm
0.0	2.127	.3447	.9489	.4705	.9702	-.213	.075
2.5	1.738	.3651	.6717	.4158	.7776	-.094	.135
5.0	1.647	.4927	.5174	.4146	.7576	-.082	.073
7.5	1.263	.5054	.3097	.2943	.6113	-.178	-.113
10.0	1.008	.4356	.1543	.2243	.4424	-.282	-.222
11.0	0.736	.3256	.0858	.1572	.3087	-.303	-.453

L = 11.1 cm, E = 200 GPa, R = 18 cm, G = 75 GPa
$\phi = 90^0$, $\rho = 0.08$ N/cm^3, $n_s = 12$.

Table 2 Fourier component amplitudes

m	F_x(N/cm) a_{mx}	b_{mx}	F_y(N/cm) a_{my}	b_{my}	M (N-cm/cm) a_{mM}	b_{mM}
0	0.0622	0.0000	-0.0064	0.0000	0.0280	0.0000
1	-0.0642	-0.0169	0.0153	-0.0392	-0.0269	-0.0173
2	0.0110	0.0140	-0.0063	0.0095	0.0037	0.0089
3	-0.0024	0.0005	0.0024	0.0005	-0.0006	0.0004
4	-0.0027	0.0013	0.0012	0.0019	-0.0010	0.0011
5	-0.0001	-0.0020	0.0007	-0.0012	0.0001	-0.0012
6	-0.0005	0.0028	-0.0018	0.0015	-0.0007	0.0017

where $[M]$ and $[K]$ are mass and stiffness matrices and the vector $\{q\}$ contains

$$\{q\}^T = \{A_i, \ldots, D_i, \ldots\}$$

A turbine blade with typical geometric and material properties given in Table 1 is considered and the eigenproblem (7) is solved to obtain natural frequencies and mode shapes.

Nozzle Passing Excitation Forces

The periodic nozzle forces $F_x(z, t)$, $F_y(z, t)$ and $M(z, t)$ on the blade in the x, y, θ directions, respectively, can be expressed in Fourier form as

$$F_x(Z, t) = a_{ox}(Z) + \sum_m a_{mx}(Z) \cos\{mn_s(\omega_o t + \frac{1}{2}\alpha t^2)\} + \sum_m b_{mx}(Z) \sin\{mn_s(\omega_o t + \frac{1}{2}\alpha t^2)\}$$

$$F_y(Z, t) = a_{oy}(Z) + \sum_m a_{my}(Z) \cos\{mn_s(\omega_o t + \frac{1}{2}\alpha t^2)\} + \sum_m b_{my}(Z) \sin\{mn_s(\omega_o t + \frac{1}{2}\alpha t^2)\}$$

$$M(Z, t) = a_{oM}(Z) + \sum_m a_{mM}(Z) \cos\{mn_s(\omega_o t + \frac{1}{2}\alpha t^2)\} + \sum_m b_{mM}(Z) \sin\{mn_s(\omega_o t + \frac{1}{2}\alpha t^2)\} \quad (8)$$

[$\alpha = 0$, for constant-speed operations]

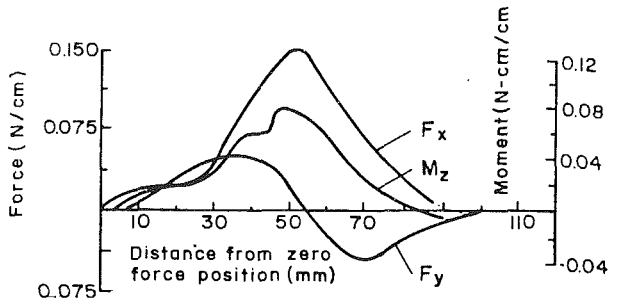


Fig. 2 Forcing functions

Typical nozzle forces simulated by electromagnets for a laboratory spin-rig are shown in Fig. 2. Table 2 gives the amplitudes of the Fourier harmonics.

Resonant frequencies for the blade are found from the Campbell diagram (Fig. 3), e.g., interaction of the I mode of vibration with the VI, V, and IV harmonics of nozzle forces gives rise to blade resonant speeds of 539, 647, and 809 rpm, respectively. It should be noted here that for the blade under consideration, the increase in natural frequencies with rotational speed is small (e.g., for the I mode it increases from 643 Hz at 0 rpm to 647 Hz at 4000 rpm) and on the Campbell diagram the natural frequencies are apparently seen as straight horizontal lines.

Nomenclature (cont.)

S_u = ultimate tensile strength
S_y = yield strength
s = surface area
T = kinetic energy
T_i = traction force in the ith direction
T_θ = twisting moment
t = time
$[U]$ = modal matrix
U^* = complementary energy density function
u_i = displacement in the ith direction
v = volume
xx, yy = coordinate axes through center of flexure
$x1x1, y1y1$ = coordinate axes through centroid
z = distance along blade length
Z = z/L
α = angular acceleration
ϵ_{ij} = strain
$\eta\eta, \xi\xi$ = coordinate axis, see Fig. 1
η = generalized coordinate
ν = nozzle passing frequency
ξ = modal damping ratio
ξ_{av} = average modal damping ratio
ρ = mass density
$\sigma_1, \sigma_2, \sigma_3$ = principal stresses
σ_{alt} = basic alternating stress
σ_{mean} = basic mean stress due to Oth NPF component
σ_{af}, σ_{mf} = failure values of basic alternating and mean stress
σ_z = bending stress
τ_{ij} = stress
τ_{xz}, τ_{yx} = shear stresses
ϕ = stagger angle
ψ_z = pretwist angle at distance z
ω = angular frequency
ω_o = initial angular frequency
$(')$ = denotes differentiation with z
$(\dot{})$ = denotes differentiation with t
$(.)$ = denotes coordinate quantity, thus, $\dot{x}$

Downloaded 02 Jun 2010 to 171.66.16.122. Redistribution subject to ASME license or copyright; see http://www.asme.org/terms/Terms_Use.cfm

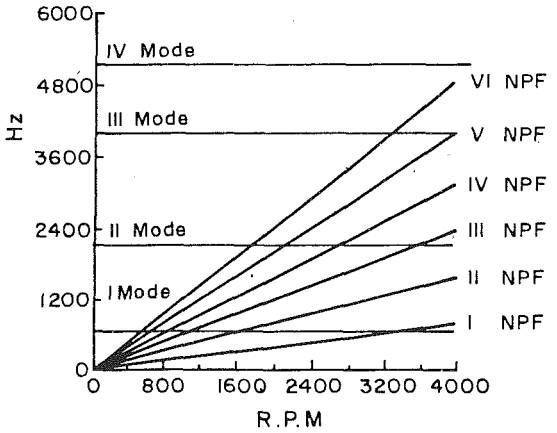


Fig. 3 Campbell diagram

Steady State Response—Constant-Speed Operation

Blade damping is modeled as a nonlinear function of strain amplitude and speed of operation for each mode of vibration. Initially, damping can be assumed to be proportional and viscous, so that the energy dissipated as

$$W = \frac{C\,T}{\rho} \tag{9}$$

The process of incorporating the nonlinear model will be considered shortly. The equations for forced damped motion are then obtained as

$$[M]\{\ddot{q}\} + [C]\{\dot{q}\} + [K]\{q\} = \{Q_o\} + \sum_m \{Q_m\} \cos m\nu t + \sum_m \{Q_{m+6}\} \sin m\nu t \tag{10}$$

$$\{q\}^T = \{A_i, \ldots, D_i, \ldots\}$$

$$M_{11} = \rho \int_o^l A_i f_i f_j \, dz$$

$$C_{11} = \frac{C\,M_{11}}{\rho}$$

$$Q_{01} = \int_0^l a_{0x} f_j \, dz, \text{ etc.} \tag{10a}$$

A modal analysis technique is employed to obtain decoupled equations of forced motion. Hence, using

$$\{q\} = [U]\,\{\eta\} \tag{11}$$

we get

$$M_k(\ddot{\eta}_k + 2\zeta_k p_k \dot{\eta}_k + p_k^2 \eta_k) = Q_{oN_k} + \sum_m Q_{mN_k} \cos m\nu t + \sum_m Q_{(m+6)N_k} \sin m\nu t \tag{12}$$

The solution of the above in terms of displacement and moment vectors, due to each harmonic, is of the form

$$H_{o_k} = \frac{Q_{oN_k}/M_k}{P_k^2}$$

$$H_{m_k} = \eta_{m_k} + \eta_{(m+6)_k} = \frac{\sqrt{Q_{mN_k}^2 + Q_{(m+6)N_k/M_k}^2}}{\sqrt{\{p_k^2 - (m\nu)^2\}^2 + 4\zeta_k^2 p_k^2 (m\nu)^2}} \cos(m\nu t - \psi_{m_k} - \delta_{m_k}) \tag{13}$$

where

$$\psi_{m_k} = \tan^{-1}\left[\frac{2\zeta_k p_k (m\nu)}{p_k^2 - (m\nu)^2}\right]$$

$$\delta_{m_k} = \tan^{-1}\left[\frac{Q_{(m+6)N_k}}{Q_{nM_k}}\right] \tag{14}$$

With the help of Eqs. (13), (11), and (5), the deflections and moments of the blade for the force harmonics can be determined. For computation of stresses, we can use the following formulae:

$$M_X = M_x \cos\psi_x - M_y \sin\psi_x$$

$$M_Y = M_y \cos\psi_x - M_x \sin\psi_x \tag{15}$$

The normal stress is

$$\sigma_z = \frac{M_Y x}{I_{yy}} + \frac{M_X y}{I_{xx}}$$

The maximum shear stress occurs in the vicinity of one of the points where the largest inscribed circle touches the boundary of the blade profile of the section (Roark and Young, 1976).

This stress is given by

$$\tau_{r\theta} = \frac{T_\theta}{k} C$$

where

$$K = \frac{\frac{1}{3}F}{1 + \frac{4}{3}F/AU^2}$$

$$F = \int_0^U t^3 \, dU$$

dU = the elemental length along the camber line
t = profile thickness as a function of U
A = area of the section

$$C = \frac{D}{1 + \frac{\pi^2 D^4}{16A^2}}\left[1 + 0.15\left(\frac{\pi^2 D^4}{16A^2} - \frac{D}{2r}\right]\right.$$

if the radius of curvature of the profile at the point is positive

$$C = \frac{D}{1 + \frac{\pi^2 D^4}{16A^2}}\left\{1 + \left[0.118 \log_e\left(1 - \frac{D}{2r}\right) - 0.238\frac{D}{2r}\right] \tanh\frac{2\phi}{\pi}\right\}$$

if the radius of curvature of the profile at the point is negative

D = diameter of the inscribed circle
r = radius of curvature of the profile at the point
ϕ = angle through which a tangent to the boundary rotates in turning or traveling around the re-entrant position (radians)

Stresses τ_{zx} and τ_{yz} are readily obtained from $\tau_{r\theta}$. The principal stresses are

$$\sigma_1 = 0$$

$$\sigma_{2,3} = \frac{\sigma_z}{2} \pm \sqrt{\left(\frac{\sigma_z}{2}\right)^2 + \tau_{zx}^2 + \tau_{yz}^2} \tag{16}$$

The basic mean stress (zeroth harmonic) and alternating stresses are determined from the principle stresses by using the following formula:

$$\sigma_{\text{mean}},\ \sigma_{\text{alt}} = \sqrt{\frac{1}{2}[\sigma_2^2 + \sigma_3^2 - 2\sigma_2\sigma_3]} \tag{17}$$

Downloaded 02 Jun 2010 to 171.66.16.122. Redistribution subject to ASME license or copyright; see http://www.asme.org/terms/Terms_Use.cfm

Transient Response—Constant Acceleration Operation

Consider now a step-up or step-down operation of the engine from an initial angular velocity ω_o, with a constant acceleration α. The kinetic energy expression in Eq. (1) gets modified to (Vyas et al., 1987)

$$T=\frac{1}{2}\rho\int_o^l A\{(\dot{x}+r_y\dot{\theta})^2+(y-r_y\dot{\theta})^2\}\,dz$$
$$+\frac{1}{2}\int_o^l I_{cg}\dot{\theta}^2 dz+\frac{1}{2}\rho(\omega_o+\alpha t)^2\Big[-\int_o^l\{(x'+r_y\theta'+r_y'\theta)^2$$
$$+(y'-r_x'\theta-r_x\theta')^2\}\,(RI_1+I_2)\,dz$$
$$+\sin^2\phi\int_o^l A(x+r_y\theta)^2\,dz+\cos^2\phi\int_o^l A(y+r_x\theta)^2\,dz$$
$$-\sin 2\phi\int_o^l A(x+r_y\theta)(y+r_x\theta)^2\,dz\Big] \quad (1a)$$

Following the procedure used before for the steady operation conditions, we get

$$M_k(\ddot{\eta}_k+2\xi_k p_k\dot{\eta}_k+p_k^2\eta_k)$$
$$=Q_{oN_k}+\sum_m Q_{mN_k}\cos\left[mn_k(\omega_o t+\frac{1}{2}\alpha t^2)\right]$$
$$+\sum_m Q_{(m+6)N_k}\cos\left[mn_k(\omega_o t+\frac{1}{2}\alpha t^2)\right] \quad (12a)$$

The solution for Eq. (12*a*) for each term in the forcing function can be written using Duhamel's integral as

$$\eta_{ok}=\int_0^l\frac{Q_{oN_k}}{p_{1k}M_k}e^{-\xi_k p_k(t-\tau)}\sin p_k(t-\tau)\,d\tau$$

$$\eta_{mk}=A_c\cos(p_{1k}t+\lambda_c)$$

$$\eta_{(m+6)k}=A_s\cos(p_{1k}t+\lambda_s) \quad (18)$$

with

$$A_c=\frac{1}{2}\sqrt{(-I_{1c}+I_{2c})^2+(I_{3c}+I_{4c})^2}$$

$$A_s=\frac{1}{2}\sqrt{(-I_{1s}+I_{2s})^2+(I_{3s}+I_{4s})^2}$$

$$\lambda_c=\tan^{-1}\frac{I_{3c}+I_{4c}}{-I_{1c}+I_{2c}}$$

$$\lambda_s=\tan^{-1}\frac{I_{3s}+I_{4s}}{-I_{1s}+I_{2s}}$$

$$I_{1c}=\int_0^l\frac{Q_{mN_k}}{p_{1k}M_k}e^{-\xi_k p_k(t-\tau)}\sin\{mn_s(\omega_o\tau+\frac{1}{2}\alpha\tau^2)-p_{1k}\tau\}\,d\tau$$

$$I_{2c}=\int_0^l\frac{Q_{mN_k}}{p_{1k}M_k}e^{-\xi_k p_k(t-\tau)}\sin\{mn_s(\omega_o\tau+\frac{1}{2}\alpha\tau^2)-p_{1k}\tau\}\,d\tau$$

$$I_{3c}=\int_0^l\frac{Q_{mN_k}}{p_{1k}M_k}e^{-\xi_k p_k(t-\tau)}\times\cos\{mn_s(\omega_o\tau+\frac{1}{2}\alpha\tau^2)-p_{1k}\tau\}\,d\tau$$

$$I_{4c}=\int_0^l\frac{Q_{mN_k}}{p_{1k}M_k}e^{-\xi_k p_k(t-\tau)}\times\cos\{mn_s(\omega_o\tau+\frac{1}{2}\alpha\tau^2)+p_{1k}\tau\}\,d\tau$$

$$I_{1s}=\int_0^l\frac{Q_{(m+6)N_k}}{p_{1k}M_k}e^{-\xi_k p_k(t-\tau)}\times\sin\{mn_s(\omega_o\tau+\frac{1}{2}\alpha\tau^2)-p_{1k}\tau\}\,d\tau$$

$$I_{2s}=\int_0^l\frac{Q_{(m+6)N_k}}{p_{1k}M_k}e^{-\xi_k p_k(t-\tau)}\times\sin\{mn_s(\omega_o\tau+\frac{1}{2}\alpha\tau^2)+p_{1k}\tau\}\,d\tau$$

$$I_{3s}=\int_0^l\frac{Q_{(m+6)N_k}}{p_{1k}M_k}e^{-\xi_k p_k(t-\tau)}\times\sin\{mn_s(\omega_o\tau+\frac{1}{2}\alpha\tau^2)-p_{1k}\tau\}\,d\tau$$

$$I_{4c}=\int_0^l\frac{Q_{(m+6)N_k}}{p_{1k}M_k}e^{-\xi_k p_k(t-\tau)}\times\sin\{mn_s(\omega_o\tau+\frac{1}{2}\alpha\tau^2)+p_{1k}\tau\}\,d\tau$$

$$p_{1k}=p_k\sqrt{1-\xi_k^2} \quad (19)$$

Damping Model

The resonant response to be determined from Eq. (13) or (19) is dependent on system parameters, the most complex among them being the modal damping ratio. Damping is a complex phenomenon by itself and for the case of turbine blades it primarily consists of friction at the mating surfaces and material hysteresis. The overall damping is known to be dependent on the rotational speed (influencing the blade-disk root friction) and strain amplitude (influencing hysteresis). The above dependency was quantitatively assessed for each mode by Rao et al. (1986) with tests conducted a vacuum spin rig. In these tests excitation was provided by DC electromagnets simulating the nozzles in a turbomachine. From the filtered decay signals of each mode, equivalent modal damping ratios were obtained as a function of rotational speed and strain amplitude. Typical equivalent modal damping values for I mode, obtained from free vibratory response, are shown in Fig. 4(*a*) as a function of strain amplitude for different rotor speeds.

The average damping value obtained from such plots for the first four modes is depicted in Fig. 4(*b*). From Fig. 4(*b*), it is clear that there is a threshold speed in each mode, below which friction damping is predominant. In the first and second modes, this threshold speed is approximately 400 rpm, and for the third and fourth modes, it is around 500 rpm. This threshold speed may be called the friction threshold speed, beyond which the effect of friction decreases due to the centrifugal force, causing increased interlocking between the blade root and the disk.

From Fig. 4(*b*), it can also be observed that the damping at higher speeds, say 1000 rpm and above, is predominantly due to hysteresis. In this region, the blade root gets totally interlocked with the disk and there is not relative movement between them. The speed beyond which there is only hysteresis available for energy dissipation may be called hysteresis threshold speed. In this region beyond the hysteresis threshold speed, say 1000 rpm in this case, there is no energy loss due to friction at the blade root-disk junction.

There is a transition region between the friction threshold speed, and the hysteresis threshold speed, where the energy dissipation occurs due to both friction and material hysteresis simultaneously. For the blade data considered in this paper, the fundamental natural frequency is 646.95 Hz. As the ex-

Downloaded 02 Jun 2010 to 171.66.16.122. Redistribution subject to ASME license or copyright; see http://www.asme.org/terms/Terms_Use.cfm

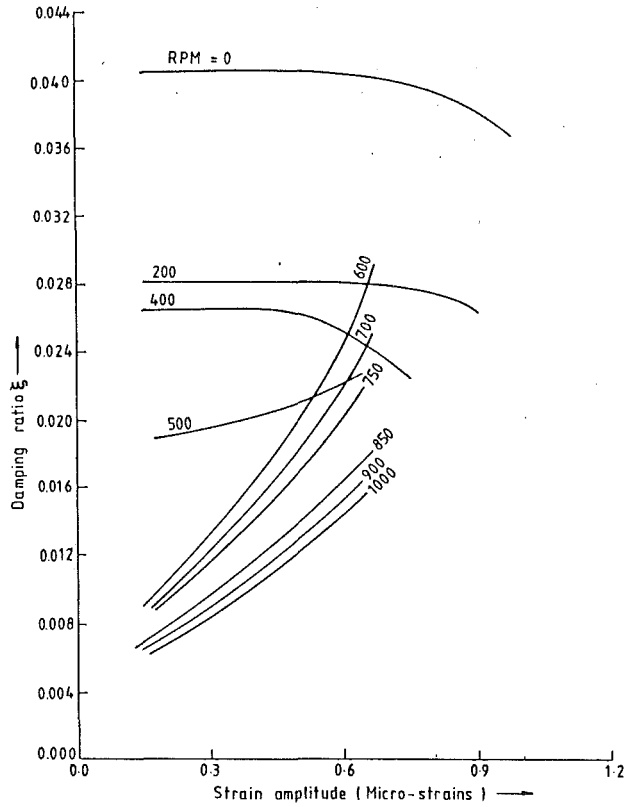


Fig. 4(*a*) Damping ratio versus strain amplitude—mode I

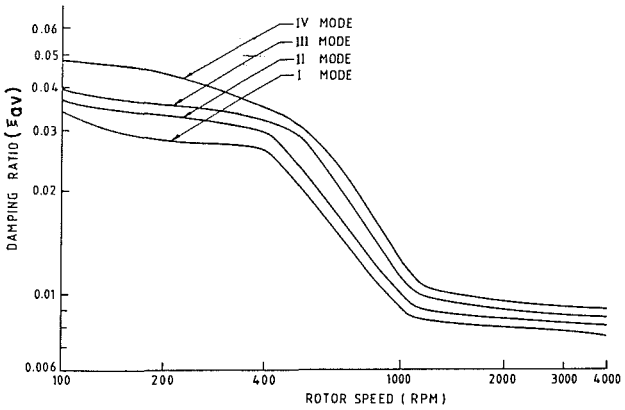


Fig. 4(*b*) Modal average damping ratios versus rotor speed

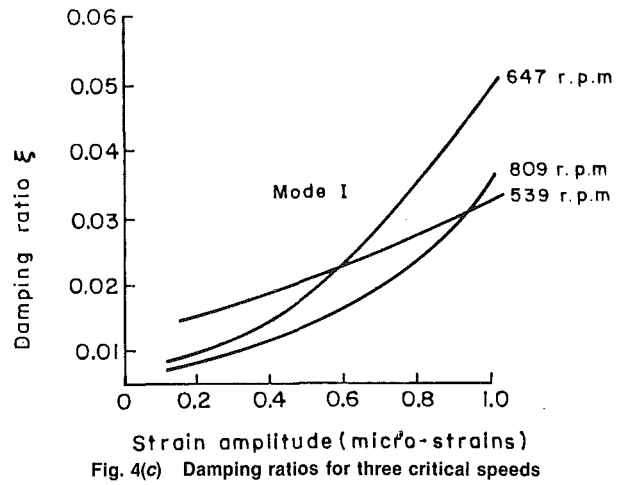


Fig. 4(*c*) Damping ratios for three critical speeds

Table 3 a_i of Eq. (20): $0.1 \times 10^{-6} < \epsilon < 1.0 \times 10^{-6}$

	Rotor Speed (RPM) 539.125	646.95	808.6875
a_0	.010287	.007240	-.001460
a_1	.029565	.004731	.057824
a_2	-.025293	.050749	-.100043
a_3	.028727	-.027351	.129434
a_4	-.010978	.008639	-.063694
a_5	.001923	.007853	.015665

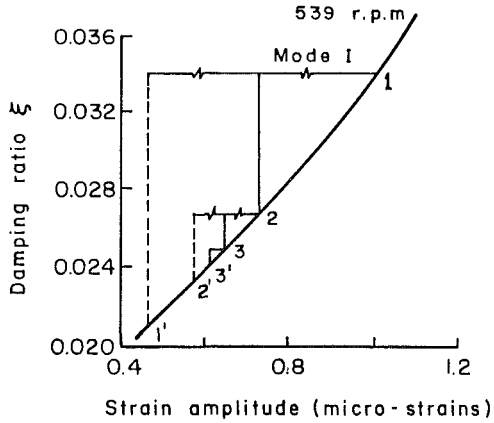


Fig. 5 Iteration procedure

citation is due to 12 magnets simulating the nozzles in a turbine stage there are three critical speeds for the blade, viz., 539.125 rpm, 646.95 rpm, and 808.6875 rpm in the transition region of Fig. 4(*b*), corresponding to the sixth, fifth, and fourth harmonics, respectively. The damping data for these speeds are obtained by interpolation from the relations in Fig. 4(*a*) and shown in Fig. 4(*c*).

The damping ratios for each mode are expressed as polynomial functions of strain amplitude at various rotor speeds, thus

$$\xi = a_o + a_1\epsilon + a_2\epsilon^2 + \ldots + a_5\epsilon^5. \tag{20}$$

The constants a_i in Eq. (20) for 1 mode are obtained by a curve fitting routine and given in Table 3.

Response Under Nonlinear Damping

Starting with an assumed value of strain and corresponding modal ratio, point 1, Fig. 5, the principal component of stress and resultant strain is estimated, point 1′. The averages of the assumed and estimated values of strain and the corresponding modal damping ratio are taken as the starting values for the next iteration. The process is repeated until two successive values of stress are obtained within a specified limit of accuracy.

For constant-speed operation at the resonant speed of 647 rpm the iterative steps and final principal stresses obtained within an accuracy of 0.1 percent are listed in Table 4.

Similarly the stresses at 539 rpm and 809 rpm are found to be 0.12551 MPa and 0.18847 MPa, respectively. These theoretical results have been found to be in good agreement with experiment (Rao and Vyas, 1989). Table 5 gives the comparison between theoretical and experimental stresses.

Table 6 lists the iterative steps and final principal stresses at instantaneous speed of 647 rpm during a start-up operation (start at 0 rpm; accln. 1600 rpm/min). The corresponding

Downloaded 02 Jun 2010 to 171.66.16.122. Redistribution subject to ASME license or copyright; see http://www.asme.org/terms/Terms_Use.cfm

Table 4 Iteration values for constant speed of 647 rpm

Starting Values μ-Strains	ξ	Final Values Stress MPa	μ-Strains
1.00000	0.05000	0.03311	0.16555
0.58276	0.02325	0.06968	0.34840
0.46557	0.01819	0.08871	0.44355
0.45456	0.01776	0.09082	0.45410

Table 5 Comparison of analytical and experimental stresses

Rotor Speed RPM	Analytical Stress (MPa)	Exptl. Stress (MPa) (Vyas,1986)	% Error
539	0.1255	0.1034	21
647	0.0908	0.0661	37
809	0.1885	0.1438	31

Table 6 Iteration values for instantaneous speed 647 rpm during start

μ-Strains	ξ	Stress 10^5Pa	μ-Strains
1.00000	0.05170	0.00000	0.00000
0.50000	0.01958	0.03925	0.01963
0.25981	0.01142	0.54126	0.27063
0.26522	0.11576	0.51698	0.25849
0.26252	0.01149	0.52903	0.26451
0.26351	0.01152	0.52456	0.26228
0.26302	0.01151	0.52679	0.26339
0.26321	0.01151	0.52594	0.26297

values at instantaneous speeds 539 rpm and 809 rpm are found as 0.31153×10^5 Pa and 0.94605×10^5 Pa (Rao and Vyas, 1990).

Fatigue Model

Consider a simplified loading process of the blade as shown in Fig. 6, where starting from 0 rpm the blade is accelerated to its constant working speed of 700 rpm. The rate of acceleration is 1600 rpm/min. This can be translated in terms of stress loading versus time with the help of the stress analysis procedure discussed earlier. The alternating stresses on the blade consist of harmonics of nozzle passing frequency corresponding to the harmonics in the excitation function. These can be treated to act independently of each other, generating independent loading patterns to have finally a cumulative damaging influence on the blade. With reference to Fig. 6, the blade passes through two resonant speeds, namely 539 rpm and 647 rpm during the start-up operation. As mentioned earlier resonance at 539 rpm is caused by the interaction of the first mode with the sixth order of excitation forces, while that at 647 rpm is caused by the interaction of the fifth-order excitation and first mode. The fifth-order vibratory stresses experienced by the blade during the loading process are shown in Fig. 7. The stresses caused by the sixth-order excitation are much smaller in comparison with those of the fifth order.

The mean stress on the blade consists of the zeroth harmonic or stress. In addition to this, the blade also experiences a mean stress due to centrifugal effects. They can be readily computed using

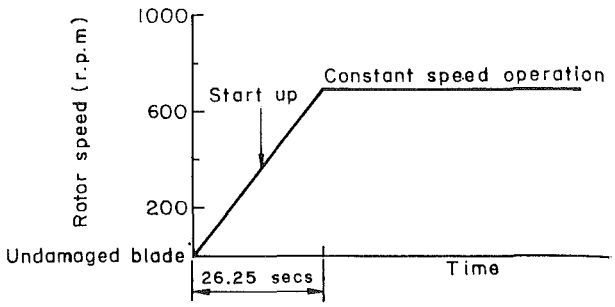


Fig. 6 Blade loading process

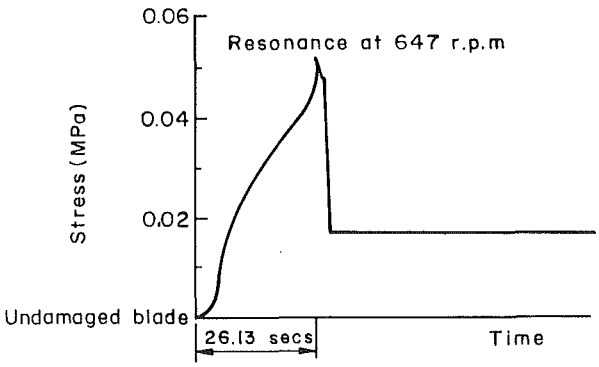


Fig. 7 Vibratory stress on blade during the loading of Fig. 6

$$\sigma_{zc} = \frac{(R+Z)}{A_z}\left(\frac{\text{RPM}}{60}\,2\pi\right)^2 \int_0^l A_z\,\rho dz \tag{21}$$

The fatigue strength of a material is defined in terms of the endurance limit of a standard rotating beam specimen of the material. The strength of the blade can be considerably smaller due to a variety of factors such as surface, k_a, size, k_b, reliability, k_c, temperature, k_d, stress concentration, k_e, and miscellaneous effects, k_f. Standard tables can be referred to broadly define these factors for specific conditions of operation.

Bagci's (1981) fatigue failure surface line, which defines the two zones, namely, the zone of fatigue failure experiencing brittle fracture and the zone of failure due to yielding, in one, by providing a unified fatigue design equation for machine members is employed to account for the mean stress effects. Figure 8 shows the Bagci line coupled with the S-N diagram defining the fatigue failure surface. The surface line is of fourth order and is given by

$$\sigma_{af} = \sigma_e\left[1 - \left(\frac{\sigma_{mf}}{S_y}\right)^4\right] \tag{22}$$

The S-N plane reads

$$\log S_e' = -A \log N + B \text{ for } 10^3 < N < 10^6$$

$$S_e' = S_e = kS_u \text{ for } N \geq 10^6$$

$$A = \frac{1}{3}\log\left(0.9\,\frac{S_u}{S_e}\right)$$

$$B = \log\left[R_f\,\frac{(0.9\,S_u)^2}{S_e}\right] \tag{23}$$

$k = 0.5$ for standard rotating beam fatigue specimen made of steel.

For the blade considered (material 40Ni3), $S_u = 900$ MPa; $S_y = 650$ MPa; $S_e = 450$ MPa. For laboratory conditions of

Downloaded 02 Jun 2010 to 171.66.16.122. Redistribution subject to ASME license or copyright; see http://www.asme.org/terms/Terms_Use.cfm

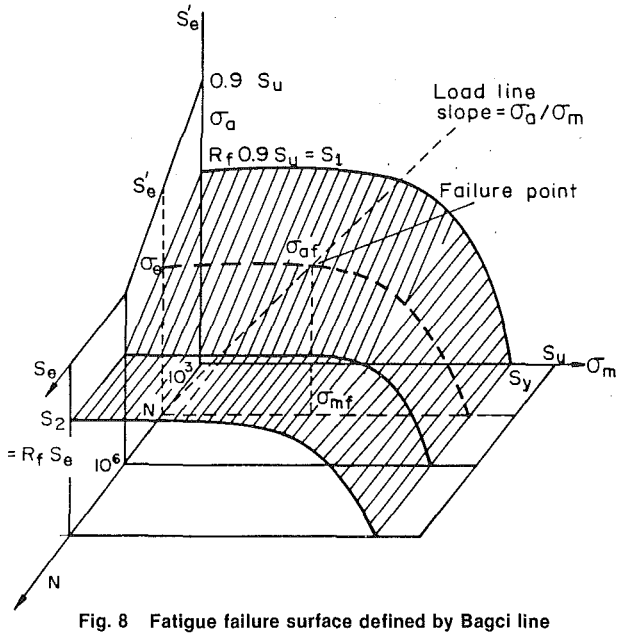


Fig. 8 Fatigue failure surface defined by Bagci line

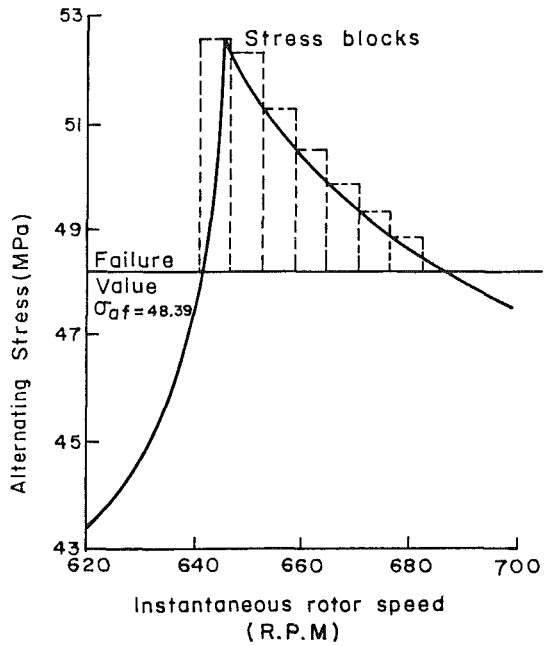


Fig. 9 Stress block construction

operating let the endurance limit modifying factor R_f be taken as 0.112. Hence the endurance limit is 50.4 MPa. Using these data the fatigue failure surface can be generated. Any load point can then be located on this surface to obtain the number of load cycles, N, to failure, if any.

Considering the fourth order of excitation the following observations can be made:

Start up

- Maximum alternating stress of 0.0526 MPa experienced momentarily while passing through resonance at 647 rpm (Ref. Fig. 7).
- Mean stress at 647 rpm due to centrifugal effects is 0.6 MPa (Eq. (21)).
- Mean stress due to static "steam/gas" force (zeroth component of excitation, cf. Table 1) is 0.29 MPa.
- Total mean stress $= 0.6 + 0.29 = 0.629$ MPa.

Constant-speed operation at 700 rpm

- Alternating stress is 0.0175 MPa (Fig. 7).
- Mean stress due to centrifugal rotation is 0.70 MPa (Eq. (21)).
- Mean stress due to static "steam/gas" force is 0.29 MPa.
- Total mean stress $= 0.70 + 0.29 = 0.99$ MPa.

The entire stress pattern can be seen to lie well below the fatigue failure surface indicating safe operation. It should be noted that the nozzle forces of Fig. 2 are simulated by electromagnets and are extremely small. In practice steam/gas forces would be large enough to drive the machine for power generation, giving rise to much larger stresses.

For the purpose of illustration let it be assumed that the excitation forces are such that the stresses are 1000 times larger. Thus for the same rotor operation of Fig. 6 we have:

Start up

- Maximum alternating stress $= 0.0526 \times 1000 = 52.6$ MPa.
- Mean stress due to centrifugal effects $= 0.6$ MPa.
- Mean stress due to static excitation force $= 0.29 \times 1000 = 290$ MPa.
- Total mean stress $= 0.6 + 290 = 290.6$ MPa.

Constant speed operation at 700 rpm

- Alternating stress $= 0.0175 \times 1000 = 17.5$ MPa.
- Mean stress due to centrifugal effects $= 0.70$ MPa.
- Mean stress due to static excitation force $= 0.29 \times 1000 = 290$ MPa.
- Total mean stress $= 0.70 + 290 = 290.70$ MPa.

In this case although the stresses during constant-speed operation lie below the failure surface, the blade experiences high resonant stresses during start up operation while passing through the resonant speed of 647 rpm. The damaging influence of this transient resonance is estimated as follows.

Using Eq. (21) the mean stress due to centrifugal effects is found to increase from a value of 0.52 MPa at 600 rpm to 0.70 MPa at 700 rpm with 0.60 MPa at 647 rpm. The mean stress due to static excitation force is constant equal to 290 MPa. Taking the total mean stress value σ_{mf} during the transit past resonance as 290.60 MPa, the failure value σ_{af} of the alternating stress is fixed using Eq. (22) (with $\sigma_e = 50.4$ MPa). The alternating stress failure value, σ_{af}, and the resonant stress peak during passage through 647 rpm are shown on an expanded scale in Fig. 9. The peak region lying above the failure value is segmented into a number of stress blocks. For each stress block the fatigue damage is separately estimated in terms of the number of cycles to failure, N, by locating the stress point on the failure surface. Simultaneously the number of stress cycles, n, experienced during each stress block is obtained from the instantaneous nozzle passing frequency and the known acceleration rate. Fatigue damage is obtained in terms of ratios n/N for all stress blocks and added to obtain the damage during the blade loading process. Miner's rule, $n/N = 1$, is employed for damage accumulation. The calculations determine that the blade can withstand approximately 31 loading cycles of the type described. For a complete fatigue damage estimate, effects during shut down and those due to other orders of engine excitation also need to be considered.

Conclusion

A blade designed for safe operation at constant rotor speeds may get damaged during transient operations. In this study blade stresses during constant and variable speed operations have been analyzed. A numerical procedure for determination of steady-state and transient stresses under nonlinear damping has been described. Fatigue life estimation technique is outlined and the damaging influences of transient operations are illustrated.

Downloaded 02 Jun 2010 to 171.66.16.122. Redistribution subject to ASME license or copyright; see http://www.asme.org/terms/Terms_Use.cfm

References

Bagci, C., 1981, "Fatigue Design of Machine Elements Using Bagci Line Defining Fatigue Failure Surface Line," *Mech and Mach Theory*, Vol. 16, No. 4, p. 239.

Irretier, H., 1986, "Transient Vibrations of Turbine Blades Due to Passage Through Partial Admission and Nozzle Excitation Resonances," *Proc. IFToMM Intl. Conf. Rotor Dynamics*, Tokyo, p. 301.

Jones, D. I. G., and Muszynska, A., 1983, "A Discrete Model of a Multiple Blade System With Interblade Slip," *Vibrations of Blades and Bladed Disk Assemblies*, ASME, p. 137.

MacBain, J. C., and Whaley, P. W., 1984, "Maximum Resonant Response of Mistuned Bladed Disks," ASME *Journal of Vibration, Acoustics, Stress, and Reliability in Design*, Vol. 106, p. 218.

Rao, J. S., Gupta, K., and Vyas, N. S., 1986, "Blade Damping Measurement in a Spin Rig With Nozzle Passing Excitation Simulated by Electromagnets," *Proc. Shock Vib. Bull.*, US Naval Res. Labs., Proc. 56, Pt 2, p. 109.

Rao, J. S., Gupta, K., and Vyas, N. S., 1986, "Analytical and Experimental Investigations on Vibratory Stresses of a Rotating Steam Turbine Blade Under NPF Excitation," *Proc. IFToMM Intl. Conf. Rotor Dynamics*, Tokyo, p. 269.

Rao, J. S., and Vyas, N. S., 1986, "On Life Estimation of Turbine Blading," *Proc. IFToMM Tech. Comm. on Rotordynamics*, Seventh IFToMM World Congress, Sevilla, Spain.

Rao, J. S., 1987, *Turbine Blade Vibration, Shock & Vib. Dig.*, Vol. 19, No. 5, p. 3.

Rao, J. S., and Vyas, N. S., 1989, "Resonant Stress Calculation of a Turbine Blade With Damping as a Function of Rotor Speed and Vibratory Amplitude," ASME Paper No. 89-GT-27.

Rao, J. S., and Vyas, N. S., 1990, "Transient Stress Response of a Turbine Blade Under Non Linear Damping Effects," ASME Paper No. 90-GT-269.

Rieger, N. F., 1985, "Factors Affecting the Fatigue Life of Turbine Blades and an Assessment of Their Accuracy," *Shock Vib. Bull.*, Proc. 55, Pt. 1, p. 51.

Roark, R. J., and Young, W. C., 1976, *Formulas for Stress and Strain*, 5th ed., McGraw-Hill, IBC.

Sinha, A., and Griffin, J. H., 1984, "Effects of Static Friction on the Forced Response of Frictionally Damped Turbine Blades," ASME JOURNAL OF ENGINEERING FOR GAS TURBINES AND POWER, Vol. 106, p. 65.

Srinivasan, A. V., 1984, "Vibration of Bladed Disk Assemblies—A Selected Review," ASME *Journal of Vibration, Acoustics, Stress, and Reliability in Design*, Vol. 106, p. 165.

Vyas, N. S., 1986, "Vibratory Stress Analysis Stress and Fatigue Life Estimation of Turbine Blade," Ph.D. Thesis, I.I.T., New Delhi, India.

Vyas, N. S., Gupta, K., and Rao, J. S., 1987, "Transient Response of Turbine Blade," *Proc. 7th IFToMM World Congress*, Sevilla, Spain, p. 697.

Downloaded 02 Jun 2010 to 171.66.16.122. Redistribution subject to ASME license or copyright; see http://www.asme.org/terms/Terms_Use.cfm

H. L. Bernstein

R. C. McClung

T. R. Sharron

Materials and Mechanics Department,
Southwest Research Institute,
San Antonio, TX 78228

J. M. Allen

Combustion Turbines Program,
Electric Power Research Institute,
Palo Alto, CA 94303

Analysis of General Electric Model 7001 First-Stage Nozzle Cracking

Analyses of first-stage nozzle cracking in General Electric Model 7001B and 7001E industrial gas turbines are presented. Empirical algorithms are developed to predict the maximum extent of cracking that is visible on these nozzles as a function of engine cyclic history and the number of fired hours. It is shown that the algorithms predict this cracking to within a factor of two. Metallurgical analyses of nozzles show that crack growth follows the carbide-matrix interface, environmental attack occurs at the crack tip, and that the microstructure changes by increasing the amount of carbide precipitation, which increases the hardness. These metallurgical results, along with mechanical test data and stress analyses from the literature, are used to understand the nature of nozzle cracking. The maximum extent of cracking coincides with locations of maximum thermal stresses as determined by finite element analyses of similar nozzle designs. This location is at the airfoil-shroud junction on the middle vanes of multivane castings. The use of these algorithms as a predictive maintenance tool and the ability to inspect nozzles visually in the engine also are discussed.

Introduction

The first-stage nozzles of gas turbines are exposed to the hottest gases in the turbine section of the engine. These components, which are also called stators or vanes, experience cracking in all types of gas turbines, whether industrial, aircraft, or marine. This cracking is usually the cause for the removal and repair of the component.

Cracking of nozzles of industrial gas turbines is particularly severe due to the long service times and, in many cases, numerous cycles that these engines are required to sustain. Individual crack lengths in the larger engines can reach 3 to over 4 in. (7 to over 10 cm) in length, and the sum of all the crack lengths over the entire nozzle can be greater than 500 in. (13 m).

Other causes of nozzle degradation include trailing edge bowing, foreign object damage, burning of the leading edge, etc. While these forms can be very important in specific instances, nozzle cracking is the principal mode of degradation of most industrial gas turbine nozzles.

The purpose of this paper is to characterize and predict the cracking that occurs on industrial gas turbine nozzles. The General Electric Model 7001 gas turbines were chosen for this study. These engines are the subject of an ongoing program to develop a Life Management System (LMS) for these engines, which is sponsored by the Electric Power Research Institute [1]. Part of this project involves the development of a computer program, called REMLIF, to compute the remaining life of the first-stage nozzle and buckets.

Contributed by the International Gas Turbine Institute and presented at the 37th International Gas Turbine and Aeroengine Congress and Exposition, Cologne, Germany, June 1–4, 1992. Manuscript received by the International Gas Turbine Institute February 21, 1992. Paper No. 92-GT-311. Associate Technical Editor: L. S. Langston.

Background

The GE MS7001 gas turbine line is composed of five models: the 7B, 7C, 7E, 7EA, and 7F. This paper will focus on the 7B and 7E engines since these have the largest database on nozzle cracking. All the engines are single shaft with an in-line canular type of combustion system. The turbine inlet temperature, or firing temperature, of the 7B is 1840 to 1850°F (1005 to 1010°C) and that of the 7E is from 1985 to 2020°F (1085 to 1105°C). These engines can burn a variety of fuels, but natural gas is the primary fuel in use today due to its lower cost. The base load power rating of these engines at ISO is 50 to 59 MW for the 7B and 72 to 78 MW for the 7E.

The design of the nozzle for the 7E engine is significantly different from that of the 7B engine. The 7B nozzle consists of 12 segments, with each segment having 4 vanes (also called partitions) in a single casting, as shown in Fig. 1. The 7E nozzle has 18 segments with two vanes per segment. The vane of the 7B is smaller than that of the 7E.

The nozzles are cast from FSX-414, a cobalt-base superalloy, and are not coated. This metal is discussed in the section on Metallurgical Analysis of Nozzle Cracking.

Both nozzles are cooled by compressor discharge air, which enters the vane from a slot in the outer sidewall and flows out of the trailing edge cooling holes. Both designs use perforated sheet metal inserts in the vane to provide impingement cooling of the interior surfaces. The 7B nozzle is a single-cavity design, whereas the 7E nozzle has two interconnected cavities. In order to lower the temperatures on the thin trailing edge, both nozzles have a row of cooling holes at the exit of the trailing edge and a row of cooling holes on the pressure side[1] near the trailing edge. In addition to these cooling holes, the 7E nozzle has two

[1]Pressure side refers to the concave side, and suction side refers to the convex side.

Copyright © 1994 by ASME
Downloaded 02 Jun 2010 to 171.66.16.122. Redistribution subject to ASME license or copyright; see http://www.asme.org/terms/Terms_Use.cfm

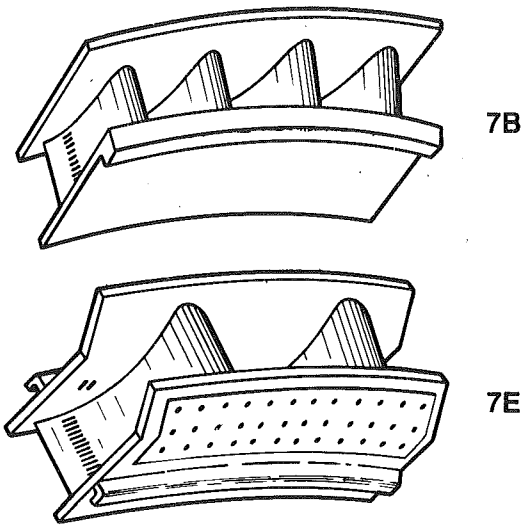


Fig. 1 Schematic of 7B and 7E nozzle segments

rows of cooling holes on the suction side near the leading edge, and it has additional cooling holes on the outer and inner sidewalls to cool the suction and pressure side fillets. These additional cooling holes provide film cooling in the regions near the holes.

The outer sidewall, or shroud, of the 7B is cooled by the compressor discharge air that passes over it. Perforated sheet metal plates have been added to the 7E nozzle to provide impingement cooling to both sidewalls.

The 7C nozzle is similar in design to the 7B nozzle. The 7EA nozzle is similar in design to the 7E nozzle, except that the nozzle has additional support at the inner diameter. The 7F nozzle incorporates additional film cooling by means of numerous cooling holes over the nozzle surface, and operates at turbine inlet temperatures of 2300°F.

Description and Inspection of Nozzle Cracking

Cracking can be found in numerous areas of the nozzle. The most severe cracking is usually restricted to certain areas, which are dependent upon the nozzle design. The following description of nozzle cracking concentrates on the vane cracking since this is the subject of the paper. Sidewall cracking also occurs, and these cracks can be both long and numerous. The description of cracking for 7B nozzles is based upon nozzles run under peaking, intermediate, and load following operation, but not baseload operation. Cracking of 7E nozzles has been observed for baseload, intermediate, and load following operation, but not peaking operation.

For the 7B nozzle, the most severe cracking is found on the suction side at the fillets with the sidewalls, as shown in Fig. 2.[2] These cracks often extend a long distance in the fillet area, then radiate to the sidewall surface. The outer sidewall will usually show this cracking earlier than the inner sidewall. In addition, the center two vanes are more heavily cracked, although the number four vane can have substantial cracking. The number one vane, whose suction side is not constrained by the other vanes, has very little suction side cracking. Pressure side cracking on 7B nozzles is also present at the fillet areas, but these cracks are not visible when inspecting the nozzle in the engine due to surface deposits and closed cracks (most likely caused by residual compressive stresses).

The trailing edge is usually cracked on the 7B nozzle, typically at the fillet and along the trailing edge (TE), as shown

[2]Suction side fillet cracking was also found by Flowers et al. [13], for first-stage MS5002A&B nozzles.

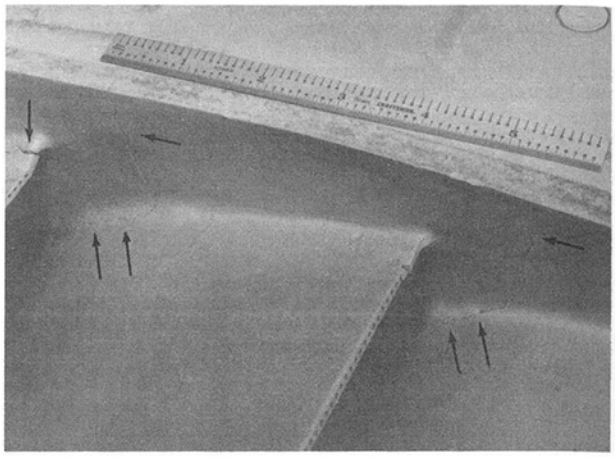


Fig. 2 Typical 7B suction side cracking with cracks radiating to the sidewall. At the left-hand side is a trailing edge crack at the fillet with the sidewall. (Scale is in inches.)

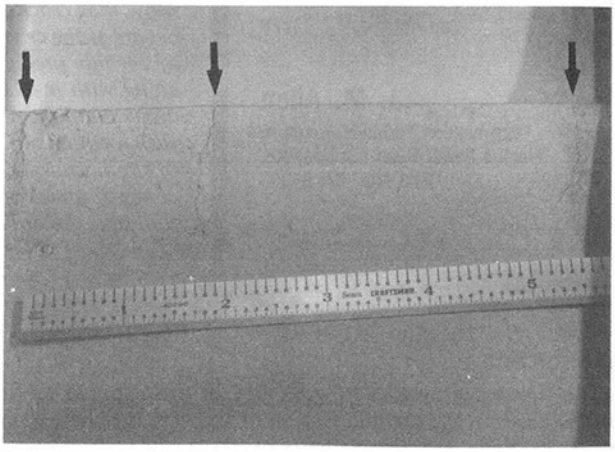


Fig. 3 Three typical 7B trailing edge cracks. The crack at the left-hand side is near the fillet. (Scale is in inches.)

in Fig. 3. Cracking starts at the end of the TE and tracks parallel to the sidewall toward the pressure side cooling holes. Leading edge (LE) damage is generally limited to foreign object damage or erosion. Cracks in this area are normally short and directed around the radius of the leading edge. Cracking along the length of the leading edge has been observed in both 7B [2] and 7C nozzles, but is not common.

The 7E nozzle shows a different characteristic set of cracks than the 7B nozzle. The majority of the cracking is located on the pressure side in an area above the pressure side cooling holes. These cracks grow from the sidewall toward the center of the partition and are generally found in a group, as shown in Fig. 4. Significant amounts of cracking occur parallel to, but not in, the fillet near the leading edge of the pressure side. These cracks are usually of a significant length and often are found as a series of cracks. Trailing edge cracks generally originate from the cooling hole nearest the sidewalls instead of the fillet area as in the B model. These cracks also migrate toward the pressure side cooling holes. Leading edge cracks have a tendency to be more severe on the E model than on the B and tend to travel in the longitudinal direction across the leading edge, as shown in Fig. 5. Finally, cracks at the fillet between the suction side and sidewall tend to grow in a diagonal manner across the vane in the direction of the leading edge.

In addition to the cracks that are visible on the exterior surfaces, cracks can also form on the interior surfaces of both

Downloaded 02 Jun 2010 to 171.66.16.122. Redistribution subject to ASME license or copyright; see http://www.asme.org/terms/Terms_Use.cfm

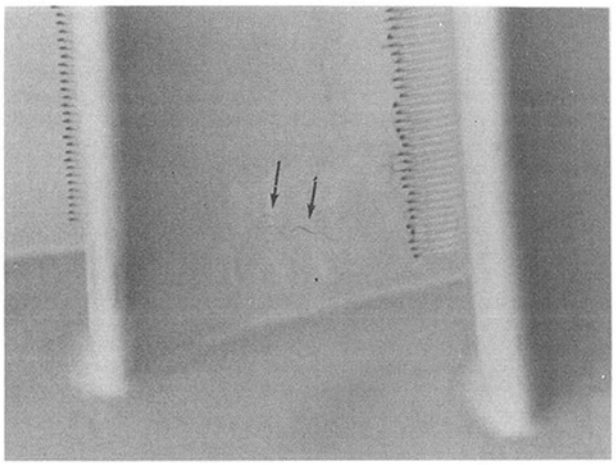


Fig. 4 Typical 7E pressure side cracking

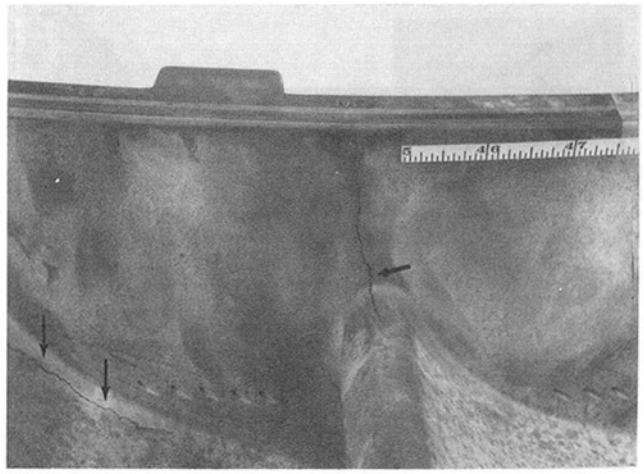


Fig. 5 Typical 7E cracking. A longitudinal, leading edge crack is continuing into the sidewall. On the left side is a pressure side crack at the fillet. (Scale is in inches.)

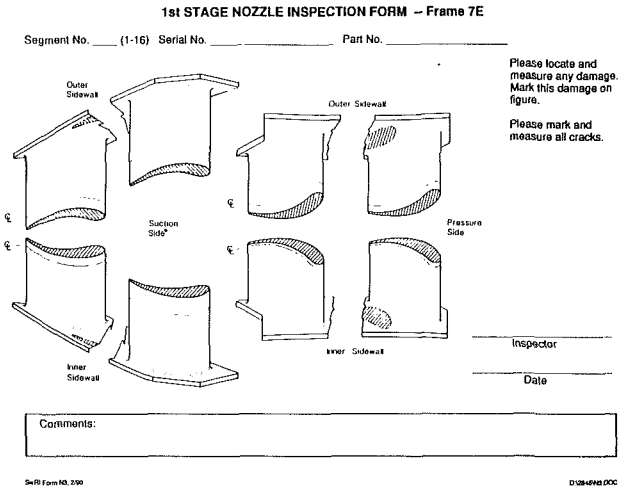


Fig. 6 Nozzle inspection form

nozzles and grow out to the exterior. Metallurgical specimens show cracks initiating from trailing edge cooling holes and from sharp fillets at the junction of the leading edge with the sidewall. These interior cracks cannot be found by visual inspection while the nozzle is in the engine. Since these cracks are not normally found during inspections, they are not normally repaired during refurbishment of the nozzle.

Inspection Techniques

Due to the difference in dominant cracking tendencies of the two types of nozzle, the problems incurred in the inspection process vary significantly. For the 7B nozzle, inspecting the suction side, the location of the most severe cracking, is the single largest obstacle to overcome for inspections done while the nozzle remains in the engine. With some degree of effort, one can see most of the pressure side of the nozzle fairly well. However, the suction side is inaccessible except by means of mirroring or some type of small video equipment. Lighting, because of the curved surface, must be reflected off some type of crook-necked device, or fiber optically transferred. Measurement of crack lengths must also be accomplished through the use of a mirror surface or with a probe such as a borescope. Even with these devices, the curved surfaces cause distortion and reduce accuracy. Methods are currently under study that should greatly enhance the ability of the inspector to acquire accurate suction side data [3]. In addition to these obstacles, the cramped conditions and poor maneuverability in the turbine make suction side inspection techniques even more difficult.

Apart from the diligence of the inspector, the key to a good inspection is the lighting technique and a good crack charting form. It is imperative that a good light source be used when doing an inspection. This means that the light must supply enough lumens to overcome the light absorption of the combustion deposits and be small enough to be moved around easily. The surface must be scanned from several angles to avoid missing any indication that could be masked by shadow or combustion deposit colorations. This is especially important on the trailing edge and pressure surfaces where deposits tend to hide small cracks. In addition, the form used to record cracks needs to convey the information accurately to an analyst using the data, perhaps several years after it was recorded. A sample of a newer type of form is shown in Fig. 6 [3]. Since each side of the vane is shown, there is no confusion in where the crack is located. Also with the connected fillets and sidewalls, cracks that migrate in this direction can be accurately displayed.

There are a number of small tools that make an inspection an easier task to perform. Some type of breathing mask is recommended, especially in the tight confines of the turbine. A collection of small paintbrushes, some of which have had the bristles cut short to make them stiffer, is needed to clear away the loose deposits. An air source, either canned or from a compressor line, is desirable. An oil or other liquid can be used to enhance the contrast of the crack. Finally, a see-through scale[3] is used to measure the crack length.

Metallurgical Analysis of Nozzle Cracking

The nozzles are air cast from FSX-414, a General Electric cobalt base superalloy similar to X-40 and X-45. High-temperature coatings are not used. The nominal chemical composition of FSX-414, in weight percent, is 29.5 percent Cr, 10.5 percent Ni, 7 percent W, 0.25 percent C, 0.01 percent B, and balance Co. The standard heat treatment is 2100°F (1150°C) for 4 hours, furnace cool to 1700°F (925°C) and hold for 10 hours, furnace cool to below 1000°F (540°C) and then air cool [4]. FSX-414 has less carbon than X-40, and thus, has better ductility and weldability. It has more chromium than either X-40 or X-45 for improved corrosion resistance. All three alloys are strengthened primarily by the formation of carbides. Typical carbide formations are shown in Fig. 7. Car-

[3]A precision reproduction of a hundreth scale works well when printed on overhead projection transparency stock.

Downloaded 02 Jun 2010 to 171.66.16.122. Redistribution subject to ASME license or copyright; see http://www.asme.org/terms/Terms_Use.cfm

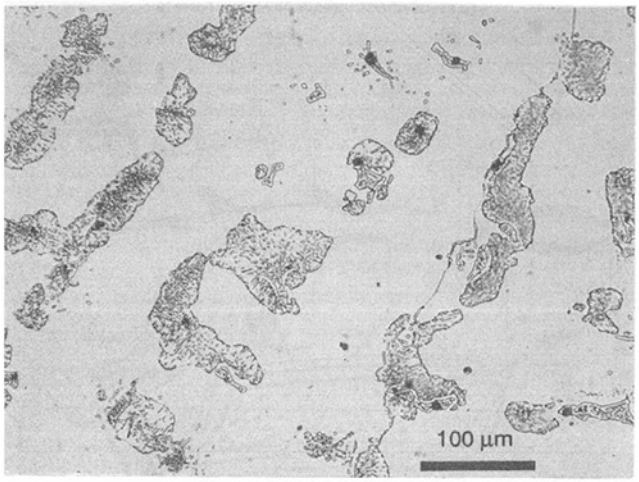


Fig. 7 Typical carbide formations in FSX-414; chromic oxide etch (#45722)

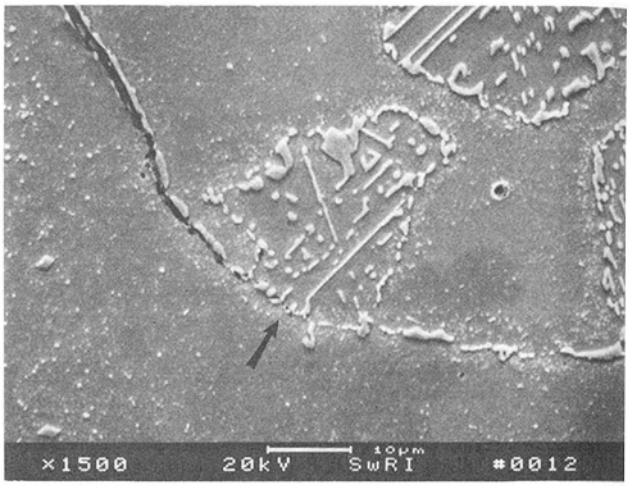


Fig. 9 Tip of trailing edge crack shown in Fig. 8. The arrow identifies small holes developing ahead of the main crack at the carbide-matrix interface. Chromic oxide etch (#46100).

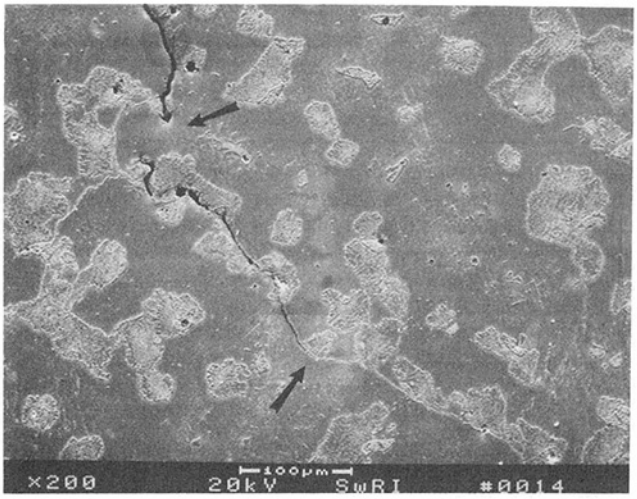


Fig. 8 Trailing edge crack in a 7B nozzle. The upper arrow identifies where the crack stopped and restarted because there were no carbides to follow. The lower arrow identifies the end of the crack, which is shown at higher magnification in Fig. 9. Chromic oxide etch (#46102).

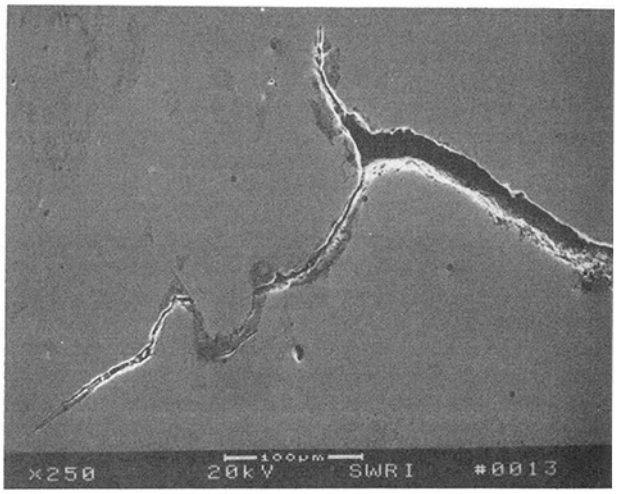


Fig. 10 Tip of pressure side crack in a 7E nozzle. The crack is filled with oxidation products. Unetched (#51338).

bides are typically of the MC, M_6C, and $M_{23}C_6$ types. Additional strengthening is provided by solid solution hardening from tungsten. General discussions of FSX-414 [4] and other cobalt-base superalloys [5, 6, 7] are available. The primary reason for using these alloys for nozzles is their good high-temperature creep strength, oxidation resistance, corrosion resistance, and their ability to be repair welded.

FSX-414 has moderate ductility at room temperature, with an elongation of about 15 percent, but good ductility at temperature, with an elongation of about 35 percent at 1600°F (870°C). However, the ductility of cobalt-base superalloys, including FSX-414 [4], decreases with high-temperature exposure [5]. This loss of ductility may be due to the secondary precipitation of $M_{23}C_6$ carbides during service exposure [5].

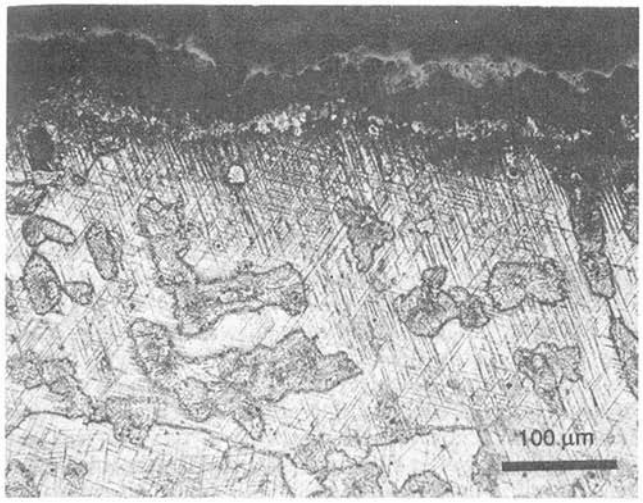
Fatigue crack initiation tests, both isothermal and thermal mechanical, and isothermal fatigue crack growth tests on FSX-414 have been conducted at elevated temperature [8]. These tests showed that increasing the strain range from 0.4 to 0.8 percent reduced the fatigue life by about a factor of four. These tests also showed that hold times of 2 and 15 minutes at the minimum strain reduced the fatigue crack initiation life by up to a factor of 1.7. Two-minute hold times at both maximum and minimum load increased the crack growth rate as much as 6 times. This behavior is consistent with isothermal data on X-45 [9].

Metallurgical analyses of samples from 7B and 7E first-stage nozzles show the development of the microstructure, the crack path, and environmental attack. Representative microstructures and cracks are discussed below.

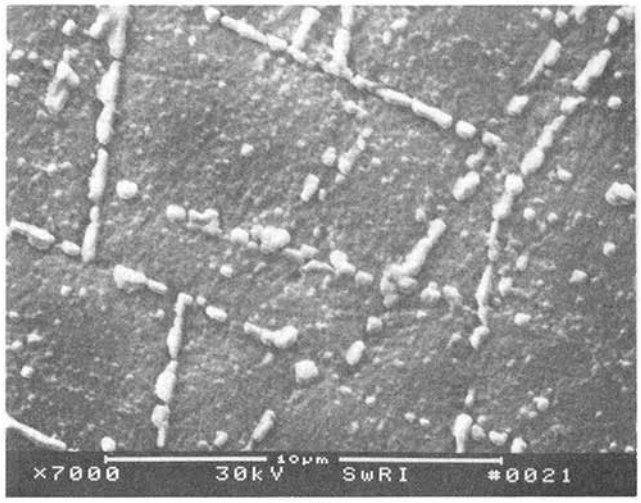
The end of a trailing edge crack in a 7B nozzle is shown in Fig. 8. The crack is 1.5 in. (38 mm) long, and it originated at a cooling hole in the trailing edge. The crack is irregular and integranular. The tip of the crack is shown in Fig. 9. It can be seen that the crack is following the carbide-matrix interface. At the end of the crack, the crack has stopped where there are no carbides in front of it. Cracking at the carbide-matrix interface has occurred ahead of the end of the crack tip. Some of this cracking may be due to the oxidation of carbides, which forms carbon monoxide pockets adjacent to the carbides [10]. This path of cracking, along the carbide-matrix interface, is seen consistently in samples from the fillets, sidewalls, and trailing edges, as well as in laboratory experiments [10].

Environmental attack of the crack is also seen in the metallurgical samples. An example of this attack is shown in Fig. 10, for a crack near the fillet of the pressure side and inner

Downloaded 02 Jun 2010 to 171.66.16.122. Redistribution subject to ASME license or copyright; see http://www.asme.org/terms/Terms_Use.cfm



(a)



(b)

Fig. 11 Secondary carbide precipitation at the trailing edge of a 7B nozzle. The top photo shows the end of the trailing edge. The bottom photo is a detailed view, showing the fine, crystallographic particles. Chromic oxide etch (#45718 and #46108).

sidewall on a 7E nozzle. The tip of the crack is filled with oxidation products.

At the end of the trailing edge of this same 7B nozzle, secondary carbide particles have formed. These appear to be needles at lower magnification, as shown in Fig. 11(*a*), but at higher magnification, they can be seen to be discrete particles along crystallographic planes, as shown in Fig. 11(*b*). This microstructure should be compared to the microstructure representative of the as-heat-treated condition, Fig. 7, which was obtained from a sample located in a cool section of the outer sidewall. The carbide network is discrete and has not coarsened or formed a fine precipitation of carbides. Much more extensive carbide precipitation occurs for 7E nozzles as shown for the trailing edge section in Fig. 12.

The microhardness of the various microstructures was determined. The as-heat-treated structure shown in Fig. 7 had a hardness of 280 DPH.[4] The trailing edge section shown in Fig. 8 had a hardness of 330 near the tip of the trailing edge, which had greater carbide precipitation, and a hardness of 305 away from the tip, which had less precipitation. The hardness of

[4]All hardness values are DPH microhardness measured in the matrix between the carbide eutectics.

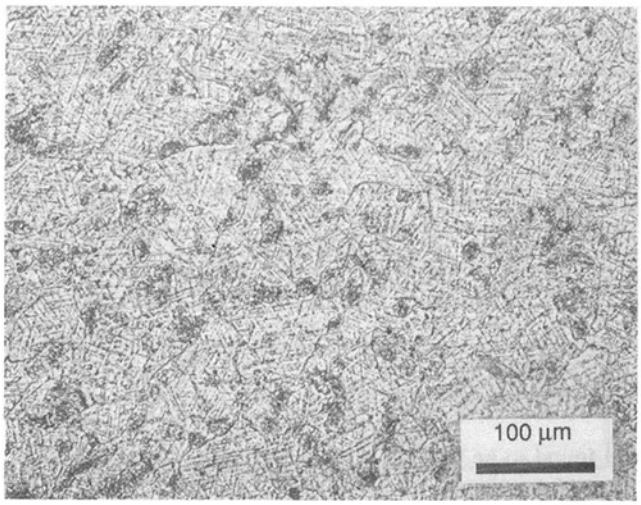


Fig. 12 Secondary carbide precipitation at the trailing edge of a 7E nozzle. The precipitation is much denser than for the 7B nozzle. Chromic oxide etch (#51389).

trailing edge samples from 7E nozzles was 360 for a nozzle that was run at lower temperatures and 410 for a nozzle that was run at higher temperatures.

In summary, the results of the metallurgical analyses are:

(1) Cracking occurs along the carbide-matrix interface; (2) high-temperature environmental attack occurs at the crack tip; (3) the microstructure changes by increasing the amount of carbide precipitation, including the formation of very fine, crystallographically oriented carbides; and (4) the hardness increases with increasing carbide precipitation.

Stress Analysis of Nozzles

Heat transfer and stress analysis of multivane nozzle segments is an involved process. Computational methods, notably finite element analysis (FEA), are well developed, but a refined inelastic model of a cooled multivane nozzle segment is a very large problem. In some cases, such models may exceed the solution capability of scientific mainframe computers. The modeling is complicated by the geometric detail associated with the convective and film cooling and with rapidly changing thermal boundary conditions, e.g., those associated with film cooling. The generation of boundary conditions for transient analyses is tedious, and long run times are required to obtain transient solutions for the various startup and shutdown conditions that can be experienced by the turbine. Procedures that have been used for performing detailed transient inelastic analysis of nozzles are described in [11], but few results from such analysis have been published. The only results for a multivane segment, such as the subject ones, that could be found were for steady-state conditions [9, 12]. Some nozzle transient temperature measurements taken during startup, at steady state, and during shutdown of a General Electric Frame MS5002A have been reported [13].

Steady-State Finite Element Analysis. Hultgren [12] describes a steady-state heat conduction and elastic FEA of a three-vane segment and a single-vane segment. It was shown that, at steady state, the highest thermal stress occurs on the suction surface of the middle vane near the outer shroud fillet at the airfoil-shroud junction, which, as stated earlier, corresponds with one of the critical areas of the subject nozzles. It was noted that this was the location where the highest incidence of cracking occurred in service and that there had been no cracking in the number one vane fillet (vane with its suction surface next to an edge of the shroud) where the thermal stress

Downloaded 02 Jun 2010 to 171.66.16.122. Redistribution subject to ASME license or copyright; see http://www.asme.org/terms/Terms_Use.cfm

Table 1 Host sites

Site	Operation	Engine
New England	Intermediate	7E
Alaska	Load Following	7E
Northern	Base Load	7E
Houston	Base Load	7E
Gulf Coast	Intermediate	7B
Southwest	Load Following	7B
East Coast	Peaking	7B

was found to be only 28 percent of that in the middle vane. For vane number 3, the stress was 75 percent as large. At the inner diameter of the nozzle sector, the relative stresses were 28, 75, and 38 percent for vanes 1, 2, and 3, respectively.

High stresses occur at the airfoil-shroud junctions due to three effects. First, there is an abrupt change in geometry and temperature between shroud and airfoil, which causes high localized stresses. Second, stresses arise due to internal bending moments and forces required to maintain slope and deflection compatibility between the vanes and shrouds in multivane segments. Third, stresses are caused by the thermal gradient between the exterior and internal surfaces of the vane, and the thermal gradients along the chord of the vane. For the 7B nozzle, the stresses are greater in vanes 2 and 3 because of the greater restraint imposed by the shroud at these locations. The maximum curvature region on the suction side of vane 1 is much less affected because it is adjacent to an edge of the shroud. For the single vane segment that was analyzed in [12], the inner and outer fillet stresses were 25 and 50 percent as large as these stresses on a three-vane segment, because the vanes could thermally deform independently of each other.

Transient Temperature Measurements. Flowers et al. [13] describe the transient and steady-state temperature response of a General Electric MS5002A nozzle vane and endwall (shroud). Large differences between the vane pitch section average temperature and average endwall temperature were measured in these tests. This difference was considered to be proportional to the thermal stress in the sidewall-vane fillet. The largest difference, during the heating part of the cycle, occurred during acceleration or at steady state, depending on the acceleration rate, but the steady-state differential was reasonably close to the maximum in any case. During shutdown, the differential was reversed with the maximum being roughly half the steady-state value for a normal shutdown and roughly two thirds as large for a full-load trip out. The suction side fillet between the endwall and vane was a principal mode of cracking for this nozzle, as it is for the subject MS7001B nozzle. This is also consistent with the experience reported by Westinghouse and MHI for two of their multivane segments [9, 12].

Prediction of Nozzle Cracking

The nozzle cracking algorithms were derived from inspection records and operating histories corresponding to eleven different engines at seven different sites. The sites are summarized in Table 1, which reveals the wide range of operating parameters and environments (including ambient temperature and humidity). The different sites also varied in their cycle types (combined versus simple) and fuel types (natural gas versus fuel oil).

A total of 22 nozzle inspections are currently represented in the data base that supports the algorithms. Five of these inspections (all on 7B nozzles) were conducted in the laboratory at SwRI for EPRI, and the remainder were conducted by either the EPRI host sites or their contractors. Engine history information corresponding to these inspections was extracted from the operating logs of the host sites. Engine histories were characterized in terms of the total number of fired starts, the total number of fired hours, and (in most cases, but not all) further information on the types of cycles experienced (normal shutdowns versus trips, for example).

The first major challenge in the development of nozzle cracking algorithms is to determine an appropriate quantitative characterization of the cracking itself. As described earlier, cracks can occur on the inner and outer sidewalls, on the pressure side (PS) and suction side (SS) of the airfoil, and on the leading and trailing edges (LE and TE). Multiple cracks with complex geometries occur frequently, but some of these cracks are much more significant than others. Cracking of the vane can lead to ejection of metal or structural failure, whereas cracking of the sidewall is usually nonthreatening. While no cracks are desirable, only heavily cracked or damaged vanes will motivate an expansive repair of the entire nozzle.

A sample of actual cracking data for a Frame 7E nozzle is shown in Fig. 13(*a*), in which the sum of the crack lengths on each vane is plotted in polar coordinates as a function of the vane number. Sidewall cracking has been neglected, and all other cracking has been partitioned between PS, SS, and TE (TE cracks are typically through-cracks, which appear on both PS and SS). While many cracks are present on all three surfaces, one vane is clearly the most heavily cracked, as was the case for most 7E nozzles. 7B nozzles generally exhibited more uniform distributions of crack lengths, with larger numbers of long cracks, but the single most heavily cracked vane still functioned as a good descriptor of the overall cracking tendencies. Typical cracking data for a 7B nozzle are shown in Fig. 13(*b*), which is similar to that of the 7E plot except that there are 48 vanes. The 6–10 in. (150–250 mm) of total cracking reported on worst-case vanes for both nozzle designs typically comprised one or two long cracks, perhaps 3–5 in. (75–125 mm) each, and sometimes one or two shorter cracks of 1–2 in. (25–50 mm) each.

SwRI inspections of 7B nozzles have shown that cracking is heaviest on the SS, and this is consistent with other available data from the 7B host sites. This is due, in part, to corrosion deposits on the PS, which conceal many cracks. If these deposits are removed by grit-blasting, which cannot be done while the nozzle is still in the engine, numerous additional cracks can be found on the PS, and a few additional cracks on the SS. Another factor influencing detection is that PS cracks are often "tighter" than SS cracks due to differences in the residual stress fields. The worst-case cracking, however, is still generally associated with the SS. On the other hand, cracking data for 7E nozzles reported by the host sites indicates that PS cracking is more severe than SS or TE cracking. This is probably due to differences in nozzle design, or it may reflect the difficulty of accessing the SS and TE during an inspection of the nozzle while still in the engine.

Based upon this evidence, the cracking description adopted for use in algorithm development is the sum of the crack lengths on the PS (7E) or the SS (7B) for the single most heavily cracked vane. This is a description that has physical significance, that is relatively easy for an inspector to determine, and that (as will be shown below) correlates successfully with engine history. Note that for the 7B nozzles, any individual cracks less than 1 in. (25 mm) in length were neglected in the summation in order to simplify the required inspection process and to avoid biasing the data base. Extremely detailed inspections in SwRI laboratories found many such short cracks, while these were almost never reported from the field or repair shops.

The second major challenge in the development of nozzle cracking algorithms is the description of the engine history:

Downloaded 02 Jun 2010 to 171.66.16.122. Redistribution subject to ASME license or copyright; see http://www.asme.org/terms/Terms_Use.cfm

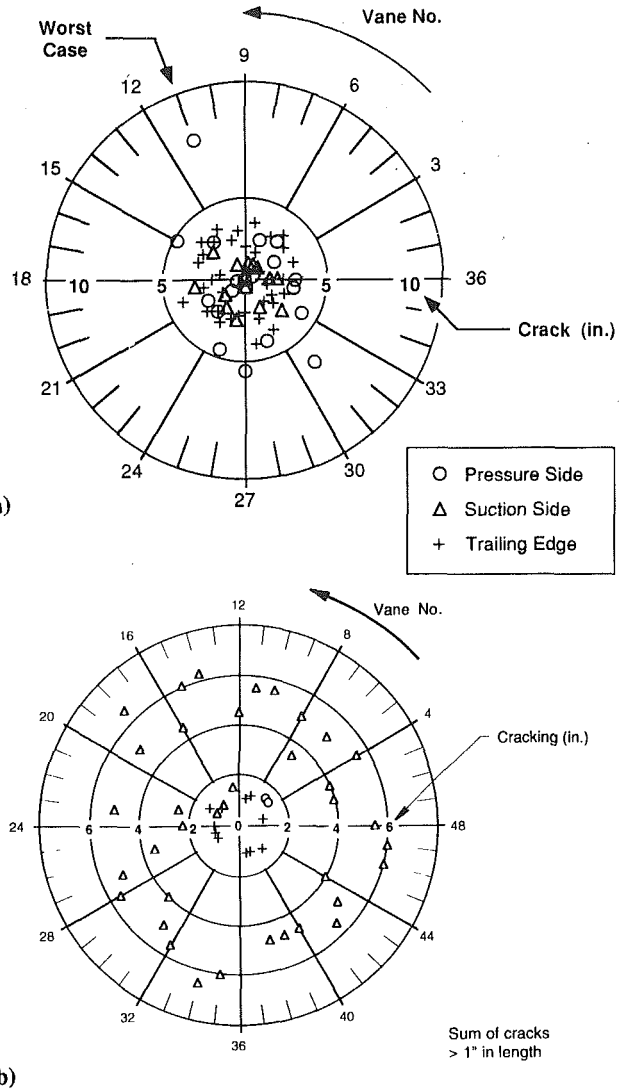


Fig. 13 Sum of crack lengths for a typical nozzle by location and vane number: (*a*) 7E, (*b*) 7B

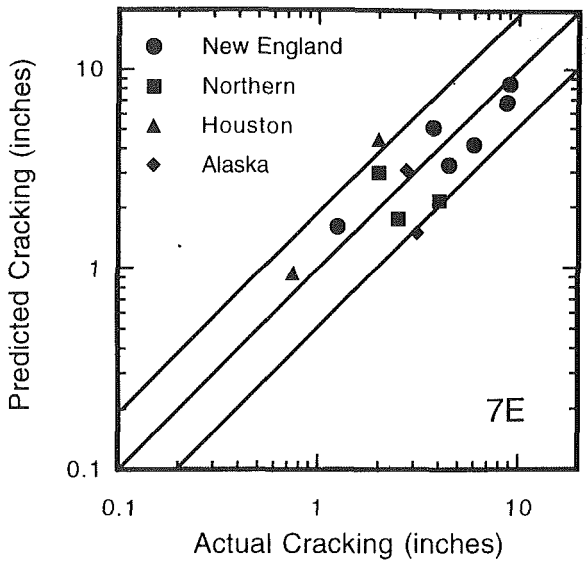


Fig. 14 Predicted versus measured 7E nozzle cracking. The outer diagonal lines represent factors of two on the predictions, and the center line shows perfect agreement.

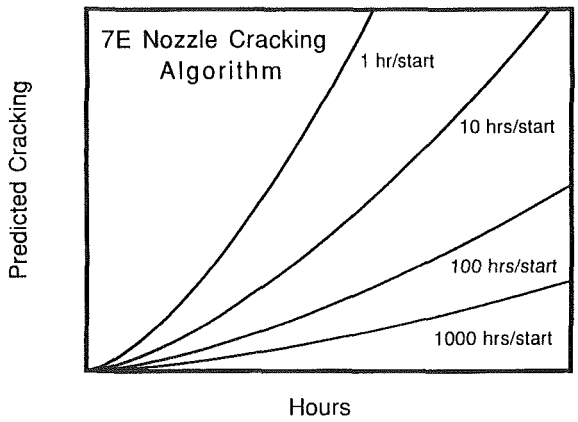


Fig. 15 Predicted 7E nozzle cracking with increasing fired hours (power law model)

How to identify and quantify those operational events that cause damage to initiate and grow. As noted above, engine history data available in the operating logs included information about fired hours, fired starts, and different cycle types.

A 7E nozzle algorithm developed earlier by General Electric (GE) for EPRI [8] computed a damage factor for each cycle type (start type–base or peak load—shutdown type) based on low cycle fatigue life equations and proprietary numerical analysis of transient strain and temperature histories in the nozzle. Miner's linear damage rule was then used to sum damage from the complete nozzle history, and the resulting total damage factor was related empirically to observed cracking. This model was unsatisfactory when applied to a data base that included both baseload and intermediate duty machines. The baseloaded engines had much more cracking than would be expected by considering only the number of starts and stops.

An improved algorithm for the frame 7E engine, which is now employed in the REMLIF code, considers both the proprietary GE damage factor and the total number of fired hours. The general form of this algorithm is

$$(\text{cracking}) = A(\text{fired hours})^B(\text{damage})^C \qquad (1)$$

Values for the constants A, B, and C were determined by a multiple linear regression with available 7E cracking data (expressed as the total length of PS cracks on the worst vane for a given nozzle). The success of this formula in describing cracking for the available data base is illustrated in Fig. 14, which compares actual cracking with the "predictions" of the REMLIF algorithm for the data from which the algorithm was derived. Here the central diagonal line indicates perfect agreement, while the two outer lines indicate factors-of-two in error. There is no segregation of the data or of the quality of fit based on site or load profile. The quality of the fit, in view of the normal $2\times$–$3\times$ scatter in laboratory fatigue life testing, is excellent. The data are correlated to within a factor of 2.0, except for two points, which are correlated to factors of 2.1 and 2.2.

A greater demand on any nozzle cracking algorithm is its ability to provide accurate predictions outside the range of data with which it was calibrated; e.g., at smaller or larger number of hours. The particular power law form of the 7E algorithm projects that cracking will initiate at time $t = 0$, which may not be physically realistic, but that crack growth will proceed at an extremely small rate during the early nozzle life. At much longer lives, the 7E algorithm projects that crack growth will continue to accelerate. These trends are illustrated in Fig. 15, which shows the predictions of the algorithm for four hypothetical engines, which see only normal start-shutdown cycles and which maintain constant ratios of fired hours per fired start.

A semi-logarithmic algorithm, which provides a fit to the

Downloaded 02 Jun 2010 to 171.66.16.122. Redistribution subject to ASME license or copyright; see http://www.asme.org/terms/Terms_Use.cfm

7E data of comparable quality, was also investigated. This type of model projects that no cracking will occur until some nonzero incubation period has been completed, that the initial cracking rate is relatively high, and that subsequent cracking rates steadily decrease throughout the life of the nozzle. But which functional form is more nearly correct, particularly at longer or shorter lives? The limited nozzle data available do not give a conclusive answer, and the complicated mechanics and materials issues involved in this long-life thermal fatigue cracking problem do not admit an obvious theoretical explanation. Some recently obtained inspection data from a Frame 7E engine at a Texas site appear to show a general acceleration of cracking at very long lives (38,000 h). While this one data set does not prove that accelerating cracking rates will always occur in 7E nozzles, it does suggest that such crack behavior cannot be ruled out. With this support, the power law 7E nozzle algorithm (Eq. (1)) was chosen for incorporation into REMLIF with the understanding that it may overpredict cracking at long lives.

The development of an algorithm for the frame 7B nozzle had the advantage of more detailed information about cracking, but it was constrained by more limited information about engine histories. The 7B sites, in general, were unable to provide sufficient information about the different types of duty cycles (the number of trips versus normal shutdowns, for example) experienced by the engines of interest. The only available history parameters, then, were the total numbers of fired starts and fired hours.

In contrast to the 7E nozzles, the total number of fired hours for the different 7B nozzles exhibited no statistical correlation with cracking. However, the 7B nozzle data base included no base-loaded engines as did the 7E data base. The total fired hours for the nine 7B nozzle inspections ranged from a low of 2400 to a high of 10,000 and all engines averaged between 2 and 8 hours per start. The available 7E data base represented a much wider spectrum of engine operations, including total fired hours ranging from 5600 to 24,000 and average hours per start ranging from about 5 for an intermediate duty site to nearly 1000 hours for a base-loaded site.

The total number of fired starts for the 7B nozzles statistically correlated with the observed cracking. A power-law model was developed with the general form,

$$\text{cracking} = D(\text{fired starts})^{\alpha} \qquad (2)$$

where the constants D and α were determined by a least-squares analysis. The power-law 7B model displays a gradual saturation of cracking with increasing starts (decelerating cracking rate). A semi-logarithmic model was also investigated, but the two models proved to be nearly identical over the range of available data. Although the semi-log model does admit a short incubation period before cracking initiates, both 7B models are probably overly conservative at very short lives. The power-law model has been chosen for incorporation into REMLIF at the present time for consistency with the 7E algorithm and because it is slightly more conservative. The quality of fit of the 7B power-law model is illustrated in Fig. 16, which (as in Fig. 14) compares the "predictions" of the model with the data from which it was derived. Again, the scatterbands indicate factors-of-two. All cracking is "predicted" within 25 percent.

These algorithms will continue to be evaluated and modified as necessary as new inspection data for both engines become available. Of particular interest will be data at larger numbers of fired starts and fired hours. Other ongoing investigations are studying the distributions of cracking on all vanes in an effort to generate a probabilistic description of cracking and, ultimately, a probabilistic life model, which may be used to estimate the likelihood that a nozzle has developed a certain amount of cracking. An initial version of this model has been developed for the 7B nozzle.

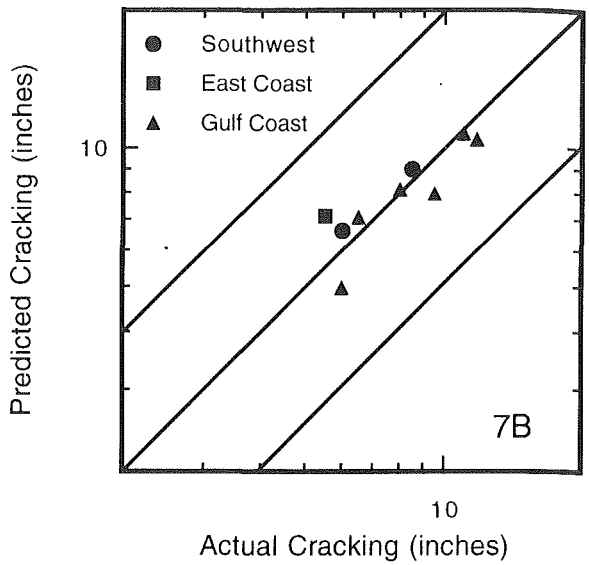


Fig. 16 Predicted versus measured 7B nozzle cracking. The lines are the same as in Fig. 14.

Discussion

The principal purpose of this paper has been to demonstrate that nozzle cracking can be characterized and that the extent of cracking can be reasonably well predicted, despite the complexity of this phenomenon. Much of this complexity is due to the three-dimensional geometry of multivane nozzle segments, which are difficult to analyze by finite element methods. Apart from an accurate stress analysis, the prediction of nozzle cracking requires a knowledge of how the material responds to the imposed thermal loads. Crack initiation and crack growth of FSX-414 under thermal mechanical loading is not well characterized, especially the effect of dwell time. Furthermore, environmental attack accelerates the cracking, and the hardness of the material increases with time. Both these effects generally reduce ductility and fatigue life. Thus, the ability to correlate nozzle cracking to within a factor of two is fairly remarkable using a simple, empirical model. Further refinements to the model await obtaining data for nozzles having hours and starts not contained in the present database.[5]

The parameter used to characterize nozzle cracking, the extent of cracking on the worst cracked vane, is simple to measure and easy to understand. Other parameters could be used, but these involve more extensive measurements or complicated formulations. For example, the sum of the length of all the cracks on the nozzle is a direct measure of the amount of weld repair that must be done, but this requires that all the cracks be carefully measured. In addition, values of this parameter, which can be hundreds of inches, are difficult to comprehend. Other parameters involving measures of the frequency and length of cracking, such as the mean, median, mode, standard deviation, etc., may provide a more accurate, statistical description of cracking, but require careful measurement of all the cracks, a statistical analysis, and their physical meaning is difficult to conceptualize.

Based upon the data collected, when the crack length of the worst cracked vane exceeds some value, the amount of cracking of the other vanes is quite extensive, and the nozzle should be removed for repair. For the 7E nozzle, this length is between 8 and 10 in. (20 to 25 cm), and for the 7B, it is between 6 and 8 in. (15 to 20 cm). (The 7E vane is larger than the 7B vane.)

[5]It should be noted that it has not been possible to monitor the growth of a single crack or the cracking of a single vane because of the lack of detail in field inspection reports.

Downloaded 02 Jun 2010 to 171.66.16.122. Redistribution subject to ASME license or copyright; see http://www.asme.org/terms/Terms_Use.cfm

The time dependence of nozzle cracking is an important technical issue. The data for the 7E nozzle clearly show that the cracking is time dependent, as well as dependent upon cycles, but the cracking of the 7B nozzle shows no correlation to service time. The existing database is too narrow to state as a fact that the cracking of 7B nozzles is *not* time dependent because the starts-to-hours ratio is too narrow to determine the effect of time. Additional data from base-loaded units are required to determine the importance of time. There may be an insufficient number of hours or too low a metal temperature for the importance of time to become manifest for the 7B engines. The metallurgical evidence points to a lack of secondary carbide precipitation in the 7B nozzles compared to the 7E nozzles, suggesting that an insufficient combination of time and temperature was present for the 7B nozzles.

The time dependence of cracking in the 7E nozzle can be explained from several causative factors. First, microstructural changes, which occur during service, result in an increase in the hardness of the metal. An increase in hardness usually correlates with a loss in ductility and a decrease in resistance to low cycle fatigue. No experimental data are available in the open literature for FSX-414, but for the cobalt base superalloy, Mar M-509, it has been shown that ductility decreases with exposure time [5]. Second, environmental attack in the form of high-temperature oxidation and nitridation is present at the crack tips of nozzles from service. Environmental attack usually accelerates cracking in superalloys, and it has been shown that air can embrittle cobalt base superalloys [14]. Third, experimental data on FSX-414 and X-45 have shown that a dwell period causes a decrease in thermal mechanical and low-cycle fatigue life and an increase in fatigue crack growth rate in isothermal tests. Thus, it is not surprising that nozzle cracking is time dependent for the 7E nozzle.

Operation and Maintenance. Nozzle cracking is inherent in the design of the nozzle. No significant reduction in nozzle cracking can be accomplished without modifying the design of the nozzle. The single largest design change that could be made to reduce the amount of nozzle cracking is to cast the nozzle in single vane segments. The benefit of the single vane segment could be a 50 percent or greater reduction in stresses, as explained in the section on stress analysis. This reduction in stress results in increased nozzle life. Esser et al. [15] have estimated a large increase in low cycle fatigue life by using a single-vane segment instead of a three-vane segment. For a General Electric MS5001 gas turbine, it has been estimated that the resistance to crack initiation increases by almost three times when a two-vane segment is used instead of a five-vane segment [16]. The penalty of single-vane segments is an increase in cost and a small decrease in performance due to additional losses at the seals between the vanes.

Operational changes that can reduce nozzle cracking are reductions in the temperature spread and in the number of emergency shutdowns. Large temperature spreads usually result from combustion problems. A combustor burning too hot discharges hotter gases directly on the first-stage nozzle. The vanes in front of the hot combustor would be expected to exhibit greater cracking. Some evidence to suggest that this is the case has been seen, but correlations of exhaust temperature readings with nozzle cracking have not been made. This correlation is made more difficult by the changes in exhaust temperature readings over time and the maintenance of combustor hardware during the service period of a nozzle.

Reduction in the number of emergency stops and fast starts benefits all the hot-section hardware. These conditions impose greater thermal cycles on the hot parts than any other cycle. For engines that sustain a large number of emergency stops, substantially greater damage to the first-stage buckets has been observed [17].

Since the cracking of the first-stage nozzle primarily determines the timing of the hot gas path inspection, it is important to be able to predict when the nozzle should be removed. If the nozzle is removed too soon, then unnecessary overhaul costs might be incurred, and if it is not removed soon enough, repair costs may become excessive.

Life management of the nozzle can be accomplished by the use of predictive program, such as the REMLIF computer program, along with a careful collection of data on nozzle cracking and engine operation. This information can be tracked with the aid of a database, such as the EPRI LMS Database [18]. The predictive program can determine the current and projected condition of the nozzle.[6] A careful collection of historical data on nozzle cracking and engine operation can then be used to modify the predictions of the program.

Finally, nozzle durability is enhanced by a quality repair job. Proper repair specifications and in-process inspections of the nozzle are essential in this regard, since it is not possible to determine the quality of the repair from a final, visual inspection of the nozzle.To assist member utilities, EPRI is developing model repair specifications for nozzles and a guidebook on the subject.

Summary

Nozzle cracking can be predicted to within a factor of two for the first-stage nozzle of the General Electric MS7001 B and E gas turbines. The measure of cracking used is the total length of cracks on one side of the worst cracked vane. For the 7B, the suction side is used, whereas for the 7E, the pressure side is used. These sides are where the most severe cracking is found. The cracking of the 7B nozzle is predicted from the number of fired starts. The number of fired hours is not significant based upon available data, and records of fast starts or trips are mostly unavailable. For the 7E nozzle, the cracking is predicted from the number of starts, fast starts, trips, and fired hours. It was not possible to account for the cracking on the 7E nozzles without the use of fired hours. The reason for the importance of fired hours for the 7E nozzle but not the 7B nozzle is not completely understood.

Metallurgical analysis showed that the cracks follow the carbide-matrix interface, and that environmental attack occurs at the crack tip. During service, additional carbide precipitation occurs, which increases the hardness of the material. Results of stress analyses of nozzles in the literature are presented. These analyses show that single vane castings have significantly less stress than multivane castings. The location of maximum stresses corresponds to the areas of maximum cracking observed in the nozzles examined in the paper.

Acknowledgments

The authors thank the host sites for making their inspection records available to us and, in several instances, sending nozzles to us to inspect. We thank the Electric Power Research Institute for supporting this work under contract No. RP 3064-01. We also thank the General Electric Company for providing algorithms and inspection information to us. Finally, we thank Mr. Harold Saldana for preparing the metallurgical samples, and Ms. Loretta Mesa for preparing this manuscript.

References

1 Bernstein, H. L., "Life Management System for Frame 7E Gas Turbine," *Life Assessment and Repair Technology for Combustion Turbine Hot Section Components*, R. Viswanathan and J. M. Allen, eds., EPRI Report GS-7031, ASM International, Materials Park, OH, 1990, pp. 111-118.

2 Steinberg, B. G., and Perez-Daple, W. R., "Practical Approach to Gas Turbine Component Life Assessment—An Electric Utility Perspective," *Life Assessment and Repair Technology for Combustion Turbine Hot Section Com-*

[6] An expert system is also under development by Southwest Research Institute under EPRI contract to predict nozzle cracking. The expert system can access nonquantitative information important to nozzle durability.

Downloaded 02 Jun 2010 to 171.66.16.122. Redistribution subject to ASME license or copyright; see http://www.asme.org/terms/Terms_Use.cfm

ponents, R. Viswanathan and J. M. Allen, eds., EPRI Report GS-7031, ASM International, Materials Park, OH, 1990, pp. 41–53.

3 EPRI RP3250-01, "Computer-Aided Inspection of Combustion Turbines," Contractor: Southwest Research Institute, 1991.

4 Foster, A. D., and Sims, C. T., "FSX-414, an Alloy for Gas Turbines," *Metal Progress*, July 1969, pp. 83–85.

5 Beltran, A., "Cobalt Base-Superalloys," in: *Superalloys II*, C. T. Sims, N. S. Stoloff, and W. C. Hagel, eds., Wiley, NY 1987, pp. 135–163.

6 Sullivan, C. P., Varin, J. D., and Donachie, M. J., Jr., "Relationship of Properties to Microstructure in Cobalt-Base Superalloys," *Metals Engineering Quarterly*, May 1969, pp. 16–29.

7 Morral, F. R., Habraken, L., Coutsouradis, D., Drapier, J. M., and Urbain, M., "Microstructure of Cobalt-Base High-Temperature Alloys," *Metals Engineering Quarterly*, May 1969, pp. 1–16.

8 Cincotta, G. A., "Gas Turbine Life Management System," Final Report, EPRI RP2421-02, 1988.

9 Sato, T., Takelishi, K., and Sakon, T., "Thermal Fatigue Life Prediction of Air-Cooled Gas Turbine Vanes," ASME JOURNAL OF ENGINEERING FOR GAS TURBINES AND POWER, Vol. 108, 1986, pp. 414–420.

10 Woodford, D. A., and Mowbray, D. F., "Effect of Material Characteristics and Test Variables on Thermal Fatigue of Cast Superalloys," *Materials Science and Engineering*, Vol. 16, 1974, pp. 5–43.

11 Schiffer, D., Singh, M. P., and Plummer, R., "Life Prediction of CAES L. P. Expander Components Using the Finite Element Method," *Life Assessment and Repair Technology for Combustion Turbine Hot Section Components*, R. Viswanathan and J. M. Allen, eds., EPRI Report GS-7031, ASM International, Materials Park, OH, 1990, pp. 107–110.

12 Hultgren, K. G., "Use of 3-Dimensional Finite Element Model in Design of First Stage Turbine Vane Segments," *14th International Conference on Combustion Engines (CIMAC)*, Helsinki, 1981, pp. GTI9-1 to GTI9-15.

13 Flowers, T. L., Anderson, A. W., and Brunso, J., "Improvement of Nozzle Life in Gas Turbines," ASME Paper No. 79-GT-50, 1979.

14 Woodford, D. A., and Bricknell, R. H., "Air Embrittlement of a Cobalt-Base Superalloy," *Metallurgical Transactions*, Vol. 12A, 1981, pp. 1945–1949.

15 Esser, W., Deblon, B., and Czech, N., "Refurbishment of Gas Turbine Blades—Concept, Development and Experience," in: *Life Assessment and Repair Technology for Combustion Turbine Hot Section Components*, R. Viswanathan and J. M. Allen, eds., EPRI Report GS-7031, ASM International, Materials Park, OH, 1990, pp. 313–322.

16 Grondahl, C. B., Linnell, R. D., and Martin, T. J., "The Modernization of a 1965 MS5001 Gas Turbine," ASME JOURNAL OF ENGINEERING FOR GAS TURBINES AND POWER, Vol. 111, 1989, pp. 631–636.

17 Bernstein, H. L., and Allen, J. M., "Analysis of Cracked Gas Turbine Blades," ASME Technical Paper 91-GT-16, 1991, to be printed in the ASME Transactions.

18 Bernstein, H. L., and Malik, J., "Relational Database for Gas Turbine Engines," *Life Assessment and Repair Technology for Combustion Turbine Hot Section Components*, R. Viswanathan and J. M. Allen, eds., EPRI Report GS-7031, ASM International, Materials Park, OH, 1990, pp. 119–124.

Downloaded 02 Jun 2010 to 171.66.16.122. Redistribution subject to ASME license or copyright; see http://www.asme.org/terms/Terms_Use.cfm

S. Aksoy

B. Mitlin

H. Borowy

Textron Lycoming,
550 Main Street,
Stratford, CT 06497

Structural Evaluation and Testing of Swept Compressor Rotor

This paper summarizes specific critical issues encountered in the structural analysis of a swept first-stage compressor blade of a gas turbine engine and the results of the test to evaluate the accuracy of the modeling and surface stress prediction procedure. The surface stresses of a three-dimensional structure were obtained using membrane elements attached to the surface of solid elements. Steady stress measurements were then made during accelerations and decelerations to and from design speed. The test was conducted in an evacuated spin rig. The measurements were used to evaluate the validity of the stress prediction from finite element analysis.

Introduction

The past 50 years have seen significant increases in the power of computers and advances in finite element techniques. Today, the finite element technique has become a standard tool in aircraft design because of its capability to analyze complex structures in a short time and at reduced cost. In spite of the impressive advances in theoretical methods and computer capacity, considerable effort is needed to develop structural data for calibration of the finite element analysis. A major reason for this is the need to determine component life accurately. For accurate life predictions, comprehensive understanding of the state of stresses in components is required under the total range of operation defined by aircraft missions. Small inaccuracies in calculated stresses can result in significant life variations. Therefore, accurate analysis and experimental verification, as integral parts of the complex design process, are necessary to attain design life goals.

The objective of this paper is to discuss the structural analysis procedure for a swept airfoil and to evaluate the accuracy of surface stress prediction technique using the results of the strain gage test.

Background

Needs. In recent years, the search for improved efficiencies for gas turbine engines has intensified. Fractional percent improvements in fuel efficiency mean important savings to an airline and greater market strength for engine producers. Improvements in efficiency have been sought in all areas and every last detail has been examined. A significant portion of the effort expended is devoted to aerodynamic design of components. The trend in design of compressors for advanced gas turbine engines is to have fewer stages and higher rotational speeds. These imply higher stage pressure ratios and supersonic Mach numbers. Consequently, the losses due to shocks have to be reduced to improve and maintain compressor efficiency. The aerodynamic objective is to control the shock structure by sweeping the blade. The shock formed is oblique to the incident flow and has a reduced loss compared to the more commonly achieved normal shock structure. The application of this principle to turbomachinery rotors gives rise to a number of significant design challenges. The design objective is to determine the aerodynamic shape ultimately required to achieve an efficiency improvement of a swept blade and the desired service life.

Challenges. The common approach taken is first to evaluate the aerodynamic feasibility of reducing loss using sweep, without considering structural requirements. In a conventional blade, the center of mass of each section is located on a radial line with minor tilt and lean to minimize peak bending stresses. With the swept design approach, the center of mass of the section does not lie on a radial line. This results in a substantial bending about the two principal axes of the cross section and twisting about an axis perpendicular to the cross section. Compared to conventional airfoils, advance airfoils are thin and highly swept back, which gives rise to complex stress fields and relatively large deflection. Thus, the structural challenge arising from the aero-driven solution is to obtain design objectives with less material margin, without sacrificing aero efficiency. Therefore, the accuracy of the prediction of stress fields is most critical for swept airfoil design. Another challenge is the modeling of the blade/disk joint zones. A small grid size or substructuring is required. The obvious disadvantages of both these approaches are high computer modeling costs.

Modeling. Using a model with reasonably sized solid elements, the finite element analysis of a swept first-stage compressor blade revealed a rapid rise in stress at the leading and trailing edges of the airfoil hub section. This rapid local stress rise is due to the combination of a modeling deficiency and the extrapolation technique used by the finite element program to calculate surface stress. A combination of the blade to disk joint geometry and the rapid change in inner flow path contour creates modeling problems in this area. In addition to this geometric difficulty, sweeping the leading edge of the airfoil

Contributed by the International Gas Turbine Institute for publication in the JOURNAL OF ENGINEERING FOR GAS TURBINES AND POWER. Manuscript received by the International Gas Turbine Institute June 15, 1992. Associate Technical Editor: L. S. Langston.

Copyright © 1994 by ASME
Downloaded 02 Jun 2010 to 171.66.16.122. Redistribution subject to ASME license or copyright; see http://www.asme.org/terms/Terms_Use.cfm

rearward and offsetting the airfoil section in the tangential direction gives rise to torsional deformation and large bending stress in the leading and trailing edge zones of blade/disk joint. Therefore, achievement of sufficient accuracy in the calculation of stresses in these areas presents a significant challenge.

Previous Research. A knowledge of the steady stress distribution is vital to determine component life accurately. Therefore, the calibration of design/analysis tools using experimental results becomes a critical step in the development of accurate life prediction systems. In the past, experimental methods have been extensively employed in design and failure investigation of gas turbine components. Strain gages were first used on compressor blades in the late 1940s to establish the reason for the fatigue failures (Carter and Kilpatric, 1957). Armstrong (1988) discussed strain gage utilization in assessment of fatigue for gas turbine components. Kuo et al. (1980) employed a full-scale spin test to measure steady stresses in an advanced centrifugal impeller using strain gages, and used the results to validate the finite element prediction of stress fields in the impeller. Srinivasan and Fulton (1984) conducted a series of tests on an advanced swept turboprop blade to develop a structural dynamic data base. Steady-state blade deformation under centrifugal loading, as well as the vibratory characteristics of the rotor assembly, was measured and compared with analytical results. A geometric nonlinear solution, provided by the finite element software NASTRAN, was used for the analytical results in this study. Recently, Chi and Jones (1988) used a noninterference technique for measuring turbine engine rotor blade stresses.

Proposed Procedure. For accurate life predictions, the accuracy of surface stresses predicted from finite element technique is critical for the design of advanced engine components where the steady stress level can approach the limit of material capabilities. Stresses calculated from finite element technique are least accurate at element corners, more accurate at midside, and most accurate at certain interior points. These interior points can be used to define a stress field that can be extrapolated to yield stresses at the element surface. The quality of stress extrapolations can be strongly affected by element geometric shape. Therefore, a procedure that calculates surface stresses directly is desirable.

The very thin membrane element attached to the free surface of solid element was proposed to predict the surface stresses as an alternative method to the extrapolation. As far as these authors are aware no previous work has been employed using membrane elements overlaid to cover the surface of a solid finite element model used for surface stress prediction.

Discussion

1.0 Steady Stress Structural Analysis

1.1 Analysis/Results. The first-stage rotor of the three-stage axial compressor used in this investigation is shown in Fig. 1. Twenty-noded isoparametric solid elements were used to construct the finite element model of the blade and disk, shown in Fig. 2. This figure also illustrates the aerodynamic characteristic of the blade; the leading edge was bulged forward to provide a rearward sweep at the tip. The steady stresses and deflections of this swept rotor were calculated using the finite element software ABAQUS. A nonlinear geometric solution was carried out to simulate properly the stiffening effect of a centrifugal field and the large-scale deflections. The three-dimensional solid modeling approach revealed a rapid rise in stress at the leading edge of the airfoil hub section. As a standard procedure, the finite element method calculates stresses at integration points, which are located inside a solid element and then extrapolates them to the surface. This procedure results in large errors in areas where elements are distorted. This is a common problem in modeling of irregular geometry, such as the leading edge of an airfoil hub section.

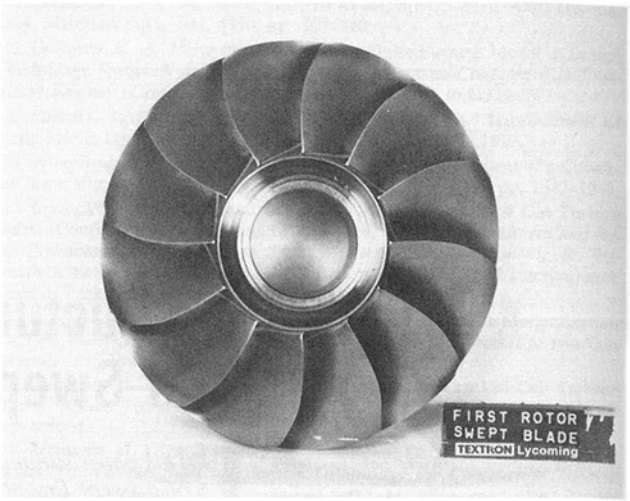


Fig. 1 Axial compressor rotor

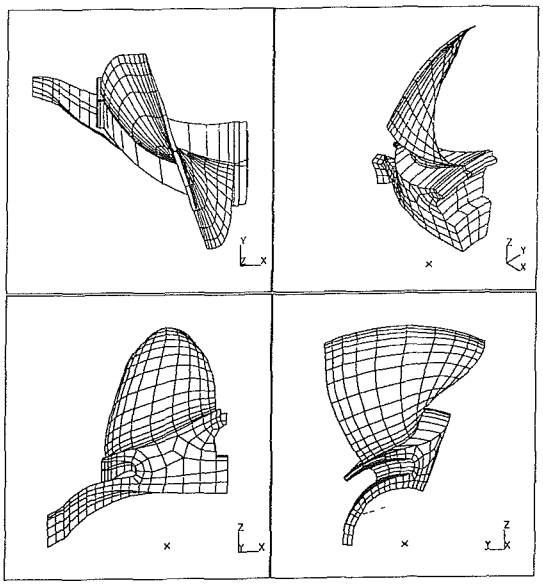
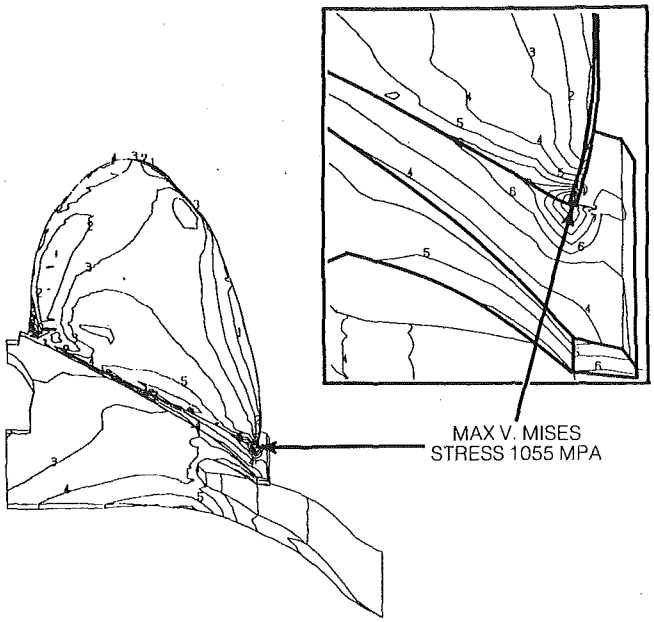


Fig. 2 Finite element model of the rotor

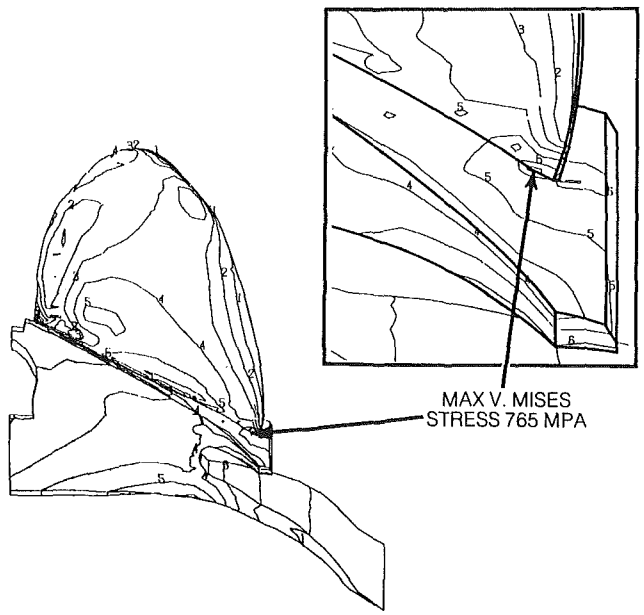
1.2 Stress/Displacement Accuracy. In the finite element representation of a structural problem, the displacement is continuous across the element boundary. However, this continuity does not mean that the element stresses are continuous across element boundary. The element stresses are predicted using derivatives of the displacements in the interior of the elements because the stresses are calculated with higher accuracy at specific points. Theoretical discussions on the optimal stress calculation location can be found from Hinton and Campbell (1974) and Barlow (1976). These interior stress fields are extrapolated to achieve stress at element boundaries. As might be expected, approximate displacements are better than approximate stresses because of the differentiation of displacement in the stress calculation. The quality of stress calculations can be strongly affected by element geometric shape. The safest rule is to avoid unnecessary irregularity. Several tests could be used: warped element checking, interior angle checking, and element distortion checking. The quality ranking of elements is likely to be different in the different test cases and could depend on whether stress or displacement is the indicator of quality. Since only one element was used through the thickness of airfoil, it is very difficult to construct a solid

Downloaded 02 Jun 2010 to 171.66.16.122. Redistribution subject to ASME license or copyright; see http://www.asme.org/terms/Terms_Use.cfm



CONTOUR LEVEL	VON MISES STRESS, MPa
1	100
2	200
3	300
4	400
5	500
6	600
7	700
8	800
9	900
10	1000

Fig. 3(A) Stress distribution calculated from solid elements



CONTOUR LEVEL	VON MISES STRESS, MPa
1	100
2	200
3	300
4	400
5	500
6	600
7	700
8	800
9	900
10	1000

Fig. 3(B) Stress distribution calculated from membrane elements attached on solid elements

element without large shape distortion at the airfoil/disk joint area.

1.3 Criteria for Accuracy. Since the derivative of displacements is involved in stress calculations, the element distortion checking test was chosen to determine the quality of element geometric shape. The distortion value is calculated by constructing a mapping from a parent element (in computational space) to the actual element. A postprocessor, CAEDS, was used to calculate the distortion value of elements. This value is one for the perfect mapping (cubic parent element to cubic actual element). It becomes zero or negative in the neighborhood of excessive distortion. If the distortion is 0.2 or less at any element, distortion is considered excessive (Nicholas and Citipitioglu, 1977). Elements in the trailing and leading edge zone had the value of 0.182, which is the lowest in the solid model of the blade. In elements with distorted shape, extrapolated stresses at the corners may be inaccurate. Face stresses are preferred to be calculated directly.

1.4 Improved Accuracy. Attaching a membrane element to the surface of a solid element will provide stresses to be calculated at the surface of the airfoil and eliminate the errors associated with stress extrapolation. Based on the solid model experience, it was decided that analysis should be performed using a model constructed from twenty-noded solid elements plus membrane elements attached to the surface. The "surface-coating" commands of the preprocessor, CAEDS, was used to generate eight-noded quadrilateral membrane elements on the free faces of twenty-noded solid brick elements. This process involves picking the element faces from which membrane elements will be generated and then choosing whether existing nodes will be used or new nodes will be generated. The existing nodes were used to define the membrane element. The solid elements were simultaneously analyzed with membrane elements having the same mechanical properties as those for the solid elements. The thickness of membrane element chosen is 0.00025 cm. In order to assure that no stiffness change occurs in the model, the displacement fields from solid and membrane-

Downloaded 02 Jun 2010 to 171.66.16.122. Redistribution subject to ASME license or copyright; see http://www.asme.org/terms/Terms_Use.cfm

solid analyses were compared. It was found that the difference between the two displacement fields was negligible for the chosen membrane thickness. Von Mises stresses calculated from the solid and membrane element attached on the solid are shown in Fig. 3. When the stress distributions from these two elements were examined, it appeared that the difference was relatively low (about 10 percent) except at the leading edge where the difference is 40 percent.

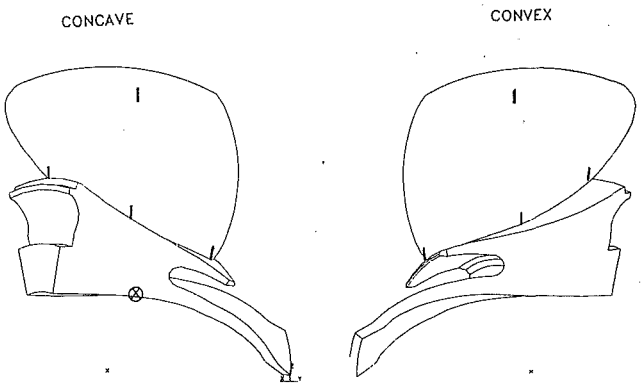
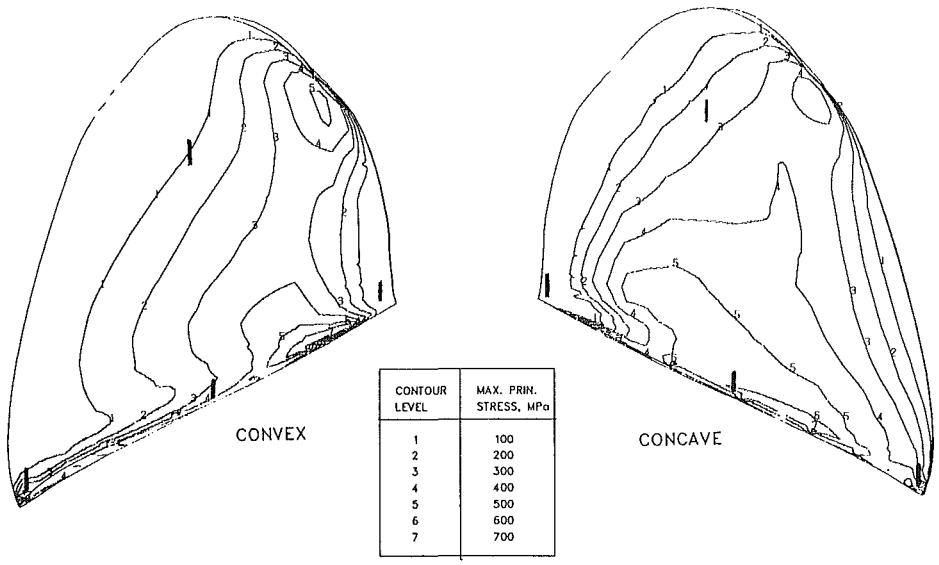


Fig. 4 Location of strain gages

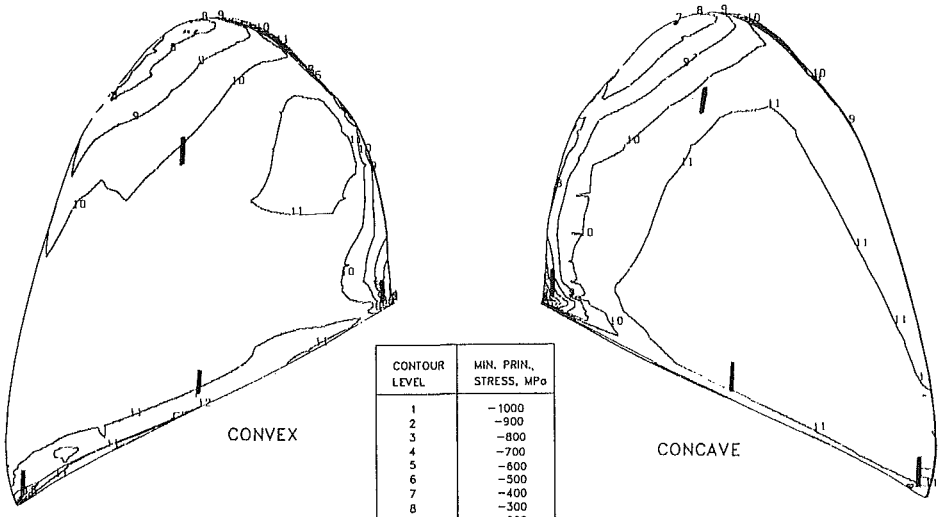
2.0 Validation

2.1 Instrumentation. The compressor blisk was instrumented with a total of nine strain gages, as shown in Fig. 4. Eight were placed at various airfoil locations. One additional gage was placed on the blisk bore. The preferred practice for determining stress is to use a strain rosette, which measures strains on each of three intersecting gage lines. This makes the calculation of the principal stresses possible regardless of orientation. Because of the high rotating speed and limited number of slip ring channels for transmitting the strain gage signal, one gage was used to measure stress at each location. This way, measurement of stress at the nine locations was made possible by utilizing the available channels on the slip ring.



CONTOUR LEVEL	MAX. PRIN. STRESS, MPa
1	100
2	200
3	300
4	400
5	500
6	600
7	700

Fig. 5 Maximum principal stress distribution and strain gage location



CONTOUR LEVEL	MIN. PRIN., STRESS, MPa
1	−1000
2	−900
3	−800
4	−700
5	−600
6	−500
7	−400
8	−300
9	−200
10	−100
11	0
12	100

Fig. 6 Minimum principal stress distribution and strain gage location

Downloaded 02 Jun 2010 to 171.66.16.122. Redistribution subject to ASME license or copyright; see http://www.asme.org/terms/Terms_Use.cfm

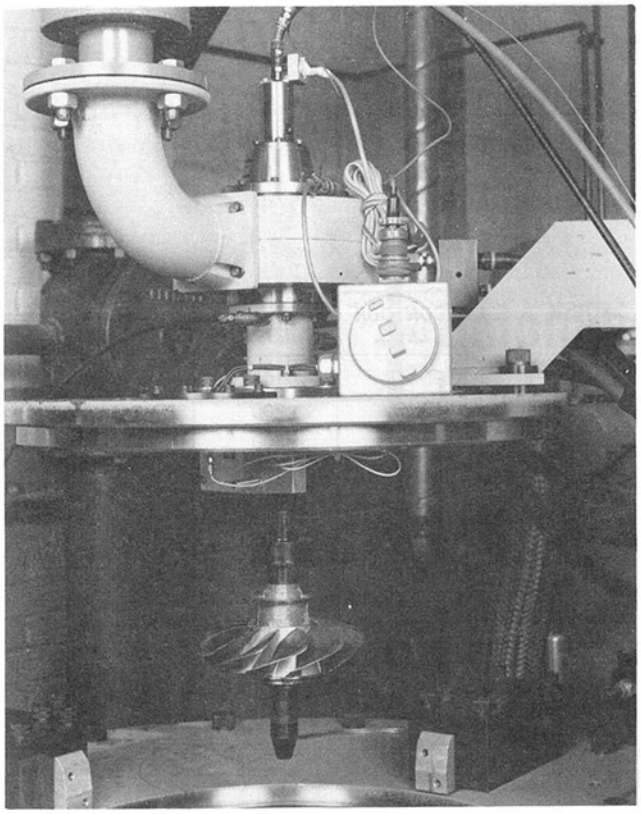


Fig. 7 Spin pit setup

The location and direction of strain gages were chosen to coincide with principal stresses, which are determined from the finite element analysis. The principal maximum and minimum stress distribution on the airfoil are shown in Figs. 5 and 6, respectively.

The spin pit setup is shown in Fig. 7. The test assembly was attached by means of the spindle to the bidirectional air turbine mounted on the cover of the pit assembly. Strain gage signals were transmitted through a Freon-cooled, high-speed slip ring assembly installed on the air turbine of the spin pit. The strain gage measurements were conducted by means of a bridge balancing technique. The bridge output of each strain gage was conditioned using a Budd Model p-350 Strain Indicator and the resulting stress versus speed was recorded on an X–Y plotter.

2.2 Test Procedure. The following schedule was used during testing: the assembly was slowly accelerated from zero speed to 40 percent of the maximum speed, dwelled at speed for 5 minutes, accelerated to 80 percent, dwelled for 5 minutes, accelerated to 100 percent, and dwelled for 5 minutes. The test assembly was then decelerated to zero speed. The procedure above was accomplished twice. The high stress location gages were observed during the initial run to assure that strain gages did not drift. The final run was an accel from zero speed to maximum speed, dwell at maximum speed for 5 minutes, and then a decel to zero speed. The variation between the results of the two runs is within 1 percent.

3.0 Comparison of Analytical and Experimental Results. In order to compare results of the test and the analysis, one-dimensional finite elements (ABAQUS's two-node truss element) representing the strain gages were added in the direction of principal stress to the membrane-solid model. Truss elements are rods that can only transmit axial force; they do not transmit moments. This element uses linear interpolation for displacement so that the strain varies linearly along the element.

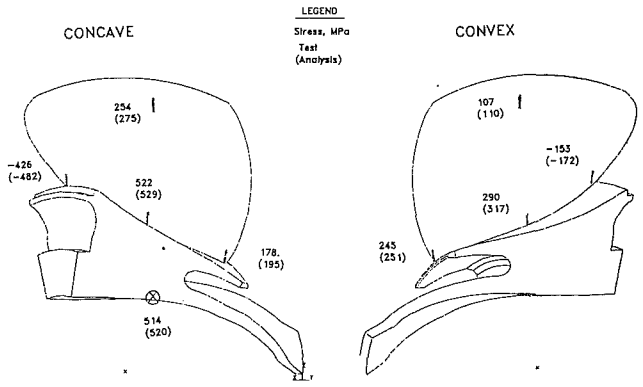


Fig. 8 Comparison of analytical results with strain gage data

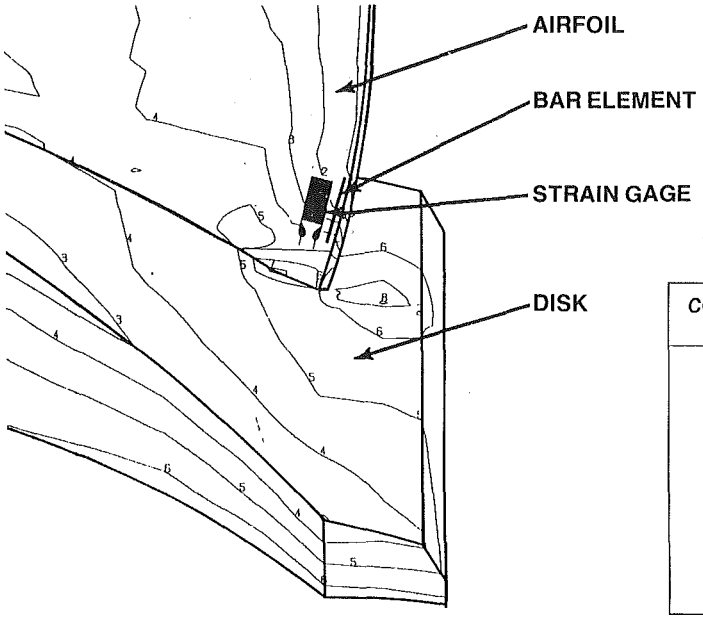
Conversion to stress occurs throughout the constitutive equations, which is Hooke's law for one dimension. The material properties of this bar element are the same as that of the component and the cross-sectional area is 0.001 mm^2. The strain gage tests introduce inaccuracies in the measurement of strain because of averaging strain over the gage finite length, which was 1.5 mm in this application. This was simulated using one-dimensional bar element with the length about the same as the strain gage's length. The comparisons of predicted stress from the one-dimensional element with the measured stress are shown in Fig. 8. As seen from this figure, the surface stress predictions, obtained from the membrane attached to the solid model, are in good agreement with the test data. However, the strain gages measured only 30 percent of the calculated stress at the trailing and leading edge of the blade's hub section where highly localized stress was predicted.

The gage length is an important parameter in strain gage selection. This parameter affects the installation and operating constraints. Accuracy, stability, simplicity, and ease of installation are the most important requirement in this experiment. The selection of gage length generally involves compromises. At the leading edge of the airfoil's hub section where the strain gradient is extremely high, one of the shortest available gages might be the obvious choice. However, small gages are generally characterized by less stable behavior and greater installation difficulty. At the same time, the space available for gage installation is very limited because of the small-radius fillet. Therefore, the strain gage length of 1.5 mm was chosen and it was installed above the fillet radius. Figure 9 shows the location of the strain gage and the bar element on the leading edge of the airfoil's concave side. Since strain gage measurement is an average of the stress over the area covered by strain gage's length, and since the average of any nonuniform stress distribution is always less than the maximum, a strain gage's measurement will indicate lower stress than the predicted values. The predicted maximum stress occurred at the blade/disk joint. However, because of the difficulty in locating the gage on the fillet at the blade/disk joint, it was necessary to place the gage at a location above the fillet radius. Therefore, there is no direct correlation between the maximum stress and a corresponding strain gage reading. Nevertheless, there is good correlation between calculated and measured values at the gage position nearest to the fillet. Effect of gage length on measured stress in the presence of a severe stress gradient is also illustrated in Fig. 9. The calculated stress in the bar element was 195 MPa, which corresponded to the average stress on the solid element. The strain gage measurement at this location is 178 MPa.

Conclusions

1 Steady-state measurements at various locations on the airfoil correspond favorably with the finite element analysis

Downloaded 02 Jun 2010 to 171.66.16.122. Redistribution subject to ASME license or copyright; see http://www.asme.org/terms/Terms_Use.cfm



CONTOUR LEVEL	MAX PRIN STRESS, MPa
1	100
2	200
3	300
4	400
5	500
6	600
7	700
8	800

Fig. 9 Location of strain gage and bar element on leading edge of airfoil's concave side

when membrane elements are used to predict surface stresses.

2 The experimental method of using a vacuum spin test with strain gage instrumentation provided an effective means of evaluating the steady stress of a swept airfoil design without the expense of an engine test.

3 Good agreement between calculated and measured stress verifies that nodal displacements are correct and provides confidence in stresses from membrane elements connected to them.

4 The investigation revealed the critical steady stress locations and the trend of stress variation along the hub section of the airfoil. Highly localized compression stress occurred at the trailing edge of blade hub, due to bending generated by centrifugal force.

5 The accuracy of stress prediction is dependent on the distortion of the finite elements. This dependence can be reduced by calculating stresses from membrane elements attached on the free surface of solid elements.

6 Obtaining stresses from the membrane elements offers an inexpensive, alternative technique to model bending problems, which usually require more than one element through the thickness of structures.

References

ABAQUS, 1989, Hibbitt, Karlsson and Sorenson Inc., 100 Medway St., Providence, RI 02906.

Armstrong, E. K., 1988, "Fatigue and Assessment Methods of Blade Vibration," *AGARD manual on Aeroelasticity in Axial Flow Turbomachines.*

Barlow, J., 1976, "Optimal Stress Locations in Finite Element Models," *International Journal for Numerical Methods in Engineering*, Vol. 10, No. 2, pp. 243–251.

CAEDS, 1988, IBM Corp., Application Systems Products, Neighborhood Rd., Kingston, NY.

Carter, A. D. S., and Kilpatric, D. A., 1957, "Self-Excited Vibration of Axial-Flow Compressor Blades," *Proceedings of the Institution of Mechanical Engineering*, Vol. 171, pp. 245–281.

Chi, R. M., and Jones, H. T., 1988, "Demonstration Testing of Noninterference Technique for Measuring Turbine Engine Rotor Blade Stresses," AIAA Paper No. 3143.

Kuo, P. S., Borowy, H. M., and Exley, J. T., 1980, "Steady Stress of a Backward Curved Impeller Blade," *Proceeding, Measurement Methods in Rotating Components of Turbomachinery*, ASME, New York, pp. 235–240.

Hinton, E., and Campbell, J. S., 1974, "Local and Global Smoothing of Discontinuous Finite Element Functions Using a Least Squares Method," *IJNME*, Vol. 8, No. 3, pp. 461–480.

NASTRAN, 1984, The MacNeal-Schwendler Corp., 815 Colorado Boulevard, Los Angeles, CA, 90041.

Nicholas, V. T., and Citipitioglu, E., 1977, "A General Isoparametric Finite Element Program SDRC SUPERB," *CompSt.*, Vol. 7, No. 2, pp. 303–313.

Srinivasan, A. V., and Fulton, G. B., 1984, "Advanced Turboprop Vibratory Characteristics," NASA CR-174708.

Downloaded 02 Jun 2010 to 171.66.16.122. Redistribution subject to ASME license or copyright; see http://www.asme.org/terms/Terms_Use.cfm

Detonation-Wave Technique for On-Load Deposit Removal From Surfaces Exposed to Fouling: Part I—Experimental Investigation and Development of the Method

K. Hanjalić[1]
Lehrstuhl für Strömungsmechanik,
University of Erlangen-Nürnberg,
Erlangen, Federal Republic of Germany

I. Smajević
Mašinksi Fakultet,
University of Sarajevo,
Bosnia Hercegovina

The paper presents a description and results of the experimental research, development, and full-scale testing of a new technique for cleaning gas-swept surfaces exposed to fouling, such as found in boilers, furnaces, heat exchangers, reactors, and gas ducts, by means of detonation waves. Part I describes the principles and reports on experimental investigations and optimization of the technique. Part II reports on several years of experience in applying the technique in full-scale operation in two large coal-fired boilers. Experiments involved detailed measurements of the pressure wave characteristics at a laboratory-scale model of a boiler furnace at a range of operating conditions and produced necessary information for optimum design and operation of the detonation wave generator. The investigation enabled a close insight into the detonation and shock wave generation, their behavior during propagation through the connecting ducts, and attenuation in the inner space of the model furnace. A good indication has also been obtained of the wave impact and effects on deposit-removal from different packages of tube bundles, which were placed in the model boiler in order to mimic boiler heating surfaces.

Introduction

The problem of surface fouling is encountered in many industrial equipment and plant components, such as coal-fired boilers, industrial furnaces, gasifiers, chemical and other type reactors, heat exchangers, industrial gas conduits, and the accompanying accessories: compressors, valves, fittings. Various techniques have been employed with more or less success, but most of the methods suffer from the drawbacks of accompanying side effects, such as abrasion and erosion of the cleaned surfaces, or are expensive to install and to operate. The problem of cleaning efficiently without incurring harmful effects is particularly pronounced in thermal power plants, metallurgical plants, cement factories, pulp and paper mills, and equipment in the chemical industry. A new technique, based on the action of detonation waves generated outside the object to be cleaned, seems to be devoid of most of the known undesirable effects and offers a number of advantages in comparison with conventional techniques. The present paper (Part I) describes such a technique and reports on the experimental investigation and development carried out in a laboratory at a model furnace of a boiler. The companion (Part II) of the paper reports on the full-scale application of the technique over a number of years in two coal-fired steam boilers in a power plant.

The basic principle of the detonation wave cleaning technique relies on utilization of shock waves generated by detonation of a fuel-oxidant mixture in a special chamber ("denotation wave generator," or simply "detonation chamber") placed outside the equipment to be cleaned. The wave generator consists basically of the ignition chamber and one (or more) cylindrical pipe of the same or smaller diameter. The connecting pipe serves a dual purpose: to enable a sufficient traveling path for the flame front to transform into the steep detonation wave front, but also to bring the wave into the boiler interior at the desired location and under desired angle, and to direct it toward the tube packages or other surfaces to be cleaned. After reaching the position beyond which there is no energy supply (i.e., at the end of the fuel-oxidant mixture zone, or at the most at the entry of the boiler interior), the detonation wave transforms into a shock wave, which propagates into the nonreactive environment and impacts on the exposed surfaces. It is the action of this impact and associated effects that produce the desired breakage and removal of the deposit from the impacted surfaces.

Theoretical Background

The basic theory of detonation waves was established more than a century ago, but has been modified considerably over

[1]On leave from the University of Sarajevo, Bosnia Hercegovina.

Contributed by the Power Division for publication in the JOURNAL OF ENGINEERING FOR GAS TURBINES AND POWER. Manuscript received by the Power Division January 12, 1992. Associate Technical Editor: R. W. Porter.

Copyright © 1994 by ASME
Downloaded 02 Jun 2010 to 171.66.16.122. Redistribution subject to ASME license or copyright; see http://www.asme.org/terms/Terms_Use.cfm

the past few decades on the basis of extensive laboratory research exploiting laser generated extremely short light pulses: photons (stroboscopic laser schlieren systems), fast transducers, and other modern instruments. The subject has been covered in detail in the literature and will not be elaborated on here except to recall some aspects relevant to the considered problem. This concerns first of all determining basic design and operational parameters of the detonation wave generating system, but also elucidating, at least in part, the wave action on destroying and removing the deposited material from impacting solid surfaces.

According to the classic detonation theory (e.g., Courant and Friedrichs, 1956), a detonation wave can easily be generated in a sufficiently long tube, closed at one end, by igniting a homogenized and premixed combustible fuel–oxidant mixture by a spark. The combustion products, bounded by the tube closed end, side walls, and the flame front, will travel toward the open end of the tube into the unburned mixture initially at a relatively slow propagation speed of a few meters per second for about ten tube diameters, but accelerating quickly toward the flame front until a steep detonation front is established. The detonation wave propagates subsequently at its own propagation velocity, which may reach several thousand meters per second. It has been maintained for a long time that it is the acceleration of the flame front that causes the formation of a series of weak compressible waves, which coelesce into stronger waves whose strength gradually increases until transforming into a shock wave, which in turn establishes conditions for the continuation of the detonating combustion.

This simple picture of the detonation wave formation has undergone a substantial modification in some details; nevertheless, the general notion in regard to the final outcome of the process is more or less the same. We know now that the process is more complex in regard to what is happening in the course of the wave formation. High-speed photographs show that the ignited flame usually has a front in the form of a smooth spheroid, initially laminar if the fuel–oxidant mixture was at rest, but wrinkling fast and generating a series of pressure waves, which may coelesce into a shock front before the flame even becomes turbulent. This shock wave will itself enhance the fast transformation of the laminar flame into a turbulent structure, which in turn will act as the source of pressure waves. Contrary to the classic theory, which presumes a gradual monotonic transition from the flame front to the detonation wave, the experimental evidence suggests that a sequence of intense pressure waves, emanating from the wrinkled surface of the highly turbulent flame, leads to several internal explosions ("explosion within the explosion"), each producing a detonation front. Some of the detonation fronts will eventually either decay, if the others consume all unburned energy, or merge into the joint strong detonation front.

Such a detonation wave, which represents basically a sharp discontinuity between the burned and unburned combustible mixture, has for long been thought to consist of a shock wave and layer of small but finite thickness where the combustion occurs, which actually follows the shock wave traveling behind it ("on its back") with the same speed. The classic detonation theory presumes the formation of a shock front as a precursor for the detonation to occur (detonation was also defined "as a combustion process initiated by a shock," Courant and Friedrichs, 1956), while the heat released due to combustion supplies the energy needed for the maintenance of the shock wave. However, high-speed photographs obtained by a stroboscopic laser-schlieren technique (e.g., Oppenheim, 1970) repudiated this oversimplified picture and showed that the detonation wave has essentially a cellular structure consisting of a number of curved intersecting shock fronts separated by strings of thin combustion fronts. It is this reactive netlike structure through which the combustion layer from behind the shock protrudes the shock front and acts as a receiver of the energy ("propulsion drive"), needed for its sustenance, from the combustible mixture encountered, Fig. 1. Such a detonation corresponds to the Chapman–Jouguet point on the detonation adiabate ("Chapman–Jouguet detonation"), which is characterized by the fact that the propagation speed of the detonation wave front relative to the combustion products just behind it equals the local speed of sound, while relative to the unburned mixture ahead of the front its speed is supersonic, though minimum for the given conditions.

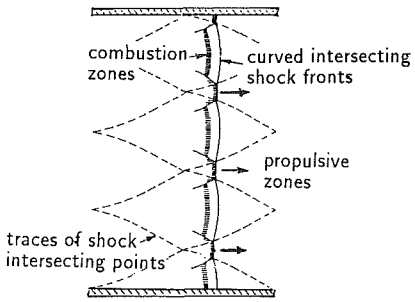


Fig. 1 Structure of a detonation front (after Oppenheim, 1970)

This brief recollection of the basic notions of the detonation theory and some recent findings is by no means complete, but could serve a purpose of creating some picture of what is actually happening in the detonation wave generator. On the basis of this description and simple relationship for the detonation wave we determined approximately the propagation speed of the detonation before it enters the boiler interior. Of course, the results could be regarded only as approximate since several parameters depart from the above idealized picture. So, e.g., in the present situation, the continuous inflow of air (kept for practical reasons over the period of running the experiment) and the presence of a turbulizer ensured turbulent regime from the start. Besides, the distance between the mixture ignition by spark plug and the position at which conditions for the formation of the detonation front are fulfilled depends also on other factors, such as the composition and premixing of the combustible gases into which the flame propagates.

Laboratory Investigations

In order to quantify and correlate the basic parameters that define the optimum operation of the equipment and the best cleaning effects, extensive laboratory investigations have been undertaken at the specially designed experimental rig in laboratory. The experimental program was set with the following goals:

- to define basic wave characteristics and to correlate them with design parameters and operational mode of the wave generator;
- to establish correlations between the wave characteristics and the deposit removal (surface cleaning) effects;
- to optimize the design of the detonation chamber and fuel–air mixture generating system as to produce the desired wave characteristics and cleaning effects;
- to ensure fully controlled, safe and reliable operation of the equipment.

The experimental rig, shown schematically in Fig. 2, consists of a reduced-size cold model of a typical boiler furnace, two detonation chambers, the system for preparing the fuel–oxidant mixture, and the control unit. A chamber of rectangular cross section ($1.6 \times 2.4 \times 3.9$ m) was adopted to mimic the boiler furnace (Fig. 3). Provision was made for placing packages of boiler or other tubes of various types in desired arrangements. A piece of the original refractory brick layer was also built in one of the model side walls in order to investigate the shock effects on the boiler structure. One of the experimental det-

Downloaded 02 Jun 2010 to 171.66.16.122. Redistribution subject to ASME license or copyright; see http://www.asme.org/terms/Terms_Use.cfm

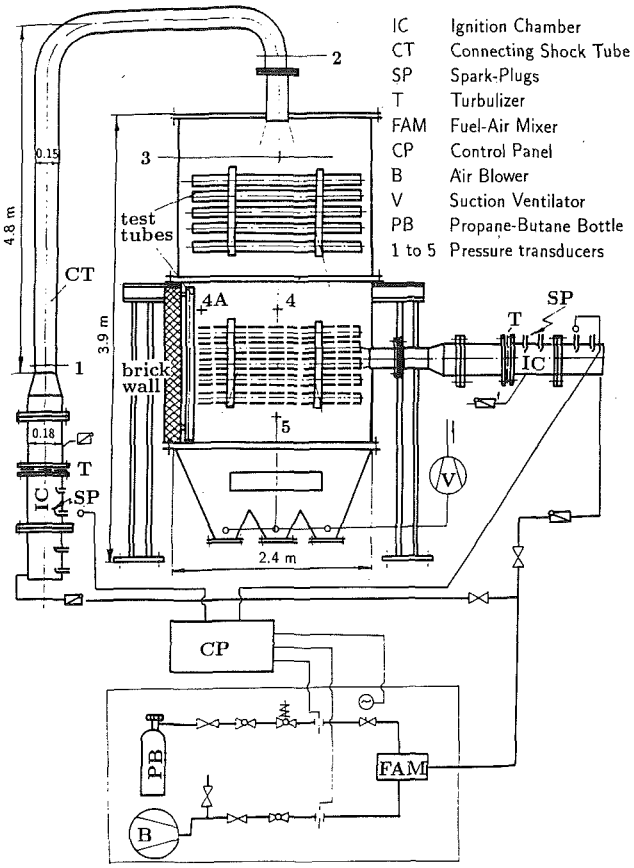


Fig. 2 Schematic layout of the experimental rig

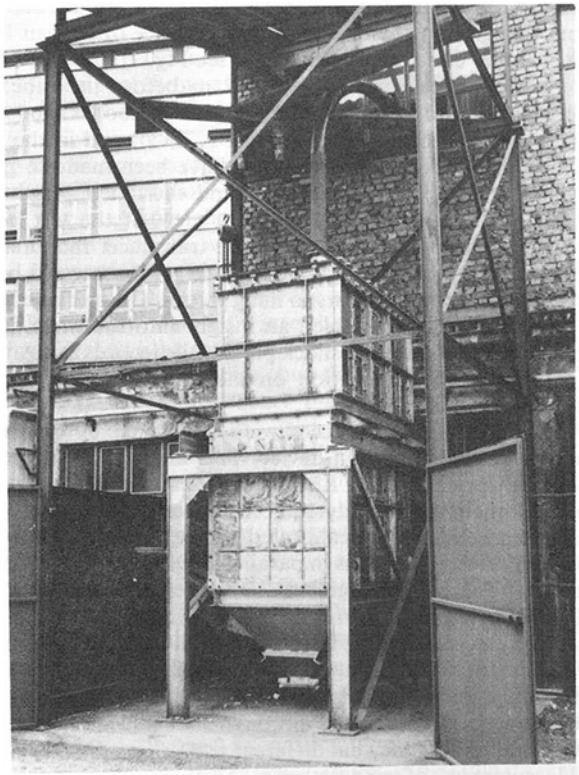


Fig. 3 Outlook of the experimental boiler furnace

onation chambers was placed vertically on the floor and its exit was connected with the model boiler by a circular pipe through which the waves have been led into the boiler interior. The connecting pipe originally directed upward was redirected

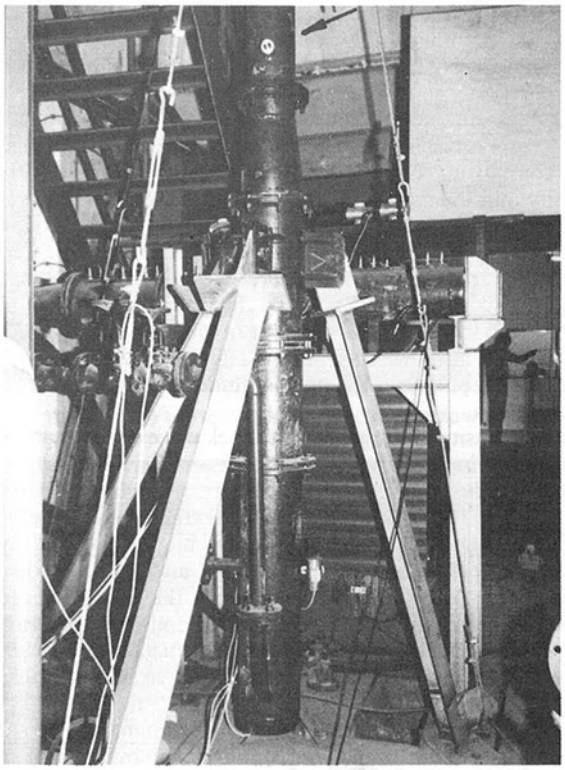


Fig. 4 A view at the vertical detonation chamber

downward by a 180 deg bend (made on purpose to simulate actual full-scale geometry) and introduced into the boiler interior through its roof, its axis at the exit being directed toward the test tube package, which was placed to hang freely in the model boiler. The other detonation chamber, positioned horizontally, is connected to the boiler model via a short straight pipe and directed toward the brick wall. The wall can be screened with a row of tubes of different size and configuration as to simulate various types of furnace tube walls.

Each of the two experimental chambers has been equipped with a number of spark plugs, turbulizers, and other elements that ensure a fully controlled detonation. A view at the vertical detonation chamber is given in Fig. 4. The fuel–oxidant mixture is prepared in the mixture generator ("mixer"), equipped with necessary control and safety valves and monitoring sensors, connected to the control panel, so that its operation is controlled automatically. A propane–butane mixture, supplied in standard industrial consumer containers, has been used as fuel in the present experiment, but other types of fuel (natural gas or liquid fuel) can also be used. Air was supplied by laboratory blower of 0.19 m^3/s capacity. A three-way valve enables a simple choice between the two detonation chambers according to needs, while nonreturn safety valves in each duct prevent any return flow or wave propagation into the mixture generator.

Each detonation chamber is supplied with a turbulizer in the form of a perforated orifice plate, which is placed usually between the ignition chamber and the connecting shock tube. Over the period of optimization of the chamber design a number of different types of turbulizing orifice plates, as well as their positioning, have been explored. Partly for that reason, but also for the sake of arriving at optimum shape and aspect ratio of the ignition chamber, the latter was composed of two or more sections, some of them in conical shape, which could be combined to give a different ratio of volumes of the ignition chamber and connecting tube, while retaining the constant total volume. Because a detonation wave is followed by a rarefaction wave, which can create a vacuum, the ignition chamber has been connected to the atmosphere via a nonreturn valve.

Downloaded 02 Jun 2010 to 171.66.16.122. Redistribution subject to ASME license or copyright; see http://www.asme.org/terms/Terms_Use.cfm

Experiments have been carried out either by triggering a single spark plug at the selected position, or several plugs simultaneously. The control unit provides a possibility to preset parameters defining the mixture formation and ignition, after which the unit can operate automatically. It controls the time of the ignition chamber feeding with fuel and its washing after the combustion is finished, regulating in such a way the intensity and the frequency of the resulting detonation waves.

The maximum flame propagation speed through the detonation chamber depends on the composition of the fuel–air mixture (air surplus factor), effective cross-sectional area of the turbulizing orifice plate, and the ignition chamber volume (relative to the total volume of the detonation chamber). These parameters have been optimized after a detailed exploration, and were kept within the narrow limits throughout the experimentations.

The intensity of the generated shock wave depends also upon the fuel filling rate n [%] of the detonation chamber, which can be defined as the ratio of the part of the chamber volume occupied by the reagents and the total chamber volume. In the course of the experiment, the filling rate was varied over a wide span between 13 and 74 percent and was controlled by measuring the volume of the mixture that was fed into the chamber before ignition. This was accomplished by controlling the time period τ_f during which the magnetic valve in the propane–butane supply line was kept open. The relationship between the chamber feeding rate n [%] and the fuel valve opening time τ_f [s], depends upon the design and size of the detonation chamber, and was established on the basis of simple calculation and by trial and error for each chamber. The approximate correlation, established for the considered configuration of the detonation wave generator, can be written as[2]

$$n\ [\%] = 4.236\tau_f\ [\text{s}] - 1.65$$

After ignition, the flame propagates into the premixed fuel–air mixture, quickly forming a detonation front. The pressure of the combustion-wave crest increases during the formation of the detonation front, reaching a characteristic value at the point of steep front formation, and then remains constant until the pipe end is reached (a slight weakening may occur due to the friction at pipe walls). A substantial reduction of the wave intensity occurs after the wave leaves the pipe and enters the boiler chamber with a much larger cross-sectional area.

The above-described picture of the wave development process will occur in full only if the connecting shock tube is sufficiently long and a sufficient amount of the fuel–air mixture has been fed into the detonation chamber. If either of these two conditions is not fulfilled, the wave development will not be completed. If the connecting tube is too short, a part of the air–fuel mixture will exit the tube and enter the boiler interior before the flame front has reached the tube end. Hence, the detonation may occur somewhere in the boiler instead of in the connecting tube, or it may not occur at all if the mixture is diluted too much after entering a much larger space of the boiler interior. In the other case, if the feeding rate is insufficient, the detonation will be too weak (or will not occur at all) and the wave will attenuate quickly while traveling along the tube.

The intensity of the detonation and wave formation will also depend upon the location of the ignition nest, i.e., number and positions of the spark plugs. Investigation of this parameter was carried out by installing a number of nests for placing spark plugs, but triggering only the selected ones in accord with a proscribed systematic testing schedule. After preliminary testing we retained only four ignition nests located all in the ignition chamber so that the lowest one was positioned at a distance of 300 mm from the chamber closed end, while the other three plugs were placed at distances of 540, 1020, and 1260 mm, respectively, all measured from the chamber end. Of several combinations that were tested, we will report on three cases, which illustrate sufficiently in detail the effect of the ignition nest position, namely when the ignition was performed by triggering only the lowest spark plug, or the uppermost, or all four plugs in the same time.

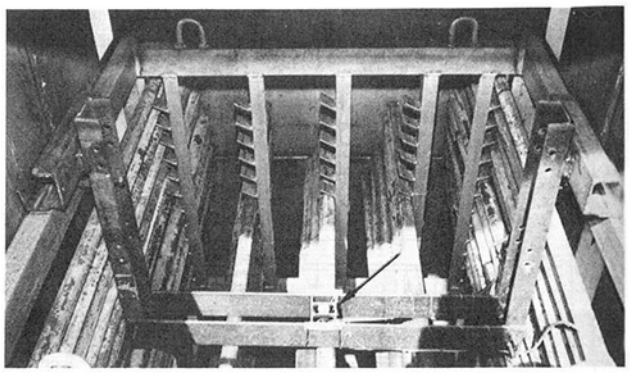


Fig. 5 Interior of model furnace with the installed pressure transducer

The recording of the transient pressure intensity was carried out by several fast pressure transducers placed at various positions in the rig. Two types of pressure transducer were used in parallel to ensure full reliability and to exclude possible systematic error: piezoelectric pressure gages Kistler, type 601A with the measuring range from 0 to 25 MPa, and DISA capacitive transducers, type 51F10 with the measuring range from 0 to 2.5 MPa. Standard measuring positions include the exit from the ignition chamber (IC) at a distance of 2.23 m from the chamber closed end (position 1, see Fig. 2), the end of the connecting shock tube (CT) at 1.2 m before the tube exit (position 2), and at several places inside the boiler model interior at the furnace axis (positions 3, 4, 5), and in the wall vicinity (4A). However, provisions have been made to place several more pressure transducers and thermocouples in the ignition chamber. Figure 5 shows a view of the test boiler interior with a Kistler 601A pressure transducer mounted on a rigid traverse in section axis, together with some old boiler tubes placed in several rows to hang freely. The measurements at positions 1 and 2 enabled an insight into the wave development in the connecting shock pipe, while records at positions 3 to 5 supplied information on the wave attenuation after entering the boiler interior.

DISA pressure transducers were calibrated by a special (though static) calibration device. This method could not be employed for calibrating Kislter piezoelectric transducers because of their inherent dynamic characeristics. Instead, the Kistler transducers were calibrated on the rig itself by placing them at the same positions in parallel to DISA transducers and recording both signals together. A number of recordings were taken at different pressure intensities, which were varied by changing the fuel feeding time in the ignition chamber. It was found that Kistler transducer, in spite of the fact that its measuring range was much larger than the measured pressure span, showed a good sensitivity, although its calibration constant was found to be somewhat different from the catalogue value.

Measurements of temperature at characteristic positions were also carried out by means of fero-constantane and chromel-alumel microthermocouples. However, the thickness of the thermocouple wires of 100 μm was too high to ensure sufficiently fast response so that the temperature records served only as an indication and have not been used for any quantitative deductions.

[2]Theoretically, n should be directly proportional to τ_f, but there is some initial "idle" time of about 0.4 seconds during which there is actually no noticeable fuel feeding.

Downloaded 02 Jun 2010 to 171.66.16.122. Redistribution subject to ASME license or copyright; see http://www.asme.org/terms/Terms_Use.cfm

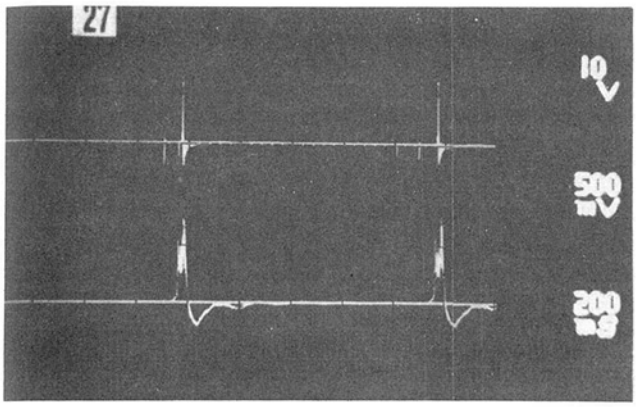


Fig. 6 Wave oscillograms at positions 1 and 2; ignition by the lowest spark, τ_f = 12 s

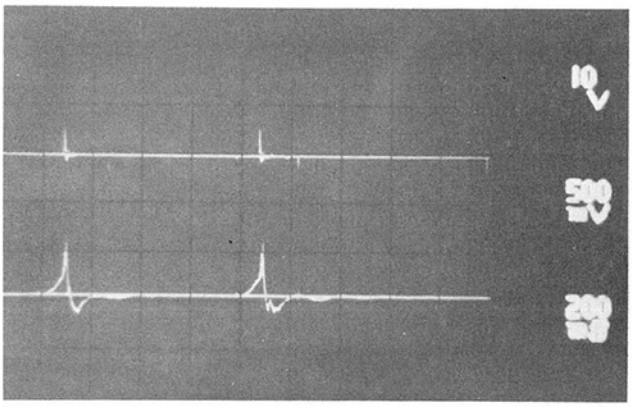


Fig. 7 The same as in Fig. 6, but ignition by the uppermost spark

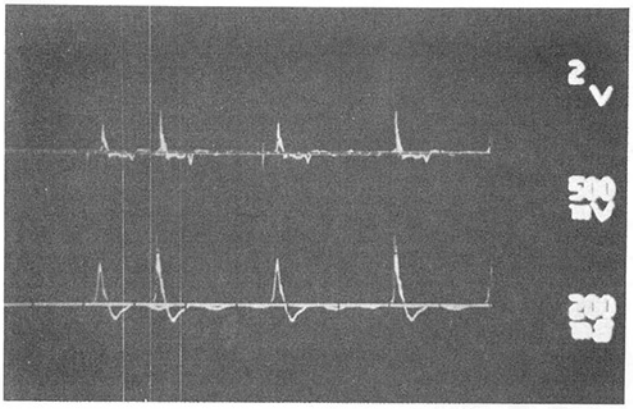


Fig. 8 Oscillograms at positions 1 and 2 for insufficient feeding, τ_f = 5 s

Results and Discussion

Wave Dynamics and Formation in the Detonation Chamber. We start by analyzing first the process of traveling and formation of the detonation wave in the connecting tube on the basis of pressure recordings at positions 1 and 2. By varying the fuel feeding time τ_f and the ignition position it was possible to obtain waves of different intensities and shapes. Figure 6 shows a typical sample of simultaneous oscilloscope recordings of both signals, obtained in this case for τ_f = 12 s (corresponding to n = 49.2 percent for the detonation chamber considered) and by igniting the combustion by the lowest spark plug. The lower signal corresponds to the position 1 and was obtained by a DISA capacitive transducer, while the upper signal was obtained by a Kistler piezoelectric transducer positioned at 2. Both signals have the same time basis, but amplitude scales are different, and so are the calibration coefficients.

Two signals differ not only in amplitude, but also in shape. The lower signal shows a typical strong compression wave with an amplitude of about 0.42 MPa, but the wave has a considerable thickness and its front does not have the character of steep detonation wave, proving that the formation of the detonation wave has not yet been completed due to an overly short distance from the ignition to the measuring point 1. Contrary to that, the wave at position 2 (upper signal) has a very sharp peak, reaching an amplitude of 1.4 MPa, which indicates that in this case the wave at the exit of the connecting tube has transformed fully into the steep detonation front.

Figure 7 shows the recordings obtained by the same feeding rate as in the previous case, but the ignition was started by triggering the uppermost spark plug. The same scaling as in the previous figure has been used to facilitate a fair comparison. As could be seen, the intensities of both waves are considerably smaller than in the previous case and although the upper signal exhibits a steep front, its intensity, about three times lower than in the previous case (about 0.5 MPa), suggests that the full development of the detonation front has not been accomplished. Even more is true for the lower signal of crest intensity of about 0.26 MPa, which has a character of a typical finite amplitude compression wave with a nonsteep front. This figure illustrates best the importance of the proper positioning of the ignition nest for the timely development of the wave front. As will be seen later, the strongest waves, for the same conditions, are obtained by igniting the fuel-oxidant mixture as close to the closed end of the chamber as possible (here with the lowest spark plug) and the weakest waves are obtained by triggering the uppermost one.

Figures 8 provides further illustrations by showing again a comparison of waves at two positions, 1 and 2 (lower and upper signal repectively), but this time with much shorter feeding time of τ_f = 5 s (n = 19 percent). The figure also shows a comparison between the ignition by single and multiple ignition nests: The right part of the record was obtained by triggering the lowest spark plug, while the left part corresponds to the case when the ignition was triggered by all four plugs. Both recordings show that the waves have considerable thicknesses; their front is not steep as in previous cases. The intensities of both waves are moderate and different in between, but their ratio is opposite from the previous cases. That is, a higher intensity has been recorded at position 1 where the wave peak reaches about 0.32 MPa while at position 2 it achieves only about 0.17 MPa. These findings confirm the fact that the feeding rate was insufficient for detonation wave to develop fully even at the end of the connecting tube.

The previous three figures illustrated the importance of establishing the two basic criteria for completion of the detonation waves formation in a selected geometry and size and length of the detonation chamber. These are: the minimum feeding time τ_f [s] or the corresponding filling rate n [percent] as discussed earlier, and the position of the ignition nest. In order to arrive at definite conclusion, a number of combinations has been explored and the results plotted in a summary diagram, as shown in Fig. 9. The figure shows the extracted values of waves intensities (peak pressure in MPa) at two positions in the connecting tube in function of the fuel feeding time or filling rate (both denoted on abscissa).

Two families of curves can be distinguished. The curves denoted by "1" represent the recordings taken at station 1 at the exit from the detonation chamber, while curves "2" correspond to recordings at position 2 at the end of the connecting pipe. Each of the two families contains three curves corresponding to three different positions and sizes of the ignition nests. The index "l" denotes that the ignition has been triggered by the lowest spark plug (at the chamber closed end) while the index "u" denotes triggering with the uppermost plug. Curves

Downloaded 02 Jun 2010 to 171.66.16.122. Redistribution subject to ASME license or copyright; see http://www.asme.org/terms/Terms_Use.cfm

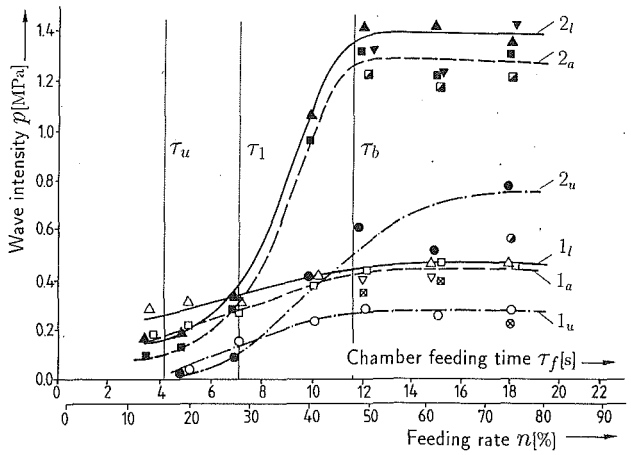


Fig. 9 Development of wave front at positions 1 and 2 with filling rate n (and feeding time τ_f)

marked by "a" correspond to the case when all plugs (here four) were triggered in the same time. For reference, three characteristic feeding times have also been denoted: τ_u, τ_1, τ_b denote feeding times needed for the fuel-air mixture to reach the uppermost spark plug, position 1, and the connection tube bend, respectively.

Attention is drawn first to the fact that the detonation wave can under no circumstances be formed at position 1, and that for its formation the wave needs a traveling path longer than the distance between the ignition nest and the position 1. Of course, higher feeding time and a larger distance of the ignition nest from the position 1 yields a stronger wave intensity, as expected. In all cases, however, after passing position 1, where the filling rate n is only about 28 percent, the wave continues to develop, achieving considerably higher strength at position 2. The completion of the detonation wave formation is accomplished when the filling rate reaches 46 percent except for the case of ignition with the uppermost spark plug. Further feeding of the chamber with fuel has no effect, which is in agreement with the earlier conclusion drawn from the basic detonation theory on the constant propagating velocity and wave intensity.

It should be noticed that for short feeding times ($\tau_f < 7$ s, $n < 30$ percent, approximately) the pressure amplitude at position 1, though small, is higher than at position 2, which indicates that due to insufficient supply of energy the combustion is terminated already in the ignition chamber or just outside it and the combustion wave decays before it manages to transform itself into the detonation front.

The ignition with the uppermost spark plug generates the weakest waves among the three cases considered, with a nonsteep front at all positions in the connecting tube. The reason is the insufficient length of the tube for the formation of the detonation wave. However, this may sound surprising, since the relative difference between the positions of spark plugs in comparison with the total length of the detonation chamber is not large enough to cause such a difference in regime. It is more likely that the distance between the ignition nest and the turbulizing orifice plate plays a more important role. Larger distance (lowest nest active) gives a change to the combustion products to expand and accelerate sufficiently before reaching the turbulizer, so that the latter could perform its "duty," i.e., deform and wrinkle the flame front and transform it into highly turbulent structure. This turbulent flame front with extended surface area enhances the generation of pressure waves, promoting a faster mixing and a better contact of the flame with the unburned mixture, accelerates quickly, and transforms into the detonation wave. In the case when only the uppermost nest was active, the flame front and the combustion products encounter the turbulizing plate in slow motion and its effect may not be sufficient to create any significant level of turbulence. Insufficient turbulence cannot be compensated in the later phase of the combustion wave traveling through the connecting tube in spite of the expansion of combustion gases. It should be mentioned that this expansion is slower than in other two cases also because combustion gases are expanding with the second flame front towards the closed tube end. As a result, the increase of pressure with the feeding time in this case at position 2 is much slower than in other two cases, as shown by curve $2u$, Fig. 9.

When igniting with all four spark plugs, flame fronts are generated around each plug. They coalesce fast, promoting an acceleration of the combustion process, and in spite of the fact that the flame front from the uppermost plug will reach turbulizer first and at a low speed, subsequent onflow of accelerated combustion gases will enhance turbulence. The pressure rise with the feeding rate in this case is close to that in case of ignition with the lowest plug. In fact, in an ideal case, for the same fuel-oxidant mixture and chamber geometry, the maximum pressure rise at the detonation wave should be the same in all cases if the wave formation is completed, regardless of the place and way of the ignition, but in a real situation a number of influencing factors seem to matter.

Ignition with the lowest spark plug yields the highest pressure at both measuring stations. This is partly a consequence of a considerable self-acceleration of the combustion products within the ignition chamber before they reach the turbulizing plate. We should not, however, exclude the possibility of achieving even better performances (development of the detonation wave at even shorter distance and with a shorter feeding time) by using more than one ignition nest, but concentrated near the tube closed end and sufficiently away from the turbulizer.

The pressure at station 1 does not exceed the value of 0.47 MPa. In an ideal situation the pressure should reach its maximum when the feeding time reaches the value of 7.1 s (which corresponds to the time in which the detonation chamber is filled just up to position 1), and should retain this value irrespective of subsequent continuation of fuel feeding. The fact that the pressure at this position continues to rise with the increase of the feeding time above this value can be explained by better conditions for combustion in the ignition chamber and by some heat accumulation in the chamber walls from previous detonation during the experiment. This effect fades away, however, and at $\tau_f > 13$ s an equilibrium has been reached when pressure remains constant irrespective of the feed time.

In spite of a considerable scatter of measured data, this discussion of Fig. 9 can serve for drawing some important conclusions:

- The wave intensity is much larger at the end of the connecting pipe (curves "2") than at the pipe inlet (curves "1"), provided the feeding rate has exceeded a certain minimum value, proving that the detonation front is generated somewhere in the pipe between these two points.
- In both families of curves the largest wave intensities are achieved if the ignition is triggered by the lowest spark plug, while the weakest waves are generated by igniting the mixture by the upper plug. In the latter case ignition occurs close to the perforated plate that serves as a turbulizer and the flame passes the plate at low velocity, diminishing its turbulizing function. The second flame front, in this case, after reflecting from the close end, follows the primary front, but they are parted and the combustion is slower than in the first case when both fronts are much closer to each other and propagate into the well-mixed mixture.
- Ignition by all spark plugs simultaneously produces results that are between these two.
- Recordings at station 2 for different feeding rates show that there exists a saturation feeding rate n [percent] (between

Downloaded 02 Jun 2010 to 171.66.16.122. Redistribution subject to ASME license or copyright; see http://www.asme.org/terms/Terms_Use.cfm

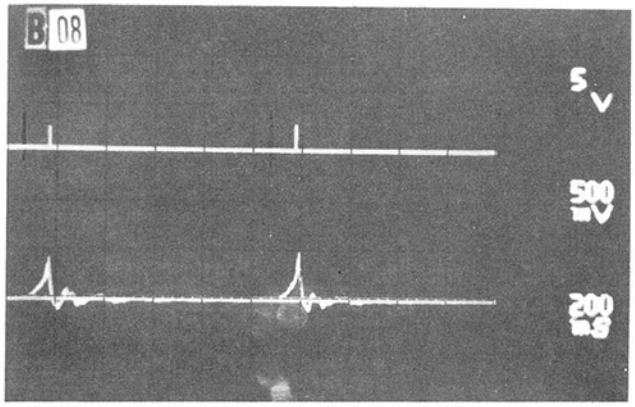


Fig. 10 Oscilloscope recording of waves at position 1 (lower signal) and position 3 (upper signal), ignition with the uppermost spark, τ_f = 12 s

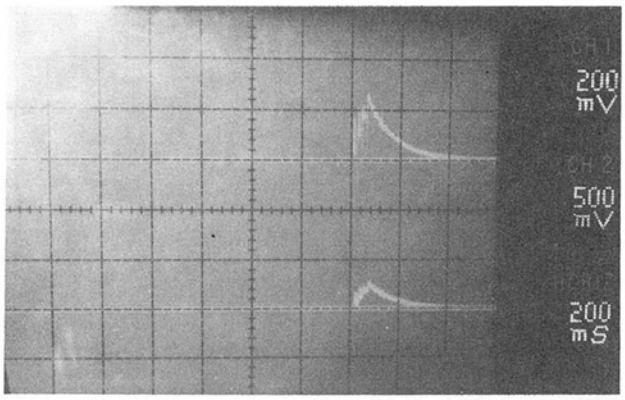


Fig. 12 Oscilloscope recordings of a wave in furnace, position 4, τ_f = 15 s

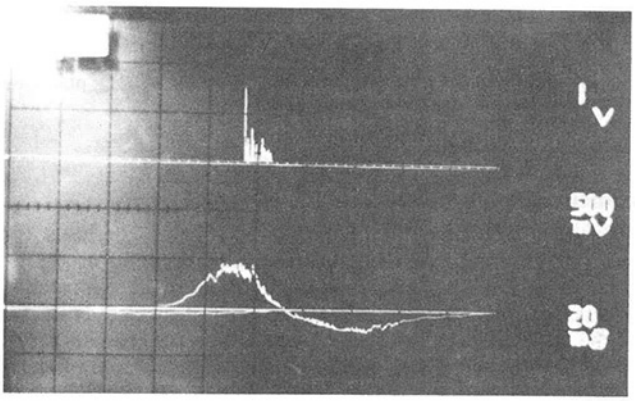


Fig. 11 The same as in Fig. 10, but ignition by all sparks, τ_f = 7 s (note the change of scales)

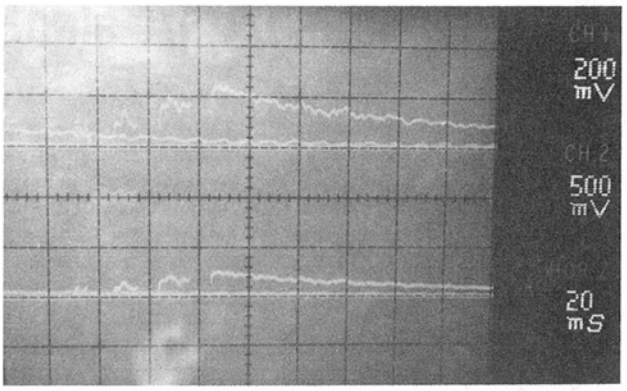


Fig. 13 The same as in Fig. 12, with time base enlarged 10 times

45 and 60 percent, depending on other conditions) beyond which further feeding yields no effect upon the wave strength; this moment corresponds to the formation of the steep detonation front and this percentage has been characterized as the *rational* feeding rate because it represents a minimum amount of fuel needed for ensuring the maximum wave intensity.

• Waves generated with a smaller amount of fuel (feeding time less than rational) reach their maximum intensity in the ignition chamber (before reaching the pipe inlet, position 1) or just after, and retain the character of a combustion wave (no steep front) and show a larger intensity at position 1 than at 2 (though considerably smaller than in case of rational feeding). This can be explained to be a consequence of attenuation of an already weak detonation wave and of a lack of further energy supply, since the combustion had been completed earlier in the chamber.

Wave Attenuation in the Model Furnace. We move now to the discussion of the process of wave attenuation after leaving the connection pipe and entering the boiler interior. These measurements have been obtained by placing pressure transducers at position 3, 4, 4A, and 5 and recording the oscilloscope reading at each position in parallel with those at reference position 1 or 2.

The shape of the wave after entering the boiler interior and the comparison with the waves in the connection tube can be seen in Figs. 10 and 11, where the same wave is shown recorded at positions "1" and "3" (the latter is already inside the model boiler) for two feeding times: τ_f = 12 and 7 s, respectively. (Note different amplitude scales for the upper signal as well as time scales in two figures!) A sharp diminution of the wave intensity is noticeable for all cases considered, which could be expected considering the large increase of the cross-sectional area. Since it is these waves here that are attacking the tube packages, it is their strength that matters and the rate of attenuation of wave intensities at this point is an important parameter, which should be known for each particular case for proper dimensioning of the chamber and connecting pipe, as well as for determining the adequate time.

Of considerable interest is also the destiny of the waves after they pass through the tube package in the boiler space. For this purpose recordings have been taken at measuring positions 4, 4A, and 5, but this time with tube packages placed in the lower portion of the boiler furnace (between measuring positions 4 and 5, see Fig. 2). The results are shown in Figs. 12 and 13, each representing the same two signals, but with the time base in the second picture enlarged by factor of 10. Two signals in each picture have been taken at the same position but using different transducers (different calibration coefficient) showing the same shape, but a difference only in amplitude, as expected. The figure shows also a further diminishing of the wave strength so that the intensity of the peak pressure at position 4 is about 0.1 MPa. This may be considered still as too high and risky for the application in a real boiler, but the wave will continue to attenuate before reaching the tubes or wall. Besides, the cross-sectional area in a full-scale boiler is much larger than in the experimental model.

Wave of almost identical form have been recorded at position 4A, as shown in Fig. 14. Here the peak intensity is somewhat smaller, but this is expected, because the spherical wave front travels longer to reach this point than position 4.

Further inspection discloses some other interesting features. For example, the compressive portion of the wave is not smooth but consists of a number of weaker waves superimposed on it, which are in fact the reflections of the original pressure wave from the side walls and obstacles. The wave tail is, however, smooth and has a mild gradient, Figs. 11–13.

Based on a large number of pressure recordings at position

Downloaded 02 Jun 2010 to 171.66.16.122. Redistribution subject to ASME license or copyright; see http://www.asme.org/terms/Terms_Use.cfm

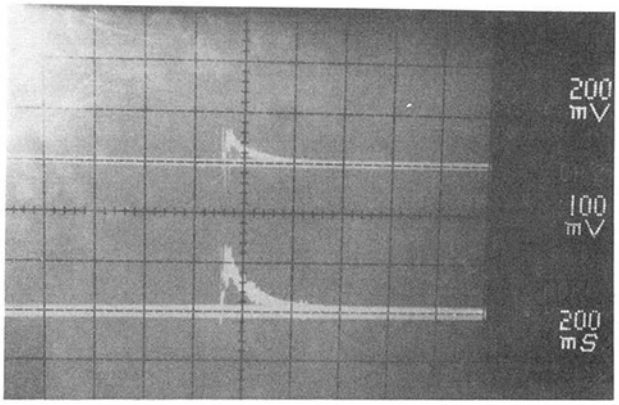


Fig. 14 Recordings of a wave in the furnace, position 4A, τ_f = 15 s

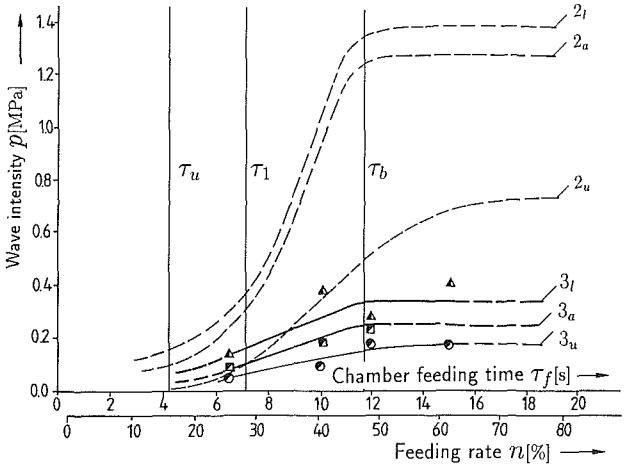


Fig. 15 Development of the wave front at positions 2 and 3 with τ_f and n

3, a diagram was constructed as shown in Fig. 15, showing the dependence of the pressure wave intensity as a function of the feeding time τ_f (and filling rate n). For comparison, three curves representing the best fit through the measurement at the position 2 have been reproduced from Fig. 9. Comparison between the wave intensities at positions 2 and 3 for corresponding feeding time and position of the ignition nests show in all cases a strong attenuation of the waves after entering larger space. It should be mentioned that the geometry of the connecting tube open end, as well as the geometry and size of the model boiler, were kept the same througout the whole experiment and the results obtained are valid for that situation. Maximum pressure in the boiler space at position 3 was 0.35 MPa and this was achieved by igniting the mixture with the lowest spark plug and with a rational feeding rate (n = 46 percent).

A summary presentation of the wave development along its path looks roughly as in Fig. 16, where the intensity of the waves is plotted along the distance from the chamber closed end (on abscissa). Three different cases are presented, corresponding to feeding times of τ_f = 7, 10, and 12 s. In all cases the ignition was performed by all four plugs simultaneously. Because of lack of measurements in the connecting pipe between the positions 1 and 2 the behavior of the curves in this region had to be guessed and should be regarded as approximate. However, the figure shows that only in case "1," which corresponds to the rational feeding time, the maximum wave strength was achieved in the pipe, remaining constant until the end of the pipe, to be strongly diminished after entering the boiler space.

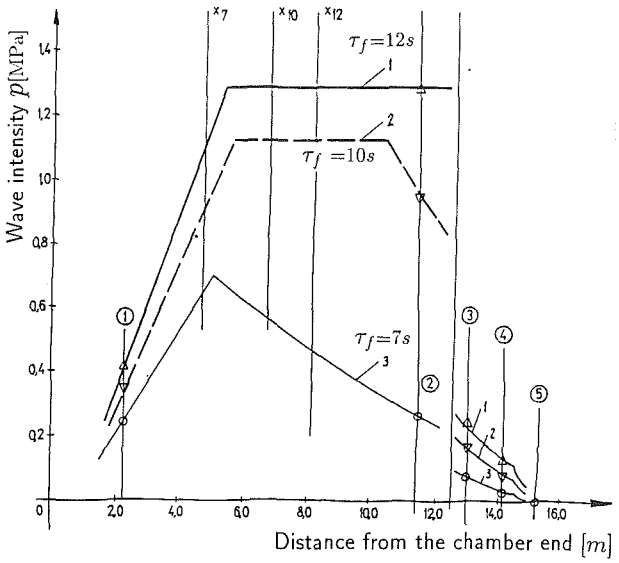


Fig. 16 Development of waves along their path: X_7, X_{10}, X_{12}; positions reached by mixture at τ_f = 7, 10 and 12 s

Conclusions

Detailed experimental investigations of the methods for cleaning gas-swept surfaces by means of detonation waves, carried out at a laboratory model of a boiler furnace, provided necessary information regarding the generation and dynamics of the wave propagation and their action on the solid surfaces. Relationships were established between various parameters, which could be used for designing the wave generator and control unit and for adequately connecting the wave generating unit to the equipment to be cleaned. The results showed that the technique could be efficiently employed for removing various types of deposite material in industrial equipment exposed to heavy fouling.

Acknowledgments

Parts of this research have been supported by the Research Fund of Bosnia Hercegovina and by the Power Plant "Kakanj." The final writing of the paper was completed during the stay of K. Hanjalić at LSTM of the University of Erlangen and this author acknowledges with thanks both the sponsorship of the Deutsche Forschungsgemeinschaft and the hospitality of the LSTM.

References

Courant, R., and Friedrichs, K. O., 1956, *Supersonic Flow and Shock Waves*, Interscience Publ., 2nd printing.

Oppenheim, A. K., 1970, "Introduction to Gasdynamics of Explosions," Int. Centre for Mechanical Sciences, Lecture notes 48, Udine.

Podimov, V. N., et al., 1979, "On the Mechanism of Impulse Cleaning" [in Russian], Kazan University.

Smajević, I., 1984, "Contribution Towards the Development of Detonation Wave Method for the Prevention of Deposit Forming on Boiler Heating Surfaces," M.Sc. Thesis [in Serbocroatian], Faculty of Mechanical Engineering, University of Sarajevo.

Smajević, I., and Hanjalić, K., 1987, "Detonation Wave Technique for On-Load Cleaning of Gas-Side Surfaces of Steam Boilers," *Proc. Joint German-Yugoslav Colloquium on Low-Grade Coal Combustion*, Special Publ., Academy of Science and Arts of Bosnia Hercegovina, Vol. LXXXI, Sarajevo.

Smajević, I., and Hanjalić, K., 1991, "Laboratory Investigation and Full-Scale Experience on Detonation-Wave Technique for On-Load Cleaning of Gas-Side Boiler Heating Surfaces," *Proc. 2nd European Conference on Industrial Furnaces and Boilers*, Vilamoura, Portugal.

Downloaded 02 Jun 2010 to 171.66.16.122. Redistribution subject to ASME license or copyright; see http://www.asme.org/terms/Terms_Use.cfm

Detonation-Wave Technique for On-Load Deposit Removal From Surfaces Exposed to Fouling: Part II—Full-Scale Application

K. Hanjalić[1]
Lehrstuhl für Strömungsmechanik,
University of Erlangen-Nürnberg,
Erlangen, Federal Republic of Germany

I. Smajević
Mašinski Fakultet,
University of Sarajevo,
Bosnia Hercegovina

The paper reports on the full-scale application and testing of the detonation-wave technique in two boilers, fired with pulverized coal, of total thermal power of 600 MW. Continuous monitoring over a period of several years confirmed earlier laboratory findings, reported in the companion Part I of the paper. The testing proved that the technique is efficient and reliable, with a number of advantages in comparison with various conventional cleaning methods. In spite of the fact that the lining of one of the boilers is made of classic refractory material, careful records and inspection over several years of daily application of the detonation wave technique showed no signs of any undesirable effects. The method was officially adopted as a routine deposit removal technique in the Power Plant "Kakanj" in Bosnia.

Introduction: Need for a New Deposit Removal Technique

A major cause of serious diminishing of efficiency, availability, and reliability of most coal and oil-fired steam boilers is the fouling of gas-side heating surfaces. The problem is particularly pronounced in cases of boilers fired with coal of low calorific value and high content of mineral constituents, especially those that tend to agglormerate on the solid surfaces. Conventional techniques for on-load cleaning of boiler heating surfaces on the gas side, such as sequence steam and air soot blowers, air, or steam lancing, shot cleaning ("iron rain"), acoustic or mechanical vibration, on-load washing, and other methods, have been employed for long in most large coal-fired boiler installations. Although these methods have proved to help generally in reducing the fouling problem and maintaining over a longer period the desired conditions of the heating surfaces, it has been frequently recorded that most of the mentioned methods fail to produce long-term satisfactory results in spite of careful operation and maintenance. In addition to the failure to ensure efficient cleaning, in spite of considerable expenditure of working fluid and energy, a number of undesired effects have been reported, the extent of which depends on the composition of minerals and characteristics of deposited ash. Perhaps the most serious side effect is the erosion and subsequent bursts of boiler tubes due to the abrasive action of hard ash components that are carried away by the steam jets. This problem is particularly pronounced in cases when the coal ash contains hard compounds, such as ferro- and aluminum silicates. The use of shields around tubes to protect them from abrasion generally helps, but in addition to extra costs, the shields often reduce heat transfer and may create new pockets for deposit agglomeration, if positioned inappropriately. Hence, a need has been recognized for a different, alternative or complementary technique, to which the ash deposit will respond more efficiently and, in the same time, will not cause any undesirable side effects. Sonic horns and air cannons are some of the more recent techniques that offer some advantages, but in turn they also have shortcomings.

The detonation wave technique, based on the action of mechanical and thermal shock on the material, deposited on gas contact surfaces, offers a convenient, inexpensive, and efficient means for ensuring on-load prevention of deposit agglomeration on surfaces exposed to heavy fouling by continuous and harmless deposit removal. It has proved to be particularly effective as a prophylactic method and as such it could be recommended as a daily routine technique, which ensures long-term desired conditions of boilers, furnaces, reactors, and surfaces of other equipment and gas ducts. In addition to utility boilers in the general area of energy engineering, the technique is especially suitable for conventional and waste heat boilers, furnaces, heat exchangers and other equipment in iron and steel works, in nonferrous metallurgy, chemical plants, cement factories, pulp and paper mills, communal and other waste processing and combustion, and in many other industries in which heavy fouling of equipment poses serious operational problems and causes the equipment efficiency to deteriorate.

Over the past decade of detailed testing the method has been applied for on-load cleaning of almost all segments of boiler heating surfaces including the radiant and convection superheaters and reheaters, economizers and air heaters. It could be stated that in all cases the method proved to be successful, with some marginal differences depending on the type and

[1]On leave from the University of Sarajevo, Bosnia Hercegovina.

Contributed by the Power Division for publication in the JOURNAL OF ENGINEERING FOR GAS TURBINES AND POWER. Manuscript received by the Power Division January 12, 1992. Associate Technical Editor: R. W. Porter.

Copyright © 1994 by ASME
Downloaded 02 Jun 2010 to 171.66.16.122. Redistribution subject to ASME license or copyright; see http://www.asme.org/terms/Terms_Use.cfm

configuration of the cleaned surfaces. The best results have been achieved on convection surfaces where the deposit is not excessively hard.

Background: Few Historical Recollections

The first ideas for employing detonation waves for cleaning boilers could be traced in the literature back in 1965, though the first experiments were not reported until 1974 (Schelokov et al.). The extensive paper of Podimov et al. (1979) on the so-called "Impulse Technique," published in Russian, revealed that this topic was researched extensively in the USSR in connection with cleaning of waste heat boilers that utilize hot gases from iron and steal-works, nonferrous smelters, and other industries. Although the report deals with various types of "Impulse Chambers," in most cases this notion basically stands for a type of valveless pulse combustors in which a series of pulses were generated by self- or operator-controlled ignition, and subsequently introduced into the furnaces in order to promote a continuous deposit removal. The authors reported several examples in which the "Impulse Technique" was successfully tested, to mention the waste heat boiler in a chromium compound factory, copper smelting industry, and several other metallurgical plants. However, very scarce information on design and operation experience could be traced in the literature cited and other sources.

In 1980 the Institute for Thermal Equipment (VUEZ) in Tlmače, Czechoslovakia, and the Thermal Power Plant "Kakanj" near Sarajevo, Bosnia, decided to test jointly the basic idea by installing a simple detonation wave generator at an old 140 *t/h* coal-fired Steinmüller boiler in the "Kakanj" Power Plant. The first results, although encouraging, brought into focus a number of queries that could not be resolved without a detailed experimental investigation (Smajevič, 1980). This motivated the management of the Power Plant "Kakanj" to commission an extensive research project at the Institute for Process-Power and Environmental Engineering (IPES) of the University of Sarajevo, aimed at providing a deeper insight into the process and establishing correlations between all important design and operation parameters, before the technique could be employed in practice. Contrary to the "Impulse Chambers" described in the report of Podimov et al. (1979), we opted for Detonation Wave Generators in which a fully controlled single wave, or a desired series of waves, of controlled intensity, could be generated and directed onto the surfaces to be cleaned. The results of the extensive research at the IPES-Institute were reported in 1984 (Smajević, 1984). Few months earlier Bobovnicki et al. (1983) reported on some laboratory investigation of the method in a simple model of the boiler furnaces, carried out in parallel in Czechoslovakia.

The research at the University of Sarajevo has been continuously pursued up to the present time, first on a laboratory-scale model of a boiler furnace and later also on a full-scale installations in the Thermal Power Plant "Kakanj," resulting in a new technique with a number of original features.[2] The method has been applied and thoroughly tested in the above-mentioned power plant where the detonation wave equipment was installed at two larger boilers fired by pulverized brown coal, of total thermal power of 600 MW. Some experience has already been reported, e.g., Smajević and Hanjalić (1985, 1987a, 1987b, 1988, 1991).

Principles of Operation

As described in Part I, the method utilizes the shock waves generated by detonation in a "detonation chamber" placed outside the boiler, by using an adequate fuel-oxidant mixture, which is ignited by means of a standard automobile spark plug. The waves are lead by one or more connecting pipes to the desired location(s) at the boiler where they protrude into the boiler wall, entering the boiler interior and direct the waves toward the surfaces to be cleaned. The length of the connecting tubes and the fuel feeding time are adjusted to enable transformation of an initially continuous combustion wave into a steep-front detonation wave, which turns into a shock after reaching the end of the fuel-oxidant mixture zone.

In principle, the wave characterisitics and their intensity and frequency can be adjusted and controlled electronically according to the composition and characteristics of the ash. Automatic guidance and control of the wave generator operation can be easily secured. An adequate monitoring parameter such as flue gas temperature at a convenient location, or the pressure drop through the chosen tube package, can be used for ensuring an automatic control of the wave generator operation. Alternatively, the generator can be operated manually. A boiler unit can be equipped with a number of wave generators, which could all be operated from the central command manually or fully automatically.

However, in order to design a reliable and fully controllable system, it is necessary to know the details of the mechanisms of the wave generation, its formation and propagation through the connecting pipe, as well as its dynamics after entering the boiler interior space and its interaction with the impinged solid surfaces. It is expected that the desired effects should be achievable with a shock wave, the intensity of which should be sufficient to cause the destruction of the deposit, but still weak enough not to cause any damage to the boiler interior structure and in particular to the refractory walls. Fortunately, as will be explained later, the major deposit destructive effects are achieved by a sequence of reflected interior stress waves within the deposited material and less by the shock front itself, so that its strength need not be very high. Instead, it appeared that the best cleaning effects are achieved if a series of shock waves is generated at regular time intervals. Although some recommendations can be given depending on deposit characteristics and surface configuration, the number and frequency of waves for a single cleaning procedure should be determined by a trial-and-error method in each particular situation.

Shock waves can be generated in various ways. The present technique uses the detonation waves as the source of shock waves for several reasons. First, their generation and control are easy, practical, and energy efficient. Second, in comparison with a shock wave generated in a shock tube by releasing compressed gas through bursting a membrane, the strong temperature gradient pertinent to the detonation-generated shock wave produces an additional effect, the thermal shock, which in some cases, such as cleaning the low temperature surfaces of air heaters and economizers, contributes further to the deposit destruction.

Wave Action and Cleaning Mechanism

Although the shock wave impingement on the solid surface and its pressure force and thermal impact are basically the major cause of destruction and subsequent removal of the deposit, it would have been an oversimplification to attribute the complete effect to the mere action of the shock wave alone. More probably it is a joint and simultaneous action of several factors associated with or generated by the shock wave that contribute each in its own way to the final effects. Although it is difficult to give a plausible explanation of the complex mechanism that occurs, a simplified picture of individual actions can be summarized as follows:

- direct removal of the deposit by the detonation chamber exhaust gases at the expense of their kinetic energy;
- combined effects due to the interaction of the detonation

[2]Patent pending.

Downloaded 02 Jun 2010 to 171.66.16.122. Redistribution subject to ASME license or copyright; see http://www.asme.org/terms/Terms_Use.cfm

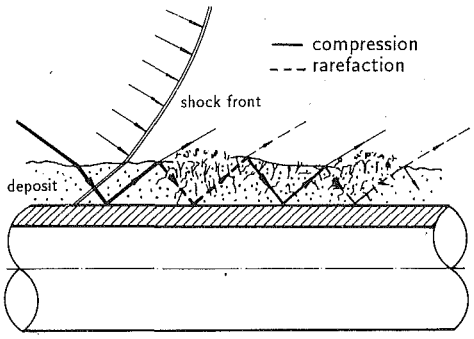


Fig. 1 Schematic representation of the wave action on deposit breakage and removal

chamber exhaust gases and the mean flow of the boiler combustion products (local acceleration, vortex shedding, recirculation, and a consequent turbulence production);

- weakening of the cohesive forces within the deposited material and adhesive forces between the deposit and the solid surface due to the intensive heating from the shock wave (particularly in the low-temperature regions, e.g., boiler air heaters and economizers);
- deposit cracking and loosening due to the stresses generated by thermal shock (steep temperature gradient);
- vibration of the tubes and other solid surfaces, caused by the mechanical shock;
- direct action of the shock wave and consequent series of compressive and tensile interior stress waves within the deposited material.

Most of the mechanism mentioned are self-explanatory. It is worthwhile, however, to dwell for a while on the last mentioned action, which is most probably the dominant one. As expected, the front of the shock wave that enters the furnace space, after leaving the connecting pipe by which it is brought from the ignition chamber, has a spherical form and the angle of its attack on the solid surface depends on the configuration of the attacked surfaces with respect to the wave front. Furthermore, the wave intensity weakens in the course of its propagation into the furnace interior which is much larger than the wave pipe. Hence its effect upon the deposit on a solid surface depends much on the exposition of that surface to the wave front.

However, in all cases the shock wave will "penetrate" the deposited material and generate an internal compressive stress wave inside the deposit, which will propagate with a speed $c = \sqrt{E_d/\rho_d}$, where E_d and ρ_d are the bulk elasticity modulus and density of the deposited material, respectively. Depending on the incoming angle, the internal wave will reflect to a larger or smaller extent from the solid wall again as a compressive wave. This reflected wave propagates through the deposited material toward its free surface and will reflect from this surface as a rarefaction wave, which will propagate back toward the solid surface. The sequence of reflection of waves and their subsequent attenuation—the deposited material in most cases could be treated as viscoelastic—will continue until the waves lose their intensity or the deposit is destroyed and removed. It is this sequence of stress waves, the frequency and amplitudes depending on the thickness, composition, and stiffness of the deposited material, that causes the shearing of the material particles with respect to their equilibrium state, loosening their interior bonds and consequent destruction and subsequent removal of the deposit from the solid surfaces. According to some authors (e.g., Borisov et al. and Kosenko et al. as quoted by Podimov et al., 1979) the rarefaction internal waves, propagating through the deposited material, have the major effect on deposit destruction and loosening, in particular if the deposited material is not very hard. In addition to this, a shear effect on the solid surface, caused by the wave sweeping along the wall, will also contribute to the deposit cracking.

This simplified, but plausible picture of the process, presented schematically in Fig. 1, demonstrates that it is not shock wave front alone, but more the sequence of reflected waves—and here mainly the rarefactive ones—that cause major effects, and explains best why an efficient cleaning has been observed with relatively weak shock waves, which will not cause any damage to the equipment structure. Some other authors came to a similar conclusion, e.g., Podimov et al. (1979), who claim that a shock wave with Mach number of about 1.3 is capable of destroying a relatively loose deposit several millimeters thick.

Of course, other mentioned effects play also important roles, among which the next most influential one comes from tube vibrations excited by the shock waves. After the shock impact, the tubes are displaced from the equilibrium position and start to oscillate with amplitudes that depend on the tube stiffness but also on the strength and angle of attack of the impacting shock front. The removal of the deposit will depend, of course, on damping of the oscillations, which in turn depend not only on the tube length and natural frequency, but also on the character, quantity and distribution of the deposited material.

As mentioned before, the thermal stresses due to the thermal shock play an important role in particular in case of low-temperature surfaces. The thermal shock itself, but also the heating of the deposit due to a series of waves impacting into the tubes, will cause the mechanical binding forces among molecules of the deposit to weaken, while a sequence of waves with a high temperature front will generate large temperature gradients and consequent thermal stresses, contributing in such a way to loosening and braking of the deposited material.

In the vicinity of the solid surface the shock waves will interact with the gas velocity field and enhance vortex shedding and recirculation, contributing in such a way to local turbulence production and local gas acceleration, which in turn would promote local removal of the deposited material.

Finally, some effects can be expected also from the change of momentum of the combusted gas jet coming behind the shock front upon their impact on the solid surfaces. However, this effect will remain limited to a narrow region of the central part of the front tube rows, since the momentum of the gas that impacts on each tube attenuates strongly in both the radial and axial directions due to the jet spreading.

The overall effects of deposit removal as well as side effects on equipment structure depend upon the initial energy of the shock wave at the detonation chamber exit, which can be assumed (e.g., Podimov et al., 1979) to be proportional to the product of the volume of the combustible mixture in the active part of the chamber and square of the flame front propagation velocity at its open end. The flame propagation velocity depends on the mixture reactivity, its composition, temperature, and pressure, as well as on turbulence level. The latter parameter in turn depends on the gas and fuel velocity, chamber shape, and the manner in which the fuel is introduced into the chamber. Better conditions are secured if the combustible mixture is fully turbulent, which is ensured by special turbulizer placed at a position somewhere in between the ignition chamber and the connecting pipe or in the chamber itself downstream of the ignition nest. Finally we should mention also the importance of the proper location of the ignition point (or points), which affects to a large degree the overall performance of the detonation wave generator.

Following the above, to a great degree simplified (and to some extent speculative) vision of the overall process, it is obvious that the total effects are difficult to quantify since the process depends on many factors, but above all on the composition and granulation of the deposit, its density and moisture. Hence, correlations between the influencing parameters and cleaning effects can be established only experimentally for

Downloaded 02 Jun 2010 to 171.66.16.122. Redistribution subject to ASME license or copyright; see http://www.asme.org/terms/Terms_Use.cfm

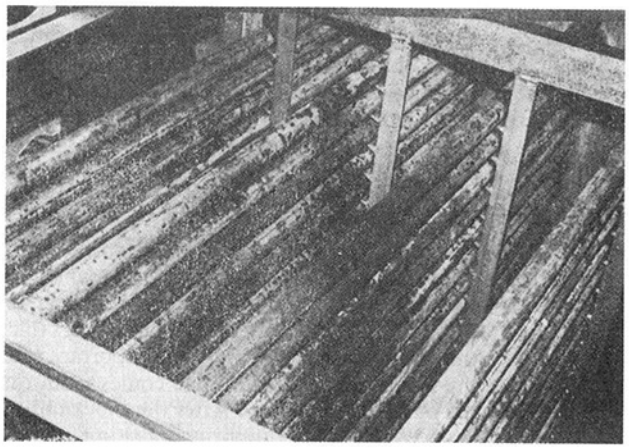


Fig. 2 Removal of hard deposit from old boiler superheater tube packages subjected to a series of detonation

a specific design of the equipment (boiler, furnace, heat exchanger) and fuel and deposited material characteristics.

Laboratory Test of Deposit Removal Action

The ability of the detonation technique to reduce the fouling cannot be easily quantified in the laboratory because it is difficult to simulate a real situation in the model. Hence these effects have been investigated in a full-scale boiler under normal operating conditions, as described later. However, some tests have been carried out by placing packages of old superheater tubes with hard deposit of ash, taken from an old boiler during the major reconstruction. Although the detonation technique is primarily a preventive one, intended to be used regularly to remove the deposit while it is still loose, the test in the model boiler with the old superheater tubes (after almost 20 years of operation and with a hard deposit about 2 mm (thick) showed clearly that the waves and the induced tube oscillations brought a removal of a large part of the hard deposit. The effect is particularly noticeable in the central area of few front rows of tubes where the wave effect was most intensive. This is clearly visible in Fig. 2 where the photograph of the tube package is shown, after being subjected to a series of detonations over the course of several days.

Experienced in Full-Scale Operation

A detailed exploration of the technique in the laboratory clarified almost all queries in regard to the control of the detonation wave generation. Also, correlations were established concerning the propagation of the waves, their transition into shock waves in the tube and attenuation after entering the furnace space of the model boiler. The shock effects upon the obstacles—model of tube packages and boiler walls—were also fully recorded and correlated with the design parameters of the detonation chamber and air-fuel mixing device. In parallel to the laboratory testing, two full-scale detonation wave chambers were installed already in 1982 at one of the major coal-fired boilers, of 300 MW thermal power in the Power Plant "Kakanj." This boiler was originally equipped with 20 soot blowers of which 12 were placed in the convective shaft while the remaining 8 were installed in the zone of the radiative superheaters. The shock wave entry ports were placed on the roof of the second shaft and directed downward toward the economizer tube packages, as indicated in Fig. 3, pipes 1 and 2. However, the application of the method to a full-scale installation at first did not yield desired long-term results due to some practical problems encountered. The major cause of the problem came from the return flow of the flue gases that brought the ash back into the detonation chamber, the deposit

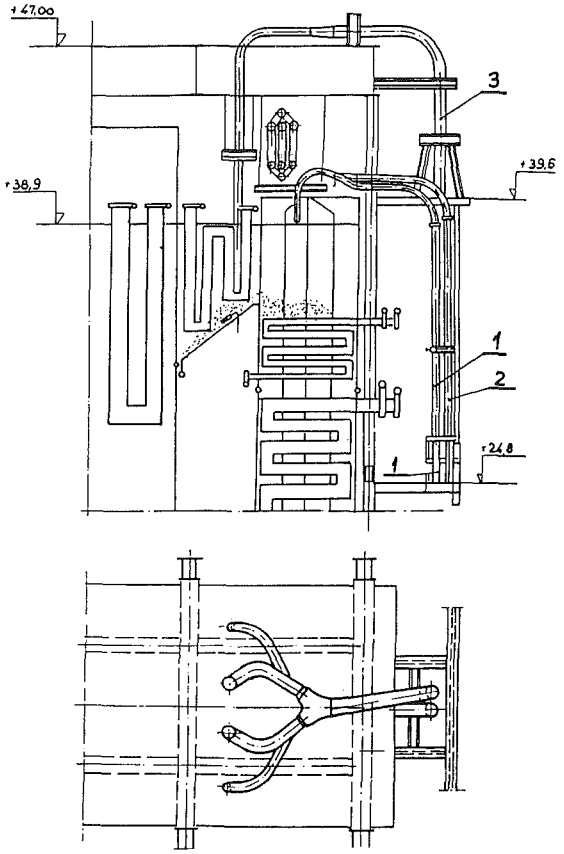


Fig. 3 Detonation wave entries into first boiler of 300 MW_{th}

of which (enhanced by the presence of oil droplets in the air that was mixed with the fuel) blocked the turbulizing plate at the chamber exit as well as clogging the spark plugs. This problem was overcome by a new design of the chamber and the connecting pipes in which a type of bypass was introduced for the air-fuel mixture into which the spark plug was displaced, together with a flow control orifice. In addition, the shock wave entry port into the furnace was redesigned by introducing three more nozzles through which a small quantity of air was continuously blown so that the pipe-furnace connection acted as an aerovalve, practically preventing the back flow. These and some other minor design interventions removed all difficulties and the equipment proved to function successfully over a period of several months. Continuous monitoring of boiler performances indicated a visible improvement. A few months later, in 1983, another detonation wave generator was added to the installation with the shock wave entry port placed at the furnace roof and directed toward the superheater tube packages (Fig. 3, denoted by 3). A view of the connecting pipes and their entries into the boiler is shown in Fig. 4. On the basis of experimental results obtained in the laboratory and after several years of satisfactory full-scale test operation, in 1986 the permission for a regular operation of the technique was granted by the state authorities. In 1987 it was decided to install two new wave generators to the second boiler of the same thermal power, but considerably older than the first one (built in 1969) and with the conventional refractory wall. In this case the entry ports were placed deep in the convective shaft. All five wave generators were connected to the common air-fuel mixture preparing equipment and the same control unit. Since then the method has been applied regularly as a daily routine operation on both boilers, repeated every 8 hours. The operation consists of a series of about 10 to 15 waves, generated automatically and applied in succession with the time interval between two detonations of about one minute.

Downloaded 02 Jun 2010 to 171.66.16.122. Redistribution subject to ASME license or copyright; see http://www.asme.org/terms/Terms_Use.cfm

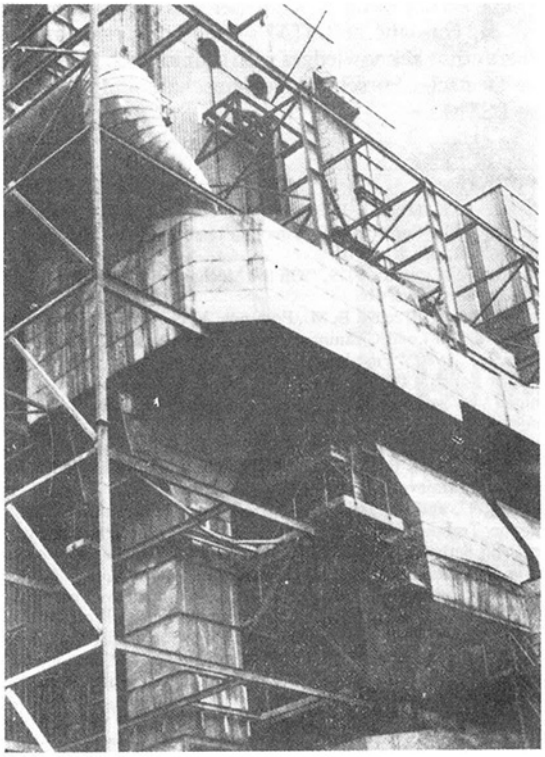


Fig. 4 Outlook of the detonation tube connection to the 300 MW_{th} boiler

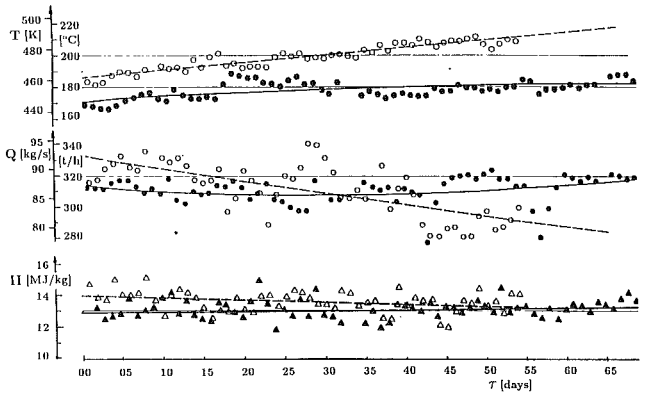


Fig. 5 Variation of flue gas temperature, steam production, and coal heat value over two successive three-month periods: empty symbols—boiler cleaning with 18 soot blowers; full symbols—detonation wave cleaning (only 6 soot blowers retained)

Table 1 Flue gas temperature drop (in °C) at three measuring points

Measurement No.	Detonation wave method 1	2	3	Conventional method 1	2	3
1	35	47	20	20	17	13
2	20	55	13	25	5	3
3	25	37	15	27	13	10
4	0	33	13	35	0	13
5	15	47	13	30	15	7

Over a number of years of continuous operation the method proved to be superior to the conventional cleaning technique and on the whole very satisfactory.

In order to illustrate the cleaning effects we carried out two three-month tests in succession during which we recorded three basic parameters that serve as an indication of the method efficiency: the flue gas temperature, the steam production, and the calorific value of the coal. Figure 5 shows the comparison of these data over the two test periods of 70 days overlaid one upon the other. As could be seen, in spite of regular use of 18 soot blowers every 8 hours (due to the failure, two blowers in the radiative zone were out of use), the flue gas temperature showed a steady increase, while the steam production was diminishing, indicating without any doubt a steady fouling of the heating surfaces (empty symbols). Contrary to that, the employment of the detonation wave technique in the convective shaft, by retaining 6 soot blowers in the furnace and eliminating all 12 in the convective shaft, showed much more steady performances (full symbols). In both cases there is no conclusive change of the fuel quality in spite of a considerable scatter of the recorded data.

In order to compare further the efficiency of the two cleaning methods, the measurements of flue gas temperature were recorded at three locations (denoted by 1, 2, and 3 in Table 1) in the boiler at instants just before and after the cleaning was applied. The measuring position 1 was placed at the entry to the last superheater tube register, whereas positions 2 and 3 correspond to the entry and exit of the economizer. The measured temperature drops given in Table 1 (only five representative sets of data, out of many are shown) illustrate the difference. The left part of the table, which refers to the detonation wave method, shows considerably higher temperature drops and, consequently, more efficient deposit removal in comparison with figures in the right part of the table, obtained after the conventional technique was applied.

In addition to the above-mentioned indicators, it is worth mentioning that the application of the shock waves resulted in some imediately visible manifestations, giving clear evidence on surface cleaning effects. These were particularly noticeable in cases when the technique was applied in less frequent time intervals during which a larger amount of deposit was allowed to accumulate on the tube surfaces. For instance, with 12 hour time intervals, it was noticed that immediately after the cleaning the steam production increases by about 5 *t/h* with the same coal consumption, contributing to an increase in boiler thermal power by about 4 MW and a consequent increase in boiler efficiency by about 1.14 percent. Another undesired manifestation was a sudden surge of dust flow toward the stack, which could not be fully handled by the precipitators, causing excess opacity in some cases. In order to meet the opacity requirements and to ensure more continuous performance characteristics, the regular cleaning intervals were subsequently reduced to 8 hours, which eliminated a possibility of ash deposition in larger quantities.

As another important indicator of the overall improvement of performances, a survey was carried out on the number of tube bursts over two longer consecutive test periods. The statistics substantiated our earlier hypothesis that the conventional cleaning methods (soot steam blowers) were the main cause of tube bursts due to the abrasive action. The application of the detonation wave technique reduced the tube bursts over a period of three months by more than 30 percent.

Finally, the most worrying effect—the impact of the shock waves on the refractory wall—was studied by careful visual inspection and recording of the refractory wall texture at regular intervals over a period of 15 months. No signs of any cracks or other damage were noticed.

Conclusions

The on-load boiler cleaning technique described here utilizes the action of detonation waves, which are generated in a chamber outside the boiler. The waves, brought into the boiler furnace and flue gas passages, impose an intensive mechanical and thermal shock on the boiler heating tubes, braking and removing the deposited ash. Besides, the shock causes tube vibrations, which contributes further to deposit removal.

Downloaded 02 Jun 2010 to 171.66.16.122. Redistribution subject to ASME license or copyright; see http://www.asme.org/terms/Terms_Use.cfm

The strength of the waves can be adjusted as desired according to the characteristics and composition of the ash, and could be made sufficiently strong to brake and remove a very hard deposit. However, depending on the design and construction of the boiler, the exceedingly strong waves may cause damages to the boiler interior structure and its wall. Hence a series of relatively weak waves may be preferred in most cases. The technique should then be used regularly at adequate intervals as to secure continuous removal of the deposited material before it becomes hard.

In fact the technique has proved to be particularly effective in removing the deposited material while it is still fairly loose, and is therefore primarily of the preventive nature. It could be employed to clean all types of boiler heating surfaces, though the best results have been achieved for cleaning the convective tube packages.

The laboratory experiments and seven years of experience with daily application of the technique on two-full-scale installations showed that the method is safe and reliable, simple to use and maintain, easy to control, and, above all, very economical. It offers a number of advantages in comparison with most conventional methods. Depending upon the type of boiler and characteristics of the fuel, the technique can be used either as self-sufficient, or as complementary to other cleaning methods.

The technique can, in particular, be recommended for the on-load cleaning of boilers fired with low-grade pulverized coal, which are usually prone to heavy fouling.

Acknowledgments

Parts of this research have been supported by the Research Fund of Bosnia Hercegovina and by the Power Plant "Kakanj." The final writing of the paper was completed during the stay of K. Hanjalić at LSTM of the University of Erlangen and this author acknowledges with thanks both the sponsorship of the Deutsche Forschungsgemeinschaft and the hospitality of the LSTM.

References

Bobovnicky, J., Murani, J., and Kovačik, Š., 1983, "An Arrangement for Cleaning of Boiler Surfaces by Means of Pressure Waves" [in Czech], *Strojirenstvi*, Vol. 12, pp. 710–716.

Podimov, V. N., et al., 1979, "On the Mechanism of Impulse Cleaning" [in Russian], Kazan University.

Schelokov, J. M., Teeing, E. M., Podimov, V. N., and Gasnikov, V. I., 1974, "Methods for On-Load Cleaning of Boilers" [in Russian], Kazan University.

Smajević, I., 1980, "First Results of the Experiments on Soot Removal in the Steinmüller Boiler at the Thermal Power Plant, 'Kakanj' by Means of Impulse Technique" [in Serbocroatian], Informat. bilten, TE "Kakanj," No. 6–11.

Smajević, I., 1984, "Contribution Towards the Development of Detonation Wave Method for the Prevention of Deposit Forming on Boiler Heating Surfaces," M.Sc. Thesis [in Serbocroatian], Faculty of Mechanical Engineering, University of Sarajevo.

Smajević, I., and Hanjalić, K., 1985, "Some Experience in Applying the Detonation Technique for Cleaning the Boiler Surfaces in the Power Plant Kakanj" [in Serbocroatian], *Proceedings, 7th Conference on Thermal Power Plants in Yugoslavia*, Ohrid.

Smajević, I., and Hanjalić, K., 1987a, "Detonation Wave Technique for On-Load Cleaning of Gas-Side Surfaces of Steam Boilers," *Proc. Joint German-Yugoslav Colloquium on Low-Grade Coal Combustion*, Special Pull., Academy of Science and Arts of Bosnia Hercegovina, Vol. LXXXI, Sarajevo.

Smajević, I., and Hanjalić, K., 1987b, "Application of Detonation Waves for Cleaning Boiler Heating Surfaces on the Side of Flue Gases" [in Serbocroatian], *Strojarstvo*, Vol. 29, (1), pp. 21–33.

Smajević, I., and Hanjalić, K., 1988, "Some Further Experience in the Application of Detonation-Wave Method for Cleaning Boilers" [in Serbocroatian], Proceedings, 8th Conference on Thermal Power Plants in Yugoslavia, Opatija.

Samjević, I., and Hanjalić, K., 1991, "Some New Results in the Investigation and Application of Detonation Waves for Cleaning Boiler Heating Surfaces" [in Serbocroatian], *Strojarstvo*, Vol. 33, (1), pp. 23–29.

Downloaded 02 Jun 2010 to 171.66.16.122. Redistribution subject to ASME license or copyright; see http://www.asme.org/terms/Terms_Use.cfm

Powder Metallurgy Repair of Turbine Components

K. A. Ellison

P. Lowden

J. Liburdi

Liburdi Engineering Ltd.
Hamilton, Ontario, Canada

An advanced powder metallurgy repair process called Liburdi Powder Metallurgy (LPM)[1] has been developed for the repair, overlay or joining of nickel and cobalt-based high-temperature alloys. This process involves mechanical cleaning, followed by the application and consolidation of a filler metal powder, which has substantially the same composition as the base metal, and produces joints with mechanical properties similar to those of the parent material. While previously activated braze or "wide-gap" repair processes have been limited to clearances of approximately 1 mm, the LPM technique has the ability to bridge larger gaps of over 5 mm. In addition, the LPM joints contain significantly lower concentrations of melting point depressants such as silicon and boron than conventional wide-gap repair techniques and exhibit superior microstructural features. The characteristics and typical applications of the LPM process for blade and vane repairs are highlighted and the results of laboratory and engine tests are discussed.

Introduction

The complexity of advanced materials combined with the escalating cost of replacement parts has resulted in a continuing need to improve the joining and repair processes used to refurbish the high-temperature materials found in gas turbine engines. The conventional fusion welding techniques are not only difficult to perform on highly alloyed nickel-based materials, but must also contend with the complex metallurgical reactions that occur when they are heated to their melting point during the welding process. This often results in the formation of microcracks in the heat-affected zone during welding or after the post-weld heat treatment, which influences the quality of the joints and limits the application of weld repairs (Owczarski, 1977; Duvall and Owczarski, 1967; Thamburaj et al., 1983).

Although automation of the welding process can significantly improve the quality (Liburdi et al., 1989; Lowden et al., 1991), the overall joint efficiency is still limited by the properties of the filler materials used. Even when higher strength or matching materials are used in either the powder or wire form, the weld build-up is limited by their low ductibility and tendency to crack under the resultant strains (Liburdi and Lowden, 1985).

In the earlier development programs, some of the difficulties associated with fusion welding and joining of the high-strength nickel alloys were overcome by the introduction of high-strength diffusion brazing processes. Previously, traditional brazing alloys or processes did not possess adequate elevated temperature properties to be used for the joining of high-temperature, highly stressed components and had to be modified by the development of filler alloys and procedures used for transient liquid phase (TLP)[2] bonding (Duvall et al., 1974; Hoppin and Berry, 1970). Boron was used as the principal melting point depressant in the new alloys since it could be diffused into the parent metal at the brazing temperature, thereby causing isothermal solidification of the braze liquid and the elimination of brittle intermetallic phases that would otherwise form during cooling from the brazing temperature. Additional homogenizing heat treatments were applied to effect interdiffusion of the parent alloying elements, which resulted in mechanical properties for the TLP bonds equivalent to those of the alloys being joined. In practice, careful surface preparation, precise control of joint clearances, and the application of moderate pressures were required to produce sound joints.

Soon after their introduction, the methods developed for TLP bonding in new part manufacturing operations were adapted to help meet the ever-increasing demands of engine users for repair procedures to extend the service lives of costly hot section components. An early example was the replacement of worn blade tips by TLP bonding cast to size tip inserts onto premachined blades (Duvall and Doyle, 1973). The next logical application for the activated brazes was the repair of thermal and/or mechanical cracks in cobalt and nickel-alloy nozzle guide vanes (NGVs). The most significant limitations to the use of diffusion braze techniques for this type of repair were the need for adequate crack surface cleaning and the limits to the size and defects that could be repaired while still producing adequate mechanical properties in the repair joint.

Without proper cleaning, the braze filler alloys will not wet and flow into cracks and proper metallurgical bonding will not take place. This usually results in incomplete filling of the

[1] LPM is a trademark and proprietary process of Liburdi Engineering Limited.

Contributed by the International Gas Turbine Institute and presented at the 37th International Gas Turbine and Aeroengine Congress and Exposition, Cologne, Germany, June 1-4, 1992. Manuscript received by the International Gas Turbine Institute February 24, 1992. Paper No. 92-GT-312. Associate Technical Editor: L. S. Langston.

[2] TLP is a Trademark of Pratt & Whitney.

Copyright © 1994 by ASME
Downloaded 02 Jun 2010 to 171.66.16.122. Redistribution subject to ASME license or copyright; see http://www.asme.org/terms/Terms_Use.cfm

crack or, if undetected, recracking of the repair after only a few thermal cycles when the component is returned to service (Schneider et al., 1985). In principle, the oxides that form in service can be more easily removed from cobalt-based superalloys than from nickel-based alloys because the nickel alloys are strengthened by precipitation hardening elements such as aluminum and titanium, which forms stable oxides that cannot be reduced using conventional heat treatments in vacuum or hydrogen atmospheres. As a consequence, specialized fluoride ion cleaning operations have been developed that attempt to overcome the problem of removing these oxides from the surfaces of nickel-based parts (Keller and Resor, 1978; Chasteen, 1983).

In practice, the effectiveness of the various fluoride ion cleaning processes appears to be inconsistent and the results can vary from excellent to poor performance. Concerns have also been raised with regard to depletion of the precipitation hardening elements from unoxidized surfaces and intergranular attack of the blade roots that can result from these operations (Brauny et al., 1985; Antony and Goward, 1988).

Another limitation in diffusion brazing repair operations is the size of the joint that can practically be used and still achieve adequate diffusion of boron out of the repair area for a reasonable time as well as bridge the gap with the liquid braze alloy. Complete isothermal solidification and joint homogenization of TLP bonds at the brazing temperatures commonly used for cast superalloys (1100–1200°C) require times on the order of 10 h for joint clearances of only 25 μm (0.001 in.) (Kang, 1989). Joints that are not given the best diffusion and homogenization heat treatments usually exhibit segregation of brittle eutectic phases along the joint centerline. In an attempt to overcome these limitations, a variety of "wide gap" brazing mixtures have been introduced by both original engine manufacturers and independent repair facilities throughout the industry (McComas and Stuart, 1987; Ferrigno et al., 1989). All are basically mixtures of a relatively low melting diffusion brazing alloy and a filler powder, which corresponds to the base alloy of the article being repaired, with minor variations in alloy compositions, heat treatments, and ratio of braze to filler powders used. Brazing is performed at a temperature above the solidus of the brazing alloy, but below the solidus of the filler powder. The filler alloy powder acts to retard the flow of the mixture, thereby allowing larger defects to be bridged than would be possible using the braze alloy alone. Furthermore, the filler powder acts as an additional sink for dissolution of the boron from the brazing liquid.

In practice, the high ratios of braze to filler alloys necessary to wet the filler powder and produce adequate flow of the mixture do not result in complete isothermal solidification of the filler alloy mixture, and the remelt temperatures of the resulting joints are roughly equivalent to the solidus temperatures of the braze alloys used (Antony and Goward, 1988). Furthermore, maximum joint clearances are still limited to 1–2 mm due to the flow or solidification properties of the wide gap mixtures and there are significant problems with residual porosity within the filler material that may constitute unacceptable defects in the article being repaired (Antony and Goward, 1988; Mattheij, 1985). In addition, the high levels of boron in the repair joints and the local segregation may also lead to reduced surface stability of coated airfoils and problems during the subsequent coating operations (Antony and Goward, 1988).

The novel LPM process developed by Liburdi Engineering Limited provides an improved "matching filler metal" repair procedure for high-temperature turbine components that overcomes the cracking problems traditionally associated with welding of nickel-based alloys, and produces joint properties equivalent to those achieved by proper diffusion or TLP bonding. In addition, the repair limits normally associated with wide gap brazing techniques have been significantly increased,

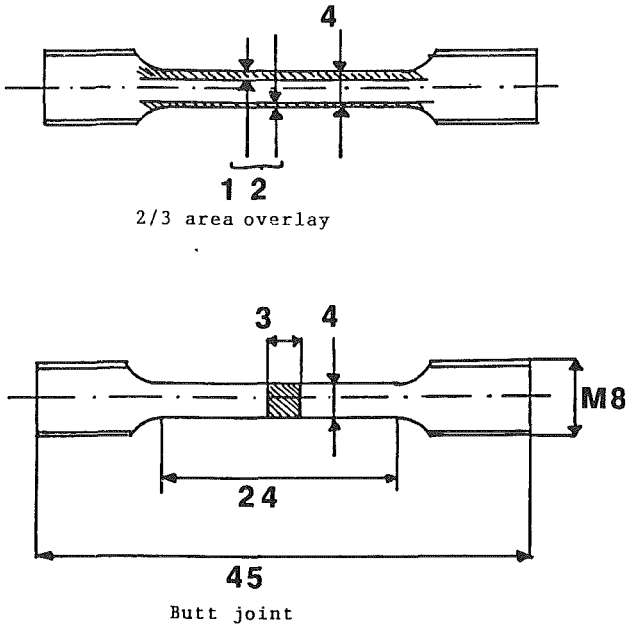


Fig. 1 Geometry of tensile and stress rupture samples used to evaluate mechanical properties of LPM joints

allowing more components to be repaired. Although the details of the process are proprietary, key material properties and several applications will be presented to illustrate the potential for the process to overlay surfaces, HIP encapsulate, join details, and repair wide structural cracks.

General Features and Properties of the LPM Process

Joint Preparation. As in previous repair operations, the surfaces to be repaired or joined must be metallurgically cleaned to assure good bonding. Due to the difficulties outlined earlier, the LPM process does not rely on fluoride cleaning. Instead, the cracks are ground out and eroded or worn areas are dressed to remove all surface oxides or corrosion products including adjacent parent material, which has been locally depleted of alloying elements due to the corrosion reactions. Furthermore, complete defect removal can be verified by the use of standard liquid penetrant inspection procedures.

Choice of Filler Materials. For components damaged in service, repairs are usually completed using matching filler materials in the form of gas atomized powders. However, there are situations in which it may be desirable to replace damaged or worm material with a filler alloy of another composition. This need may arise due to design modification, the need for modified material properties such as wear or oxidation resistance, the joining of dissimilar materials or lack of availability of matching filler materials. When performing such material substitutions, care must be exercised to ensure chemical, physical, and mechanical compatibility with the base alloys.

Application Techniques. Various application techniques have been evaluated for the LPM process. In most cases the process is carried out using slurries of the filler metal powders, which can be applied by syringe, by spraying, or by transfer tapes, depending on the repair geometry.

Thermal Cycles. The LPM process is performed in conventional vacuum heat-treating furnaces. The thermal cycles are designed not only to achieve consolidation of the LPM repairs, but are compatible with standard heat treatments for the parent material. Typically, the LPM processing is completed at temperatures between 1100–1200°C and for times of 2–10 hours.

Downloaded 02 Jun 2010 to 171.66.16.122. Redistribution subject to ASME license or copyright; see http://www.asme.org/terms/Terms_Use.cfm

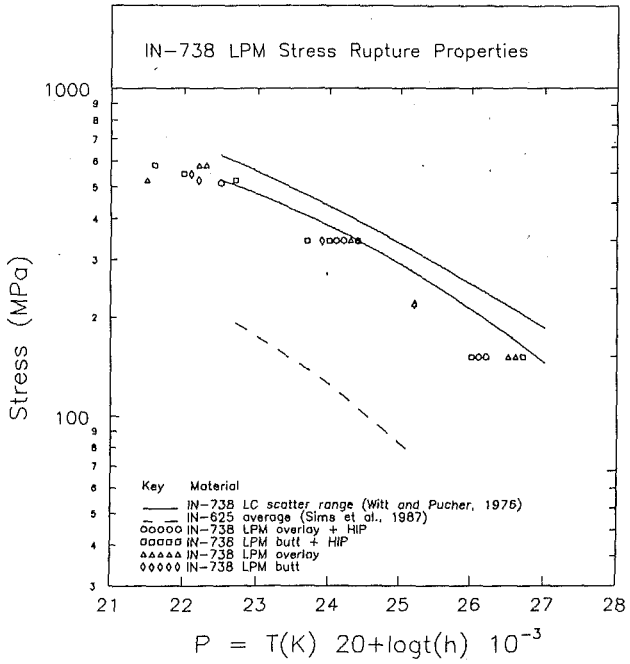


Fig. 2 Larsen and Miller (1952) representation of stress rupture properties of LPM joints using IN-738 filler alloy. For comparison, data are shown for cast IN-738 LC and IN-625, a typical weld filler metal.

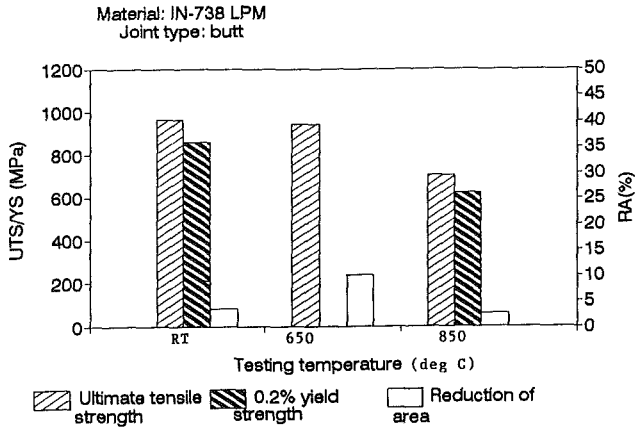


Fig. 3 Tensile properties of LPM joints in IN-738 test bars

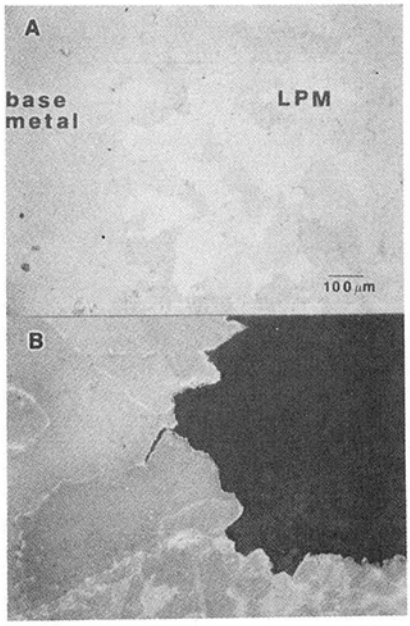


Fig. 4 Photomicrographs showing (A) a typical LPM microstructure using IN-738 filler material and (B) a fracture cross-section from an IN-738 LPM tensile bar tested at 650°C

Table 1 Quantitative chemical analysis of IN-738 filler material

ELEMENT	COMPOSITION	IN–738 LC SPEC.
Cr	13.97	15.7 – 16.3
V	0.13	–
Ti	4.04	3.2 – 3.7
Mo	1.25	1.5 – 2.0
Nb	0.79	0.6 – 1.1
Ta	2.08	1.5 – 2.0
Ni	Bal.	Bal.
Co	8.34	8.0 – 9.0
Fe	0.19	< 0.5
Mn	0.03	–
W	1.62	2.4 – 2.8
Si	0.40	–
Al	3.45	3.2 – 3.7
B	0.31 (wet chemical analysis)	

Mechanical Properties. The tensile and stress rupture properties of LPM joints in IN-738 test bars were determined using butt and overlay sample geometries, as shown in Fig. 1, which imposed both tensile and shear loading on the interface. The stress rupture data presented in Fig. 2 rank the efficiencies of the LPM joints at over 80 percent of the published values for the IN-738LC base metal (expressed in terms of stress). Note that the LPM data exhibit normal Larsen–Miller behavior for tests at different temperatures and for reasonable porosity levels. There is no significant improvement in the properties of joints given a hot isostatic pressing (HIP) cycle. In essence, the LPM properties are typical of fine-grained powder metallurgy superalloys, which are slightly weaker in high-temperature creep than the same coarser grained cast alloys. However, when compared to conventional IN-625 repairs, the IN-738 joints have far superior mechanical properties as well as a matching coefficient of expansion for thermal cycling.

The IN-738 LPM tensile data presented in Fig. 3 also exhibits normal powder metallurgy properties. The test samples generally failed in normal transgrandular or intergranular modes in the filler or base metal and not at the interface of the joints as illustrated in Fig. 4.

Structure and Composition. The LPM microstructure shown in Fig. 4 reveals the excellent fusion obtained between the filler deposit and the base metal as well as the absence of segregation of brittle intermetallic compounds that are often found in conventional braze repair joints. Equally important is the absence of microcracking in the adjacent base metal due to the low stresses and limited melting and fusion of the base metal, which are central features of this process. In some cases, a hot isostatic pressing (HIP) cycle has been used to increase the final density of the LPM joints; however, the use of HIP does not significantly affect the stress rupture properties of the joints, as shown by the test data in Fig. 2, provided that porosity levels are within acceptable levels.

The chemical analysis of an LPM sample is given in Table 1 and confirms that the joint composition is similar to the nominal composition of the IN-738 base alloy. The total concentrations of boron and silicon are significantly lower than the nominal concentrations found in the wide gap brazing filler materials described earlier and can be lowered even further.

Downloaded 02 Jun 2010 to 171.66.16.122. Redistribution subject to ASME license or copyright; see http://www.asme.org/terms/Terms_Use.cfm

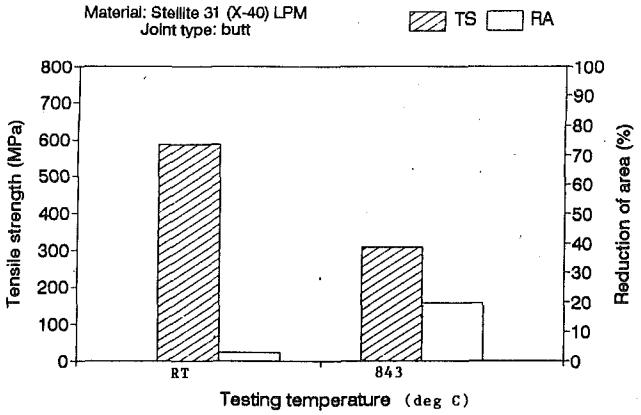


Fig. 5 Tensile properties of LPM joints using cobalt-based Stellite 31 (X-40) powder

This should result in improved oxidation resistance and higher remelt temperatures for the LPM filler material.

The LPM process has also been tested using cobalt-based alloys as filler materials. The tensile results are shown in Fig. 5 and the microstructure for X-40 LPM repairs is shown in Fig. 8(*b*). In this case, matching X-40 powder was used instead of the stronger nickel-based alloys normally used to braze repair cobalt-based components in order to achieve a complementary coefficient of thermal expansion. The resultant strength is typical of cobalt-based alloys.

The test properties confirm that the LPM process could be used in a number of repair or joining schemes for stationary and rotating components. For example, matching high-strength powders could be used to extend the repair limits in crack-sensitive turbine blade alloys as well as to repair cracks and restore airfoil contours in nozzle guide vanes. Typical applications include high-pressure blade tip restoration, repair of worn shrouds, airfoil crack repair, insert attachment, build up of eroded or oxidized airfoils to restore throat area, and HIP encapsulation of casting or welding defects.

Applications

The following cases outline how the LPM process can be applied to nickel and cobalt-based components to perform unique repairs that are beyond the scope of current welding and brazing processes.

Repair of Aero Nickel-Based Nozzle Guide Vanes. The ability of the LPM process to repair cracks beyond the limits for activited diffusion brazes was first demonstrated on René 80, second-stage nozzle guide vanes (NGV), which exhibited cracking extending around the leading edge shroud fillet as well as through the shroud section (Fig. 6).

In each case, the cooling inserts were removed and the cracks were routed by mechanical means to ensure their complete removal. The resultant cavities, which ranged up to 1 cm in width and 3 cm in length, were filled using matching René 80 powder and given a full heat treatment. The parts were then aluminide coated and submitted for future low-cycle fatigue testing by the engine manufacturer. The metallographic examination revealed excellent fusion between the cast vane and the filler powder with an acceptable level of microporosity (Fig. 6) in both areas.

It was also proposed that the LPM wide gap process for structural cracks could be combined with the standard diffusion brazes and fluoride ion cleaning to repair the less critical craze cracks. This would minimize the mechanical removal of defects and make the repairs more economical.

Shroud and Airfoil Crack Repairs for Nickel Alloy Turbine Second-Stage Aero/Industrial Vane Segments. NGVs shown

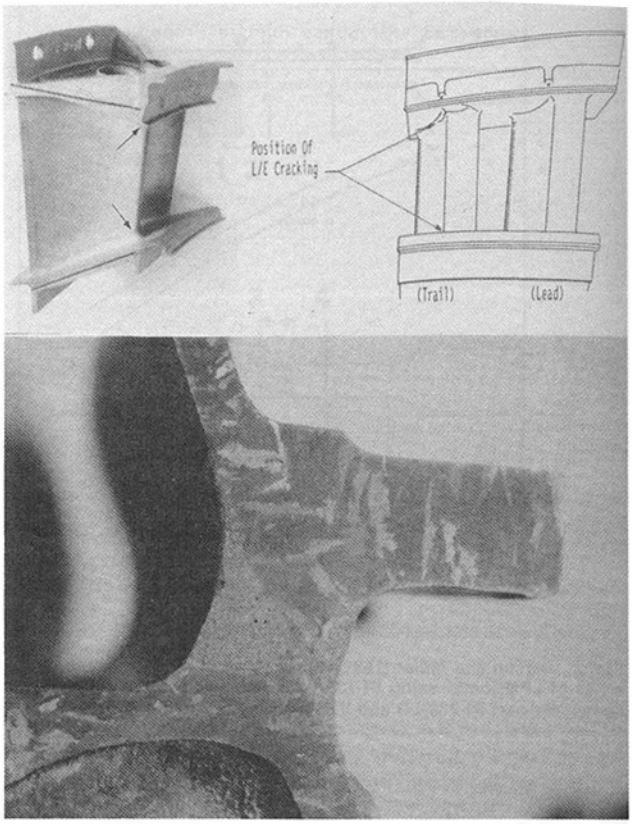


Fig. 6 Matching filler metal repair of a nickel-based (René 80) nozzle guide vane. Thermal fatigue cracks in airfoil fillet radii extended through the shroud wall or wrapped around the airfoil as shown on the sketch.

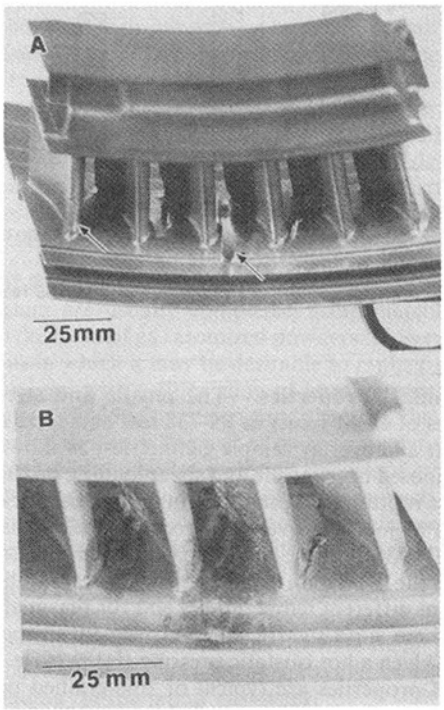


Fig. 7 Repair of thermal fatigue cracks in IN-738 nozzle guide vane: (A) repair areas after grinding to remove cracks and depleted base metal; (B) LPM repair areas prior to final blending

in Fig. 7 are cast from the nickel-based IN-738 alloy and coated using an electrophoretic aluminide process.

In service, the second-stage NGVs experience thermal fatigue cracking through the shroud sections, in the fillet radii, and

Downloaded 02 Jun 2010 to 171.66.16.122. Redistribution subject to ASME license or copyright; see http://www.asme.org/terms/Terms_Use.cfm

and at airfoil leading and trailing edges. The outer shroud cracks in almost all cases extend completely through the shroud wall and render the parts unserviceable. Reportedly, various attempts had been made to repair these parts by welding and brazing processes, but they had not been successful. Prior to the LPM repair, the vanes had been stripped to remove the aluminide coating, and then ground locally to ensure complete removal of the cracks and oxides. The extent of crack removal and blending is shown in Fig. 7(*a*). The airfoil leading edges, which contained several adjoining cracks, were cut back to remove both the cracks and oxidized base metal prior to the LPM repair. It should be noted that the resultant joint clearances were well beyond current wide-gap brazing process capabilities and represent a significant departure from the previous practice of only cleaning the oxide in the cracks or surface and then diffusion brazing.

A typical shroud repair immediately following the LPM process is shown in Fig. 7(*b*). The cracks had been effectively repaired with matching IN-738 powder and the small amount of overfill present was removed during the final blending stage to re-establish the proper dimensions and contours.

The repaired components were then submitted for repair evaluation and rebuilt into a service engine. The NGVs were first subjected to accelerated throttle excursions in the engine test cell and visually examined for defects during a partial disassembly. Since no defects were observed, the vanes were released for field evaluation in a hydrofoil engine, which would subject the repairs to strenuous load cycling. The parts were re-examined after 2409 hours of service and found to be in excellent condition. The only signs of material distress were small cracks in the airfoil trailing edges in nonrepaired areas that were within serviceable limits. It is interesting to note that the major repairs in the leading edge and shroud areas did not show any evidence of cracking in cyclic service. The components were therefore deemed fit to return to service until the next scheduled overhaul.

Repair of Cobalt-Based Industrial Turbine Vane Segments. The Stellite 31 (X-40) third and fourth-stage stators from an industrial engine had suffered extensive damage during a failure. Large sections of the airfoil trailing edges were missing as a result of impact and there were cracks up to 10 cm in length in the fillet radii between the airfoils and shroud sections. One third-stage vane contained cracks that extended completely through the outer shroud wall. A combined TIG welding and LPM approach was used to return these vanes to a serviceable condition. The trailing edges were repaired by welding inserts using matching filler materials. However, due to the high restraint and variations in section thickness, it was not possible to weld the shroud cracks. The fillet cracks were therefore removed by grinding and repaired using the LPM process with an X-40 based filler powder.

In order to ensure the removal of all the cracks including the tip, the blended areas were periodically checked using fluorescent penetrant inspection. The resultant cavities were typically 1 cm deep by 1 cm wide by 10 cm 25–180 g, or 3–20 cm^3 of added material to repair the cavities. Due to the large section sizes, a HIP cycle was used to ensure complete consolidation of the filler material as well as the original casting porosity.

The repaired vane segments shown in Fig. 8 were fully heat treated and inspected thoroughly to ensure their serviceability. All repaired areas were checked by x-ray to verify internal soundness and by fluorescent penetrant for surface indications. The fit-up of the shrouds was verified using appropriate fixtures and the airfoil throat areas were reset to provide proper aerodynamic flow.

With regard to mechanical properties, the LPM process for X-40 was qualified at the start of the program and the results shown in Fig. 5. Matching X-40 alloy was chosen instead of stronger nickel-based alloys in order to provide uniform expansion under thermal cycling. The microstructure produced by the LPM process (Fig. 8(*b*)) shows excellent fusion at the joint interface and fine-grained filler alloy with no porosity following the HIP treatment. Due to the unique ability of the LPM process to affect a matching material repair in the high restraint fillet areas, it was possible to repair all the vane segments and provide needed spares that were not readily available.

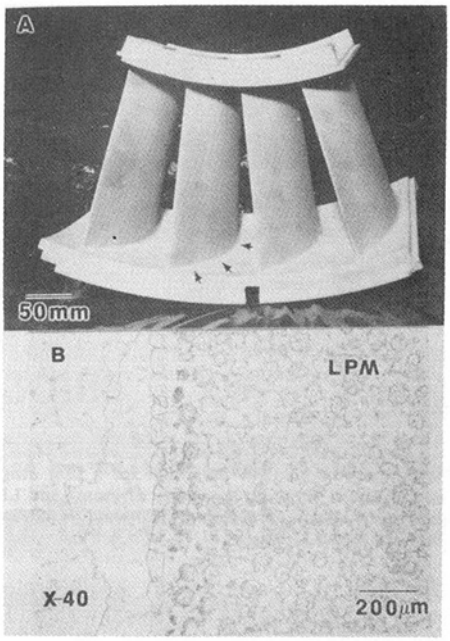


Fig. 8 (A) Stellite 31 (X-40) industrial turbine vane segment. Airfoil trailing edges were replaced by TIG welding matching filler inserts. Cracks in airfoil fillet radii (locations shown by arrows) were repaired using the X-40 LPM process. (B) The microstructure of the X-40 LPM joint.

Repair of First-Stage Nickel Alloy Turbine Blades. LPM repairs have also been applied to large IN-738 industrial turbine buckets that experienced rubbing and cracks at the tip and material loss due to foreign object impact damage. Conventional weld repairs using IN-625 filler alloy are very difficult on IN-738 due to problems with HAZ microcracking, especially during the post-weld heat treatment (Jahnke, 1982). Therefore, repairs are limited to the squealer tip area and the welds will often exhibit varying degrees of cracking. By using the LPM process with matching IN-738 powder, it was possible to extend the repair limit significantly because of the improved stress rupture properties of the IN-738 LPM filler material. This allowed more blades to be repaired than oridinarily would have been possible using welding and avoided the potential problems with HAZ cracks. In order to minimize the machining of the tip cavities, a combination of preformed IN-625 inserts and IN-738 LPM filler materials was chosen to make repairs on the damaged blades. Following the prerepair inspections and stripping of the existing aluminide coating, the blades were ground to remove the damaged material. IN-625 inserts were fabricated to replace the missing squealer walls and joined to the cast blade tips using the IN-738 LPM process, which was also used to repair damage beyond the IN-525 repair limits. An example of a repaired blade after the LPM processing is shown in Fig. 9(*a*). The LPM area can be seen clearly before final airfoil contour restoration. In addition, a blended and etched section is shown in Fig. 9(*b*) in order to highlight the areas repaired by the different materials.

This case also serves to illustrate the versatility of the LPM process. In the same application the IN-738 LPM powders were used to join a wrought detail to a cast part, fill in the wide gaps of missing airfoil material below the insert and

Downloaded 02 Jun 2010 to 171.66.16.122. Redistribution subject to ASME license or copyright; see http://www.asme.org/terms/Terms_Use.cfm

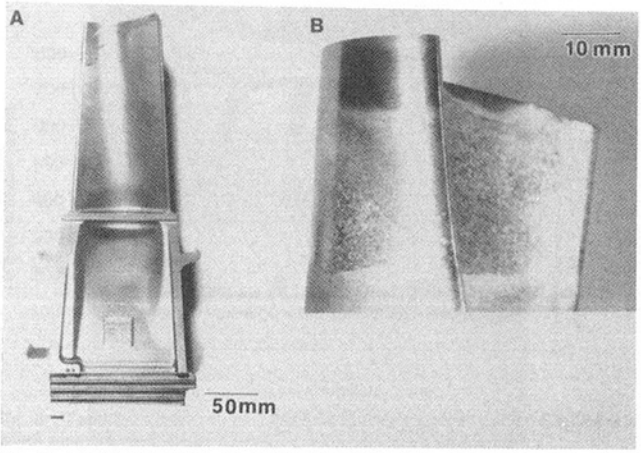


Fig. 9 Photographs of an LPM tip repair for a first stage industrial turbine blade: (A) view showing locations of insert and LPM joint; (B) close-up view of tip after macro-etching to reveal IN-625 insert and IN-738 LPM filler material

overlay thin areas of the squealer tip. As illustrated in Fig. 4, the deposit is well fused to the base metal with no HAZ cracks and exhibits good mechanical properties (Fig. 2). The result is an improved, engineered repair that should provide greater reliability and repairability for various turbine blades or buckets.

Conclusions

As illustrated by the preceding applications, the LPM process provides a novel approach to the joining or repair of superalloys that combines the mechanical removal of the defect as in welding with the convenience of a wide gap powder metallurgy process. The resultant microstructure is well-fused to the base material and exhibits mechanical properties typical of finer grained powder metallurgy deposits.

The LPM process can be engineered for both cobalt and nickel-based alloys and used to join details, fill wide gaps, and overlay surfaces. When used in conjunction with HIP, LPM can effectively encapsulate and heal defects and produce a dense structure. LPM can also be applied to advanced materials such as customized tips for single crystal blades and can be combined with diffusion brazes to produce both narrow and wide gap repairs.

Acknowledgments

Liburdi Engineering Limited is grateful for the support of the National Research Council of Canada in the development of high-strength repairs for superalloys. The authors wish to express their thanks to Joe Daleo, Jim Wilson, Vince Lamanna, and Randy Schaubel for their technical assistance and Yvonne Gautreau for help with preparation of the manuscript.

References

Antony, K. C., and Goward, G. W., 1988, "Aircraft Gas Turbine Blade and Vane Repair," *Superalloys 1988*, D. N. Duhl, G. Maurer, S. Antolovich, and C. Lund, eds., The Metallurgical Soceity, pp. 745–754.

Brauny, P., Hammerschmidt, M., and Malik, M., 1985, "Repair of Air-Cooled Turbine Vanes of High Performance Aircraft Engines—Problems and Experience," *Materials Science and Technology*, Vol. 1, pp. 719–727.

Chasteen, J. W., 1983, "Method for Cleaning Metal Parts," U.S. Patent 4,405,379, Sept. 20.

Duvall, D. S., and Owczarski, W. A., 1967, "Further Heat-Affected Zone Studies in Heat Resistant Nickel Alloys," *Welding Research Supplement*, Sept., pp. 423s–432s.

Duvall, D. S., Owczarski, W. A., and Paulonis, D. F., "TLP Bonding: A New Method for Joining Heat Resistant Alloys," *Welding Journal*, Apr., Vol. 53(4), pp. 203–214.

Duvall, D. S., and Doyle, J. R., 1973, "Repair of Turbine Blades and Vanes," ASME Paper No. 73-GT-44.

Ferrigno, S. J., Somerville, M., and Young, R., 1989, "Alloy Powder Mixture for Treating Alloys," U.S. Patent 4,830,934, May 16.

Hoppin, G. S., and Berry, T. F., 1970, "Activated Diffusion Bonding," *Welding Research Supplement*, Nov., pp. 505s–509s.

Jahnke, B., 1982, "High-Temperature Electron Beam Welding of the Nickel-Based Superalloy IN-738LC," *Welding Research Supplement*, Nov., pp. 343s–347s.

Kang, C. H., 1989, Ph.D. Thesis, Dept. of Welding and Production Engineering, Osaka University, Osaka, Japan.

Keller, D. L., and Resor, D. L., 1973, "Superalloy Article Cleaning and Repair Method," U.S. Patent 4,098,540, July 4.

Larsen, F. R., and Miller, J., 1982, "A Time-Temperature Relationship for Rupture and Creep Stresses," *Trans. ASME*, Vol. 74, p. 765.

Liburdi, J., and Lowden, P., 1985, "Repair Technologies for Gas Turbine Components," *AGARD Conference Proceeding No. 398, Advanced Joining of Aerospace Metallic Materials*, Sept., pp. 22.1–22.12.

Liburdi, J., Lowden, P., and Pilcher, C., 1989, "Automated Welding of Turbine Blades," ASME JOURNAL OF ENGINEERING FOR GAS TURBINES AND POWER, Vol. 112, pp. 550–554.

Lowden, P., Pilcher, C., and Liburdi, J., 1991, "Integrated Weld Automation for Gas Turbine Blades," ASME Paper No. 91-GT-159.

Mattheij, J. H. G., 1985, "Role of Brazing in Repair of Superalloy Components—Advantages and Limitations," *Materials science and Technology*, Vol. 1, pp. 608–612.

McComas, C. C., and Stuart, D. C., 1987, "Repair of Surface Defects in Superalloy Articles," U.S. Patent 4,705,203, Nov. 10.

Owczarski, W. A., 1977, "Process and Metallurgical Factors in Joining Superalloys and Other High Service Temperature Materials," *AGARD Lecture Series No. 91, Advanced Manufacturing Techniques in Joining of Aerospace Materials*, Sept., pp. 3.1–3.32.

Schneider, K., Jahnke, B., Bürgel, R., and Ellner, J., 1985, "Experience With Repair of Stationary Gas-Turbine Blades—View of a Turbine Manufacturer," *Materials Science and Technology*, Vol. 1, pp. 613–619.

Sims, C. T., Stoloff, N. S., and Hagel, W. C., 1987, *Superalloys II*, Wiley, New York, Appendix B.

Thamburaj, R., Wallace, W., and Goldak, J. A., 1983, "Post-weld Heat-Treatment Cracking in Superalloys," *International Metals Reviews*, Vol. 28(1), pp. 1–22.

Downloaded 02 Jun 2010 to 171.66.16.122. Redistribution subject to ASME license or copyright; see http://www.asme.org/terms/Terms_Use.cfm

A High-Speed Capacitance-Based System for Gaging Turbomachinery Blading Radius During the Tip Grind Process

A. G. Sheard

G. C. Westerman

B. Killeen

Rotadata Ltd.,
Bateman Street,
Derby, United Kingdom

M. Fitzpatrick

Dean Smith & Grace Ltd.,
Keighley,
West Yorkshire, United Kingdom

During the manufacture and overhaul of gas turbines, it is necessary to ensure that all blades in a stage are of an equal and known length to minimize the loss in performance that arises as a consequence of the clearance between rotor tip and engine casing. Modern compressor and turbine blades are generally loose fitting in their root fixings and only adopt their true working position when running. In this paper, a new technique for measuring the rotor radius over individual blades is described. The measurement technique utilizes a capacitance-based clearance measurement system, which enables rotor radius to be measured over each blade while spinning fast enough to ensure that the blades are centrifugally loaded into their true working position. The measurement technique is described, as is the system utilized to calibrate and reduce output into engineering units. The mechanical design of the "measurement head" is presented and the CNC lathe to which it interfaces described. Finally, the results of an experimental program, utilizing a fully bladed compressor disk undertaken to ascertain system performance, are presented.

1 Introduction

The continuing effort by gas turbine manufacturers to improve the efficiency of their product has led to the use of sophisticated computer codes to minimize aerodynamic losses through the blading. This has resulted in complex three-dimensional aerofoil designs, which minimize the losses associated with the various secondary flow mechanisms in the gas path. As aerodynamic losses have been reduced, so losses associated with tip clearance effects have become a larger proportion of the remaining loss.

The use of an abrasive material over rotating blading is common as it allows the blades to cut their own path when the engine is new, so ensuring that the clearance is the result of blade-to-casing contact at some point during the flight cycle and, therefore, the minimum that may be achieved. Clearly, the technique of allowing the blading to cut its own path through an abradable over-tip material will not work well if one blade is significantly longer than the rest. The long blade will cut a path that will result in larger clearances over every other blade. At first sight the problem may seem trivial: Simply ensure all blades are the same length; however, the design of modern blade root fixings in their disk is such that they are a loose fit and do not adopt their true working position until centrifugally loaded.

In order to measure the radius of a bladed disk over each blade it is necessary to spin it fast enough to load the blading into its working position. The problems associated with measuring the radius of a bladed disk while rotating are formidable and, until recently, were simply not addressed. This has, however, changed and the V2500 engine, for example, now specifies in its build and overhaul procedures that the bladed disks must be machined to a known diameter as an assembly. The technique of grinding individual blades to a known length and fitting them in a disk of known diameter has specifically been cited as inadequate to meet the required initial build and overhaul performance.

In this paper two techniques for measuring the radius of a bladed disk are described. The first of these techniques has been in service with engine manufacturers and overhaul shops for over five years. The second utilizes a new measurement system, which is a development of the original technique and was produced in response to the changing needs of the gas turbine community.

2 Radius to the Longest Blade

During the early 1970s the desire to machine bladed disks became a need and the gas turbine community began to look for machine tools that could meet it. The problem was not one of machining because, although the machining of a bladed disk does present problems, they can be addressed using those methods and techniques commonly utilized within the machine tool trade. The problem was one of measurement, when a blade does not adopt its true working position until centrifugally loaded by revolving at over 1000 rpm.

Contributed by the International Gas Turbine Institute and presented at the 37th International Gas Turbine and Aeroengine Congress and Exposition, Cologne, Germany, June 1-4, 1992. Manuscript received by the International Gas Turbine Institute January 13, 1992. Paper No. 92-GT-365. Associate Technical Editor: L. S. Langston.

Copyright © 1994 by ASME
Downloaded 02 Jun 2010 to 171.66.16.122. Redistribution subject to ASME license or copyright; see http://www.asme.org/terms/Terms_Use.cfm

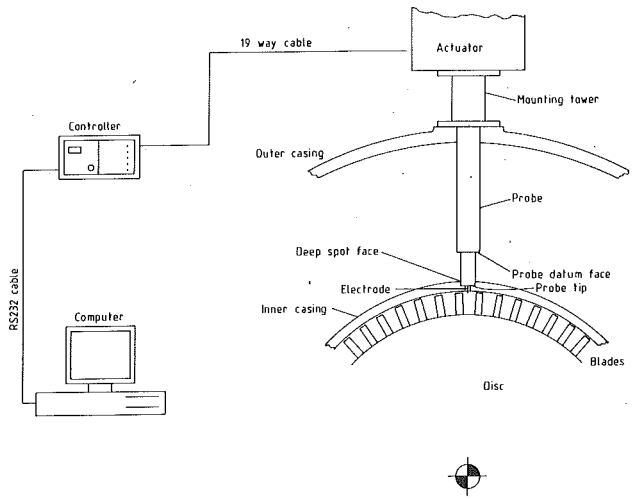


Fig. 1 A schematic view of the electromechanical SMP probe and actuator mounted on a gas turbine, with the controller displaying distance from the probe datum to the rotating blading

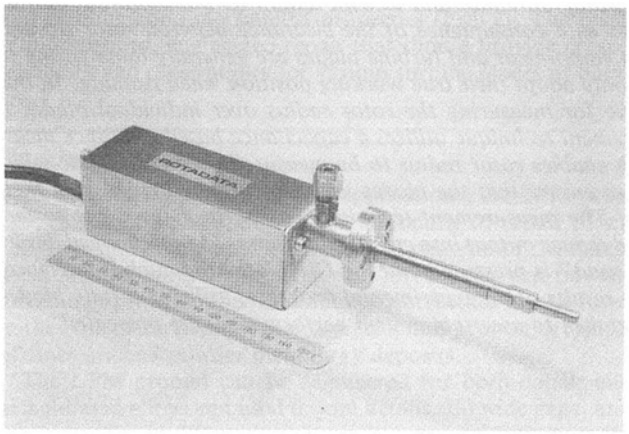


Fig. 2 The electromechanical SMP. For tip grind applications a bayonet-type probe cartridge with a soft copper tip is used to facilitate rapid probe changes and to prevent the probe electrode damaging the blading in the event that the electrode physically contacts the blade.

2.1 Measurement Technique Selection. Standard machine tool gaging techniques were simply never intended to measure the position of the discontinuous surface represented by the blades of a disk while rotating. Some other technique was required. The gas turbine industry has developed techniques for measuring the clearance between the compressor and turbine blading and the casings in which they run. While this measurement is different from that required for the measurement of a bladed disk during machining, it was recognized that the techniques used for tip clearance measurement in gas turbines might be more applicable to the measurement of bladed disk radius during machining than conventional machine tool techniques.

A Stepper Motor driven Probe (SMP) utilizing a spark/discharge principle of operation was originally developed by Davidson et al. (1983) for clearance measurement in gas turbines. The development of a miniaturized SMP and a detailed description of its principle of operation are given by Sheard and Turner (1992). The original SMP of Davidson et al. has been in use for over twelve years measuring blade-to-casing running clearances and over five years in tip grinding applications. The system comprises a probe, actuator, and electronic controller, Fig. 1. In its original application the probe would be inserted into an engine and spring loaded onto an inner casing on which a datum face had been machined.

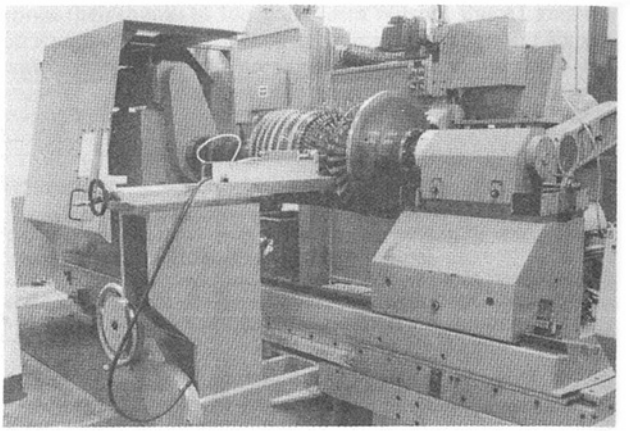


Fig. 3 A typical tip grind machine, based on a manual grinding machine fitted with three-axis read out and the electromechanical measurement system developed by Davidson et al. (1983)

The actuator, Fig. 2, contains a stepper motor drive assembly and an electronics module. The electronics module generates 400 V, which is applied to an insulated electrode running down the probe. The controller provides stepper motor drive pulses and interrogates the electronics module after each step. As the stepper motor drives the insulated electrode forward, the electrode is pushed out of the probe tip toward the rotating blading. When the electrode comes within 3 to 4 μm. of an electrically grounded target, such as a passing blade, there is a breakdown of the air in the gap and a spark jumps from the electrode to the blade.

The electromechanical system measures to the longest blade around a disk, as this is the first one encountered. While this was recognized as a limitation, after machining the blades should all be the same length so an accurate measurement of the finished diameter would be provided.

2.2 Operating Procedure. All tip-grind installations of SMPs are on manual grinding machines, with Fig. 3 being a typical example. Each machine has a different specification and, therefore, a different operating procedure is used when tip grinding. The operating procedure described below is typical of those used routinely.

The tooling used to hold the compressor drum to be machined incorporates a datum face and datum disks of known dimensions, Fig. 4. After mounting on the grinding machine, concentricity of the datum disk and a second reference diameter, such as a bearing surface at the far end of the assembly, are checked as is the swash of the datum face. These are typically set to better than 0.025 mm. The SMP actuator and probe are mounted on the grinding machine, Fig. 5. In some installations the actuator is free to move axially over the datum disks, blading, and second reference diameter. In other installations it is fixed with the tooling and compressor drum being moved relative to it. The probe is datumed against the axial datum face so its axial location is known. The assembly is rotated at between 1000 and 2000 rpm, depending on rotor diameter.

The measurement system is brought up to the datum disk radial face and a measurement made to the datum disk. It is then moved the appropriate axial distance, Fig. 4, over the first set of blades. A second measurement is taken, this time to the rotating blading. From a knowledge of the datum disk diameter, the first and second measurements, the radius of the bladed disk may be calculated. Once the rotating radius of the bladed disk is known, the grinding wheel is used to grind it to the required radius. The blades are then deburred with a wire wheel and the measurement technique repeated. If necessary, further cuts are taken.

Downloaded 02 Jun 2010 to 171.66.16.122. Redistribution subject to ASME license or copyright; see http://www.asme.org/terms/Terms_Use.cfm

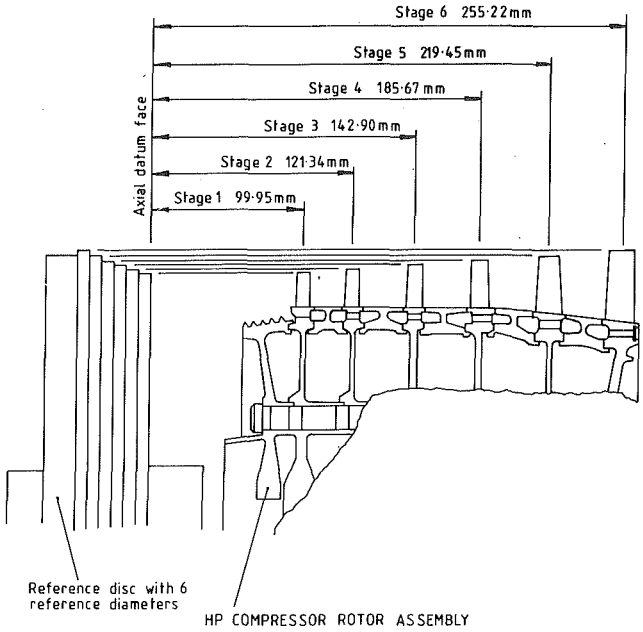


Fig. 4 The blading of a typical compressor drum and the datum disks illustrating how the radial and axial datum faces enable blades with a hade angle to be machined

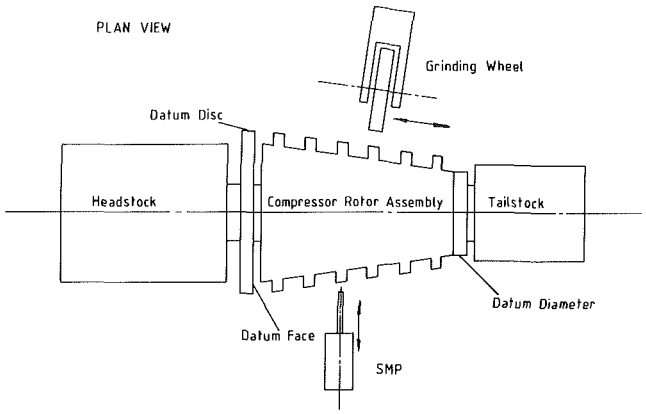


Fig. 5 A schematic view of a bladed disk assembly fitted on a grinding machine with datum disks and SMP measurement system

The procedure described above is a reliable and cost-effective solution to the problem of machining bladed disk assemblies when the blades are a loose fit in their root fixings. For many applications this is adequate, as the total accuracy that may be achieved on radius for a well set-up rotor on a good grinding machine is ± 0.025 mm and typically no more than ± 0.05 mm on diameter.

3 Radius Over Every Blade

There are instances where there is a need to measure radius over every blade around a disk and in these cases the SMP of Davidson et al. is not suitable. Optical triangulation systems, such as that described by Barranger and Ford (1981), use a laser to measure clearance over individual blades. These systems are large and inherently fragile and therefore are not ideal for use in the tip grinding process. Capacitance probes are small, rugged devices that are routinely used to measure tip clearance in gas turbines. A capacitance-based clearance measurement system was designed by Chivers (1989) and developed by Killeen et al. (1991). This system was further developed by Sheard et al. (1991) who designed a "measurement head" able

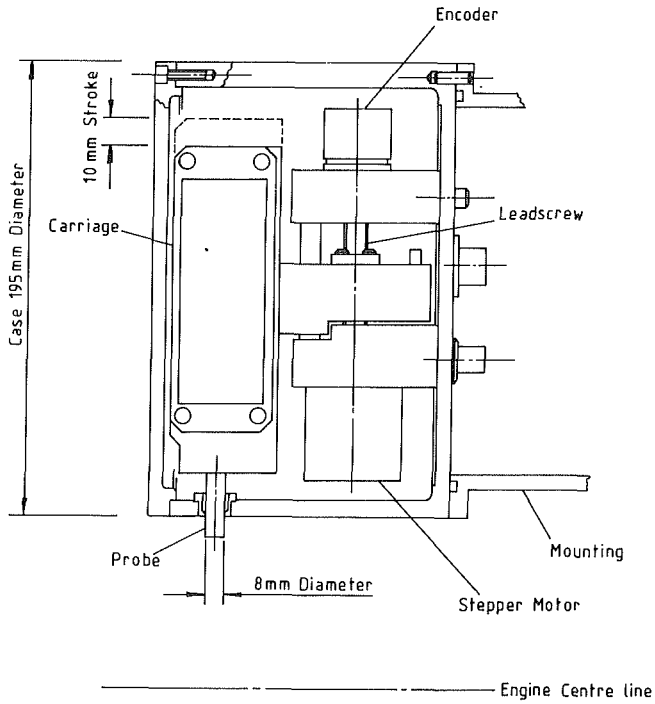


Fig. 6 Layout of the measurement head designed for measuring radius of individual rotor and stator blades during their machining, developed by Sheard et al. (1992)

to measure clearance over individual blades to an accuracy of ± 0.01 mm. The measurement head was shown to be insensitive to variations in blade thickness and could be calibrated on line immediately prior to use, thus eliminating any errors due to drift with temperature.

3.1 A Capacitance-Based Measurement System. The measurement head contains a traverse actuator, electronics module, and capacitance probe oscillator, Fig. 6. The compact design enables this to be fitted within a 195-mm-dia hermetically sealed case, which enables it to be used to measure internal stator blade radius down to a minimum stator internal diameter of 200 mm. The 8-mm-dia probe incorporates an insulated electrode and capacitance probe. The electronics module, oscillator, and probe are mounted on a traverse actuator carriage and may be stepped in toward the blading, which facilitates probe calibration.

A capacitance probe utilizes its own tip and a target as the two plates of a capacitor. As capacitance is proportional to plate separation, so the capacitance measured as a blade passes is proportional to the distance of that blade from the probe tip. The probe tip capacitance tunes an oscillator circuit. As the value of capacitance at the probe tip changes, so the resonant frequency of the circuit changes. The blade passing results in a modulation of the oscillator's natural frequency, which is known as a Frequency Modulated (FM) mode of operation.

4 System Commissioning

In order to establish that the capacitance clearance measurement system of Sheard et al. could measure the radius of a bladed disk during the tip grinding process, a two-stage commissioning exercise was undertaken. A CNC lathe was fitted with a measurement head and grinding spindle. Two-cycle scrapped compressor disks were acquired, a Pratt & Whitney JT8 Stages 7 and 11, each with a full blade set. These were chosen as being typical of the type of disk that is routinely ground to size by engine manufacturers and overhaul shops. The commissioning was then split into two stages. The first

Downloaded 02 Jun 2010 to 171.66.16.122. Redistribution subject to ASME license or copyright; see http://www.asme.org/terms/Terms_Use.cfm

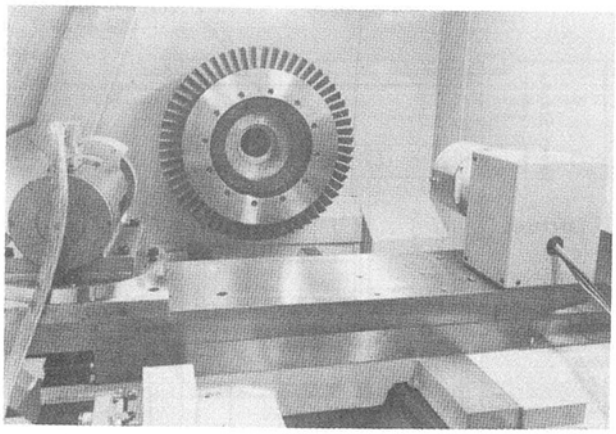


Fig. 7 The CNC lathe fitted with a grinding spindle, prototype measurement head, datum disk, and Pratt & Whitney JT8 Stage 11 bladed compressor disk

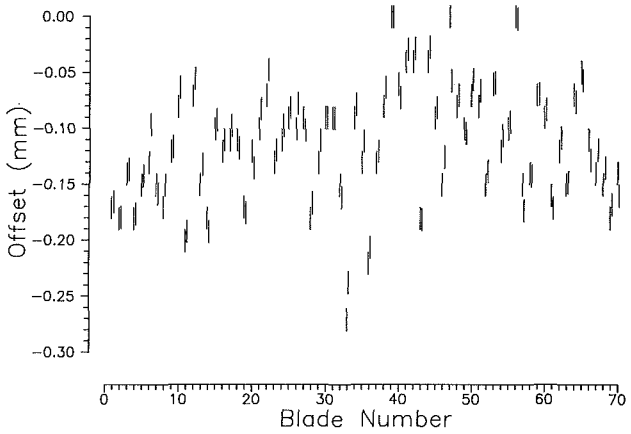


Fig. 8 Offset of the JT8 Stage 11 compressor blades from the longest blade, measured statically using a dial gage and at 1800 rpm using the measurement head. Dial gage measurements are offset to the left and measurement head measurements to the right for clarity.

stage utilized the Stage 11 disk, which has blades wedged out into their working position. This enabled the radius over individual blades to be measured using a dial gage. Static measurement of radius provided a useful benchmark against which to gage the accuracy with which the measurement head could measure blade tip radius under rotation. The second phase of the commissioning utilized the Stage 7 disk, which had pin fixed blades that did not adopt their true working position until centrifugally loaded.

4.1 Phase One Commissioning. Suitable fittings and a datum disk were manufactured to enable the Stage 11 disk to be mounted on a CNC lathe, Fig. 7.

The disk was spun to 1800 rpm and the measurement head brought over the datum disk. The measurement head is driven in a similar manner to the SMP of Davidson et al. with a measurement from its internal datum to the datum disk being made. This procedure is then repeated over the rotating blading, thus enabling radius of the longest blade to be calculated.

The capacitance probe is calibrated on-line while making the measurement to the longest blade; the method used is described in detail by Sheard et al. (1992). The capacitance probe provides a measurement of the clearance over every blade relative to the capacitance probe tip. This is used in conjunction with the measured radius of the longest blade to calculate radius over each blade.

The radius of the Stage 11 disk was measured over each blade using a dial gage. Dial gage measurements were estimated

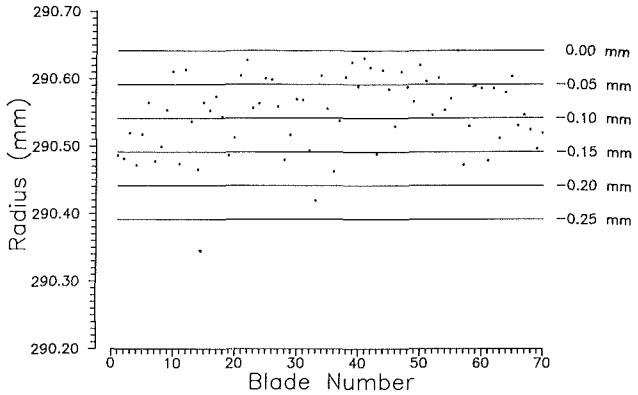


Fig. 9 Radius of the JT8 Stage 11 compressor blades prior to grinding, measured at 1800 rpm using the measurement head

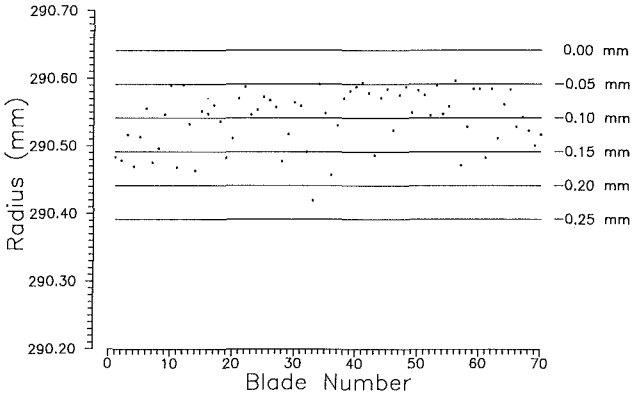


Fig. 10 Radius of the JT8 Stage 11 compressor blades after a 0.05 mm cut, measured at 1800 rpm using the measurement head

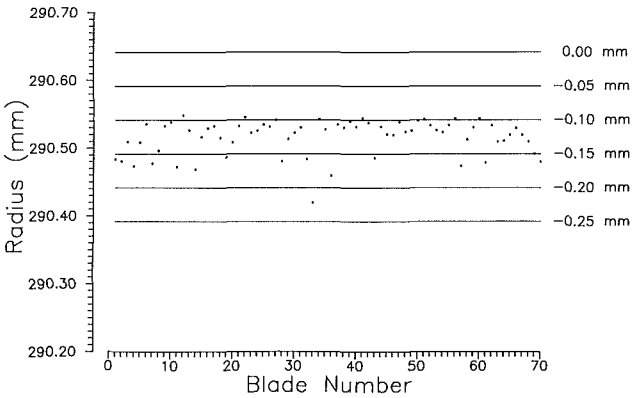


Fig. 11 Radius of the JT8 Stage 11 compressor blades after a 0.10 mm cut, measured at 1800 rpm using the measurement head

to be accurate to ±0.01 mm. Sheard et al. (1992) concluded that the measurement head was also accurate to ±0.01 mm. Dial gage and measurement head radii were each plotted against blade number, with the vertical axis plotted as offset from the longest blade to enable the scale to be expanded sufficiently for the ±0.01 mm error bar to be visible, Fig. 8. The error bars of the two data sets show a high degree of overlap giving confidence in their accuracy. To facilitate comparison with results obtained during grinding, the measurement head data were re-plotted against radius, Fig. 9.

The grinding wheel was used to take a 0.05 mm cut, Fig. 10. The repeatability of measured radius for the blades before grinding, Fig. 9, and after a 0.05 mm cut, Fig. 10, was considered excellent, with the exception of those blades that had been ground that were now correspondingly shorter. The process was repeated with a 0.10 mm cut, Fig. 11, 0.15 mm cut,

Downloaded 02 Jun 2010 to 171.66.16.122. Redistribution subject to ASME license or copyright; see http://www.asme.org/terms/Terms_Use.cfm

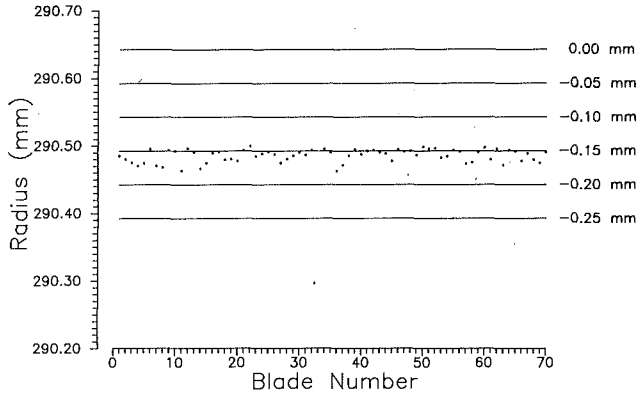


Fig. 12 Radius of the JT8 Stage 11 compressor blades after a 0.15 mm cut, measured at 1800 rpm using the measurement head

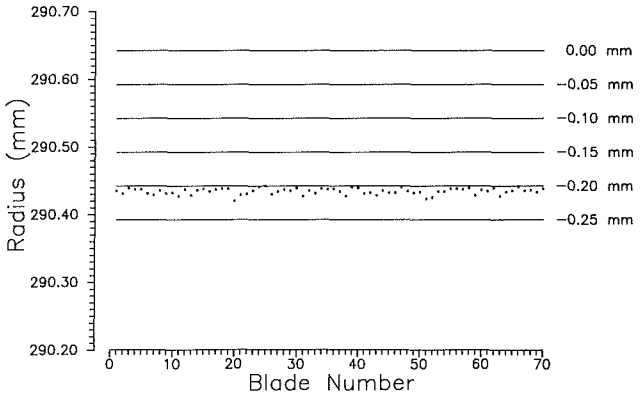


Fig. 13 Radius of the JT8 Stage 11 compressor blades after a 0.20 mm cut, measured at 1800 rpm using the measurement head

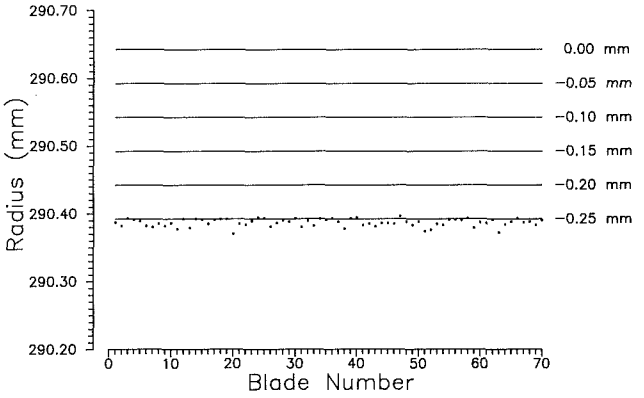


Fig. 14 Radius of the JT8 Stage 11 compressor blades after a 0.25 mm cut, measured at 1800 rpm using the measurement head

Fig. 12, 0.20 mm cut, Fig. 13, and finally a 0.25 mm cut, Fig. 14. The progression to a finished diameter may be clearly seen from one cut to the next. A dial gage was used to check the finished radius, which was 290.39 mm, ±0.01 mm, over each blade. The measurements made after the final cut exhibited a blade-to-blade variation in radius of 0.02 mm, which compares well to the ±0.01 mm variation in radius measured with the dial gages.

The final check on measurement system performance utilized the measurement head to measure radius over each blade six times. The measurement head was moved from its park to measure position, calibrated, then used to measure radius. This procedure was repeated six times. The repeatability of measurement, Fig. 15, is ±0.01 mm, in agreement with the ±0.01 mm error of Sheard et al. and therefore considered excellent.

At this point phase one commissioning was considered complete as the prototype measurement system had demonstrated that it could make reliable and repeatable measurements of radii over fixed blades while rotating.

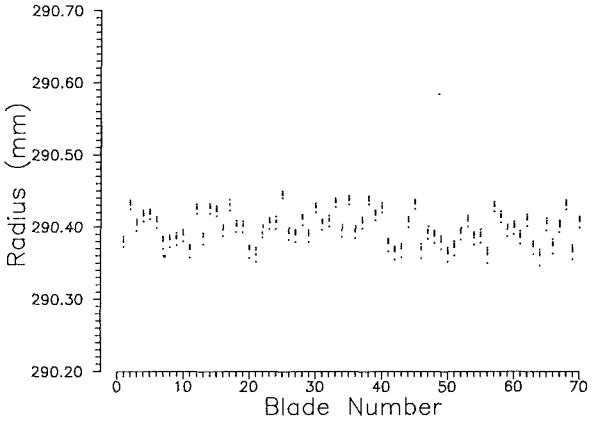


Fig. 15 Repeatability test conducted on the Pratt and Whitney JT8 Stage 11 bladed disk at 1800 rpm. The capacitance probe used in the measurement head was recalibrated prior to each of the six measurements of radius.

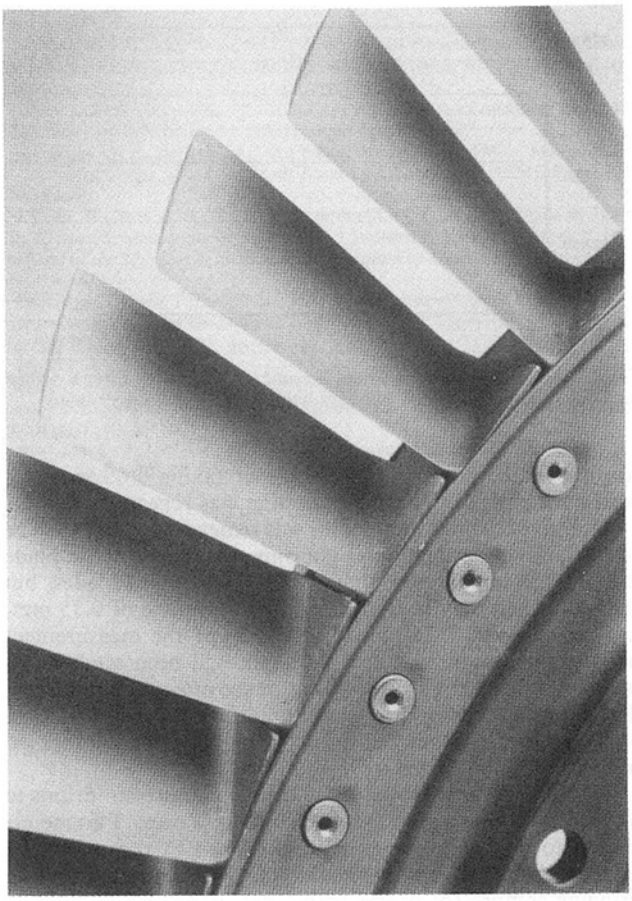


Fig. 16 A close-up view of the pin fixed blade root fixing arrangement of the Pratt & Whitney JT8 Stage 7 blades

4.2 Phase Two Commissioning. The commissioning exercise continued with the Pratt & Whitney JT8 Stage 7 disk. The blades in this disk are pin fixed, Fig. 16, and therefore do not adopt their true working position until centrifugally loaded.

The prototype measurement head was used to measure radius over individual blades, Fig. 17, with the variation in blade heights being typical of that which would be expected of engine

Downloaded 02 Jun 2010 to 171.66.16.122. Redistribution subject to ASME license or copyright; see http://www.asme.org/terms/Terms_Use.cfm

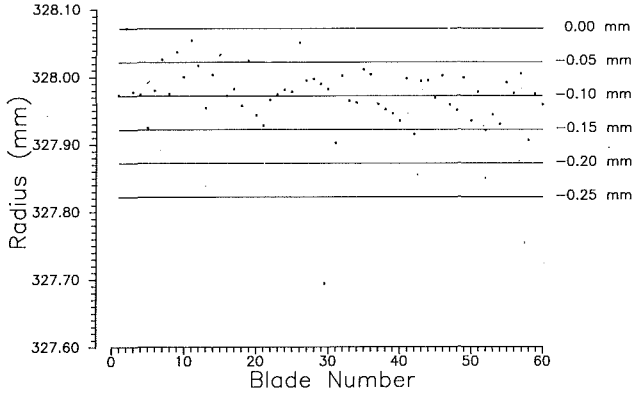


Fig. 17 Radius of the JT8 Stage 7 compressor blades prior to grinding, measured at 1800 rpm using the measurement head

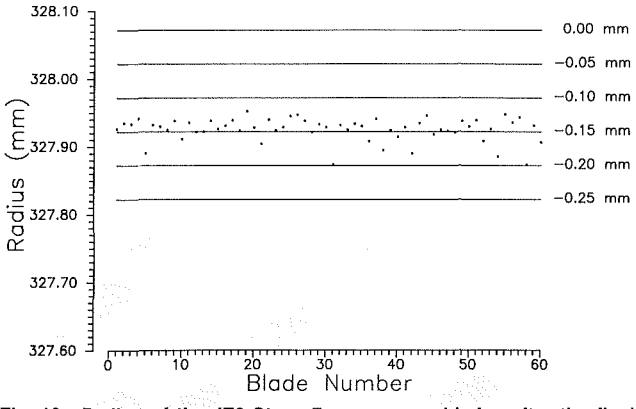


Fig. 18 Radius of the JT8 Stage 7 compressor blades after the final 0.25 mm cut, measured at 1800 rpm using the measurement head

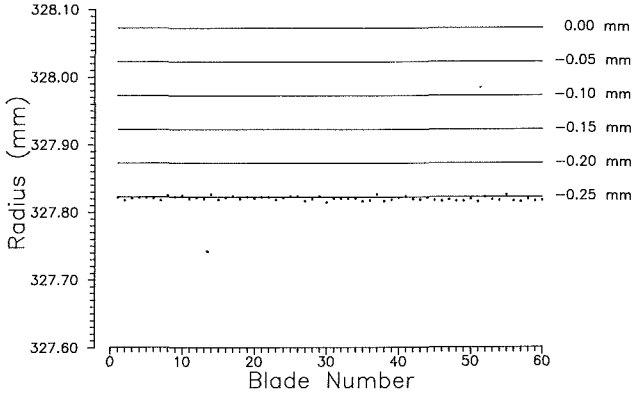


Fig. 19 Radius of the JT8 Stage 7 compressor blades after completing the 0.25 mm cut following the recommendations of Winfield (1991), measured at 1800 rpm using the measurement head

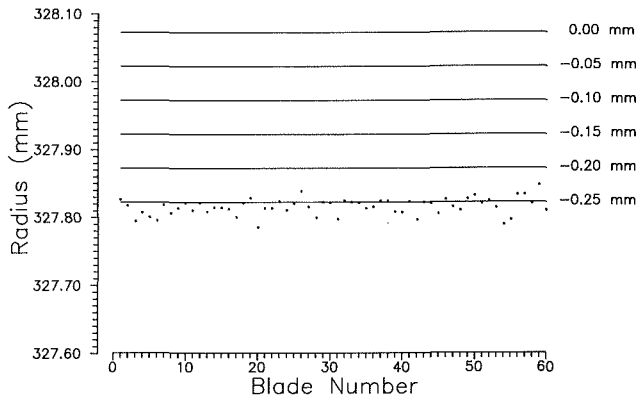


Fig. 20 Radius of the JT8 Stage 7 compressor blades after de-burring of the blades, measured at 1800 rpm using the measurement head

run hardware. The same procedure of taking 0.05 mm cuts used during phase one commissioning was repeated.

After five 0.05 mm cuts radius was remeasured, Fig. 18. The results were disappointing as not only was the scatter in blade radius large compared to that achieved with fixed blades, but the radius had only been reduced by an average of 0.15 mm, not the expected 0.25 mm. The ability of the measurement head to measure radius to ±0.01 mm had been established, both by Sheard et al. and during phase one commissioning. The authors, therefore, reasoned that the grinding technique, which was satisfactory for fixed blades, was not suitable for use with pin fixed blades.

The accurate grinding of loose-bladed compressor drums to a specific radius is a specialized machining process. Parameters critical to its success have been established by those working in the field. The recommendations of Winfield (1991) when grinding compressor drums with loose blades are as follows. Use a relatively soft grinding wheel, which is dressed immediately prior to use. After completing the final cut, allow the grinding wheel to remain over the blading for several minutes. This minimizes deflection of the blading due to cutting forces by allowing the blades to "relax" back to their true radial location under the action of centrifugal force. With the grinding wheel still over the blading this minimizes blade-to-blade variation in radius. Lastly, measure the ground compressor after grinding without stopping the machine, as loose blades always reseat in slightly different positions.

After implementing the recommendations of Winfield the blades were ground to the desired radius, Fig. 19. The blade-to-blade variation in radius was 0.01 mm, which was an improvement over that achieved previously, Fig. 18. This result confirmed that the discrepancy between the expected results and those initially obtained with loose blades was due to the use of a grinding technique inappropriate to the machining of a compressor drum with loose blading.

Once the required radius over each blade had been achieved, the blades were de-burred by stopping the machine and manually removing the burr on each blade. The bladed disk was then spun back up to 1800 rpm and radius remeasured, Fig. 20. The act of de-burring the blades combined with stopping and starting the machine caused the blades to reseat. This resulted in an increase in the blade-to-blade variation of radius to 0.06 mm, of which 0.05 mm may be attributed to the reseating of the blades as blade-to-blade variation in radius had been 0.01 mm.

The variation in blade radius of 0.01 mm, Fig. 19, is within the ±0.01 mm error associated with the measurement head. This suggests that the grinding technique used achieved near the limiting accuracy with which blade lengths could be machined to a known diameter. The design of the blade root fixings appears to introduce a variation in blade seating of 0.05 mm; therefore grinding to a more accurate radius would not significantly improve the variation in blade-to-blade radius of the compressor after the blades had reseated.

The measurement head was able to measure radius to ±0.01 mm, with a 0.06 mm variation in radius being seen following the reseating of the blades. The limiting accuracy with which radius over each blade may be machined to a specified value is, therefore, a function of blade root fixing design and not the ±0.01 mm error inherent in the measurement technique. The measurement head was, hence, concluded to be suitable for measuring blade radius during the tip grind process.

Commissioning concluded with an investigation of the ef-

Downloaded 02 Jun 2010 to 171.66.16.122. Redistribution subject to ASME license or copyright; see http://www.asme.org/terms/Terms_Use.cfm

fects of disk speed on measured blade radius. Changing wheel speed from 1400 rpm to 2200 rpm was found to have no effect on the relative heights of the blades. This was not unexpected as even at 1400 rpm the blades experience a centrifugal load of over 400 g, so they should be seated in their root fixing. An important result, however, was that the measurement head remained unaffected by changes in blade passing frequency.

5 Conclusions

1 An electromechanical measurement system originally developed by Davidson et al. (1983) has been successfully used for over five years on manual grinding machines to enable bladed rotors to be machined to an accuracy of ± 0.025 mm on radius.

2 There are some situations where an inspection capability to enable the radius of the rotor over every blade to be measured is desirable to ascertain, for example, whether a previously run rotor requires reblading.

3 A two-stage commissioning trial was undertaken to verify the functionality of a capacitance based measurement head, using a CNC lathe as a base. The conclusion of the trial was that the measuring head could measure radius over individual blades to ± 0.01 mm.

4 De-burring rotor blades after the grinding operation combined with stopping and starting the grinding machine introduces a variation in the radial seating of the blades in their root fixing of 0.05 mm. This indicates that the ± 0.01 mm measurement error is significantly less than the blade-to-blade variation of radius that is achieved after de-burring of the blading.

5 Increasing the accuracy with which blade radius may be measured beyond that achieved with the measurement head would not decrease the final blade-to-blade variation in radius, because of the variation in blade seating.

6 The accuracy, compact size, tolerance to blade width, and blade passing frequency plus the inherent ruggedness of the measurement head were concluded to make it ideal for use during the tip grinding of rotor and stator blade sets.

Acknowledgments

The assistance of D. P. Winfield of Rolls-Royce plc during the program of work reported and the preparation of this manucript was much appreciated by the authors. The assistance of J. B. Macindoe and Dr. J. W. H. Chivers, also of Rolls-Royce plc, is acknowledged.

The author gratefully acknowledge the assistance of Dr. J. H. Nicholson, Caledonia Airmotive plc, who provided the disk and blade sets used in the program of work reported.

The contribution of A. Wooler, B. H. Edmundson, G. Brock, and R. J. Gent of Rotadata Ltd. is acknowledged.

The authors would like to thank Rotadata Ltd. and Dean Smith & Grace Ltd. who funded the work reported in this paper. Lastly, the authors would like to thank D. P. Davidson, Chairman of the Rotadata Group, for permission to publish this work.

References

Barranger, J. P., and Ford, M. J., 1981, "Laser Optical Blade Tip Clearance Measurement System," ASME JOURNAL OF ENGINEERING FOR POWER, Vol. 103, p. 457.

Chivers, J. W. H., 1989, "A Technique for the Measurement of Blade Tip Clearance in a Gas Turbine," AIAA Paper No. 89-2916.

Davidson, D. P., De Rose, R., and Wennerstrom, A. J., 1983, "Measurement of Turbomachinery Stator to Drum Running Clearances," ASME Paper No. 83-GT-204.

Killeen, B., Sheard, A. G., and Westermann, G. C., 1991, "Blade by Blade Tip Clearance Measurement in Aero and Industrial Turbomachinery," *Proceedings of the 37th ISA International Symposium of Measurement Techniques*, pp. 429–447.

Sheard, A. G., and Turner, S. R., 1992, "An Electromechanical Measurement System for the Study of Blade Tip to Casing Running Clearances," ASME Paper No. 92-GT-50.

Sheard, A. G., Westermann, G. C., and Killeen, B., 1992, "An On-Line Calibration Technique for Improved Blade by Blade Tip Clearance Measurement," *Proceedings of the 38th ISA International Symposium of Measurement Techniques*, pp. 31–51.

Winfield, D. P., 1991, Rolls-Royce plc, Product Engineering Manager Repair and Overhaul ATO, Private Communication.

Downloaded 02 Jun 2010 to 171.66.16.122. Redistribution subject to ASME license or copyright; see http://www.asme.org/terms/Terms_Use.cfm

The Evolution of Thermal Barrier Coatings in Gas Turbine Engine Applications

S. M. Meier

D. K. Gupta

Pratt & Whitney,
East Hartford, CT 06109

Thermal barrier coatings (TBCs) have been used for almost three decades to extend the life of combustors and augmentors and, more recently, stationary turbine components. Plasma-sprayed yttria-stabilized zirconia TBC currently is bill-of-material on many commercial jet engine parts. A more durable electron beam–physical vapor deposited (EB–PVD) ceramic coating recently has been developed for more demanding rotating as well as stationary turbine components. This ceramic EB–PVD is bill-of-material on turbine blades and vanes in current high thrust engine models and is being considered for newer developmental engines as well. To take maximum advantage of potential TBC benefits, the thermal effect of the TBC ceramic layer must become an integral element of the hot section component design system. To do this with acceptable reliability requires a suitable analytical life prediction model calibrated to engine experience. The latest efforts in thermal barrier coatings are directed toward correlating such models to measured engine performance.

Introduction

Commercial gas turbine engines typically use combustor and turbine superalloys, which melt in the range of 1230°C to 1315°C. These materials operate in a combustion gas environment typically above 1370°C. To avoid structural failure by melting, creep, oxidation, thermal fatigue, and other mechanisms, the airfoils are made hollow, and compressor discharge air is injected to cool the component. To maximize efficiency, it is desirable to minimize the use of this air for cooling purposes and to use it to perform work in the turbine. This has been traditionally accomplished by designing more effective cooling geometries within the component and by film cooling the surface of the component with drilled cooling holes. As this cooling technology matures, however, the technical community is searching for innovative technologies to increase efficiency further (Duvall and Ruckle, 1982; Miller and Lowell, 1982).

One method of protecting gas turbine engine components is through the use of thermal barrier coatings. TBC typically is a two-layer system (Fig. 1), which incorporates a thin layer of ceramic approximately 0.254 mm thick applied to the outer gas path surface of the engine component and an underlying metallic "bond coat" approximately 0.127 mm. The metallic bond coat performs two functions: (1) to provide oxidation resistance and (2) to adhere the ceramic physically and chemically to the underlying superalloy structure.

The use of thermal barrier coatings on noncritical turbine components has provided substantial improvements in system performance through increased turbine efficiency, reduction in maintenance requirements, and fuel usage. These insulative coatings can reduce the turbine airfoil temperature by as much as 167°C, thereby improving the component durability by as much as three to four times and/or specific fuel consumption by more than 1 percent (Miller and Lowell, 1982; Sheffler and Gupta, 1988).

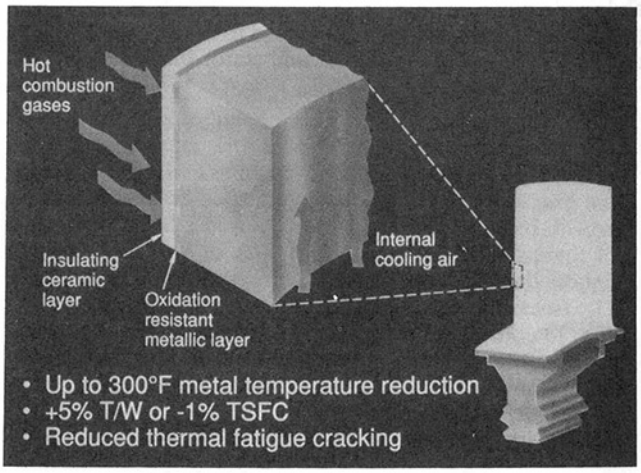


Fig. 1 Thermal barrier coating benefits

Ceramic thermal barrier coatings, however, have a tendency to spall upon experiencing thermal cycling from ambient conditions to extremely high operating conditions encountered in the hot section of a gas turbine engine. Improvements have been made to extend coating life and life prediction models have been formulated to permit utilization of thermal barriers in such a way as to attain maximum benefits. This has led to

Contributed by the International Gas Turbine Institute and presented at the 37th International Gas Turbine and Aeroengine Congress and Exposition. Cologne, Germany, June 1–4, 1992. Manuscript received by the International Gas Turbine Institute February 21, 1992. Paper No. 92-GT-203. Associate Technical Editor: L. S. Langston.

Copyright © 1994 by ASME
Downloaded 02 Jun 2010 to 171.66.16.122. Redistribution subject to ASME license or copyright; see http://www.asme.org/terms/Terms_Use.cfm

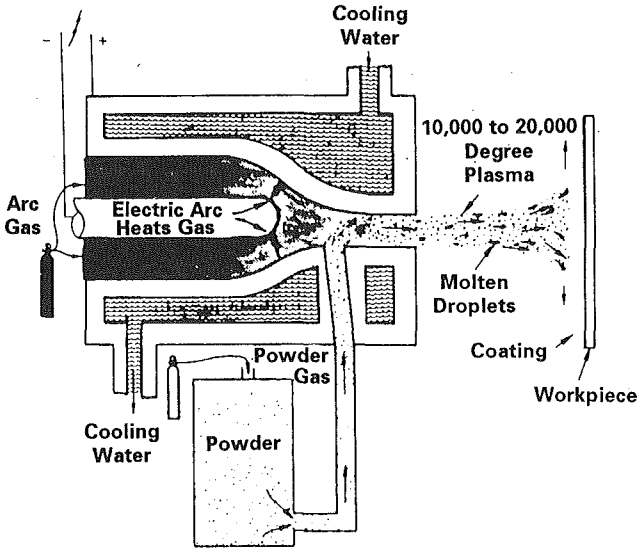


Fig. 2 Plasma-deposited TBC process schematic

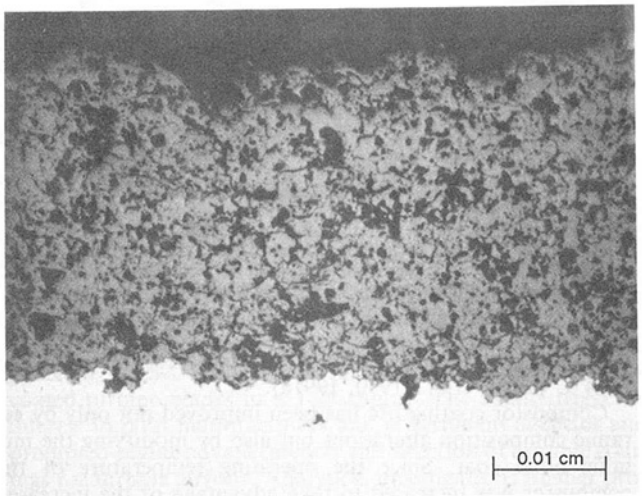


Fig. 3 The microstructure of air plasma-deposited 7 weight percent yttria partially stabilized zirconia

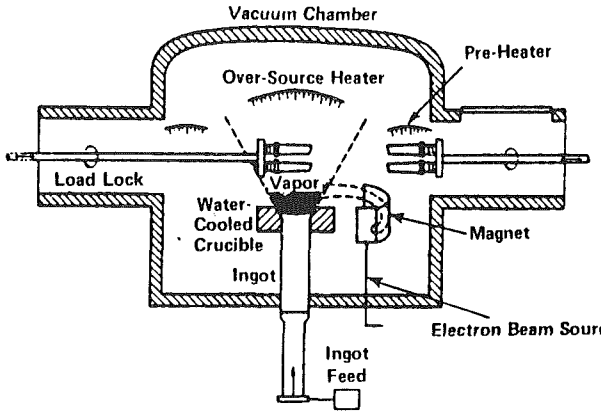


Fig. 4 Electron beam-physical vapor deposited TBC process schematic

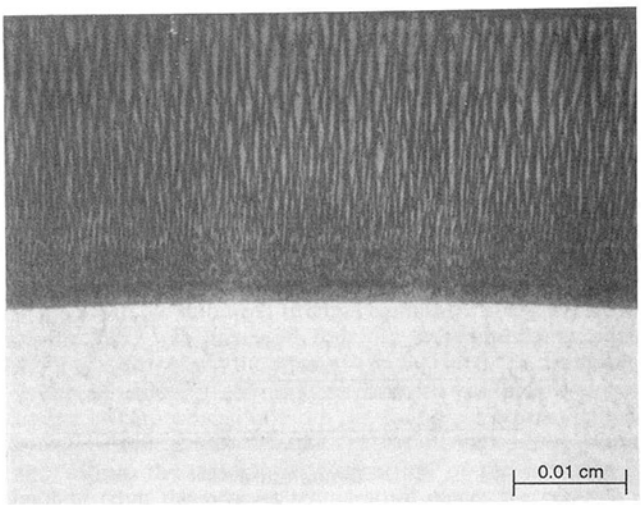


Fig. 5 The microstructure of an electron beam-physical vapor deposited ceramic coating, showing the highly columnar microstructure produced by the EB-PVD process.

more widespread use of thermal barrier coatings throughout the gas turbine engine.

Processing Approaches

Two major approaches are currently used for deposition of thermal barrier coatings: plasma deposition and electron beam–physical vapor (EB-PVD) deposition. Plasma deposition is essentially an adaption of the flame spray process. An electric arc in the water-cooled plasma gun is used to ionize argon gas, converting it into a plasma (Fig. 2). The powder is injected into the flame at the nozzle of the gun, where the ions and electrons of the plasma recombine. The flame heats metal or ceramic powder particles to a semiplastic state and accelerates them toward the workpiece. Upon impact, the semiplastic particles deform to produce a complex, interlocking structure, which is tightly bonded to the substrate. This plasma-sprayed structure (Fig. 3) is quite porous and extensively microcracked. The interface between the ceramic and the metal possesses a very complex topology characteristic of the original metallic bond coat surface. This surface includes small, almost free-standing peninsular metal deposits, which penetrate relatively deeply and are surrounded by ceramic. This feature creates angles and pockets that promote mechanical interlocking between the ceramic and the metal (DeMasi-Marcin et al., 1990).

The EB-PVD ceramic process is a more advanced method of ceramic deposition (Strangman, 1982). In the fabrication of EB-PVD coatings, an electron beam is directed onto the surface of material contained within a crucible (Fig. 4). The material in the crucible is heated, melted, and then evaporated to a vapor of atomic proportions. The parts are positioned above the molten material in the crucible to receive the vapor. The EB-PVD ceramic grows in columnar form when processed under the appropriate conditions (Fig. 5). In contrast to the mechanical interlocking adhesion mechanism of the plasma-sprayed coatings, the EB-PVD coating bonding method is chemical in nature.

In the following sections, evolutionary improvements of the plasma and the EB-PVD deposited coatings will be reviewed and compared, and laboratory and field experience with these coatings will be discussed.

Combustor Coatings

Ceramic coating systems have been used for approximately three decades to decrease the severity of oxidation damage and to improve the cracking resistance of combustors and augmentors. The early combustor coatings consisted of an outer ceramic insulative layer of air plasma deposited fully stabilized 22 weight percent MgO stabilized ZrO_2 and an inner metallic

Downloaded 02 Jun 2010 to 171.66.16.122. Redistribution subject to ASME license or copyright; see http://www.asme.org/terms/Terms_Use.cfm

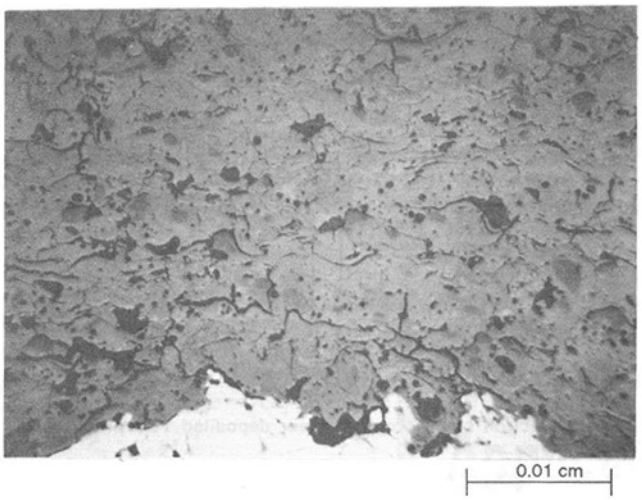


Fig. 6 The microstructure of air plasma-deposited 22 weight percent magnesia stabilized zirconia

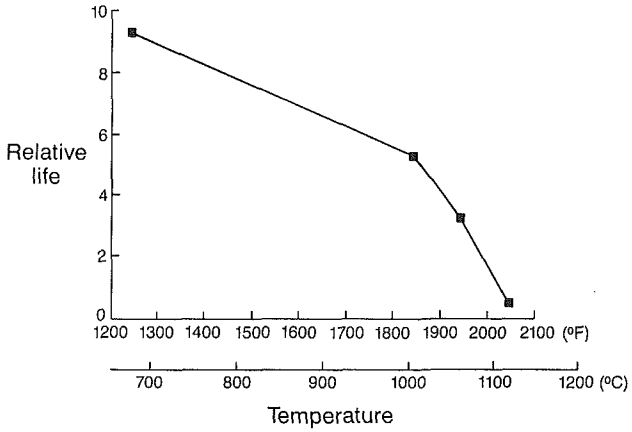


Fig. 7 Influence of temperature on the relative cyclic thermal spallation life of a magnesia-stabilized zirconia thermal barrier coating

bond coat of air plasma deposited Ni-Cr or Ni-Al. After thermal exposure, this inner metallic bond coat bonds chemically to the underlying metallic substrate and provides a topologically suitable surface for mechanical bonding with the overlay ceramic. The magnesia-stabilized zirconia microstructure shown in Fig. 6 has a relatively small amount of porosity, is extensively microcracked, and contains a significant volume fraction of finely distributed free magnesia. It is thought that differential thermal expansion between this free magnesia and the surrounding zirconia matrix assists in the creation and maintenance of the high level of microcrack toughening achieved in this system. The extensive microcracking provides significant toughening and increased tolerance to cyclic thermal strains imposed by repeated heating and cooling (Meier et al., 1990, 1991a).

As the temperatures in the combustor have been increased, the durability of this early combustor coating has become inadequate. The maximum use temperature of the plasma-sprayed magnesia-stabilized zirconia coating is on the order of 982°C since magnesia-stabilized zirconia crystallographically destabilizes above 954°C (Fig. 7). By replacing the 22 weight percent magnesia with the 7 weight percent yttria composition used successfully in the turbine section of the engine, the spallation life at temperatures above 982°C has been substantially improved (Stecura, 1979). Figure 8 shows that the thermal spallation life of a 7 weight percent yttria partially stabilized zirconia is approximately four times that of the 22

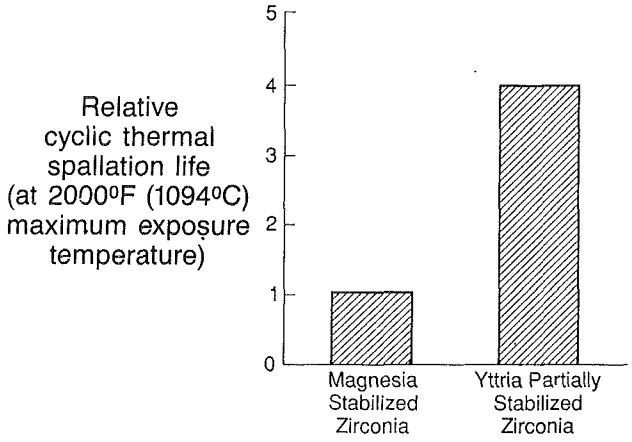


Fig. 8 Relative cyclic thermal spallation life at a maximum exposure temperature of 1094°C

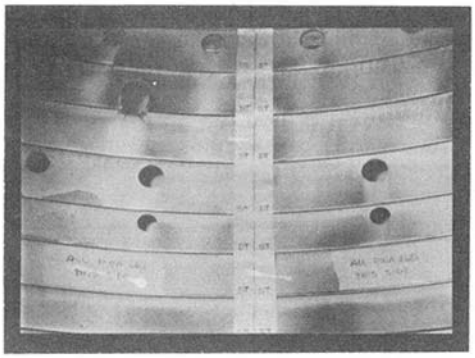


Fig. 9 Engine operated JT9D combustor panels, which clearly demonstrate the durability benefit of 7 percent yttria partially stabilized zirconia (on the right, designated PWA 265) as compared to magnesia-stabilized zirconia (on the left, designated PWA 261)

weight percent magnesia fully stabilized zirconia coating at 1094°C (Meier et al., 1990, 1991a).

Combustor coating life has been improved not only by ceramic composition alterations but also by modifying the metallic bond coat. Since the operating temperature of the combustor was increased to take advantage of the increased temperature capability of the yttria-stabilized zirconia, the underlying bond coat oxidation became a problem. By adopting a more oxidation-resistant NiCoCrAlY bond coat composition from the turbine section of the engine, the performance of the combustor has been improved. Pratt & Whitney has designated this 7 percent yttria-stabilized zirconia plasma-sprayed ceramic over air plasma-sprayed NiCoCrAlY bond coat PWA 265. The earlier magnesia stabilized system was labeled as PWA 261. An in-house JT9D engine test of PWA 265 and PWA 261 combustor panels clearly demonstrated the durability benefit of the 7 percent ytrria partially stabilized zirconia as compared to magnesia-stabilized zirconia (Fig. 9) (Meier et al., 1990, 1991a). Similar favorable results have been achieved with PWA 265 in over 3000 hours and 15,000 cycles of commercial engine testing. Also, PWA 265 has accumulated about 100,000 cumulative flight hours and 70,000 cumulative flight cycles of combined fighter and commercial engine field experience with no reported problems. In order to improve component performance and durability as well as to achieve commonality across the product line, Pratt & Whitney has incorporated PWA 265 in all combustor applications.

Plasma-Sprayed TBC Laboratory and Field Experience

Although ceramic coating systems have been used for decades to decrease the severity of oxidation damage and improve

Downloaded 02 Jun 2010 to 171.66.16.122. Redistribution subject to ASME license or copyright; see http://www.asme.org/terms/Terms_Use.cfm

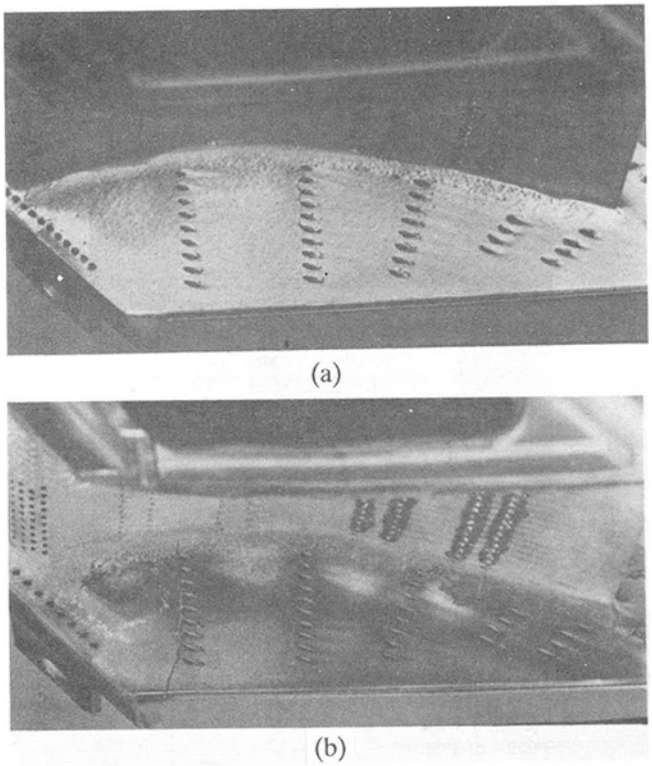


Fig. 10 (*a*) A thermal barrier coated JT9D vane platform after 2778 endurance test cycles; (*b*) a metallic coated vane platform from the same engine after 1500 endurance test cycles. The thermal barrier coating clearly reduces burning and thermal fatigue cracking.

the cracking resistance of combustors, it was not until the mid-70s that many important developments were made, which led to extension of thermal barrier coating application to the turbine section of the engine (Grisaffe and Levine, 1979; Ruckle, 1979). One major development was the successful test conducted by NASA-Lewis (Liebert et al., 1976) on thermal barrier coated turbine blades in a J-75 engine. The results triggered interest in both manufacturers and government agencies and prompted engine advancement in the direction of ceramic coatings for turbine airfoils. Analytical investigations further promoted the use of thermal barrier coatings since they established the large overall engine performance benefits achievable from successful utilization of ceramic thermal barrier coatings on turbine airfoils.

Two factors distinguish plasma-sprayed turbine thermal barriers from the combustor coatings. The first is that the ceramic composition is 7 weight percent yttria partially stabilized zirconia, which was originally developed for the turbine section and only later retrofitted for the combustor (Miller and Lowell, 1982). The second is the substitution of a more oxidation resistant low-pressure plasma-sprayed (LPPS) bond coat for the air plasma sprayed bond coat in the combustor. This modification of the bond coat fabrication method improves the performance by as much as 2.5 × due to its increased resistance to oxidation damage.

The cyclic thermal spallation life may be improved by altering ceramic compositions, residual stress control, and most importantly, careful control of ceramic microstructure (Duvall, 1977; Sumner and Ruckle, 1980; and Grot and Martyn, 1981). Progressive improvements have been made to the ceramic microstructure over the past 15 years (Grisaffe and Levine, 1979; Ruckle, 1979). A relatively dense plasma-sprayed ceramic coating portrays a typical brittle ceramic failure and a relatively short cyclic thermal stability life. By incorporating porosity and microcracking to the plasma-sprayed ceramic, the ceramic compliance is enhanced and the coatings have

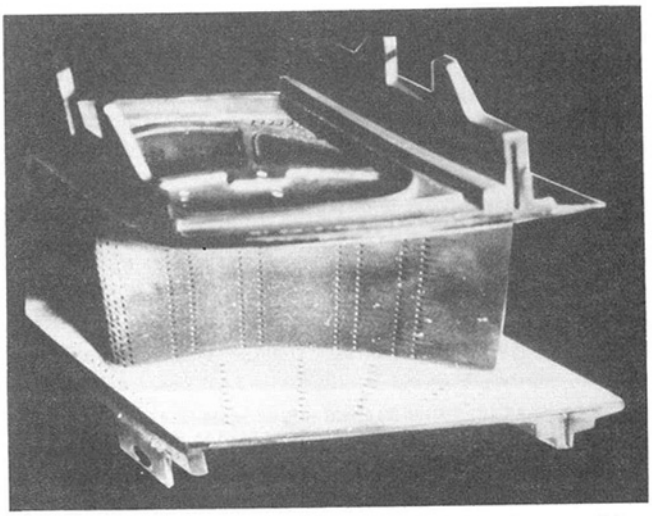


Fig. 11 JT9D-7R4G first-stage turbine vane is in excellent condition after 9300 hours flight engine service

greater spalling resistance than high-density coatings. The incorporation of a columnar structure further improves the coating durability life, offering improvements as much as 15 times more than the life of plasma-sprayed coatings. Plasma sprayed coating process studies have shown that a higher porosity level is usually associated with a coarse particle size (−120 mesh) and finer particle size (−325 mesh) is associated with denser structures. The ceramic composition is an important life critical parameter. As previously mentioned, by substituting yttria for magnesia in the stabilized zirconia combustor coatings, the life of the TBC was increased fourfold at temperatures above 1094°C. Controlling the state of residual stress in the coating is also an important life critical parameter. This can be controlled by careful regulation of the workpiece processing temperature. If the metal substrate is heated too high during coating application, the differential contraction of the substrate on cooling from the process temperature places the ceramic in excessive compression at room temperature, ultimately decreasing the coating durability significantly (Sheffler et al., 1982).

One of the first ground-based test engines to comparatively test the degrees of durability enhancement provided by this TBC was the JT9D first vane platforms (Fig. 10). The plasma-sprayed TBC coated vane platforms were operated side by side in the engine. After 1500 endurance test cycles, the coating without the ceramic insulating layer was removed due to burning and cracking damage as seen in Fig. 10(*a*). The vane in Fig. 10(*b*) was subsequently operated an additional 1278 cycles with little damage prior to termination of the test campaign. This comparative engine test clearly showed the durability enhancement supplied by the TBC.

This current generation plasma-deposited ceramic coating is designated PWA 264. Several million cumulative engine flight hours have been accumulated on turbine vanes in several engines. These engines include the JT9D, PW2037, the PW4000, and the V2500. The experience has been highly favorable (Fig. 11). The high time component has over 18,000 engine flight hours with the coating still in serviceable condition (Meier et al., 1990, 1991a).

EB-PVD Laboratory and Field Experience

As discussed previously, the PWA 264 plasma-sprayed ceramic coating has demonstrated acceptable life in commercial engines, but as turbine inlet temperatures continue to increase, an improved electron beam–physical vapor deposited (EB-PVD) coating was developed. As shown in Fig. 12, the structure produced by this process consists of individual, free-standing

Downloaded 02 Jun 2010 to 171.66.16.122. Redistribution subject to ASME license or copyright; see http://www.asme.org/terms/Terms_Use.cfm

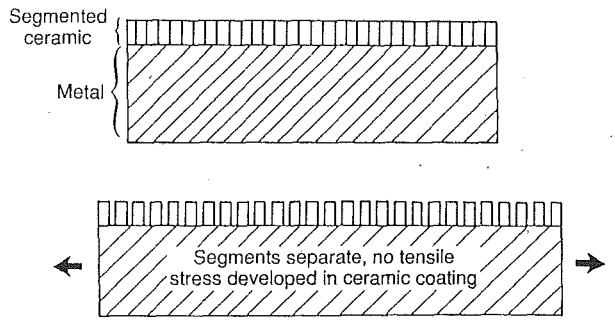


Fig. 12 Illustration of an idealized strain tolerant ceramic structure

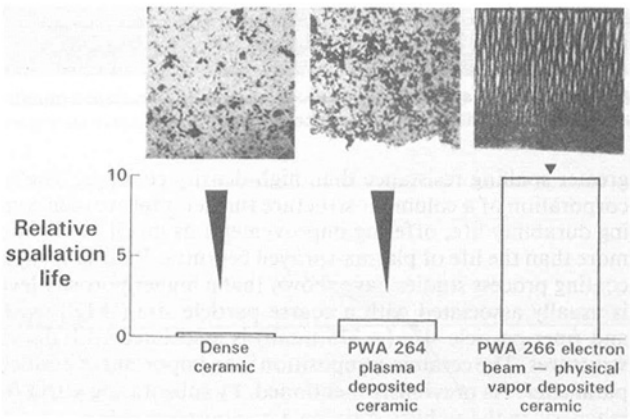


Fig. 13 The improvement in relative spallation life provided by modification of the ceramic microstructure: (*a*) dense ceramic; (*b*) plasma-deposited ceramic; (*c*) EB-PVD ceramic

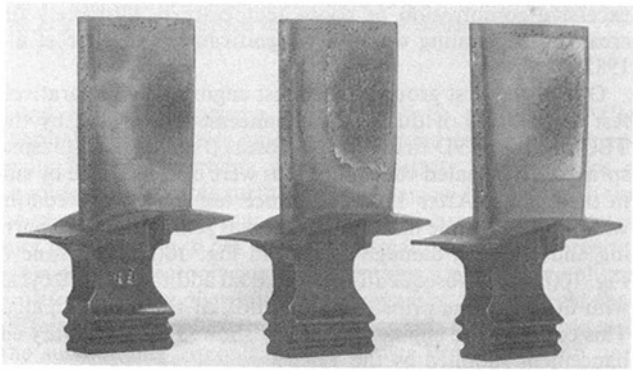


Fig. 14 The relative durability of (*a*) metallic coating, (*b*) plasma-deposited ceramic, and (*c*) EB-PVD ceramic as demonstrated in JT9D flight service. While the other samples show damage, the EB-PVD ceramic-coated turbine blade exhibits discoloration due to engine deposits.

ceramic columns, each of which is very tightly bonded to the substrate but essentially free to separate from adjacent columns as the substrate thermally expands relative to the ceramic. Consequently, this structure prevents the build-up of long range stresses. As previously mentioned, the most important element of improvement of ceramic spallation has been through the increased understanding and control of ceramic microstructure. The improvements to ceramic coating durability that have been achieved are summarized in Fig. 13 (Duvall, 1977; Sumner and Ruckle, 1980; Grot and Martyn, 1981). Whereas relatively

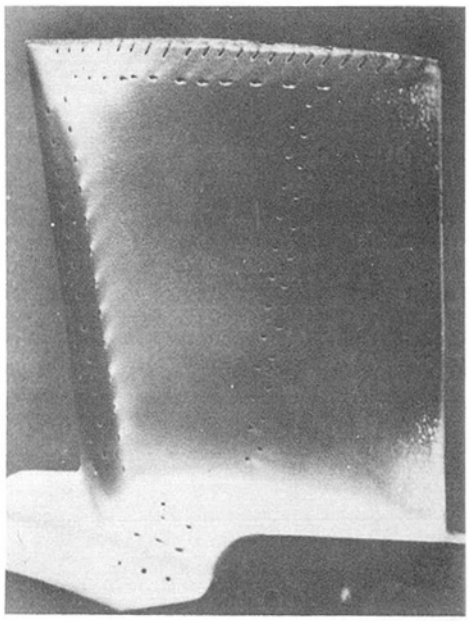


Fig. 15 An EB-PVD ceramic-coated PW2000 first-stage turbine blade exposed in a 150 hour endurance test. Color variations, and especially the mottled appearance near the tip of the trailing edge, are the result of engine deposits.

dense ceramic fails very quickly, the porous, microcracked plasma-deposited and columnar EB-PVD ceramic structures provide progressively increasing coating durability. The current embodiment of this EB-PVD ceramic TBC concept is designated PWA 266, and it incorporates EB-PVD 7 weight percent yttria partially stabilized zirconia over a low-pressure chamber-sprayed NiCoCrAlY bond coat.

The earliest engine demonstration of the EB-PVD ceramic durability benefit was achieved in flight service testing of this coating side-by-side with PWA 264 plasma-sprayed ceramic and nonceramic coated JT9D first turbine blades. As shown in Fig. 14, both the nonceramic and the PWA 264 plasma ceramic coated blade exhibited significant damage. The PWA 266 EB-PVD ceramic, on the other hand, was in good condition (Meier et al., 1990, 1991a).

Demonstration of the EB-PVD ceramic thermal benefit has been obtained in successful ground-based experimental engine testing on the PW2000 first turbine blade (Fig. 15) (Meier et al., 1991a). Earlier attempts to incorporate plasma-sprayed ceramic were unsuccessful due to the cyclic thermal spallation. This test not only demonstrated the durability against spallation in high strain, high heat flux environments, but it also allowed assessment of the thermal benefit by post-test metallographic evaluation. Base metal temperatures of adjacent ceramic and nonceramic coated blades showed the blade with 5 mils of ceramic operated up to 139°C cooler in the hot spot, thereby demonstrating a very substantial thermal benefit (Fig. 16) (Meier et al., 1990, 1991a).

Additional confirmation of the EB-PVD ceramic durability benefit has been obtained in field testing on JT9D second vanes. Without TBC, this vane can suffer significant thermal distress. Flight service evaluation has demonstrated that PWA 266 can reduce the thermal distress dramatically (Fig. 17). Based on this demonstration, PWA 266 EB-PVD ceramic was incorporated as bill-of-material on this part in mid-1989 (Meier et al., 1990, 1991a).

Further substantiation of the EB-PVD ceramic durability benefits was demonstrated in field testing on the JT9D-7R4 first-stage high turbine blades. Figure 18 shows a blade before engine operation and after nearly 4000 hours of hot operation.

Downloaded 02 Jun 2010 to 171.66.16.122. Redistribution subject to ASME license or copyright; see http://www.asme.org/terms/Terms_Use.cfm

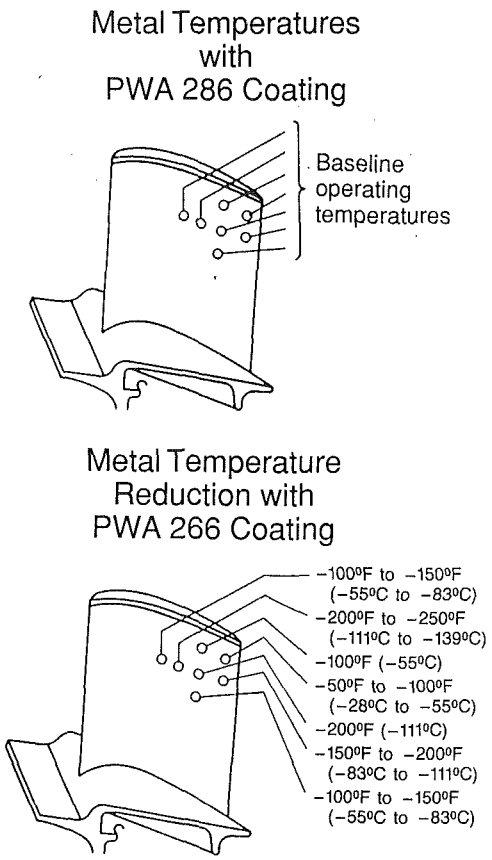


Fig. 16 PW2000 engine demonstration of PWA 266 EB-PVD ceramic durability and temperature reduction benefits

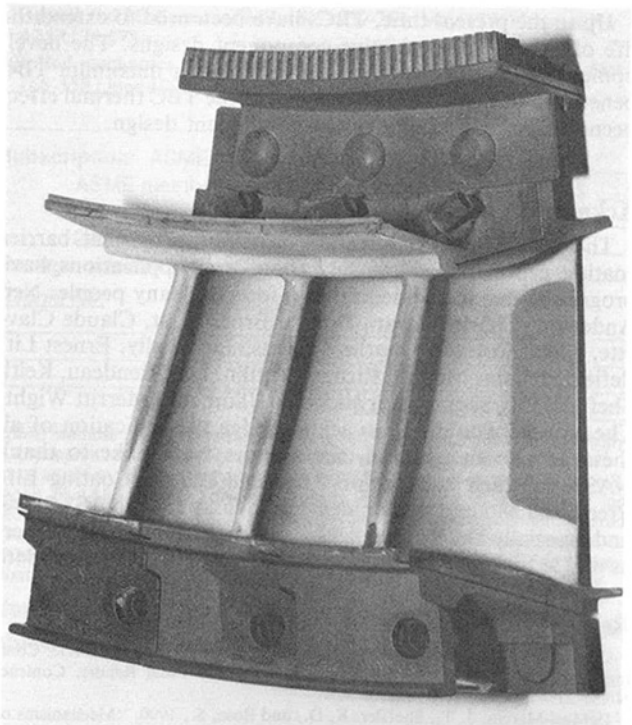


Fig. 17 A JT9D-7Q second-stage turbine vane after 4200 hours of field service, which is known to cause significant degradation of uncoated vanes. This vane was coated with EB-PVD ceramic.

This engine test provided dramatic evidence of the durability of the ceramic and was incorporated as bill-of-material on this part in 1990.

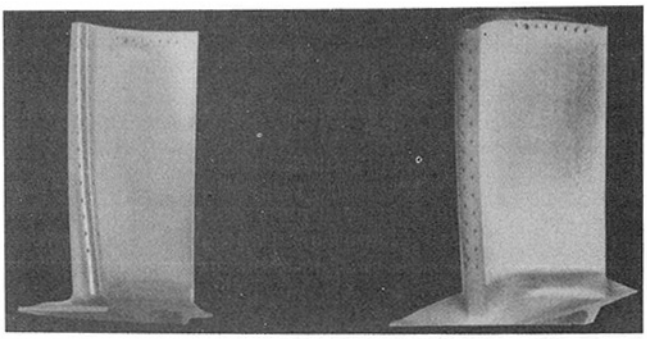


Fig. 18 A JT9D first-stage turbine blade (*a*) before engine exposure and (*b*) after 3085 hours of field service

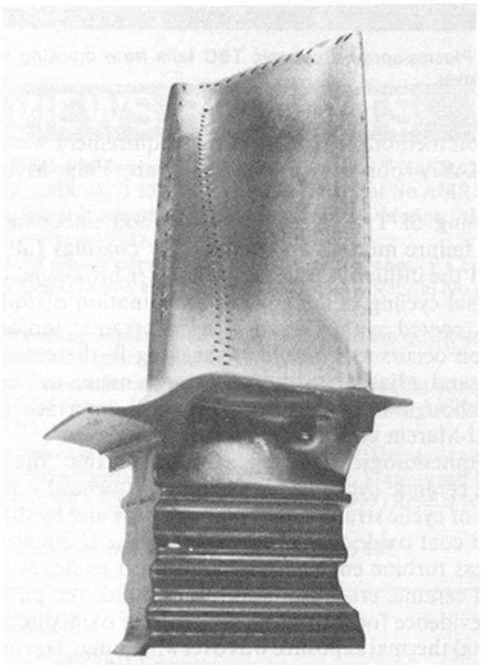


Fig. 19 A PW4000 first-stage turbine blade after ground-based engine testing shows improved durability

Ground-based experimental engine testing on the PW4000 first turbine blade (Fig. 19) has shown significant increases in component durability. No appreciable reduction of cooling airflow was evident after deposition of the EB-PVD ceramic coating. This is in contrast to an essentially 100 percent closure of the cooling holes when plasma-sprayed ceramic is applied.

The EB-PVD ceramic TBC offers numerous advantages in addition to minimal reduction of flow. Aerodynamically, the most important benefit is the smooth surface finish. This is achieved because the EB-PVD ceramic structure duplicates the surface finish of the substrate on which it is applied. In contrast, plasma-sprayed TBCs require a mechanical surface finishing after deposition. In terms of processing the EB-PVD process provides a more reproducible coating by the control of process parameters as opposed to the plasma-sprayed process.

TBC Life Prediction Modeling

Achievement of the maximum TBC benefit potential will require incorporation of the TBC thermal effect as an integral element of initial component design. This will in turn require development of a TBC design system and supporting TBC life

Downloaded 02 Jun 2010 to 171.66.16.122. Redistribution subject to ASME license or copyright; see http://www.asme.org/terms/Terms_Use.cfm

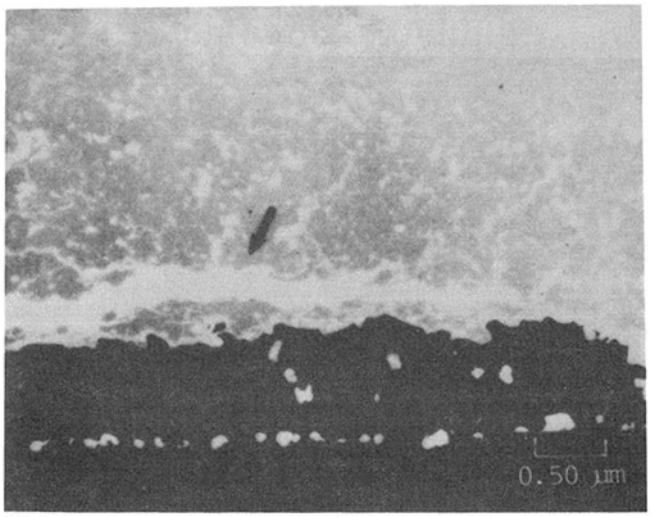


Fig. 20 Plasma-sprayed ceramic TBC fails from cracking within the ceramic layer

prediction methodology. This latter requirement was pursued under NASA sponsorship (DeMasi et al., 1989; Meier et al., 1991b).

Modeling of TBC life requires a good understanding of coating failure modes. Thermal barrier coatings fail by spallation of the insulative ceramic layer after prolonged exposure to thermal cycling in the engine. Examination of failed components coated with plasma-sprayed ceramic indicates that spallation occurs as a result of cracking in the ceramic layer parallel and adjacent to the very rough metal-ceramic interface, although not coincident with this interface (Fig. 20) (DeMasi-Marcin et al., 1990).

Phenomenological evidence indicates that the plasma-sprayed ceramic cyclic life is strongly influenced both by the severity of cyclic strain in the ceramic phase and by the amount of bond coat oxide that results from cyclic thermal exposure in the gas turbine engine. While no direct evidence of oxide-induced ceramic crack initiation was found, the phenomenological evidence for the strong influence of oxidizing (and only oxidizing) thermal exposure was overwhelming. The interactive life model developed for plasma-sprayed ceramic was designed to account for both the oxidative and mechanical forms of TBC degradation (DeMasi et al., 1989).

Engine failure of EB-PVD ceramic occurs by cracking associated with the thermally grown oxide layer that forms at the interface between the insulative zirconia ceramic and the underlying metallic bond coat (Fig. 21). While this layer is predominantly aluminum oxide, it also may incorporate oxides of other bond coat or substrate metals such as nickel, cobalt, chromium, etc. (Meier et al., 1990, 1991b).

Past experience with plasma-sprayed TBC indicated that inelastic deformation of the ceramic was a critical life parameter. However, nonlinear analysis of the EB-PVD ceramic behavior during thermal cycling indicated that the EB-PVD ceramic remained elastic. For that reason and because spallation failure of the EB-PVD TBC system is caused by cracking at the thermally grown oxide/metallic bond coat interface, life modeling efforts for the EB-PVD coating have used TGO elastic strains instead of EB-PVD ceramic strains (Meier et al., 1991b).

Laboratory generated EB-PVD thermal barrier coating cyclic thermal test results have been used to define a fatigue life model to correlate the TBC spallation lives (Meier et al., 1991b). The fatigue model includes the combined effects of cyclic thermal loading and oxide scale growth due to elevated temperatures during test. The model is the same as that used in the evaluation of plasma-sprayed thermal barrier coatings except

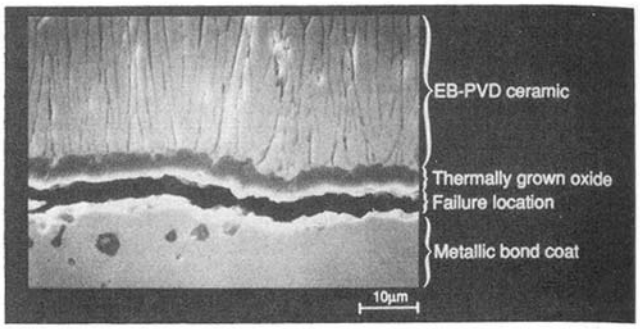


Fig. 21 Ceramic EB-PVD TBC fails from cracking at the thermally grown oxide/bond coat layer

the mechanical damage parameter in the EB-PVD model is the thermoelastic stress within the actual oxide layer, where spallation fracture occurs.

Summary

The thermal insulation benefit provided by plasma-deposited zirconia thermal barrier coatings (TBC) extends the durability of gas turbine engine combustors. Improvements to the underlying metallic bond coat, the ceramic composition, and the ceramic microstructure have lead to the use of TBCs in the turbine section of the engine. More recent optimization of the composition and processing for increased durability electron beam-physical vapor deposited zirconia has allowed TBCs to be successfully utilized in the most demanding stationary and rotating components. Production of JT9D vanes and blades with EB-PVD ceramic commenced in mid-1989. Performance of this coating in the field has been highly favorable and has led to more widespread use in developmental situations.

Up to the present time, TBCs have been used to extend the life of existing or derivative component designs. The development of a TBC design system is allowing maximum TBC benefits to be achieved in the engine as the TBC thermal effect becomes an integral part of the component design.

Acknowledgments

The state-of-the-art advances in ceramic thermal barrier coating processing, characterization, and applications have progressed due to the dedicated efforts of many people: Neil Anderson, Charles Bevan, Donald Broadhurst, Claude Clavette, Glenn Cotnoir, Charles Giggins, Jack Lally, Ernest Littlefield, Jeanine Marcin, Richard Mullin, Leo Riendeau, Keith Sheffler, Ray Skurzewski, Nicholas Ulion, and Merritt Wight. The authors would like to acknowledge the dedication of all these people. In addition, the authors would like to thank NASA for their support of "Thermal Barrier Coating Life Prediction Model Development" under contract NAS3-23944 and especially Dr. Robert A. Miller, NASA program manager, as well as the Navy for support on contract N00140-90-C-1846.

References

DeMasi, J. T., Ortiz, M., and Sheffler, K. D., 1989, "Thermal Barrier Coatings Life Prediction Model Development," Phase I Final Report, Contract NAS3-23944, NASA CR-182230.

DeMasi-Marcin, J. T., Sheffler, K. D., and Bose, S., 1990, "Mechanisms of Degradation and Failure in a Plasma-Deposited Thermal Barrier Coating," ASME Journal of Engineering for Gas Turbines and Power, Vol. 112, pp. 521-526.

Duvall, D. S., 1977, "Processing Technology for Advanced Metallic and Ceramic Turbine Airfoil Coating," *Proc., Second Conf. on Advanced Materials for Fuel Capable Heat Engines*, Palo Alto, CA, Electric Power Research Institute, pp. 6-102.

Duvall, D. S., and Ruckle, D. L., 1982, "Ceramic Thermal Barrier Coatings for Turbine Engine Components," ASME Paper No. 82-GT-332.

Downloaded 02 Jun 2010 to 171.66.16.122. Redistribution subject to ASME license or copyright; see http://www.asme.org/terms/Terms_Use.cfm

Grisaffe, S. J., and Levine, S. R., 1979, *Proc. First DOE/EPRI Conf. on Advanced Materials for Alternative Fuel Capable Directly Fired Heat Engines*, Palo Alto, CA, Electric Power Research Institute, p. 680.

Grot, A. S., and Martyn, J. K., 1981, "Behavior of Plasma-Sprayed Ceramic Thermal Barrier Coatings for Gas Turbine Applications," *ACerS Bull.*, Vol. 60, No. 8, p. 807.

Liebert, C., et al., 1976, "Durability of Zirconia Thermal Barrier Ceramic Coatings on Air Cooled Turbine Blades in Cyclic Jet Engine Operation," NASA TM X-3410.

Meier, S. M., Nissley, D. M., and Sheffler, K. D., 1990, "Status of Ceramic Thermal Barrier Coatings—Gas Turbine Applications and Life Prediction Methods," *Proceedings of the 1990 Coatings for Advanced Heat Engines Workshop*, CONF-9008151, Castine, ME.

Meier, S. M., Gupta, D. K., and Sheffler, K. D., 1991a, "Ceramic Thermal Barrier Coatings for Commercial Gas Turbine Engines," *JOM*, pp. 50–53.

Meier, S. M., Nissley, D. N., and Sheffler, K. D., 1991b, "Thermal Barrier Coating Life Prediction Model Development," Phase II Final Report, Contract NAS3-23944, NASA CR-189111.

Miller, R. A., and Lowell, C. E., 1982, "Failure Mechanisms of Thermal Barrier Coatings Exposed to Elevated Temperature," *Thin Solid Films*, Vol. 99, p. 265.

Ruckle, D. L., 1979, "Evaluation of Plasma-Sprayed Ceramic Coatings for Turbine Engine Components," *Thin Solid Films*, Vol. 64, p. 327.

Sheffler, K. D., Graziani, R. A., and Sinko, G. C., 1982, "JT9D Thermal Barrier Coated Vanes," Final Report, Contract No. NAS3-20630, NASA CR-167964.

Sheffler, K. D., and Gupta, D. K., 1988, "Current Status and Future Trends in Turbine Application of Thermal Barrier Coatings," ASME JOURNAL OF ENGINEERING FOR GAS TURBINES AND POWER, Vol. 110, pp. 605–609.

Stecura, S., 1979, "Effect of Compositional Changes on the Performance of a Thermal Barrier Coating System," NASA TM-78976.

Strangman, T. E., 1982, U.S. Patent No. 4,321,311, "Columnar Grain Ceramic Thermal Barrier Coatings."

Sumner, I. E., and Ruckle, D. L., 1980, "Development of Improved Durability Plasma Sprayed Ceramic Coatings for Gas Turbine Engines," AIAA Paper No. 80-1193.

Downloaded 02 Jun 2010 to 171.66.16.122. Redistribution subject to ASME license or copyright; see http://www.asme.org/terms/Terms_Use.cfm

Microstructural Investigations of Plasma-Sprayed Yttria Partially Stabilized Zirconia TBC (In Relation to Thermomechanical Resistance and High-Temperature Oxidation Mechanisms)

S. Alpérine[1]

L. Lelait[2]

O.N.E.R.A. Materials Science Department,
B.P. 72,
92322 Chatillon Cedex, France

This study deals with microstructural investigations of plasma-sprayed yttria partially stabilized zirconia thermal barrier coatings, performed by classical and analytical transmission electron microscopy. The aim of the study was to determine eventual relationships between coating microstructure and toughness. The ceramic/metal interface, which plays an important role during TBC thermomechanical solicitation, has also been studied. In the 6–8 wt. percent Y_2O_3 range, the metastable tetragonal t' phase is observed, showing special faulted microstructural features, such as grain twinning and antiphase boundary planes. Moreover, after high-temperature annealing in air, a very fine and stable precipitation of the equilibrium cubic phase appears. It is believed that these microstructural elements could act as crack deviation sites and enhance the coatings' intrinsic toughness. Microstructural investigations of the alumina scales grown during high-temperature annealing reveal yttrium segregation at oxide grain boundaries as well as significant quantities of zirconium inside the alumina grains. The oxide growth seems to be dominated by a classical grain boundary oxygen diffusion mechanism. The presence of zirconium inside the alumina grains suggests that Al_2O_3 also partially forms by chemical reduction of ZrO_2 by Al.

Introduction

Yttria stabilized zirconia (YPSZ) ceramic coating are currently used for thermal insulation of hot stage gas turbine superalloy components, the current challenge being the application of TBC on rotating parts (Levine and Miller, 1982). The most critical requirements for the application of such ceramic coatings on metallic substrates are, on the one hand, a high intrinsic thermomechanical resistance of the ceramic and, on the other, a high bond strength between the metallic bond coat and the ceramic overlayer (Miller et al., 1981).

It is widely believed that in the case of yttria partially stabilized zirconia top coat, plasma sprayed on a metallic bond coat, oxide scale growth at the ceramic/metal interface is a major factor contributing to interfacial strength. However, very few studies in the literature try to interpret this interfacial strengthening phenomenon in relation to structural investigations at a microscopic level.

It is also well known that the thermomechanical resistance of thermal barrier coatings in the zirconia–yttria system is strongly dependent upon the amount of yttria added to the zirconia (Stecura, 1985; Miller et al., 1981, 1983). It is generally observed that the coating lifetime in high-temperature cyclic conditions shows a sharp maximum at intermediate yttria contents, which correspond to zirconia partial stabilization (7–8 wt. percent Y_2O_3) associated with the presence of a nonequilibrium tetragonal t' phase. At higher yttria contents corresponding to the fully stabilized zirconia cubic phase, the thermomechanical resistance of the coatings drops significantly (Fig. 1, reproduced from Stecura, 1985). The usual explanation of this phenomenon is twofold: first, the t' phase obtained during plasma spraying for yttria partially stabilized zirconia TBC is a metastable phase, which does not easily decompose into the equilibrium $t+c$ phases (see Fig. 2, reproduced from Scott, 1975) and consequently does not undergo martensitic transformation into monoclinic. Second, the intrinsic toughness of the t' phase is believed to be higher than that of the

[1]Present address: SNECMA Materials and Process Department, RN7, B.P. 81, 91003 Evry Cedex, France.

[2]Present address: Electricité de France, Materials Science Department, Centre des Renardières, B.P. 01, Ecuelle 77250 Moret-sur-Loing, France.

Contributed by the International Gas Turbine Institute and presented at the 37th International Gas Turbine and Aeroengine Congress and Exposition, Cologne, Germany, June 1–4, 1992. Manuscript received by the International Gas Turbine Institute February 24, 1992. Paper No. 92-GT-317. Associate Technical Editor: L. S. Langston.

Copyright © 1994 by ASME
Downloaded 02 Jun 2010 to 171.66.16.122. Redistribution subject to ASME license or copyright; see http://www.asme.org/terms/Terms_Use.cfm

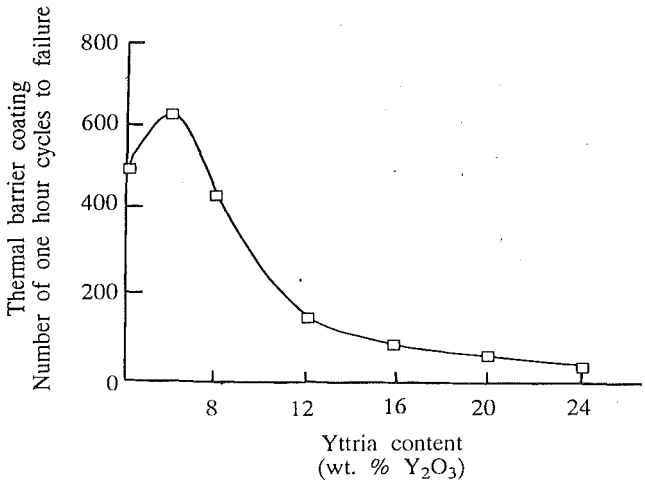


Fig. 1 Influence of Y_2O_3 content in ZrO_2 on thermomechanical resistance of thermal barrier coatings in cyclic oxidation conditions (from Stecura, 1985)

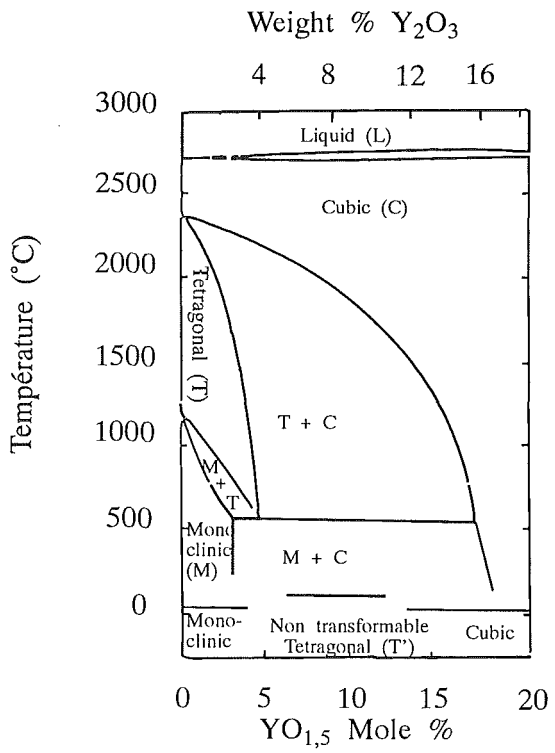


Fig. 2 Low yttria region of the zirconia-yttria phase diagram (from Scott, 1975)

FSZ cubic phase (Michel et al., 1983). However, to our knowledge, the reasons t' is tougher than c phase remain unclear and are not well documented in the literature. A possible answer to this particular question could be found through microstructural investigations of both cubic and t' phases. However, although many fundamental studies have been devoted to the mechanical resistance and microstructure of monolythic zirconia base ceramics (Garvie et al., 1975; Gupta et al., 1977; Anderson and Gupta, 1981; Butler, 1985; Lanteri, 1986; Lanteri et al., 1986), only a few studies report fine microstructural investigations of plasma-sprayed zirconia TBC (Trémouille et al., 1986; Suhr et al., 1984).

In this paper, we try to draw a synthesis of several recent studies (Lelait and Alpérine, 1991; Lelait et al., 1991; Lelait, 1991) whose general scope was twofold. Attempts were made to shed some light on the high thermomechanical resistance of the ZrO_2-8 wt. percent Y_2O_3 nonequilibrium t' phase in plasma-sprayed TBC through examination of its fine microstructure. We also tried to evaluate the influence of oxide scale formation mechanisms on the strength of the zirconia/bond coat interface. To this end, crystallographic and analytical examinations of coating fine microstructures were obtained by conventional, analytical, and high-resolution transmission electron microscopy on transverse thin foils, of plasma-sprayed YPSZ coatings. The influence of high-temperature annealing on the microstructural features of the coatings and on the formation of an interfacial oxide scale has also been studied.

Experimental

The substrates used were $25 \times 40 \times 2$ mm^3 coupons of Hastelloy X superalloy (Ni-22Cr-18.5Fe-6Ta-9Mo-1.5Co-0.6W-0.1C-0.5Si, wt. %), which were grit-blasted (Al_2O_3 220 mesh, 2 bars) and degreased (vapor phase trichloroethylene). The substrates were first coated with a 100 μm thick NiCrAlY bondcoat deposited by low-pressure plasma spraying (from Ni-23Cr-6Al-0.5Y wt. %, AMDRY 963 powder). The samples were then heat treated during four hours at 1080°C under secondary vacuum ($P_{tot} < 10^{-5}$ Torr) for bondcoat diffusion and finally covered with a 300 μm thick layer of air plasma-sprayed ZrO_2-8.5 wt. % Y_2O_3 (starting from MEL SCZ8 powder). Isothermal annealing of the specimen was carried out at 1100 or 1200°C in a tube furnace, in air, for 100 hours, followed by an air quench.

Transverse thin foils for transmission electron microscopy (TEM) were prepared following a procedure derived and adapted from the one described by King et al. (1984). This procedure is explained in full detail elsewhere (Lelait et al., 1989). Samples were studied using conventional and high-resolution microscopy with Jeol 200CX and 4000FX microscopes, the latter equipped with a S.T.E.M. unit. HREM images were digitized with a video camera and processed using Fourier filtering, for signal-to-noise ratio enhancement. The distributions of the alumina grain sizes and anisotropy were determined by image analysis routines from a population of at least 100–150 grains. Grain size determination refers to the diameter of equivalent circular grains (computed from an area/perimeter ratio); anisotropy of the grains refers to the ratio of their Feret radii. Chemical microanalysis was performed on the thin foils by E.D.S. technique (KEVEX device equipped with a "Quantum" diode) using a probe diameter of about 10 nm. Moreover, a Gatan 666 magnetic prism spectrometer for parallel simultaneous detection of electron energy losses (P.E.E.L.S) was used. All such measurements were made in diffraction mode, with a collecting angle β of 15.0 mrad. The recorded spectra were calibrated for cell collecting efficiency following a standard procedure; background was subtracted by a least-square, fitting procedure, assuming a classical exponential decay.

Microstructure of As-Sprayed and Annealed t' Phase

As-Sprayed Specimens. The ceramic coating is composed of a single metastable t' tetragonal phase. This phase is, indeed, crystallographically very close to the equilibrium cubic phase, since its c/a ratio only differs from unity by around 1.3 percent (Lelait et al., 1989). At the level of magnification of TEM observations, the coating is composed of small, well-defined elongated t' grains (typically 1×0.25 μm^2). Indeed, the tetragonality of the t' phase is revealed in diffraction mode by the presence of weak reflections of the type {odd, odd, even} (with the relevant index permutations). Imaging of the t' phase is hence achieved with the *dark field* technique using these reflections. These conditions are used in Fig. 3. Inside this t' grain (and, generally speaking, inside all t' grains), one can

Downloaded 02 Jun 2010 to 171.66.16.122. Redistribution subject to ASME license or copyright; see http://www.asme.org/terms/Terms_Use.cfm

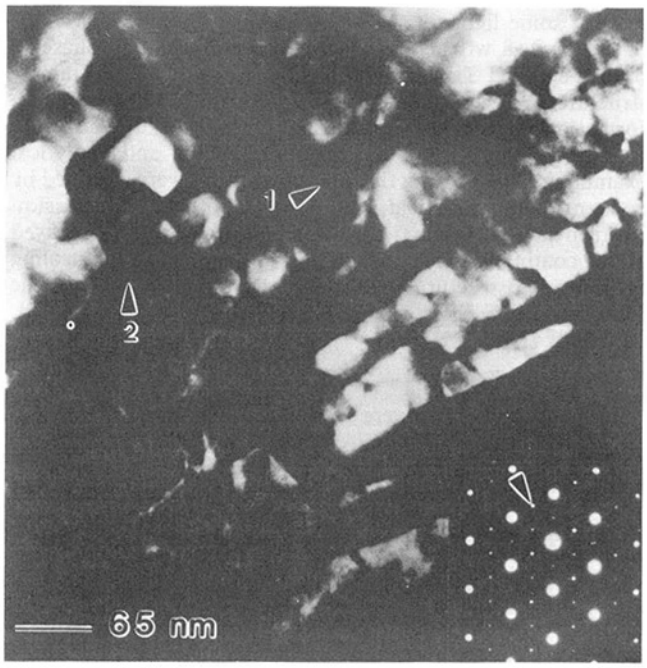


Fig. 3 Dark field image and diffraction pattern of a tetragonal t' grain with ⟨111⟩ zone axis; $g = \{112\}$; (1) extinguished twin, (2) APB; the arrow in the diffraction pattern indicates {112} spot

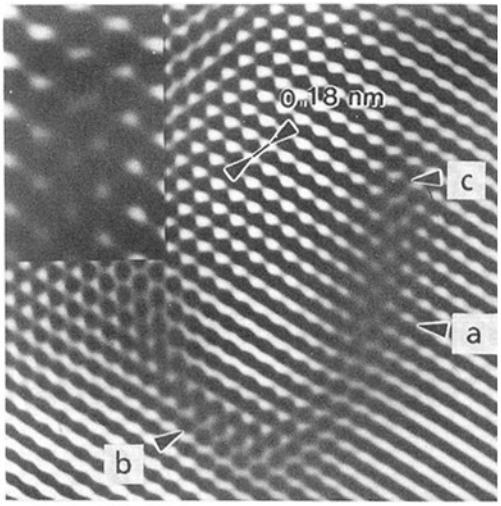


Fig. 4 HREM image of an APB edge on (*a*), twisting inside the foil (*b*), and ending in the t' grain (*c*); the zone axis is ⟨110⟩

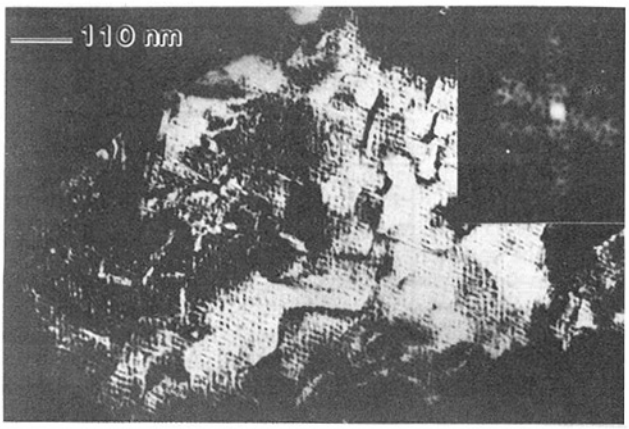


Fig. 5 Microstructure of samples annealed 100 h at 1100°C; dark field image with ⟨110⟩ zone axis; $g = \{112\}$

observe two particular microstructural features: twinning of the grain and a domain structure inside each difracting twin; these elements of the microstructure will be explained below.

One can see in Fig. 3 that for a given selected reflection, some twins appear bright while the others remain dark. However, when the three first-order {odd, odd, even} reflections are consecutively selected, it is possible to lighten the whole t' grain in sequence. This twin microstructure is a consequence of the theoretically equal probability that the small distortion of the cubic lattice leading to the tetragonal symmetry be along any of the three original ⟨100⟩ cubic axes. When the high-temperature cubic phase transforms into t', nucleation occurs leading to individuals having three possible orientations of their tetragonal fourfold axis (relative to their former cubic unit cell). The tetragonal distortion of the cubic lattice then propagates, leading to a globally tetragonal t' grain divided into a limited number of tetragonal variants (usually in the order of magnitude of ten per grain).

The domain microstructure inside the twins, observed in Fig. 3, arises because of the lowering of the crystal symmetry during the $c \rightarrow t'$ transformation (Lelait and Alpérine, 1991). If two t' domains, one nucleated at (0, 0, 0) in the parent cubic cell and the other at (1/2, 0, 1/2) or (0, 1/2, 1/2), grow and come into contact, they will be separated by an antiphase boundary (APB). This APB contrast is clearly observed inside the different variants in Fig. 3. It is to be noted that APB lines generally tend to curve. A high resolution image of an APB in a t' grain is visible on Fig. 4. The ending of this APB is further magnified in the box inside Fig. 4; the dislocations that encapsulate the APB are clearly visible.

Annealed Samples. The two main microstructural features observed on as-sprayed specimens are also present after annealing at 1100°C for 100 hours (Fig. 5). The APB structure has somewhat varied: The boundaries have straightened. This is a classical ripening phenomenon leading to a minimal energy configuration; the basal plane of the APBs tends to follow low-order crystallographic planes. A new important microstructural feature has appeared during annealing. Inside all t' grains, the precipitation of a second phase is observed. The precipitates are very fine and well defined (Fig. 5); they form a "tweed" microstructure. The typical size of the precipitates is of the order of 10×6 nm^2. The box in Fig. 5 presents a numerical diffraction pattern of the grain (Fraunhoffer diffraction). This diffraction pattern reveals that the precipitates are arranged on a pseudoperiodic lattice with an intermediate range positional and orientational order. The peculiar arrangement of the precipitates forming the tweedlike structure could be one solution that minimizes the total elastic strain energy, by the creation of a BCC pseudonetwork (pseudocell parameter ≈ 20 nm) where local strains generated by many individuals cancel out (Katchaturyan and Shatalov, 1968; Wen et al., 1981). It is likely (Lelait, 1991) that these precipitates, which contain more yttrium than the matrix, are composed of the equilibrium cubic phase, which appears as soon as solid-state diffusion has allowed the migration of yttrium ions. The appearance of these precipitates can thus be looked at as the first stage of the return to equilibrium of the t' phase. It is important to note that these precipitates also appear after 100 h annealing at 1200°C and that *they do not age during further annealing at this temperature*. After 500 hours their typical dimension has scarcely varied.

Discussion

It is important to note that the three microstructural features described above (t' twins + APB + tweed microstructure) can

Downloaded 02 Jun 2010 to 171.66.16.122. Redistribution subject to ASME license or copyright; see http://www.asme.org/terms/Terms_Use.cfm

only be obtained under two conditions. Firstly, suitable chemical composition of the ceramic coating must be used (the range of yttria content where zirconia is partially stabilized). Secondly, its deposition process must involve high quenching rates (plasma spraying) or evaporation on a cold substrate (such as PVD methods). The twinning inside the grains as well as the APB structure can only appear during a solid-solid phase transformation involving a decrease of the symmetry (for instance the $t' \rightarrow c$ reaction); in the yttria–zirconia system, such a transformation can only occur for partially stablized zirconia, if the t' phase is quenched during the elaboration process (this is the case during plasma spraying). In the same way, the appearance of the "tweed microstructure" is related to a slow decomposition of the t' phase; this microstructure thus requires the pre-existence of a metastable, quenched phase. Indeed, none of these microstructural features are expected in cubic Y–FSZ since, in this case, no phase transformation occurs upon cooling (twins, APB) and no metastable phase is retained at room temperature (tweed). They have actually been unsuccessfully looked for in a recent study (Lelait, 1991).

The fact that special microstructural elements are being observed in the t' region of the zirconia–yttria phase diagram, which cannot be observed in the high yttrium content cubic region, may help to understand the high intrinsic toughness of the t' phase, with its associated microstructure; it could, in fact, be thought of in terms of structural toughening, i.e., the ability of a t' grain to dissipate crack propagation energy. A crack propagating in a zirconia grain will follow one of the easiest cleavage planes. In the FCC cubic cell these planes are the eight ⟨111⟩ planes. In a tetragonal phase such as t', this situation differs somewhat. A projection of the crystallographic cell along the ⟨100⟩ axis is shown schematically in Fig. 6. Atomic bonds are there of two different kinds: shorter bonds (more energetic) and longer bonds (easier to break). One can see in Fig. 6 that some planes normal to the fourfold axis of the tetragonal cell only intercept low energy bonds. These planes could be the ones along which a crack would propagate with a minimum consumption of crack energy. These planes are less numerous in a tetragonal cell than ⟨111⟩ planes in a cubic cell (which is due to the fact that the medium has a lower symmetry). A first consequence of this is that a crack meeting a twin boundary must deviate at right angles, since the tetragonal c axes are orthogonal to each other in two neighboring twins. Also, the propagation of a crack through an APB is likely to consume some energy, for similar reasons. This analysis finds some support in the work by Michel et al. (1983), dealing with toughness measurements and fracture of cubic and t' zirconia single crystals, the latter showing a twin structure similar to the one described here. These authors indicate that the intrinsic toughness of t' is about three times that of the cubic phase.

Let us now consider the propagation of a crack in a t' grain having developed the "tweed" microstructure. The crack tip is likely to deviate each time it meets a precipitate, for two reasons. First, the easy cleavage plane differs in the t' matrix and in the cubic precipitate, so that the crack should deviate from $(100)_t$, or $(010)_t$, to $\langle 111 \rangle_c$. Second, before meeting the precipitate, the crack tip will meet the stress field developed near the interface between the matrix and the precipitate. No exact calculation of this stress field is currently available, but it is high enough to prevent the cubic precipitates from growing beyond a critical size of about 10 nm at 1200°C, in our case. This stress field could well also oblige the crack to bypass the precipitate. So we see that chances are that the tweed microstructure is able to dissipate a lot of crack propagation energy, by a mechanism related to "microcomposites."

It should be noted here that the fact that the precipitates are of cubic symmetry does not account for the toughening mechanism described here above. The authors suggest that this is the stress field generated by mismatch between matrix and

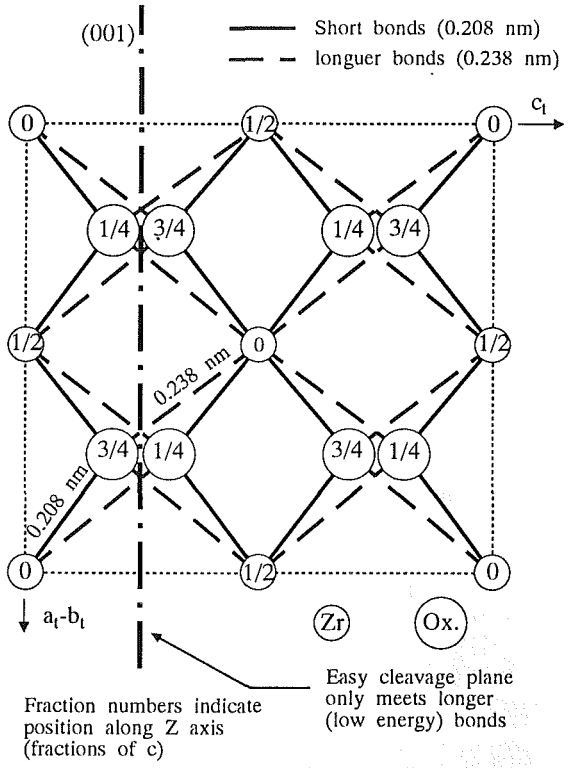


Fig. 6 Schematic representation of a t' crystallographic cell; projection along (100) axis; existence of an easy cleavage plane perpendicular to (001)

precipitates, whatever their respective crystallographical nature and intrinsic toughness, which could make the crack "zig-zag" through the "pseudo-ordered" network of the precipitates and consume an important amount of propagation energy. This mechanism is made possible by the fact that the tweed precipitates are themselves stabilized by the stress field at temperatures up to 1200°C. At higher temperatures (1300°C and above, cf. Lelait, 1991), the stress field no longer constitutes a high enough potential barrier to prevent solid-state yttrium diffusion; the cubic precipitates grow, leading to a progressive disruption of the tweed microstructure and transformation of the matrix t' into the stable, low yttrium content, tetragonal t phase.

Oxidation Mechanisms and Interfacial Strength

During annealing, an α-alumina scale grows between the NiCrAlY bondcoat and the zirconia topcoat. After 100 hours at 1200°C the thickness of the scale is 6 ± 0.5 μm.

Oxide Scale Morphology and Microstructure. Typical bright field micrographs of the alumina scale grown at 1200°C and representative of its inner region (close to the NiCrAlY/Al_2O_3 interface) can be seen on Fig. 7. Micrographs taken in the median and external regions (close to the zirconia/Al_2O_3 interface) can be seen in Figs. 7(*b*) and 7(*c*), respectively. The morphology of the oxide scale significantly changes throughout its thickness. Close to the NiCrAlY, the alumina grains are elongated (typical aspect ratio between two and four), columnar, and display numerous intergranular pores, whereas near the Al_2O_3/ZrO_2 interface, they are smaller, more equiaxed (typical aspect ratio between one and two) and pore free. In the inner region of the alumina scale, besides the microvoids mentioned above, defects such as dislocation pile-ups can be seen, as well as low angle grain boundaries (Fig. 7*d*). Very fine spinel oxides ($Ni(Al, Cr)_2O_4$ according to S.A.D. observations and E.D.S. analysis) have also been detected in this region.

Downloaded 02 Jun 2010 to 171.66.16.122. Redistribution subject to ASME license or copyright; see http://www.asme.org/terms/Terms_Use.cfm

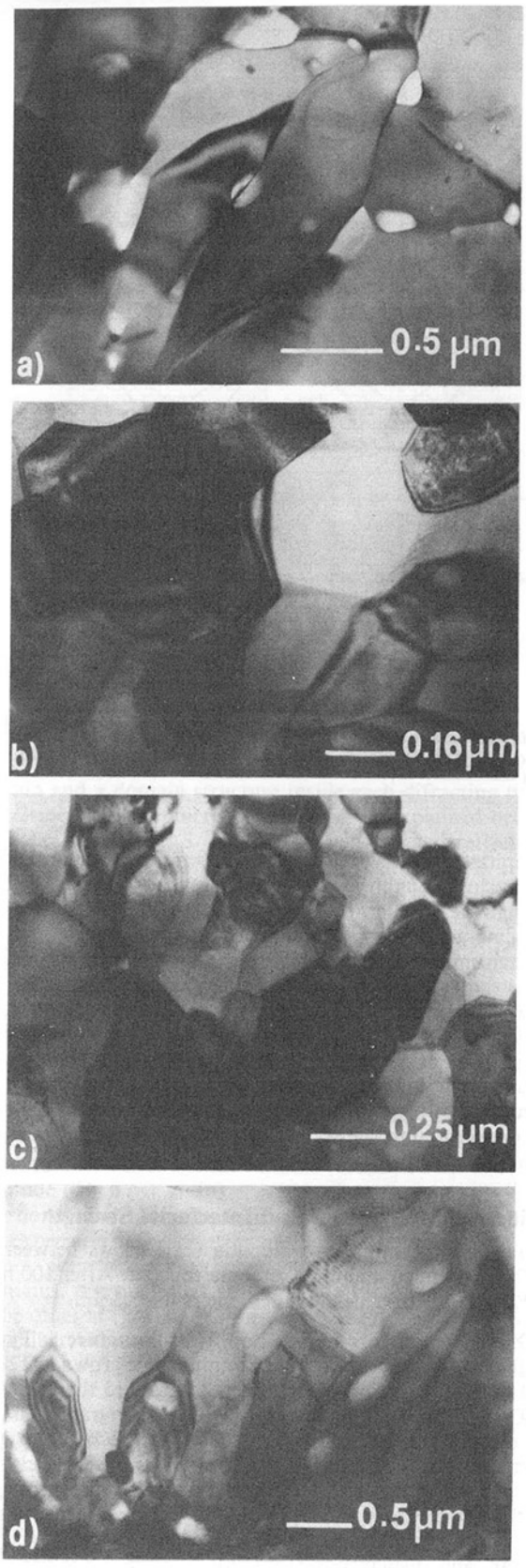


Fig. 7 Microstructure of the alumina scale grown during 100 h annealing at 1200°C in air; (*a*) near NiCrAlY/Al_2O_3 interface, (*b*) median zone, (*c*) near Al_2O_3/ZrO_2 interface, (*d*) typical defects near NiCrAlY/Al_2O_3 interface

At the zirconia/alumina interface there is a fine dense microstructure of small equiaxial grains (Fig. 7*c*): $(Al, Cr)_2O_3$, $Ni(Al, Cr)_2O_4$ spinels, and NiO. Inside these alumina grains,

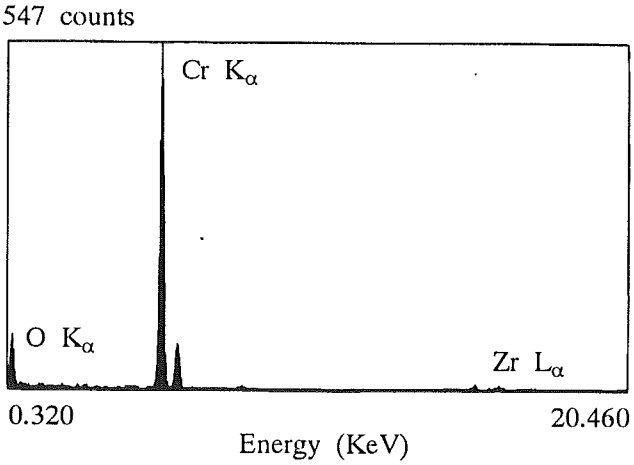


Fig. 8 E.D.S. analysis of a chromia grain near the MCrAlY/Al_2O_3 interface

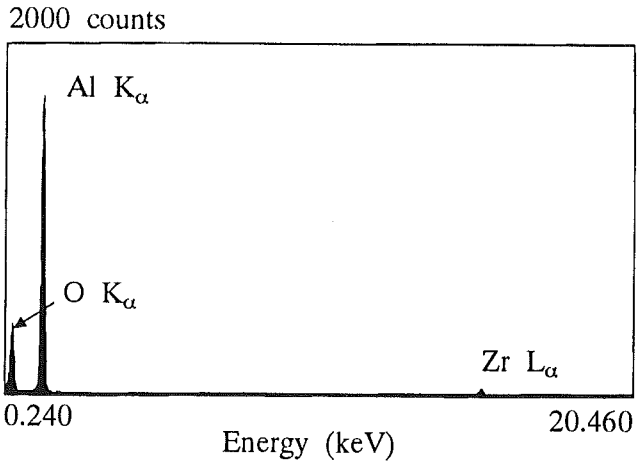


Fig. 9 E.D.S. analysis in an alumina grain showing the presence of zirconium

small round ZrO_2 inclusions have been identified by E.D.S. This coexistence of zirconia grains with aluminum-based oxides is not really surprising. Is a consequence of the "roughness" of the ZrO_2/Al_2O_3 interface: The zirconia "islands" are not inclusions but indeed connected to the ceramic layer, the connection path being located below or above the cross section plane.

The distributions of grain sizes, determined from T.E.M. observations, show that the average grain size regularly increases from the scale external surface to the oxide–metal interface. After 100 h at 1200°C, the distribution of alumina grains near the alumina/zirconia interface is relatively sharp, the grain sizes ranging from 0.02 to 0.25 μm. In the inner region, the size distribution is more scattered and spreads out between 0.04 and 1.00 μm.

Chemical Microanalysis. Chemical microanalysis experiments show that the oxide scale grown at 1200°C at the zirconia/NiCrAlY interface is not composed of pure α-alumina. The alumina scale is bordered, on the NiCrAlY side, by a fine layer of pure chromia (≈ 0.25 μm thick), as evidenced by E.D.S. (Fig. 8). Moreover, most Al_2O_3 grains contain small amounts of chromium (in the order of 1 wt. percent).

The presence of zirconium is detected almost everywhere in the alumina scale (see the E.D.S. spectrum in Fig. 9), both in the bulk of the oxide grains and in the oxide grain boundaries (within the limitation of a 10 nm E.D.S. probe). The fact that the edge of zirconium is also observed by P.E.E.L.S. (Fig. 10)

Downloaded 02 Jun 2010 to 171.66.16.122. Redistribution subject to ASME license or copyright; see http://www.asme.org/terms/Terms_Use.cfm

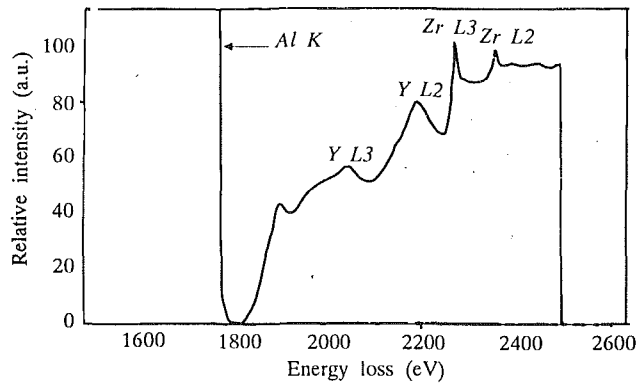


Fig. 10 P.E.E.L.S. spectrum inside an alumina grain showing the presence of zirconium and, to a lesser extent, yttrium in solid solution

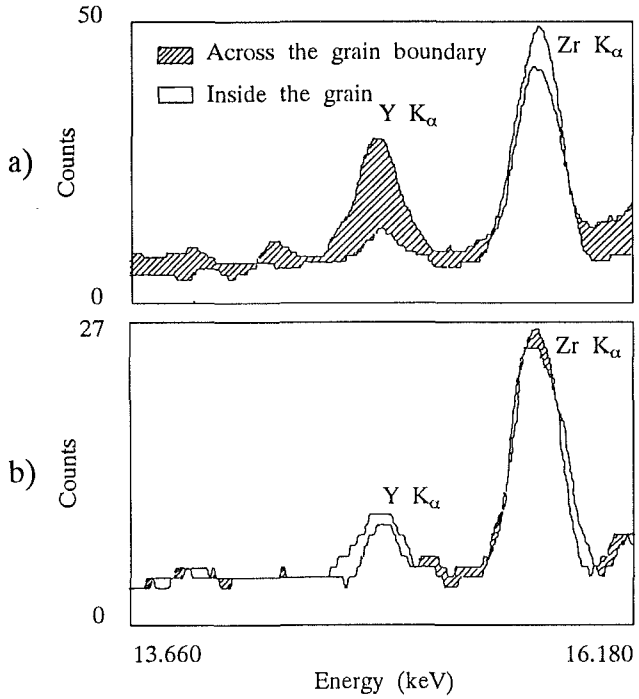


Fig. 11 E.D.S. spectra in the Y and Zr high energy peak region: superposition of spectra recorded in the grain bulk and at a grain boundary; (*a*) near NiCrAlY/Al_2O_3 interface, (*b*) near ZrO_2/Al_2O_3 interface

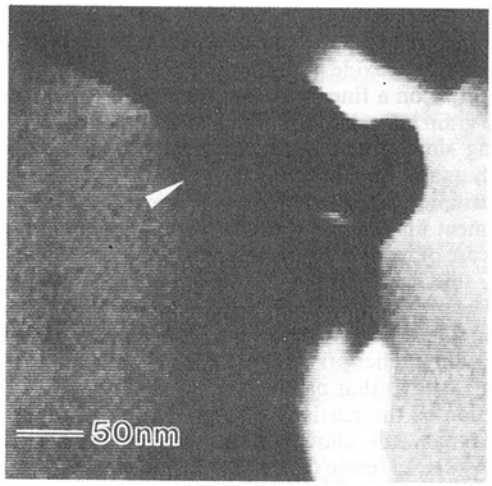


Fig. 12 $Y_3Al_5O_{12}$ garnet at a triple grain boundary near the Al_2O_3/MCrAlY interface (STEM imaging)

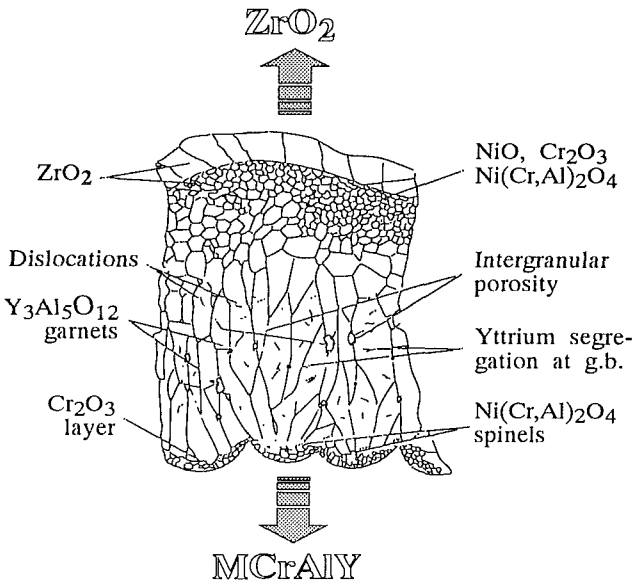


Fig. 13 Schematic representation of the oxide scale grown during 100 h annealing in air at 1200°C at zirconia /MCrAlY interface

indicates that the Zr signal detected by E.D.S. is not merely due to the fluorescence of Zr from the nearby zirconia coating. A rough estimate of the zirconium content in the Al_2O_3 grains (using the thin foil approximation) is about 1 wt. percent. It is worth pointing out that the zirconium content decays farther and farther away from the alumina/zirconia interface.

Figures 11(*a*) and 11(*b*) present detailed energy dispersive X-ray spectra around the high energy Y and Zr peaks, collected from regions near the NiCrAlY/Al_2O_3 and Al_2O_3/zirconia interfaces, respectively. In each figure, one can see the super position of two spectra: one recorded with the 10 nm probe centered in the bulk of a grain, the other with the probe across a grain boundary. On the NiCrAlY side of the alumina scale (Fig. 11*a*), an yttrium signal is clearly visible, strongly reinforced in the grain boundary. On the other side of the alumina scale (Fig. 11*b*), no such reinforcement is visible. This experiment reveals yttrium segregation at the oxide grain boundary near the NiCrAlY/Al_2O_3 interface: The yttrium concentration as indicated by this analysis is of course lower than the real yttrium concentration inside the grain boundary, because of the probe size smearing effect. The presence of yttrium in the oxide scale is also detected in the form of small $Y_3Al_5O_{12}$ garnets lying in some grain boundaries of the inner region (Fig. 12).

Discussion. The principal microstructural features of the alumina scales grown at the ZrO_2/NiCrAlY interface are schematically represented on Fig. 13. The mechanisms of formation of the oxide scale in the NiCrAlY-YPSZ system can be discussed on the basis of these microstructural observations and also from a comparison between the microstructures of the oxide scale grown on the duplex system and on bare MCrAlY (Choquet and Mévrel, 1989). The structural modifications that can be attributed to the presence of a zirconia top coat essentially consist of an inward diffusion of zirconium (and to a lesser extent yttrium) inside the alumina grains. The microstructure of the oxide scales grown at the zirconia/NiCrAlY interface needs to be discussed in terms of oxide growth mechanisms, oxide composition, and scale plasticity.

Growth Mechanisms. The presence of large elongated grains near the metal/oxide interface suggests that the oxide growth occurs predominantly at this interface and hence that

Downloaded 02 Jun 2010 to 171.66.16.122. Redistribution subject to ASME license or copyright; see http://www.asme.org/terms/Terms_Use.cfm

oxygen diffusion through the Al_2O_3 layer is faster than aluminum diffusion. It also leads one to believe that yttrium segregation in the oxide grain boundaries—either as $Y_3Al_5O_{12}$ precipitates or on a finer scale—enhances oxygen diffusion at the oxide grain boundaries (bulk diffusion of aluminum probably being slow at this temperature). This assumption was previously made by Choquet (1988), although he could not detect yttrium segregation on oxide thin foils by E.D.S., due to instrument limitation.

In the case of oxide growth at a MCrAlY/Zirconia interface, however, this mechanism may well not be the only one involved. The presence of significant amounts of zirconium (and lesser amounts of yttrium) inside the oxide layer, with a positive concentration gradient from the inner to the outer part of the oxide scale, shows that part of the alumina layer has formed by reduction of the partially stabilized zirconia layer, which is thermodynamically allowed at these temperatures (at 1200°C, $\Delta G_{ZrO_2} = -816$ kJ/mole $O_2 < \approx \Delta G_{Al_2O_3} = -802$ kJ/mole O_2). Zirconium and yttrium atoms thus "trapped" in the alumina layer can further diffuse toward the inner zone of the scale. This secondary growth mechanism, which takes place at the oxide/zirconia interface, is probably of limited extent (as indicated by the grain morphology typical of a scale growth at the metal/oxide interface), since it is limited by the slow volume diffusion of Al atoms through the oxide scale. However, it probably has the consequence of substantially strengthening the ZrO_2/Al_2O_3 interface because of the chemical reaction taking place there.

Other Oxides. The presence of a thin chromia layer at the NiCrAlY/oxide interface, after 100 h at 1200°C, is also somewhat unexpected (Cr_2O_3 being less stable than Al_2O_3 at this temperature). It probably forms at the end of the oxidizing treatment after important aluminum depletion of the NiCrAlY has taken place, preventing further formation of a continuous alumina layer. This argument is supported by the relatively low initial aluminum content of the bond coat alloy (6.5 wt. percent) and by T.E.M. E.D.S. measurements in the NiCrAlY near the metal/oxide interface (confirming important aluminum depletion during Al_2O_3 scale formation). Some chromium has also diffused and partially substitutes for aluminum in the Al_2O_3 grains.

Oxides other than alumina and chromia have been identified in the oxide scale. The presence of nickel oxides and very small spinels in the outermost region of the scale is not surprising: They were formed during the early stages of oxidation, when a stationary oxidation regime is not yet established. On the other hand, the presence of $NiAl_2O_4$ spinels near the MCrAlY/oxide interface is not so easily explained. One notices that the small spinel grains are localized in convoluted regions of the alumina scale. This spinel formation could be due to a local aluminum depletion in an alumina encapsulated metallic "pouch."

Plasticity. The presence, in relatively large quantities, of dislocation pile-ups inside the oxide scale grown at 1200°C is not easy to interpret. Choquet and Mévrel (1989) demonstrated that the high value of residual stresses ($\approx -5.7 \pm 0.4$ GPa) measured at room temperature on an alumina scale grown at 1100°C on a bare MCrAlY corresponded to the calculated thermal stresses; this means that the level of oxide growth stress, at the oxidation temperature, is likely to be lower than the flow stress of alumina at this temperature. It is thought therefore that plastic deformation inside the scale could occur during cooling, at intermediate temperature, as a result of thermal stresses. This would not be too surprising since, according to Castaing et al. (1981), the flow stress associated with prismatic slip varies from about 500 MPa to 1 GPa when the temperature varies between 1200°C and 900°C.

It is also difficult to tell how the presence of the top coat would influence the plasticity of the thermally grown alumina layer. The fact that some zirconium dissolves into the scale could possibly alter the mechanical properties of the material one way or another. No such evidence has been reported in the literature to our knowledge. The topcoat in itself is microcracked and would most probably deform itself, following the deformation of the alumina scale.

Conclusion

It is reported here how microstructural investigations can provide valuable insight into the relationship between the chemical composition and thermomechanical resistance of yttria stabilized zirconia thermal barrier coatings. It has been confirmed that when such coatings are processed through fusion with a high quenching rate (as in plasma spraying) and with an adequate composition (6–8 wt. percent Y_2O_3, corresponding to zirconia partial stabilization), a single metastable tetragonal t' phase is being obtained. This particular phase exhibits fine microstructures of twins and antiphase boundaries, which are likely to enhance its toughness through microcrack deviation mechanisms. Upon annealing at service temperatures, a new stable "tweed" microstructure appears, which had not been previously reported in plasma-sprayed TBC, and probably provides additional toughness to the material. The toughening mechanisms obtained with these microstructural elements would be very specific to the t' phase and could not be achieved in cubic fully stabilized zirconia coatings. This difference observed at a microscopic scale could help to understand why the t' phase is much tougher than the FCC cubic phase.

It has also been reported here that alumina scale growth at the PSZ/MCrAlY interface could be a major contribution to the strength of this interface. Significant amounts of zirconium inside the alumina grains have been observed, sustaining the hypothesis that the oxide scale has partially grown by reduction of the zirconia top coat. This could be a reason the zirconia/alumina interface is so strong. Otherwise, the oxide grain morphology is typical of oxide growth at the metal/oxide interface suggesting that the scale still mainly forms by oxygen grain boundary diffusion. Segregation of yttrium at oxide grain boundaries has been observed, leading us to think that yttrium segregation enhanced oxygen diffusion. The large quantities of defects observed in the alumina scale formed at 1200°C suggest that in this range of temperature, a significant plasticity of alumina can be obtained, which could help in relieving the thermal stresses due to expansion coefficient mismatch in the TBC.

Finally, it should be repeated here that the thermomechanical resistance of thermal barrier coatings does not rely exclusively on the intrinsic toughness of the ceramic and the strengthening mechanisms of the ceramic/metal interface. At least two other factors contribute to this resistance. The first one is the good oxidation resistance of the MCrAlY bond layer, which is achieved through the selection of appropriate plasma spraying parameters for the bondcoat. The second one is the very special structure of the porosity in the ceramic coating, which relieves some of the compressive stresses generated by thermal expansion coefficient mismatch between the ceramic and the underlying metal. This structure is very much dependent on the plasma spraying parameters of the ceramic topcoat. The authors think, however, that the large differences observed between the thermomechanical resistance of coatings made of partially and fully stabilized zirconia should not be attributed to some variations in the coatings deposition parameters (in each case, appropriate plasma spraying parameters have been used for the topcoat as well as for the MCrAlY bondcoat), but rather to the *real intrinsic differences*, detailed above, between the coatings respective toughness.

Downloaded 02 Jun 2010 to 171.66.16.122. Redistribution subject to ASME license or copyright; see http://www.asme.org/terms/Terms_Use.cfm

Acknowledgements

The authors gratefully acknowledge the help of HEURCHROME for plasma spraying the coatings observed in this study.

References

Anderson, C. A., and Gupta, T. K., 1981, "Phase Stability and Transformation Toughening in Zirconia," *Advances in Ceramics*, Vol. 3, The Am. Ceram. Society, Columbus, OH, pp. 184–201.

Butler, E. P., 1985, "Critical Assessment: Transformation Toughened Zirconia Ceramics," *Materials Science and Technology*, Vol. 1, pp. 417–432.

Castaing, P., Cadoz, J., and Kirby, S. H., 1981, "Deformation of Al_2O_3 Single Crystal Betwen 25°C and 1800°C: Basal and Prismatic Slip," *J. Phys.*, Paris, Vol. 42, pp. 43–47.

Choquet, P., 1988, "Etude de l'Oxydation á Haute Temperature de Dépôts D'Alliages Ni(Co)CrAlY Réalisés par Pulvérisation Cathodique. Influence des Éléments d'Addition Y, Hf et Zr," Thése d'état, Orsay, France.

Choquet, P., and Mévrel, R., 1989, "Microstructure of Alumina Scales Formed on NiCoCrAl Alloys With and Without Yttrium," *Materials Science and Engineering*, Vol. A 120/A121, pp. 153–159.

Garvie, R. C., Hannink, R. H., and Pascot, R. T., 1975, *Nature*, Vol. 258, p. 703.

Gupta, T. K., Bechtold, J. H., Kuznicnw, R. C., Cadoff, L. H., and Rossing, B. R., 1977, "Stabilization of Tetragonal Phase in Polycrystalline Zirconia," *Journal of Materials Science*, Vol. 12, pp. 2421–2426.

Katchaturyan, A. G., and Shatalov, G. A., 1968, "Elastic Interaction Potential of Defects in a Crystal," *Soviet Physics—Solid State*, Vol. 11, No. 1, pp. 118–123.

King, W. E., Peterson, N. L., and Reddy, J. F., 1984, "Application of Transverse-Section Analytical Electron Microscopy to the Study of Oxidation of Metal Alloys," *Proc. Int. Cong. on Metallic Corrosion*, Toronto, Canada, June, Vol. 4, pp. 28–35.

Lanteri, V., 1986, "The Tetragonal Phase in Yttria Partially Stabilized Zirconia," PhD. thesis, Case Western Reserve University, Cleveland, OH.

Lanteri, V., Chaim, R., and Heuer, A. H., 1986, "On the Microstructures Resulting From the Diffusionless Cubic → Tetragonal Transformation in ZrO_2–Y_2O_3 Alloys," *J. Amer. Ceram. Soc.*, Vol. 69, No. 10, pp. 258–261.

Lelait, L., Alpérine, S., Diot, C., and Mévrel, R., 1989, "Thermal Barrier Coatings: Microstructural Evolution During Annealing," *Materials Science and Engineering*, Vol. A121, pp. 475–482.

Lelait, L., and Alpérine, S., 1991, "T.E.M. Investigations of High Toughness Non-equilibrium Phases in the ZrO_2–Y_2O_3 System," *Scripta Metallurgica et Materialia*, Vol. 25, pp. 1815–1820.

Lelait, L., Alpérine, S., and Mévrel, R., 1991, "Alumina Scale at Zirconia/MCrAlY Interface: a Microstructural Study," *Journal of Materials Science*, in press.

Lelait, L., 1991, "Etude Microstructurale Fine de Revêtements Céramiques de Type Barriére Thermique; Incidence sur la Résistrance Thermomécanique de ces Revêtements," Thèse de Doctorat, Université d'Orsay, France, Nov.

Levine, K. D., and Miller, R. A., 1982, "Thermal Barrier Coatings for Utility Gas Turbine," EPRI AP-2618, Electric Power Research Institute, Palo Alto, CA.

Michel, D., Mazerolles, L., and Perez Y Jorba, M., 1983, "Fracture of Metastable Tetragonal Zirconia Crystals," *Journal of Materials Science*, Vol. 18, pp. 2618–2628.

Miller, R. A., Smialek, J. L., and Garlick, R. G., 1981, "Phase Stability in Plasma Sprayed Partially Stabilized Zirconia-Yttria," A. H. Heuer and L. W. Hobbs, eds., *Advances in Ceramics*, Vol. 3, The Am. Ceram. Society, Columbus, OH, pp. 241–253.

Milelr, R. A., Garlick, R. G., and Smialek, J. L., 1983, "Phase Distribution in Plasma-Sprayed Zirconia-Yttria," *Ceramic Bulletin*, Vol. 62, No. 12 pp. 1355–1358.

Scott, M. G., 1975, "Phase Relationship in the Zirconia-Yttria System," *Journal of Materials Science*, Vol. 10, pp. 1527–1535.

Stecura, S., 1985, "Optimization of NiCrAl/ZrO_2–Y_2O_3 Thermal Barrier System," NASA Technical Memo 86905.

Suhr, D. S., Mitchell, T. E., and Keller, R. J., 1984, "Microstructure and Durability of Zirconia Thermal Barrier Coatings," in: *Science and Technology of Zirconia, Adv. in Ceramics*, Vol. 12, pp. 503–517.

Trémouille, G., Derep, J. L., and Portier, R., 1986, "Plasma Coated Metal-Zirconia Interface," *Advances in Thermal Spraying*, Proc. of International Thermal Spraying Conference, Montreal, Canada, Sept. 8–12, pp. 445–454.

Wen, S. H., Katchaturyan, A. G., and Morris, J. W., Jr., 1981, "Computer Simulation of a 'Tweed-Transformation' in an Idealized Elastic Crystal," *Metal. Trans. A*, Vol. 12A, pp. 581–587.

Downloaded 02 Jun 2010 to 171.66.16.122. Redistribution subject to ASME license or copyright; see http://www.asme.org/terms/Terms_Use.cfm

Y. R. Takeuchi

K. Kokini

Purdue University,
Ray W. Herrick Laboratories,
School of Mechanical Engineering,
West Lafayette, IN 47907

Thermal Fracture of Multilayer Ceramic Thermal Barrier Coatings

Controlled experiments and a corresponding analytical model were developed to investigate the reasons for crack initiation in multilayer ceramic thermal barrier coatings. The experiments and model determined that surface cracks form as a result of tensile stresses created following stress relaxation in the ceramic at steady-state high temperatures (about 900°C–1100°C). Interface cracks generated by out-of-plane stresses are affected by the presence of these surface cracks and thermal transients and, possibly, edge effects.

1 Introduction

Ceramic thermal barrier coatings have been developed for diesel engines and gas turbines to improve efficiency, increase power output of the engine, and increase the life of the metal parts. Initial ceramic coating development efforts were conducted by the gas turbine engine community [1–5]. More recently, the diesel engine industry has actively participated in similar efforts [6–9]. The level of temperatures to which thermal barrier coatings are exposed during their use results in different types of failure modes. For high-temperature applications such as gas turbines, bond coat oxidation and possibly crystalline phase change have a significant effect in damage initiation [1–3]. For lower temperatures and thicker ceramic coatings such as the ones used in diesel engines, these factors do not affect the failure. However, the thermal cyclic stresses occurring during engine operation usually result in coating delamination and spalling. This paper considers the latter case.

Ultimately, the failure process is a result of thermomechanical stresses generated by the mismatch in properties of the different materials and the application of transient temperature distributions.

A number of previous studies have consisted of testing until spalling occurred [2, 4–7, 9, 10]. These investigations have yielded information on the *total* life of the coating, where the cracks had already initiated and propagated. However, the mechanisms behind crack initiation and propagation could be different, and therefore, require more detailed investigations. To study crack initiation, the experiment should investigate the life of the coating until the first crack forms. Thermal stress analysis can be used to study crack initiation, but once the first crack forms, the stress fields and the mechanics of the problem change and require the use of fracture mechanics. This paper presents a controlled study of a multilayer ceramic thermal barrier coating on a metal substrate subjected to a controlled heat flux with the objective of developing a fundamental understanding of the crack initiation process. The stresses due to the experimental thermal loads are calculated numerically and related to the actual experimental measurements.

2 Description of Study

2.1 Experiments. The experiment consisted of subjecting a beam-shaped specimen to two high-intensity infrared lamps that resulted in the boundary conditions shown in Fig. 1. This is an approximation of a concentrated heat flux region in the engine. While the experiment itself is not exactly two dimensional, a two-dimensional model was used to study first-order effects in the failure behavior of the coating. The specimen is shaped like a multilayer beam, where the coating materials and thicknesses are representative of thermal barrier coatings used for gas turbine metal shrouds. Because the applied heat flux is at the center of the specimen, concentrated along a line across its width, failures occur in this region, away from the specimen edges.

A significant advantage of this experiment is the ease with which the cracks can be viewed from the side. The length of the surface crack and the presence of the delamination crack can be observed visually without the need for additional destructive or nondestructive methods.

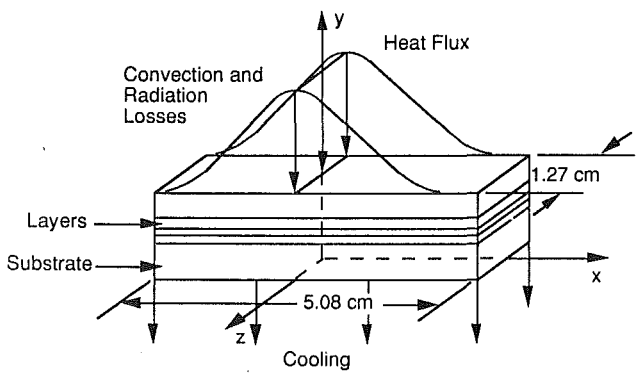


Fig. 1 Schematic diagram of the experimental boundary condition

Contributed by the International Gas Turbine Institute and presented at the 37th International Gas Turbine and Aeroengine Congress and Exposition, Cologne, Germany, June 1–4, 1992. Manuscript received by the International Gas Turbine Institute February 24, 1992. Paper No. 92-GT-318. Associate Technical Editor: L. S. Langston.

Copyright © 1994 by ASME
Downloaded 02 Jun 2010 to 171.66.16.122. Redistribution subject to ASME license or copyright; see http://www.asme.org/terms/Terms_Use.cfm

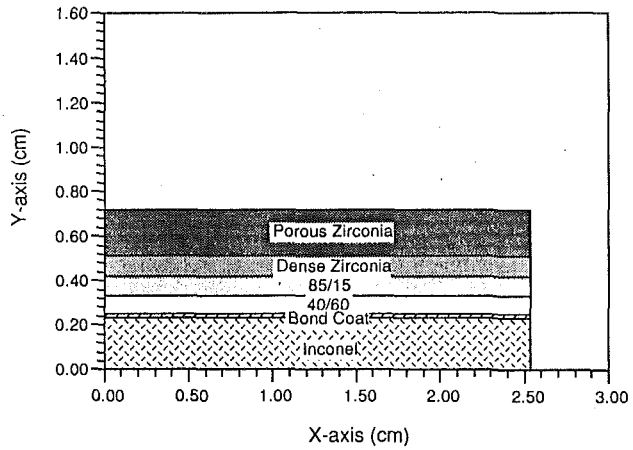


Fig. 2 Diagram of the specimen cross section

A schematic of the specimen cross section is shown in Fig. 2. As indicated in the figure, the thermal barrier coating has a multilayered structure. The materials chosen for the specimen were the same as materials used in the actual diesel engines. For instance, the ceramic was 20 percent weight yttria-stabilized zirconia. This is fully stabilized zirconia, i.e., no phase change occurs during the thermal loading.

The concentrated line heat flux across the beam-shaped specimen surface was provided by two focused infrared lamps (see Fig. 3). The lamps were 5.08 cm (2 in.) long argon-filled quartz tungsten filament light bulbs with a spectral peak of 1.1 μm. The power rating of the bulbs was 1000 W. A bulb was set in one focal point of a highly polished water-cooled aluminum reflector shaped as a half-elliptical tube. The light rays emitted by the bulb reflect off the reflector, then converge at the second focal point of the ellipse, which concentrates the heat flux into a line. The resulting peak heat flux was 335 kW/m^2. This method of heating the specimen is noncontact and controlled, compared to the more common burner rig heating method, which blasts hot gases on a rotating specimen surface. The heat sink is a water-cooled copper plate upon which the specimen rests without any restraints. Conductance grease is used to minimize contact resistance between the cooling plate and the specimen.

The heat source and the heat sink create temperature distributions in the specimen similar to the coatings in the diesel engine environment. Such a temperature distribution is a better representation of actual engine conditions than the uniform temperatures created in oven tests. The heat flow from the coating surface to the substrate creates a temperature gradient in the y direction (see Fig. 1). Also, the line heat flux at the center of the specimen creates a hot spot, where temperatures vary in the x direction, peaking at the center ($x = 0$). The two dimensionality of the specimen temperature distribution in this experimental setup facilitates the mathematical modeling of the experiment.

Thermocouples were attached to the surface of the specimen coating and the bottom of the substrate. The thermocouple was bonded to the ceramic surface using a paste, which also shielded the thermocouple from the incident radiation. A high-temperature strain gage was mounted on the substrate to measure strain changes during transient and steady-state heating. The specimen surface was also coated with a high-temperature paint to increase absorptivity and the sides of the specimen were insulated to prevent incident radiation from heating the sides and to insure that the temperature distribution obtained was two dimensional. Temperature measurements were recorded by a data acquisition system and strain gage measurements were recorded onto a strip chart recorder.

The current to the lamps was provided by a power controller.

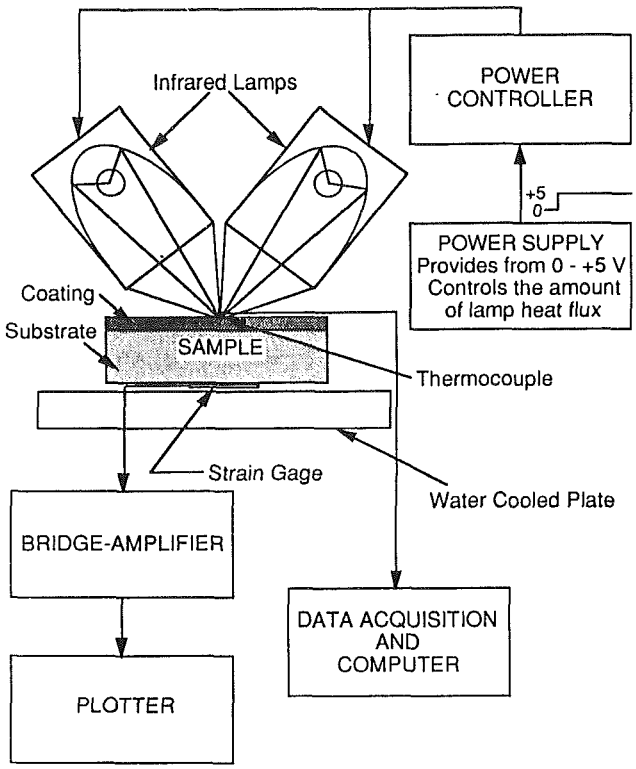


Fig. 3 Diagram of the two-lamp experimental setup

The amount of output from the lamp was determined by an input voltage to the controller that may range from 0 to 5 V. This determined the percent power emitted from the lamps.

The experimental procedure consisted of immediately bringing the lamps to full power, thus, heating the specimen until steady-state temperatures were reached. The specimen was held at these temperatures for a period of one hour, and then cooled back to room temperature.

2.2 Analysis. In order to develop a quantitative understanding of the experimental results, an analytical model of the experiment was developed. The purpose of the analysis was to study the stress distribution in the specimen. The magnitude of these stresses was related to the initiation of cracks. Specifically, it was assumed that the in-plane σ_x stress in the top ceramic layer caused the formation of the surface crack and that the σ_y stress at an interface was related to the initiation of delamination cracks. Shear stresses were also calculated and determined to be significantly smaller than the normal stresses.

The distributions of temperatures and thermal stresses were calculated using the finite element method.[1] The finite element mesh consisted of 739 eight-node plane strain isoparametric elements. The model was made up of 2350 nodes. The details of the model are given in [12]. The temperatures and thermal stresses were determined in the following four consecutive steps:

1 A uniform stress-free state for all layers was assumed at 618°C (1144°F) corresponding to the average temperature obtained during the plasma spray process. Therefore, when the specimen was cooled to room temperature, the mismatch in coefficients of thermal expansion among the various layers of the coating and the substrate resulted in residual stresses.
2 In the second step of the analysis, the transient temperatures and stresses resulting from the applied heat flux and the corresponding steady-state values were calculated.

[1]A program called ABAQUS, developed by HKS, Inc., Providence, RI, was used for the calculations.

Downloaded 02 Jun 2010 to 171.66.16.122. Redistribution subject to ASME license or copyright; see http://www.asme.org/terms/Terms_Use.cfm

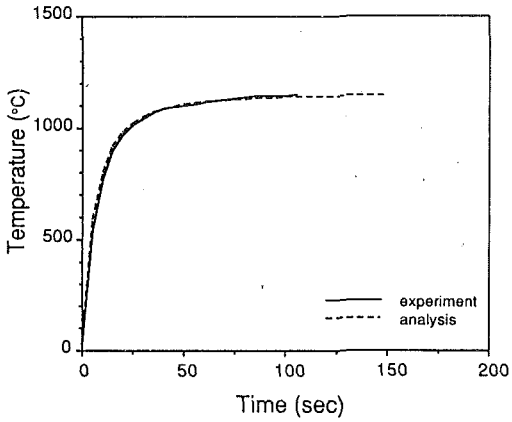


Fig. 4 Temperature versus time of the surface of the coating at $x = 0$

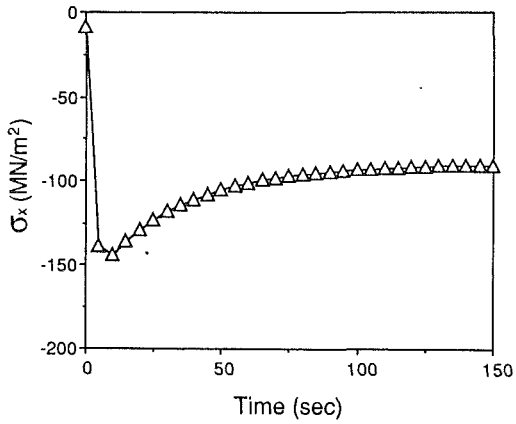


Fig. 5 σ_x stress versus time at $x = 0$, on the surface of the specimen

Table 1 Time-dependent properties of zirconia

Constants	Value
ΔH $(\frac{kJ}{atm})$	4.605×10^{-19}
R $(\frac{kJ}{atm\ K})$	1.38×10^{-23}
A $(\frac{N}{m^2})^{-n} (\frac{1}{t})$	1.89×10^{-6}
n	1.59

3 In the third step, stress relaxation of the ceramic coating in the high-temperature regions was allowed to take place for a period of one hour. The temperature distribution was assumed to remain at the steady state previously reached.

4 In the fourth and final step, the stresses when the specimen was cooled back to room temperature were calculated. The stress distribution was different than the original residual stress because of the stress relaxation that had occurred during heating.

The transient temperature distributions in the second step and the steady-state temperature in the third step were calculated by solving the corresponding heat transfer problem. The temperature distributions in all four steps were then used to calculate the corresponding thermal stresses.

The boundary conditions for the model were determined by comparing experimentally and analytically obtained temperature distributions. Both the steady-state and the transient behavior of the temperatures were in agreement with the proper boundary conditions. A comparison between the experimental and calculated temperatures is shown in Fig. 4.

The material properties used in the calculations were provided by United Technologies Research Center, based on their in-house measurements [11] and are given in [12].

The stress relaxation properties for the particular zirconia coatings used were not available through direct measurements and were estimated as described in [12]. However, the estimated properties were within the range of published data given in [13]. The effects of stress relaxation behavior was modeled as:

$$\frac{d\epsilon}{dt} = A\ \sigma^n e^{-\Delta H/RT} \tag{1}$$

where

σ = Von Mises equivalent stress
ΔH = activation energy
R = Universal Gas Constant
A, n = experimentally determined constants

These constants are presented in Table 1.

3 Results

The experimental and analytical results obtained in this study are presented and compared in order to be able to better determine the mechanisms for crack initiation in ceramic thermal barrier coatings.

The measured temperature on the specimen surface, due to heating at full power, reached a steady-state value of 1140°C (2080°F). The maximum temperature at the bond coat was 190°C (380°F), which was below the bond coat oxidation temperature for the material.

Surface and interface cracks formed as a result of one cycle of heating at full power, one hour at steady state, and cooling. The surface crack formed along the line of maximum heat flux ($x = 0$) and the interface crack appeared at the specimen edge between the top two coating layers. The mechanisms behind the initiation of the cracks are different and will be discussed separately.

3.1 Initiation of Surface Cracks. The surface σ_x stress was determined to initiate surface cracks. Before and during heating, the ceramic surface is subjected to only compressive stresses. However, the steady-state compressive stress at the surface is not large enough to fail the coating. A transient thermal stress analysis shows that a compressive transient peak stress occurs during transient heating (see Fig. 5). The magnitude of this peak stress at 10 seconds is 143 MN/m^2 (21 kpsi). However, experiments performed by heating the specimens for only 30 seconds, and cooling them immediately afterward, did not produce any cracking. This confirmed that the transient process did not cause the surface cracks. Also, the stress value was far below the compressive strength of plasma-sprayed zirconia of 380 MN/m^2 (55 kpsi). The experiments also showed that the cracks on the surface opened after cooling, suggesting that the surface stresses were tensile.

Therefore, the crack initiation mechanism was explained by considering the time-dependent behavior of zirconia at high temperature. It is believed that stress relaxation was the most significant effect in this behavior.

The stress distribution at $x = 0$ resulting from the analysis is shown in Fig. 6. Each curve on this figure represents the four stages of the stress states that the specimen undergoes:

Stage (1) the residual at room temperature
Stage (2) the stress distribution at steady-state temperatures
Stage (3) the stress distribution at steady-state after one hour of stress relaxation
Stage (4) the stress after uniform cooling back to room temperature

Figure 6 shows that the surface of the specimen is initially in compression. As the heat flux is applied on the specimen, the compressive stresses become larger. The time-dependent behavior of the material, in regions that experience a large

Downloaded 02 Jun 2010 to 171.66.16.122. Redistribution subject to ASME license or copyright; see http://www.asme.org/terms/Terms_Use.cfm

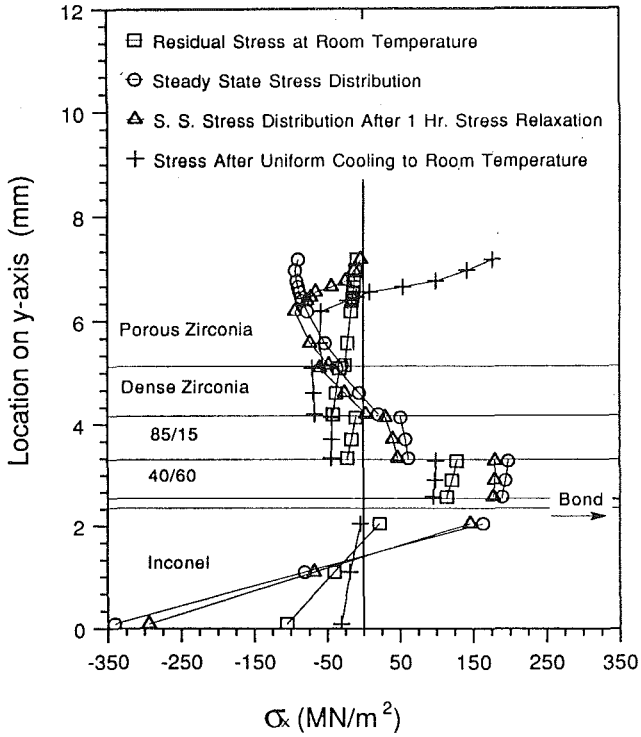


Fig. 6 σ_x stress distribution at $x = 0$ with one hour of stress relaxation

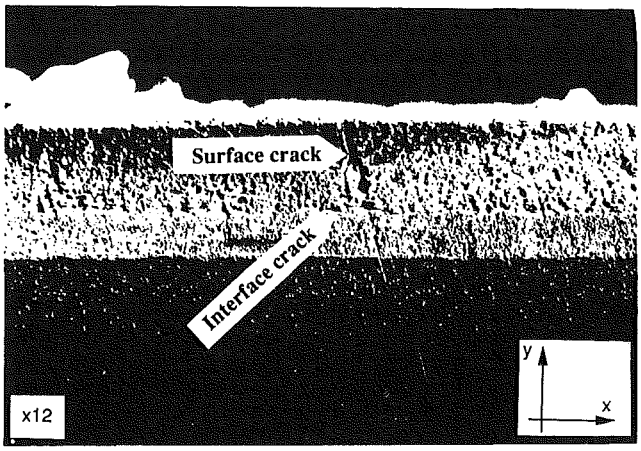


Fig. 7 Surface and interface cracks in a specimen after one hour of steady-state heating

temperature increase, results in the compressive surface stress decreasing at the end of one hour. Finally, upon uniform cooling to room temperature the surface stresses become tensile. The value of 176 MN/m^2 obtained for the tensile stress was above the nominal tensile strength of dense zirconia of 21 MN/m^2 (3.0 kpsi). It is believed that this tensile σ_x stress results in the initiation of surface cracks in the specimen. An example of a cracked specimen is shown in Fig. 7.

The presence of stress relaxation was verified by mounting a strain gage on the bottom side of the specimen substrate. The temperature dependence of the stress relaxation in the ceramic was verified by performing experiments with lower applied heat fluxes (1/5, 2/5, and 3/5 power). In these cases, the surface temperature was not large enough to result in significant stress relaxation for a time period of 1 hour. Indeed, no strain change was measured at steady-state temperatures for these cases. However, at full power, a steady change of strain of 30 μm/m was measured (Fig. 8), thus indicating that stress relaxation does occur at higher temperatures.

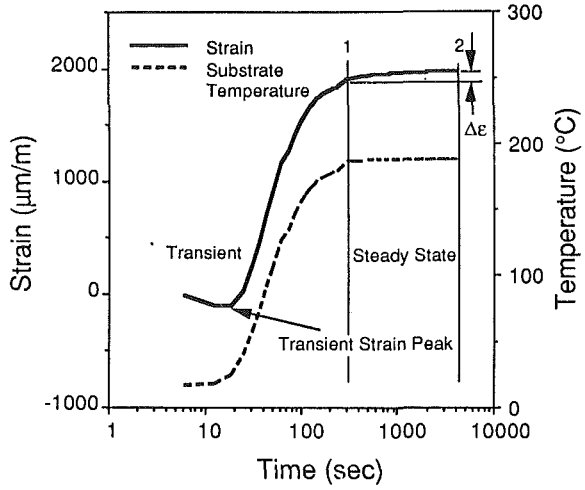


Fig. 8 Measured strain versus time at $x = 0$, $y = 0$

These results show that the mechanism of surface crack initiation in thermal barrier coatings consists of stress relaxation due to the time dependent behavior of the zirconia at large temperatures, followed by cooling, which creates tensile stresses on the surface.

3.2 Initiation of Interface Cracks. The mechanism controlling the initiation of interface cracks was different from that of the surface crack. The analysis showed that the tensile σ_y stresses necessary to initiate such cracks were decreased as a result of stress relaxation and became compressive upon cooling to room temperature. Therefore, several possible modes of crack initiation were considered for interface cracks: (1) Tensile stresses normal to the interface are generated during the transient heating process. These stresses could be large enough to break the interfacial bond. (2) After surface cracks were initiated, the presence of these cracks caused interfacial σ_y stresses to become larger and initiated the interface cracks. (3) A three-dimensional σ_y stress distribution near the interfaces was considered as a possibility.

Figure 9 shows the σ_y stress distribution in the specimen at $x = 0$. The initial residual σ_y stresses are small. During subsequent heating, the σ_y stresses become tensile. After one hour of stress relaxation, the magnitude of the stresses decreases and upon cooling to room temperature, they become compressive. This suggests that the time-dependent behavior would not cause the interface crack. Instead, it is during transient heating that the largest tensile σ_y stresses are obtained (see Fig. 10). In the experiments, the interface crack formed between the top two layers, centered directly beneath the surface crack. A transient tensile σ_y stress peak occurred in 10 seconds of heating. However, the magnitude of this stress was well below the strength of the zirconia. It is possible that the interface itself could be weaker than the actual material. However, experiments that heated the specimen for only 30 seconds without subsequent stress relaxation produced no failure. The case of fatigue failures is not considered in this paper but it is currently being investigated.

The second mode for the initiation of interface cracks was the effect of the surface crack on the σ_y stresses at the interface. On cooling, a surface crack forms due to the tensile σ_x stress at the surface. It should be remembered that the cooling in these experiments was provided by natural convection. Experiments with forced convection cooling will be conducted in future studies. Once the crack forms, the stress profile in the specimen completely changes. The effects of the surface crack on the σ_y stresses at the interface were estimated by introducing a surface crack into the model during the fourth stage of the

Downloaded 02 Jun 2010 to 171.66.16.122. Redistribution subject to ASME license or copyright; see http://www.asme.org/terms/Terms_Use.cfm

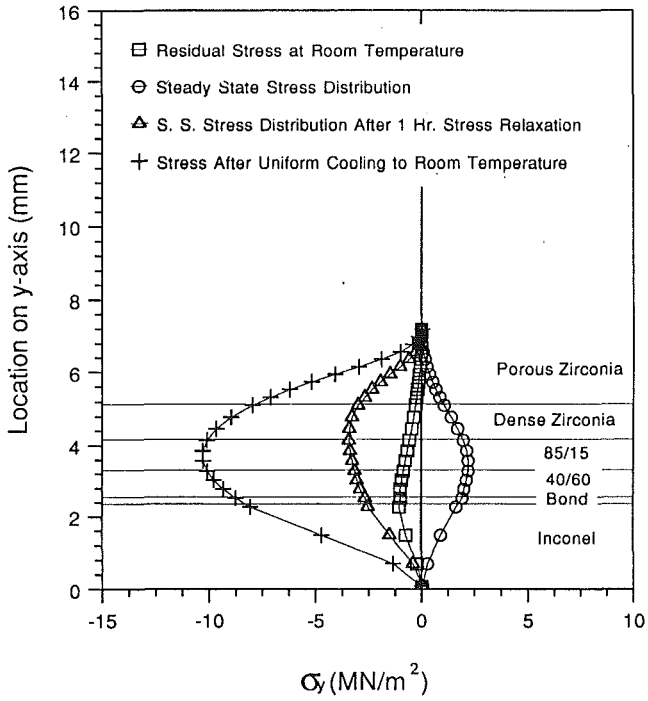


Fig. 9 σ_y stress distribution at $x = 0$ with one hour of stress relaxation

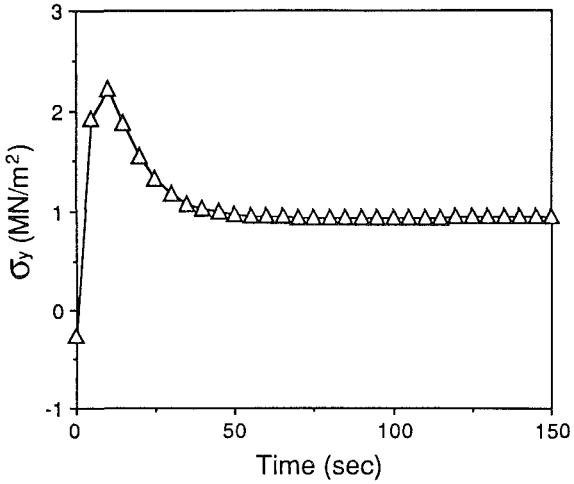


Fig. 10 σ_y stress versus time at $x = 0$ at the interface between the top two layers

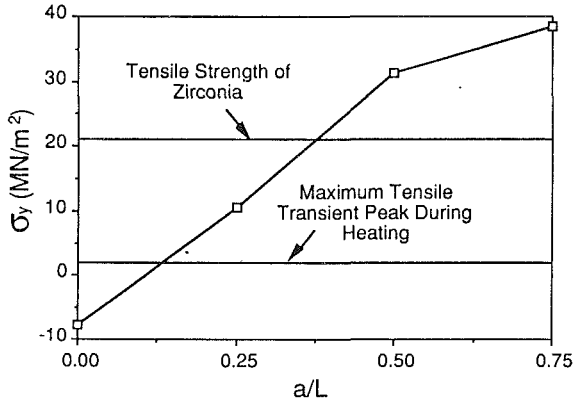


Fig. 11 σ_y versus crack length at the porous/dense zirconia interface at $x = 0$ after cooling

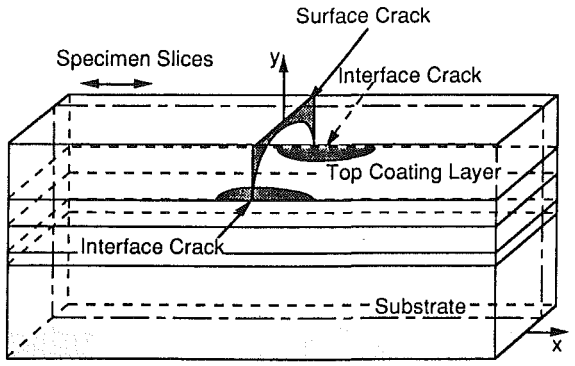


Fig. 12 Schematic diagram of the interface and surface crack

analysis where the specimen was uniformly cooled to room temperature and the surface tensile stresses were formed.

The result of the analysis is shown in Fig. 11. In this figure, a and L represent respectively the length of the surface crack and the thickness of the top layer. It can be noted that, as the surface crack propagates, the tensile σ_y stress at the interface increases significantly. The stress values calculated for this case were much larger than the σ_y stresses created during the transient heating, and were large enough to cause crack initiation. In Fig. 11, a tensile stress of 31.4 MN/m^2 (45.5 kpsi) occurred at a crack length of 0.5 mm (0.0197 in.). This stress exceeded significantly the tensile stress of 2.0 MN/m^2 (0.29 kpsi), which occurred during transient heating.

Experimental evidence seemed to support the hypothesis that the presence of the surface crack helped initiate the delamination crack. For instance, the interface crack did not appear immediately after cooling in a number of cases, even though the surface cracks had formed. For these cases, the surface crack was relatively short in length immediately after the test was finished. However, room temperature slow crack growth seemed to occur, which resulted in extension of the surface crack. There were several samples where the cracks extended in this manner. It is clear that this behavior requires further careful investigation. In some cases, the delamination crack appeared after the surface crack grew near the interface. In all cases where the interface crack was observed, it was located directly beneath the surface crack.

The third possibility for causing the initiation of interface cracks was three-dimensional stresses due to edge effects. In the x direction, the heat flux was concentrated at the center and did not directly affect the edges (at $x = \pm 2.54$ cm (± 1 in.)), thus preventing any edge cracking. However, the specimen was heated uniformly in the z direction. Therefore, stress relaxation occurred along the entire width of the specimen. This could cause a negative bending moment about the x axis. This loading would result in large peel stresses caused by the singular behavior of the stresses at the free edges.

This possibility was studied by slicing a specimen into thin strips along the x direction and measuring the three-dimensional crack profile. The measurements showed that both the vertical and interface cracks have a three-dimensional configuration. The surface crack was longer at the edges and shorter at the center of the specimen. The interface crack had a thumbnail shape, as shown in Fig. 12. It is clear that the two-dimensional model used in this study cannot be used to analyze the three-dimensional nature of these cracks. A three-dimensional model is currently being developed for this purpose.

The preceding discussion shows that the understanding of the mechanism for the initiation of the interface cracks is not as clear as the one obtained for the surface crack. Any one of the three mechanisms presented above or some combination of them could lead to interface cracks. While in all cases σ_y is

Downloaded 02 Jun 2010 to 171.66.16.122. Redistribution subject to ASME license or copyright; see http://www.asme.org/terms/Terms_Use.cfm

believed to cause the cracks, this stress component itself is influenced by different factors as discussed previously. In order to separate the different effects, more experiments need to be performed.

4 Conclusions

An experimental investigation, coupled with an analytical study was performed to determine the mechanisms of crack initiation in ceramic thermal barrier coatings. The objective was to develop a fundamental understanding of such mechanisms in order to extend the life of the coating.

The experimental methodology was developed to model a concentrated heat flux, where failure of thermal barrier coatings was observed to occur. The experiments were performed on two-dimensional specimens in order to obtain controlled thermal loads and visually observe the resulting cracks. The corresponding analytical model was developed using the finite element method.

Two types of cracks were observed: surface and interface. The mechanism for the initiation of surface cracks was determined to be stress relaxation in the ceramic. Time-dependent changes of strains were measured in the experiments during heating, which resulted in in-plane tensile stresses in the coating surface upon cooling to room temperature. The mechanism for the initiation of interface cracks was related to stresses normal to the interface, which are affected by the presence of the surface crack and/or three-dimensional effects, such as edge singularities.

Acknowledgments

Support of this research by Cummins Engine company is gratefully acknowledged. In particular, we would like to thank Thomas M. Yonushonis for valuable discussions. Thermal barrier coatings were produced by United Technologies Research Center through a Cummins-funded subcontract.

References

1 Liebert, C. H., and Miller, R., "Ceramic Thermal Barrier Coatings," *I&EC Product Research and Development*, Sept. 1984, pp. 334–349.

2 Levine, S. R., Miller, R., and Hodge, P. E., "Thermal Barrier Coatings for Heat Engine Components," *Sampe Quarterly*, Vol. 12, Oct. 1980, pp. 20–26.

3 Levine, S. R., and Miller, R., "Ceramic-Coated Metals Can Survive Contact With Hot Working Fluids," *Research and Development*, Vol. 26, Mar. 1984, pp. 122–1254.

4 Liebert, C. H., and Stepka, F. S., "Ceramic Thermal-Barrier Coatings for Cooled Turbines," *AIAA Journal of Aircraft*, Vol. 14, No. 5, May 1977, pp. 487–493.

5 Miller, R. A., and Berndt, C. C., "Performance of Thermal Barrier Coatings in High Heat Flux Environments," *Thin Solid Films*, Vol. 119, 1984, pp. 195–202.

6 Brink, R. C., "Material Property Evaluation of Thick Thermal Barrier Coating Systems," ASME JOURNAL OF ENGINEERING FOR GAS TURBINES AND POWER, Vol. 111, 1989, pp. 570–577.

7 Yonushonis, T. M., Roehling, D. P., Hoag, K. L., Novak, R. C., Matarese, A. P., and Huston, R. P., "Thick Thermal Barrier Coatings for Diesel Engines," *Proceedings of the 25th Automotive Technology Development Contractors Coordination Meeting*, SAE Publication P2009, Oct 26–29, 1987.

8 Alexander, W. D., and Wallace, F. J., "A Thermal Shock Facility for Testing Diesel Engine Ceramic Materials," *Ceramic Materials and Components for Engines: Proceedings of the Third International Symposium*, Las Vegas, NV, Nov. 27–30, 1988, pp. 1449–1458.

9 DeMasi, J. T., Sheffler, K. D., and Ortiz, M., "Thermal Barrier Coating Life Prediction Model Development," NASA CR 182230, Dec. 1989.

10 Berndt, C. C., and Herman, H., "Failure During Thermal Cycling of Plasma-Sprayed Thermal Barrier Coatings," *Thin Solid Films*, Vol. 108, 1983, pp. 427–437.

11 United Technologies Research Center, personal communication.

12 Takeuchi, Y., "Thermal Fracture of Ceramic Thermal Barrier Coatings," M.S. Thesis, Purdue University, Aug. 1991.

13 *Ceramic Source*, The American Ceramic Society, 1989, p.T89.

Downloaded 02 Jun 2010 to 171.66.16.122. Redistribution subject to ASME license or copyright; see http://www.asme.org/terms/Terms_Use.cfm

T. Cosack
MTU Motoren- und Turbinen-Union,
Dachauerstr. 665D-8000,
Munchen 50, Federal Republic of Germany

L. Pawlowski
CSM Centro Sviluppo Materiali,
I-38057 Pergine di Valsugana (TN), Italy

S. Schneiderbanger
MTU Motoren- und Turbinen-Union,
Munchen 50, Federal Republic of Germany

S. Sturlese
CSM Centro Sviluppo Materiali,
I-38057 Pergine di Valsugana (TN), Italy

Thermal Barrier Coatings on Turbine Blades by Plasma Spraying With Improved Cooling

Turbine blades were coated with a thermal barrier coating system consisting of an MCrAlY bond coat about 100 μm thick deposited by Low-Pressure Plasma Spraying (LPPS) and a 300 μm thick ZrO_2–7 wt. % Y_2O_3 top coat. The latter was manufactured by both Atmosphere and Temperature Controlled Spraying (ATCS) and Air Plasma Spraying (APS) using internal air cooling through the cooling holes of the turbine blades. Coated blades were submitted to thermal cycling tests in a burner rig with hot gas temperature of 1485°C. In the case of ATCS coated blades the number of cycles until the first spallation at the leading edge of the blade was between 350 and 2400. The number of cycles of the thermal barrier coatings sprayed with internal cooling was between 1200 and 1800. Furnace cycling tests were also carried out with ATCS coated blades at temperatures of 1100 and 1200°C. The results of thermal cycle tests and the investigations of the microstructure are discussed.

Introduction

Extensive research efforts have been devoted to the manufacture of plasma sprayed thermal barrier coatings (TBCs) on turbine parts for aeroengines (Meetham, 1985). The advantages and improvements of TBCs on turbine blades and vanes are as follows:

1 increase of the turbine thermal efficiency due to a higher stator outlet temperature (SOT),
2 increase of the compressor efficiency due to a reduced air flow for the turbine cooling,
3 longer service life of the metallic substrate material due to a decreased thermal fatigue load.

Part of these efforts focuses on improving the high-temperature behavior of ceramic coatings. The development should lead to an increase in cyclic thermal spallation time. This depends strongly on the strain tolerance of the ceramic coatings. This tolerance can be improved by an appropriate microstructure. This can be achieved with the help of ATCS, which has frontal cryogenic cooling system. However, this system is sophisticated and needs a careful analysis.

Another way to improve the TBC service life is by an application of internal blade cooling during plasma spraying. The internal cooling should lead to a decrease of residual tensile stresses in the TBCs.

All turbine blades were coated with a 100 μm thick MCrAlY bond coat. An yttria (7 wt. %) stabilized zirconia was used for the 300 μm thick top coat. Thermal cycle tests were carried out in a burner rig with a hot gas temperature of 1480°C. Additionally, blades were cycled in a furnace with temperatures of 1100 and 1200°C. All coats were investigated by microstructural analysis.

Situation of Plasma-Sprayed TBCs

One of the widely discussed reasons for the early spallation of plasma-sprayed TBCs is the residual stress in the composite system consisting of ceramic top coating–metallic bond coating–metallic substrate. The residual stresses are mainly caused by the mismatch of the thermal expansion coefficients and also by oxidation of the bond coat.

Previous investigations of TBCs sprayed with zirconia powders having different stabilizers have shown that the best results were obtained with 6 wt. % Y_2O_3. In a further step toward optimization of TBCs, the temperature during spraying was investigated. The best results were obtained with 20 percent yttria-stabilized zirconia at low deposition temperatures of 20 and 315°C. Thermal cycling tests were subsequently carried out at temperatures between 260 and 1010°C. After final engine tests, TBCs were qualified for turbine applications (Sheffler et al., 1982; Duvall and Ruckle, 1982; Sumner and Ruckle, 1980; Manning Meier et al., 1991). Today such TBCs possess an acceptable service lifetime, e.g., on vane platforms.

However, it seems to be difficult to produce TBCs with sufficient service life on airfoils. Obviously the most critical location for TBCs is the airfoil of turbine vanes or blades, where high temperatures up to 1150°C are experienced at the surface of the leading edge. In order to improve the TBC quality, investigations were carried out to avoid disadvantageous residual stresses and to increase the strain tolerance. The favorable microcracking pattern consisting of small vertical

Contributed by the International Gas Turbine Institute and presented at the 37th International Gas Turbine and Aeroengine Congress and Exposition, Cologne, Germany, June 1–4, 1992. Manuscript received by the International Gas Turbine Institute February 24, 1992. Paper No. 92-GT-319. Associate Technical Editor: L. S. Langston.

Copyright © 1994 by ASME
Downloaded 02 Jun 2010 to 171.66.16.122. Redistribution subject to ASME license or copyright; see http://www.asme.org/terms/Terms_Use.cfm

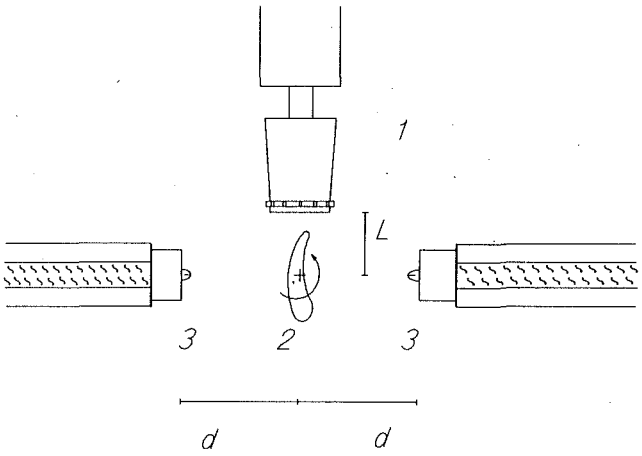


Fig. 1 Sketch of principal elements of ATCS processing: (1) plasma torch, (2) workpiece (blade), (3) atomizing nozzle of cryogenic liquid

Table 1 List of main parameters influencing the workpiece temperature during ATCS

COOLING FLUX PARAMETERS	HEATING FLUX PARAMETERS
- CRYOGENIC LIQUID PRESSURE	- POWER INPUT TO PLASMA
- ATOMIZING GAS FLOW RATE	- DISTANCE BETWEEN PLASMA TORCH AND WORKPIECE (L IN FIG. 1)
- GEOMETRY OF ATOMIZING NOZZLES	- PARAMETERS OF THE TORCH MOVEMENT (VELOCITY, AMPLITUDE...)
- DISTANCE BETWEEN NOZZLES AND WORKPIECE	- INITIAL TEMPERATURE PRIOR TO THE DEPOSITION

microcracks obtained by ATCS seems to be an appropriate solution to the problem of the strain tolerance of the coating (Ducos, 1989; Sturlese et al., 1991).

The internal blade cooling concept was triggered by the temperature measurements during plasma spraying. In particular, the spray distance between the substrate and the plasma torch influences strongly the substrate temperature. Some investigations have shown an increase of the temperature up to a constant value if there is no cooling during spraying (Pawlowski, 1981; Pawlowski et al., 1982; Balting et al., 1990; Knotek et al., 1991). Probably, the temperature increase at the beginning of the spraying process causes disadvantageous residual stresses at the interface between the bond coat and the top coat. The internal cooling is a way to have low, and regular temperatures over the whole coating process for the creation of favorable residual stresses.

Experimental

Spraying of the Bond Coat. A Low-Pressure Plasma Sprayed (LPPS) bond coat is proven to resist well against oxidation and has high hot gas corrosion resistance. The MCrAlY powders (32 Ni 21 Cr 8 Al 0.5 Y bal. Co) with different grain size distributions were sprayed in a LPPS-coater on IN-100 blades. At first a dense coat was sprayed with a fine powder. Thereafter, a coarse powder with the same composition was used to produce a rough surface, giving better bonding to the ceramic layer. The bond coat was sprayed onto a rotating blade by an oscillating plasma torch in a vacuum atmosphere. Finally, the complete bond coat was heat treated for about 4 h in a vacuum furnace at 1050°C.

ATCS of the Top Coating. The basic idea of ATCS is simultaneous control of the atmosphere and the substrate temperature during deposition (Fig. 1).

The plasma torch (1), installed on the arm of an industrial robot, is closed in a chamber. The workpiece (2) is mounted on a rotating table. The liquid gas (e.g., Ar) is transported to the atomizing nozzles (3) where the mixing with an atomizing gas (e.g., Ar) takes place. The droplets of atomized cryogenic liquid are sprayed toward the workpiece and cool it down. At the same time the workpiece is heated by the fluxes coming from (Pawlowski, 1981):

- convection of the plasma flame
- solidification of plasma-sprayed particles
- plasma-sprayed particles cooling to the actual temperature of the coatings

The temperature of the substrate during deposition results from the balance between heating and cooling fluxes coming from the workpiece. As the fluxes are relatively large (the heating flux could be as high as 2.3×10^6 W/m^2) (Pawlowski et al., 1982), the balance is very delicate and the establishment of the desired deposition temperature takes a long time. More than 10 parameters such as initial temperature, liquid argon flow rate, etc., were selected and correlated with deposition temperature ranging from 0°C to 200°C. Precise control of all the processing parameters (Table 1) is necessary and they were set up also by means of Fast Fourier Transforms (Bertamini et al., 1991).

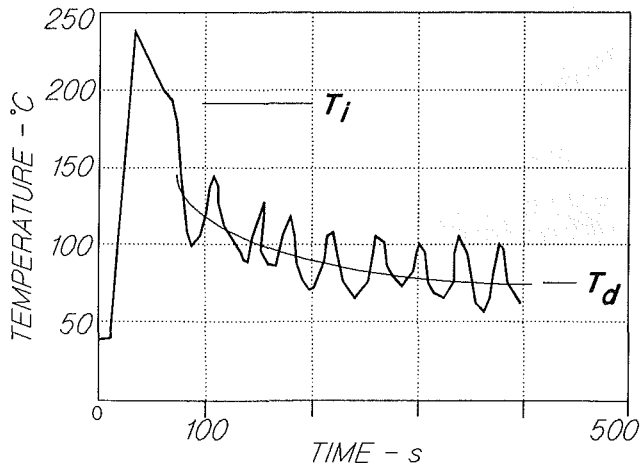


Fig. 2 Typical temperature versus time profile during spraying of TBCs by ATCS; T_i—initial temperature; T_d—deposition temperature

The ceramic coatings were deposited with the use of the ATCS technique. Deposition temperature was measured with the use of a thermocouple inserted inside one hole in the blade. The signal coming from the thermocouple was collected by a Linseis X-T recorder, connected with a PC in which recorded raw data were treated. A typical temperature versus spraying time is shown in Fig. 2. Spraying starts at T_i and terminates at T_d. The temperature reaches an average value marked with a line T_d. The recorded temperature shows periodic oscillations, which are attributed mainly to the imperfections of the cooling system.

APS of the Top Coat With Internal Blade Cooling. High pressure turbine blades are ideally suited for internal cooling during plasma spraying since coolants can flow through holes that are already drilled for cooling purpose in an engine. A

Downloaded 02 Jun 2010 to 171.66.16.122. Redistribution subject to ASME license or copyright; see http://www.asme.org/terms/Terms_Use.cfm

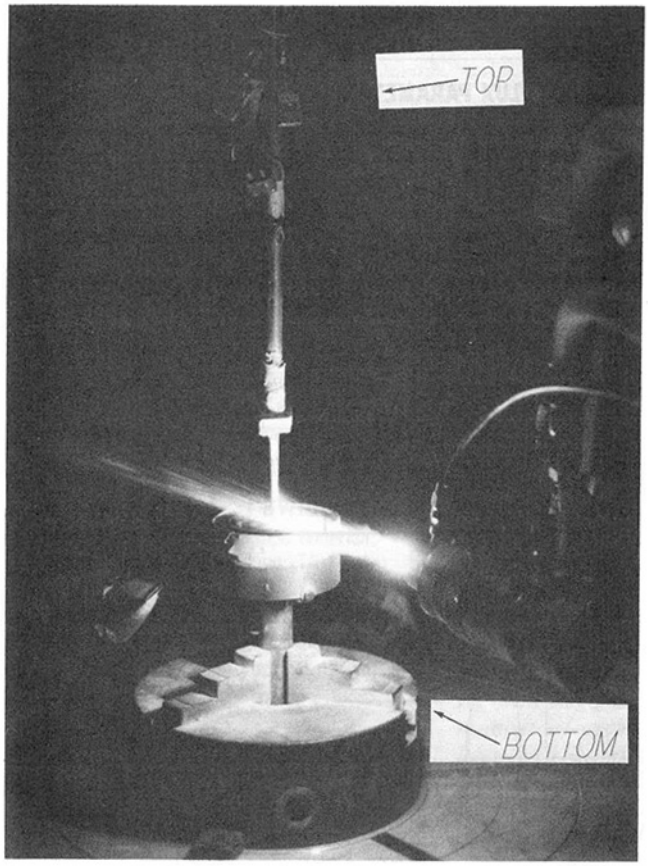


Fig. 3 A turbine blade installed in a fixture for cooling (bottom) and temperature measurement with a thermocouple (top)

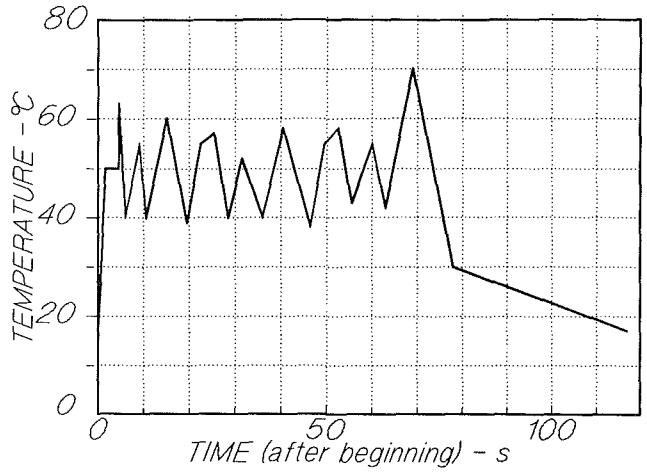
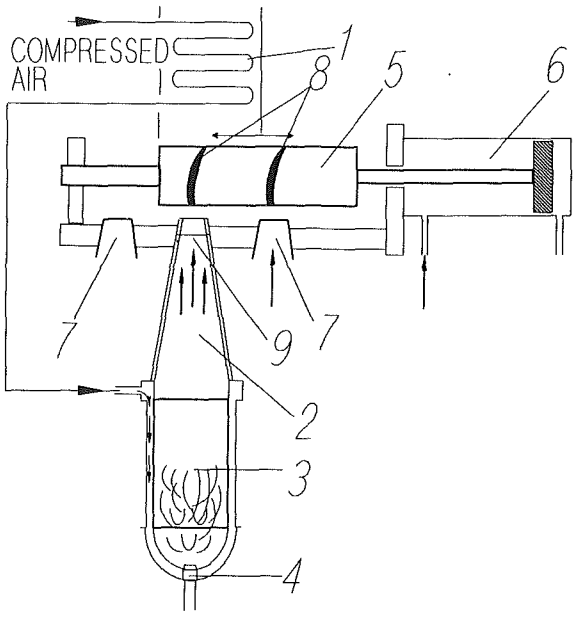


Fig. 4 A temperature versus time profile during plasma spraying of a TBC on a turbine blade with internal cooling

special fixture is used to cool the rotating blade with compressed air during plasma spraying (Fig. 3).

A thermocouple is arranged in one of the drilled holes, which is plugged by a wire from the cooling side. The position of the thermocouple is in the middle of the blade. The thermocouple voltage is transferred to a recorder by means of a slip ring. Figure 4 shows a typical temperature versus time curve with internal blade cooling. The oscillation is caused by the plasma torch moving.

Burner Rig Tests. The test facility consists mainly of an upright combustor equipped with a slide above the hot gas



THERMAL CYCLING RIG

1. HEAT EXCHANGER
2. CERAMIC HOT GAS NOZZLE
3. COMBUSTOR
4. FUEL NOZZLE
5. SPECIMEN CARRIER
6. PNEUMATIC CYLINDER
7. COOLING AIR NOZZLE
8. TEST SPECIMEN
9. Pt/PtRh THERMO-COUPLE

Fig. 5 Burner rig for thermal cycling tests

nozzle (Fig. 5). Two specimens at a time are mounted on the rig: one in the stream of hot gases and the other over the cold air nozzle. During testing, blades can be cooled internally by forced air circulation. The air flows from the front to the rear of the blade. The position of the specimens can be alternated by moving the sample-holder. This generates a cyclic change in temperature.

The temperature of the hot gas is measured with a Pt/PtRh thermocouple located inside the hot gas nozzle 20 mm from the outlet opening. The temperature can be controlled by varying the fuel/air ratio. This is obtained by maintaining a constant flow of fuel and adjusting the air flow.

Instrumented blades are used for temperature measurement of the specimens themselves. Dummies were used for determining gas temperature, fuel flow, and internal cooling pressure as well as the specimen angle at which the requested temperature distribution patterns were obtained. Measurements were made by NiCr–Ni thermocouples embedded beneath the bond coat (Fig. 6*a*). Testing of the coated rotor blades was carried out under the conditions specified in Table 2.

Furnace Cycle Tests. The furnace cycling was carried out at two temperatures: 1100°C and 1200°C. The blades were kept at these temperatures for 20 minutes. The cooling part of the cycle lasted for 10 minutes in air at room temperature. Figure 6(*b*) shows temperature versus time profile in the case of heating at 1200°C. The test ended at the appearance of first spallation in TBCs.

Results

As-Sprayed TBCs. Figure 7(*a*) shows the TBC microstructure of the APS coat with internal cooling. Pores with different sizes are regularly distributed in the TBC. The ceramic layer follows the roughness contour at the interface top-bond coat.

Downloaded 02 Jun 2010 to 171.66.16.122. Redistribution subject to ASME license or copyright; see http://www.asme.org/terms/Terms_Use.cfm

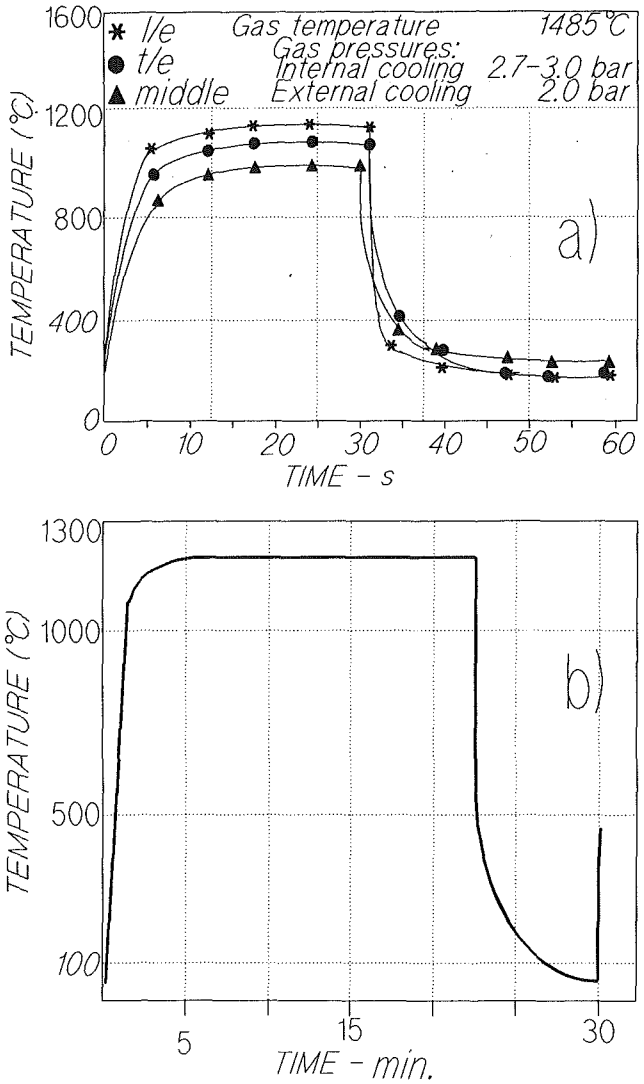
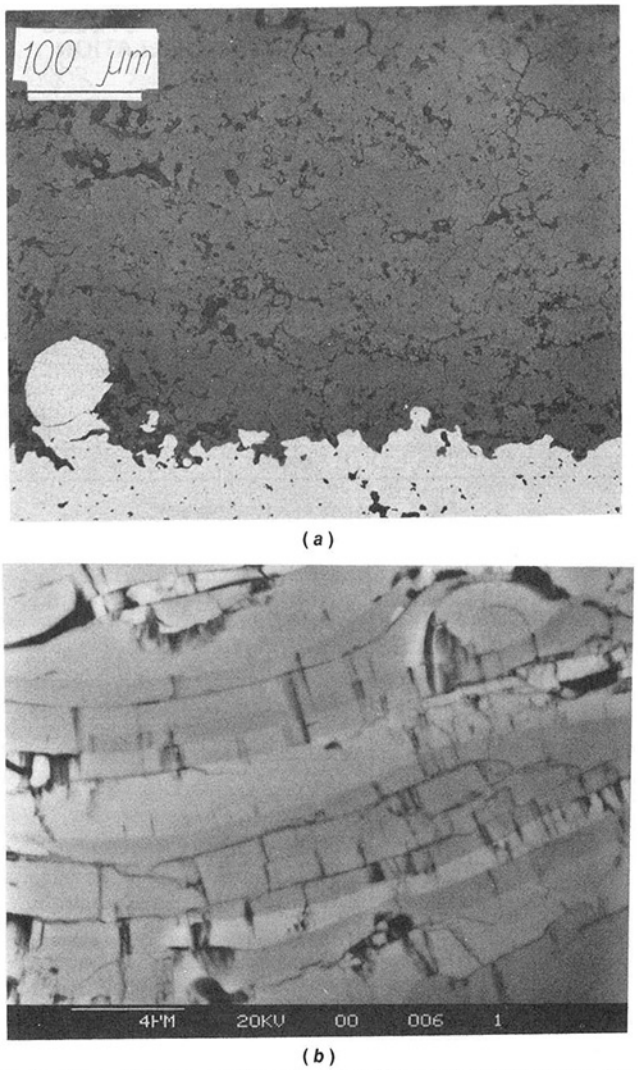


Fig. 6 Temperature versus time profile for thermal cycling tests: (*a*) burner rig test; (*b*) furnace cycling test; l/e = leading edge, t/e = trailing edge



(*a*)

(*b*)

Fig. 7 Microstructures of the as-sprayed TBCs: using APS with internal cooling (*a*); using ATCS (*b*)

Table 2 Operating conditions of the burner rig test

FUEL:	JPL
DIMENSION OF HOT GAS NOZZLE:	28 X 13 mm^2
DURATION OF HEATING / COOLING CYCLE:	30 s EACH
HOT GAS TEMPERATURE:	1485 °C
PRESSURE OF GAS APPLIED FOR BLADE INTERNAL COOLING:	2.4 - 3.0 bar
PRESSURE OF GAS APPLIED FOR BLADE EXTERNAL COOLING:	2 bar

The microstructure of the as-sprayed TBC is typical for the use of agglomerated and sintered zirconia powder.

Figure 7(*b*) shows the typical microstructure of a TBC sprayed by ATCS. A pattern of small vertical microcracks is apparent inside individual layers.

Burner Rig Tested TBCs. Three coated blades from CSM and MTU were thermally cycled until first spallation of the top coat occurred at the trailing edge and at the leading edge. Every 100–200 cycles the blades were removed for visual inspection. All blades showed cracking 100–200 cycles prior to spallation. Figure 8 shows the results of the burner rig tests. The TBCs sprayed by CSM on turbine blades have a wide scatter in the number of cycles until first spallation. The service life of CSM TBCs is partly poor and partly very high at the leading edge. In comparison, the number of cycles for TBCs sprayed by MTU (APS with internal cooling) is less scattered and ranges from 1200 to 1800 cycles. The results shown in Fig. 8 indicate that the damage, while thermal cycling, always occurs at the trailing edge prior to being visible at the leading edge.

Furnace Cycled TBCs. The results of cyclic furnace thermal tests are shown in Fig. 9. TBCs show spallation after 240. . .530 furnace cycles with a maximum temperature of 1100°C and 35. . .57 furnace cycles with a maximum temperature of 1200°C.

Concluding Remarks

Since plasma-sprayed TBCs had been already introduced in commercial aeroengines on platforms of turbine vanes, the investigations in this paper have been focused on application of plasma-sprayed TBCs on airfoils. That is why real turbine blades were used for plasma spraying and the subsequent ther-

Downloaded 02 Jun 2010 to 171.66.16.122. Redistribution subject to ASME license or copyright; see http://www.asme.org/terms/Terms_Use.cfm

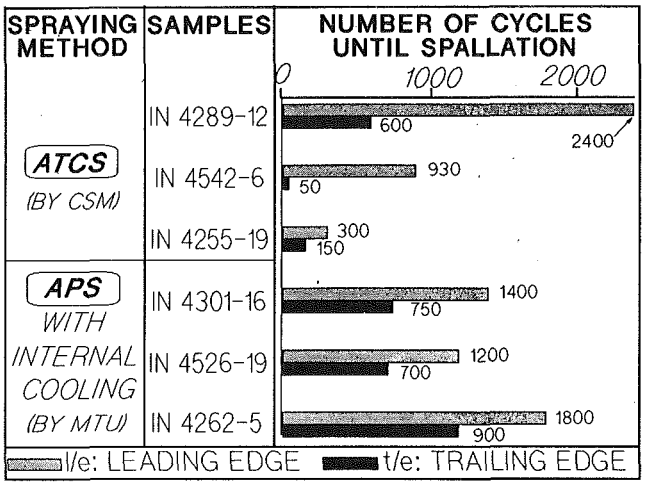


Fig. 8 Results of burner rig test

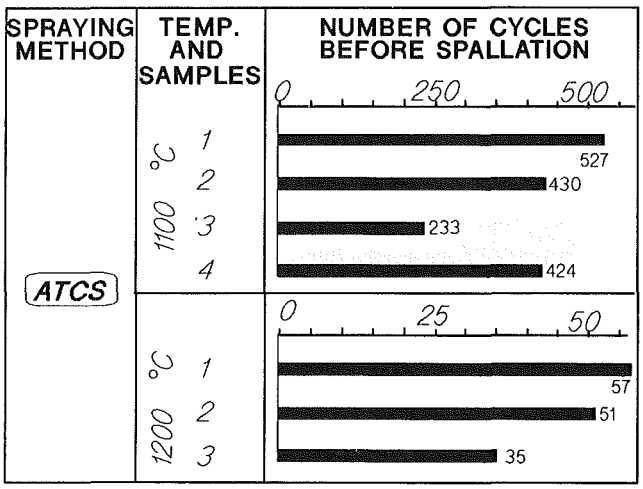


Fig. 9 Results of furnace thermal cycling tests

mal cycle tests. At the moment zirconia partially stabilized with 7–8 wt. % of yttria is the optimal material for TBC applications. The burner rig test conditions were very hard with a hot gas temperature up to 1480°C and a surface temperature up to 1150°C at the blade surface. MTU has sprayed TBCs with internal blade cooling. The blade temperatures between 35 and 70°C during plasma spraying reduced the residual stresses at the interface between the bond coat and the top coat. The control of the deposition temperature resulted in an increase of the number of thermal cycles at the trailing edge from 20 (for the blades deposited without internal cooling) up to 700–900 cycles (for the blades deposited in the controlled temperature conditions). The increase in the number of thermal cycles at the leading edge is even more spectacular and this number can reach 1200–1800.

The TBCs deposited with the use of ATCS technique can withstand up to 2400 cycles at the trailing edge and up to 600 cycles at the leading edge. However, the ATCS needs a careful analysis of the factors affecting the deposition temperature in a way that enables these parameters to be precisely controlled. Further process analysis would also be required to improve the homogeneity of the microcracking induced by ATCS. Particular attention has to be paid to understand the thermal stress pattern during thermal cycling of the TBCs.

The results of this paper show that improved cooling systems can increase the service life of plasma-sprayed TBCs. The present investigations seem to be the beginning of an improvement in TBCs and consequently, the first use of such TBCs on airfoils of turbine vanes appears to be conceivable. Normally vanes have cooling holes at the trailing edge so that the lower resistance against thermal fatigue can be avoided at the trailing edge.

Acknowledgments

The contributions of Dr. Bertamini, Mr. Scaccia, and Mr. Beber to the development of the ATCS technique and the help in carrying out this study are gratefully acknowledged.

References

Balting, U., Knotek, O., Elsing, R., and Cosack, T., 1990, "Comparison of Temperature Curve Calculations and Measurements in Coating Substrate Composites During Plasma Spraying," 3rd NTSC, Long Beach, CA, May 21–24, ASM International, in press.

Bertamini, L., Galvanetto, E., Manini, L., Marchese, M., and Pawlowski, L., 1991, unpublished data, Trento.

Ducos, M. P., 1989, "Atmosphere and Temperature Control Plasma Spraying Thick Coatings on Composite Resin Fibers," presented at the 12th Thermal Spraying Conference, London, United Kingdom, June 4–9, Paper No. 66.

Duvall, D. S., and Ruckle, D. L., 1982, "Ceramic Thermal Barrier Coatings for Turbine Engine Components," *27th International Gas Turbine Conference and Exhibit*, London, United Kingdom, Apr. 18–22, pp. 1–9.

Knotek, O., Balting, U., Cosack, T., and Pantucek, P., 1991, "Measurements and Mathematical Modelling of Heat Flow Into Substrates During APS of Coated Compounds as a Starting Point for Strain Calculation," *Proc. 2nd Plasma Technik Symposium*, Lucerne, Switzerland, Vol. 1, pp. 103–110.

Manning Meier, S., Gupta, D. K., and Sheffler, K. D., 1991, "Ceramic Thermal Barrier Coatings for Commercial Gas Turbine Engines," *J. Metals*, Mar., pp. 50–53.

Meetham, G. W., 1985, "Coating Requirements in Gas Turbine Engine," *J. Vac. Sci. Technol.*, Vol. A 3(6), Nov/Dec., pp. 2509–2515.

Pawlowski, L., 1981, "Temperature Distribution in Plasma Sprayed Coatings," *Thin Solid Films*, Vol. 81, pp. 79–88.

Pawlowski, L., Vardelle, M., and Fauchais, P., 1982, "A Model of the Temperature Distribution in an Alumina Coating During Plasma Spraying," *Thin Solid Films*, Vol. 94, pp. 307–319.

Sheffler, K. D., Graziani, R. A., and Sinko, G. C., 1982, "JT9D Thermal Barrier Coated Vanes," NASA CR-167964, Apr.

Sturlese, S., Dal Maschio, R., Bartuli, C., Zacchetti, N., and Berardo, M., 1991, "Effect of Deposition Temperature on Thermal Fatigue Resistance of Thermal Barrier Coatings," Materials Science Monographs, No. 67, *High Performance Ceramic Films and Coatings*, P. Vincenzini, ed., Elsevier, pp. 353–363.

Sumner, I. E., and Ruckle, D. L., 1980, "Development of Improved Durability Plasma-Sprayed Ceramic Coatings for Gas Turbine Engines," NASA TM-81512, E-451.

Downloaded 02 Jun 2010 to 171.66.16.122. Redistribution subject to ASME license or copyright; see http://www.asme.org/terms/Terms_Use.cfm